

# XXII RINEM

## Riunione Nazionale di Elettromagnetismo

September 3-6, 2018

Cagliari, Italy



## Proceedings



# XXII RINEM

**Cagliari, Italy**

**September 3-6, 2018**

## **Conference Chair**

Giorgio Montisci, *University of Cagliari*

## **Promoting Committee**

Graziano Cerri, *Marche Polytechnic University*

Giorgio Montisci, *University of Cagliari*

Stefano Selleri, *University of Parma*

Gino Sorbello, *University of Catania*

## **Organizing Committee**

Giovanni Andrea Casula, *University of Cagliari*

Alessandro Fanti, *University of Cagliari*

Giorgio Montisci, *University of Cagliari*

Alessandro Navarrini, *INAF-Cagliari Astronomical Observatory*

## **Conference Venue:**

**Faculty of Engineering**

**University of Cagliari**

Via Marengo, 2

09123 Cagliari

**ISBN: 978-88-907599-2-5**

## Sponsors



**CST**



*joins*



**ROHDE & SCHWARZ**



**nurjanatech**  
THINKING HIGHER



# Program Overview

	Monday Sept., 3	Tuesday Sept., 4	Wednesday Sept., 5	Thursday Sept., 6	
8:30-8:40	REGISTRATION (AULA MAGNA)	REGISTRATION (AULA MAGNA)	REGISTRATION (AULA MAGNA)		
8:45-9:00					
9:00-9:15					
9:15-9:30		Session 5 (AULA ALFA) EMF Propagation & Remote Sensing	Session 6 (AULA MAGNA) Measurements & Diagnostics	URSI SESSION (AULA MAGNA)	Session 9 (AULA ALFA) Optics I
9:30-9:45					Session 10 (AULA MAGNA) Inverse Problems
9:45-10:00					
10:00-10:15					
10:15-10:30					
10:30-10:45					
10:45-11:00					
11:00-11:15			Coffee Break (AULA BI)	Coffee Break (AULA BI)	Coffee Break (AULA BI)
11:15-11:30					
11:30-11:45					
11:45-12:00			INAF SESSION (AULA MAGNA)	Session 7 (AULA ALFA) RFID	Session 11 (AULA ALFA) Optics II
12:00-12:15				Session 8 (AULA MAGNA) Microwaves	Session 12 (AULA MAGNA) Antennas I
12:15-12:30					
12:30-12:45				Closing and awards (BarZola)	
12:45-13:00					
13:00-13:15	REGISTRATION (AULA MAGNA)				
13:15-13:30		Lunch (AULA BI)	Lunch (AULA BI)	Lunch (AULA BI)	
13:30-14:00					
14:00-14:15					
14:15-14:30					
14:30-14:45					
14:45-15:00	Open and salutations (AULA MAGNA)	PLENARY SESSION (AULA MAGNA)	Poster (AULA BI)	(ST (AULA MAGNA)	
15:00-15:15					
15:15-15:30	Session 1 (AULA ALFA) Antennas I				
15:30-15:45	Session 2 (AULA MAGNA) Computational Electromagnetics				
15:45-16:00					
16:00-16:15					
16:15-16:30					
16:30-16:45					
16:45-17:00					
17:00-17:15					
17:15-17:30					
17:30-17:45	Session 3 (AULA ALFA) Bioelectromagnetics & Biomedical applications				
17:45-18:00	Session 4 (AULA MAGNA) RADAR				
18:00-18:15					
18:15-18:30					
18:30-18:45					
18:45-19:00					
19:00-19:30					
19:30-20:00					
20:00-20:30					
20:30-21:00					
21:00-21:30					
21:30-22:00		Dinner**	Social Dinner*** Awards (CNT, Sarsileo, Lateral)		

## Invited Speakers

**Tuesday, September 4th, 2018, 14:00-15:30**

**Chairperson: Giuseppe Mazzarella**

**Prof. Yang Hao**

School of Electronic Engineering and Computer Science  
Queen Mary, University of London

### ***"Nanoelectromagnetics at Microwave Frequencies and Beyond"***

**Abstract:** Classic electromagnetics has witnessed novel developments in recent years due to the emergence of novel materials and concepts such as metamaterials and transformation optics. The theory of near-field electromagnetism has enabled us to explore structures in sub-wavelength scales and opens up new possibilities of imaging, sensing and characterization of materials. In this talk, I will review our recent research activities related to nanoelectromagnetics applied to microwave frequencies and beyond. In particular, how novel electromagnetic modelling tools have been developed and applied for the development of device innovation.

**Dr. Francesco Bonaccorso**

Graphene Labs  
IIT Central Research Lab, Genova

### ***"Solution processed 2D-materials for printed electronics"***

**Abstract:** Graphene and other 2D crystals are emerging as promising materials to improve the performance of existing devices or enable new ones. A key requirement for flexible and printed electronics is the development of industrial-scale, reliable, inexpensive production processes, while providing a balance between ease of fabrication and final material quality. Solution-processing is a simple and cost-effective pathway to fabricate various 2D crystal-based (opto)electronic devices, presenting huge integration flexibility compared to conventional methods. Here, I will present an overview of graphene and other 2D crystals for flexible and printed (opto)electronic applications, starting from solution processing of the raw bulk materials, the fabrication of large area electrodes and their integration in the final devices.

**Prof. Alexander I. Nosich**

Institute of Radio-Physics and Electronics

National Academy of Sciences

Kharkiv, Ukraine

***"Periodicity matters: ultrahigh-Q resonances on the grating modes of large arrays of sub-wavelength scatterers"***

**Abstract:** This talk reviews the nature and history of the discovery of extremely high-quality natural modes existing on periodic arrays of many subwavelength scatterers. Thanks to these modes, infinite and large arrays can be viewed as specific periodically structured open resonators. These grating or lattice modes (GMs), like any other natural modes, give rise to the associated resonances in electromagnetic-wave scattering and absorption. Their complex wavelengths are always located very close to (but not exactly at) the well-known Rayleigh anomalies (RAs), determined only by the period and the phase shift between adjacent elements. This circumstance has long been a reason for their misinterpretation as RAs, especially in the measurements and simulations using low-resolution methods. On the frequency scans of the reflectance or transmittance, GM resonances usually develop as asymmetric Fano-shape double extrema. In the microwave range, GM resonances can spoil the performance of large phased-array antennas assembled on flat surfaces. In the optical range, GM resonances are found behind exotic phenomena such as "anomalous" transmission, reflection and absorption, giant Faraday, Kerr and Kerker effects, etc., and also behind the principle of operation of Distributed Feedback Lasers. If a grating is made of subwavelength-size noble metal elements, then collective GMs exist together with better-known localized surface-plasmon modes on individual particles. Their interplay can result in the effect of induced optical transparency. Thanks to high tunability and considerably higher Q-factors, the GM resonances can potentially replace the plasmon-mode resonances in the design of nanosensors, nanoantennas, and solar-cell nanoabsorbers.

### INAF SESSION

**Chairperson: Alessandro Navarrini**

**Prof. Paul Goldsmith**

Jet Propulsion Laboratory, California Institute of Technology  
Pasadena CA 91109, USA

#### ***"The Renaissance of Submillimeter Astronomical Spectroscopy"***

**Abstract:** High resolution spectroscopy is recognized as a powerful astrophysical tool. For understanding many critical aspects of the formation and evolution of interstellar clouds and how new stars are formed within them, the most important spectral lines are at submillimeter wavelengths, corresponding to the terahertz frequency range between 300 and 6000 GHz, (0.3 to 6 THz). In many astronomical situations, line widths resulting from Doppler shifts arising from gas motions can be significantly less than 1 km/s. Thus, extracting the full information available about the kinematics of gas in the source being observed requires resolution  $R = f / \Delta f \geq 3 \times 10^5$ . This requires a heterodyne system, which can readily achieve the required frequency resolution. Exploiting the wealth of ionic, atomic, and molecular transitions has been hampered by the nearly total absorption by the Earth's atmosphere and the relatively low sensitivity of available detectors. The situation has improved dramatically over the last decade. The development of the Heterodyne Instrument for Far Infrared (HIFI), on board the Herschel Space Observatory launched in 2009 encouraged a continuing technological transformation that includes vastly improved mixers, local oscillators, optics, and the development of focal plane arrays. The data from Herschel have inspired improved laboratory measurements generating spectral line catalogs, quantum calculations, and measurements of collision rates and chemical reaction rates for key astrophysical species. New observing platforms including the SOFIA airborne observatory and long-duration balloons flying at 40 km altitude have resulted in a stream of data of ever-increasing frequency coverage and range and extent of sources observed. Anticipated ultra-long-duration balloons and the possibility of space missions ranging from small satellites to a large-aperture major (Flagship) mission are generating great excitement about possible future observations. In this talk I will review the importance of high resolution spectroscopy and will briefly highlight recent astronomical results, including high-sensitivity observation of water in collapsing cloud cores and the solar system and velocity-resolved large-area studies of Giant Molecular Clouds and nearby galaxies in the 158 micron fine structure transition ([CII]) of C+. I will then turn to the technological developments that have made this dramatic progress possible, including detectors, local oscillators, and spectrometers. I will conclude by talking about some possibilities for the future.

**Dr. Federica Govoni**

INAF – Osservatorio Astronomico di Cagliari, Italy

***"Scientific involvement of the Italian radio astronomical community in national and international facilities"***

**Abstract:** The attention of the Italian radio astronomy is currently distributed across various world-class facilities which includes both single-dish radio telescopes, such as the Sardinia Radio Telescope, and radio interferometers, such as the Square Kilometre Array, its precursors (e.g. MeerKAT, ASKAP, MWA), and its pathfinders (e.g. LOFAR, APERTIF, GMRT). I will compare the strengths of single-dish radio telescopes to radio interferometers and I will show the research which is performed by the Italian community using these instruments.

**Dr. Tonino Pisanu**

INAF – Osservatorio Astronomico di Cagliari, Italy

***"The Front-Ends of the Sardinia Radio Telescope"***

**Abstract:** The Sardinia Radio Telescope (SRT), a challenging scientific project of the Italian National Institute for Astrophysics (INAF), is a new general purpose fully steerable 64 m diameter radio telescope designed to operate with high efficiency across the 0.3-116 GHz frequency range. The SRT is located 35 km North of Cagliari, Sardinia, Italy, at about 600 m above the sea level. The telescope, equipped with an active surface, three first-light receivers and various backends, successfully completed a six-month early science program in 2016. Following the refurbishment of its active surface in 2017, the telescope is currently being recommissioned for its technical and scientific capabilities with the goal of opening it to the international community by the end of 2018. I will describe the SRT first-light instrumentation, in particular the three radioastronomy receivers, that were all developed by INAF: a double frequency L-P band (305-410 MHz, 1.3-1.8 GHz) coaxial receiver for the primary focus, a K-band (18-26.5 GHz) 7-beam multibeam receiver for the Gregorian focus and a single feed high C-band (5.7-7.7 GHz) receiver for the Beam Waveguide focus. Furthermore, I will describe the receivers planned to be built and installed on SRT during the next few years.

### URSI SESSION

**Chairperson: Stefano Selleri**

**Mauro Messerotti**

INAF-Astronomical Observatory of Trieste, Loc. Basovizza 302, 34149 Trieste, Italy

#### **“Solar Radio Interferences on Radio Systems: A Direct Space Weather Effect”**

**Abstract:** The Sun is a source of broadband radio noise, which can reach quite high levels at different phases of the solar activity cycle. In particular, very intense solar radio bursts can significantly affect the quality of radio communications, e.g. in HF and UHF (mobile phones, radars), up to the interruption of services like satellite geolocation via GNSS in L-band. The Trieste Solar Radio System (TSRS) has played a key role in the detection of one of the first GNSS solar RFI published in literature. In this work, we briefly review the phenomenological scenario by focussing on the observational requirements for GNSS, which operate in the Right-Hand Circular Polarisation mode, and point out the need of a network of dedicated multichannel solar radio polarimeters for providing alerts and warning to enhance the quality of GNSS services and their resilience with respect to solar RFIs, a direct Space Weather effect on technological systems.

**Prof. Alain Sibille**

LTCI, Telecom ParisTech  
46 rue Barrault 75013, Paris, France

#### **“Statistical methods for joint antenna-radio channel modelling”**

**Abstract:** The description of the electromagnetic behavior of antennas needs a large amount of data to be complete, since it requires complex numbers for the radiated far field in all possible directions and polarizations, for all frequencies of interest and all antenna elements in case of arrays or multiport antennas, plus the full impedance matrix. In addition, since most of the time the radio channel linking the transmitting and receiving antennas in a wireless communication is not in free space, many propagation effects are involved and result in the particularities of the received signals. Finally, while it is often designed and measured in nearly ideal conditions (e.g. anechoic chamber) an antenna is rarely used in emptiness and its close environment does impact its performance, sometimes dramatically. While strong close disturbers can be taken into account at the design phase (such as a casing or a human head), variations in the effective impact of such disturbers can take place, which to

some extent can unpredictably affect the antenna characteristics. Deterministic methods can hardly take into account all the variabilities that occur in real life and would be much too expensive to implement and to use. The natural approach, widely practiced in other domains, is to resort to statistical descriptions, based on metamodels able to represent these variabilities with a limited number of parameters while achieving an adequate trade-off between accuracy and simplicity. The presentation will address these issues for joint antenna-channel modelling, giving some examples about the development and use of such methods.

**Prof. Ludger Klinkenbusch**

Technische Fakultät der Christian-Albrechts-Universität zu Kiel  
Kiel University

***"Scattering and Diffraction of Complex-Source Beams by Canonical Objects"***

**Abstract:** The presentation reviews recent advances in the application of complex-source beams (CSB) as incident fields in the context of scattering and diffraction by canonical objects like wedges, cones and sector-like structures. A CSB can be achieved by simply replacing the source coordinates in the Green's function by suitably chosen complex numbers. Nearby the axis it then represents half of a Gaussian beam which – except of the waist – exactly satisfies the Maxwell or Helmholtz equations. The main advantages of using CSBs as compared to the commonly applied illuminating plane waves are a dramatically improved convergence of the resulting series expansions of the scattered far fields and the opportunity to illuminate just the desired part of the canonical object, for example the tip of the cone. To achieve results comparable to the case of an incident plane wave a uniform CSB will be employed representing a full Gaussian beam. The uniform CSB will be located such that its waist where the field can be interpreted as a local plane wave interacts with the structure of interest, for example the tip. The outcomes can be used to extend the application of asymptotic methods like the Geometrical Theory of Diffraction (GTD) or the Uniform Theory of Diffraction (UTD). More generally, (uniform) CSBs can also be used as wave propagators in different applications where localized or beam-like fields are more suitable than omnidirectionally radiated fields or full plane waves.

**Prof. Gabriele Gradoni**

School of Mathematical Sciences, and George Green Institute for  
Electromagnetics Research University of Nottingham  
University Park NG7 2RD  
United Kingdom

***"Wave Chaos for Electromagnetic Environment Modelling and Control"***

**Abstract:** The propagation of waves through real-life electromagnetic environments, e.g., structures, channels and media, involves multiple components and space-time scales. In particular, the modelling of high frequency fields poses computational challenges when the environment is large and irregular. Recently, it has been shown that wave interference driven by multiple reflections and scattering ignites collective phenomena whose physics is beyond the obvious, e.g., wave localisation, diffusion, and rogue states. This opens up new exciting modelling avenues to understand and design complex electromagnetic environments. Collective phenomena are universal in the sense they depend on system generic symmetries and can be predicted by chaos theory with a few global parameters. Based on this phenomenology, statistical methods have been successfully used to devise simulation tools that characterise the electromagnetic energy flow through large structures with a reasonable computational effort. A specific model, the random coupling model, which describes the high-frequency excitation of irregular environments, is derived and applied to cavity problems of practical interest. The derivation is outlined following the wave chaos theory paradigm, which brings together semiclassical analysis and random matrix theory. In a linear eigenvalue problem, semiclassics is used to replace exact eigenfunctions with putative modes made of a superposition of random plane waves, while random matrix theory is used to replace the exact spectrum of resonances with universal distributions of eigenvalues. The two prescriptions are motivated by field mixing, ray instability, and high modal overlapping: collective wave phenomena of systems whose underlying classical dynamics is chaotic. A few advanced applications are discussed in the context of wave control of energy diffusion and focusing in dynamic confined environments. Results are relevant in wireless channels in telecommunications, wavefront shaping in imaging and radars, reverberation chambers in electromagnetic compatibility, and microwave applicators in material processing engineering.

# **Conference Sessions**

## Session 1: Antennas I

**Chairperson: Giovanni Andrea Casula**

### **ANGLE AND POLARIZATION TUNING OF THE SECOND HARMONIC RADIATION PATTERN IN DIELECTRIC NANOANTENNAS**

Carletti L.<sup>1</sup>, D. Rocco<sup>1</sup>

<sup>1</sup>Department of Information Engineering, Università degli Studi di Brescia

p. .... 1

### **OPTIMAL SYNTHESIS OF SHAPED BEAMS FOR GENERIC FIXED GEOMETRY ARRAYS**

G. M. Battaglia<sup>1</sup>, G. G. Bellizzi<sup>1</sup>, T. Isernia, A. F. Morabito<sup>(1,2)</sup>

<sup>1</sup>DIIES, Università Mediterranea di Reggio Calabria

<sup>2</sup>CNIT, Consorzio Nazionale Interuniversitario per le Telecomunicazioni

p. .... 5

### **OPTIMAL SYNTHESIS OF SUM AND DIFFERENCE PATTERS OF CENTRO-SYMMETRIC ARRAYS**

G. Bellizzi<sup>(1,2,3)</sup>, O.M. Bucci<sup>(1,2,3)</sup>

<sup>1</sup>DIETI Università di Napoli Federico II

<sup>2</sup>IREA-CNR

<sup>3</sup>CNIT

p. .... 9

### **AUTOMATIC DESIGN OF A RHCP LINEAR SLOTTED ARRAY FOR LAST-MILE APPLICATIONS AT MICROWAVES**

S. C. Pavone<sup>1</sup>, M. Casaletti<sup>2</sup>, M. Albani<sup>1</sup>

<sup>1</sup>Department of Information Engineering and Mathematics (DIISM), University of Siena,

<sup>2</sup>Laboratory of Electronics and Electromagnetics (L2E), University Pierre and Marie Curie, Paris

p. .... 13

### **A WIDEBAND PHASED ARRAY**

C. Novi<sup>1</sup>, M. Righini<sup>2</sup>

<sup>1</sup>Antennas and EMC Development Unit Research and Development Department, Rheinmetall Italia S.p.A., Rome

<sup>2</sup>Department of Information Engineering, University of Florence

p. .... 17

### **DESIGN OF CRYOGENIC PHASED ARRAY FEED FOR 4-8 GHZ**

A. Navarrini<sup>1</sup>, et al.

<sup>1</sup>INAF-Osservatorio Astronomico di Cagliari, via della Scienza 5, Selargius, Italy

p. .... 21

### **DEVELOPMENT OF HIGH-FREQUENCY RADOMES FOR POLAR GROUND STATIONS**

A. Martellosio<sup>1</sup>, M. Pasian<sup>1</sup>, F. Concaro<sup>2</sup>, L. Perregrini<sup>1</sup>

<sup>1</sup>Department of Electrical, Computer and Biomedical Engineering, University of Pavia

<sup>2</sup>Department of Ground Systems Engineering, European Space Agency (ESA)

p. .... 25

## Session 2: Computational Electromagnetics

**Chairperson: Gino Sorbello**

### **ANALYSIS OF INHOMOGENEOUS WAVEGUIDE COMPONENTS BY THE BI-RME METHOD**

S. Battistutta<sup>1</sup>, M. Bozzi<sup>1</sup>, M. Bressan<sup>1</sup>, L. Perregrini<sup>1</sup>

<sup>1</sup>Department of Electrical, Computer and Biomedical Engineering, University of Pavia

p. .... 29

### **CLOSED-TO-OPEN CROSS-SECTION CONVERSION OF MM-WAVE DEVICES BY MEANS OF THE MODE MATCHING THEORY**

G. Torrisi<sup>1</sup>, G. Castorina<sup>2</sup>

<sup>1</sup>Istituto Nazionale di Fisica Nucleare -Laboratori Nazionali del Sud, Catania

<sup>2</sup>Università degli Studi di Roma La Sapienza, Dip. SBAI

p. .... 33

### **AN OPTIMISED APPROACH TO NUFFT**

A. Capozzoli<sup>1</sup>, C. Curcio<sup>1</sup>, A. Liseno<sup>1</sup>

<sup>1</sup>Dept. of Information Technology and Electrical Engineering, University of Naples "Federico II"

p. .... 37

### **A GENERAL ANALYTICAL METHOD, BASED ON SLATER'S PERTURBATION THEOREM, FOR MESH GENERATION IN FEM SIMULATION OF RF CAVITIES**

G. S. Mauro<sup>(1,2)</sup>, L. Celona<sup>3</sup>

<sup>1</sup>Istituto Nazionale di Fisica Nucleare - Laboratori Nazionali di Legnaro

<sup>2</sup>Università degli Studi "Mediterranea" di Reggio Calabria

<sup>3</sup>Istituto Nazionale di Fisica Nucleare - Laboratori Nazionali del Sud, Catania

p. .... 41

### **MESHLESS METHODS APPLIED TO ELECTROMAGNETIC EIGENPROBLEMS**

V. Lombardi<sup>1</sup>, M. Bozzi<sup>1</sup>, L. Perregrini<sup>1</sup>

<sup>1</sup>Department of Electrical, Computer and Biomedical Engineering, University of Pavia

p. .... 45

### **AN ANALYTICAL APPROACH FOR THE EFFICIENT EVALUATION OF A CLASS OF IMPROPER INTEGRALS INVOLVING OSCILLATING AND SLOWLY DECAYING FUNCTIONS**

M. Lucido<sup>1</sup>, G. Panariello<sup>1</sup>, C. Santomassimo<sup>1</sup>, F. Schettino<sup>1</sup>

<sup>1</sup>Department of Electrical and Information Engineering, University of Cassino and Southern Lazio

p. .... 49

### **APERTURE TRUNCATION AND EXCITATION ERROR ANALYSIS FOR A SPACE DEBRIS RADAR ANTENNA ARRAY**

G. Siciliano<sup>1</sup>

<sup>1</sup>Dept. of Electrical, Electronic and Biomedical Engineering, University of Pavia

p. .... 53

## Session 3: Bioelectromagnetism & Biomedical applications

**Chairperson: Rosa Scapaticci**

### **EXPERIMENTAL STUDY UP TO 50 GHZ ON TISSUE-MIMICKING MATERIALS FOR BREAST PHANTOMS**

S. Di Meo<sup>1</sup>, L. Pasotti<sup>(1,2)</sup>, G. Matrone<sup>(1,2)</sup>

<sup>1</sup>Dept. of Electrical, Computer and Biomedical Engineering University of Pavia

<sup>2</sup>Centre for Health Technologies, University of Pavia, Pavia

p. .... 57

### **QUANTITATIVE MICROWAVE BRAIN STROKE IMAGING: INVERSION PROCEDURE AND PRELIMINARY EXPERIMENTAL RESULTS**

I. Bisio<sup>1</sup>, C. Estatico<sup>2</sup>, A. Fedeli<sup>1</sup>, F. Lavagetto<sup>1</sup>, G. L. Mancardi<sup>3</sup>, M. Pastorino<sup>1</sup>, A. Randazzo<sup>1</sup>, A. Sciarrone<sup>1</sup>, E. Tavanti<sup>1</sup>

<sup>1</sup>Department of Electrical, Electronic, Telecommunications Engineering, and Naval Architecture, University of Genoa

<sup>2</sup>Department of Mathematics, University of Genoa

<sup>3</sup>Department of Neuroscience, Rehabilitation, Ophthalmology, Genetics, Maternal and Child Health, University of Genoa

p. .... 61

### **SYNTHESIS OF TARGET-CONFORMAL FIELD INTENSITY PATTERNS FOR HEAD & NECK HYPERTHERMIA TREATMENT**

G. G. Bellizzi<sup>(1,2)</sup>, L. Crocco<sup>2</sup>

<sup>1</sup>DIIES, Università Mediterranea di Reggio Calabria

<sup>2</sup>CNR-IREA, Napoli

p. .... 65

### **NEW IN-VIVO MAPPING OF HUMAN TISSUES VIA PHASELESS INVERSE SCATTERING AND MRI/CT SEGMENTATION**

M. T. Bevacqua<sup>1</sup>, G. G. Bellizzi<sup>(1,2)</sup>, L. Crocco<sup>2</sup>, T. Isernia<sup>(1,2)</sup>

<sup>1</sup>DIIES, Università Mediterranea di Reggio Calabria

<sup>2</sup>CNR-IREA, Napoli

p. .... 69

### **AN EXPERIMENTAL ASSESSMENT OF THERMAL ABLATION MONITORING VIA MICROWAVE TOMOGRAPHY**

R. Scapaticci<sup>1</sup>, M. Cavagnaro<sup>2</sup>, V. Lopresto<sup>3</sup>, R. Pinto<sup>3</sup>, L. Crocco<sup>1</sup>

<sup>1</sup>IREA, National Council of Research of Italy, Naples

<sup>2</sup>DIET, Sapienza University of Rome, Rome

<sup>3</sup>ENEA, Division of Health Protection Technologies, Casaccia Research Center, Rome

p. .... 73

### **MAGNETIC BIOMATERIALS FOR BONE TUMOR HYPERTHERMIA: A NUMERICAL STUDY**

A. Fanti<sup>1</sup>, M.B Lodi<sup>1</sup>, G. Vacca<sup>1</sup>, G. Mazzearella<sup>1</sup>

<sup>1</sup>Department of Electrical and Electronic Engineering, University of Cagliari, Cagliari

p. .... 77

### **NUMERICAL RESULTS ON A MILLIMETER-WAVE CONFORMAL ARRAY FOR BREAST CANCER DETECTION**

S. Di Meo<sup>1</sup>, G. Matrone<sup>1</sup>

<sup>1</sup>Dept. of Electrical, Computer and Biomedical Engineering University of Pavia

p. .... 81

## Session 4: RADAR

**Chairperson: Sandra Costanzo**

### **A MICROWAVE RADAR SYSTEM FOR INDOOR POSITIONING TRACKING OF ELDERLY AND DEPENDENT PEOPLE**

G. Paolini<sup>1</sup>

<sup>1</sup>DEI – University of Bologna

p. .... 85

### **INTEGRATED RADAR TILE FOR X/KA BAND SAR APPLICATIONS**

E. Arnieri<sup>1</sup>, L. Boccia<sup>1</sup>, G. Amendola<sup>1</sup>, C. Mao<sup>2</sup>, S. Gao<sup>2</sup>, T. Rommel<sup>3</sup>, S. Glisic<sup>6</sup>, P. Penkala<sup>4</sup>, M. Krstic<sup>5</sup>, A. Ho<sup>7</sup>, U. Yodprasit<sup>6</sup>, O. Schrape<sup>5</sup>, M. Younis<sup>3</sup>

<sup>1</sup>DIMES, University of Calabria

<sup>2</sup>School of Engineering and Digital Arts, University of Kent, Canterbury

<sup>3</sup>Microwaves and Radar Institute, German Aerospace Center (DLR)

<sup>4</sup>Evatronix S.A. Bielsko-Biała, Poland.

<sup>5</sup>IHP, 15236 Frankfurt (Oder)

<sup>6</sup>Silicon Radar GmbH, 15236 Frankfurt (Oder)

<sup>7</sup>Innovative Solutions In Space BV, 629 JD, Delft

p. .... 89

### **ANALYTICAL MODEL FOR THE BISTATIC RCS OF SHIPS BASED ON THE GEOMETRICAL OPTICS APPROXIMATION**

A. Di Simone<sup>1</sup>, W. Fuscaldo<sup>2</sup>, L. M. Millefiori<sup>3</sup>, G. Di Martino<sup>1</sup>, A. Iodice<sup>1</sup>, G. Ruello<sup>1</sup>, D. Riccio<sup>1</sup>, P. Braca<sup>3</sup>, P. Willett<sup>4</sup>

<sup>1</sup>Dept. of Information Technology and Electrical Engineering, University of Naples "Federico II"

<sup>2</sup>Dept of Information Engineering, Electronics and Telecommunications, Sapienza Univ. Rome

<sup>3</sup>NATO-STO Centre for Maritime Research and Experimentation, La Spezia

<sup>4</sup>Department of Electrical and Computer Engineering, University of Connecticut

p. .... 93

### **THE DELAY AND SUM ALGORITHMS FOR THROUGH THE WALL RADAR IMAGING SYSTEMS**

S. Pisa<sup>1</sup>, E. Piuze<sup>1</sup>, E. Pittella<sup>1</sup>, G. Sacco<sup>1</sup>, P. d'Atanasio<sup>2</sup>, A. Zambotti<sup>2</sup>

<sup>1</sup>Dept. of Information Engineering, Electronics and Telecommunications, Sapienza Univ. Rome

<sup>2</sup>Italian National Agency for New Technologies, Energy and Sustainable Economic Development, Casaccia Research Centre, Rome

p. .... 97

### **SOFTWARE-DEFINED RADAR FOR VITAL SIGN MONITORING**

A. Raffo<sup>1</sup>, V. Cioffi<sup>1</sup>, S. Costanzo<sup>1</sup>

<sup>1</sup>Dept. of Informatics, Modeling, Electronics and System Engineering, University of Calabria

p. .... 101

### **DUAL-RECEIVER FMCW RADAR FOR SNOWPACK MONITORING: SYSTEM VALIDATION AND PRELIMINARY RESULTS**

P. F. Espin-Lopez<sup>1</sup>, M. Pasian<sup>1</sup>

<sup>1</sup>Department of Electrical, Computer and Biomedical Engineering, University of Pavia

p. .... 105

### **UPGRADING THE P-BAND RECEIVER OF THE SARDINIA RADIO TELESCOPE FOR SPACE DEBRIS MONITORING**

L. Schirru<sup>(1,2)</sup>, G. Muntoni<sup>1</sup>, G. Montisci<sup>(1,2)</sup>

<sup>1</sup>Department of Electrical and Electronic Engineering, University of Cagliari

<sup>2</sup>National Institute for Astrophysics, Cagliari Astronomical Observatory, Selargius

p. .... 109

## Session 5: EMF Propagation & Remote Sensing

**Chairperson: Lorenzo Luini**

### **TWO-SCALE MODEL FOR THE EVALUATION OF SEA-SURFACE SCATTERING IN CIRCULAR POLARIZATION**

G. Di Martino<sup>1</sup>, A. Di Simone<sup>1</sup>, A. Iodice<sup>1</sup>, D. Riccio<sup>1</sup>, G. Ruello<sup>1</sup>

<sup>1</sup>Department of Electrical Engineering and Information Technology, University of Napoli Federico II

p. .... 113

### **FLOOD MAPPING USING SENTINEL-1 SAR DETECTED IMAGES**

D. Amitrano<sup>1</sup>, G. Di Martino<sup>1</sup>, A. Iodice<sup>1</sup>, D. Riccio<sup>1</sup>, G. Ruello<sup>1</sup>

<sup>1</sup>Department of Electrical Engineering and Information Technology, University of Napoli Federico II

p. .... 117

### **A NEW METHOD TO ENHANCE SPATIAL RESOLUTION OF MICROWAVE EARTH OBSERVATION MEASUREMENTS**

M. Alparone<sup>(1,2)</sup>, F. Nunziata<sup>1</sup>

<sup>1</sup>Dipartimento di Ingegneria, Università degli Studi di Napoli Parthenope

<sup>2</sup>Centro Direzionale - Isola C4, Napoli

p. .... 121

### **STUDY ON MM-WAVE MULTI-USER BEAMFORMING BASED ON MEASUREMENTS AND RAY TRACING SIMULATIONS**

M. Zoli<sup>1</sup>, F. Fuschini<sup>1</sup>

<sup>1</sup>Department of Electrical, Electronic and Information Engineering (DEI), University of Bologna

p. .... 125

### **PROGRESS ON THE REALIZATION OF A LOR® BASED COMMUNICATION SYSTEM FOR ATMOSPHERIC MONITORING PROBES**

S. Bertoldo<sup>(1,2)</sup>, M. Paredes<sup>(1,3)</sup>, L. Carosso<sup>(1,2)</sup>, C. Lucianaz<sup>(1,2)</sup>, M. Allegretti<sup>(1,2,3)</sup>, F. Canavero<sup>1</sup>, G. Perona<sup>2</sup>

<sup>1</sup>Politecnico di Torino, DET

<sup>2</sup>Consorzio Interuniversitario Nazionale per la Fisica delle Atmosfere e delle Idrosfere, Politecnico di Torino

<sup>3</sup>Envisens Technologies s.r.l., Torino

p. .... 129

### **EM WAVE PROPAGATION EXPERIMENT AT E BAND AND D BAND FOR 5G MOBILE NETWORKS**

L. Luini<sup>1</sup>, G. Roveda<sup>2</sup>, M. Zaffaroni<sup>2</sup>, M. Costa<sup>2</sup>, C. Riva<sup>1</sup>

<sup>1</sup>DEIB, Politecnico di Milano

<sup>2</sup>Huawei Microwave Centre, Milano

p. .... 133

### **RAY TRACING PATH LOSS PREDICTION IN URBAN ENVIRONMENT @ 26, 28 AND 38 GHZ**

F. Mani<sup>1</sup>, E. M. Vitucci<sup>1</sup>, M. Barbiroli<sup>1</sup>, F. Fuschini<sup>1</sup>, V. Degli Esposti<sup>1</sup>

<sup>1</sup>Dept. of Electrical, Electronic and Information Eng. "G. Marconi", University of Bologna

p. .... 137

## Session 6: Measurements & Diagnostics

**Chairperson: Graziano Cerri**

### **PERFORMANCES ESTIMATION AND MEASUREMENT OF A SOURCE STIRRED REVERBERATION CHAMBER**

G. Cerri<sup>1</sup>, A. De Leo<sup>1</sup>, V. Mariani Primiani<sup>1</sup>, P. Russo<sup>1</sup>

<sup>1</sup>Dipartimento di Ingegneria dell'Informazione, Università Politecnica delle Marche

p. .... 141

### **AN ITERATIVE TECHNIQUE TO CORRECT PROBE POSITIONING ERROR AFFECTED PLANAR WIDE-MESH SCANNING NF DATA**

F. D'Agostino<sup>1</sup>, F. Ferrara<sup>1</sup>, C. Gennarelli<sup>1</sup>, R. Guerriero<sup>1</sup>, M. Migliozzi<sup>1</sup>

<sup>1</sup>D.I.In., Università di Salerno, Fisciano

p. .... 145

### **FAST DIAGNOSTICS OF LARGE CONFORMAL ARRAY BY MATRIX METHOD**

G. Di Massa<sup>1</sup>, S. Costanzo<sup>1</sup>

<sup>1</sup>DIMES-University of Calabria, Rende

p. .... 149

### **NEAR-FIELD VALIDATION OF THE ELECTROMAGNETIC MODELS FOR LOFAR LBA-OUTER ARRAY**

P. Di Ninni<sup>1</sup>, P. Bolli<sup>1</sup>, F. Paonessa<sup>2</sup>, G. Pupillo<sup>3</sup>, G. Virone<sup>2</sup>, S. J. Wijnholds<sup>4</sup>

<sup>1</sup>INAF-Osservatorio Astrofisico di Arcetri, Firenze

<sup>2</sup>CNR-Istituto di Elettronica ed Ingegneria dell'Informazione e delle Telecomunicazioni, Torino

<sup>3</sup>INAF-Istituto di Radio Astronomia, Medicina

<sup>4</sup>Netherlands Institute for Radio Astronomy, Dwingeloo, The Netherlands

p. .... 153

### **FIRST TESTS OF A TORALDO PUPIL OPTICAL MODULE FOR THE 32M MEDICINA ANTENNA**

L. Olmi<sup>1</sup>, P. Bolli<sup>1</sup>, L. Carbonaro<sup>1</sup>, L. Cresci<sup>1</sup>, A. Maccaferri<sup>2</sup>, G. Maccaferri<sup>2</sup>, P. Marongiu<sup>3</sup>, D. Mugnai<sup>4</sup>, R. Nesti<sup>1</sup>, A. Orfei<sup>2</sup>, D. Panella<sup>1</sup>, S. Righini<sup>2</sup>

<sup>1</sup>INAF – OAA, Firenze

<sup>2</sup>INAF – IRA, Villafontana

<sup>3</sup>INAF – OAC, Selargius

<sup>4</sup>CNR – IFAC, Firenze

p. .... 157

### **A VALID ANGLE CRITERION IN NEAR FIELD MEASUREMENTS BASED ON ANALYTICAL SVD**

M.A. Maisto<sup>1</sup>

<sup>1</sup>Dipartimento di Ingegneria, Università della Campania L. Vanvitelli, Aversa

p. .... 161

### **MEASUREMENTS-BY-DESIGN: A NOVEL APPROACH FOR FAST AND RELIABLE ANTENNA CERTIFICATION**

M. Salucci<sup>1</sup>

<sup>1</sup>ELEDIA Research Center (ELEDIA@UniTN - University of Trento), Trento

p. .... 165

## Session 7: RFID

**Chairperson: Luca Catarinucci**

### **AN EPIDERMAL CONFIGURABLE ANTENNA SYSTEM FOR THE MONITORING OF BIOPHYSICAL PARAMETERS**

C. Miozzi<sup>1</sup>, G. Marrocco<sup>1</sup>

<sup>1</sup>University of Roma "Tor Vergata", Roma

p. .... 169

### **UHF RFID 3-D LOCALIZATION IN RETAIL SHOP SCENARIOS**

A. Motroni<sup>1</sup>, P. Nepa<sup>1</sup>

<sup>1</sup>Dipartimento di Ingegneria dell'Informazione, University of Pisa

p. .... 173

### **GOSPER SPACE-FILLING RADIOFREQUENCY-SKIN FOR THE DETECTION AND IDENTIFICATION OF SURFACE CRACKS**

S. Nappi<sup>1</sup>, G. Marrocco<sup>1</sup>

<sup>1</sup>Department of Civil and Informatic Engineering, University of Rome Tor Vergata

p. .... 177

### **TIME-BASED ARRAYS FOR PRECISE TAGS LOCALIZATION**

M. Shanawani<sup>1</sup>, D. Masotti<sup>1</sup>, A. Costanzo<sup>2</sup>

<sup>1</sup>DEI – University of Bologna, Bologna

<sup>2</sup>DEI – University of Bologna, Cesena

p. .... 181

### **RADIO FREQUENCY SENSORS BASED ON CHIPLESS RFID TECHNOLOGY**

F. Costa<sup>1</sup>, S. Genovesi<sup>1</sup>, S. Terranova<sup>1</sup>, G. Manara<sup>1</sup>

<sup>1</sup>Dipartimento di Ingegneria dell'Informazione, University of Pisa

p. .... 185

### **UHF RFID TAG DETECTION IN CYLINDRICAL WAVEGUIDES**

A. Michel<sup>1</sup>

<sup>1</sup>Dipartimento di Ingegneria dell'Informazione, University of Pisa

p. .... 189

### **ROTATION-INSENSITIVE RF-TO-DC LINK FOR IPT IMPLANTS**

A. Pacini<sup>1</sup>, F. Benassi<sup>1</sup>

<sup>1</sup>Department of Electrical, Electronic and Information Engineering "Guglielmo Marconi", University of Bologna

p. .... 193

## Session 8: MICROWAVES

**Chairperson: Luca Perregrini**

### **FOCUSING THROUGH CYLINDRICAL LEAKY WAVES**

D. Comite<sup>1</sup>, W. Fuscaldo<sup>1</sup>

<sup>1</sup>Department of Information Engineering, Electronics, and Telecommunications, "Sapienza" University of Rome

p. .... 197

### **SPATIAL CONFINEMENT OF LOCALIZED BEAMS AND PULSES FOR NEAR-FIELD FOCUSING APPLICATIONS AT MILLIMETER WAVES**

W. Fuscaldo<sup>1</sup> and S. C. Pavone<sup>2</sup>

<sup>1</sup>Dept. of Information Engineering, Electronics and Telecommunications, Sapienza Univ. Rome

<sup>2</sup>Department of Information Engineering and Mathematics, University of Siena

p. .... 201

### **ADDITIVE MANUFACTURING OF HIGH PERFORMANCES FILTERS**

G. Addamo<sup>1</sup>, O.A. Peverini<sup>1</sup>, F. Calignano<sup>2</sup>, D. Manfredi<sup>2</sup>, F. Paonessa<sup>1</sup>, G. Virone<sup>1</sup>

<sup>1</sup>Istituto di Elettronica ed Ingegneria dell'Informazione e delle Telecomunicazioni, Torino

<sup>2</sup>Dipartimento di Ingegneria Gestione della Produzione, Politecnico di Torino

p. .... 205

### **PERFORMANCE STUDY OF COMPACT SUBSTRATE INTEGRATED WAVEGUIDE RESONATORS**

N. Delmonte<sup>1</sup>, C. Tomassoni<sup>2</sup>, M. Bozzi<sup>1</sup>, L. Perregrini<sup>1</sup>

<sup>1</sup>Department of Electrical, Computer and Biomedical Engineering, University of Pavia

<sup>2</sup>Department of Engineering, University of Perugia

p. .... 209

### **CORRUGATED RECTANGULAR WAVEGUIDE FOR PULSE COMPRESSION SYSTEMS**

G. Di Massa<sup>1</sup>, S. Costanzo<sup>1</sup>

<sup>1</sup>Department of Informatics, Modeling, Electronics and System Engineering, University of Calabria

p. .... 213

### **3D-PRINTED SUBSTRATE INTEGRATED WAVEGUIDE CAVITY FOR FLUIDS CHARACTERIZATION**

G. M. Rocco<sup>1</sup>, M. Bozzi<sup>1</sup>, D. Schreurs<sup>2</sup>, S. Marconi<sup>3</sup>, G. Alaimo<sup>3</sup>, F. Auricchio<sup>3</sup>

<sup>1</sup>Department of Electrical, Computer and Biomedical Engineering, University of Pavia

<sup>2</sup>Department of Electrical Engineering, KU Leuven, Belgium

<sup>3</sup>Department of Civil Engineering and Architecture, University of Pavia

p. .... 217

### **Low-power Eco-friendly Sensors for the Internet of Things**

Valentina Palazzi<sup>1</sup>, Federico Alimenti<sup>1</sup>, Luca Roselli<sup>1</sup>, P. Mezzanotte<sup>1</sup>

<sup>1</sup>Dipartimento di Ingegneria, Università degli studi di Perugia

p. .... 221

## Session 9: OPTICS I

**Chairperson: Stefano Selleri**

### **A GENERAL PURPOSE APPROACH FOR DIPSTICK ANALYSIS USING SMARTPHONES AND COLORIMETRIC EQUALIZATION CHART**

F. Biasion<sup>1</sup>, M. Barozzi<sup>1</sup>, F. Pasquali<sup>2</sup>, A. Tonelli<sup>2</sup>, S. Selleri<sup>1</sup>

<sup>1</sup>Dipartimento di Ingegneria e Architettura - Università di Parma

<sup>2</sup>DNAPhone s.r.l., Parma

p. .... 225

### **DESIGN OF AN IN-BAND PUMPED DYSPROSIUM-DOPED ZBLAN FIBER AMPLIFIER OPERATING AT 2.9-3.2 MICRON**

M.C. Falconi<sup>1</sup>, D. Laneve<sup>1</sup>, M. Bozzetti<sup>1</sup>, T. T. Fernandez<sup>2</sup>, G. Galzerano<sup>2</sup>, F. Prudenzeno<sup>1</sup>

<sup>1</sup>Department of Electrical and Information Engineering, Polytechnic of Bari

<sup>2</sup>Istituto di Fotonica e Nanotecnologie - CNR, Department of Physics, Politecnico di Milano

p. .... 229

### **ELECTROMAGNETIC PROPAGATION FOR ON-CHIP WIRELESS COMMUNICATIONS**

F. Fuschini<sup>1</sup>, M. Barbiroli<sup>1</sup>, M. Zoli<sup>1</sup>, P. Bassi<sup>1</sup>, G. Bellanca<sup>2</sup>, A.E. Kaplan<sup>2</sup>, G. Calò<sup>3</sup>, V. Petruzzelli<sup>3</sup>

<sup>1</sup>Dept. of Electrical, Electronic and Information Eng. "G. Marconi", University of Bologna

<sup>2</sup>Dept. of Engineering, University of Ferrara

<sup>3</sup>Department of Electrical and Information Engineering, Polytechnic of Bari

p. .... 233

### **EXPERIMENTAL DEMONSTRATION OF PROTEIN DETECTION USING HOLLOW-CORE TUBE LATTICE FIBERS**

F. Giovanardi<sup>1</sup>, A. Cucinotta<sup>2</sup>, A. Rozzi<sup>3</sup>, R. Corradini<sup>3</sup>, F. Benabid<sup>(4,5)</sup>, L. Vincetti<sup>1</sup>

<sup>1</sup>Department of Engineering "Enzo Ferrari", University of Modena and Reggio Emilia

<sup>2</sup>Department of Engineering and Architecture, University of Parma

<sup>3</sup>Department of Chemistry, Life Sciences and Environmental Sustainability, University of Parma

<sup>4</sup>GPPMM group, Xlim Research Institute, CNRS UMR 7252, Université de Limoges, Limoges

<sup>5</sup>GLOphotonics SAS, Ester Technopole, Limoges Cedex

p. .... 237

### **COUPLED MODE THEORY ASSESSMENT FOR SEMICONDUCTOR CODIRECTIONAL COUPLERS**

Kaplan Ali Emre<sup>(1,2)</sup>, G. Bellanca<sup>1</sup>, J. Van Der Tol<sup>2</sup>, P. Bassi<sup>3</sup>

<sup>1</sup>DI, University of Ferrara

<sup>2</sup>DEE, Technical University of Eindhoven, The Netherlands

<sup>3</sup>DEI, University of Bologna

p. .... 241

### **NON-VOLATILE FERROELECTRIC ACTUATORS INTEGRATED IN SILICON PHOTONIC CIRCUITS**

I. Maqueira Albo<sup>1</sup>, S. Varotto<sup>2</sup>, M. Asa<sup>2</sup>, C. Rinaldi<sup>2</sup>, M. Cantoni<sup>2</sup>, A. Melloni<sup>1</sup>, R. Bertacco<sup>2</sup>, F. Morichetti<sup>2</sup>

<sup>1</sup>Dipartimento di Elettronica, Informazione e Bioingegneria, Politecnico di Milano

<sup>2</sup>Dipartimento di Fisica, Politecnico di Milano

p. .... 245

## Session 10: INVERSE PROBLEMS

**Chairperson: Giovanni Leone**

### **THE REDUCED SCATTERED FIELD AS A TOOL FOR FOCUSING IN AN UNKNOWN SCENARIO**

M. T. Bevacqua<sup>1</sup>, R. Palmeri<sup>1</sup>, L. Crocco<sup>2</sup>, T. Isernia<sup>(1,2)</sup>

<sup>1</sup>DIIES, Univ. Mediterranea of Reggio Calabria

<sup>2</sup>CNR-IREA, National Research Council of Italy, Naples

p. .... 249

### **THE ROLE OF VIEW DIVERSITY ON LINEAR SCATTERING OPERATOR IN FRESNEL-ZONE**

M.A. Maisto<sup>1</sup>, F. Munno<sup>1</sup>

<sup>1</sup>Dipartimento di Ingegneria, Università della Campania "L. Vanvitelli", Aversa

p. .... 253

### **FAULTS DIAGNOSTICS OF A CONICAL ARRAY**

G. Leone<sup>1</sup>, G. Buonanno<sup>1</sup>

<sup>1</sup>Dipartimento di Ingegneria, Università della Campania "L. Vanvitelli", Aversa

p. .... 257

### **ON THE FEASIBILITY OF PHASELIFT IN CIRCULAR GEOMETRY**

M.A. Maisto<sup>1</sup>, R. Moretta<sup>1</sup>, R. Solimene<sup>1</sup>, R. Pierri<sup>1</sup>

<sup>1</sup>Dipartimento di Ingegneria, Università della Campania "L. Vanvitelli", Aversa

p. .... 261

### **TWO-DIMENSIONAL PHASE RETRIEVAL AS A 'CROSSWORDS' PROBLEM**

A.F. Morabito<sup>1</sup>, P. G. Nicolaci<sup>(1,2)</sup>, T. Isernia<sup>1</sup>

<sup>1</sup>DIIES, Univ. Mediterranea of Reggio Calabria

<sup>2</sup>Space Engineering S.p.A., Roma

p. .... 265

### **THEORETICAL ADVANCES ON NON-DETECTABLE OBJECTS WITH FREQUENCY-SHIFTING AND SPATIAL-SQUEEZING COATINGS**

R. Palmeri<sup>1</sup>, G. Labate<sup>2</sup>

<sup>1</sup>DIIES, Univ. Mediterranea of Reggio Calabria

<sup>2</sup>DET, Politecnico di Torino

p. .... 269

## Session 11: OPTICS II

**Chairperson: Stefano Trillo**

### **NONLINEAR PROPAGATION IN OPTICAL FIBERS FOR SPACE-DIVISION SPACE-DIVISION MULTIPLEX TRANSMISSION**

C. Antonelli<sup>1</sup>, Mecozzi A. <sup>1</sup>, and M. Shtaif<sup>2</sup>

<sup>1</sup>Department of Physical and Chemical Sciences, University of L'Aquila

<sup>2</sup>Department of Physical Electronics, Tel Aviv University, Tel Aviv

p. .... 273

### **OBSERVING THE BROKEN SYMMETRY OF FERMI-PASTA-ULAM RECURRENCES IN OPTICAL FIBERS**

A. Mussot<sup>1</sup>, C. Naveau<sup>1</sup>, M. Conforti<sup>1</sup>, A. Kudlinski<sup>1</sup>, F. Copie<sup>1</sup>, P. Szriftgiser<sup>1</sup>, and S. Trillo<sup>2</sup>

<sup>1</sup>Univ. Lille, CNRS, UMR 8523 - PhLAM, Lille

<sup>2</sup>Department of Engineering, University of Ferrara

p. .... 277

### **MULTI-CORE OPTICAL FIBERS FOR HIGH POWER LASERS**

L. Rosa<sup>1</sup>, F. Poli<sup>2</sup>, S. Selleri<sup>2</sup>, L. Vincetti<sup>1</sup>, A. Cucinotta<sup>2</sup>

<sup>1</sup>Department of Engineering "Enzo Ferrari", University of Modena and Reggio Emilia

<sup>2</sup>Department of Engineering and Architecture, University of Parma

p. .... 281

### **NESTED PLASMONIC RESONANCES IN OPTICAL ANTENNAS LOADED WITH EPSILON-NEAR-ZERO NANOPARTICLES**

D. De Ceglia<sup>1</sup>, M. A. Vincenti<sup>2</sup>, N. Akozbek<sup>3</sup>, M. J. Bloemer<sup>4</sup>, M. Scalora<sup>4</sup>

<sup>1</sup>Department of Information Engineering, University of Padova

<sup>2</sup>Department of Information Engineering, University of Brescia

<sup>3</sup>Aegis Technologies Inc., Huntsville (AL) - USA

<sup>4</sup>US Army AMRDEC, Redstone Arsenal (AL) - USA

p. .... 285

### **TUNABLE OPTICAL ANTENNAS USING VO<sub>2</sub> METAL-INSULATOR PHASE TRANSITIONS**

A. Tognazzi<sup>1</sup>, F. Baronio<sup>(1,2)</sup>, A. Locatelli<sup>(1,2)</sup>, M. A. Vincenti<sup>1</sup>, F. Banfi<sup>3</sup>, C. Giannetti<sup>3</sup>, C. De Angelis<sup>(1,2)</sup>

<sup>1</sup>Dipartimento di Ingegneria dell'Informazione, Università degli Studi di Brescia

<sup>2</sup>Istituto Nazionale di Ottica, Consiglio Nazionale delle Ricerche, Brescia

<sup>3</sup>Dipartimento di Fisica, Università Cattolica del Sacro Cuore, Brescia

p. .... 289

### **ANALYSIS OF THE THERMAL EFFECTS ON A FULLY APERIODIC LARGE PITCH FIBER AMPLIFIER**

K. Tragni<sup>1</sup>, C. Molardi<sup>(1,3)</sup>, F. Poli<sup>1</sup>, R. Dauliat<sup>2</sup>, B. Leconte<sup>2</sup>, D. Darwich<sup>2</sup>, R. du Jeu<sup>2</sup>, M.A. Malleville<sup>2</sup>, S. Selleri<sup>1</sup>, P. Roy<sup>2</sup>, A. Cucinotta<sup>1</sup>

<sup>1</sup>University of Parma, Dept. of Engineering and Architecture, Parma

<sup>2</sup>University of Limoges, CNRS, XLIM, UMR 7252, Limoges

<sup>3</sup>Electrical and Electronic Eng. Dept., Nazarbayev University, Astana, KZ

p. .... 293

## Session 12: ANTENNAS II

**Chairperson: Alessandro Fanti**

### **REDUCED SIZE PLANAR GRID ARRAY ANTENNA FOR AUTOMOTIVE RADAR SENSOR**

E. Arnieri<sup>1</sup>, F. Greco<sup>1</sup>, L. Boccia<sup>1</sup>, G. Amendola<sup>1</sup>

<sup>1</sup>Università della Calabria

p. .... 297

### **RECENT ADVANCES ON EBG CAVITY ANTENNAS**

P. Baccarelli<sup>1</sup>, S. Ceccuzzi<sup>2</sup>, V. Jandieri<sup>3</sup>, C. Ponti<sup>1</sup>, G. Schettini<sup>1</sup>

<sup>1</sup>Department of Engineering, Roma Tre University

<sup>2</sup>ENEA, Fusion and Nuclear Safety Department, Frascati

<sup>3</sup>Faculty of Engineering, University of Duisburg-Essen, and CENIDE–Center for Nanointegration  
Duisburg-Essen

p. .... 301

### **PROPOSAL OF A MILLIMETER-WAVE ANTENNA ARRAY FOR CUBESATS**

G. Buttazoni<sup>1</sup>, F. Pelusi<sup>1</sup>, R. Vescovo<sup>1</sup>

<sup>1</sup>Department of Engineering and Architecture, University of Trieste

p. .... 305

### **A COMPACT SERIES ARRAY FOR SHORT RANGE COMMUNICATION**

S. Maddio<sup>1</sup>, G. Pelosi<sup>1</sup>, M. Righini<sup>1</sup>, S. Selleri<sup>1</sup>

<sup>1</sup>Department of Information Engineering, University of Florence

p. .... 309

### **ESTIMATION OF THE ANTENNA PHASE CENTER POSITION IN ANECHOIC CHAMBER**

C. Esposito<sup>1</sup>, A. Gifuni<sup>2</sup> and S. Perna<sup>(1,2)</sup>

<sup>1</sup>Institute for Electromagnetic Sensing of the Environment (IREA) of Consiglio Nazionale delle  
Ricerche (CNR), Napoli

<sup>2</sup>Dipartimento di Ingegneria (DI), Università degli Studi di Napoli "Parthenope"

p. .... 313

### **SPATIAL DISPERSION OF METASURFACES FOR LEAKY-WAVE ANTENNAS IN THE TERAHERTZ RANGE**

S. Tofani<sup>1</sup>, W. Fuscaldo<sup>1</sup>, D. C. Zografopoulos<sup>2</sup>, P. Baccarelli<sup>3</sup>, P. Burghignoli<sup>1</sup>, R. Beccherelli<sup>2</sup>, A.  
Galli<sup>1</sup>

<sup>1</sup>Dept. of Information Engineering, Electronics and Telecommunications, Sapienza Univ. Rome

<sup>2</sup>Institute for Microelectronics and Microsystems (CNR-IMM), National Research Council, Rome

<sup>3</sup>Department of Engineering, "Roma Tre" University

p. .... 317

## Poster Session

### THE QV-LIFT PROJECT: A GROUND SEGMENT FOR THE FUTURE Q/V BAND SATELLITE SYSTEMS

G. Amendola<sup>1</sup>, L. Boccia<sup>1</sup>, F. Greco<sup>1</sup>, E. Arnieri<sup>1</sup>, C. Riva<sup>2</sup>, L. Luini<sup>2</sup>, R. Nebuloni<sup>3</sup>, G. Codispoti<sup>4</sup>, G. Parca<sup>4</sup>, G. Valente<sup>4</sup>, G. Goussetis<sup>5</sup>, S. Kosmopoulos<sup>5</sup>, M. Siegler<sup>6</sup>, R. Martin<sup>7</sup>, J. Moron<sup>7</sup>, R. Eleuteri<sup>8</sup>, M. Bergmann<sup>8</sup>, F. Massaro<sup>9</sup>, R. Campo<sup>9</sup>, F. Vitobello<sup>10</sup>

<sup>1</sup>CNIT-Università della Calabria (I)

<sup>2</sup>CNIT-Politecnico di Milano(I)

<sup>3</sup>IEIIT/CNR (I)

<sup>4</sup>ASI-Agenzia Spaziale Italiana (I)

<sup>5</sup>Heriot Watt University (UK)

<sup>6</sup>ERZIA (S)

<sup>7</sup>Ommic (F)

<sup>8</sup>Skytech (I)

<sup>9</sup>Eutelsat (F)

<sup>10</sup>European Commission

p. .... 321

### INVERSE SCATTERING METHODOLOGIES AND APPLICATIONS @ELEDIA RESEARCH CENTER

N. Anselmi<sup>1</sup>, A. Gelmini<sup>1</sup>, G. Gottardi<sup>1</sup>, G. Oliveri<sup>1</sup>, L. Poli<sup>1</sup>, P. Rocca<sup>1</sup>, M. Salucci<sup>1</sup>, and A. Massa<sup>(1,2)</sup>

<sup>1</sup>ELEDIA Research Center, Trento

<sup>2</sup>ELEDIA Research Center, Madrid

p. .... 325

### EM EDUCATION TOOLS & PROGRAMS @ ELEDIA RESEARCH CENTER

N. Anselmi<sup>1</sup>, G. Oliveri<sup>1</sup>, L. Poli<sup>1</sup>, A. Polo<sup>1</sup>, F. Robol<sup>1</sup>, P. Rocca<sup>1</sup>, M. Salucci<sup>1</sup>, A. Massa<sup>(1,2)</sup>

<sup>1</sup>ELEDIA Research Center, Trento

<sup>2</sup>ELEDIA Research Center, Madrid

p. .... 329

### ANTENNA SYNTHESIS AND OPTIMIZATION @ ELEDIA RESEARCH CENTER

Anselmi N.<sup>1</sup>, R. Azaro<sup>1</sup>, P. Bui<sup>1</sup>, A. Gelmini<sup>1</sup>, G. Gottardi<sup>1</sup>, M. A. Hannan<sup>1</sup>, G. Oliveri<sup>1</sup>, L. Poli<sup>1</sup>, A. Polo<sup>1</sup>, F. Robol<sup>1</sup>, P. Rocca<sup>1</sup>, M. Salucci<sup>1</sup>, and A. Massa<sup>(1,2)</sup>

<sup>1</sup>ELEDIA Research Center, Trento

<sup>2</sup>ELEDIA Research Center, Madrid

p. .... 333

### DISTRIBUTED WIRELESS SENSING, MONITORING, AND DECISION SUPPORT: CURRENT ACTIVITIES @ ELEDIA RESEARCH CENTER

M. Bertolli<sup>1</sup>, G. Oliveri<sup>1</sup>, A. Polo<sup>1</sup>, F. Robol<sup>1</sup>, P. Rocca<sup>1</sup>, F. Viani<sup>1</sup>, A. Massa<sup>(1,2)</sup>

<sup>1</sup>ELEDIA Research Center, Trento

<sup>2</sup>ELEDIA Research Center, Madrid

p. .... 337

### THE CASE OF MICROWAVE DISINFECTION OF RAISED BEDS CULTIVATIONS – NUMERICAL ASSESSMENT

S.Casu<sup>1</sup>, A. Fanti<sup>1</sup>, M.B. Lodi<sup>1</sup>, M. Spanu<sup>1</sup>, M. Renzi<sup>1</sup>, G. Mazzarella<sup>1</sup>

<sup>1</sup>Department of Electrical and Electronic Engineering, University of Cagliari, Cagliari

p. .... 341

### DESIGN OF AMC STRUCTURES FOR UHF APPLICATIONS

G.A. Casula<sup>1</sup>, G. Montisci<sup>1</sup>, P. Maxia<sup>1</sup>

<sup>1</sup>Department of Electrical and Electronic Engineering, University of Cagliari, Cagliari

p. .... 345

**ENHANCED COLE-COLE DIELECTRIC MODEL FOR ACCURATE BLOOD GLUCOSE SENSING**

V. Cioffi<sup>1</sup>

<sup>1</sup>DIMES, University of Calabria, Rende (CS)

p. .... 349

**ANALYSIS OF PROPAGATION IN URBAN AREAS AT 3.7 AND 28 GHz FOR 5G WIRELESS NETWORKS**

G. Di Martino<sup>1</sup>, A. Iodice<sup>1</sup>, D. Riccio<sup>1</sup>, G. Ruello<sup>1</sup>

<sup>1</sup>Department of Electrical Engineering and Information Technology, University of Napoli Federico II

p. .... 353

**ON THE REPEATABILITY OF THE EXPERIMENTAL CHARACTERIZATION UP TO 50 GHz OF EX-VIVO BREAST TISSUES**

S. Di Meo<sup>1</sup>, P. F. Espin-Lopez<sup>1</sup>, A. Martellosio<sup>1</sup>

<sup>1</sup>Dept. of Electrical, Computer and Biomedical Engineering, University of Pavia

p. .... 357

**SVM CLASSIFICATION OF ALZHEIMER'S DISEASE USING MRI AND FMRI**

C. Dachena<sup>1</sup>, A. Allocca<sup>1</sup>, I. Meloni<sup>1</sup>, A. Fanti<sup>1</sup>, G. Mazzarella<sup>1</sup>

<sup>1</sup>Department of Electrical and Electronic Engineering, University of Cagliari, Cagliari

p. .... 361

**EFFECTIVE ANTENNA DESIGN METHODOLOGIES FOR NEW GENERATION 5G MIMO SYSTEMS**

G. Gottardi<sup>1</sup>

<sup>1</sup>ELEDIA Research Center, Trento

p. .... 365

**FEASIBILITY STUDY ON THE USE OF MICROWAVE IMAGING FOR IN-LINE MONITORING OF FOOD CONTAMINATION**

L. Farina<sup>1</sup>, J. A. Tobon Vasquez<sup>1</sup>, and R. Scapatucci<sup>2</sup>

<sup>1</sup>DET, Politecnico di Torino, Torino

<sup>2</sup>IREA, National Council of Research of Italy, Naples

p. .... 369

**SOLUTION-PROCESSABLE ORGANIC SEMICONDUCTORS FOR INTEGRATED PHOTONICS APPLICATIONS**

I. Maqueira Albo<sup>1</sup>, M. Caironi<sup>2</sup>, F. Morichetti<sup>1</sup>

<sup>1</sup>Dipartimento di Elettronica, Informazione e Bioingegneria, Politecnico di Milano, Milano

<sup>2</sup>Center for Nano Science and Technology, Istituto Italiano di Tecnologia, Milano

p. .... 373

**ADDITIVE MANUFACTURING OF A SUBSTRATE INTEGRATED SLAB WAVEGUIDE FOR SINGLE-MODE BANDWIDTH ENHANCEMENT**

E. Massoni<sup>1</sup>, L. Silvestri<sup>1</sup>, G. Alaimo<sup>2</sup>, S. Marconi<sup>2</sup>, M. Bozzi<sup>2</sup>, L. Perregrini<sup>2</sup>, and F. Auricchio<sup>2</sup>

<sup>1</sup>Department of Electrical, Computer and Biomedical Engineering, University of Pavia

<sup>2</sup>Department of Civil Engineering and Architecture, University of Pavia

p. .... 377

**DESIGN OF ROBUST WEARABLE UHF RFID TAGS THROUGH THE OPTIMUM POSITIONING OF A PIFA RADIATING ELEMENT ON A COMPACT GROUND PLANE**

A. Michel<sup>2</sup>, R. Colella<sup>1</sup>, G. A. Casula<sup>3</sup>, P. Nepa<sup>2</sup>, L. Catarinucci<sup>1</sup>, G. Montisci<sup>3</sup>, G. Mazzarella<sup>3</sup>, G. Manara<sup>2</sup>

<sup>1</sup>Dept. of Innovation Engineering, Univ. of Salento, Lecce

<sup>2</sup>Dept. of Information Engineering, Univ. of Pisa, Pisa

<sup>3</sup>Dept. of Electrical and Electronic Engineering, Univ. of Cagliari, Cagliari

p. .... 381

**MODELING AND EXPERIMENTATION OF A UHF-RFID TRANSCUTANEOUS WIRELESS COMMUNICATION SYSTEM FOR THE MYOELECTRIC CONTROL OF PROSTHETIC HAND**

C. Miozzi<sup>1</sup>, S. Guido<sup>1</sup>, G. Saggio<sup>1</sup>, E. Gruppioni<sup>2</sup>, G. Marrocco<sup>1</sup>

<sup>1</sup>University of Roma "Tor Vergata", Roma

<sup>2</sup>INAIL Centro Protesi, Research and Training Area, Budrio (BO)

p. .... 385

**DESIGN OF ACTIVE WAVEGUIDE OMT FOR RADIO ASTRONOMY RECEIVER ARRAY IN THE 3 MM BAND**

A. Navarrini<sup>1</sup>, G. Valente<sup>2</sup>, P. Serres<sup>3</sup>, F. Schaefer<sup>4</sup>, F. Thome<sup>5</sup>, O. Garnier<sup>3</sup>

<sup>1</sup>INAF-Osservatorio Astronomico di Cagliari, via della Scienza 5, Selargius, Italy

<sup>2</sup>Agenzia Spaziale Italiana, Via del Politecnico snc, Rome, Italy

<sup>3</sup>IRAM-Istitut de RadioAstronomie Millimétrique, Grenoble, France

<sup>4</sup>MPIfR-Max Planck Institute for Radio Astronomy, Bonn, Germany

<sup>5</sup>IAF-Fraunhofer Inst. Appl. Solid State Physics, Friburg, Germany

p. .... 389

**INVESTIGATING EM WAVE DEPOLARIZATION DUE TO RAIN USING A PHYSICALLY-BASED MODEL**

E. Regonesi<sup>1</sup>, L. Luini<sup>1</sup>

<sup>1</sup>Dipartimento di Elettronica, Informazione e Bioingegneria, Politecnico di Milano

p. .... 393

**A FMCW RADAR AS ELECTRONIC TRAVEL AID FOR VISUALLY IMPAIRED SUBJECTS**

G. Sacco<sup>1</sup>, E. Piuze<sup>1</sup>, E. Pittella<sup>1</sup>, S. Pisa<sup>1</sup>

<sup>1</sup>Dept. of Information Engineering, Electronics and Telecommunications, Sapienza Univ. Rome

p. .... 397

**FIRST EXPERIMENTAL ASSESSMENT OF A MICROWAVE IMAGING PROTOTYPE FOR CEREBROVASCULAR DISEASES MONITORING**

J. A. Tobon Vasquez<sup>1</sup>, R. Scapaticci<sup>2</sup>, G. Turvani<sup>1</sup>, G. Dassano<sup>1</sup>, N. Joachimowicz<sup>3</sup>, B. Duchêne<sup>4</sup>, M. R. Casu<sup>1</sup>, L. Crocco<sup>2</sup>, and F. Vipiana<sup>1</sup>

<sup>1</sup>DET, Politecnico di Torino, Torino, Italy

<sup>2</sup>IREA, National Council of Research of Italy, Naples

<sup>3</sup>GeePs, CNRS-Centrale Supélec-Université Paris Saclay, Gif-sur-Yvette

<sup>4</sup>L2S, CNRS-Centrale Supélec-Univ Paris Sud, Gif-sur-Yvette

p. .... 401

**NOVEL CLASS OF DUAL-MODE AIR FILLED SIW FILTERS**

C. Tomassoni<sup>1</sup>, L. Silvestri<sup>2</sup>, M. Bozzi<sup>2</sup>, L. Perregrini<sup>2</sup>, A. Ghiotto<sup>3</sup>

<sup>1</sup>University of Perugia, Department of Engineering, Perugia

<sup>2</sup>University of Pavia, Department of Electrical, Computer and Biomedical Engineering, Pavia

<sup>3</sup>University of Bordeaux, IMS Laboratory, Talence, France

p. .... 405

**GRAPHENE MICROSTRIP ATTENUATOR WITH HIGH TUNABILITY AND MINIMUM REFLECTION**

M. Yasir<sup>1</sup>, M. Bozzi<sup>1</sup>, L. Perregrini<sup>1</sup>

<sup>1</sup>Department of Electrical, Computer and Biomedical Engineering, University of Pavia, Pavia

p. .... 409

# ANGLE AND POLARIZATION TUNING OF THE SECOND HARMONIC RADIATION PATTERN IN DIELECTRIC NANOANTENNAS

L. Carletti<sup>(1)</sup>, D. Rocco<sup>(1)</sup>

<sup>(1)</sup> Department of Information Engineering, Università degli Studi di Brescia, Via Branze 38, 25123 Brescia, Italy  
[luca.carletti@unibs.it](mailto:luca.carletti@unibs.it), [d.rocco003@unibs.it](mailto:d.rocco003@unibs.it)

## Abstract

*High-permittivity semiconductor nanoresonators recently demonstrated a huge potential for nanoscale nonlinear light sources by second and third harmonic generation. While achieving a high conversion efficiency has been the first milestone, directionality and control of the emitted light pattern will also be crucial for applications. In this work, we use numerical simulations to demonstrate the tunability of the directionality of the second harmonic radiation pattern generated in AlGaAs nanodisks by varying the polarization and angle of incidence of the pump beam. Our results show that this technique allows improving the collection efficiency of the second harmonic signal and selectively controlling the second harmonic emission angle. Our approach further demonstrates a novel scheme for all-optical angular measurements by background-free nanoscopic goniometry with high sensitivity.*

**Index Terms** – Dielectric nanoantennas, Nonlinear Optics, Second Harmonic Generation.

## I. INTRODUCTION

Nanostructures based on high refractive index dielectric materials are receiving more and more attention in the nanophotonics field [1]. These structures offer unpaired characteristics such as negligible absorption loss in the visible and near-infrared wavelength range and both electric and magnetic Mie type resonances. Moreover, access to materials with strong second and third order nonlinear optical response provided a new approach for nonlinear optics at the nanoscale. Concerning second-order nonlinear optical effects, aluminum gallium arsenide (AlGaAs) is emerging as a very promising material platform. In fact, AlGaAs is characterized by a high second-order nonlinear optical response, a large bandgap energy allowing two-photon absorption free operation in the near-infrared spectrum, and it is associated with a mature nanofabrication technology. In this context, our first numerical investigation of the potential of AlGaAs nanodisks for second harmonic generation (SHG) [2] have soon been followed by experimental characterization reporting record high SHG conversion efficiencies from nanoscale structures [3,4]. The richness of resonance types that govern the optical response of such nanostructures allows obtaining complex radiation patterns for the nonlinearly generated light. Careful engineering of these modes will pave the way towards nanoscale devices featuring controlled and dynamically tunable

nonlinear optical response. Our preliminary investigations showed the shaping of the SHG radiation pattern by engineering the nanodisk geometry and pump polarization state [4,5]. Demonstrations from either isolated nanodisks or dimers also featured generation of second harmonic (SH) with complex radiation patterns [6,7]. In this work, we conduct a detailed numerical characterization of the shaping of the radiation pattern of the SHG in AlGaAs nanodisks on a low refractive index substrate through manipulation of the polarization state and the directionality of the pump beam. We demonstrate the capability to dynamically change the directionality of the SH radiation pattern. Our results also inspire a new approach towards all-optical background-free angle sensor that could be of paramount importance in modern nanometrology setups.

## II. RESULTS AND DISCUSSION

We consider an AlGaAs nanodisk with a radius of 220 nm and a height of 400 nm on a low refractive index substrate ( $n=1.6$ ) as depicted in Fig. 1(a). This structure is compatible with the AlGaAs-on-AlOx material platform for monolithic nanoantenna fabrication [3]. We use three-dimensional electromagnetic simulations to characterize the linear and nonlinear response of the proposed structure [2]. The dispersion of the nanodisk material refractive index is modeled from experimental data and the nonlinear susceptibility tensor is  $\chi_{ijk}^{(2)}=100$  pm/V with  $i \neq j \neq k$  [3,4]. The pump beam is modelled as a plane wave at a wavelength of 1.6  $\mu\text{m}$ , i.e. at the magnetic dipole resonance. Both electric field polarization and angle of incidence,  $\theta$ , of the pump beam are defined with respect to the plane of incidence as shown in Fig. 1(a). The SH radiation pattern generated by our nanodisk is projected on a plane parallel to the nanodisk base in the backward direction and is shown as a function of the incidence angle,  $\theta$ , in Figures 1(b,c) for either *s* or *p* pump beam polarizations. For a *p*-polarized pump beam, the radiation pattern does not show significant variations as  $\theta$  is increased up to 45°. On the other hand, in the case of *s*-polarized incident electric field, SH emission along the normal direction occurs for  $\theta$  larger than 10° and it is enhanced until  $\theta=45^\circ$ . Thus, as shown in Fig. 1(b,c), we achieve angular and polarization sensitive shaping of the SH radiation pattern. The SH power collected through a solid angle corresponding to a numerical aperture of 0.85 is shown in Fig. 2(a). As it can be seen, SHG from *s*-polarized pump beam undergoes a strong enhancement, of a factor of 10, when the angle of incidence,  $\theta$ , increases up to 45°. On the other hand, the SH enhancement is considerably reduced for *p*-polarized incident electric field. We also observe that the collected SH power increases monotonically as  $\theta$  augments. This feature can be used to implement a sensor for the angle of the nanoparticle with respect to the pump propagation direction, i.e. a nanoscopic all-optical goniometer. By

applying a linear fit of the data for  $\theta$  between  $15^\circ$  and  $40^\circ$ , we estimated a sensitivity of  $0.15\text{ }(^{\circ})^{-1}$  for  $s$ -polarization and  $0.04\text{ }(^{\circ})^{-1}$  for  $p$ -polarization. To perform angular measurements at angles smaller than  $15^\circ$ , the SH collected power is not a sufficient parameter. Thus we define the normalized intensity difference as  $D_\theta = (I_a - I_b)/I$ , with  $I = (I_a + I_b)/2$ , where  $I_a$  and  $I_b$  are the measured intensity at one side,  $I_a$ , and at the center,  $I_b$ , of the SH radiation pattern in Fig. 1(b,c). Hence,  $D_\theta$  represents the angular parameter, which is shown as a function of the angle of incidence,  $\theta$ , and pump beam polarization in Fig. 2(b). For angles between  $0^\circ$  and  $10^\circ$ ,  $D_\theta$  and  $\theta$  have a linear relation with a slope of  $0.087\text{ }(^{\circ})^{-1}$  for  $s$ -polarization and  $0.008\text{ }(^{\circ})^{-1}$  for  $p$ -polarization.

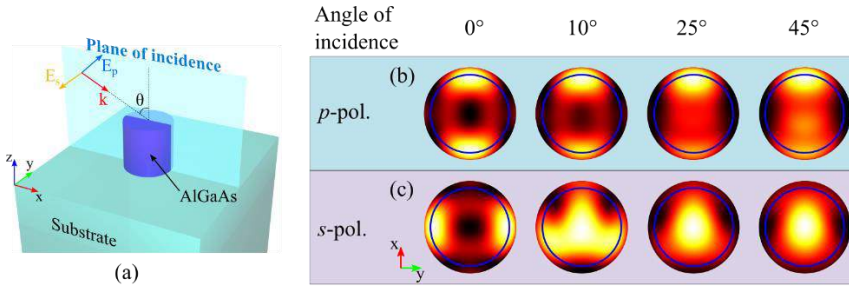


**FIG. 1** – (a) Schematic representation of AlGaAs nanodisks on low refractive index substrate. The wavevector,  $k$ , and the electric field vectors for  $p$ ,  $E_p$ , and  $s$ ,  $E_s$ , polarizations on the plane of incidence are shown. (b,c) SH radiation projected on a plane parallel to the nanodisk base in the backward direction, as a function of the angle of incidence of the pump,  $\theta$ , from  $0^\circ$  to  $45^\circ$  for  $p$  and  $s$  polarized incident electric field respectively. The blue circle in (b,c) represents the NA = 0.85.

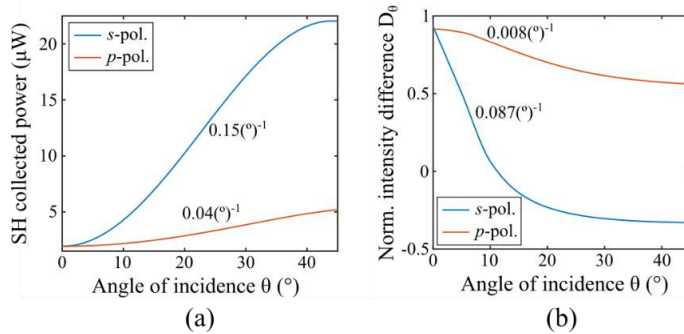


**FIG. 2** – (a) Second Harmonic power collected in the backward direction through an area corresponding to an NA of 0.85 and (b) normalized intensity difference estimated from back focal plane images for  $s$  and  $p$  pump beam polarizations respectively. Proportionality constants of linear fit are reported next to the respective data.

### III. CONCLUSION

We demonstrate active tunable angular emission of SHG from AlGaAs nanodisks on low refractive index substrate, compatible for fabrication

on the AlGaAs-on-AlOx material platform. Our results show a strong sensitivity of the SH response emission angle and power on both polarization and directionality of the incident pump beam. For an s-polarized electric field of the pump beam, due to the reshaping of the SH radiation pattern, the collected SH power is enhanced by more than one order of magnitude while changing the angle of incidence from 0° to 45°. This feature can be used to realize an all-optical background-free nanoscopic goniometer with an estimated sensitivity up to 0.15 (°)<sup>-1</sup> for angles between 15° and 40°. Our results represent a significant step towards the long-sought goal of controlling the nonlinear optical response of nanoantennas that will foster the development of active tunable nonlinear metasurfaces.

#### ACKNOWLEDGMENT

The paper has been made possible in the framework of the Erasmus Mundus NANOPHI project, contract number 2013 5659/002-001.

#### REFERENCES

- [1] S. Kruk and Y. Kivshar, "Functional Meta-Optics and Nanophotonics Governed by Mie Resonances," *ACS Photonics* vol. 4(11), pp. 2638-2649, Oct. (2017).
- [2] L. Carletti, A. Locatelli, O. Stepanenko, G. Leo, and C. De Angelis, "Enhanced second-harmonic generation from magnetic resonance in AlGaAs nanoantennas," *Optics Express*, vol. 23(20), pp. 26544-26550, Oct. (2015).
- [3] V. F. Gili, L. Carletti, A. Locatelli, D. Rocco, M. Finazzi, L. Ghirardini, I. Favero, C. Gomez, A. Lemaitre, M. Celebrano, C. De Angelis and G. Leo, "Monolithic AlGaAs second-harmonic nanoantennas," *Optics Express*, vol. 24(14), pp. 15965-15971, Jul. (2016).
- [4] L. Carletti, D. Rocco, A. Locatelli, C. De Angelis, V. F. Gili, M. Ravaro, I. Favero, G. Leo, M. Finazzi and L. Ghirardini, "Controlling second-harmonic generation at the nanoscale with monolithic AlGaAs-on-AlOx antennas," *Nanotech.*, vol. 28(11), pp. 114005, Feb. (2016).
- [5] L. Carletti, A. Locatelli, D. N. Neshev, and C. De Angelis, "Shaping the radiation pattern of second-harmonic generation from AlGaAs dielectric nanoantennas," *ACS Photonics*, vol. 3(8), pp. 1500-1507, Apr. (2016).
- [6] D. Rocco, V. F. Gili, L. Ghirardini, L. Carletti, I. Favero, A. Locatelli, G. Marino, D. N. Neshev, M. Celebrano, M. Finazzi, G. Leo, and C. De Angelis, "Tuning the second-harmonic generation in AlGaAs nanodimers via non-radiative state optimization [Invited]," *Photonics Research*, vol. 6(5), pp. B6-B12, May (2018).
- [7] S. S. Kruk, R. Camacho-Morales, L. Xu, M. Rahmani, D. A. Smirnova, L. Wang, H. H. Tan, C. Jagadish, D. N. Neshev and Y. Kivshar, "Nonlinear Optical Magnetism Revealed by Second-Harmonic Generation in Nanoantennas," *Nano Lett.*, vol. 17(6), pp. 3914-3918, May (2017).

# OPTIMAL SYNTHESIS OF SHAPED BEAMS FOR GENERIC FIXED GEOMETRY ARRAYS

G. M. Battaglia<sup>(1)</sup>, G. G. Bellizzi<sup>(1)</sup>, T. Isernia<sup>(1,2)</sup>, A. F. Morabito<sup>(1,2)</sup>

<sup>(1)</sup> DIIES, Università Mediterranea di Reggio Calabria  
Loc. Feo di Vito, I-89124 Reggio Calabria, Italy

<sup>(2)</sup> CNIT, Consorzio Nazionale Interuniversitario per le  
Telecomunicazioni

[{giada.battaglia, gennaro.bellizzi,tommaso.isernia, andrea.morabito}@unirc.it](mailto:{giada.battaglia,gennaro.bellizzi,tommaso.isernia,andrea.morabito}@unirc.it)

## Abstract

*In this work we propose an innovative approach to the mask-constrained synthesis of shaped beams through fixed-geometry array antennas. The problem is cast as a (limited) number of convex programming optimizations and can deal with all kinds of arrays, including planar and conformal arrays.*

**Index Terms** – Antenna synthesis, Array antennas, Shaped beams.

## I. INTRODUCTION

The optimal synthesis of shaped beams by means of antennas array is a classical problem of interest from both a theoretical and applicative point of view [1-2]. Accordingly, it implies well-defined constraints on the far-field pattern, on the antenna geometry and structures, and on the feeding network. A popular approach has been given by Woodward and Lawson in [3] where the ‘shaped’ beam is conceived as the superposition of many ‘pencil’ beams which are steered, one by one, and then summed to achieve the desired shaping. Unfortunately, the synthesized pattern is restricted within the class of *real* patterns which are not exploiting all the available degrees of freedom of the problem [4]. Moreover, this method does not allow enforcing constraints on the amplitude in the side-lobe region.

The ‘Spectral Factorization’ (SF) [1,5] is a very powerful method able to cast the beam synthesis problem in a computationally effective way as a mask-constrained one and it allows avoiding undesired limitations on the degrees of freedom. Interestingly, the approach is able to find all the different possible solutions to the problem at hand, so that the “more convenient” one can be selected according to some additional performance parameter. Unfortunately, the approach can only be applied to those cases where the far field can be written in terms of a 1-D polynomial<sup>1</sup>. Such limitation does not allow, for instance, considering generic planar arrays or conformal arrays.

A more general approach relies on the so-called ‘semidefinite relaxation’ framework which allows dealing with generic (fixed-geometry) arrays.

---

<sup>1</sup> see [1] for more details.

On the other side, such approach suffers serious computational issues<sup>2</sup> and only one solution is eventually found, thus eventually omitting (see above) a number of potentially interesting solutions.

In the attempt of overcoming the disadvantages of the above-mentioned methods, in the following section we propose a novel synthesis approach.

## II. RATIONALE OF THE PROPOSED APPROACH AND NUMERICAL RESULTS

The far-field of a generic N-elements array can be written as:

$$F(\underline{r}) = \sum_{n=1}^N I_n \Psi_n(\underline{r}) \quad (1)$$

wherein  $\underline{r}$  denote the coordinate spanning the observation space,  $\Psi_n(\underline{r})$  the total field induced by the unitary excited  $n$ -th antenna in  $\Omega$  when all the other antennas are off, and  $I_n$  ( $n=1, \dots, N$ ) a set of complex excitation coefficients.

By the sake of simplicity, let us suppose the goal is to synthesize a ‘flat-top’ [1] beam having a square amplitude lower than an upper-bound function  $UB(\underline{r}) \forall \underline{r} \in \Omega$  ( $\Omega$  is the region of interest) and being as close as possible to a constant  $A^2$  in the region  $\forall \underline{r} \in \Lambda$  (so to minimize the intensity ripple in such a region and respect some lower bound as well). Moreover, let us consider a set of “control points”  $\underline{r}_i$  ( $i=1, \dots, L$ ) located into  $\Lambda$  and, for a better understanding, let us focus on the case of  $L=2$ . Then, by introducing an auxiliary variable (say  $\varphi$ ), the problem can be cast in the unknowns,  $I_1, \dots, I_n$ , as:

$$\Re\{F(\underline{r}_1)\} = A \quad (2)$$

$$\Im\{F(\underline{r}_1)\} = 0 \quad (3)$$

$$\Re\{F(\underline{r}_2)\} = \Re\{F(\underline{r}_1)\} \cos \varphi \quad (4)$$

$$\Im\{F(\underline{r}_2)\} = \Re\{F(\underline{r}_1)\} \sin \varphi \quad (5)$$

$$|F(\underline{r})|^2 \leq UB(\underline{r}) \quad \underline{r} \in \Omega \quad (6)$$

Notably, for any fixed value of  $\varphi$ , which has the physical meaning of phase shift between the fields at the two ‘control points’, constraints (4) and (5) enforce the equality of the corresponding field’s intensities, whereas constraint (6) allows enforcing arbitrary upper-bounds outside  $\Lambda$ . Constraints (2)-(5) are linear functions of the unknown whereas constraint (6) is a positive semi-definite quadratic form, so that the intersection of constraints (2)-(6) still defines a convex set in the space of the unknowns. The overall problem is cast as a convex programming (CP) problem. As such, for each  $\varphi$ , the globally optimal solution of the problem can be efficiently determined via local optimization procedures.

<sup>2</sup> The number of unknowns grows in a quadratic way with the antennas number [6].

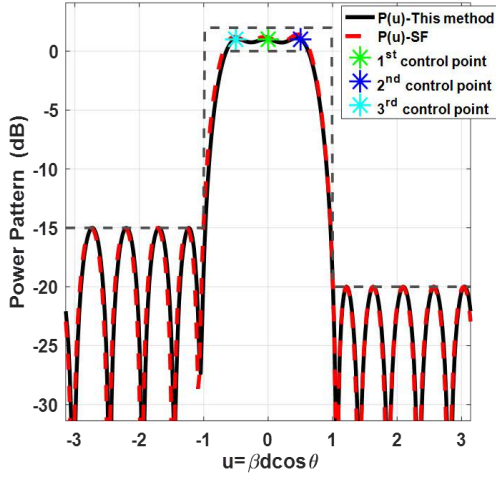


**FIG. 1** – Flat-top power pattern synthesized through the proposed procedure (black line) and the approach introduced in [1] (red line), and adopted mask (dashed gray line).

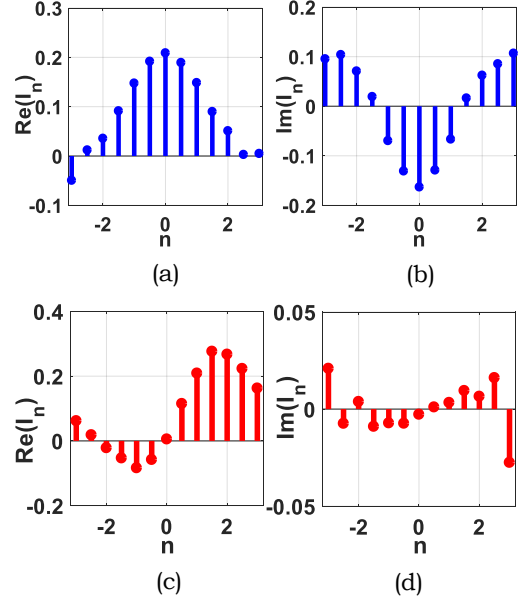


**FIG. 2** – Two different excitation sets (real parts 2.a-2.c and respective imaginary parts 2.b-2.d) synthesized by the proposed method which generate the same pattern of Fig.1.

Then, exploring the space of the possible  $\varphi$  values, the “most convenient” solution (according to some criterion) (and the corresponding excitations), can be finally picked. One possible criterion amounts to minimize the ripple of the square amplitude of the field within  $\Lambda$ :

$$\Phi = \min_{\varphi} \left\{ \int_{u \in \Lambda} [P(u) - \bar{P}]^2 du \right\} \quad (7)$$

where

$$P(u) = \left| \sum_{n=1}^N I_n e^{jnu} \right|^2 \text{ is the power pattern} \quad (8)$$

and  $\bar{P}$  is its average value within  $\Lambda$ .

Extension to larger target regions will require more control points and, of course, a higher computational complexity. Considering  $L$  control points and  $M$  sampling points for each of the  $L-1$  auxiliary variables, the overall number of CP problems raises as  $M^{(L-1)}$ . Note however one can take profit of parallel computing.

Exploiting a set of properly spaced control points where the field intensity has a given intensity, the proposed approach is similar in spirit to [3]. However, as all the available degrees of freedom are exploited, the proposed method removes the aforementioned limitation related to the Woodward-Lawson approach [4].

In the following, the proposed procedure has been compared to the SF approach exploiting an equi-spaced array composed by 13 antennas with  $\lambda/2$  inter-element spacing. As an example, we considered the synthesis of a flat-top shaped power pattern exploiting three control points. The mask, i.e.,  $UB(u)$ , is designed to enforce a maximum ripple

equal to  $\pm 1$  dB in  $\Lambda$  and different side-lobe levels outside (see Fig. 1). The far-field power pattern and the corresponding synthesized excitations are depicted in Fig. 1 and 2.(a)-(b), respectively.

Notably, the proposed approach achieves performances equal to SF ones as adapted to the case of ripple minimization. As for the SF method, the proposed approach also has the capability to determine the different excitation sets satisfying the initial constraints. For example, Fig. 2 depicts two different excitation coefficient sets delivering the same far-field pattern reported in Fig. 1.

#### IV. CONCLUSION

A new approach for a generic fixed-geometry array antennas radiating shaped beams lying in a given power pattern mask has been presented and assessed. A major advantage concerns the generality of the proposed approach. Besides its possible application to any kind of fixed-geometry array, it can also deliver every desired beam shape (by properly modifying constraints (2), (4) and (5)). On the other side, particularly in case of larger target regions, it is of the utmost importance reducing as much as possible the overall number of CP problems, which can be done through a *smart exploration* of the phase shift's space.

#### REFERENCES

- [1] T. Isernia, O. M. Bucci, N. Fiorentino, "Shaped beam antenna synthesis problems: feasibility criteria and new strategies," *J. Elect. Wav. and App.*, vol.12, pp.103-137,1998.
- [2] O.M. Bucci, G. D'Elia, G. Mazzarella, G. Panariello, "*Antenna pattern synthesis: A new general approach*," *Proc. IEEE*, Vol. 82, No. 3, 358-371, March 1994.
- [3] P.M.Woodward, J.D.Lawson, "The theoretical precision with which an arbitrary radiation-pattern may be obtained from a source of finite size," *J. of the Institution of Electrical Engineers*, vol. 95, n. 37, pp. 363-370, 1948.
- [4] R.S. Elliott, "Criticisms of the Woodward-Lawson method," *IEEE Antennas and Propagation Society Newsletter*, vol. 30, n. 3, p. 43, 1988.
- [5] O.M.Bucci, T.Isernia, A.F.Morabito, "Optimal synthesis of circularly symmetric shaped beams", *IEEE Trans. on Ant. and Prop.*, vol.62, n.4, pp.1954-1964, 2014.
- [6] B.Fuchs, "Application of convex relaxation to array synthesis problems," *IEEE Transactions on Antennas and Propagation*, vol. 62, n. 2, pp. 634-640, 2014.

# OPTIMAL SYNTHESIS OF SUM AND DIFFERENCE PATTERS OF CENTRO-SYMMETRIC ARRAYS

G. Bellizzi<sup>(1,2,3)</sup>, O.M. Bucci<sup>(1,2,3)</sup>

<sup>(1)</sup> DIETI Università di Napoli Federico II, Via Claudio 21, 80125, Napoli, Italy

<sup>(2)</sup> IREA-CNR, Via Diocleziano 328, 80124, Napoli, Italy

<sup>(3)</sup> CNIT, Viale G.P. Usberti 181/A, 43124, Parma, Italy  
gbellizz@unina.it, bucci@unina.it

## Abstract

*This communication deals with the optimal synthesis of sum or difference patterns radiated by an array of fixed geometry. The aim is to identify the most general class of arrays for which such problems admit an optimal real solution in the radiated far field, thus allowing their reduction to a linear programming problem. It is shown that an optimal real solution there exists if and only if the array layout is centro symmetric and the element patterns are either equal or, more generally, the patterns of symmetric elements are the complex conjugate of each other. Furthermore, the corresponding optimal excitations of symmetric elements are complex conjugate of each other as well, so that the number of unknowns is halved. Some numerical examples are provided to give an idea of the geometries to which the achieved result successfully applies.*

**Index Terms** – array synthesis, centro-symmetric arrays, linear programming sum and difference patterns,.

## I. INTRODUCTION

The problem of the synthesis of the excitations of an array, of fixed geometry, radiating in some optimal fashion in a given angular sector and subject to arbitrary upper bounds for the side-lobe levels, is of interest in many contexts, from satellite communication to radar localization, for both civil and defense applications [1].

Among such kind of problems, there are relevant cases, such as the synthesis of sum patterns, for which the original problem can be cast into a convex programming (CP) ones [2], which, as well known, admit only one minimum, and therefore can be solved exploiting a local optimization algorithm. An important aspect of this formulation is that it holds whatever the geometry of the array, including non-uniformly spaced, linear and planar, arrays, circular arrays, and so forth.

Moreover, it has been shown that, in the case of uniformly spaced, linear or planar, arrays of identical elements, the optimal synthesis of both sum and difference patterns can be further recast as a simpler (and computationally less expensive) linear programming (LP) problem, with a halved number of unknown [3], [4]. Interestingly, in [3], it has been shown that the above results also extend to non-uniformly spaced

arrays and nonrectangular boundaries, provided that the array layout is centro-symmetric.

The aim of this communication is to identify the most general class of arrays for which such kind of synthesis problems can be reduced to a LP problem. We show that this class consists of all (and only) the arrays whose layout is centro-symmetric and whose element patterns are either all equal (so that an array factor can be defined) or, more generally, Hermitian symmetric with respect to the inversion center. The class of centro-symmetric arrays is obviously much wider than that of uniformly spaced, linear or planar, arrays, and includes those with elements located on concentric rings, on the arms of double spiral, or conformal arrays having, for instance, a cylindrical, bi-conical or spherical shape and so on.

A numerical example is reported in this communication. Other examples will be presented at the Conference.

## II. FORMULATION OF THE PROBLEM

To simplify the notation we will refer to the case of 1D arrays. The extension to 2D arrays is straightforward.

Let us consider an array of  $N'$  radiating elements. The radiated far field,  $E(\phi, \underline{w})$ , can be expressed as:

$$E(\phi, \underline{w}) = \sum_{-N}^N w_n g_n(\phi) e^{i\beta \mathbf{r}_n \cdot \mathbf{i}(\phi)}. \quad (1)$$

In Eq. (1)  $\mathbf{r}_n$ ,  $w_n$  and  $g_n(\phi)$  are the position vector, the excitation ( $\underline{w}$  is the excitation vector) and the element pattern of the  $n$ -th element,  $\beta$  the free space propagation constant,  $\mathbf{i}(\phi)$  the unit vector along the observation direction,  $i$  the imaginary unit and “ $\cdot$ ” denotes the dot products between vectors. The summation in (1) includes the term of index  $n=0$  when  $N'=2N+1$ ; it does not include the term of index  $n=0$  when  $N'=2N$ .

Let us notice that the derivative of  $E(\phi, \underline{w})$  has the same form as in Eq. (1), provided to replace  $g_n(\phi)$  with:

$$g_n'(\phi) = \frac{dg_n(\phi)}{d\phi} + i\beta \mathbf{r}_n \cdot \frac{d\mathbf{i}(\phi)}{d\phi} g_n(\phi) \quad (2)$$

Therefore, all the results found for sum patterns will hold for difference patterns as well, provided to replace  $g_n(\phi)$  with  $g_n'(\phi)$ .

The optimal synthesis of a sum pattern consists of finding the excitations  $w_n$  such to maximize  $|E(\phi, \underline{w})|$  in a given direction  $\phi = \phi_0$ , subject to given upper bounds  $|E(\phi_m, \underline{w})| \leq c_m$ , along the  $M$  directions,  $\phi_m$ .

Now, it is easy to realize that this problem can be reduced to a LP problem *if and only if* an optimal real solution in the far field pattern there exists. Accordingly, we must determine *necessary and sufficient*

conditions under which the above problem admits a solution with real far field.

Let us consider necessary condition first. If  $E(\phi, \underline{w})$  is an optimal real field, then  $E(\phi, \underline{w})=E^*(\phi, \underline{w})$ , the asterisk denoting complex conjugation. Hence, from Eq. (1) we get:

$$\sum_{-N}^N w_n g_n(\phi) e^{i\beta \mathbf{r}_n \cdot \mathbf{i}(\phi)} = \sum_{-N}^N w_{-n}^* g_{-n}^*(\phi) e^{-i\beta \mathbf{r}_{-n} \cdot \mathbf{i}(\phi)} \quad (3)$$

The last equality follows from the fact that summing from  $-N$  to  $N$  or from  $N$  to  $-N$  does not change the result and that  $n$  is a dummy index.

Now, in order that two arrays can radiate the same field, it is necessary that the elements locations and patterns coincide. Regarding the first and last term in Eq. (3) as two distinct arrays, we must have:

$$\mathbf{r}_{-n} = -\mathbf{r}_n \quad (4)$$

$$g_{-n}(\phi) = g_n^*(\phi) \quad (5)$$

Eq. (4) states that the array must be centro-symmetric with respect to the origin of the coordinate system; Eq. (5) states that the patterns of symmetric elements must be the complex conjugate of each other. Note that Eq. (5) can be assumed verified when all the element patterns are equal. Indeed, in this case Eq. (1) factorizes in the usual product of the element pattern by the array factor. As the phase of the element pattern does not influence the amplitude of the radiated field, it can assumed equal to zero, which makes Eq. (5) trivially satisfied.

Concerning the sufficient condition, let us assume that Eq. (4) and (5) are satisfied. Denoting with  $\underline{w}_-^*$  the excitation vector whose  $n$ -th entry is  $w_{-n}^*$ , from Eq. (1) we immediately infer that if  $\underline{w}$  is a solution of the synthesis problem, then  $\underline{w}_-^*$  is a solution as well, being the corresponding fields the complex conjugate of each other. As the set of solutions is convex and the objective functional is real and linear, this implies that  $\underline{w}_{\text{opt}}=(\underline{w}+\underline{w}_-^*)/2$  is also a solution, to which a real radiated field does correspond. Notice that  $\underline{w}_{\text{opt}}$  is Hermitian so that we get the further result that the number of unknowns to be searched is halved.

As final remark, it can be shown that if Eq. (4) and (5) are satisfied then  $g_n(\phi)$  in Eq. (2) satisfies Eq. (5) as well. Therefore, Eq. (4) and (5) are necessary and sufficient also for the optimal synthesis of difference patterns.

### III. NUMERICAL EXAMPLES

As a numerical example, we have report the synthesis of a sum pattern radiated by an array of  $N=40$  infinitely extended current wires, oriented along the  $z$ -axis and uniformly spaced of half-wavelength ( $\lambda/2$ ) along a

circle of radius  $a \approx 3 \lambda$  in the  $xy$ -plane. According to the above results, the excitations have been determined by solving the associated LP problem, by exploiting the *linprog* routine of MatLab (running on a laptop PC mounting an Intel I7-4710 MQ-2.5 GHz, as CPU and a RAM of 16 GB).

Figure 1a reports the synthesized complex excitations (normalized real and imaginary parts), while Fig. 1b shows the power pattern, normalized to the maximum SLL upper bound, the imposed constraint mask and the direction of maximum,  $\phi_0 = 250^\circ$ . As foreseen, the synthesized excitations have a Hermitian symmetry and the corresponding power pattern is maximum at  $\phi_0$  and completely fulfills the imposed mask.

Finally, in order to show the advantages of the results provided in Section II, we have also determined the excitations by solving directly the CP problem (exploiting the *fmincon* routine of MatLab, and setting both the *interior point* and *active set* algorithms of this routine). It turned out that, while the synthesized excitations are, of course, exactly the same as in the LP case, the computation time was 28 s by CP vs 2.5 s by LP, i.e. about 10 times larger in the CP case. Such computational cost is even more larger by increasing the radius  $a$  of the array (hence the number of elements), becoming at least 100 times larger for  $a > 10 \lambda$ .

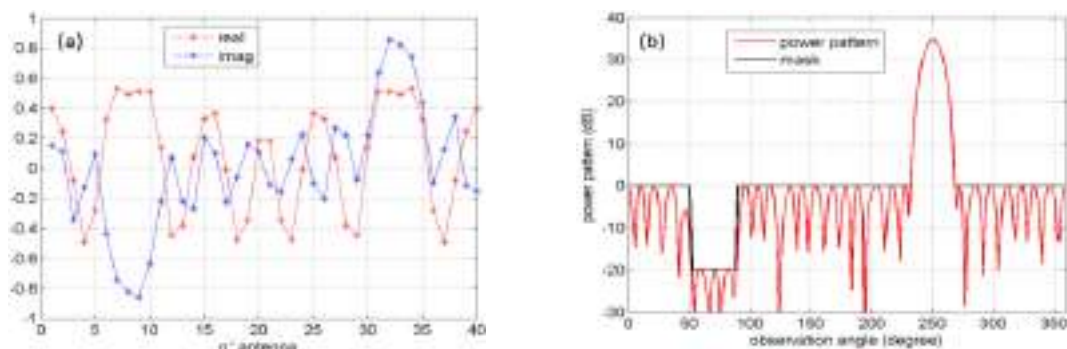


**FIG. 1** – Circular array: (a) synthesized excitations; (b) radiated power pattern.

## REFERENCES

- [1] C. Balanis, *Antennas Theory Analysis and Design*, Wiley, New York, 1997.
- [2] T. Isernia and G. Panariello, “Optimal focusing of scalar fields subject to arbitrary upper bounds”, *Electronic Lett.*, vol. 34, pp.162-164, January 1998.
- [3] O.M. Bucci, L. Caccavale, and T. Isernia, “Optimal focusing of uniformly spaced arrays subject to arbitrary upper bounds in non-target directions”, *IEEE Trans. Antennas Propag.*, vol. 50, pp. 1539–1553, November 2002.
- [4] O.M. Bucci, M. D’Urso, and T. Isernia, “Optimal synthesis of difference patterns subject to arbitrary sidelobe bounds by using arbitrary array antennas”, *IEE Proc. Microw. Antennas Propag.*, vol. 152, pp. 129–137, June 2005.

# AUTOMATIC DESIGN OF A RHCP LINEAR SLOTTED ARRAY FOR LAST-MILE APPLICATIONS AT MICROWAVES

S. C. Pavone<sup>(1)</sup>, M. Casaletti<sup>(2)</sup>, M. Albani<sup>(1)</sup>

<sup>(1)</sup> Department of Information Engineering and Mathematics (DIISM),  
University of Siena, 52100 Siena, Italy, [santi.pavone@unisi.it](mailto:santi.pavone@unisi.it)

<sup>(2)</sup> Laboratory of Electronics and Electromagnetics (L2E),  
University Pierre and Marie Curie, Paris 6, France.

## Abstract

*A full automatic procedure for the optimization of a linear slot array in SIW is presented here. A simplified analytical model for the minimization of back-reflection and of the cross-polarized component of the total magnetic dipole moment of a single slot pair, etched on the top plate of the SIW, is derived. Suitable functionals are introduced for single slot pair optimization. The last part is devoted to the entire RHCP linear slot array optimization.*

**Index Terms** – antennas, linear slotted array, substrate integrated waveguide (SIW), circular polarization.

## I. INTRODUCTION

Substrate integrated waveguides (SIWs) are a promising technology for the design of low-cost and low-profile planar electromagnetic (EM) devices at microwaves/millimeter waves [1], [2].

Different approaches were developed for the analysis and design of SIW devices, mainly based on numerical techniques such as method of moments (MoM) [2]. An interesting field of application of SIWs is the design of very compact planar antennas, in which both feeding networks and radiating slots can be efficiently integrated in the same dielectric host.

Here, the techniques developed for the automatic optimization of circularly-polarized radial line slot array (RLSA) antennas [3], together with the previous works on this topic [4-5], are profitably adopted and generalized for the design of compact linear arrays in SIW technology. For the analysis of such structures, an in-house MoM has been used [2], and an optimization loop, i.e. proper functionals and geometry-based update rules, has been proposed.

We present a procedure for fully automatic design of a right-handed circular polarized (RHCP) linear slot array for “last-mile” communications, characterized by a broad (narrow) pattern in the azimuthal (elevation) plane. Starting from single slot pair geometrical parameter optimization, a database is filled.

The optimized set of slot pairs is then used for the definition of the “starting guess” for optimizing the entire RHCP linear array in SIW.

## II. ANALYTICAL MODEL FOR SINGLE SLOT PAIR DESIGN AND OPTIMIZATION

In this Section, a simplified analytical model is proposed for defining the relevant parameters for the optimization of linear array unit cell, i.e. a RHCP slot pair with centers in  $P_{1,2} \equiv (\mp d_x, 0, \mp d_z)$  and directed along  $\hat{\mathbf{u}}_{1,2} = \pm \sin \theta_1 \hat{\mathbf{x}} + \cos \theta_2 \hat{\mathbf{z}}$ , as shown in Fig. 1.

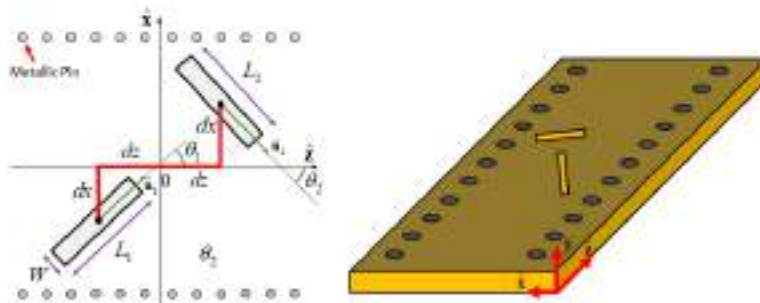


**FIG. 1** – Geometrical parameters for single slot pair design and optimization.

The slots can be considered as two equivalent magnetic dipole moments  $\mathbf{M}_{1,2} = M_{1,2} \hat{\mathbf{u}}_{1,2}$ . The waveguide is supposed to be fed by the fundamental  $\text{TE}^{10}$  mode, that exhibits a field distribution of the form  $\mathbf{h}_{10}^{\mp} = h_x^{\mp} \hat{\mathbf{x}} + h_z^{\mp} \hat{\mathbf{z}}$ ,  $\mathbf{e}_{10}^{\mp} = e_y^{\mp} \hat{\mathbf{y}}$  [6], in which the minus (plus) sign applies to outward (inward) waves along  $z$ -direction [1]. As a starting point for the optimization, we imposed  $\theta_1 = -\theta_2 = \theta_s = \pi/4$ , and  $d_x = d_z = \lambda_g/8$ . In order to optimize the slot pair positions and orientation for the linear array design, it is mandatory *i*) to reduce their back-scattering to the feeding point ( $|S_{11}| < -30\text{dB}$ ) and *ii*) to ensure their RHCP polarization purity ( $|AR| \approx 0\text{dB}$ ).

The minimization of the back-reflection by a single slot pair requires the modal amplitude  $A_{10}$  of the back-reflected wave to be theoretically zero. By resorting to the reciprocity theorem [6] and by identifying with  $\mathbf{M}_{\text{tot}} = M_1 \hat{\mathbf{u}}_1 + M_2 \hat{\mathbf{u}}_2$  the total magnetic dipole moment of the slot pair, one can easily calculate  $A_{10}$ . In order to cancel out the single slot pair back-reflection to the feeding point, we have to satisfy  $M_1 e^{j\beta d_z} = M_2 e^{-j\beta d_z}$ . Therefore, a functional  $G$  can be defined in order to minimize the slot pair back-reflection, namely  $G = (M_1 / M_2) e^{2j\beta d_z}$ , that should be optimized in order to obtain  $|G| = 1$ ,  $\angle G = 1$ . Also a set of update rules has to be defined in order to close the optimization loop. In particular, slots have to be enlarged/reduced of an amount  $\Delta L$  with respect to their starting length  $L_c$  in order to adjust  $|G|$ , but also moved close/apart of an amount  $\Delta Z$  in order to tune  $\angle G$ , hence  $\Delta L^{(s+1)} = \Delta L^{(s)} - \chi_{\Delta L} (1 - |G^{(s)}|) L_c$ ,

$\Delta Z^{(s+1)} = \Delta Z^{(s)} - \chi_{\Delta z} \frac{\angle G^{(s)}}{4\beta}$ , in which a suitable set of damping factors  $\chi_{\Delta L}$ ,  $\chi_{\Delta z}$

was introduced in order to ensure the algorithm convergence.

In order to radiate right-handed circular polarization (RHCP), the cross-polarized LHCP of  $\mathbf{M}_{tot}$  has to be set equal to zero, that is  $\mathbf{M}_{tot} \cdot \hat{\mathbf{p}}_{RH}^* = 0$ , being  $\hat{\mathbf{p}}_{RH,LH} = (\hat{\mathbf{x}} \mp j\hat{\mathbf{y}}) / \sqrt{2}$ . With some manipulations, one finds that  $M_1 e^{-j\theta_s} = -M_2 e^{j\theta_s}$ . Also in this case, a proper functional  $H$  can be defined for rejecting the cross-polarized component of the total magnetic dipole moment, namely  $H = -\frac{M_1}{M_2} e^{-2j\theta_s}$ . Since by definition

$|G| = |H|$ , only the condition  $\angle H = 0$  has to be achieved by modifying the slot pair orientation angle  $\theta_s$  of an amount  $\Delta\theta$  with respect to the starting angle  $\theta_s = \pi/4$ . Hence, only one more update rule must be added to (1), namely  $\Delta\theta^{(s+1)} = \Delta\theta^{(s)} + \chi_{\Delta\theta} \angle H^{(s)} / 2$ , where the additional damping factor  $\chi_{\Delta\theta}$  was introduced. Such functionals are used for filling a database of optimized single slot pairs of suitable lengths and then to generate the aperture distribution of the entire linear array in SIW.

### III. OPTIMIZATION OF THE ENTIRE LINEAR ARRAY IN SIW

In order to design a full broadside linear slot array, a target uniform aperture distribution has to be imposed, namely  $A(z) = \mathbf{H}(z + L_A/2) - \mathbf{H}(z - L_A/2)$ , in which  $\mathbf{H}(\cdot)$  is the Heaviside step function and  $L_A$  is the linear array length. A global functional  $F$  can be profitably introduced to optimize slot pair positions and lengths in order to match the desired distribution to the actual co-polar component of the total magnetic dipole moment as  $F = \frac{(\mathbf{M} \cdot \hat{\mathbf{p}}_{RH}) \bar{A}}{A \bar{M}}$  [3], in which two average parameters are introduced, namely  $\bar{A} = 1/N_p \sum_{n=1}^{N_p} |A_n|$  and  $\bar{M} = 1/N_p \sum_{n=1}^{N_p} |\mathbf{M}_n \cdot \hat{\mathbf{p}}_{RH}|$ , being  $N_p$  the number of slot pairs. The following update rules of the global slot pair lengths  $L_c$  and positions  $Z_c$  can be used to close the global optimization loop, namely  $L_c^{(s+1)} = L_c^{(s)} \left[ 1 + \chi_l \left( 1 - |F^{(s)}| \sqrt{\eta_{so}^{(s)}} \right) \right]$ ,  $Z_c^{(s+1)} = Z_c^{(s)} + \chi_z \angle F^{(s)} / \beta$ , in which other two damping factors  $\chi_l$ ,  $\chi_z$  were used, together with the spill-over efficiency  $\eta_{so}$ . By assuming a RHCP linear slot array of length  $L_A = 220\text{mm}$ , at the design frequency  $f = 24.27\text{GHz}$ , etched on the top plate of a SIW characterized by  $d_{pin} = 0.5\text{mm}$ , period  $P = 2d_{pin} = 1\text{mm}$ , equivalent width  $a_e = 6.5\text{mm}$ , and thickness  $h = 1.5\text{mm}$ , we have found the results briefly

provided in Fig. 2, showing that a sectoral directivity pattern can be profitably designed for applications at microwaves.

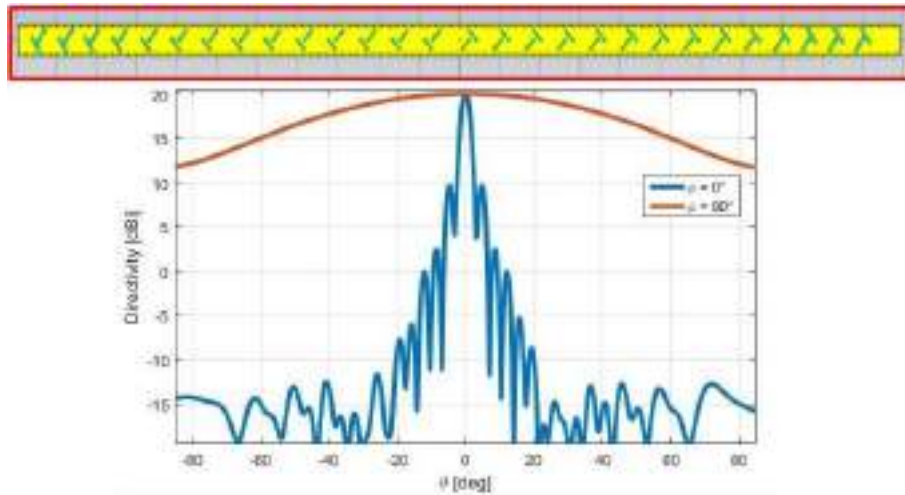


**FIG. 2** – Directivity pattern in both directive and non-directive planes.

#### IV. Conclusion

In this paper, an automatic procedure for the design and optimization of a linear slot array in SIW has been presented. An optimization procedure to reduce back-reflection and cross polarized component of the total magnetic dipole moment of each single slot pair, etched on the top plate of the SIW, was derived. The results achieved by designing the entire linear array have shown the proposed approach effectiveness.

#### REFERENCES

- [1] D. Deslandes and K. Wu, “Accurate modeling, wave mechanisms, and design considerations of a substrate integrated waveguide,” *IEEE Trans. Microw. Theory Tech.*, vol. 54, n. 6, pp. 2516–2526, 2006.
- [2] M. Casaletti, G. Valerio, R. Sauleau, and M. Albani, “Mode-matching analysis of lossy SIW devices,” *IEEE Trans. Microw. Theory Techn.*, vol. 64, n. 12, pp. 4126–4137, 2016.
- [3] M. Albani, A. Mazzinghi, and A. Freni, “Automatic design of CP-RLSA antennas,” *IEEE Trans. Anten. Propag.*, vol. 60, pp. 5538–5547, 2012.
- [4] G. Montisci, M. Musa, and G. Mazzarella, “Waveguide slot antennas for circularly polarized radiated field,” *IEEE Trans. Antennas Propag.*, vol. 52, n. 2, pp. 619–623, 2004.
- [5] G. Montisci, “Design of circularly polarized waveguide slot linear arrays,” *IEEE Trans. Antennas Propag.*, vol. 54, n. 10, pp. 3025–3029, 2006.
- [6] C. Balanis, *Advanced Engineering Electromagnetics*, John Wiley & Sons, 2013.

# A WIDEBAND PHASED ARRAY

C. Novi<sup>(1)</sup>, M. Righini<sup>(2)</sup>

<sup>(1)</sup> Antennas and EMC Development Unit  
Research and Development Department, Rheinmetall Italia S.p.A.  
Via Affile, 102, 00131 Rome Italy  
C.Novi@rheinmetall.it

<sup>(2)</sup> Department of Information Engineering, University of Florence  
Via di S. Marta, 50139 Florence, Italy  
monica.righini@unifi.it

## Abstract

*A broadband linearly polarized phased array comprising 16 radiating elements is presented. The system is designed to work on a 13 % bandwidth centered at 3.1 GHz, therefore the single elements is based on the multilayer architecture. Since compactness and lightweight are a requirement, a low dielectric constant layer, either air or rohacell has been used. Actually, this layer allows both the reduction of the structure weight and the large bandwidth. Measurements show an active reflection coefficient lower than -10 dB over a 13 % of bandwidth.*

**Index Terms** – wideband antenna, phased array, liner polarization array, multilayer architecture.

## I. INTRODUCTION

In many of the most important modern applications, like communication, radar and surveillance systems the Electronically Scanned Array (ESA) architecture has gained popularity.

This kind of antenna takes advantage of a large number of elements, which are appropriately fed and placed, in order to generate a steerable and reconfigurable pattern.

If a broadband is a requirement, Vivaldi antennas could be a choice as an element. Anyway, it is bulky, prone to high mutual coupling, and difficult to pack close enough to have wide steering angles. Hence a multilayer patch antenna becomes an attractive choice even if a thicker antenna heavier than a single patch, and weight is usually required to be low as possible, [1]-[3].

On the basis of the above considerations, the aim of this paper is to design a 4x4 linearly polarized phased array breadboard, working on a 13 % bandwidth at 3.1 GHz with reduced weight.

This paper is organized as follows: Section II shows the architecture of the designed structure while in Section III the comparison between simulated and measurements result are presented.

## II. PHASED ARRAY ARCHITECTURE

The designed antenna is a multilayer 4x4 rectangular patch array composed of two RO4350B ( $\epsilon_r=3.66$ ,  $\tan \delta=0.031$ ) layers in air, spaced by calibrated nylon hoses since their influence on the electromagnetic performances is negligible.

The choice of a multilayer architecture allows to obtain a wideband behavior, as shown in the next section, moreover the use of a commonly available material allows to keep a low cost of manufacturing.

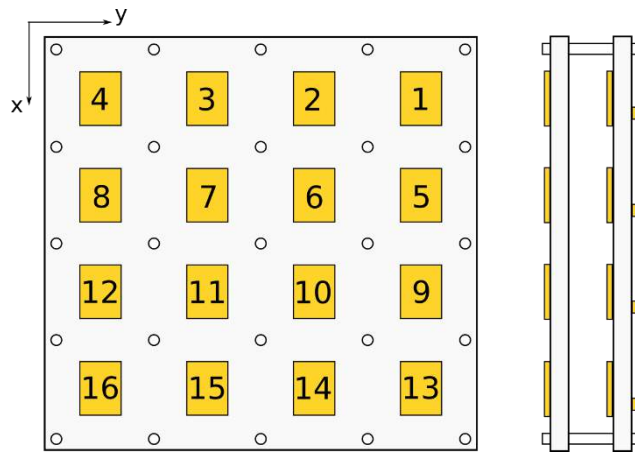


**Fig. 1** – Top and side view of the 4x4 rectangular patch phased array antenna.

The presence of an air layer, although it increases the size of patches and the thickness of the whole array, reduces the weight of the structure and contributes to the bandwidth increasing

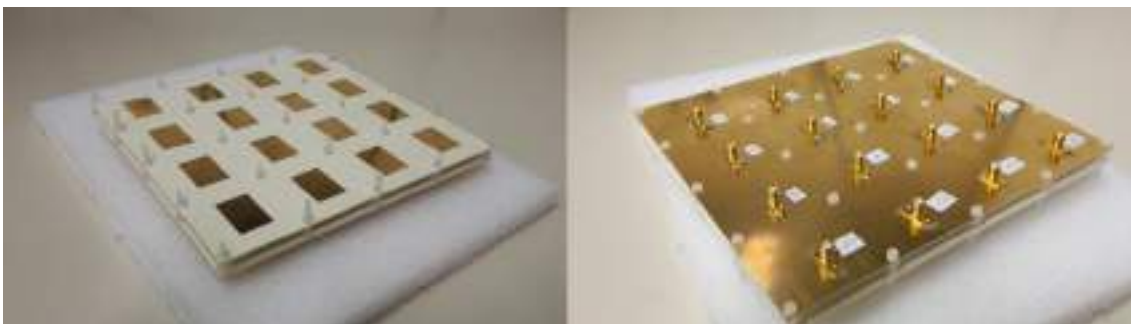


**Fig. 2** –Prototype of the designed antenna.

In order to allow the beam steering each element has its own feeding point, through which receives the prescribed amplitude and phase. As a

consequence, 16 standard 50- $\Omega$  SMA connector has been used as is shown in Fig. 2, where the top and the bottom view of the array prototype are presented.

### III. COMPARISON BETWEEN MEASUREMENTS AND SIMULATION RESULTS

The measurements have been carried out in a semi-anechoic chamber, where the transmitter antenna, a single multilayer radiating element, has been fed by the HP 83621 signal generator, while the receiving 4x4 elements array has been connected to the HP 8510 B Network analyzer. A characterization of the antenna in terms of S-parameters has been carried out in order to check the bandwidth of antenna when the return loss is better than 10 dB.

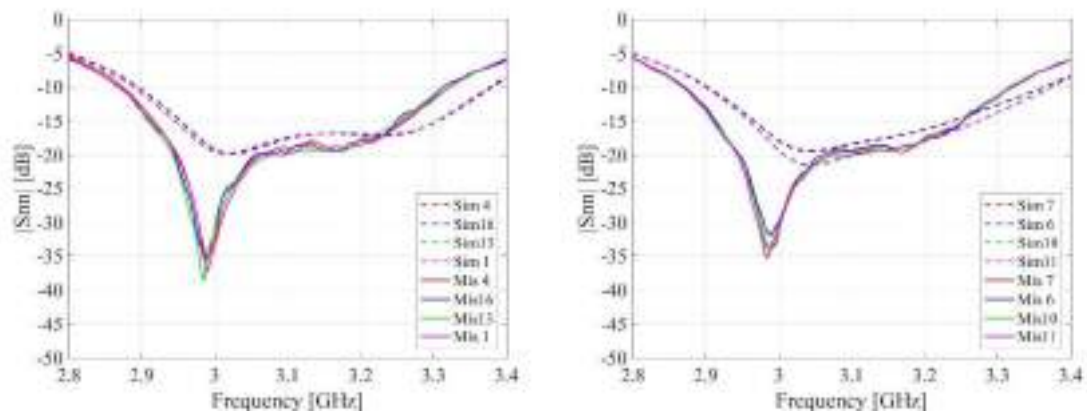


**Fig. 3** – Comparison on the reflection coefficient between measurements (solid lines) and simulations (dotted lines). On the left the results of the corner elements have been show, while on the right are presented the ones of the central elements.

Fig. 3 shows the comparison between the simulated and measured reflection coefficients at several ports. Considering the numeration in Fig. 1, the plot on the left presents the response of the four corner elements: 4, 1, 16 and 13 while the plot on the right presents the response of the four central elements: 7, 6, 11 and 10. Very good agreement is apparent, except for a slight shift towards lower frequencies in the measured results [4]. Despite the presence of the mutual coupling, which degrades the antenna performances, the measured bandwidth for the worst case, that is for the central elements, is 13.1 %.

In addition, an analysis of the pattern has been carried out, both at broadside ( $\theta=0$ ) and at  $\theta=30^\circ$  pointing. Comparison between simulated and measured results are presented in Fig. 4. As it is shown measured results matches very well the simulated ones, especially close to the direction of maximum radiation. The larger error on the side and back lobes is due to multipath effects occurring in the semi-anechoic chamber.

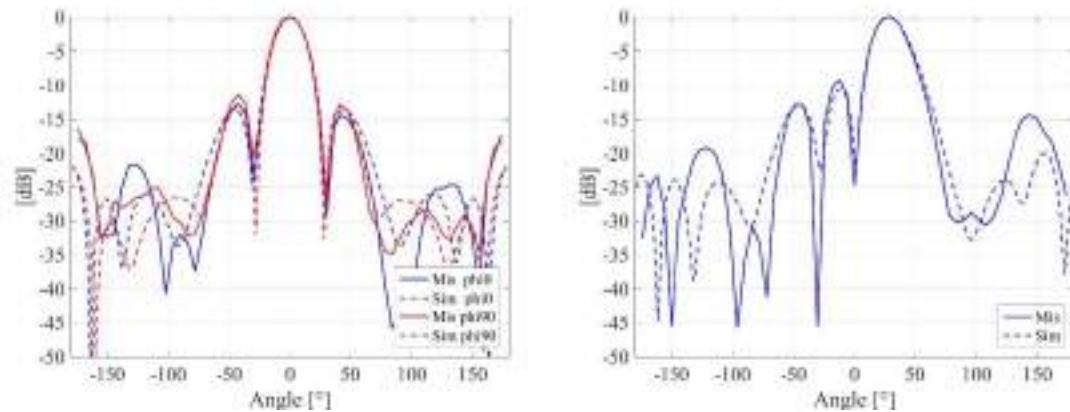


**Fig. 3** – Comparison between the array pattern at  $\theta=0$  (left) on both the E-plane (blue lines) and the H-plane (red lines) at 3.1 GHz and at  $\theta=30^\circ$  only on the E-plane, containing the direction of maximum radiation (blue lines). On both graphs dotted lines represent simulations results while the solid lines represent measured data.

#### IV. CONCLUSION

A wideband linearly polarized phased array comprising 16 multilayer rectangular patches has been proposed. Thanks to their architecture the structure presents a broadband behavior and a weight reduction. The measured results confirm behavior predicted by the simulations, and a return loss better than 10 dB over a 13.1 % bandwidth at 3.1 GHz for the worst case. Furthermore, an analysis of the patterns has been carried out, both at broadside and at a squint angle.

#### REFERENCES

- [1] Y. Yang, Y. Wang and A. E. Fathy, “Design of compact Vivaldi antenna arrays for UWB see through all applications,” *Progress in Electromagnetic Research, PIER* 82, pp. 401-418, Feb. 2008.
- [2] P. Capece, L. Lucci, G. Pelosi, M. Porfilio, M. Righini and W. Steffè “A multilayer PCB dual-polarized radiating element for future radar applications,” *IEEE Antennas and Propagation Letters*, 2014, pp. 297-300.
- [3] P. Capece, L. Lucci, G. Pelosi, M. Porfilio, M. Righini and W. Steffè “A fully integrated multilayer power distribution network for SAR dual-polarized linear arrays,” *IEEE Microwaves and Wireless Components Letters*, 2014, pp. 760-762.
- [4] G. Giunta, C. Novi, S. Maddio, G. Pelosi, M. Righini and S. Selleri, “Efficient tolerance analysis on low cost, compact size, wideband multilayer patch antenna,” *Antennas and Propagation & USNC/URSI National Radio Science Meeting, 2017 IEEE International Symposium on*, 2017, pp. 2113-2114.

## DESIGN OF CRYOGENIC PHASED ARRAY FEED FOR 4-8 GHz

A. Navarrini<sup>(1)</sup>, J. Monari<sup>(2)</sup>, A. Scalambra<sup>(2)</sup>, A. Melis<sup>(1)</sup>, R. Concu<sup>(1)</sup>, G. Naldi<sup>(2)</sup>, A. Maccaferri<sup>(2)</sup>, A. Cattani<sup>(2)</sup>, P. Ortu<sup>(1)</sup>, J. Roda<sup>(2)</sup>, F. Perini<sup>(2)</sup>, G. Comoretto<sup>(3)</sup>, M. Morsiani<sup>(2)</sup>, A. Ladu<sup>(1)</sup>, S. Rusticelli<sup>(2)</sup>, A. Mattana<sup>(2)</sup>, P. Marongiu<sup>(1)</sup>, A. Saba<sup>(1)</sup>, M. Schiaffino<sup>(2)</sup>, E. Carretti<sup>(2)</sup>, F. Schillirò<sup>(4)</sup>, E. Urru<sup>(1)</sup>, G. Pupillo<sup>(2)</sup>, M. Poloni<sup>(2)</sup>, T. Pisanu<sup>(1)</sup>, R. Nesti<sup>(3)</sup>, G. Muntoni<sup>(1)</sup>, K. Zarb Adami<sup>(5,6)</sup>, A. Magro<sup>(5)</sup>, R. Chiello<sup>(6)</sup>, L. Liu<sup>(6)</sup>, K. Grainge<sup>(7)</sup>, M. Keith<sup>(7)</sup>, M. Pantaleev<sup>(8)</sup>, W. van Cappellen<sup>(9)</sup>

<sup>(1)</sup> INAF-Osservatorio Astronomico di Cagliari, via della Scienza 5, Selargius, Italy, [alessandro.navarrini@inaf.it](mailto:alessandro.navarrini@inaf.it)

<sup>(2)</sup> INAF-Istituto di Radioastronomia, Bologna, Italy

<sup>(3)</sup> INAF-Osservatorio Astrofisico di Arcetri, Florence, Italy

<sup>(4)</sup> INAF-Osservatorio Astrofisico di Catania, Catania, Italy

<sup>(5)</sup> University of Malta, Malta

<sup>(6)</sup> University of Oxford, Department of Physics, UK

<sup>(7)</sup> University of Manchester, Jodrell Bank Observatory, UK

<sup>(8)</sup> Onsala Space Observatory, Chalmers, Sweden

<sup>(9)</sup> ASTRON, Dwingeloo, The Netherlands

### Abstract

*We describe the design and architecture of PHAROS2, a cryogenically cooled 4-8 GHz Phased Array Feed (PAF) demonstrator with digital beamformer for radio astronomy application. The instrument will be capable of synthesizing four independent single-polarization beams by combining 24 active elements of an array of Vivaldi antennas.*

*PHAROS2, the upgrade of PHAROS (PHased Arrays for Reflector Observing Systems), features: a) commercial cryogenic LNAs with state-of-the-art performance, b) a “Warm Section” for signal filtering, conditioning and single downconversion to select a  $\approx 275$  MHz Intermediate Frequency (IF) bandwidth within the 4-8 GHz Radio Frequency (RF) band, c) an IF signal transportation by analog WDM (Wavelength Division Multiplexing) fiber-optic link, and d) a FPGA-based Italian Tile Processing Module (iTPM) digital backend.*

**Index Terms** – Antennas, digital backend, down-conversion, Phased Array Feed (PAF).

### I. PHASED ARRAY FEEDS

Phased Array Feeds (PAFs) are a key technology enabling the next major advancement in radio astronomy. In contrast to multi feeds, the elements of a PAF are densely packed ( $\approx 0.5 \lambda$  at the highest design frequency) and combined in weighted sums to form multiple independent beams. The beams and the antenna properties resulting from a PAF equipped with a digital beamformer can be optimized, using frequency-dependent weights, for each of the backend frequency channels (of order  $\approx 1$  MHz) leading to high antenna aperture efficiencies and low spillover losses for

all the synthesized beams over the entire band. The flexibility of a PAF allows achieving a complete coverage of the available radio telescope Field of View (FoV,) thus increasing the survey speed if compared to a single-pixel feed.

## II. PHAROS PHASED ARRAY FEED

PHAROS is a C-band cryogenically cooled low noise PAF with analogue beamformer designed to operate at the focus of a large single-dish radio telescope. Figures 1 and 2 show respectively, a schematic system diagram of PHAROS and a more detailed block diagram of the front-end. Views of the PHAROS PAF and of the dome-shaped vacuum window with array of antennas are shown in Fig. 3. A description of the instrument can be found in [1, 2]. PHAROS consists of a 220-element Vivaldi array cooled at  $\approx 20$  K along with 24 low noise amplifiers (LNAs) mounted behind the antenna elements. The LNAs are cascaded with low-loss low-thermal conduction RF connections to the analogue beam former designed to operate at  $\approx 77$  K. The RF signals of the active elements are distributed to the beam formers by passive splitters, while the non-active elements are terminated into  $50 \Omega$  loads. Four beam former modules are available inside the cryostat, each with 13 RF inputs and 13 individually controllable phase and amplitude control units (PACs), along with 13

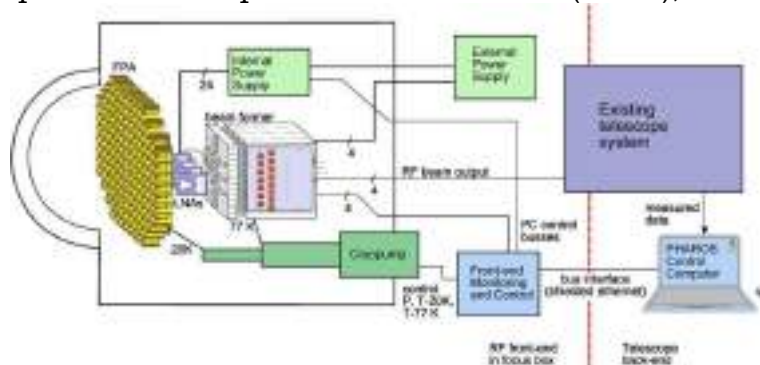


**FIG. 1** – PHAROS system diagram.

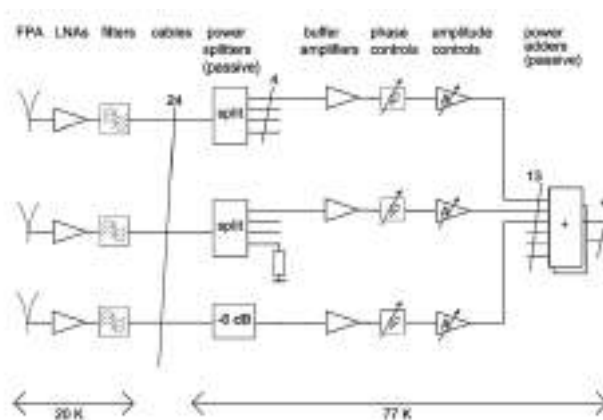


**FIG. 2** – PHAROS system diagram showing the analog beamformer components (including buffer amplifier, phase controls, amplitude controls and passive power adders).

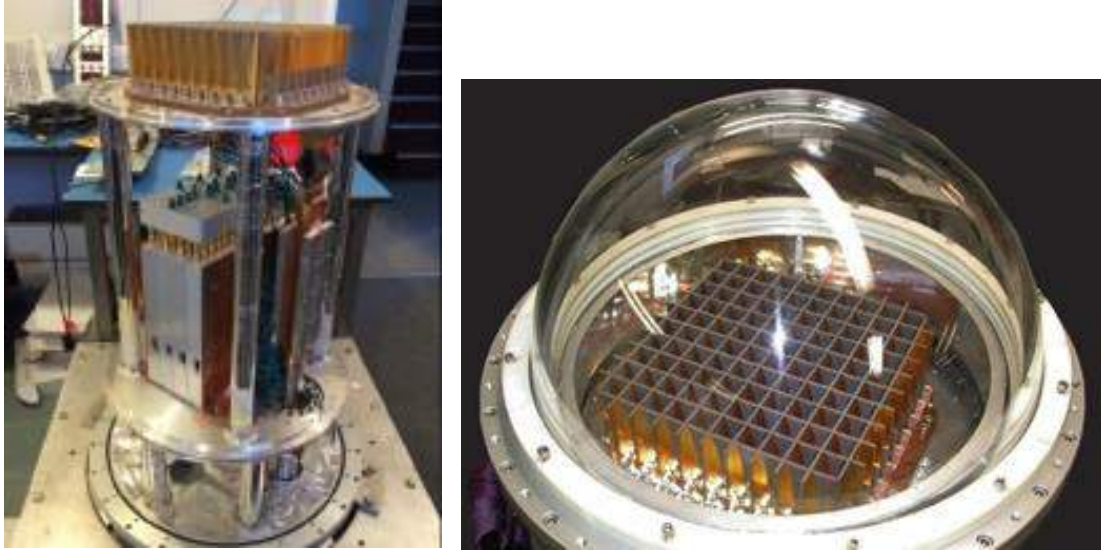


**FIG. 3** – View of PHAROS instrument: left) during assembly, right) showing half-dome vacuum window and array of Vivaldi antennas.

amplifiers to compensate for system losses. The last stage of the analogue beam forming system is a 16-way Wilkinson combiner (with three unused inputs). Each analog beam former controls the weights of the amplitude and of the phase from 13 antenna elements to produce a single (compound) one-polarization beam.

### III. PHAROS2

PHAROS is being upgraded to PHAROS2, a new PAF with digital beamformer. The latter re-uses part of the existing PHAROS hardware, including the cryostat and the array of Vivaldi antennas. PHAROS2 is under development in the framework of the SKA (Square Kilometer Array) PAF Advanced Instrumentation Program as a collaboration among the following institutions: the National Institute for Astrophysics (INAF, Italy), the Jodrell Bank Observatory (University of Manchester, UK), the Netherland Institute for Radio Astronomy (ASTRON, the Netherland), the Onsala Space Observatory (OSO, Sweden) and the University of Malta (Malta). In PHAROS2 a digital beamformer (at room temperature) replaces the four PHAROS analog beamformers.

The main PHAROS2 capability will be the possibility of digitally forming four independent beams on the sky using 24 antenna elements, each beam covering an instantaneous IF bandwidth of  $\approx 275$  MHz across 375-650 MHz [3]. We aim at completing and installing PHAROS2 on a large European single-dish radio telescope and carry out the technical validation of the instrument, including antenna efficiency optimization and multi-beaming scientific observations for demonstration of the adopted technologies that may find application in the SKA.

The architecture of PHAROS2 (see schematic layout in Fig. 3) consists of three main blocks: a) the “PHAROS2 cryostat,” to be equipped with new LNAs and possibly a new vacuum window; b) the “Warm Section,” to be

located in the primary focus receiver room, next to the cryostat; c) the “iTPM digital backend,” to be located in the backend room.

The Warm Section (WS) is connected to the digital backend through analog WDM fiber optic links allowing to transport two IF signals over a single fiber.

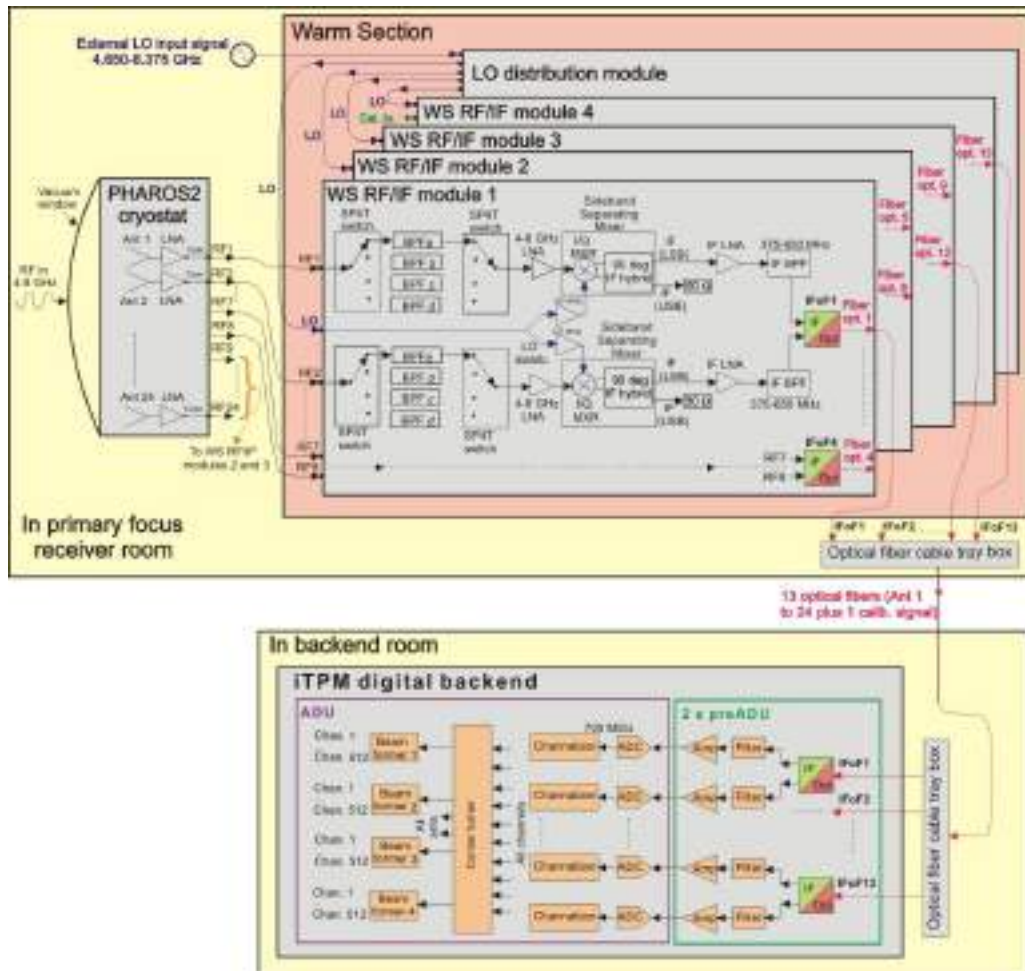


**FIG. 4** – Schematic diagram of PHAROS2.

## REFERENCES

- [1] J. Simons, J.G. Bij de Vaate, M.V. Ivashina, M. Zulliani, V. Natale, N. Roddis, “Design of a Focal Plane Array system at cryogenic temperatures,” Antennas and Propagation, EuCAP 2006, Nice, France, Nov. 2006.
- [2] L. Liu, K. Grainge, A. Navarrini, “Analysis of Vivaldi array antenna for phased array feeds application,” International Conference on NEMO, IEEE MTT-S, Sevilla, Spain, 17-19 May, 2017, doi 10.1109/NEMO.2017.7964244.
- [3] G. Naldi, G. Comoretto, R. Chiello, S. Pastore, A. Mattana, A. Melis, R. Concu, M. Alderighi, J. Monari, A. Navarrini, F. Schillirò, K. Zarb Adami, “Development of a digital signal processing platform for the Square Kilometre Array,” To be published in Proceedings of URSI-AT RASC Conference, Gran Canaria, Spain, May 28th-June 1st, 2018.

# DEVELOPMENT OF HIGH-FREQUENCY RADOMES FOR POLAR GROUND STATIONS

Andrea Martellosio<sup>1</sup>, Marco Pasian<sup>1</sup>,  
Filippo Concaro<sup>2</sup> and Luca Perregrini<sup>1</sup>

<sup>1</sup> Department of Electrical, Computer and Biomedical Engineering,  
University of Pavia  
andrea.martellosio01@universitadipavia.it  
marco.pasian@unipv.it  
luca.perregrini@unipv.it

<sup>2</sup> Department of Ground Systems Engineering, European Space  
Operations Center (ESOC),  
European Space Agency (ESA)  
filippo.concaro@esa.int

## Abstract

*At low frequencies, e.g., at S-band and X-band, the radome design for ground stations can be considered consolidated and a reasonable microwave transparency can be usually obtained with minimal compromises on the structure stiffness. Conversely, at high frequencies, e.g., at K-band and above, the two domains, electromagnetics and mechanics require a joint design to achieve best performance, especially when installations at environmentally extreme locations are required.*

*This paper discusses the design and performance of a multilayer radome for a 6.4-m ground station installed in Svalbard, at around 78° North, where the combination of high-speed winds and low temperature is particularly severe.*

**Index Terms** – Arctic regions, ground station, harsh environment, high frequency, induced field ratio, K band, Ka band, polar regions, multilayer radome, radome joint, radome panel, space frame radome.

## I. INTRODUCTION

Satellites for Earth Observation (EO) missions, possibly launched at Polar orbits, thus benefiting from ground stations at Polar latitudes able to exploit all satellite passes, have been traditionally designed to operate downlink channels at S band (around 2 GHz) and X band (around 8 GHz). New missions, e.g., the European Metop-SG from a cooperation between the European Space Agency (ESA) and the European Organisation for the Exploitation of Meteorological Satellites (EUMETSAT), and the American JPSS-1 from a cooperation between the National Aeronautics and Space Administration (NASA) and the National Oceanic, and Atmospheric Administration (NOAA), make use of higher frequencies, in particular the K band (around 26 GHz). Because of the Polar environment, the ground stations serving these missions practically always require a radome to protect the antenna against strong winds, low temperatures, and snow [1]. The most common

radome technologies suitable to protect medium-to-large reflector antennas are the multilayer (MLR), and the metal space frame (MSF) radomes, whose typical geometries are shown in Fig. 1, respectively [2]. This paper presents the design and performance of a MLR radome for a 6.4-m ground station installed in Svalbard, intended to provide adequate electromagnetic transparency from 25.5 GHz to 27 GHz, while operating at temperatures as low as around  $-45$  °C, and winds as strong as 200 km/h (surviving threshold 280 km/h), thus allowing to serve both JPSS-1 and Metop-SG.

## II. ENVIRONMENTAL AND MECHANICAL ASPECTS

A detailed environmental analysis of the installation site, shown in Fig. 1, based on the statistics recorded from on-site weather stations, spanning several years, is used to derive adequate specifications for the robustness of the radome. In particular, the minimum temperature is  $-46.3$  °C, the maximum wind gust is 277 km/h, and the maximum wind speed averaged over 10 minutes is 173 km/h. It is calculated that a radome able to operate against winds as strong as 200 km/h will provide a ground station availability better than 99.99%. In addition, a design based on a MLR approach can be tuned to provide a survival threshold of around 280 km/h without catastrophic failures (i.e., accepting panel distortions but avoiding a collapse over the antenna). Finally, a proper MLR outer coating can also provide an adequate protection against rain and snow, with minimum maintenance cost and effort.

## III. RADOME DESIGN

A MLR radome is composed by panels and joints, as shown in Fig. 2a. Panels usually comprises different layers of low- and high-dielectric constant materials, most typically foam and fiberglass, respectively (Fig. 2b). The panels are tapered at the sides to form a joint, usually reinforced by metal nuts. The effect of the panel is normally quantified using the scattering parameters at plane-wave incidence, while joints are evaluated using the Induced Field Ratio (IFR) [3].



**Fig. 1.** Aerial view of the communication complex (SvalSat), located in Svalbard at a latitude of around  $78^\circ$  N (credits of KSAT).

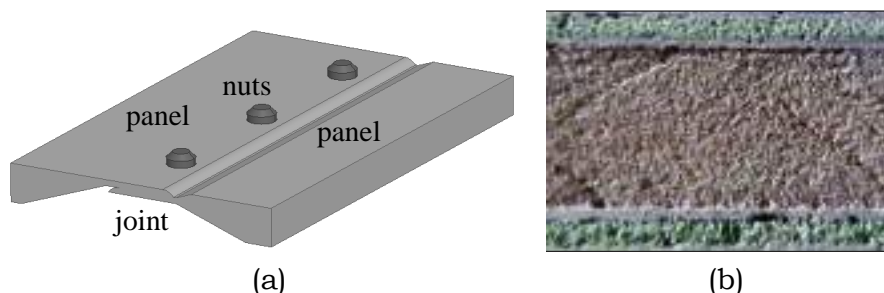


**Fig. 2.** MLR radome: (a) schematic view; (b) magnified side view of a panel.

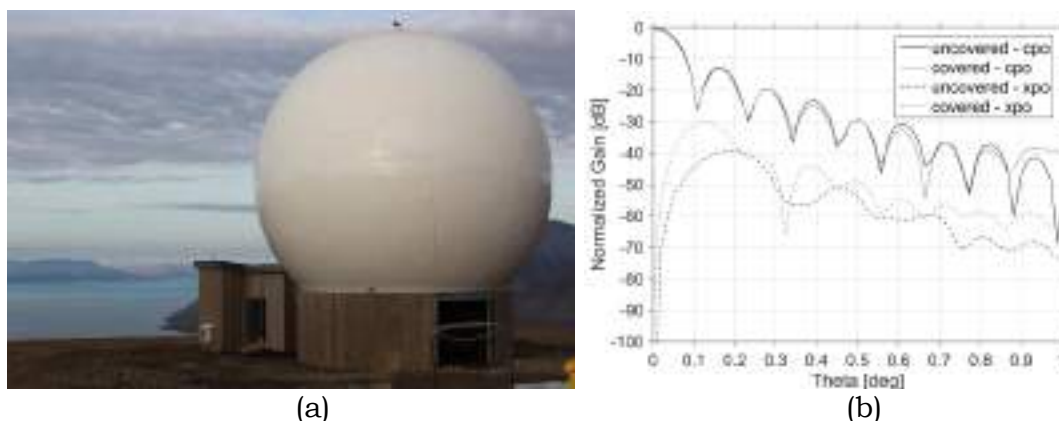


**Fig. 3.** (a) Photograph of the ground station; (b) simulated normalized radiation patterns for an antenna elevation of 90 degrees, comparison between with (covered) and without (uncovered) radome, for both the co-polar (cpo) and the cross-polar (xpo) component.

However, for brevity and to show the overall impact on the antenna performance, the entire ground station (Fig. 3a), with and without radome, is modelled using Tiera GRASP, and the changes on the radiation patterns are calculated. An example is shown in Fig. 3b, and it can be appreciated that the impact can be considered modest.

The key point for achieving a good transparency, while maintaining the mechanical robustness required to withstand the condition outlined in Sec. II, is to provide a panel layering comprising two outer half-wavelength stratifications, divided by an inner low-loss foam. This way, the thickness of the inner layer, strongly influencing the mechanical robustness, can be determined with minimum constraints on the electromagnetic design. At the same time, it is also vital to minimize the overall joint length, a factor where MLR radomes normally performs very well due to the large size of the panels.

#### IV. MLR HYDROPHOBICITY

The MLR radome is provided with an outer finishing, called gelcoat, able to provide an adequate hydrophobic response, with minimum (virtually no) maintenance. In particular, the hydrophobicity is measured calculating experimentally the contact angle of a water drop, using the optical device shown in Fig. 4.

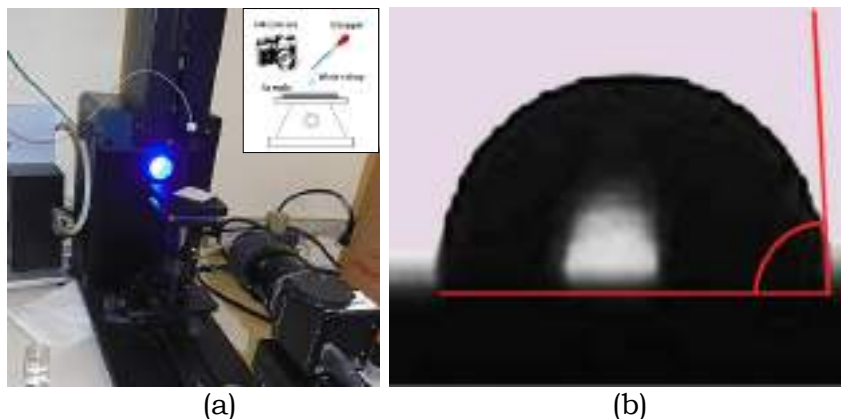


**Fig. 4.** Hydrophobicity measurements: (a) experimental setup; (b) magnified view of a water drop, contact angle highlighted by the red lines.

The mean value is 91 degrees, with a standard deviation of 2 degrees. Therefore, this type of gelcoat provides a stable contact angle exceeding the hydrophobicity threshold, i.e., 90 degrees. It is pointed out that other special finishing can provide even higher contact angle (a proprietary treatment returned a mean value of 107 degrees), but normally these treatments have a limited life, in the order of 6-to-12 months, thus requiring periodic (and costly) maintenance.

## V. CONCLUSION

This paper presented some of the most important aspects related to the design and manufacturing of a radome for Polar ground stations, working at K band. The radome covers a 6.4-m reflector antenna, and a compromise between environmental, mechanical, electromagnetic, and maintenance specification is taken into account.

It is pointed out that MLR radome can provide an optimized response to this compromise. The radome was installed in Summer/Autumn 2017 in Svalbard, and start working with the satellite JPSS in Spring 2018.

## ACKNOWLEDGEMENTS

The authors would like to thank FDS Italy and KSAT.

## REFERENCES

- [1] D. J. Kozakoff, *Analysis of radome-enclosed antennas*, Second edition, Artech House, Norwood, U.S.A., 2010.
- [2] A. Martellosio *et al.*, "High-frequency radomes for polar region ground station," *IEEE Antennas and Propagation Magazine*, Vol. 59, No. 6, pp. 88-101, December 2017.
- [3] W. Rusch, J. Appel-Hansen, C. Klein, and R. Mittra, "Forward scattering from square cylinders in the resonance region with application to aperture blockage," *IEEE Transactions on Antennas and Propagation*, Vol. 24, No. 2, pp. 182-189, February 1976.

# ANALYSIS OF INHOMOGENEOUS WAVEGUIDE COMPONENTS BY THE BI-RME METHOD

S. Battistutta, M. Bozzi, M. Bressan, L. Perregrini

Department of Electrical, Computer and Biomedical Engineering  
University of Pavia, Pavia, Italy

## Abstract

*This paper presents the application of the generalized Boundary Integral-Resonant Mode Expansion (BI-RME) method to the analysis of arbitrarily-shaped waveguide components. The proposed algorithm is based on the segmentation and recombination technique, which permits to divide the component into homogeneously filled building blocks. Each block is analysed by the BI-RME method through the formulation of an integral equation converted into a linear eigenvalue problem, whose solution leads to the determination of a generalized admittance matrix (GAM). By cascading the GAMs, the frequency response of the whole component is finally obtained. Two examples demonstrate the capabilities of the proposed algorithm.*

**Index Terms** – BI-RME method, Segmentation technique.

## I. INTRODUCTION

Even if the general-purpose numerical methods, such as the Finite Element Method (FEM) and the Finite Difference Time Domain (FDTD) methods, offer high flexibility, they typically require long computational times and large memory allocation [1]. The combination of the specialized algorithms with the segmentation technique are sometime preferred to reduce the computational burden especially in case of waveguide components filled with piecewise homogeneous materials. The numerical algorithm proposed in this paper adopts an approach similar to [2], but without using a mode-matching technique to combine the electromagnetic modal field representation of each building block (BB). In particular, simple Rao Wilton Glisson (RWG) basis functions [3] are used to represent the unknown electric and magnetic surface currents on the interconnecting surfaces between blocks, thus avoiding the limitation to use only some simple canonical shapes for the interconnecting surfaces. The component is preliminary segmented into homogeneously filled building blocks, and each block is analysed with the Boundary Integral-Resonant Mode Expansion (BI-RME) method in conjunction with the Ewald technique [4]. In fact, the Electric-Field Integral Equation (EFIE) resulting by imposing the appropriate boundary conditions is solved by exploiting the BI-RME representation of the Green's functions [5]. This method leads to a wide-band and material independent generalized admittance matrix (GAM) for each BB, then cascaded in the frequency domain to retrieve the response of the whole component [6]. The analysis of two complex waveguide components demonstrates the effectiveness of the proposed algorithm.

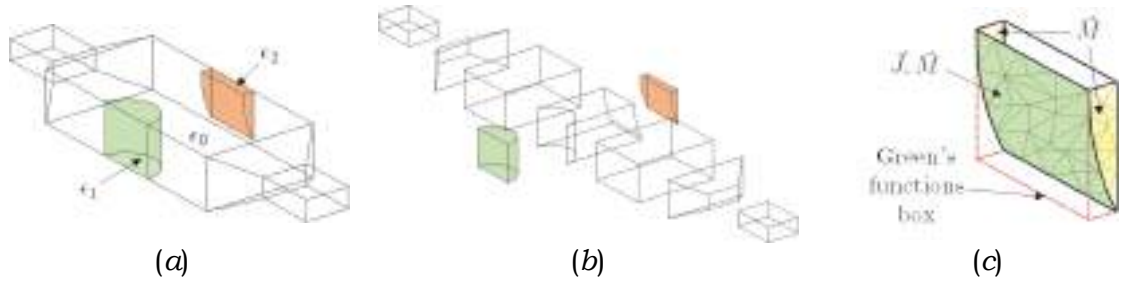


**FIG. 1** - Generalized BI-RME approach for the analysis of inhomogeneous waveguide components: (a) Whole component; (b) Segmentation into homogeneous building blocks; (c) Arbitrarily shaped block enclosed in a box for the definition of the Green's functions.

## II. OUTLINE OF THE ALGORITHM

The waveguide component (Fig. 1a) is segmented into homogeneously filled building blocks (Fig. 1b). Each block is analysed by the BI-RME method, which provides its GAM representation. The GAM represents the relation between RWGs, defined on a triangular mesh on the interconnecting surfaces to represent the electric and magnetic unknown surface currents (Fig. 1c). To determine the GAM of an arbitrarily-shaped BB, an EFIE is formulated by imposing the electric wall condition on the BB surface. The electromagnetic field inside the block can be determined through the Green's integrals which link the effect of electric ( $\mathbf{J}$ ) and magnetic ( $\mathbf{M}$ ) surface currents on volume surface  $S_V$ . Subsequently, each block is closed into a fictitious external cavity resonator with a boxed shape (Fig. 1c) and the particular BI-RME representation of the Green's functions [4] is exploited to represent each function as the sum of a frequency-independent quasi-static Green's function of the box, and a modal correction term. Aiming at the calculation of the admittance matrix, the electric wall boundary condition must be enforced on the whole surface  $S_V$  to determine the unknown currents  $\mathbf{J}$  for a given surface excitation  $\mathbf{M}$ . The resulting EFIE is solved by the Method of Moments discretizing the surface  $S_V$  by using triangular patches, and representing the surface currents as sum of RWG basis functions. After some manipulations, the integral equation is converted into a linear eigenvalue problem and its solution leads to a wideband representation of the GAM. It is worth noting that the surface currents are not defined on the whole surface  $S_V$ . In particular,  $\mathbf{J}$  is not defined on the part of  $S_V$  coincident with the cavity walls, since the electric wall condition is automatically satisfied on them. On the other hand, the magnetic current  $\mathbf{M}$  (which represent the excitation of the BB at the interconnecting surfaces) is not defined on the part of  $S_V$  bounded by a metallic surface. In case of boxed-shaped blocks, since this is the same shape of the external cavity, it is not necessary to enforce the boundary condition. Therefore, the GAM terms are simply obtained as the projection of the Green's functions on the basis functions representing the surface magnetic current  $\mathbf{M}$  [6]. Once the GAMs of all

the BBs (either arbitrarily shaped or boxed shaped) are calculated, the overall frequency response is obtained by cascading them along the lines discussed in [4]. More details about the theory and implementation of the method can be found in [4]-[6].

## I. VALIDATION EXAMPLES

**Example 1** - A WR90 Riblet junction with compensation metallic post [7] is analysed to validate the proposed algorithm (Fig. 2a). For the BI-RME analysis, the structure was segmented into twenty-two BBs. The number of electric and magnetic basis functions required for the analysis of all the BBs varied from 88 to 375 and from 248 to 1046, respectively. The computed scattering parameters are shown in (Fig. 2c-d): in all cases, the agreement with HFSS simulation is fairly good.

**Example 2** - The second example is a four-pole dielectric-loaded filter [8] (Fig. 3a). For the BI-RME analysis, the structure was segmented into thirteen BBs. In this case, more basis functions were necessary due to the high dielectric constant of the cylindrical resonators ( $\epsilon_r = 50$ ). Both the passband and the wideband responses are in good agreement with HFSS simulation and with the data taken from [8], where a specialized method was used.

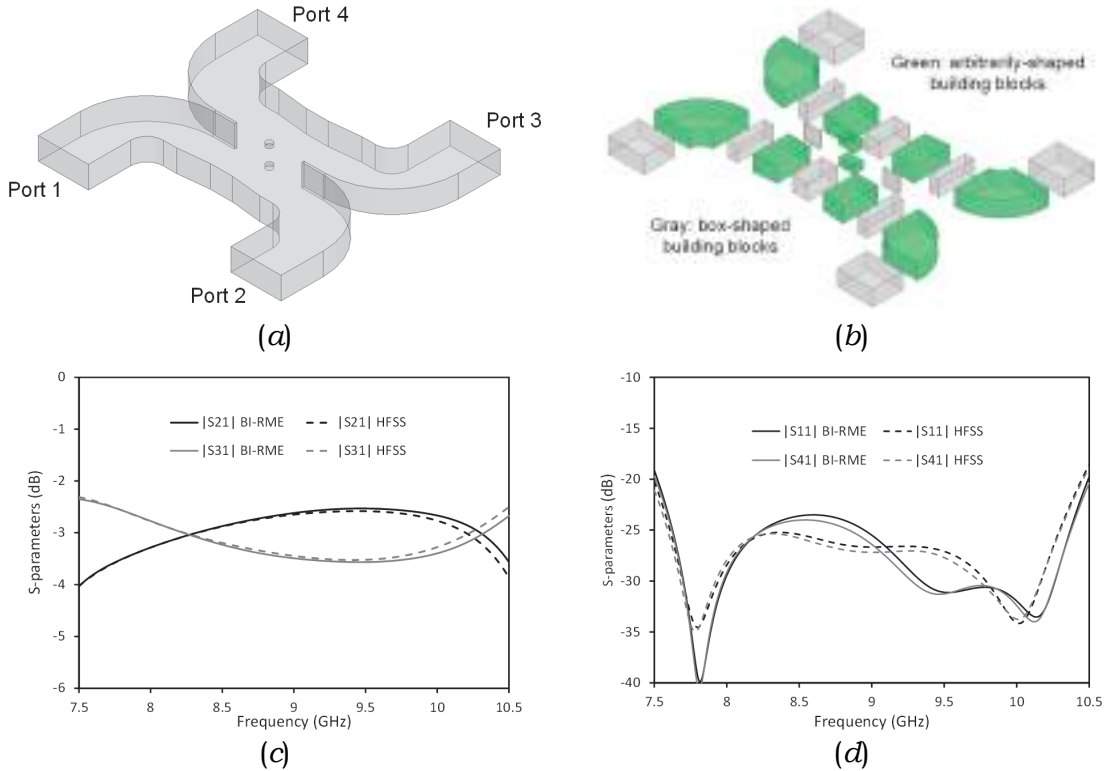


**FIG. 2** - A WR90 Riblet coupler with compensating capacitive posts: (a) Whole structure; (b) Segmented structure. Calculated frequency response compared with the HFSS simulation: (a) Coupling coefficients; (b) Matching and isolation.

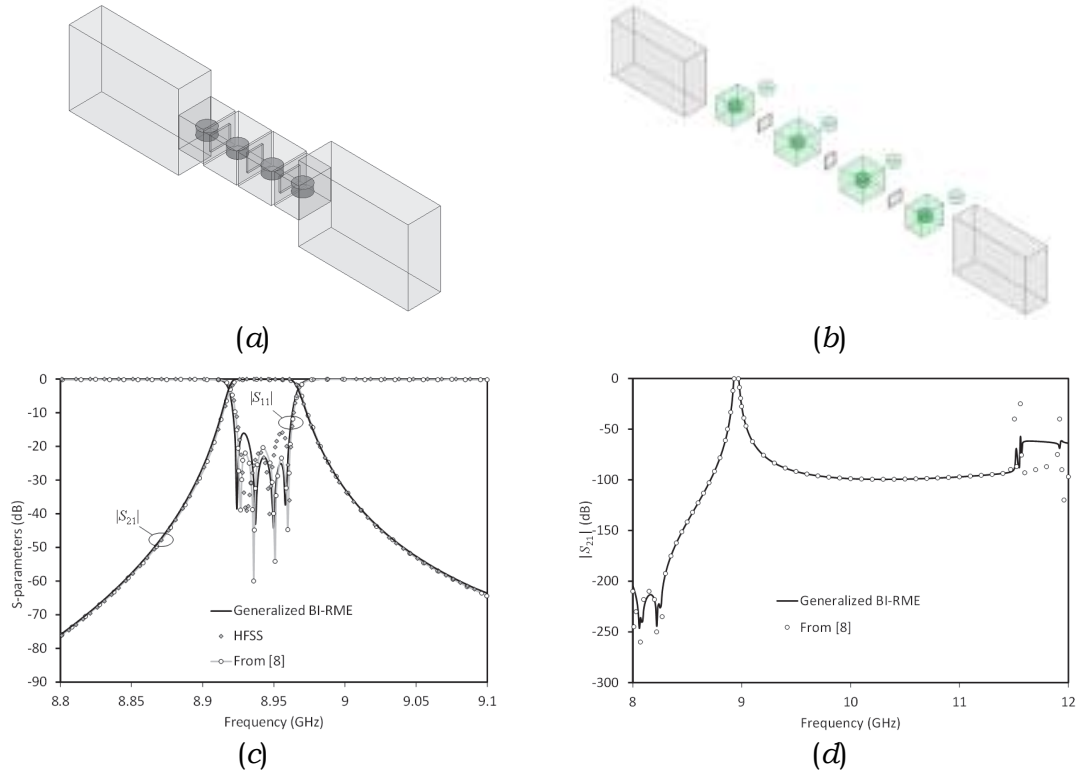


**FIG. 3** - Four-pole dielectric-loaded filter: (a) Whole structure; (b) Segmented structure. Calculated frequency response compared with the HFSS simulation and with the data taken from [8]: (a) Passband; (b) Wideband.

## II. REFERENCES

- [1] D.G. Swanson and W.J.R. Hofer, *Microwave Circuit Modeling Using Electromagnetic Field Simulation*, Artech House, Norwood (MA), 2003.
- [2] F. Alessandri *et al.*, "A technique for the fullwave automatic synthesis of waveguide components: application to fixed phase shifters," *IEEE Trans. Microw. Theory Techn.*, Vol. 40, No. 7, pp. 1484-1495, Jul. 1992.
- [3] S.M. Rao *et al.*, "Electromagnetic scattering by surfaces of arbitrary shape," *IEEE Trans. Antennas Propag.*, Vol. 30, No. 3, pp. 409-418, May 1982.
- [4] M. Bressan *et al.*, "Modeling of Inhomogeneous and Lossy Waveguide Components by the Segmentation Technique Combined with the Calculation of the Green's Function by the Ewald's Method," *IEEE Trans. Microw. Theory Techn.*, Vol. 66, No. 2, pp. 633-642, Feb. 2018.
- [5] S. Battistutta *et al.*, "Extension of the BI-RME Method to the Analysis of Piecewise-Homogeneous Waveguide Components Including Arbitrarily Shaped Building Blocks," *EuMC2017*, Oct. 8-13, 2017.
- [6] S. Battistutta *et al.*, "Modeling of Waveguide Components by the BI-RME Method with the Ewald Green's Function and the Segmentation Technique," *IMS2016*, May 22 - 27, 2016.
- [7] A. A. Sarhan *et al.*, "Optimized Broad Band Riblet Short-Slot Waveguide Coupler for X-Band Applications," *Int. J. Scientific & Eng. Research*, Vol. 4, No. 8, Aug.-2013.
- [8] J. Gil *et al.*, "Full-Wave Analysis and Design of Dielectric-Loaded Waveguide Filters Using a State-Space Integral-Equation Method," *IEEE Trans. Microw. Theory Techn.*, Vol. 57, No. 1, pp. 109-120, Jan. 2009.

# CLOSED-TO-OPEN CROSS-SECTION CONVERSION OF MM-WAVE DEVICES BY MEANS OF THE MODE MATCHING THEORY

G. Torrisi <sup>(1)</sup>, G. Castorina <sup>(2)</sup>

<sup>(1)</sup> Istituto Nazionale di Fisica Nucleare - Laboratori Nazionali del Sud, Via S. Sofia 62, Catania, Italy.

<sup>(2)</sup> Università degli Studi di Roma La Sapienza, Dip. SBAI – Via Antonio Scarpa 14, Roma, Italy.

giuseppe.torrisi@lns.infn.it

## Abstract

*This paper presents an application of the powerful field modal expansion theory, to derive a mm-wave “open” cross-section Gaussian horn antenna starting from a standard closed cross section design. The proposed approach is based on the expansion of the open-structure field in the orthonormal basis of the closed structure. The calculation of an inner product between the closed- and open-structures electromagnetic modes (commonly known as “overlap” integral) allows to mathematically evaluate the error introduced in the open structure and the quality of the mode matching in the obtained structure. The proposed methodology has been successfully tested by comparing FDTD simulation results between the closed and the open mm-wave  $TE_{11}$ -Gaussian converter.*

**Index Terms** – antenna, propagation, measurement, gap waveguide.

## I. INTRODUCTION AND MOTIVATION

Waveguide devices at millimeter wavelength are of increasing interest in many applications. At frequencies above 100 GHz, the typical structure dimensions (in the millimeter or submillimeter range) make the manufacturing very difficult and expensive. In fact, due to the small size of the waveguides, the usual fabrication technique based on joining or brazing two or several parts, results in several drawbacks such as: increase of losses, local modification of metal/copper properties, increased breakdown probability and reduced power handling capacity. An attempt to overcome metal joint is represented by the gap waveguide technology [1] based on the band gap of a PEC and PMC surfaces facing each other at a distance smaller than  $\lambda/2$ . However, since PMC surfaces may be difficult to realize, two simple PEC metal plates separated by a distance smaller than  $\lambda/2$  can be adopted, in order to relax the fabrication difficulties. This configuration still maintains band gap properties only for electric field parallel to the plates [2].

In this work we study devices with an open cross section,  $S^{(o)}$  (see Fig. 1), made of two halves with an infinite lateral extension of the gap. In practice, the gap has a height,  $g < \lambda/2$ , and a finite lateral extension. Starting from a “well-functioning” closed  $TE_{11}$ -Gaussian horn converter, designed by the authors of ref. [3], we propose a very efficient method to

optimally convert the design into an equivalent open device having the same performances. The proposed method relies on the modal analysis of the device. In particular, we demonstrate that the fields of the open structure can be expanded in the orthogonal basis of the fields of the closed structures.

A hybrid “overlap” integral between modes of the closed and open structures is defined and computed to check if the new open structures still meet the specification of the closed ones.

The performances of the obtained open structure have been successfully verified by:

- evaluating the above-mentioned hybrid overlap integral;
- carrying out FDTD simulations in CST Microwave Studio [4], in order to compare the numerical reflection coefficient  $S_{11}$  of a closed and an open design. The simulated results demonstrate that we are able to optimally “open” the Gaussian horn antenna.

## II. OVERLAP COEFFICIENT DEFINITION

The proposed method is based on the fact that the generic closed cross-section structure can be represented by a proper discretization along the  $z$  axis as a cascade of junction. If only one polarization is used an appropriate modification of the closed cross sections into an open one, would allow to preserve similar the modal contents of the original closed design and the derived open one. This circumstance can be verified rigorously by solving 2D eigenvalue problems on the original closed cross section and on the new derived open cross section and introducing a metric to evaluate the distance between the modes supported by the two structures (without performing time consuming 3D simulations).

Assuming only the presence of the appropriate polarization, the field does not extend much in the open regions, where it exponentially decays. Therefore, it is possible to expand the field of the open transversal mode basis,  $e_m^o$ , (said hereinafter “pseudo-modes”), in the orthogonal closed basis  $e_m^c$  of the closed structure, where the superscript (c) and (o) stand for closed and open cross section, respectively (and viceversa). Provided that the perturbation is small, the coupling matrix of the step junctions of the closed and open devices are similar as well as the overall scattering parameters derived from the coupling matrix ( $[S]^{(o)} \approx [S]^{(c)}$ ); moreover, also the fields (mode profiles and relative amplitude) are preserved. In order to optimally derive an open design from the closed one, the gap needs to be cut in the wall such that its long dimension runs along the current line or along a region of the wall where the surface current  $\mathbf{J}_s$  is zero.

Moreover, the gap orientation has to be chosen with respect to the polarization of the modal vectors in the modal content. Finally, the gap size  $g$  (see Fig. 1), in analogy to the behavior observed in Non-Radiative (NR) waveguides [2], [10], has to be sensibly lower than  $\lambda/2$ .

An inner product can be defined as an overlap coefficient between the transversal modes of two different structures, namely the open structure

populated by the pseudo-modes  $e_{\mu t}^{(o)}$  and the closed structure with its unperturbed modal content  $e_{\nu t}^{(c)}$ :

$$C_p = e_{\mu t}^{(o)} \cdot e_{\mu t}^{(c)} > \int_{S=S^{(o)} \cap S^{(c)}} e_{\mu t}^{(o)} \cdot e_{\mu t}^{(c)*} dS \quad (1)$$

The notation underlines that, when the modes  $\mu$  and  $\nu$  are “similar” in the sense that the  $\mu$  mode is approximately equal to  $\nu$  mode, both are remapped as  $p$ . It is worth to note that the unity normalization of the transversal field vectors brings the values of Eq. (1) into the  $[0; 1]$  range: as the common sense suggests, if the two modes are actually identical, we obtain  $C_p=1$ , on the contrary  $C_p=0$  means complete “mode orthogonality”. Therefore, the  $C_p$  value is a metric to evaluate how much the two transverse modal fields  $e_{\mu t}^{(o)}$  and  $e_{\nu t}^{(c)}$  overlap each other. This two-dimensional “overlap” integral over the cross-section of the structure represents a useful and operative parameter that can be calculated by 2D simulations.

With the above remapping it can be demonstrated that  $C_p$  close to unit, for all the relevant modal content, will result in similar coupling matrix  $[W]^{(o)}$  and  $[W]^{(c)}$ .

The mode overlap integral-based design provides a simple methodology to “convert” a closed cross section design into an open one having same performances in terms of fields confinement and distribution.

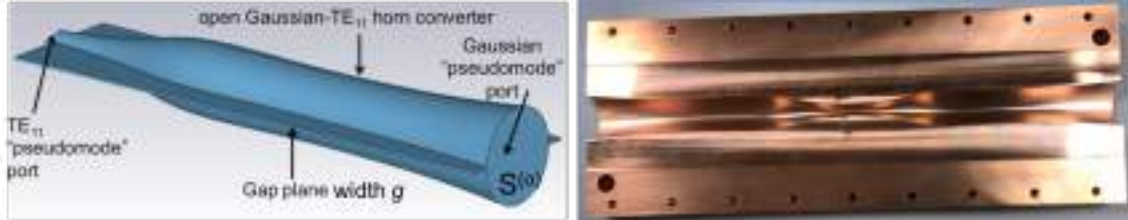


**FIG. 1** – Geometry of the (a) simulated and (b) one-half back-to-back manufactured by micro-milling Open Gaussian-TE11 horn converter.

### III. NUMERICAL RESULTS

In this section we test the proposed method combined with FDTD calculations on a Gaussian-TE<sub>11</sub> horn converter used for launching accelerating mode in RF LINACs cavities [3].

Our strategy consists of firstly following the guidelines explained in Sec. II to derive the gap in the geometry and obtain open structures with unaltered functionality. Then, we calculate the  $C_p$  integrals in order to quantitatively verify that the modal content of the obtained open structure is similar to the closed one. Finally, we compare the  $|S_{11}|$  on the horn aperture of the closed and the open structures obtained from FDTD simulations in CST Microwave Studio [4].

Starting from the closed structure, it is possible to derive the gap by inserting the “gap plane” between the two halves. Figure 1 shows the

resulting geometry of open Gaussian-TE<sub>11</sub> horn. In particular, we include a gap plane having a gap size  $g = 0.4 \text{ mm} \approx \lambda/15$ . For the TE<sub>11</sub>-Gaussian horn converter, considering that the relevant modal content is limited only to two modes, we computed the value of  $C_{TM_{11}}^{(o),(c)}$  and  $C_{TE_{11}}^{(o),(c)}$  for two representative sections of the step model: the section at the smallest radius  $r_{\min} = 1.5 \text{ mm}$  and at the largest one  $r_{\max} = 7.53 \text{ mm}$ . Being  $C_{TM_{11}}^{(o),(c)} \approx 1$  and  $C_{TE_{11}}^{(o),(c)} \approx 1$  in each section of the step model, we can assert that  $[W]^{(o)} \approx [W]^{(c)}$ . This demonstrates that the open structure still fulfills the same requirements of the closed one.

Full wave simulations confirm this. In Fig. 2 (a) it is possible to observe that the Electric field of the closed (bottom) and the open (top) Gaussian-TE<sub>11</sub> horn converter circular simulated in CST Microwave Studio, remains mostly unaltered, confirming that the opening cut is optimally operated. Figure 2 (b) shows the comparison between the simulated reflection coefficient  $|S_{11}|$  for the closed and open structure. The similar trend demonstrates that the obtained matching of the open is not destroyed by the presence of the gap.

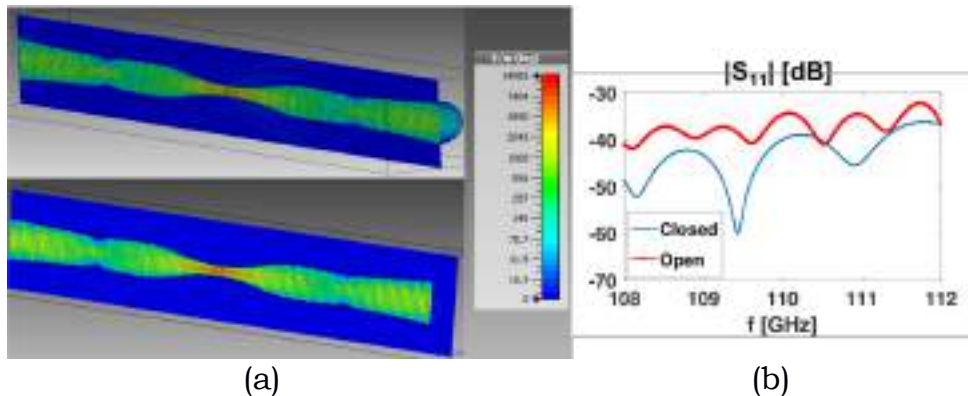


**FIG. 2** – a) CST Electric field of the closed (bottom) and open (top) back-2-back Gaussian-TE<sub>11</sub> mode converter (b) Reflection coefficient  $|S_{11}|$  (dB) for the open and closed Gaussian horn

## REFERENCES

- [1] P.-S. Kildal, E Alfonso, A Valero-Nogueira, and E. Rajo-Iglesias, “Local metamaterial-based waveguides in gaps between parallel metal plates,” *IEEE Antennas and Wireless Propagation Letters*, vol. 8, pp. 84–87, 2009.
- [2] T. Yoneyama and S. Nishida, “Nonradiative dielectric waveguide for millimeter-wave integrated circuits,” *IEEE Transactions on Microwave Theory and Techniques*, vol. 29, no. 11, pp. 1188–1192, 1981
- [3] E. Nanni, M. Dal Forno, V. Dolgashev, J. Neilson, S. Schaub, S. Tantawi, and R. Temkin, “mm-Wave Standing-Wave Accelerating Structures for High-Gradient Tests,” in *Proceedings, 7th International Particle Accelerator Conference (IPAC 2016): Busan, Korea, May 8-13, 2016*, 2016, THPOR044.
- [4] CST Microwave Studio. “3D EM simulation software.” *Computer Simulation Technology* (2017).

# AN APPROACH TO NUFFT OPTIMIZATION

Amedeo Capozzoli, Claudio Curcio, Angelo Liseno

Università di Napoli Federico II  
Dipartimento di Ingegneria Elettrica e delle Tecnologie  
dell'Informazione  
via Claudio 21, I 80125 Napoli (Italy)  
[a.capozzoli@unina.it](mailto:a.capozzoli@unina.it)

## Abstract

*We deal with an optimized approach for implementing Non-Uniform Fast Fourier Transform (NUFFT) algorithms under a general and new perspective for 1d transformations. A case study of electromagnetic interest is carried out by applying the developed NUFFT to the radiation of a linear irregular array onto a set of regular spectral points.*

**Index Terms** – Non-Uniform FFT, interpolation windows, Kahan summation formula, aperiodic arrays

## I. INTRODUCTION

Non-uniform Fourier transforms arise in many instances of applied electromagnetics [1, 2] to evaluate the “spectral” values corresponding to a given set of  $N$  sample data from/to non-uniform grids.

For uniform samplings, a standard Discrete Fourier Transform (DFT) relates the samples. In this case, the FFT algorithm takes  $O(M \log M)$  operations. On the contrary, when the sampling is non-uniform in at least one domain, the FFT does not apply anymore.

Algorithms overcoming this limitation [1, 2] are named Non-Uniform FFTs (NUFFT), which rely on interpolation schemes designed to represent the “non-uniformly sampled” exponentials by “uniformly sampled” ones, so that the standard FFT can be used on an oversampled grid and the  $O(M \log M)$  complexity can be restored. The literature approaches mainly differ in the choice of the interpolating windows, which governs the trade-off between accuracy and computational complexity and whose choice is critical in that the parameters enabling their correct usage may lead to a useless computational burden [3]. Here, we present a new approach for implementing a NUFFT algorithm using a general and new perspective to select the interpolation window for one-dimensional transformations. The attention is focused on the case of Non-Equispaced Data (NED) NUFFTs and the algorithm is applied to the radiation of a linear irregular array onto a set of regular spectral points. Here, some aspects of the approach are presented. The details can be found in [1].

## II. THE NON-EQUISPACED DATA (NED) NUFFT PROBLEM

The NED Non-Uniform DFT (NUDFT) of samples  $\{z_l\}_{l=1}^M$ , located at non-equispaced points  $\{x_l\}_{l=1}^M$  and evaluated on an equispaced grid, is defined as

$$\hat{z}_k = \sum_{l=1}^M z_l e^{-j2\pi x_l \frac{k}{N}}, k = -\frac{N}{2}, \dots, \frac{N}{2} - 1 \quad (1)$$

To guarantee fast and accurate processing, the “non-uniformly sampled” exponentials  $e^{-j2\pi x_l \frac{k}{N}}$ , appearing in Eq. (1), require to be properly interpolated. The idea behind NUFFTs is to use “uniformly sampled” exponentials  $e^{jm\xi}$  [1, 2] which is made possible by using the Poisson summation formula [1] leading to

$$e^{-jx\xi} = \frac{(2\pi)^{-1/2}}{\varphi(\xi)} \sum_{m \in \mathbb{Z}} \hat{\varphi}(x - m) e^{-jm\xi}, |\xi| \leq \pi/c \quad \forall x \in \mathbb{R} \quad (2)$$

where  $\varphi(\xi)$  is a window having compact support  $(-\pi/c, \pi/c)$ ,  $c$  is an oversampling factor and  $\hat{\varphi}(x)$  is its Fourier transform. To be of interest in a NUFFT implementation,  $\hat{\varphi}$  must be essentially bounded to  $[-K, K]$ , so as to ensure a finite summation in eq. (2).

### III. REPRESENTATION OF THE WINDOW FUNCTION AND ITS OPTIMIZATION

For fixed values of  $K$  and  $c$ , the determination of  $\varphi$  “minimizing” the representation error of  $e^{-j\xi x}$  in Eq. (2) when a finite summation is considered is now in order. Since  $\varphi$  must be compactly supported and  $\hat{\varphi}$  must be essentially compactly supported in  $[-K, K]$ ,  $\varphi$  must belong to the space spanned by the Prolate Spheroidal Wave Functions (PSWFs) corresponding to the singular values of the Fourier transform operator before the “knee” [3]. The expansion coefficients  $\underline{\gamma}$  onto the PSWFs are determined to optimize the error functional

$$\Gamma(\underline{\gamma}) = \int_{-x_M}^{x_M} \int_{-\frac{\pi}{c}}^{\frac{\pi}{c}} d\xi dx \left| e^{-jx\xi} - \frac{\sqrt{2\pi}}{\varphi(\xi; \underline{\gamma})} \sum_{|m| \leq K} \hat{\varphi}(x - (\lfloor x \rfloor + m); \underline{\gamma}) e^{-j(\lfloor x \rfloor + m)\xi} \right|, \quad (3)$$

### IV. THE NED-NUFFT ALGORITHM

Using Eq. (2), Eq. (1) becomes

$$\hat{z}_k = \underbrace{\frac{(2\pi)^{-1/2}}{\varphi\left(\frac{2\pi k}{cN}\right)} \sum_{i=-\frac{cN}{2}}^{\frac{cN}{2}-1} U_i}_{\text{Step 3}} e^{-j2\pi \frac{ik}{cN}} \quad (4)$$

where

$$U_i = \sum_{l \in \mathbb{Z}} \sum_{m \in \mathbb{Z}} z_l \hat{\varphi}_{l i + cmN - \mu_l}, \quad (5)$$

$\hat{\varphi}_{lm} = \hat{\varphi}(cx_l - (\mu_l + m))$ ,  $\mu_l = \lfloor cx_l \rfloor$  and the domains of definition of  $z_l$ ,  $\mu_l$  and  $\hat{\varphi}_{lm}$  have been extended so that  $z_l$  and  $\mu_l$  vanish for  $l < 1$  and  $l > M$ , and  $\hat{\varphi}_{lm}$  vanishes for  $l < 1$ ,  $l > M$  and for  $|m| > K$ . The algorithm involves

three steps [1]: Step 1, i.e., the calculation of  $U_i$ , is an interpolation step; Step 2 can be performed by a standard FFT over  $cN$  points and Step 3 is scaling.

## V. KAHAN SUMMATION FORMULA

It is worth noting that the performance of a method in terms of accuracy and speed must be evaluated following an appropriate professional implementation optimizing the use of the computing platform thanks to extremely sophisticated techniques [4]. To maximize the achievable accuracy, the developed NUFFT algorithm employs, just to show an example, the Kahan scheme [5] to perform summations, so keeping a separate running sequence to compensate floating point truncation errors in long summation sequences.

## VI. NUMERICAL RESULTS

The numerical performance of the optimized NUFFT approach is here analyzed and compared with that of the Gaussian and Kaiser-Bessel (KB) literature schemes [1]. An extensive analysis, with typical values of  $c$  and  $K$ , has been worked out [1]. For the sake of brevity, we report only the case with  $c = 2$  and  $K = 6$ . For it,  $\Gamma_{opt}=9.98 \cdot 10^{-8}$  and the value of (3) for the KB window is  $\Gamma_{KB}=8.15 \cdot 10^{-7}$  providing an improved accuracy of more than one order of magnitude against the KB window.

Considering now an aperiodic array comprising  $N$  elements located at the points  $\{x_k\}_{k=0}^{N-1}$ , the array factor can be written as

$$f(\bar{u}) = \sum_{k=0}^{N-1} c_k e^{jx_k \bar{u}}, \quad (6)$$

where  $\bar{u} = \beta \cos \psi$  and  $\beta$  is the wavenumber. If the array factor is computed at a regular set of  $M$  points in the  $\bar{u}$  variable, then the samples of  $f$  can be computed via a NED-NUFFT [1]. The accuracy of the NUFFT algorithm on the calculation of the radiated pattern has been examined. To this end, an aperiodic array of 40 elements, synthesized by the algorithm in [6] for a choice of  $c = 1.5$  and  $K = 1$ , has been considered. Fig. 1 illustrates the comparison between the array factor obtained by a Matrix-Vector Multiplication (MVM) approach [7] and that evaluated by the NUFFT algorithm, based on the Gaussian, KB and optimized windows, respectively. Fig. 1 also shows the differences between the reference pattern (MVM) and the NUFFT-evaluated patterns. It can be seen that even with significantly low values for  $c$  and  $K$ , the accuracy of the optimized NUFFT appears to be very satisfactory, which is at variance with the other NUFFT implementations (see [1] too).

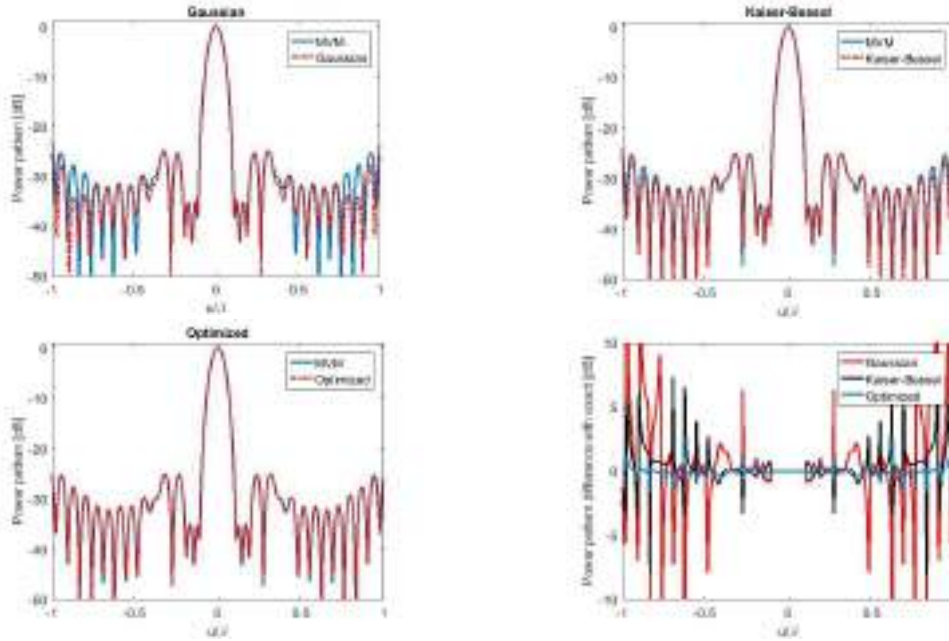


**FIG. 1** – Field radiated by the aperiodic array (solid blue line), as evaluated by a NUFFT (dash-dot red line), using Gaussian (up-left), Kaiser-Bessel (up-right) or optimized windows (down-left). Differences among the MVM evaluations of the field and those evaluated by the three compared NUFFTs (down-right).

## VII. CONCLUSION

We have presented a novel NUFFT for which: 1) the performance is superior to that of currently available NUFFTs; 2) the accuracy reaches machine precision earlier than other NUFFTs; 3) even for low values of  $c$  and  $K$ , it is capable of yielding satisfactory results. We plan to extend the approach to 2D, also using parallelization on Graphics Processing Units.

## REFERENCES

- [1] A. Capozzoli, C. Curcio, A. Liseno, "Optimized Non-Uniform FFTs (NUFFTs) and their application to array factor computation," submitted on Aug. 9, 2016, *in press on IEEE Trans. Antennas Prop.*
- [2] K. Fourmont, "Non-equispaced fast Fourier transforms with applications to tomography," *J. Fourier Anal. Appl.*, vol. 9, n. 5, pp. 431-450, Sept. 2003.
- [3] A. Capozzoli, *et al.*, "Parameter selection and accuracy in type-3 non-uniform FFTs based on Gaussian gridding," *Progr. Electromagn. Res.*, vol. 142, pp. 743-770, 2013.
- [4] M. Frigo, S.G. Johnson, "The design and implementation of FFTW3" *Proc. of the IEEE*, vol. 93, n. 2, pp. 216-231, Feb. 2005.
- [5] N.J. Higham, "The accuracy of floating point summation," *SIAM J. Sci. Comput.*, vol. 14, n. 4, pp. 783-799, Jul. 1993.
- [6] A. Capozzoli, *et al.*, "FFT & aperiodic arrays with phase-only control and constraints due to super-directivity, mutual coupling and overall size", *Proc. of the 30th ESA Antenna*, Noordwijk, The Netherlands, May 27-30, 2008, pp. 213-216.
- [7] A. Capozzoli, *et al.*, "Fast CPU/GPU pattern evaluation of irregular arrays", *Applied Comput. Electromagn. Soc. J.*, vol. 25, n. 4, pp. 355-372, Apr. 2010.

# **A GENERAL ANALYTICAL METHOD, BASED ON SLATER'S PERTURBATION THEOREM, FOR MESH GENERATION IN FEM SIMULATION OF RF CAVITIES**

G. S. Mauro<sup>(1,2)</sup>, L. Celona<sup>(3)</sup>

<sup>(1)</sup> Istituto Nazionale di Fisica Nucleare - Laboratori Nazionali di Legnaro -  
Viale dell'Università' 2, 35020 Legnaro PD, Italy.

<sup>(2)</sup> Università' degli Studi "Mediterranea" di Reggio Calabria - Salita  
Melissari, 89124 Reggio Calabria RC, Italy.

<sup>(3)</sup> Istituto Nazionale di Fisica Nucleare - Laboratori Nazionali del Sud - Via  
S. Sofia 62, 95125 Catania CT, Italy.

[gsmuro@lnl.infn.it](mailto:gsmuro@lnl.infn.it)

## **Abstract**

*When simulating electrically large complex structures such as Drift Tube Linac (DTL) cavities in 3D simulators, it is important to choose a model representation that is a compromise between accuracy and time/resource cost. This paper presents an analytical method, based on Slater's perturbation theorem, to obtain a fairly accurate 3D mesh to represent cylindrical structures.*

**Index Terms** – Slater's theorem, RF cavities, FEM simulations.

## **I. INTRODUCTION AND MOTIVATION**

3D simulators have becoming very useful nowadays to reduce the cost and delay of experimental tuning. When modeling complex structures in 3D FEM solvers the real structure is discretized in a finite number of mesh elements, usually tetrahedrons. This results in an approximation of the real structure thus introducing a systematic geometric error when curved boundaries are present.

In this paper we find an analytical relation between the (above) introduced geometric approximation and the error in the solution. As an example we consider a Drift Tube Linac (DTL) tank but the methodology is general. Fig. 1(a) shows a front view of a circular cavity. When representing the structure using a 3D simulator such Ansys HFSS [1] the mesh engine creates a regular polygon mesh inscribed inside the cylindrical real structure. Whatever the mesh size/precision chosen, the real simulated volume will be lower than the real cylindrical volume. The more the mesh is coarse, the greater will be the geometrical error and thus the frequency and field error

since the inscribed polygon fails to represent the real structure in a satisfactory and coherent way. Obviously, if the mesh density is increased, the real structure can be represented in a more accurate way and thus the simulated results will be more accurate. 3D simulators allow users to set the beginning mesh density, but for complex structures it is not straightforward to choose between a coarse mesh that could lead to inaccurate results, and an overly accurate mesh that could cost in resources and simulation time. In this work we find an analytical relation, based on the Slater's perturbation theorem, to predict the numerical error introduced by any local geometrical approximation.

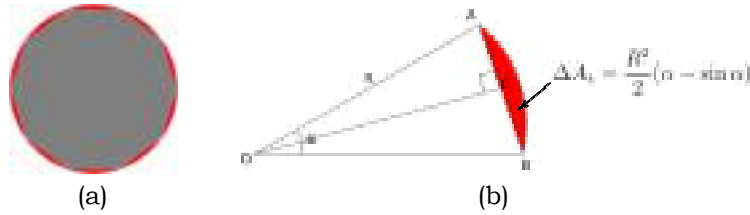


Figure 1: (a) Front view of a simulated circular cavity. Red area is the difference between real and simulated profile. (b) Circular sector of a cylindrical cavity.

## II. MESH RELATED FREQUENCY ERROR

In the above example, since the actual simulated volume is lower than the real one, an error is introduced in the simulated resonant frequency with respect to the real one  $f_0$ . The frequency variation could be taken as an index of mesh quality.

Figure 1(b) shows how a generic tetrahedron edge approximate the actual curved boundary. The cross section area difference between the real cavity profile and the simulated one is highlighted in red where the edge  $AB$  approximates the real circumference arc; the quantity  $\alpha$ , known as normal deviation angle<sup>1</sup>, can be enforced to be lower than a prefixed value to give a good geometrical approximation of the curved surfaces [1].

The objective is to find an appropriate value of  $\alpha$  that corresponds to a minimum but computationally reasonable frequency shift from the real one. Frequency shift  $\Delta f_0$  can be related to the difference in volume  $\Delta V$  between real profile and simulated one by using Slater perturbation theorem [2]. From the theory we have

$$\frac{\Delta\omega_0}{\omega_0} = \frac{\int_{\Delta V} (\mu_0 H^2 - \epsilon_0 E^2) dV}{\int_V (\mu_0 H^2 + \epsilon_0 E^2) dV} = \frac{\Delta U_m - \Delta U_e}{U} \quad (1)$$

<sup>1</sup>The normal deviation angle is defined as the maximum angular deviation between the normals of the faceted triangles and the normals of the true surfaces they represent.

where  $U = \frac{1}{4} \int_V (\mu_0 H^2 + \varepsilon_0 E^2) dV$  is the total stored energy inside the cavity,  $\Delta U_m = \frac{1}{4} \int_{\Delta V} \mu_0 H^2 dV$  is the time average of the stored magnetic energy removed and  $\Delta U_e = \frac{1}{4} \int_{\Delta V} \varepsilon_0 E^2 dV$  is the time average of the stored electric energy removed. Equation (1) can be approximated as  $\frac{\Delta f_0}{f_0} \approx \frac{\Delta V}{4U} (\mu_0 H^2 - \varepsilon_0 E^2)$ . Inside a DTL cavity, the tank outer wall is interested by a predominance of magnetic field. So we obtain  $\frac{\Delta f_0}{f_0} \approx \frac{1}{4U} \mu_0 H^2 \Delta A_s b_{tot} L$ , where  $\Delta A_s$  is the difference, referred to a circular sector, between real curved DTL cross section area and the discretized cross section,  $b_{tot}$  is a factor to consider the total circular cross section, and  $L$  is the cavity length. From Fig. 1(b), after some geometrical calculations we can evaluate the removed area  $\Delta A_s$ .

In the end we have

$$\frac{\Delta f_0}{f_0} \approx \frac{\frac{R^2}{2} (\alpha - \sin \alpha) b_{tot} L}{4U} \mu_0 H^2 \quad (2)$$

It is clear that (2) requires the knowledge of the field  $H$  at the point where the volume is subtracted, that is the cavity outer wall. However this value can be evaluated in a variational fashion, for example on an idealized 2D model with a known solution or even on the 3D model with the above mentioned local geometrical errors (thanks to variational considerations).

### III. ESTIMATED ERROR AND NUMERICAL RESULTS

In the following we test the formula (2) on a rotationally symmetric DTL without stems. However this is not strictly necessary. Thanks to the rotation symmetry both 2D and 3D simulations can be performed and in particular we can use a very accurate mesh in 2D simulation to obtain a virtually error free reference simulation. As 2D simulator we use Superfish [3].

We consider a tank with the following specifications obtained using Superfish:  $U = 22.431$  J, total stored energy inside the cavity;  $R = 0.2605$  m, cavity radius;  $H = 3719.38$  A/m, average magnetic field on the cavity outer wall;  $L = 7.52$  m, cavity length;  $f_0 = 351.28$  MHz, cavity operating frequency. Remembering that in magnetic zone a decrease in cavity volume corresponds to a frequency increase, choosing  $\alpha = 10^\circ$  so that  $b_{tot} = \frac{360}{10}$ , from equation (2) we estimate/predict an error of  $\Delta f_0 \cong 560$  kHz compared to the nominal frequency  $f_0$ , so  $f_0 + \Delta f_0 = 351.84$  MHz. Choosing instead  $\alpha = 5^\circ$ , an error of  $\Delta f_0 \cong 137$  KHz is estimated/predicted, so  $f_0 + \Delta f_0 = 351.42$  MHz.

Based on the above result we carry full wave 3D simulation in Ansys HFSS. Choosing  $\alpha = 5^\circ$ , an  $f_0 = 351.29$  MHz is obtained. Choosing  $\alpha = 10^\circ$ , an  $f_0 = 351.70$  MHz is obtained. Simulated frequency results are in good agreement with the values calculated with (2).

Fig. 2 shows accelerating field  $E_0$  on the axis of the DTL structure, obtained with HFSS at different setting for  $\alpha$  along with the reference field  $E_0$  obtained in Superfish. The use of  $\alpha = 5^\circ$ , chosen by analytical calculations, allowed us to control the frequency error below 137 KHz and also determines an on axis field comparable between HFSS and Superfish.

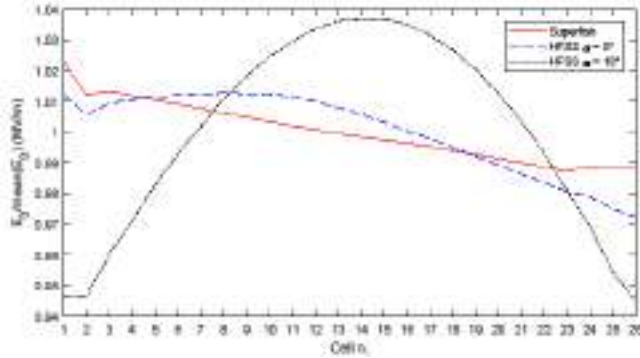


Figure 2: Comparison between  $E_0$  field curve obtained in Superfish and in HFSS for  $\alpha = 5^\circ$  and  $\alpha = 10^\circ$ .

#### IV. CONCLUSIONS

In this work an analytical relation, based on the Slater's theorem, to predict the numerical error introduced by any local geometrical approximation has been presented. The method allow to predict and control frequency error  $\Delta f_0$  by setting the simulator parameter called normal deviation angle, or  $\alpha$ , by using a simple analytical formula. The study has been validated on a full size DTL tank model and the error prediction is quite accurate. Results in terms of frequency and field are presented, showing that numerically simulated values are in good agreement with reference ones within the requie frequency error. The user can set an appropriate value of  $\alpha$  that guarantee a minimum reasonable frequency shift from the nominal frequency  $f_0$ . By applying the method we predicted a required deviation angle of  $\alpha = 5^\circ$  to enforce an error lower than 137 KHz.

The above settings, for the DTL tank 4 of project ESS, results in a mesh of more than 10 million of elements and a simulation time of 9 h and 41 m. Enforcing a finer mesh would result in an unnecessary longer simulation.

#### REFERENCES

- [1]. Ansys, Inc. [Online]. Available: <https://www.ansys.com/products/Electronics>.
- [2]. T. P. Wangler, RF Linear Accelerators. 2008.
- [3]. Los Alamos Accelerator Code Group. [Online]. Available: [http://laacg.lanl.gov/laacg/services/download\\_sf.phtml](http://laacg.lanl.gov/laacg/services/download_sf.phtml).

# MESHLESS METHODS APPLIED TO ELECTROMAGNETIC EIGENPROBLEMS

V. Lombardi, M. Bozzi, L. Perregrini

Dept. of Electrical, Computer and Biomedical Engineering  
University of Pavia, Pavia, Italy

[vincenzo.lombardi01@ateneopv.it](mailto:vincenzo.lombardi01@ateneopv.it), [Maurizio.bozzi@unipv.it](mailto:Maurizio.bozzi@unipv.it), [luca.perregrini@unipv.it](mailto:luca.perregrini@unipv.it)

## Abstract

*This paper describes the application of the meshless method to the analysis of waveguide eigenvalue problems. Both the cases of homogeneous and inhomogeneous waveguides is addressed, requiring a scalar and a vector implementation, respectively. The combination of the variational technique and the meshless method lead to a well-conditioned matrix eigenproblem, and its solution permits to obtain a large number of modes with high accuracy. Some examples demonstrate the effectiveness of the method.*

**Index Terms** – Meshless method, radial basis functions, variational method, waveguide modes.

## I. INTRODUCTION

During the last decade, the scientific community has given a lot of attention to the Meshless Method [1]–[4]. When applied to the EM eigenproblems, the Meshless Method based on radial basis functions (RBFs) presents some limitations. The first one is the critical dependence of the solution on the position of the collocation points, in particular on the boundary of the domain under study [4], and a low precision in the evaluation of the first eigensolution with the Dirichlet boundary condition [4]. In [5] a very simple and no-time consuming technique has been presented to overcome these issues, which is based on a randomized definition of the RBFs with a particular statistical distribution of the shape parameter. Another problem of the Meshless Method with RBFs is that, in its original form based on the Point Matching technique, it leads to a non-symmetric eigenproblem and sometimes to singular matrices, thus making the problem potentially ill-conditioned [6].

To overcome these drawbacks, in [7] the use of the Variational Formulation in conjunction with the Meshless Method has been proposed for the first time for the solution of homogeneous waveguides. Although in the simplified case of the scalar potential formulation, the Variational Meshless Method led to well-conditioned problems in various kind of geometries, also including sharp metal edges. In [8] the Variational Meshless Method has been extended to the more general case of inhomogeneous domains, considering rectangular waveguides filled with piecewise homogeneous dielectric, for which a vector formulation is required [9]. In section II the theory is briefly outlined, and section III reports numerical examples to demonstrate the effectiveness of the proposed method.

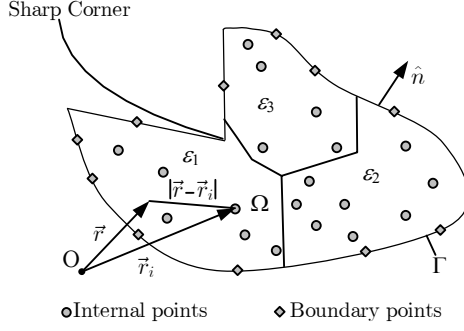


**FIG. 1** – WR90 Cross section of a generic waveguide

## II. OUTLINE OF THE THEORY

In Fig. 1 the generic cross section of a waveguide is presented. In the case of homogeneous domains [7] the functional is

$$I(\Phi) = \frac{1}{2} \iint_{\Omega} (\nabla\Phi \cdot \nabla\Phi - k^2\Phi^2) dS \quad (1)$$

where  $\Phi$  is the Hertz-Debye potential and  $k$  is the wavenumber on the medium. In the case of the TM modes, the Dirichlet boundary condition must be imposed explicitly.

In the case of inhomogeneous domains [8] the functional is

$$I(\Phi) = \iint_{\Omega} (\frac{1}{\epsilon_r} \nabla \times \vec{H} \cdot \nabla \times \vec{H} - \mu_r k^2 \vec{H} \cdot \vec{H}) dS \quad (2)$$

where  $\vec{H}$  is the magnetic field,  $\epsilon_r$  and  $\mu_r$  are respectively the relative permittivity and permeability of the medium. In this case the divergence condition  $\nabla \cdot \vec{H} = 0$  and the boundary condition on the PEC  $\hat{n} \times \vec{H} = 0$  must be imposed explicitly for all modes.

The Meshless Approximation with RBFs consists in substituting every generic scalar function  $f$  (i.e.  $\Phi$ ,  $H_x$ ,  $H_y$ , and  $H_z$ ) as follow

$$f(x, y) = \sum_{i=1}^N a_i f_i(x, y) \quad (3)$$

where  $a_i$  are unknown coefficients,  $f_i(x, y)$  are the RBFs used as basis.  $N$  is the number of the collocation points. Each RBF is centered on a collocation point. During this activity the Gaussian RFBs have been used. By applying the RBFs substitution and extremizing the functional, (1) and (2) are transformed into a generic eigenproblem  $A a = k^2 B a$  where the matrices  $A$  and  $B$  are both real and symmetric.

## III. NUMERICAL RESULTS

In this section, two numerical results are reported and discussed to validate the proposed technique.

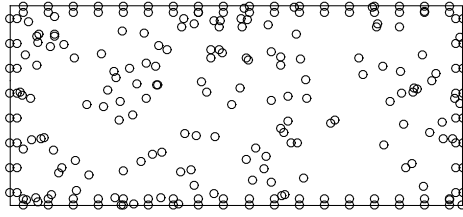


**FIG. 1** – WR90 rectangular waveguide (22.86\_10.16 mm<sup>2</sup>) and the collocation points used for the analysis by the variational meshless method.

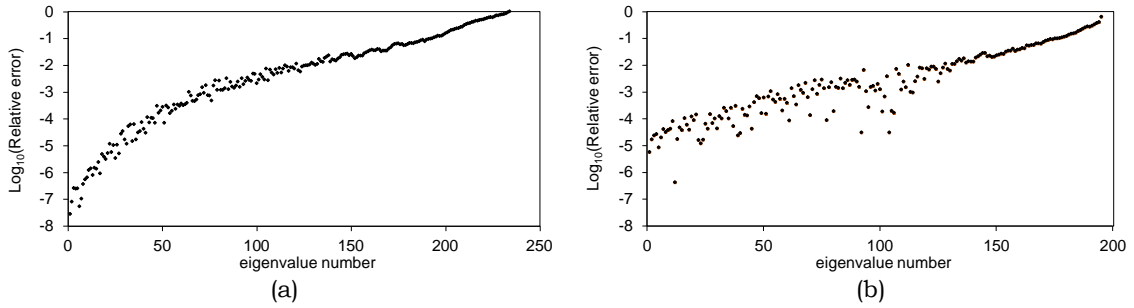


**FIG. 2** – Error in the calculation of the cut-off frequency of a WR90 rectangular waveguide by the variational meshless method with 248 collocation points: (a) TE modes; (b) TM modes.

All the simulations were run on a computer with an Intel Corei7-6700 CPU @ 3.40 GHz (8 CPUs), and 16 GB of RAM.

In Fig. 1 is shown a WR90 homogeneous waveguide simulated and the position of the collocation points. With 248 collocation points and less than 1 s of simulation the program gave 248 TE and 196 TM eigenvalues with the precision shown in Fig. 2

The second example refers to the analysis of a shielded insulated image waveguide analyzed in [10]. The domain is shown in Fig. 5(a), where all the relevant dimensions and informations about the dielectric are also provided. The number of collocation points used to define the unknown is  $N = 570$ . The simulation needed 47 s to compute the initial matrices and the reported 33 cycles. In Fig. 5(b) the obtained dispersion diagram is shown and compared with the results given by ANSYS HFSS after a port only simulation with 696 triangles on the input port.

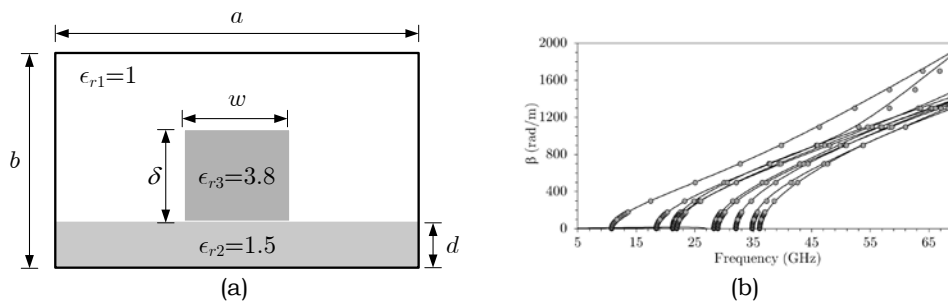


**FIG. 5** – Shielded Insulated Image Guide: (a) Geometry of the structure ( $\delta = 1$  mm,  $w = 2.25$  mm,  $d = 0.5$  mm,  $a = 13.5$  mm,  $b = 8$  mm); (b) Dispersion diagram calculated by the variational meshless method (gray circles) compared with the HFSS simulation (solid line).

#### IV. CONCLUSION

In this manuscript a brief overview of the activities conducted by the Microwave Group of the University of Pavia in the field of the Meshless Method in conjunction with the Variational Approach have been reported. The developed theory has been applied to the solution of the guided modes in a shielded waveguide with both homogenous and inhomogeneous domains. Some numerical examples demonstrated the effectiveness of the proposed technique.

#### REFERENCES

- [1] Y. Yu and Z. Chen, "A 3-D radial point interpolation method for meshless time-domain modeling," *IEEE Trans. Microw. Theory Techn.*, Vol. 57, No. 8, pp. 2015–2020, Aug. 2009.
- [2] Y. Yu and Z. Chen, "Towards the development of an unconditionally stable time-domain meshless method," *IEEE Trans. Microw. Theory Techn.*, Vol. 58, No. 3, pp. 578–586, Mar. 2010.
- [3] W. L. Nicomedes, R. C. Mesquita, and F. J. d. S. Moreira, "The meshless local Petrov-Galerkin method in two-dimensional electromagnetic wave analysis," *IEEE Trans. Antennas Propag.*, Vol. 60, No. 4, pp. 1957–1968, Apr. 2012.
- [4] R. B. Platte and T. A. Driscoll, "Computing eigenmodes of elliptic operators using radial basis functions," *Computers & mathematics with applications*, Vol. 48, No. 3, pp. 561–576, Mar./Apr. 2004.
- [5] V. Lombardi, M. Bozzi, and L. Perregrini, "An improved meshless method for waveguide eigenvalue problems," *IEEE Microw. Compon. Lett.*, Vol. 27, No. 12, pp. 1047–1049, Dec. 2017
- [6] T. Kaufmann, C. Engström, C. Fumeaux, and R. Vahldieck, "Eigenvalue analysis and longtime stability of resonant structures for the meshless radial point interpolation method in time domain," *IEEE Trans. Microw. Theory Techn.*, Vol. 58, No. 12, pp. 3399–3408, Dec. 2010.
- [7] V. Lombardi, M. Bozzi, and L. Perregrini, "A novel variational meshless method with radial basis functions for waveguide eigenvalue problems," *IEEE Trans. Microw. Theory Techn.*, (in print).
- [8] V. Lombardi, M. Bozzi, and L. Perregrini, "Analysis of Inhomogeneous Rectangular Waveguides by the Variational Meshless Method," *48<sup>th</sup> European Microwave Conference (EuMC2018)*, Madrid, Spain, 23-28 Sep. 2018, (Submitted)
- [9] J. M. Jin, *The finite element method in electromagnetics*, John Wiley & Sons, 2015.
- [10] V. J. Brankovic, D. V. Krupezevic, and F. Arndt, "An efficient two dimensional graded mesh finite-difference time-domain algorithm for shielded or open waveguide structures," *IEEE Trans. Microw. Theory Techn.*, Vol. 40, No. 12, pp. 2272–2277, Mar. 1992.

# AN ANALYTICAL APPROACH FOR THE EFFICIENT EVALUATION OF A CLASS OF IMPROPER INTEGRALS INVOLVING OSCILLATING AND SLOWLY DECAYING FUNCTIONS

M. Lucido<sup>(1)</sup>, G. Panariello<sup>(1)</sup>, C. Santomassimo<sup>(1)</sup>, F. Schettino<sup>(1)</sup>

<sup>(1)</sup> Department of Electrical and Information Engineering, University of Cassino and Southern Lazio  
Via G. Di Biasio, 43, 03043 Cassino, Italy  
[lucido@unicas.it](mailto:lucido@unicas.it)

## Abstract

*The analysis of a wide class of electromagnetic propagation, radiation and scattering problems can be readily carried out by means of suitable full-wave spectral domain formulations and the method of analytical preconditioning which allows us to transform the obtained integral equation in a matrix equation at which Fredholm/Steinberg theory can be applied. Hence, the convergence of the discretization scheme is guaranteed. Moreover, the choice of expansion functions reconstructing the physical behavior of the unknowns leads to a fast convergence. Unfortunately, the matrix coefficients are improper integrals involving oscillating and, in the worst cases, slowly decaying functions. Thus, the computation time rapidly increases as higher is the accuracy required for the solution. The aim of this paper is to show an analytical technique for the efficient evaluation of such kind of integrals even when high accuracy for the solution is required.*

**Index Terms** – Analytical technique, Improper integrals of oscillating and slowly decaying functions, Method of analytical preconditioning, Spectral domain.

## I. INTRODUCTION

Spectral domain formulations are particularly suitable for the analysis of a wide class of electromagnetic problems ranging from the propagation in planar guides and waveguides or the radiation by planar antennas, to the scattering from cylindrical structures or planar surfaces involving homogeneous or stratified media, just to give some examples. In general, the obtained integral equation in the spectral domain does not admit closed form solutions, hence, numerical schemes have to be adopted. The fast convergence of such methods is a key point. When dealing with polygonal cross-section cylindrical structures or canonical shape planar surfaces, a well-posed matrix operator equation can be obtained by means of the method of analytical preconditioning [1]. It consists in the discretization of the integral equation by means of Galerkin's method with a suitable set of expansion functions leading to a matrix equation at which Fredholm/Steinberg theorems can be applied. In the literature, it has been widely shown that this goal can be fully reached by selecting expansion functions reconstructing the physical behaviour of the fields

on the involved objects with a closed-form spectral domain counterpart [2], [3]. With such a choice, few expansion functions are needed to achieve highly accurate results and the convolution integrals are reduced to algebraic products. However, the obtained matrix coefficients are improper integrals of oscillating and, in the worst cases, slowly decaying functions to be numerically evaluated. The classical analytical asymptotic acceleration technique (CAAAT), consisting of the extraction from the kernels of their asymptotic behavior while the slowly converging integrals of the extracted parts are expressed in closed form, allows us to obtain faster decaying integrands without overcoming the most important problem of their oscillating nature. For this reason, the convergence of the accelerated integrals becomes slower and slower as the accuracy required for the solution is higher. On the other hand, by means of algebraic manipulations and a suitable integration procedure in the complex plane, the matrix coefficients can be expressed as linear combinations of proper integrals and/or improper integrals of non-oscillating functions which can be accurately and quickly evaluated. Such a technique is very effective and drastically outperforms the CAAAT.

## II. PROPOSED SOLUTION

The procedure outlined above can be readily shown by referring to a practical case. The analysis of the electromagnetic scattering from a zero-thickness perfectly electrically conducting disk in vacuum shown in [3], formulated as integral equation in the vector Hankel transform domain for the surface current density and discretized by means of Galerkin's method, leads to the numerical evaluation of the following integrals of oscillating and slowly decaying functions

$$I_{k,h}^{(|n|)} = \int_0^{+\infty} J_{|n|+2k+3/2}(aw) J_{|n|+2h+3/2}(aw) \frac{dw}{\sqrt{k_0^2 - w^2}}, \quad (1)$$

where  $a$  is the radius of the disk,  $k_0$  is the wavenumber in vacuum,  $J_\nu(\cdot)$  is the Bessel function of first kind and order  $\nu$  [4],  $n$  is the general cylindrical harmonic, while  $k$  and  $h$  denote the general test function and basis function indexes, respectively. For the sake of symmetry, it can be supposed  $k \geq h$ . Now, the functions

$$F_{k,h}^{(|n|,l)}(az) = \frac{1}{\sqrt{k_0^2 - z^2}} J_{|n|+2k+3/2}(az) H_{|n|+2h+3/2}^{(l)}(az), \quad (2)$$

with  $l \in \{1, 2\}$ , where  $H_\nu^{(l)}(\cdot) = J_\nu(\cdot) + j(-1)^{l+1} Y_\nu(\cdot)$  is the Hankel function of  $l$ th kind and order  $\nu$  and  $Y_\nu(\cdot)$  is the Bessel function of second kind and

order  $\nu$  [4], are analytical in the regions of the complex plane  $z = w + j\bar{w}$  delimited by the contours  $C_l$  sketched in Fig. 1.

Hence, by means of Cauchy's integral theorem it is possible to write

$$\lim_{\substack{R \rightarrow +\infty \\ r_0, r \rightarrow 0}} \oint_{C_l} F_{k,h}^{(|n|,l)}(az) dz = 0. \quad (3)$$

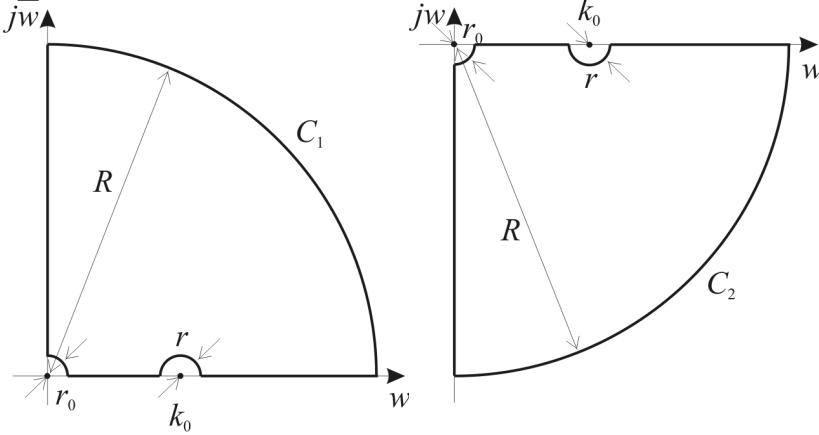


**FIG. 1** – Integration contours in the complex plane.

Starting from the behavior for small and large argument of the Bessel functions of first kind and the Hankel functions [4], it is simple to conclude that the integrands in (3) have no singularity in  $z=0$ , being  $k \geq h$ , while they decay asymptotically as  $1/z^2$  for  $l=1$  and  $0 \leq \arg(z) < \pi$ , and for  $l=2$  and  $-\pi < \arg(z) \leq 0$ .

Therefore, by means of Jordan's lemma, it is simple to rewrite formula (3), for  $l=1$  and  $l=2$ , respectively, as follows

$$\int_0^{+\infty} F_{k,h}^{(|n|,1)}(aw) dw = j \int_0^{+\infty} F_{k,h}^{(|n|,1)}(ja\bar{w}) d\bar{w}, \quad (4a)$$

$$\int_0^{k_0} F_{k,h}^{(|n|,2)}(aw) dw - \int_{k_0}^{+\infty} F_{k,h}^{(|n|,2)}(aw) dw = j \int_0^{+\infty} F_{k,h}^{(|n|,1)}(ja\bar{w}) d\bar{w}, \quad (4b)$$

where the relations  $J_\nu(z e^{jq\pi}) = e^{jq\nu\pi} J_\nu(z)$  with  $q$  integer, and  $H_\nu^{(2)}(z e^{-j\pi}) = -e^{j\nu\pi} H_\nu^{(1)}(z)$  have been used [4].

By taking the difference between (4a) and (4b), and making the substitution  $w = k_0 \sin t$ , it is simple to conclude that

$$I_{k,h}^{(|n|)} = \int_0^{k_0} F_{k,h}^{(|n|,2)}(aw) dw = \int_0^{\pi/2} J_{|n|+2k+3/2}(ak_0 \sin t) H_{|n|+2h+3/2}^{(2)}(ak_0 \sin t) dw \quad (5)$$

for  $k \geq h$ , which are proper integrals of bounded continuous functions.

### III. NUMERICAL RESULTS

This section shows the efficiency of the presented technique. In Fig. 2 the ratio between the CPU time needed to fill the coefficients' matrix as obtained by using CAAAT with respect to the presented technique is reported for  $k_0a=5$  by using 17 cylindrical harmonics to reconstruct the unknowns, as a function of the number of expansion functions used to reconstruct the radial behavior of each harmonic ( $N$ ) and by changing the accuracy in the numerical evaluation of the integrals ( $R$ ). In a first case, the CAAAT is applied by extracting only the first order asymptotic behavior of the integrands while, in a second case, the first order and second order asymptotic behavior of the integrands in (2b) are pulling out leading to 6 times faster converging integrals than the first case. Despite that, the proposed technique drastically outperforms the CAAAT in both the examined cases as higher is number of expansion functions used and as higher is the accuracy required for the solution.

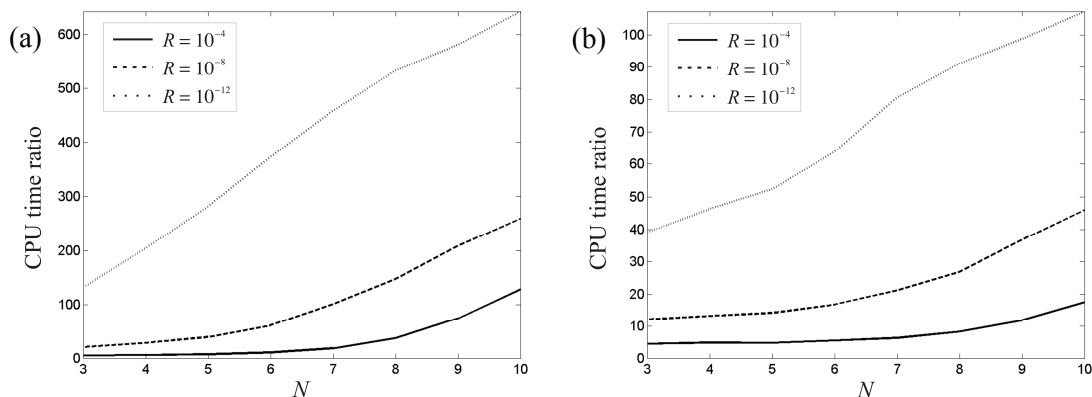


**FIG. 2** – Ratio between the CPU time needed to reconstruct the solution as obtained by using CAAAT with respect to the presented technique with varying  $N$  and for different values of  $R$ . The CAAAT is applied by extracting only the first order (a) or the first order and the second order (b) asymptotic behavior of the integrand.  $k_0a=5$ , 17 cylindrical harmonics.

### IV. REFERENCES

- [1] A. I. Nosich, “Method of Analytical Regularization in Computational Photonics,” *Radio Science*, vol. 51, no. 8, pp. 1421–1430, Aug. 2016.
- [2] M. Lucido, G. Panariello, and F. Schettino, “Scattering by Polygonal Cross-Section Dielectric Cylinders at Oblique Incidence,” *IEEE Transactions on Antennas and Propagation*, vol. 58, no. 2, pp. 540–551, Feb. 2010.
- [3] M. Lucido, G. Panariello, and F. Schettino, “Scattering by a Zero-Thickness PEC Disk: A New Analytically Regularizing Procedure Based on Helmholtz Decomposition and Galerkin Method,” *Radio Science*, vol. 52, no. 1, pp. 2–14, Jan. 2017.
- [4] M. Abramowitz, I.A. Stegun, *Handbook of Mathematical Functions*, The Netherlands: Verlag Harri Deutsch, 1984.

# APERTURE TRUNCATION AND EXCITATION ERROR ANALYSIS FOR A SPACE DEBRIS RADAR ANTENNA ARRAY

Giuseppe Siciliano

Dept. of Electrical, Electronic and Biomedical Engineering, University of Pavia, Pavia, Italy  
giuseppe.siciliano01@universitadipavia.it

## Abstract

*This paper investigates the consequences of aperture truncation and random element-excitation phase errors on the radiation performance of a moderate-sized array to be used as a preliminary antenna module for a large phased array radar belonging to ESA space-debris-detection projects. To take aperture truncation into account, the internal and the boundary elements are separately analyzed through a full-wave electromagnetic simulation software, revealing a significant gain reduction. Moreover, a Monte Carlo analysis is performed to investigate the effects of element excitation phase errors, revealing radar performance degradation such as sidelobe-level increase, gain reduction, and pointing inaccuracy.*

**Index Terms** – Array truncation, embedded element pattern, phased arrays, phase errors, surveillance radar

## I. INTRODUCTION

The European Space Agency is developing a surveillance radar based on a phased array architecture under the Space Situational Awareness programme, aimed at the generation of a European space debris catalogue. The system currently under development consists of a multi-array antenna architecture [1] where each single array has to scan a rectangular portion of the sky (Field of Regard). An optimization of the array lattice to minimize the total number of elements was carried out in previous works [1], [2], where a patch antenna was selected as elementary radiator. To calculate the array radiation pattern, the embedded element pattern was used in [2], simulating an indefinitely large array of patch elements. Although this approximation is quite accurate for large arrays, it may not be for moderate-sized arrays, where edge effects due to the finite aperture can arise, degrading the radiation performance.

In this paper, the array truncation analysis is refined and the simulation results are compared with [2]. Moreover, the effect of random phase errors on the element excitation is also studied, which had not been addressed in [1], [2].

## II. ARRAY TRUNCATION ANALYSIS

The analysis of truncation effects for finite arrays of patches has been extensively discussed in [3]. In this paper, this effect has been evaluated by using ANSYS HFSS simulation tool. To introduce in first instance such

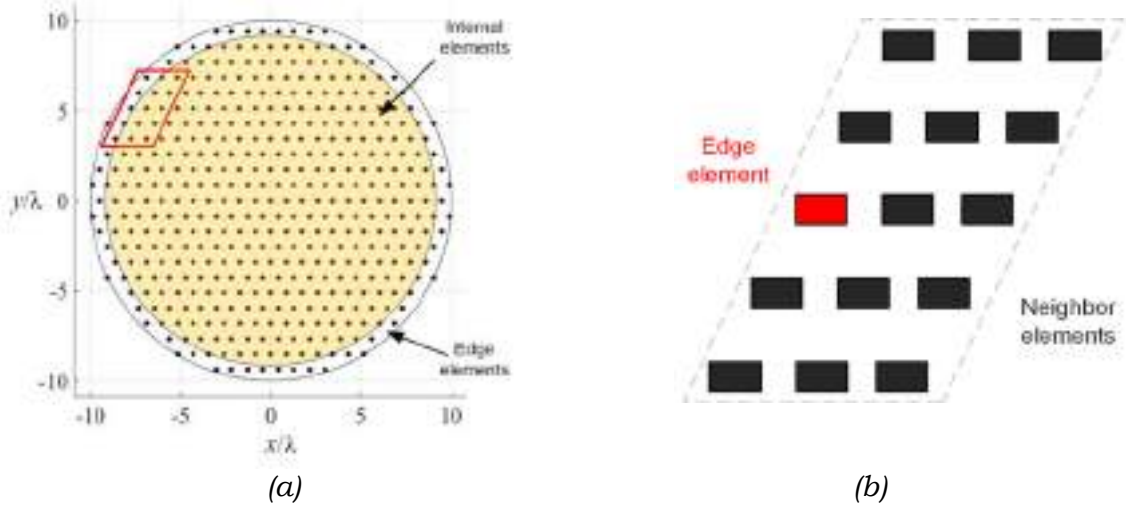


**FIG. 1** – Array element distribution: (a) total aperture size; (b) portion of the array edge simulated on HFSS for evaluation of truncation effect.

effects, the edge elements (i.e., the elements at the border of the array, Fig. 1a) have been simulated surrounded by some other more internal neighbor elements, Fig. 1b). The radiation patterns of the internal and edge elements are used together with the array factor to calculate the effect of the array truncation. In particular, two array factors are generated, namely  $AF_{int}$  and  $AF_{edge}$ , which take into account only the internal and only the edge elements, respectively (Fig. 1a). Assuming  $\mathbf{E}_{0\_int}$  and  $\mathbf{E}_{0\_edge}$  are the electric field generated by the internal and edge elements, respectively, the electric field  $\mathbf{E}$ , of the overall array, can be obtained by

$$\mathbf{E} = \mathbf{E}_{0\_int} \times AF_{int} + \mathbf{E}_{0\_edge} \times AF_{edge} \quad (1)$$

Therefore, the radiation intensity of the overall array results

$$K = |r\mathbf{E}|^2 / 2\eta_0 \quad (2)$$

where  $r$  is the observation distance and  $\eta_0$  is the characteristic impedance of vacuum.

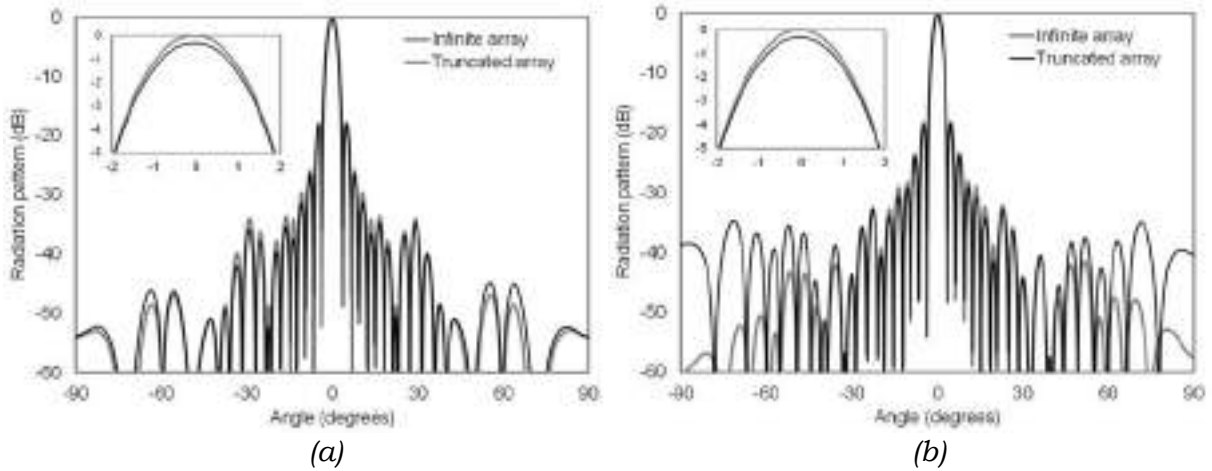


**FIG. 2** – H-plane (a) and E-plane (b) radiation pattern of the array considering all identical elements (black line) and specific elements for the array edge (gray line). The insets show a close-up view around the main beam.

The normalized array radiation pattern with no truncation effects (infinite array) and with truncation effects (truncated array) are depicted in Fig. 2a and Fig. 2b, for the H-plane and E-plane, respectively. The differences around the main lobe can be appreciated in the insets, revealing a maximum gain reduction of 0.32 dB.

### III. PHASE ERROR ANALYSIS

Phase errors are treated in a number of previous works (e.g., [4]), and a simple way to evaluate them is to consider the excitation phase of each element in the array as a Gaussian random variable  $\Phi_{\text{err}}$  with zero mean and standard deviation  $\sigma_{\text{err}}$ . The array factor, in case of uniform amplitude tapering, can be written as:

$$AF = \sum_n \exp(j\Phi_{\text{err}}) \exp(jk\mathbf{r}_n \cdot \hat{\mathbf{u}}_r) \quad (3)$$

where  $k = 2\pi/\lambda$  is the wave number,  $\mathbf{r}_n$  is the vector radial position of the  $n^{\text{th}}$  element of the array and  $\hat{\mathbf{u}}_r$  is the unit vector of the pointing direction. A MATLAB routine has been run 10 000 times recalculating the AF given such a random distribution of phase errors, obtaining a Monte Carlo analysis, with the possibility to work out some interesting statistical quantities regarding gain reduction, sidelobe level variation, and pointing error. To test the array performance in an extreme-case scenario,  $30^\circ$  phase errors were assumed. Since 99.7% of the values of a Gaussian random variable fall below  $3\sigma$  from the mean value, it is reasonable to set  $3\sigma_{\text{err}}$  equal to  $30^\circ$ , i.e.  $\sigma_{\text{err}}$  equal to  $10^\circ$ . Fig. 5 shows a result of a Monte Carlo analysis obtained with MATLAB iterations, where the red curve represents the ideal array factor. Table I presents some statistical results on the principal array performances, which better permits to appreciate

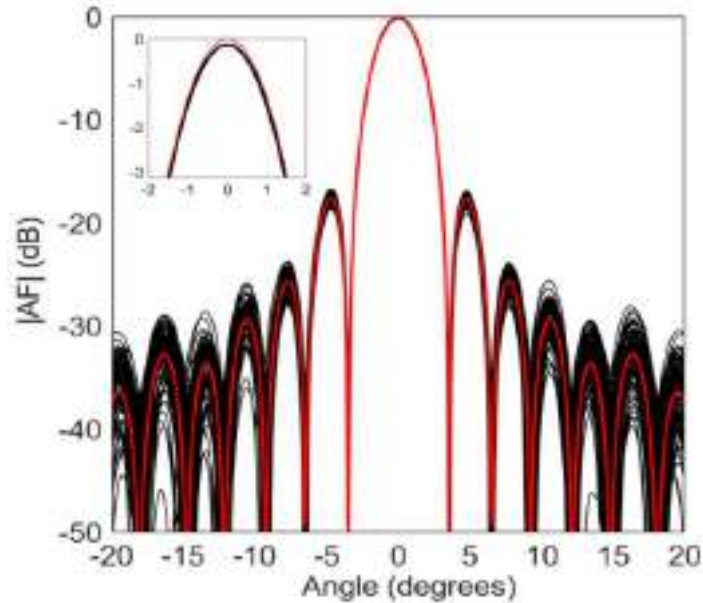


**FIG. 3** – Monte Carlo analysis of the broadside array radiation pattern with normally distributed random phase errors.

**TABLE I - MONTE CARLO STATISTICS AFTER PHASE ERRORS.**

Statistical quantity	Quantity	Standard deviation	Maximum value
Pointing Error	0°	1.15°	3.61°
Gain reduction	-0.13 dB	0.009 dB	-0.17 dB
Sidelobe level	-17.46 dB	0.23 dB	-16.24 dB

the effect of phase errors. In particular, the pointing error is expected to be less than  $2.3^\circ$  with a probability of 95.45%, which, due to the large distances of the target objects, may result into unacceptably large inaccuracies in the estimation of the position of the debris. As regards the gain, such phase errors lead to an average reduction of 0.13 dB with small variations around this value. Finally, the maximum sidelobe level is also affected by random phase errors, with an average value of -17.46 dB, very close to the ideal array case, and variations within 0.46 dB from the mean value with 95.45% probability.

#### IV. CONCLUSION

In this paper, the finite size of a phased array for ESA space debris radar as well as the inaccuracies of the phase excitation of the array elements have been investigated. Results from the array truncation analysis showed a significant degradation of the radiation pattern, especially in the E-plane. The element excitation phase errors have been studied through a Monte Carlo analysis for an extreme-case scenario. Results showed a degradation of the array radiation performances, with limited gain reduction and sidelobe level increase, and with non-negligible pointing error. However, such effects could also be considerably mitigated in a more realistic scenario where a proper phase-monitoring system is adopted.

#### REFERENCES

- [1] G. Siciliano, M. Mendijur, P. Besso, M. Pasian, and L. Perregrini, "A multi-array antenna system with optimal lattice for rectangular pyramidal scanning of space debris," *10<sup>th</sup> EuCAP*, Davos, Switzerland, April 10-15, 2016.
- [2] G. Siciliano, M. Mendijur, P. Besso, M. Pasian, and L. Perregrini, "Time-Space Optimization of Uniform Array Lattices for Space Debris Radars," *IEEE Trans. Antennas Propag.*, (in print).
- [3] A. K. Skrivervik and J. R. Mosig, "Analysis of Finite Phased Arrays of Microstrip Patches," *IEEE Trans. Antennas Propag.*, Vol. 41, No. 8, Aug. 1993.
- [4] C. A. Greene and R. T. Moller, "The Effect of Normally Distributed Random Phase Errors on Synthetic Array Gain Patterns," *IRE Trans. on Military Electronics*, Vol. MIL-6, No. 2, pp. 130-139, April 1962.

# EXPERIMENTAL STUDY UP TO 50 GHz ON TISSUE-MIMICKING MATERIALS FOR BREAST PHANTOMS

S. Di Meo<sup>1</sup>, L. Pasotti<sup>1,2</sup>, G. Matrone<sup>1,2</sup>

<sup>1</sup> Department of Electrical, Computer and Biomedical Engineering,  
University of Pavia, Pavia, Italy

<sup>2</sup> Centre for Health Technologies, University of Pavia, Pavia, Italy  
simona.dimeo01@universitadipavia.it

## Abstract

*Breast cancer is the most widespread disease among women around the world. In recent years, the interest toward the use of microwaves and mm-waves for diagnostic and screening purposes has been growing. These frequencies in principle give the possibility of making a diagnosis without risks and involving low cost instrumentation. Past dielectric characterizations of human breast samples have shown that a significant difference is present between healthy and malignant tissues, and that a reasonable penetration depth is possible for detecting a cancer of some millimeters, even in the mm-wave frequency range. A fundamental step toward the development of these systems is the test phase on breast phantoms. In this paper, the dielectric characterization of easy-to-produce and cheap mixtures mimicking the dielectric properties of human breast healthy tissues up to 50 GHz is presented. Similar mixtures are currently used for ultrasound breast phantoms, and so far they have been unexplored in the radiofrequency regime. All measurements have been compared to the data derived from the dielectric characterization of human breast samples, and the good agreement between them shows that they could be an excellent alternative to the current tissue mimicking materials.*

**Index Terms** – Breast cancer detection/screening, breast phantoms, dielectric properties, early diagnosis, mixtures, mm-wave imaging system, tissue-mimicking materials.

## I. INTRODUCTION

Breast cancer is the main cause of death among women in industrialized countries [1]. The range of diagnostic tools for breast cancer detection is wide, and the most common is the X-ray mammography. However, the research for new diagnostic methods is growing, because of its limitations (in particular, the woman exposition to ionizing radiations).

A promising alternative is the use of radiofrequencies. In this frequency range, indeed, several campaigns of dielectric characterization on human breast *ex-vivo* samples were performed at microwave [2] and mm-wave frequencies [3]–[5], and all of them have shown that the dielectric difference between healthy and neoplastic tissues is suited to build an imaging system based on the detection of the energy backscattered by the anomaly.

Different prototypes working at microwave [6]–[9] and mm-wave [10] frequencies have been proposed. In particular, mm-waves have been

proposed to achieve a satisfying resolution for early diagnosis, while maintaining a penetration depth in the order of 4 cm below the skin, especially for breast with an high fat content [10].

A fundamental step in the development and optimization of this type of system is represented by the test phase using realistic breast phantoms. To this aim, several solutions have been proposed for 3-D printing technology and not, however the high costs and the risks of the proposed materials are pushing the research of different mixtures.

In this paper, starting from blends currently used for ultrasound breast phantoms [11]–[13], composed by deionized water, sunflower seed oil, dishwashing liquid, and a safe and low cost gelling material, i.e., gelatin, an easy-to-produce and cheap mixture mimicking the dielectric properties of human breast healthy tissues, is presented. For the first time, these mixtures are characterized up to 50 GHz.

The main point is to control the dielectric variations of the produced mixtures changing the percentages of water and oil, without compromising the mixture capability. Indeed, different human tissues are composed by various percentage of water, which in turn represent a major driver for the dielectric properties of the tissues themselves. In particular, the realization of healthy tissues with a large percentage of adipose content, which require a high quantity of oil in the preparation and thus minimum quantities of water, represents one of the most interesting challenges.

## II. EXPERIMENTAL CAMPAIGN

The method of dielectric spectroscopy used for performing all measurements is based on a commercial (Keysight) open-ended coaxial probe, suitable for measurements on liquid and semi-solid materials, in a wide frequency band from 0.5 GHz to 50 GHz and from  $-40^{\circ}\text{C}$  to  $220^{\circ}\text{C}$ . The measurement setup is shown in figure 1, and it is the same used in [3]–[5].

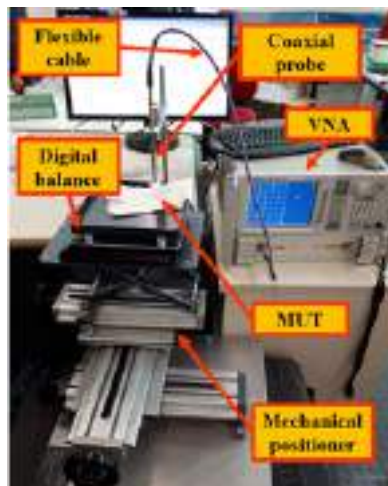


**FIG. 1** – Measurement setup.

The mixture preparation is reported in [14].

According to the different percentages of adipose content characterizing human breast healthy tissues, it is possible to divide them in three different categories of density ([3]-[5]):

- Adipose content  $\geq 80\%$  are indexed as *Low density tissues*;
- Adipose content from 20% to 80% are indexed as *Medium density tissues*;
- Adipose content  $\leq 20\%$  are indexed as *High density tissues*.

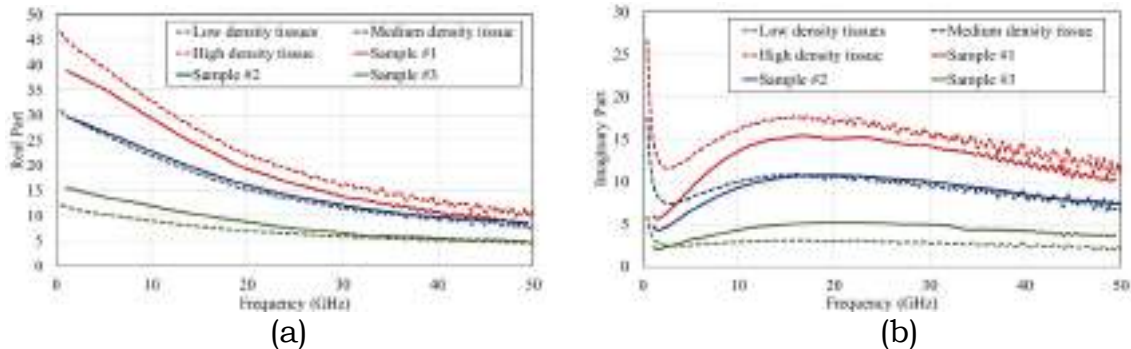


**FIG. 2** – Comparison of the dielectric properties of human healthy breast tissues (dotted lines [5]) and of the produced mixtures.

The dielectric properties for the three categories, as reported in [5], derived from *ex-vivo* samples, were compared with the dielectric properties of the prepared mixtures. The results are shown in fig. 2 (a) and (b) for the real and imaginary part, respectively.

### III. DISCUSSION AND CONCLUSION

In this paper, the dielectric characterization in the frequency range 0.5-50 GHz of three cheap and easy-to-produce mixtures mimicking the dielectric behavior of human healthy breast tissues was presented.

The mixtures presented are composed by deionized water, sunflower seed oil, dishwashing liquid, and a gelatin. The investigated blends for the first time have been characterized up to 50 GHz. The final aim of this work is the creation of a realistic breast phantom to test imaging systems, including prototypes working in the mm-wave frequency range. Results show that by carefully changing the percentages of water and oil it is possible to have a strict control of the resulting dielectric properties for the produced material.

Good agreement between the average values derived from the dielectric characterization of women *ex-vivo* samples and the produced materials is achieved both for real and imaginary part.

### ACKNOWLEDGEMENT

The authors would like to thank the European Institute of Oncology in Milan, Italy, and the Italian Association for Cancer Research. This work

is currently supported by the University of Pavia under the Blue Sky Research project MULTIWAVE.

## REFERENCES

- [1] “International Agency for Research on Cancer,” <http://globocan.iarc.fr/>.
- [2] M. Lazebnik, *et al.*, “A large-scale study of the ultrawideband microwave dielectric properties of normal breast tissue obtained from reduction surgeries,” *Physics in Medicine and Biology*, Vol. 52, No. 10, pp. 2637–2656, 2007.
- [3] A. Martellosio, *et al.*, “Dielectric properties characterization from 0.5 to 50 GHz of breast cancer tissues,” *IEEE Trans. Microw. Theory Techn.*, Vol. 65, No. 3, pp. 998–1011, March 2017.
- [4] A. Martellosio, *et al.*, “0.5–50 GHz Dielectric Characterization of Breast Cancer Tissues,” *IET Electronics Letters*, Vol. 51, No. 13, pp. 974–975, June 2015.
- [5] S. Di Meo, *et al.*, “Dielectric properties of breast tissues: experimental results up to 50 GHz”, *EuCAP2018*, London, UK, April 9–13, 2018.
- [6] N. K. Nikolova, “Microwave imaging for breast cancer,” *IEEE Microwave Magazine*, Vol. 12, No. 7, pp. 78–94, December 2011.
- [7] T. M. Grzegorzczuk *et al.*, “Fast 3-D tomographic microwave imaging for breast cancer detection,” *IEEE Transactions on Medical Imaging*, Vol. 31, No. 8, pp. 1584–1592, August 2012.
- [8] E. C. Fear, *et al.*, “Microwave breast imaging with a monostatic radarbased system: a study of application to patients,” *IEEE Transactions on Circuits and Systems*, Vol. 61, No. 5, pp. 2119–2128, May 2013.
- [9] H. Bahramiabarghouei, *et al.*, “Flexible 16 antenna array for microwave breast cancer detection,” *IEEE Transactions on Biomedical Engineering*, Vol. 62, No. 10, pp. 2516–2525, October 2015.
- [10] S. Di Meo, *et al.*, “On the Feasibility of Breast Cancer Imaging Systems at Millimeter-Waves Frequencies,” *IEEE Trans. Microw. Theory Techn.*, Vol. 65, No. 5, pp. 1795–1806, May 2017.
- [11] E.L. Medsen, *et al.*, “Stability of Heterogeneous Elastography Phantoms Made From Oil Dispersions in Aqueous Gels”, *Ultrasound in Med. & Biol.*, Vol. 32, No. 2, pp. 261–270, February 2006.
- [12] E.L. Medsen, *et al.*, “Tissue-mimicking agar/gelatin materials for use in heterogeneous elastography phantoms”, *Phys. Med. Biol.* 50 (2005) 5597–5618. Doi: 10.1088/0031-9155/50/23/013.
- [13] E.L. Medsen, *et al.*, “Oil-in-Gelatin Dispersions for Use as Ultrasonically Tissue-Mimicking Materials”, *Ultrasound in Med. & Biol.*, Vol. 8, No. 3, pp. 277–287, March 1982.
- [14] S. Di Meo, *et al.*, “Realization of breast tissue-mimicking phantom materials: dielectric characterization in the 0.5–50 GHz frequency range”, *2018 IEEE International Microwave Biomedical Conference (IMBioC)*, Philadelphia, PA, USA, June 14–15, 2018.

# QUANTITATIVE MICROWAVE BRAIN STROKE IMAGING: INVERSION PROCEDURE AND PRELIMINARY EXPERIMENTAL RESULTS

I. Bisio<sup>(1)</sup>, C. Estatico<sup>(2)</sup>, A. Fedeli<sup>(1)</sup>, F. Lavagetto<sup>(1)</sup>, G. L. Mancardi<sup>(3)</sup>,  
M. Pastorino<sup>(1)</sup>, A. Randazzo<sup>(1)</sup>, A. Sciarrone<sup>(1)</sup>, and E. Tavanti<sup>(1)</sup>

<sup>(1)</sup> Department of Electrical, Electronic, Telecommunications  
Engineering, and Naval Architecture, University of Genoa,  
Via Opera Pia 11A, 16145 Genoa, Italy

[matteo.pastorino@unige.it](mailto:matteo.pastorino@unige.it)

<sup>(2)</sup> Department of Mathematics, University of Genoa,  
Via Dodecaneso 35, 16146 Genoa, Italy

[estatico@dima.unige.it](mailto:estatico@dima.unige.it)

<sup>(3)</sup> Department of Neuroscience, Rehabilitation, Ophthalmology,  
Genetics, Maternal and Child Health, University of Genoa,  
Largo Paolo Daneo 3, 16132 Genoa, Italy

[glmancardi@neurologia.unige.it](mailto:glmancardi@neurologia.unige.it)

## Abstract

*This paper reports some recent advancements of the SIEM Unit of Genoa in the development of a microwave imaging system for brain stroke detection. In the proposed approach, the inverse scattering problem is solved by using a quantitative inversion procedure based on an inexact-Newton/conjugate-gradient scheme in  $L^p$  Banach spaces. Numerical and experimental results obtained with a preliminary experimental setup are reported.*

**Index Terms** – Microwave imaging, inverse problems, Banach spaces, brain stroke detection.

## I. INTRODUCTION

Microwave imaging has been considered for a long time as a very promising tool in biomedical applications [1]. Recently, this imaging modality has been proposed for brain stroke detection and very interesting results have been already reported in the scientific literature [2]–[4]. In this framework, this paper reports some recent results obtained by the SIEM Unit of Genoa in the development of a low-cost and portable imaging system for brain stroke detection. In particular, the inverse scattering problem is formulated in terms of integral equations, which are quantitatively solved by an efficient inversion procedure exploiting the regularization properties of the  $L^p$  Banach spaces in conjunction with a nonlinear inexact-Newton/conjugate-gradient inversion scheme. Moreover, a preliminary measurement setup is also described and a first experimental result is reported.

## II. OUTLINE OF THE MATHEMATICAL FORMULATION

With reference to a two-dimensional configuration (characterized by complex dielectric permittivity  $\epsilon_r(\mathbf{r})$ ,  $\mathbf{r} \in D$ , and immersed in a coupling medium with complex dielectric permittivity  $\epsilon_b$ ) under time-harmonic transverse-magnetic incident conditions, the ill-posed nonlinear inverse scattering problem can be formulated in terms of the following operator equation that combines the so-called data and state equations [5]

$$\Psi_t(\mathbf{x}) = \Psi_i(\mathbf{x}) + G_d c (I - G_s c)^{-1} \Psi_i(\mathbf{x}) = F(c)(\mathbf{x}), \quad \mathbf{x} \in D_{obs} \quad (1)$$

where  $\Psi_t$  and  $\Psi_i$  are the  $z$ -components of the total and incident electric fields,  $D_{obs}$  is the observation domain,  $c = (\epsilon - \epsilon_{ref})/\epsilon_b$  is the unknown contrast function ( $\epsilon_{ref}$  being a known reference dielectric profile, e.g., a healthy or homogeneous head), and  $G_{s/d}(\cdot)(\mathbf{x}) = \int_D (\cdot)(\mathbf{x}') g_{ref}(\mathbf{x}, \mathbf{x}') d\mathbf{x}'$ ,  $\mathbf{x} \in D/D_{obs}$ ,  $g_{ref}$  being the inhomogeneous Green's function for the dielectric distribution  $\epsilon_{ref}$ .

Such inverse problem is solved by means of a quantitative iterative procedure performing a regularization in  $L^p$  Banach spaces. In particular, the algorithm is composed by two nested loops. In the outer one (Newton steps), the non-linear problem is linearized around the  $n$ th estimate of the solution  $c_n$  by means of the Fréchet derivative  $F'_n$  of the operator  $F$ . The obtained linear equation,  $F'_n h_n = \Psi_t - F(c_n)$ , is solved in regularized sense by using a truncated conjugate-gradient method in Banach spaces [5], which is based on the following iterative update formula

$$h_{n,k+1} = J_q(J_p(h_{n,k}) + \alpha_k d_k^*), \quad d_k^* = -F_n'^* J_p(F_n' h_{n,k} - e_n) + \beta_{k-1} d_{k-1}^* \quad (2)$$

where  $e_n = F(c_n) - \Psi_t$ ,  $J_p$  is the duality map of  $L^p$ ,  $q$  is the Holder conjugate of  $p$ ,  $F_n'^*$  is the adjoint operator of  $F_n'$ ,  $\alpha_k = \arg \min_{\alpha > 0} \|F_n' J_q(h_k^* + \alpha d_k^*) - e_n\|_p^2$ , and  $\beta_{k-1} = \|F_n'^* J_p(F_n' h_k - e_n)\|_2^2 / \|F_n'^* J_p(F_n' h_{k-1} - e_n)\|_2^2$ . The current estimate of the solution is then updated with  $c_{n+1} = c_n + h_{n,\tilde{k}}$  ( $\tilde{k}$  being the iteration at which the inner loop is stopped). The outer loop is initialized with a starting guess  $c_0$  and it is stopped when a proper termination criterion is satisfied.

## III. NUMERICAL AND EXPERIMENTAL RESULTS

The developed inversion procedure has been firstly tested by using realistic numerical head models. An example of the obtained results, concerning the *AustinMan* 3D phantom shown in Fig. 1(a), is reported in the following. An ellipsoidal model of hemorrhagic brain stroke (semi-axes:  $a_{hs} = 1.5$  cm,  $b_{hs} = 2$  cm, and  $c_{hs} = 1.5$  cm; complex relative dielectric permittivity:  $\epsilon_r = 56 - j53$  at 600 MHz) has been inserted at position  $\mathbf{r}_s = (12, 17.7, 16.5)$  cm. The head is immersed in a 70% glycerin/water mixture.  $S = 20$  antennas (modeled as  $z$ -polarized Hertzian dipoles) are equally

distributed on an elliptic line surrounding the head (semi axes:  $a_{D_{obs}} = 9.5$  cm,  $b_{D_{obs}} = 11.5$  cm) at a height  $z = 16.5$  cm. Each antenna acts sequentially as transmitter and the remaining  $M = 19$  ones are used to collect the  $z$ -component of the scattered field. The scattered-field data have been computed by using the *gprMax* open-source FDTD software and they have been corrupted with an additive Gaussian noise with  $SNR = 25$  dB. A two-dimensional elliptic investigation domain at the same height of the antennas has been considered in the inversion procedure (semi-axes:  $a_D = 8$  cm and  $b_D = 10.5$  cm; discretized into  $N_t = 1741$  square subdomains of side 4.4 mm). The healthy head is used as reference dielectric profile. The inner and outer loops are stopped when a maximum number of 100 iterations is reached or when the normalized difference between the residuals on the data in two subsequent steps falls below 1%. The reconstructed distribution of the relative dielectric permittivity (difference between the retrieved and reference profile) obtained at 600 MHz (for the optimal value of the norm parameter  $p = 1.4$ ) is shown in Fig. 1(b). As can be seen, the stroke is correctly detected and sized.

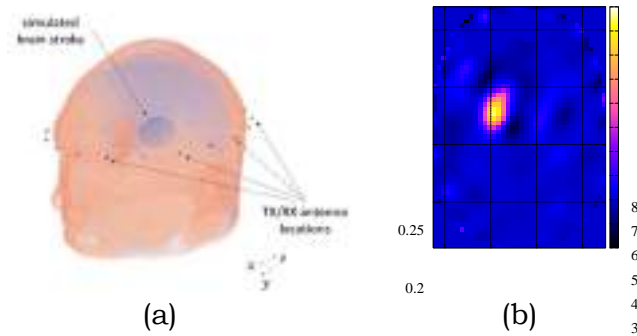


**FIG. 1** – (a) Three-dimensional head model and (b) reconstructed distribution of the real part of the relative dielectric permittivity.

A preliminary experimental setup has also been designed in order to test the developed inversion procedure with real data. A simplified cylindrical phantom with circular cross section, filled with a glycerin/water mixture simulating the average dielectric properties of the human head (i.e.,  $\epsilon_r^{av} = 50 - j17$  at 600 MHz) has been considered. A cylindrical inclusion with dielectric properties simulating blood (i.e.,  $\epsilon_r^{blood} = 60 - j11$  at 600 MHz) has been inserted in the tank (Fig. 2(a)). Ad-hoc designed cavity-backed antennas, shown in the inset of Fig. 2(a), have been used to perform the measurement in  $S = 16$  positions equally distributed on a circumference surrounding the tank. A layer of matching medium ( $\epsilon_r^b = 50 - j17$  at 600 MHz) has been put between the antennas and the structure. The parameters of the inversion procedure are the same as in the previous numerical results. An example of reconstructed distribution of the relative dielectric permittivity obtained at 630 MHz is shown in Figure 2(b). In this case, too, the developed approach is able to correctly locate the inclusion.

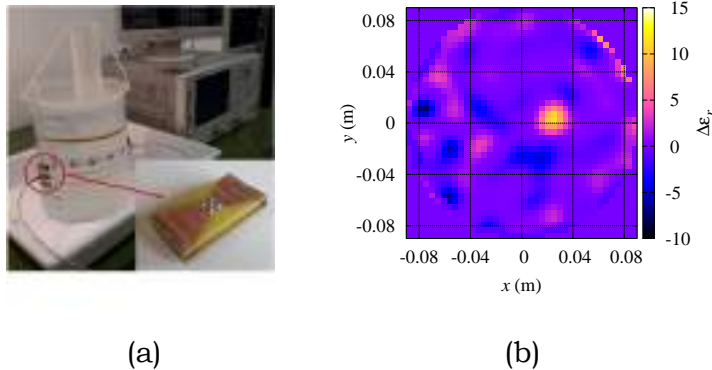


**FIG. 2** – (a) Experimental setup and (b) reconstructed distribution of the real part of the relative dielectric permittivity.

#### IV. CONCLUSION

Some recent results obtained by the SIEM Unit of Genoa in the development of a microwave imaging system for brain stroke detection have been reported in this paper. An inexact-Newton/conjugate gradient inversion procedure in  $L^p$  Banach spaces has been developed for solving the underlying inverse scattering problem. The approach has been validated by using both numerical and real data obtained with a simplified preliminary experimental setup.

#### ACKNOWLEDGEMENT

The present work is partially supported by Compagnia di San Paolo, Italy.

#### REFERENCES

- [1] O. M. Bucci and E. Bucci, “Electromagnetism, nanotechnologies and biology: New challenges and opportunities,” *URSI Radio Sci. Bull.*, vol. 2012, no. 341, pp. 10–21, Jun. 2012.
- [2] P.-H. Tournier *et al.*, “Numerical modeling and high-speed parallel computing: New perspectives on tomographic microwave imaging for brain stroke detection and monitoring,” *IEEE Antennas Propag. Mag.*, vol. 59, no. 5, pp. 98–110, Oct. 2017.
- [3] A. Zamani, A. M. Abbosh, and A. T. Mobashsher, “Fast frequency-based multistatic microwave imaging algorithm with application to brain injury detection,” *IEEE Trans. Microw. Theory Techn.*, vol. 64, no. 2, pp. 653–662, Feb. 2016.
- [4] L. Crocco, I. Karanasiou, M. James, and R. C. Conceição, Eds., *Emerging electromagnetic technologies for brain diseases diagnostics, monitoring and therapy*. Springer International Publishing, 2018.
- [5] C. Estatico, S. Gratton, F. Lenti, and D. Titley-Peloquin, “A conjugate gradient like method for p-norm minimization in functional spaces,” *Numer. Math.*, vol. 137, no. 4, pp. 895–922, Dec. 2017.

# SYNTHESIS OF TARGET-CONFORMAL FIELD INTENSITY PATTERNS FOR HEAD & NECK HYPERTHERMIA TREATMENT

Gennaro G. Bellizzi<sup>(1,2)</sup>, Lorenzo Crocco<sup>(2)</sup>

<sup>(1)</sup> DIIES, Università Mediterranea di Reggio Calabria, Italy

<sup>(2)</sup> CNR-IREA, Napoli, Italy

[gennaro.bellizzi@unirc.it](mailto:gennaro.bellizzi@unirc.it), [crocco.l@irea.cnr.it](mailto:crocco.l@irea.cnr.it)

## Abstract

*This work presents an assessment of the clinical potential of a recently proposed synthesis approach to plan hyperthermia treatments, the multi-target focusing via constrained power optimization. This method pursues, via convex programming, a uniform target-conformal shaping of the specific absorption rate distribution, while avoiding hot-spots in normal tissue. This capability allows a tight control of the administered heating and is crucial for large and irregularly shaped target volumes. The study is concerned with the planning of the treatment of some challenging patient models and its results indicate an average gain of 0,8°C on the median temperature, as compared to the case in which the synthesized field intensity is focused in one point of the target region, rather than conformed to it.*

**Index Terms** – Hyperthermia Treatment Planning, Shaping, Target Conformal Heating, Sim4Life.

## I. INTRODUCTION

Hyperthermia is an anti-cancer treatment that consists in raising the tumor temperature up to 40-44°C for 60-90min. Its related benefits, in combination with radio- and chemo-therapy, have been demonstrated through clinical trials [1]. In delivering the treatment, it is essential to selectively convey the energy in the target region, while preserving healthy tissue from occurrence of “hot-spots”. To this end, given the impossibility of performing direct temperature measurements, the treatment has to be properly planned, through electromagnetic and thermal simulations.

Hyperthermia treatment planning (HTP) aims at synthesizing, based on patient-specific models, the complex excitation coefficients of the applicator (typically a phase array), in order to uniformly shape the specific absorption rate (SAR) over the target volume, while avoiding heating of healthy tissues. In fact, it has been shown that optimizing SAR is not only suitable to enforce the sought temperature distribution (the ultimate HTP goal), but possibly even more robust than directly optimizing the temperature pattern, owing to uncertainties on thermal tissue properties. However, despite many approaches have been proposed, the possibility of uniformly shaping SAR distribution over an extended (possibly irregular) target volume is still an open issue. In fact, such a synthesis goal is not achieved by available synthesis strategies, which aim at “just” focusing the SAR into a given point within the target volume.

Recently, the so called multi-target focusing via constrained power optimization (mt-FOCO) has been proposed to address such a need [2].

This method achieves a sharp loco-regional power deposition control by properly extending the FOCO focusing approach [3] to the shaping problem, while preserving the remarkable advantages of standard FOCO (e.g., optimization via convex programming and control over hot-spots).

In this work, we present an initial assessment of the clinical potential of mt-FOCO as compared to FOCO, in a study concerned with actual HTP of head and neck (H&N) cancer treatment. It is worth noting that the H&N site is highly suited for such a purpose, as patient specific HTP is mandatory for regular clinical practice [1].

## II. MULTI-TARGET FOCUSING VIA CONSTRAINED POWER OPTIMIZATION

Let  $\Omega$  denote the target volume and let  $N$  be the number of (monochromatic) electric sources constituting the applicator. Denoting with  $\Phi_n = \Phi_{x,n}\mathbf{i}_x + \Phi_{y,n}\mathbf{i}_y + \Phi_{z,n}\mathbf{i}_z$  the total electric field induced by the unitary excited by  $n$ -th antenna in  $\Omega$  when the other antennas are off, the overall field in a generic point  $\underline{r} \in \Omega$  can be expressed as:

$$\mathbf{E}(\underline{r}) = \sum_{n=1}^N I_n \Phi_n(\underline{r}) \quad (1)$$

where  $I_n$  ( $n = 1 \dots N$ ) are the complex excitations and  $\mathbf{E} = E_x\mathbf{i}_x + E_y\mathbf{i}_y + E_z\mathbf{i}_z$ .

Assuming that one field component is dominant and considering, for the sake of simplicity, two *control points*, i.e.,  $\underline{r}_{t_1}$  and  $\underline{r}_{t_2}$  arbitrary located into the target volume (rather than just one *target point* as done in FOCO), mt-FOCO is cast as:

*For each point of a sufficiently dense grid of sampling points of  $\phi \in [-\pi, \pi]$ , determine  $I_n$  such to:*

$$\max \Re\{E_i(\underline{r}_{t_1})\} \quad (2.a)$$

*Subject to:*

$$\Im\{E_i(\underline{r}_{t_1})\} = 0 \quad (2.b)$$

$$\Re\{E_i(\underline{r}_{t_2})\} = \Re\{E_i(\underline{r}_{t_1})\} \cos\phi \quad (2.c)$$

$$\Im\{E_i(\underline{r}_{t_2})\} = \Re\{E_i(\underline{r}_{t_1})\} \sin\phi \quad (2.d)$$

$$|\mathbf{E}(\underline{r})|^2 \leq MF(\underline{r}) \quad \underline{r} \in \Omega / \Pi(\underline{r}_t) \quad (2.e)$$

where  $\phi$  is an auxiliary variable encoding the phase shift between the fields in the *control points* and the degree of freedom on the phase in  $\underline{r}_{t_1}$  has been used to cast SAR maximization in this control point in terms of a linear function of the unknown coefficients. In (2), constraints (2.c)-(2.d) enforce the uniformity of the field at target points, while  $MF(\underline{r})$  is a non-negative arbitrary function enforcing patient-specific constraints on the power deposition outside the chosen target volume  $\Pi(\underline{r}_t)$ .

For any fixed value of  $\phi$ , problem (2) is cast as the maximization of a linear function in a convex set, which corresponds to a CP problem [3].

As such, mt-FOCO is able to determine the globally optimal solution by solving different CP problems and then a-posteriori picking the most convenient one, e.g., the one maximizing the SAR into the target volume. Interestingly, such a global search is intrinsically parallel. Moreover, when the number of control points is limited, it can be pursued in an enumerative fashion, whereas more effective strategies are required when the number of control points increases.

Note the assumption that one component is dominant is not mandatory, as, in the general case, the same concept as above can be developed, by relying on the vector FOCO formulation [4]. Of course, this entails an increase of computational burden. Finally, it is worth noting that mt-FOCO provides a general tool to deal with shaping problems. As such, it can be applied to electromagnetic and ultrasound waves in applications as different as high-focused ultrasound, far-field pattern shaping, RFID design and energy harvesting.

### III. EXPERIMENTAL RESULTS

To assess the clinical potential of mt-FOCO, a dataset obtained using the clinical HTP procedure [5], consisting of three 3D patient's models planned for treatment with the HYPERcollar3D [6] has been considered. The HYPERcollar3D is a ring-shaped phased array of 20 patch antennas operating at 434MHz. As 12 amplifiers are available for the clinical treatment, 12 out of 20 antennas are selected. A water bolus fills the space between the applicator and the patient to enhance electromagnetic coupling and avoid undesired heating at the patient's skin [6]. The treatment was evaluated through the temperature distribution simulated using the Penne's Bio-Heat equation, achieved by adjusting SAR to a maximum of 44°C in normal tissue. Electromagnetic and thermal tissues parameters have been assigned according to [5]. The water bolus, external and internal air boundary conditions have been modelled as a mix of convective and Neumann boundary conditions [5].

As standard hyperthermia treatment quality parameter for the comparison, we assumed the T50 prediction, defined as the isotherm volume that covers 50% of the target volume, when the maximum temperature reached in healthy tissues is 44°C. For head and neck hyperthermia, T50 correlates to a good treatment outcome.

Figure 1 shows a cut view along sagittal coronal and transverse planes of the temperature distribution obtained with both FOCO and mt-FOCO for the three considered patient models. In patient A, the T50 raises up to 40,2°C to 41,5°C by means of FOCO and mt-FOCO, respectively. Analogously, T50 for patients B and C increases up to 39,9°C and 40,4°C (FOCO) and to 41,0°C and 40,5°C (mt-FOCO), respectively.

### IV. CONCLUSION

The results of this preliminary study show that, for the patient models at hand, mt-FOCO outperforms FOCO, with an average T50

improvement of 0,8°C. According to the CEM43 model, these results correspond to a thermal dose increased by a factor of 4 for patients A and B. Hence, this confirms the importance of basing HTP on the shaping of the field intensity, rather than simply focusing it in one point.

#### ACKNOWLEDGEMENT

This work has been carried out in collaboration with Erasmus MC, Department of Radiation Oncology, Rotterdam (NL), supported by MIUR under PRIN “FAT SAMMY” and by COST Action MiMed TD1301. Simulations are on Sim4Life, Zurich MedTech AG (CH).

#### REFERENCES

- [1] Paulides et al., *Status quo and directions in deep head and neck hyperthermia*, Rad. Onc. 11:21, 2016.
- [2] Bellizzi et al., *3D Field Intensity Shaping: The Scalar Case*, IEEE Ant. and Wir. Prop. Let., 2017.
- [3] Iero et al., *Optimal Constrained Field Focusing for Hyperthermia Cancer Therapy: a feasibility assessment on realistic phantoms*, PIER, vol.102, 2010.
- [4] Iero et al., *Constrained power focusing of vector fields: an innovative globally optimal strategy*, J. Elec. Wave, vol.29(13), no.5, pp.1708–1719, 2015.
- [5] Verhaart et al., *CT-based patient modeling for head and neck hyperthermia treatment planning: Manual versus automatic normal-tissue segmentation*, Rad. and Onc., vol. 1, no. 111, pp. 158-163, 2014.
- [6] Togni et al., *Electromagnetic redesign of the HYPERcollar applicator: toward improved deep local head-and-neck hyperthermia*, Phys Med Biol., no. 58(17), pp. 5997–6009, 2013.

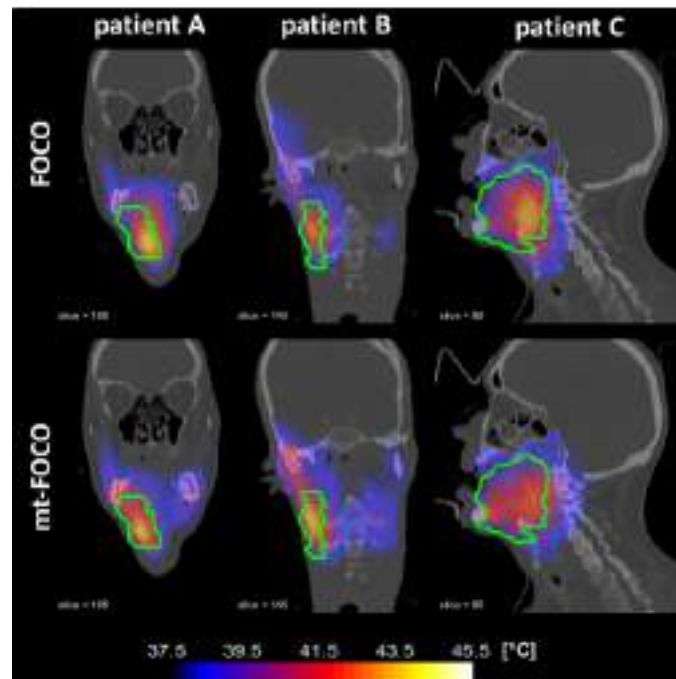


**FIG. 1** – Off center cut views of the temperature distribution obtained by means of FOCO and mt-FOCO. Target area is in green.

# NEW IN-VIVO MAPPING OF HUMAN TISSUES VIA PHASELESS INVERSE SCATTERING AND MRI/CT SEGMENTATION

M. T. Bevacqua<sup>(1)</sup>, G. G. Bellizzi<sup>(1,2)</sup>, L. Crocco<sup>(2)</sup>, T. Isernia<sup>(1,2)</sup>

<sup>(1)</sup> DIIES, Univ. Mediterranea of Reggio Calabria, Italy,  
(martina.bevacqua,gennaro.bellizzi,tommaso.isernia)@unirc.it

<sup>(2)</sup> CNR-IREA, National Research Council of Italy, Naples, Italy,  
crocco.l@irea.cnr.it

## Abstract

*This contribution introduces a novel approach for in-vivo estimation of electrical properties of biological tissues based on the solution of an inverse scattering problem from total field phaseless measurements and on an innovative use of morphological maps derived by magnetic resonance imaging or other medical imaging techniques. This issue is relevant in different medical applications, ranging from hyperthermia treatment planning to dosimetry. A preliminary numerical example of the proposed mapping is given dealing with a realistic anthropomorphic head and neck model.*

**Index Terms** – electrical properties, inverse scattering problem, phaseless data, segmentation.

## I. INTRODUCTION

The knowledge of the electrical properties (EPs) of biological tissues, namely, conductivity and permittivity, has an intrinsic interest for its relevance in different biomedical applications, such as cancer detection, hyperthermia treatment planning (HTP) [1] and electromagnetic dosimetry [2]. Indeed, the accuracy of the assumed electrical model plays a key role on actual in-vivo performances of the therapy and the estimation of field exposition.

Nowadays, the electrical model is built according to the morphological information derived by the segmentation of medical images, e.g. obtained through magnetic resonance imaging (MRI) or computed tomography (CT), and by associating to each tissue of the images the electromagnetic parameters measured in ex-vivo condition. Several ex-vivo EPs databases exist in literature, which are also on-line available, but unfortunately there is no certainty about their reliability with respect to the EPs exhibited by tissues in-vivo conditions [3].

For this reason, this contribution aims at introducing an innovative and low-cost approach for in-vivo estimation of specific patients' EPs. In particular, the mapping is pursued by performing a microwave (MW) tomography and by solving the related inverse scattering problem from phaseless total field measurements [4,5]. In several areas of applied science, the phase distribution of the scattered fields is often too corrupted by noise or are not available phase measurement. As a

consequence, it is of great importance to develop approaches that process only amplitude data, as they can also imply the design of more simple and cheap experimental setups.

As second innovative aspect, the approach benefits in an original way from the patient specific spatial priors extracted from MRI or CT in order to partially overcome the well-known difficulties corresponding to the solution of phaseless inverse scattering problem as well as the reduced spatial resolution of MW imaging.

Throughout the paper we consider the canonical 2D scalar problem (TM polarized fields) and we assume and drop the time harmonic factor .

## II. IN-VIVO ESTIMATION VIA PHASELESS INVERSE SCATTERING PROBLEM AND MRI/CT BASED PROJECTION

Let us encode the EPs of the targets in the contrast function  $\chi(\mathbf{r}) = \epsilon_s(\mathbf{r})/\epsilon_b(\mathbf{r}) - 1$ , wherein  $\epsilon_s$  and  $\epsilon_b$  are respectively the complex permittivities of the tissues and the coupling medium, and denote with  $\mathbf{r} = (x, y)$  a generic point belonging to the investigation domain  $\Omega$ . This latter is probed by means of a set of antennas located in  $\mathbf{r}_t$  on a closed curve  $\Gamma$ , while the resulting scattered fields are measured by receiver antennas also located in  $\mathbf{r}_r$  on  $\Gamma$ . The equations describing the scattering problem are [4]:

$$E_t(\mathbf{r}_r, \mathbf{r}_t) = E_i(\mathbf{r}_r, \mathbf{r}_t) + \mathcal{A}_e[W(\mathbf{r}, \mathbf{r}_t)] \quad (1)$$

$$W(\mathbf{r}, \mathbf{r}_t) = \chi E_i(\mathbf{r}, \mathbf{r}_t) + \chi \mathcal{A}_i[W(\mathbf{r}, \mathbf{r}_t)] \quad (2)$$

where  $E_i$ ,  $E_t$  and  $W$  are the incident field, total field and contrast source induced in the scatterer, respectively, and  $\mathcal{A}_e$  and  $\mathcal{A}_i$  are a short notation for the integral radiation operators. As well-known, the problem is non-linear and it is also ill-posed due to the properties of the involved operator  $\mathcal{A}_e$  [4]. Moreover, these difficulties are further worsened when, as the case at hand, only phaseless total field measurements  $|E_t|^2$  are available [5].

Very many different approaches have been developed in literature in order to partially take on such difficulties. In the following we consider the single step approach in [5], wherein the unknowns  $W$  and  $\chi$  are simultaneously estimated by minimizing a non-linear functional, i.e.:

$$\Phi(W, \chi) = \sum_t \frac{\|W - \chi E_i - \chi \mathcal{A}_i[W]\|_{l_2}^2}{\|E_i\|_{l_2}^2} + \sum_t \frac{\||E_t|^2 - |E_i + \mathcal{A}_e[W]|^2\|_{l_2}^2}{\||E_t|^2\|_{l_2}^2} \quad (3)$$

wherein the illumination and spatial dependences are neglected for the sake of brevity. Due to the strongly non-linearity of the problem, the functional (3) is non-quadratic. Moreover, due to the huge number of the involved unknowns, gradient-based minimization schemes could be trapped in local minima.

In order to avoid the occurrence of *false* solutions and simplify the complexity of the inverse scattering problem, some priori information on  $\chi$  can be exploited. To this end, the proposed approach introduces an innovative representation basis conveniently derived from the segmentation of the MRI or CT images, which allows to restrict the dimensionality of the unknown space and to fall into the right attraction basin. Accordingly, the contrast function  $\chi$  is projected into a ‘tissue space’, i.e.:

$$\chi(r) = \sum_{n=1}^N \hat{\chi}_n \mathcal{T}_n(r) \quad (4)$$

where  $N$  is the number of tissues arising in the MRI images and  $\mathcal{T}_n$  is a basis function which assumes non-zero values only in those pixels belonging to the considered tissue. By using representation (4) into minimization of  $\Phi$  (3), the actual unknowns of the problem become the coefficients  $\hat{\chi}_n$ , which represent the EPs corresponding to the  $n$ -th tissue. The inverse scattering problem is hence turned into a parameter estimation problem, wherein only a single (complex) parameter is looked for in each different tissue. By so doing, the number of unknown parameters is strongly reduced to  $N$ , and this results in a strongly reduction of the ill-posedness and non-linearity.

Note that the tissue projection (4) represent a general approach to deal with in-vivo estimation of patient specific EPs and it can be used in conjunction with other different and well assessed inversion techniques.

### III. NUMERICAL VALIDATION

In order to assess the capability of the proposed in-vivo EPs estimation, a preliminary numerical example dealing with a transversal slice of an anthropomorphic 3D head and neck model is provided. The model is derived by merging the morphological information gathered from a high-resolution voxel-based anthropomorphic phantom [6] with the results from *ex-vivo* tissue dielectric spectroscopy [7]. In particular, on the basis of the results in [3], these values have been increased of about 25% for permittivity and 30% for conductivity. Moreover, in order to consider a more realistic scenario, the EPs in each voxel of the model have been perturbed by a  $\pm 10\%$  uniformly distributed random fluctuation.

The data have been simulated by using a full wave forward simulator based on the method of moments and corrupted with a random Gaussian noise with a given SNR. In particular, a set of incident fields radiated by 30 line sources evenly spaced on a circumference with radius of 0.3 m has been considered. Following [1], the working frequency is  $f=434\text{GHz}$ , while the matching medium has permittivity 78 and conductivity 0.04 S/m. The subdomain has been discretized in  $64 \times 64$  cells of size 0.2295 m.

In figures 1(a)-(b) are reported the permittivity and conductivity values of the retrieved profiles corresponding to different SNR and the different tissues. As it can be seen the estimation of the EPs is extremely accurate, thanks to the basis representation (4) which is composed of just eight functions. The obtained mean square error with respect to the actual complex permittivities values are about 0.00018, 0.00041 and 0.0032, respectively for SNR=70 dB, 60 dB and 50 dB. Note that 30 line sources correspond to a number of independent data, which is less than the actual degrees of freedom of the original problem [5].

More details and other examples will be given at the conference, together with an assessment of a recently introduced hyperthermia treatment planning technique.

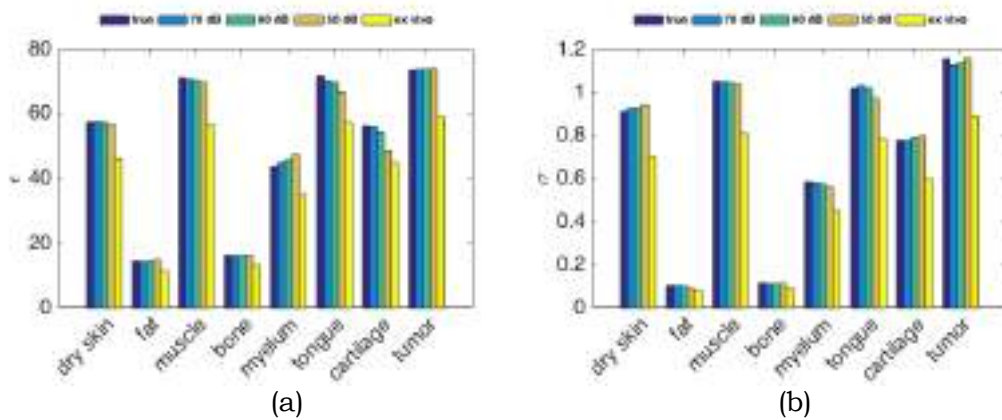


**FIG. 1** – In-vivo estimation of head and neck EPs: Retrieved values of (a) permittivity and (b) conductivity corresponding to different SNR.

## REFERENCES

- [1] Rijnen et al., Quality and comfort in head and neck hyperthermia: A redesign according to clinical experience and simulation studies, *Int J Hyperthermia*, 31(8): 823–830, 2017.
- [2] Durney, C H., Electromagnetic dosimetry for models of humans and animals: A review of theoretical and numerical techniques, *Proceedings of the IEEE*, 68(1): 33-40, 1980.
- [3] R J Halter et al, The correlation of in-vivo and ex-vivo tissue dielectric properties to validate electromagnetic breast imaging: initial clinical experience, *Physiol. Meas.* 30(6): S121, 2009.
- [4] D. Colton and R. Kress. *Inverse Acoustic and Electromagnetic Scattering Theory*, Springer-Verlag, Berlin, Germany, 1998.
- [5] M. D'Urso, K. Belkebir, L. Crocco, T. Isernia, and A. Litman, "Phaseless imaging with experimental data: facts and challenges," *J. Opt. Soc. Am. A* 25, 271-281, 2008.
- [6] Zubal, C. Harrell, E. Smith, Z. Rattner, G. Gindi, and P. Hoffer, Computerized three-dimensional segmented human anatomy, *Med. Phys.*, 21(2): 299–302, 1994.
- [7] P. A. Hasgall, F. D. Gennaro, C. Baumgartner, E. Neufeld, M. Gosselin, D. Payne, A. Klingenbock, and N. Kuster, *IT'IS Database for thermal and electromagnetic parameters of biological tissues*, Version 3.0, 2015.

# AN EXPERIMENTAL ASSESSMENT OF THERMAL ABLATION MONITORING VIA MICROWAVE TOMOGRAPHY

R. Scapaticci<sup>(1)</sup>, M. Cavagnaro<sup>(2)</sup>, V. Lopresto<sup>(3)</sup>, R. Pinto<sup>(3)</sup>, L. Crocco<sup>(1)</sup>

<sup>(1)</sup>IREA, National Council of Research of Italy, Naples, Italy  
[scapaticci.r,crocco.l](mailto:{scapaticci.r,crocco.l}@irea.cnr.it) @irea.cnr.it

<sup>(2)</sup>DIET, Sapienza University of Rome, Rome, Italy  
[cavagnaro@diet.uniroma1.it](mailto:cavagnaro@diet.uniroma1.it)

<sup>(3)</sup>ENEA, Division of Health Protection Technologies, Casaccia Research  
Center, Rome, Italy  
[vanni.lopresto,rosanna.pinto](mailto:{vanni.lopresto,rosanna.pinto}@enea.it)@enea.it

## Abstract

*This communication reports a first experimental assessment of the use of microwave tomography for monitoring thermal ablation for cancer treatments. In particular, the monitoring of a controlled microwave thermal ablation experiment on ex-vivo bovine liver sample is presented. The results confirm the capability of microwave tomography of providing information on the performed treatment.*

**Index Terms** – Microwave imaging, microwave ablation, image guided therapy.

## I. INTRODUCTION

Thermal ablation (TA) is a cancer treatment consisting in the induction of coagulative necrosis of tumour cells by local heating, which can be achieved by using various sources (radio-frequency, ultrasound, microwaves). Thanks to its minimal invasiveness, TA is gaining importance in clinical practice. However, its beneficial effects would be significantly improved if treatment delivery would be paired with imaging tools, able to monitor the evolution of the ablated tissue in real-time. Currently, the temperature in the region under treatment is monitored by local thermometric probes, which, besides being invasive, can only provide local measurements. Moreover, “standard” clinical imaging modalities (such as computed tomography or magnetic resonance imaging) suffer limitations, either related to cost or the unhealthy side-effects for the patient and operator. This motivates the interest in alternative techniques.

Recently, microwave tomography (MWT) was proposed as a low-cost and portable modality to monitor the overall thermal ablation treatment [1], enabled by the temperature-dependent changes occurring in the dielectric properties of tissue during the treatment [2]. In [3], a first feasibility study concerning the use of MWT as a tool to monitor changes of tissue dielectric properties (and therefore of temperature) during thermal ablation was presented. Based on the positive outcomes, a first experimental campaign aimed at validating the idea has been

carried out. This communication presents the initial results of this proof-of-concept study. In particular, the experiment was concerned with the microwave thermal ablation (MTA) of *ex-vivo* bovine liver tissue, under laboratory-controlled conditions. A time domain processing was adopted to analyze the measured data, confirming the great potential of MWT as a non-invasive tool to monitor TA.

## II. EXPERIMENTAL SET-UP AND MEASUREMENT PROTOCOL

The experimental set-up was composed by two independent devices. The first device is aimed at performing the ablation experiment. This was carried out with a commercial MTA apparatus inserted in an *ex-vivo* specimen of bovine liver, delivering to the applicator an average net power of about 60 W at 2.45 GHz (CW) for a time of 8 minutes. Such a protocol (power and time) was chosen in order to achieve an ablated zone completely included in the tissue sample [4].

The second device performs the monitoring task via MWT. To this end, a Vivaldi antenna was connected to a vector network analyzer (VNA) to measure the antenna's reflection coefficient (S11) in the 1–4 GHz frequency band, sampled over 201 points. The MWT antenna, positioned at a distance of about 1 cm from the (raw) liver surface, was moved along a line orthogonal to the shaft of the applicator (Fig. 1). Measurements were carried out in 13 positions, ranging from -3 cm to 3 cm, with respect to the applicator's axis, which was positioned at the zero of the assumed reference system, as shown in Fig. 1.

MWT measurements were performed before the ablation (untreated tissue, taken as "reference" condition) and after completion of the MTA procedure. At the end of the experiment, the specimen was sectioned along the coronal plane, i.e., the plane coplanar with the shaft of the applicator, to allow visual inspection of the ablated zone. In the coronal plane (XY in Fig. 1), the typical ellipsoidal-shaped thermally coagulated area can be appreciated. In the transverse plane, (YZ), i.e., the plane orthogonal to the shaft of the applicator, the thermal lesion has typically a circular shape. From the visual inspection, the ablated area has been gauged to a radius of 23 mm, while 4 mm of tissue remained untreated. Moreover, a shrinkage effect, that is, a contraction of 7 mm in the central area of the sample, was also observed [4,5].

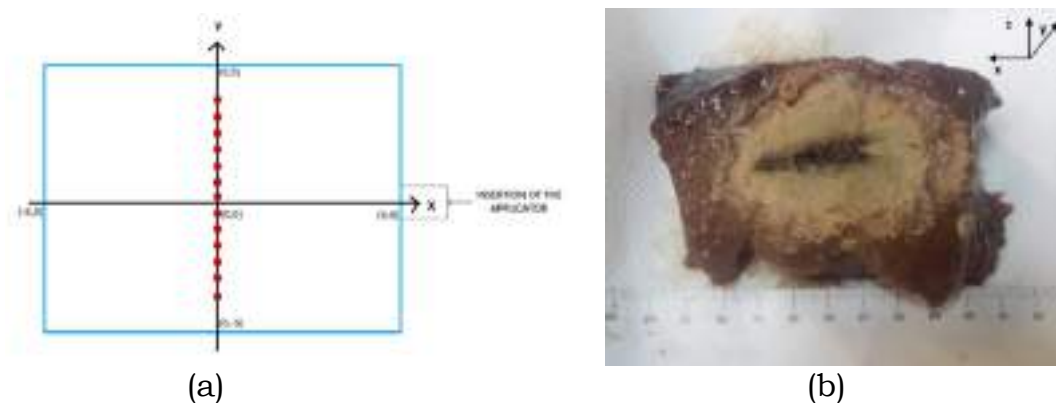


**FIG. 1** – (a) 2D Geometry of the experiment (coronal plane). The red circles denote the positions of the MWT antenna. Distances are in centimeters. (b) Inspection of the tissue specimen after MTA treatment.

### III. PROCESSING OF THE DATA

The possibility of using MWT to monitor the evolution of MTA relies on the changes in the dielectric properties of tissue during the treatment [2]. As such, a “simple” differential processing the MWT data collected at various time instants (e.g., before and after ablation) should be in principle sufficient to achieve the sought information, and in particular to image the boundary between treated and untreated tissue. In practice, treatment outcomes are not so straightforward, since the change in dielectric properties of tissue is not the only phenomenon occurring during ablation. As a matter of fact, as highlighted by the visual inspection, the treatment may induce a deformation of the sample [5], which obviously influences the differential data.

In order to cope with this issue, the data measured by the MWT system were pre-processed. In particular, the (differential) time-harmonic signals measured for each MWT antenna position were converted into time domain via 1-D Inverse Fourier Transform (IFT) and windowed. Such a windowing had to be such to filter out the contribution of the MWT antenna ringing, that of the air-liver interface, and the effect of the deformation of the liver surface. Moreover, it had to avoid the occurrence of replicas due to the limited bandwidth. Taking into account these constraints, the time window in the presented experiment was set to about 0.45 ns, which corresponds to about 1 cm in liver. Note this window can be shifted in time to inspect the specimen at different depths. Finally, the windowed signal (in time domain) was converted to frequency domain (via FFT) and fed into a tomographic algorithm based on the truncated singular value decomposition [3].

By means of the above procedure, the tomographic reconstruction shown in Fig. 2a was obtained. In this image, the origin of the reference system is located at the quota of the MWT antenna, so that the top of the image corresponds to the position of the untreated liver surface. This result allows appraising the treated-to-untreated boundary, which, in agreement with visual inspection, is located at about 1 cm from the

original surface (instead of 1.1 cm, given by 7mm due to shrinkage effect plus 4 mm of tissue remained untreated). It is interesting to observe how the tomographic image obtained from the windowed data after ablation (shown in Fig.2b) does not give a meaningful result, thus showing the relevance of performing both the difference of the signals and the time-domain preprocessing.

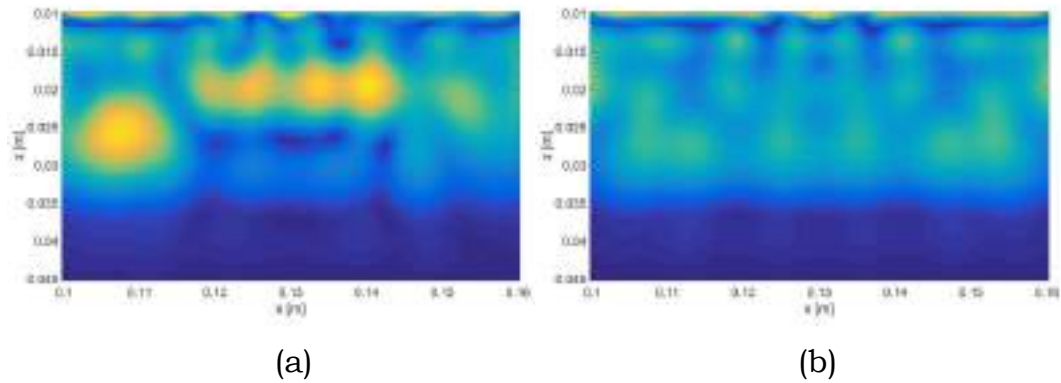


**FIG. 2** – Tomographic reconstructions obtained with (a) differential data; (b) post-treatment data

#### IV. CONCLUSIONS

The results of an experiment aimed at validating the use of microwave tomography to monitor microwave thermal ablation treatments have been presented. The initial outcomes herein described confirm the potential of the technique and have also highlighted the need of suitable preprocessing strategies, required to achieve data that can be properly handled by means of tomographic algorithms.

#### REFERENCES

- [1] R. Hoffmann et al., “Comparison of four microwave ablation devices: An experimental study in ex vivo bovine liver,” *Rad.*, vol. 268(1), pp. 89–97, 2013.
- [2] V. Lopresto et al., “Changes in the dielectric properties of ex vivo bovine liver during microwave thermal ablation at 2.45 GHz”, *Phys. Med. Biol.* Vo.57, pp. 2309–27, 2012.
- [3] R. Scapatucci et al., “Exploiting Microwave Imaging Methods for Real-Time Monitoring of Thermal Ablation,” *Int. J. Ant. Propag.*, vol. 2017, Article ID 5231065, 13 pages, 2017.
- [4] C. Amabile et al., “Tissue shrinkage in microwave ablation of liver: an ex vivo predictive model”, *Int. J. Hyperth.* Vol.33, pp. 101-109, 2017
- [5] V. Lopresto et al., “CT-based investigation of the contraction of *ex vivo* tissue undergoing microwave thermal ablation”, *Phys. Med. Biol.* Vol. 63, no. 5, pp. 055019, 2018.

# MAGNETIC BIOMATERIALS FOR BONE TUMOR HYPERTHERMIA: A NUMERICAL STUDY

A. Fanti <sup>(1)</sup>, M. B. Lodi<sup>(1)</sup>, G. Vacca<sup>(1)</sup>

<sup>(1)</sup> Department of Electrical and Electronic Engineering, University of Cagliari  
Cagliari  
Piazza D'Armi, 09123 Cagliari, Italy  
[alessandro.fanti@diee.unica.it](mailto:alessandro.fanti@diee.unica.it)

## Abstract

*Bone tumors can be treated via in situ hyperthermia employing novel magnetic biomaterials. In this work, magnetic hydroxyapatite and poly-ε-caprolactone scaffolds are investigated. The non-linear temperature dependence is included, moreover a Cole-Cole model is proposed to describe the frequency response of material magnetic susceptibility and to assess their use as therapeutic tools. Employing proper magnetic, dielectric and thermal properties for scaffold and tissues, in this work the effectiveness of magnetic induction hyperthermia against Osteosarcomas and Fibrosarcoma is investigated through an in silico model. The strength and frequency of external magnetic field were tuned to increase temperature above 43°C for at least 60 min in each tumor region without affecting healthy bone tissue.*

**Index Terms** – bone tumors, cole-cole model, hyperthermia, magnetic nanoparticles.

## I. INTRODUCTION

Hyperthermia treatment is widely recognized as a powerful clinical tool against tumors [1]. The aim of this therapy is to selectively rise tumor temperature above 42.5 °C for a time sufficient to cause protein aggregation and denaturation, inducing cytotoxicity, then altering tumor blood flow and microenvironment, causing cancer cells death [1]. Electromagnetic (EM) energy can be employed to increase cancer tissue temperature, as investigated by Fan et al. exploiting microwave (MW) irradiation of pathologic bone tissue [3]. Bone cancers are a wide class of neoplasms estimated to afflict 3 cases a year per 100'000 persons, between 10 to 20 years, with survival rate from 30% to 40% [1]. Such lesions cause pain, chronic inflammation, discomfort and movement limitations, even pathologic fractures in affected patients [3]. Among bone tumors, bone-forming, i.e. Osteosarcoma (OS), and cartilage-forming, i.e. Fibrosarcoma (FS), are most diffuse one [3]. Hence, in this work they are considered as target of the hyperthermia treatment. Anyway, the MW treatment [2] determines an 8% recurrence rate and several pathological fractures after surgery. This implies that grafts or the use of bone scaffolds to withstand tissue regeneration should be employed in clinical practice [2], [3]. This orthopedic oncology neediness

lead to the development of functional magnetic biomaterials to withstand healthy bone healing while allowing in situ hyperthermia via power dissipation under the action of an external time-varying magnetic field [4]. Innovative scaffolds biomaterials, able to perform in situ hyperthermia of bone tumor, are based on magnetic nanoparticles (MNPs), which are embedded in traditional bone tissue materials [4].

The aim of this paper is to investigate major influence parameters for in situ hyperthermia treatment of bone tumors exploiting magnetic scaffolds.

## II. MAGNETIC PROPERTIES MODELING AND BIO-HEAT EQUATION

The power per unit volume dissipated by magnetic scaffolds can be described as suggested by Roseinzweig [5]:

$$P_M = \mu_0 \pi f H^2 \chi'' \quad (1)$$

where  $\mu_0$  is vacuum permeability in  $\text{Hm}^{-1}$ ,  $f$  is the frequency of the applied alternating magnetic field,  $H$  is its strength in  $\text{Am}^{-1}$  and  $\chi''$  is the imaginary part of material magnetic susceptibility. This last term has been traditionally evaluated using Debye model [5], as for the ferrofluids case. Anyway, recently it was demonstrated that a Cole-Cole scheme [5] allows a more appropriate description of experimental heating curves [5]. Therefore, the complex magnetic susceptibility,  $\chi(\omega)$ , of both magnetic hydroxyapatite and poly- $\epsilon$ -caprolactone scaffolds can be written as [5]:

$$\chi(\omega) = \chi' - j\chi'' = \frac{\chi_0}{1 + (j\omega\tau)^{1-\gamma}} \quad (2)$$

where  $\chi'$  is the magnetic susceptibility real part,  $\omega$  is the angular frequency and  $\gamma$  is the so-called Cole-Cole exponent, which can be assumed equal to 0.75 [5]. The characteristic Néel relaxation time  $\tau$  follows the definition given in Ref. [4]. Moreover, in this model, the pre-exponential constant  $\tau_0$  is assumed to be a decreasing function of temperature [6]. Finally, the equilibrium susceptibility,  $\chi_0$ , is assumed inversely dependent from system temperature [5], [6]. From the solution of Maxwell equations in the frequency domain, the computed EM power is inserted in the Pennes equation to determine the spatio-temporal distribution of temperature in tissues [7].

## III. SIMULATIONS

Osteosarcomas and Fibrosarcoma affect mainly long bones extremities [2]. Therefore, in this paper, the case of a magnetic scaffold implanted in distal femur after surgical intervention is analyzed (Fig. 1). The software COMSOL Multyphysics is employed, especially Magnetic Fields and Heat Transfer Modules (COMSOL inc., Burlington, MA).

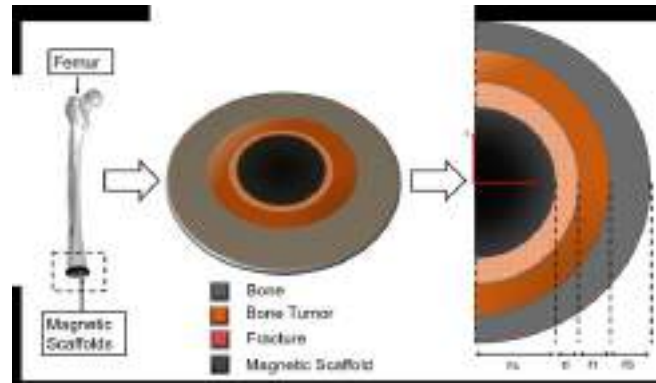


**FIG. 1** – A scaffold implanted after long bone tumor surgical treatment is analyzed. A transverse section of bone, residual cancer tissue, fracture gap and scaffold are considered, with radius  $r_b$ ,  $r_t$ ,  $r_i$ ,  $r_s$  respectively.

A homogenous uniform external magnetic flux density field  $B_0(t)$  is assumed applied along the  $z$ -axis. The orthopedic implant has a radius of 5 mm. Nearby the scaffold, there is a region where new bone forms to heal surgical fracture, its radius was set to 0.1 mm. For both OS and FS, tumor radius was varied between 1 mm to 5 mm.

#### IV. RESULTS

The non-linear dependence from temperature of material magnetic properties causes the magnetic field to vary with time, implying a stationary condition for the heating phenomenon (data not shown). Temporal and spatial distribution of temperature is qualitatively similar for both bone cancers. Therefore, as an example, in Fig. 2 it is shown  $T(r,z)$  in the case of a OS, with  $r_t = 0.5$  mm, when a 30 mT and 293.15 kHz is applied.

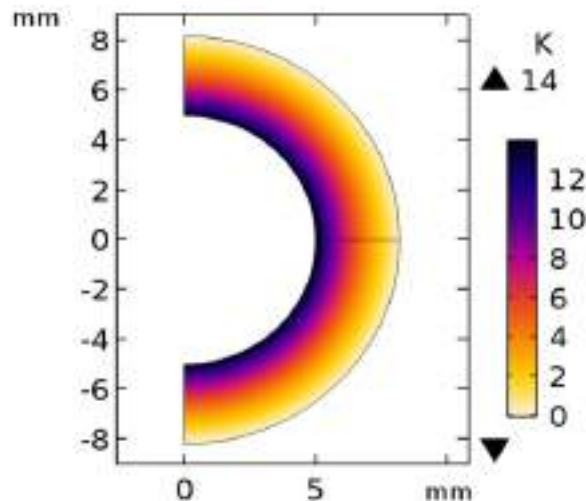


**FIG. 2** – 2D temperature distribution after 85 min of exposure to the eternal magnetic radiofrequency field.

Finally, the volume averaged temperature increase in tumor region was monitored to assess if the lethal threshold of 43 °C was overcome for

more than 60 min [1]. From Fig. 3, it can be noticed that the magnetic hydroxyapatite is the most performant biomaterials for in situ hyperthermia of bone tumors. Finally, an efficient treatment can be devised for both OS and FS.

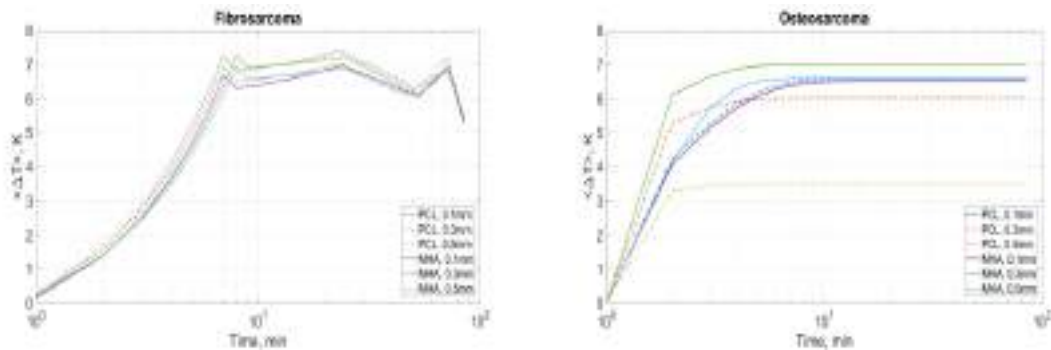


**FIG. 3** – Mean temperature in the tumor region as a function of time. Both scaffolds material performances are reported with varying  $r_t$ .

### REFERENCES

- [1] B. Hildebrandt, P. Wust, O. Ahlers, A. Dieing, G. Sreenivasa, T. Kerner, R. Felix, & H. Riess. "The cellular and molecular basis of hyperthermia," *Critical reviews in oncology/hematology*, vol. 43, no.1, pp. 33-56, 2002.
- [2] Q. Y. Fan, B. A. Ma, X. C. Qiu, Y. L. Li, J. Ye, Y. Zhou, "Preliminary report on treatment of bone tumors with microwave- induced hyperthermia," *Bioelectromagnetics*, vol. 17, no. 3, pp. 218-222, 1996.
- [3] C. D. Fletcher, K. K. Unni, & F. Mertens, "*Pathology and genetics of tumors of soft tissue and bone*", vol. 4, Iarc, 2002, cap. 11, 12, pp. 224-231, 253-290.
- [4] M. Bañobre-López, Y. Pineiro-Redondo, M. Sandri, A. Tampieri, R. De Santis, V. A. Dediu, J. Rivas, "Hyperthermia induced in magnetic scaffolds for bone tissue engineering," *IEEE Transactions on Magnetics*, vol. 50, no. 11, Nov. 2014, Art. no. 5400507.
- [5] A. Fanti, M. B. Lodi, G. Mazzarella, "Enhancement of Cell Migration Rate Toward a Superparamagnetic Scaffold Using LF Magnetic Fields," *IEEE Transactions on Magnetics*, vol. 52, no. 10, Art. no. 5200508 Oct. 2016.
- [6] S. Laurent, D. Forge, M. Port, A. Roch, C. Robic, L. Vander Elst, R. N. Muller, "Magnetic iron oxide nanoparticles: synthesis, stabilization, vectorization, physicochemical characterizations, and biological applications," *Chemical reviews*, vol. 108, no. 6, pp. 2064-2110, 2008.
- [7] H. Arkin, L. X. Xu, K. R. Holmes, "Recent developments in modeling heat transfer in blood perfused tissues," *IEEE Transactions on Biomedical Engineering*, vol. 41, no. 2, pp. 97-107, 1994.

# NUMERICAL RESULTS ON A MILLIMETER-WAVE CONFORMAL ARRAY FOR BREAST CANCER DETECTION

S. Di Meo<sup>1</sup>, G. Matrone<sup>1</sup>

<sup>1</sup>Dept. of Electrical, Computer and Biomedical Engineering University of Pavia, Pavia, Italy  
simona.dimeo01@universitadipavia.it

## Abstract

*Breast cancer places fifth as a cause of death from cancer, especially among women. However, screening techniques have increased the success rate of medical therapies. Based on the well-known limitations of the most commonly used screening methods, microwave imaging has been proposed as an alternative solution. By detecting the dielectric discontinuities in the tissues, microwave imaging systems are able to detect malignant lesions, without exposing the patient to ionizing radiations. With respect to the actual microwave prototypes, the novel system proposed in this paper works at a higher central frequency, i.e. 33.25 GHz, and with a bandwidth of about 13.5 GHz. These two values determine a higher achievable resolution, which would make it possible an early-stage cancer detection. However, at these frequencies the propagation medium is particularly challenging in terms of loss and penetration depth. Consequently, the beam-forming algorithms used to form the image play a crucial role to obtain optimum results even in a lossy medium. In this paper, the feasibility study of a system based on a mm-waves multi-static radar architecture is presented, focusing the attention on the comparison between two different beam-forming algorithms.*

**Index Terms** – Biomedical applications; breast cancer detection; beamforming; link budget; microwave and mm-wave imaging.

## I. INTRODUCTION

Breast cancer is one of the most common type of tumor among women. However, the continuous development of diagnostic devices and imaging techniques have allowed to achieve increasingly accurate and early diagnosis [1]. The most used imaging technique is X-ray mammography, but its drawbacks prevent its use on a large scale for screening applications. For this reason, microwave imaging has been recently proposed as a complementary imaging technique [2]–[5]. Indeed, microwave systems make use of non-ionizing radiations, are available at relatively low-cost, and are suitable for an operator-independent implementation, thus allowing for a possible periodic screening of a large fraction of the population. Different system architectures have been proposed, and they all rely on the dielectric contrast between normal and tumorous breast tissues [6], [7]. However, all of them share similar operational frequencies, not exceeding a few GHz, and consequently in some cases they prevent achieving an early detection, because of the reduced image resolution [2], [8]. The use of higher

frequencies, in the mm-wave range, envisaged by a number of works, would yield to better spatial resolution and to the downscaling of many components, but unfortunately at the cost of an higher signal attenuations inside breast tissues [9]–[11]. Therefore, an accurate feasibility study, on the grounds of recent experimental results on the dielectric properties of breast tissues up to 50 GHz ([12], [13]), is very important to assess the potentials of such an approach. In particular, a key point is the represented by the beam-forming algorithms, which are fundamental to obtain optimal image even for lossy media. This paper presents a multi-static radar architecture for breast cancer detection working at a central frequency of 30 GHz.

## II. MULTI - STATIC RADAR ARCHITECTURE

In the design of a new imaging system for breast cancer detection based on mm-waves, it is fundamental to increase as much as possible the Signal-to-Noise ratio (S/N) to compensate for the large propagation losses. For this reason, in the present work a multi-static radar architecture is considered.

The multi-static radar architecture considered in this paper is based on a 2-port Vector Network Analyzer (VNA) (or on a dedicated transceiver), an array of  $M$  antennas, and a  $2:M$  switch matrix, either electro-mechanical or integrated, to connect the VNA ports to the antennas. The working principle is named Synthetic Aperture Focusing (SAF) technique and it is explained in [MIO MTT]. A sketch of the proposed system is shown in Fig. 1. The circular (conformal) layout appears to be the best solution for breast cancer imaging.

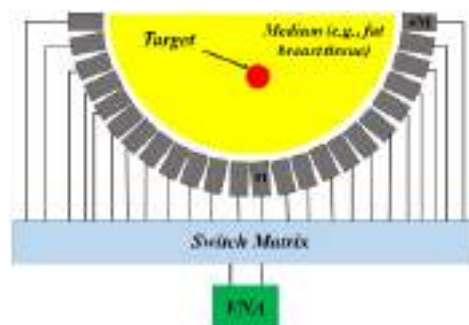


**FIG. 1** – Sketch of the multi-static radar architecture.

## III. FULL-WAVE MODELS AND IMAGE ALGORITHMS

*Full-wave simulations* were carried out using the Ansys EM solver HFSS. Open-ended WR28 waveguides, with a mono-modal bandwidth of 13.5 GHz [26.5 – 40] GHz, were used as radiators. The complete simulated models are described in [9].

Given the large importance of image reconstruction algorithms for this type of applications, two different approaches were implemented to evaluate different possibilities. In particular, the performance obtained

with standard DAS beam-forming was compared to that achieved by F-DMAS [14], i.e. a non-linear beam-forming algorithm developed for ultrasound B-mode imaging, which derives from the DMAS beam-former introduced for breast confocal microwave imaging in [15]. The image reconstruction procedure is described in [16].

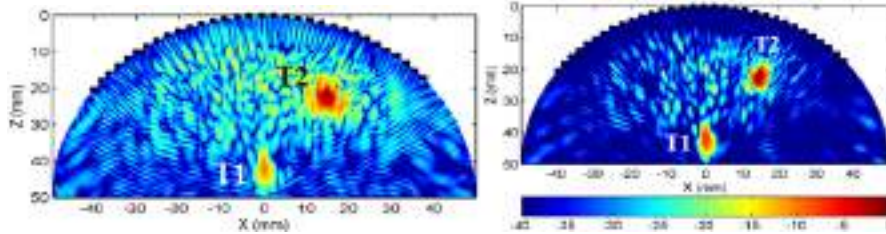


**FIG. 2** – Reconstructed image for circular configuration using: DAS beam-forming (left); F-DMAS beam-forming (right). Color scale in dB.

#### IV. RESULTS AND CONCLUSIONS

Fig. 2 shows the image reconstructed with both the approaches. Target 1 (T1) refers to the tumor on the central  $x = 0$  mm axis, Target 2 (T2) refers to the off-axis one. For T1, resolutions are:  $\delta R = 8.1$ mm and  $\delta L = 3.4$ mm (DAS);  $\delta R = 6.4$ mm and  $\delta L = 2.3$ mm (F-DMAS). For T2, resolutions are:  $\delta R = 5.1$ mm and  $\delta L = 3.7$ mm (DAS);  $\delta R = 4.4$ mm and  $\delta L = 2.4$ mm (F-DMAS).

In this paper some preliminary results of a feasibility study of a new mm-wave imaging system for breast cancer detection are discussed. A full-wave model, implementing the dielectric properties of breast tissues (normal and tumorous) experimentally derived from ex-vivo samples, were implemented, and two different image reconstruction algorithms (DAS and F-DMAS) were compared, showing the possibility to image targets at a depth of 4 cm.

#### ACKNOWLEDGEMENT

The authors would like to thank the Italian Association for Cancer Research.

#### REFERENCES

- [1] “Cancer Treatment and Survivorship Facts & Figures 2014-2015,” *Atlanta: American Cancer Society; 2014*.
- [2] N. K. Nikolova, “Microwave imaging for breast cancer,” *IEEE Microw. Mag.*, Vol. 12, No. 7, pp. 78-94, December 2011.
- [3] T. M. Grzegorzczuk *et al.*, “Fast 3-D tomographic microwave imaging for breast cancer detection,” *IEEE Trans. Med. Imag.*, Vol. 31, No. 8, pp. 1584-1592, August 2012.
- [4] E. C. Fear, *et al.*, “Microwave breast imaging with a monostatic radar-based system: a study of application to patients,” *IEEE Trans. on Circuits and Systems*, Vol. 61, No. 5, pp. 2119-2128, May 2013.

- [5] H. Bahramiabarghouei, *et al.*, “Flexible 16 antenna array for microwave breast cancer detection,” *IEEE Trans. Biomed. Eng.*, Vol. 62, No. 10, pp. 2516–2525, October 2015.
- [6] M. Lazebnik, *et al.*, “A large-scale study of the ultrawideband microwave dielectric properties of normal breast tissue obtained from reduction surgeries,” *Physics in Medicine and Biology*, Vol. 52, No. 10, article 001, pp. 2637–2656, 2007.
- [7] M. Lazebnik, *et al.*, “A large-scale study of the ultrawideband microwave dielectric properties of normal, benign and malignant breast tissues obtained from cancer surgeries,” *Physics in Medicine and Biology*, vol. 52, no.20, pp. 6093–6115, 2007.
- [8] M. Klemm, *et al.*, “Contrast-enhanced breast cancer detection using dynamic microwave imaging,” *2012 IEEE Antennas and Propagation Society International Symposium*, Chicago, U.S.A., July 8–14, 2012.
- [9] S. Di Meo, *et al.*, “On the Feasibility of Breast Cancer Imaging Systems at Millimeter-Waves Frequencies,” *IEEE Trans. Microw. Theory Techn.*, Vol. 65, No. 5, pp. 1795-1806, May 2017.
- [10] S. Moscato, *et al.*, “A mm-Wave 2D ultra-wideband imaging radar for breast cancer detection,” *Int. J. Antennas Propag.*, Vol. 2013, Article ID 475375, 8 pages, 2013, doi:10.1155/2013/475375.
- [11] L. Chao, M. Afsar, and K. Korolev, "Millimeter wave dielectric spectroscopy and breast cancer imaging," *2012 7th European Microwave Integrated Circuits Conference (EuMIC)*, Amsterdam, The Netherlands, October 28 - November 2, 2012.
- [12] A. Martellosio, *et al.*, “Dielectric properties characterization from 0.5 to 50 GHz of breast cancer tissues,” *IEEE Trans. Microw. Theory Techn.*, Vol. 65, No. 3, pp. 998-1011, March 2017.
- [13] A. Martellosio, *et al.*, “0.5-50 GHz Dielectric Characterization of Breast Cancer Tissues,” *IET Electron. Lett.*, Vol. 51, No. 13, pp. 974-975, June 2015.
- [14] G. Matrone, *et al.*, “The Delay Multiply and Sum beamforming algorithm in ultrasound B-mode medical imaging,” *IEEE Trans. Med. Imag.*, vol. 34, no. 4, pp. 940-949, 2015.
- [15] G. Matrone, *et al.*, “Depth-of-field enhancement in Filtered-Delay Multiply and Sum beamformed images using Synthetic Aperture Focusing,” *Ultrasonics.*, vol. 75, pp. 216-225, 2017.
- [16] S. Di Meo, *et al.*, “High-Resolution mm-Wave Imaging Techniques and Systems For breast Cancer Detection”, *IEEE MTT-S International Microwave Workshop Series on Advanced Materials and Processes*, Pavia, Italy, September 20-22, 2017.

# **A MICROWAVE RADAR SYSTEM FOR INDOOR POSITIONING TRACKING OF ELDERLY AND DEPENDENT PEOPLE**

Giacomo Paolini

DEI – University of Bologna, viale Risorgimento 2, 40136, Bologna, Italy  
giacomo.paolini4@unibo.it

## **Abstract**

*In this paper, a portable RFID reader operating at the frequency of 2.45 GHz is described: it exploits the Monopulse RADAR technique with the added capability of electronic beam-steering. This architecture has already demonstrated its effectiveness in multiple tags accurate localization in harsh electromagnetic indoor environments, detecting the angular position of the tags, and, with a simple algorithm based on the received signal strength, to fast estimate the distance of the tags from the reader with centimeter-level accuracy. This work has been developed within the framework of the Regional Operative Project “HABITAT” and is part of a research presented in [1]. Thanks to this simple and light reader, long-term people habits and ambient occupancy in typical indoor scenarios can be accurately monitored in almost real time.*

**Index Terms** – Monopulse RADAR, RFID reader, tags selection, tracking old people.

## **I. INTRODUCTION**

Over the last few years, with the growing availability of low-cost and low-power wireless sensor networks, there has been an ever-increasing trend to include innovative wireless technologies in living spaces in order to create Smart Spaces and allow different Internet of Things (IoT) operations.

Moreover, in the last decades, the average age of the population is rising and, as a consequence, also the number of retired people is significantly increasing and their monitoring to detect as soon as possible any kind of disease or issue related to the age is becoming a matter of urgency; it's demonstrated that the early detection of disorders such as Alzheimer's disease or other types of senile dementia, can be accomplished by analyzing the movements and the behavior of high-risk patients [2].

In this work we show how this operation can be performed by a simple and light-weight reader operating at 2.45 GHz.

## **II. READER ARCHITECTURE**

The reader has been presented for the first time in [3], for the detection of fixed tags in hostile electromagnetic environments.

Fig. 1 shows the photographs of the prototype and its hardware architecture.

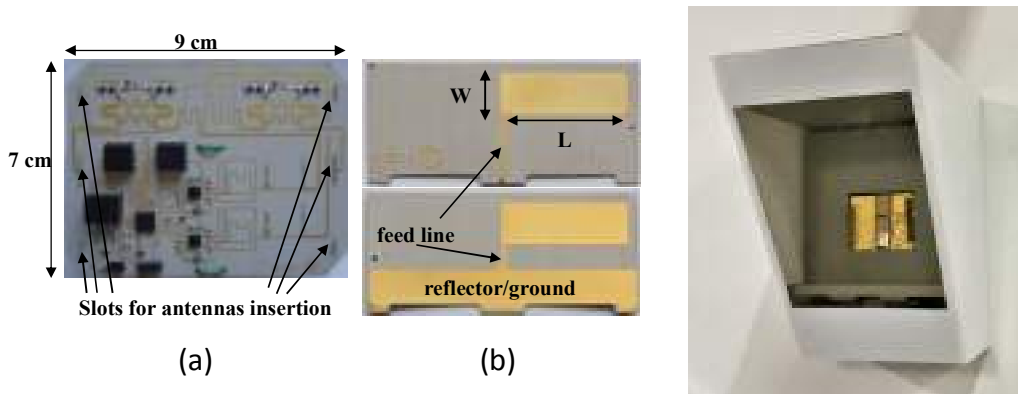


**FIG. 1** – Reader prototype: in the left, (a) circuit back view and (b) antennas layout; in the right, the adopted solution to include the smart object in everyday environments (a lamp, in this case).

Through the electromagnetic/circuitual design of a reflection-type phase shifter [4] (Fig. 1(a)), given by a meandered branch-line coupler whose inner ports are loaded by nonlinear reflective loads (two series varactors), a continuous tuning of the excitation phase of a couple of planar antennas can be obtained. An additional meandered rat-race coupler makes available a couple of array ports: the sum ( $\Sigma$ ) and the difference ( $\Delta$ ). In this way the Monopulse RADAR principles (based on the combination of the  $\Sigma$ - and  $\Delta$ -enhanced radiation patterns information) is exploited while scanning both the patterns. As radiating elements, two planar flag-shaped dipole antennas are adopted (Fig. 1(b)): the double-sided topology allows to obtain a smooth transition from the balanced antenna port to the unbalanced microstrip circuitry, without any additional balun.

This architecture has demonstrated its effectiveness in indoor environments where both the tag-reader distances are not too big (up to 5 m) and clutter or fast fading effects must be faced. In [3], accuracies of few centimetres are feasible up to 3 m-distance.

### III. MOVING TAGS LOCALIZATION

In order to add the capability of the reader to track the movements of tagged people in a bi-dimensional area, additional data processing has been included. Of course, a preliminary calibration is still needed, but it can be very simple thanks to the high accuracy of the angular position measurement previously described. Under the hypothesis of static channel, only three measurements of the maximum  $\Sigma$  RSSI received from the tag are performed: indeed, the room is sectorized into three radial reading zones, where the tag is placed at a reference distance.

After the calibration and the real-time measurement of the received RSSI signals, the distance  $d$  of the tag from the reader is given as:

$$d = 10^{\frac{(P_0 - P_R)}{10 \cdot n}} \quad (1)$$

where  $P_0$  and  $P_R$  are the maximum values of the RSSI received at the  $\Sigma$  port during calibration at one meter and in real-time, respectively, whereas  $n$  is the path-loss exponent [5].

The overall time required for a single-measurement is 200 ms (40 steps), including the initial overhead for tags ID acquisition and 60 ms dedicated to the dialogue with each tag.

As an experiment, the reader has been placed in a real office scenario with an estimated path-loss exponent of  $n=2$ ; the corresponding measured results are reported in Tab. I for the first position of the reader, considering the average of 10 successive measures.

**TABLE I: MEASUREMENTS IN THE OFFICE SCENARIO (N=2)**

Point	Actual Position ( $x_0; y_0$ )	Measured Position ( $x_m; y_m$ )	Distance Reader-Tag	Percentage Error
Point #1	(5.15;1.50)	(5.85;1.25)	1.75	13.86%
Point #2	(2.45;1.20)	(3.10;0.55)	3.79	33.70%
Point #3	(3.35;0.60)	(3.56;0.50)	2.77	6.83%
Point #4	(4.55;0.90)	(4.66;0.90)	1.75	2.37%
Point #5	(5.75;2.00)	(5.96;1.99)	2.02	3.45%

All the coordinates and distances are expressed in meters.



**FIG. 2** – A typical everyday life environment where the measurements took place (Expo Sanità, Bologna, 18-20 April 2018).

From Tab. I inspection, it is easy to notice that the highest errors occur for both higher reader-tag distances and in proximity to the calibration zone boundaries (points #1 and #2).

As a further experiment, a real tracking of a tagged person in the same office has been carried out: excellent agreement with actual track is achieved in real-time, in case of reader-tag Line of Sight (LoS).

#### IV. CONCLUSION

In this work, a portable microwave reader realizing real-time movement analysis has been presented to identify the positions of people moving in an indoor environment considering a static channel. The effectiveness of the reader operations has been demonstrated by detecting the tags' position even in harsh electromagnetic areas, with the possibility to early diagnose specific age-related diseases strictly connected to the repetition of particular movements.

#### ACKNOWLEDGEMENT

This work was funded by the EU-supported Regional Operative Project HABITAT — Home Assistance Based on Internet of Things for the Autonomy of Everybody (<http://www.habitatproject.info>).

I want to thank my PhD supervisor, Prof. Alessandra Costanzo, and co-supervisor, Prof. Diego Masotti, for the helpful support and the successful collaboration in the framework of the project.

#### REFERENCES

- [1] G. Paolini, D. Masotti, and A. Costanzo, "Hand-Held Radar for People Tracking in Indoor Scenarios", *2<sup>nd</sup> URSI AT-RASC*, 28 May-1<sup>st</sup> June 2018 [Accepted Paper].
- [2] M. F. Mendez, J. S. Shapira, and B. L. Miller, "Stereotypical movements and frontotemporal dementia", *Movement Disorders*, vol. 20(6), pp. 742-745, Mar. 2005.
- [3] M. Del Prete, D. Masotti, N. Arbizzani, A. Costanzo, "Remotely Identify and Detect by a Compact Reader with Mono-Pulse Scanning Capabilities," *IEEE Trans. Microwave Theory Tech.*, vol. 61(1), pp. 641-650, Jan. 2013.
- [4] H. Kwon, H. Lim, B. Kang, "Design of 6–18 GHz Wideband Phase Shifters Using Radial Stubs", *IEEE Microw. Wirel. Comp. Lett.*, vol. 17(3), pp. 205 – 207, 2007.
- [5] P. C. Liang, and P. Krause, "Smartphone-Based Real-Time Indoor Location Tracking With 1-m Precision", *IEEE J. Biomedical and Health Informatics*, vol. 20(3), pp. 756-762, May 2016.

# INTEGRATED RADAR TILE FOR X/KA BAND SAR APPLICATIONS

Emilio Arnieri<sup>1</sup>, Luigi Boccia<sup>1</sup>, Giandomenico Amendola<sup>1</sup>, Chunxu Mao<sup>2</sup>, Steven Gao<sup>2</sup>, Tobias Rommel<sup>3</sup>, Srdjan Glisic<sup>6</sup>, Piotr Penkala<sup>4</sup>, Milos Krstic<sup>5</sup>, Anselm Ho<sup>7</sup>, Uroschanit Yodprasit<sup>6</sup>, Oliver Schrape<sup>5</sup>, Marwan Younis<sup>3</sup>

<sup>1</sup> DIMES, University of Calabria, Italy. <sup>2</sup> School of Engineering and Digital Arts, University of Kent, Canterbury, UK. <sup>3</sup> Microwaves and Radar Institute, German Aerospace Center (DLR), 82234 Wessling, Germany. <sup>4</sup> Evatronix S.A. Bielsko-Biala, 43-300 Bielsko-Biala, Poland. <sup>5</sup> IHP, 15236 Frankfurt (Oder), Germany. <sup>6</sup> Silicon Radar GmbH, 15236 Frankfurt (Oder), Germany. <sup>7</sup> Innovative Solutions In Space BV, 629 JD, Delft, Netherlands.

[emilio.arnieri@unical.it](mailto:emilio.arnieri@unical.it)

## Abstract

*The paper presents an integrated radar tile for X/Ka band digital beamforming (DBF) space-borne Synthetic Aperture Radar (SAR) receiver. The system is a low-cost, lightweight, low-power consumption, and dual-band (X/Ka) dual-polarized module ready for the next-generation spaceborne SAR missions.*

**Index Terms** – Digital beamforming (DBF), dual-band, dual-polarized, synthetic aperture radar (SAR)

## I. INTRODUCTION

DIFFERENT project [1] proposes a multi-static SAR based on formation flying small satellites to solve the existing problems of traditional SAR systems. DIFFERENT is an abbreviation for “digital beamforming for low-cost multistatic spaceborne SARs”. The objective of the DBF-SAR system is to achieve a low cost, lightweight, low-power consumption, and dual-band (X/Ka) dual-polarized module for the next-generation spaceborne SAR system in Europe. In [1] a general description of the SAR system were provided. In this paper the integration of all subsystems in a complete radar tile will be presented and discussed. The radar tile has been realized using an innovative 15 layers stack-up where all involved components have been integrated together.

## II. RADAR ARCHITECTURE

Antennas are integrated in a RF board that accommodates also 60 MMICs (Monolithic Microwave Integrated Circuit) chips. The function of each RF MMIC unit is to down-convert the received V- and H-polarized signals to an intermediate frequency (IF) band, generating 60 output channels (48 at Ka-band and 12 at X-band). The RF board can be divided in 12 tiles, each of them generates five output channels (4 at Ka-band and 1 at X-band). The tile is the fundamental functional unit of the SAR array. The output down-converted signals are routed to an ADC board where are processed in the digital back-end block. Finally,

digitized data corresponding to each channel and polarization are weighted and combined in the DBFN implemented in six digital boards. This paper deals with the design, manufacturing, and testing of a single radar tile, demonstrating the correct operation of the whole systems composed by several components integrated in an advanced PCB stack-up. Fig. 1 (a) shows the architecture of the proposed radar tile. Each tile accommodates:

- one H-polarized X-band antenna;
- one V-polarized X-band antenna;
- eight Ka-band (two in elevation, four in azimuth) dual-polarized antennas.
- two MMIC chips at X band (for V and H polarized signals);
- four MMIC chips at Ka band (two for V and two for H polarized signals);
- two local oscillator distribution networks for the two bands ( X and Ka).

Each X-band antenna is connected to a single MMIC chip, the signal is down-converted using a 9.6-GHz local oscillator (LO) signal. Each Ka-band chip is connected to four Ka-band antenna elements. The signal from every antenna element are summed on-chip and then down-converted using an off-chip LO signal of 35.75 GHz. In this way every  $2 \times 2$  Ka-band antennas is actively combined in the tile to form a single channel.

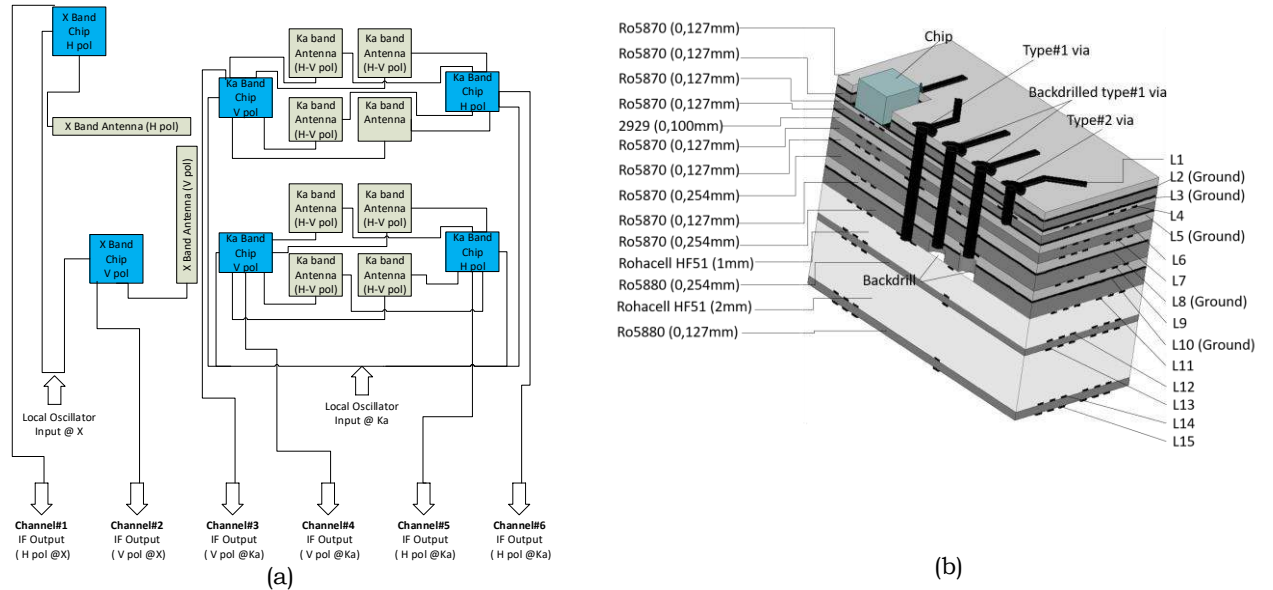


**FIG. 1** – (a) Digital beamforming synthetic aperture radar (SAR) architecture; (b) 15 Layers Board Stack-up

### III. MANUFACTURED RADAR TILE

Fig. 1 (b) shows the proposed stack-up used to design the radar tile. The technology used in this work is based on an advanced multilayer PCB technology, which includes fifteen layers of metallization. Laser

cavities are carved between layers L1 and L3 to accommodate the MMIC chips.

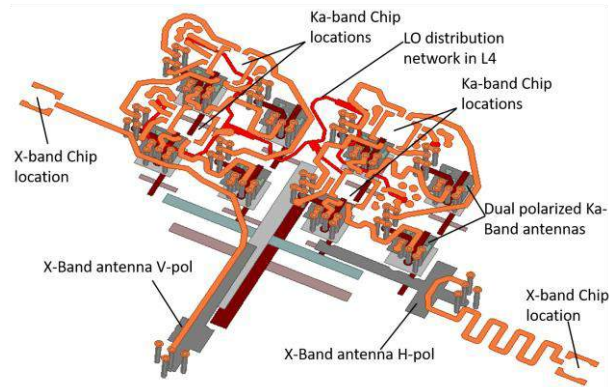


**Fig. 2** Integration of the antennas in the 15 layer stack-up of a single tile.

Ka band antennas are dual-polarized stacked patches electromagnetically coupled to the feeding lines via dedicated slots (Fig. 2). The driven patch has been integrated in the layer L11 of the stack-up. A slot in the ground layer L10 is used to couple the patch with the feeding stripline printed in L9. Connection between microstrips in the top L1 layer and feeding strips in L9 is obtained using the quasi-coaxial vertical transitions. Two orthogonal parasitic dipoles and a patch are added near the driven patch to improve the radiation patterns. The X-band antenna is realized with a pair of cross-dipole antennas printed on layers L13 and L15 proximately coupled to a driven dipole printed on L11. Fig. 3 shows the the manufactured radar tile.

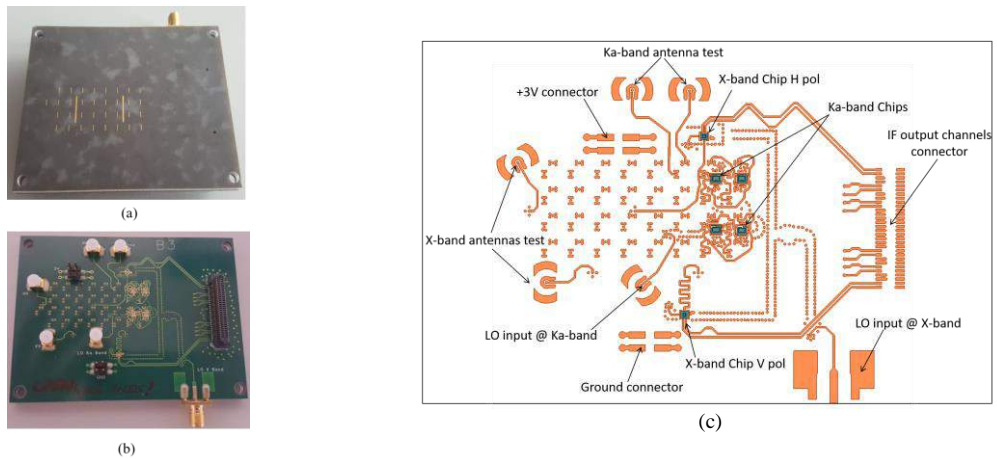


**Fig. 3** Manufactured tile: (a) Antenna side (b) Chip side. (c) architecture of the manufactured tile.

#### IV. MEASUREMENTS

Manufactured board (Fig. 3) has been tested with two set of measurements: direct antenna characterization measuring S-parameters and radiation patterns; Antenna+chip characterization

realized illuminating the board with horn antennas and measuring the IF signal of the six output channels. The purpose of the measurements is to demonstrate the correct operation of the whole system composed by several components integrated in the proposed 15 layers stack-up. Fig 4 shows the Measured S-parameters and gain of the Ka band antennas. Fig. 5 (a) shows the measurement setup used to measure the conversion gain of the Ka-band chip as shown in Fig. 5 (b). Similar results have been obtained for the X-band case.

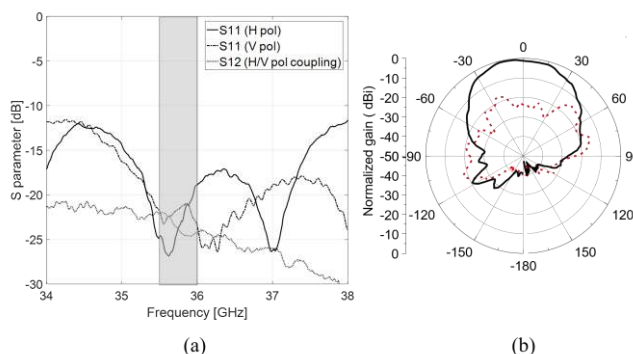


**Fig. 4**(a) Measured S parameters of the Ka-band antenna; (b) Normalized gain of the Ka-band antenna at 35.75 GHz,

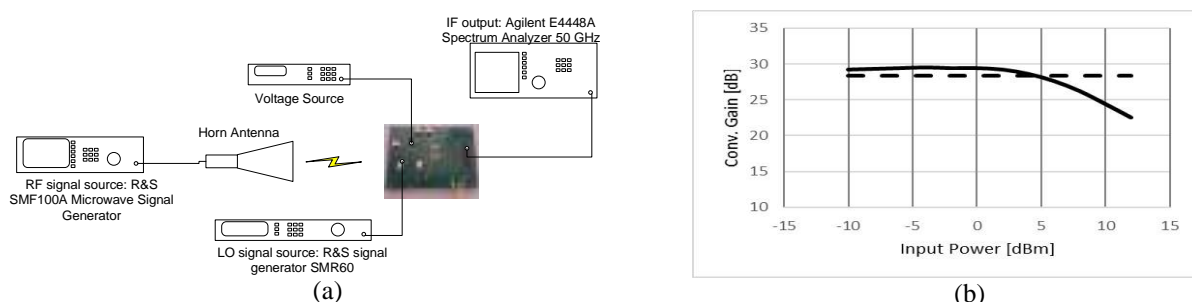


**Fig. 5** (a) Measurement setup at Ka-band; (b) Measured conversion gain of the Ka-band receiver vs. RF input power. Continuous line: current prototype; dashed line: on wafer measurement.

## V. CONCLUSION

In this work an integrated radar tile for X/Ka band Synthetic Aperture Radar Instruments were presented. The tile has been realized as a single integrated component, comprising a dual-band dual-polarized sub-array, related feeding and distribution networks and MMICs. A more detailed account of the system and of measurements will be given in the course of the presentation.

## REFERENCES

- [1] C. X. Mao et al., "X/Ka-Band Dual-Polarized Digital Beamforming Synthetic Aperture Radar," in *IEEE Transactions on Microwave Theory and Techniques*, vol. 65, no. 11, pp. 4400-4407, Nov. 2017.

# ANALYTICAL MODEL FOR THE BISTATIC RCS OF SHIPS BASED ON THE GEOMETRICAL OPTICS APPROXIMATION

A. Di Simone<sup>(1)</sup>, W. Fuscaldo<sup>(2)</sup>, L. M. Millefiori<sup>(3)</sup>, G. Di Martino<sup>(1)</sup>, A. Iodice<sup>(1)</sup>, G. Ruello<sup>(1)</sup>, D. Riccio<sup>(1)</sup>, P. Braca<sup>(3)</sup>, P. Willett<sup>(4)</sup>

<sup>(1)</sup> Department of Information Technology and Electrical Engineering, University of Naples “Federico II”, 80125 Naples, IT

<sup>(2)</sup> Department of Information Engineering, Electronics and Telecommunications, “Sapienza” University of Rome, 00184 Rome, IT

<sup>(3)</sup> NATO-STO Centre for Maritime Research and Experimentation, 19126 La Spezia, IT

<sup>(4)</sup> Department of Electrical and Computer Engineering, University of Connecticut, Storrs, CT 06269 USA

[alessio.disimone@unina.it](mailto:alessio.disimone@unina.it), [walter.fuscaldo@uniroma1.it](mailto:walter.fuscaldo@uniroma1.it)

## Abstract

*This paper deals with the theoretical derivation of an electromagnetic (EM) model for the bistatic radar cross section (RCS) of ship targets. In particular, here we focus on the modelization of the double scattering contributions arising from the interaction between the ship hull and the sea surface. The overall scattered EM field is derived under the Kirchhoff approximation and the Geometrical Optics solution. Closed-form expressions for the scattering matrix and the radiation integral are provided. Numerical results show the role of the acquisition geometry and ship orientation on the bistatic RCS.*

**Index Terms** – Electromagnetic scattering, geometrical optics, radar cross section, ship detection.

## I. INTRODUCTION

In this work, we analytically evaluate the bistatic radar cross section (RCS) of a ship, under the Kirchhoff Approximation (KA) and geometrical optics (GO). Taking cues from [1], where a rigorous theoretical framework has been developed for modeling the backscattering RCS of buildings in urban scenarios, we extend the previous results to the most generic bistatic configuration. Specifically, a ship in open sea is represented as a parallelepiped lying over a rough surface [1]. The GO approximation allows us to clearly distinguish the different contributions arising from multiple bounces between the sea surface and the ship hull. In particular, here we focus on the double-bounce contributions (i.e., sea-to-hull, and hull-to-sea), since they turn out to be the most relevant ones [1]. Furthermore, the material composition of the ship, as well as the geometry of acquisition, the ship orientation, sea state, polarization of the incident and reflected electromagnetic (EM) waves are accounted for.

## II. BISTATIC RCS MODEL OF THE SHIP TARGET

In this paper, we consider the same geometry and symbols reported in [1], and aim at extending the backscattering RCS model in [1] to generic bistatic configurations. The ship target is modeled as a parallelepiped with smooth dielectric surfaces, lying on a rough sea surface, modeled as a two-dimensional (2-D) zero mean isotropic Gaussian stochastic process with standard deviation  $\sigma$ , and auto-correlation function  $\rho(\cdot)$ . The transmitter position is described by the radar look angle  $\theta$ , while the receiver position by the look angle  $\theta_s$  and the azimuthal angle  $\varphi_s$ . In the framework of the KA-GO approach, and assuming an incident plane wave, the scattered EM field can be expressed as [1], [2]:

$$\begin{bmatrix} E_{sh} \\ E_{sv} \end{bmatrix} = jk \frac{e^{jkr}}{4\pi r} \begin{bmatrix} S_{hh} & S_{vh} \\ S_{hv} & S_{vv} \end{bmatrix} \begin{bmatrix} E_{0h} \\ E_{0v} \end{bmatrix} \underbrace{\iint_{A_0} e^{j(\underline{k}_i - \underline{k}_s) \cdot \underline{r}'} d\underline{r}'}_{I_{A_0}}$$

where all the symbols are defined in [1]. The single scattering contribution arising from the ship deck is a plane wave propagating in the specular direction  $\hat{k}_{s,top} = -\sin\theta \hat{y} + \cos\theta \hat{z}$ . Its evaluation is straightforward and omitted here. The scattered field is fully described by the scattering matrix  $\underline{\underline{S}}$  accounting for the material composition of the surface and the scattering integral  $I_{A_0}$  accounting for the surface roughness. Analytical closed-form expressions for  $\underline{\underline{S}}$  and  $I_{A_0}$  are reported in Table I and Table II for the ship-sea and sea-ship reflections, respectively.

## III. NUMERICAL RESULTS

In this section, numerical results of the model presented in the previous section are reported. The dimensions of the simulated ship target are 250 x 30 x 10 m<sup>3</sup>. We considered a sea surface with Douglas sea-state equal to 2, corresponding to standard deviation equal to 0.1 m and root mean square (rms) slope  $\sigma\sqrt{2|\rho''(0)|}$  equal to 0.073 [3]; sea water dielectric constant is evaluated via the Klein-Swift model with sea salinity 35 ppm, and temperature 19 °C. Figure 1 shows the bistatic RCS as a function of  $\varphi_s$  for  $\varphi = 0^\circ$  (long side of the ship facing the transmitter),  $\varphi = 15^\circ$ ,  $\varphi = 30^\circ$ , and  $\varphi = 45^\circ$  for linear co-pol HH, VV, and cross-pol HV channels. It is worth noting that larger values of the aspect angle  $\varphi$  will give similar results due to the symmetry of the ship target. Contributions from the different ship sides are clearly visible as local peaks of the RCS. The ship orientation dictates the angular position of such peaks. Co-pol channels give similar results in the considered scenario. Finally, it is demonstrated that, for a large range of ship orientations, the backscattering acquisition

geometry (where  $\varphi_s = 90^\circ$ ) represents the most favorable configuration for ship detection applications in multistatic systems, such as GNSS-R [4].

#### IV. CONCLUSION

In this paper, an analytical model for the bistatic RCS of ship targets has been presented and analyzed in numerical results. The KA-GO solution has been exploited for the derivation of closed-form expressions of the scattered EM field. For the sake of mathematical tractability, the ship target has been modeled as a parallelepiped with smooth dielectric surfaces, while a 2-D Gaussian stochastic process has been introduced for the sea surface roughness. In this paper, we focused on the double-bounce scattering contributions ship-sea and sea-ship, thus neglecting the higher-order triple-bounce term. The numerical analysis has emphasized the impact of the ship orientation and acquisition geometry on the RCS. It is demonstrated that, for a large range of ship orientations, the backscattering acquisition geometry represents the most favorable configuration for ship detection applications in multistatic systems, such as GNSS-R [4].

#### ACKNOWLEDGEMENT

This research has been funded by the Office of Naval Research under contract N00014-16-13157, and this support is acknowledged with thanks to John Tague and Michael Vaccaro. There is parallel support to ONR-Global. This research has also been funded by the Department of Information Technology and Electrical Engineering of the University of Naples, “Federico II”, in the framework of the MORES project.

**Table I – Double Scattering Contribution (ship-sea)**

$$\begin{aligned}
S_{hh} &= \frac{\cos\psi_1}{\sin^2\psi_1 \sin^2\zeta \cos\zeta} \left[ A_{pp} \left( R_{\perp} R_{\perp W} T' \cos\theta \cos\phi + R_{\parallel} R_{\parallel W} U \sin\phi \right) + A_{pp} \left( R_{\perp} R_{\parallel W} T' \sin\phi - R_{\parallel} R_{\perp W} U \cos\theta \cos\phi \right) \right] \\
S_{sh} &= \frac{\cos\psi_1}{\sin^2\psi_1 \sin^2\zeta \cos\zeta} \left[ A_{ps} \left( -R_{\perp} R_{\perp W} T' \sin\phi + R_{\parallel} R_{\parallel W} U \cos\theta \cos\phi \right) + A_{ps} \left( R_{\perp} R_{\parallel W} T' \cos\theta \cos\phi + R_{\parallel} R_{\perp W} U \sin\phi \right) \right] \\
S_{hs} &= \frac{\cos\psi_1}{\sin^2\psi_1 \sin^2\zeta \cos\zeta} \left[ A_{sp} \left( -R_{\perp} R_{\perp W} U \cos\theta \cos\phi + R_{\parallel} R_{\parallel W} T' \sin\phi \right) - A_{sp} \left( R_{\perp} R_{\parallel W} U \sin\phi + R_{\parallel} R_{\perp W} T' \cos\theta \cos\phi \right) \right] \\
S_{sv} &= \frac{\cos\psi_1}{\sin^2\psi_1 \sin^2\zeta \cos\zeta} \left[ A_{pp} \left( R_{\perp} R_{\perp W} U \sin\phi + R_{\parallel} R_{\parallel W} T' \cos\theta \cos\phi \right) + A_{ps} \left( -R_{\perp} R_{\parallel W} U \cos\theta \cos\phi + R_{\parallel} R_{\perp W} T' \sin\phi \right) \right] \\
A_{pp} &= U' \sin\phi - T \cos\theta \cos\phi, \quad A_{ps} = T \sin\phi + U' \cos\theta \cos\phi \\
T &= \sin\theta \cos\theta_s + \cos\theta \sin\theta_s \sin(\phi_s + 2\phi), \quad T' = \sin\theta_s \cos\theta + \cos\theta_s \sin\theta \sin(\phi_s + 2\phi) \\
U &= \sin\theta \cos(\phi_s + 2\phi), \quad U' = \sin\theta_s \cos(\phi_s + 2\phi) \\
\psi_1 &= \cos^{-1}(\sin\theta \cos\phi), \quad \zeta = \cos^{-1} \left( \sqrt{\frac{1 - \sin\theta_s \sin\theta \sin(\phi_s + 2\phi) + \cos\theta_s \cos\theta}{2}} \right) \\
\langle I_{A_0} \rangle &= A_0 \exp \left[ -\frac{k^2 \sigma^2}{2} (\cos\theta + \cos\theta_s)^2 \right] \text{sinc} \left[ \frac{kf}{2} (\sin\theta \sin\phi - \sin\theta_s \cos(\phi_s + \phi)) \right] \text{sinc} \left[ \frac{kf \tan\theta}{2} (\sin\theta - \sin\theta_s \sin(\phi_s + 2\phi)) \right] \\
&\quad \exp[jk|x_0|(\sin\theta \sin 2\phi - \sin\theta_s \cos\phi_s) + y_0(\sin\theta \cos 2\phi - \sin\theta_s \sin\phi_s)] \exp \left[ \frac{jkf \tan\theta}{2} (\sin\theta - \sin\theta_s \sin(\phi_s + 2\phi)) \right] \\
\langle |I_{A_0}|^2 \rangle &= A_0 \frac{2\pi}{(\cos\theta + \cos\theta_s)^2 k^2 r^2 |\rho^u(0)|} \exp \left( -\frac{\sin^2\theta + \sin^2\theta_s - 2\sin\theta \sin\theta_s \sin(\phi_s + 2\phi)}{2\sigma^2 |\rho^u(0)| (\cos\theta + \cos\theta_s)^2} \right) \\
A_0 &= \begin{cases} kh \cos\theta \tan\theta, & \text{if } \sin(\phi_s + \phi) > 0 \\ kh \cos\phi [\tan\theta + \tan\theta_s \sin(\phi_s + \phi)], & \text{if } \sin(\phi_s + \phi) \leq 0 \text{ and } \theta \geq \tan^{-1}(\tan\theta_s |\sin(\phi_s + \phi)|) \\ 0, & \text{otherwise} \end{cases}
\end{aligned}$$

**Table II – Double Scattering Contribution (sea-ship)**

$$\begin{aligned}
 S_{AA} &= \frac{\cos\psi_2}{\sin^2\psi_2\sin^2\zeta\cos\zeta} [A_{pp}[R_{\perp}R_{\perp}T\cos\theta_s\sin(\theta_s+\phi)+R_{\parallel}R_{\parallel}U'\cos(\theta_s+\phi)]+A_{ss}[R_{\perp}R_{\parallel}T\cos(\theta_s+\phi)-R_{\parallel}R_{\perp}U'\cos\theta_s\sin(\theta_s+\phi)] \\
 S_{sA} &= \frac{\cos\psi_2}{\sin^2\psi_2\sin^2\zeta\cos\zeta} [A_{ps}[-R_{\perp}R_{\parallel}U'\cos\theta_s\sin(\theta_s+\phi)+R_{\parallel}R_{\parallel}T\cos(\theta_s+\phi)]-A_{sp}[R_{\perp}R_{\parallel}U'\cos(\theta_s+\phi)+R_{\parallel}R_{\perp}T\cos\theta_s\sin(\theta_s+\phi)] \\
 S_{ss} &= \frac{\cos\psi_2}{\sin^2\psi_2\sin^2\zeta\cos\zeta} [-A_{pp}[R_{\perp}R_{\perp}T\cos(\theta_s+\phi)-R_{\parallel}R_{\parallel}U'\cos\theta_s\sin(\theta_s+\phi)]+A_{ps}[R_{\perp}R_{\parallel}T\cos\theta_s\sin(\theta_s+\phi)+R_{\parallel}R_{\perp}U'\cos(\theta_s+\phi)] \\
 S_{sv} &= \frac{\cos\psi_2}{\sin^2\psi_2\sin^2\zeta\cos\zeta} [A_{pp}[R_{\perp}R_{\perp}U'\cos(\theta_s+\phi)+R_{\parallel}R_{\parallel}T\cos\theta_s\sin(\theta_s+\phi)]+A_{ps}[-R_{\perp}R_{\parallel}U'\cos\theta_s\sin(\theta_s+\phi)+R_{\parallel}R_{\perp}T\cos(\theta_s+\phi)] \\
 &\quad A_{pp}=U\cos(\theta_s+\phi)-T'\cos\theta_s\sin(\theta_s+\phi), \quad A_{ps}=2'\cos(\theta_s+\phi)+U\cos\theta_s\sin(\theta_s+\phi) \\
 &\quad T=\sin\theta_s\cos\theta_s+\cos\theta_s\sin\theta_s\sin(\theta_s+2\phi), \quad T'=\sin\theta_s\cos\theta_s+\cos\theta_s\sin\theta_s\sin(\theta_s+2\phi) \\
 &\quad U=-\sin\theta_s\cos(\theta_s+2\phi), \quad U'=-\sin\theta_s\cos(\theta_s+2\phi) \\
 &\quad \psi_2=\cos^{-1}(\sin\theta_s\sin(\theta_s+\phi)), \quad \zeta=\cos^{-1}\left(\sqrt{\frac{2-\sin\theta_s\sin\theta_s\sin(\theta_s+2\phi)+\cos\theta_s\cos\theta_s}{2}}\right) \\
 (J_{A_s}) &= A_0 \exp\left[-\frac{k^2\sigma^2}{2}(\cos\theta_s+\cos\theta_s')^2\right] \sin\left[\frac{kT}{2}(\sin\theta_s\sin\phi-\sin\theta_s'\cos(\theta_s+\phi))\right] \sin\left[\frac{kT'\tan\theta_s}{2}(\sin\theta_s\sin\phi+\sin\theta_s'\cos(2\theta_s+2\phi))\right] \\
 &\quad \exp[-jk(\sin\theta_s\cos(\theta_s+2\phi)+\sin(\theta_s-\sin\theta_s'\sin(\theta_s+2\phi)))] \exp\left[\frac{-jkT\tan\theta_s}{2}(\sin\theta_s\sin\phi+\sin\theta_s'\cos(2\theta_s+2\phi))\right] \\
 (J_{A_s})^2 &= A_0 \frac{2\pi}{(\cos\theta_s+\cos\theta_s')^2 k^2 \sigma^2 |r^s(\theta)|} \exp\left(-\frac{\sin^2\theta_s+\sin^2\theta_s'-2\sin\theta_s\sin\theta_s'\sin(\theta_s+2\phi)}{2r^s(\theta)|\cos\theta_s+\cos\theta_s'|^2}\right) \\
 A_0 &= \begin{cases} kT\tan\theta_s\sin(\theta_s+\phi) & \text{if } \sin(\theta_s+\phi) > 0 \\ 0 & \text{otherwise} \end{cases}
 \end{aligned}$$

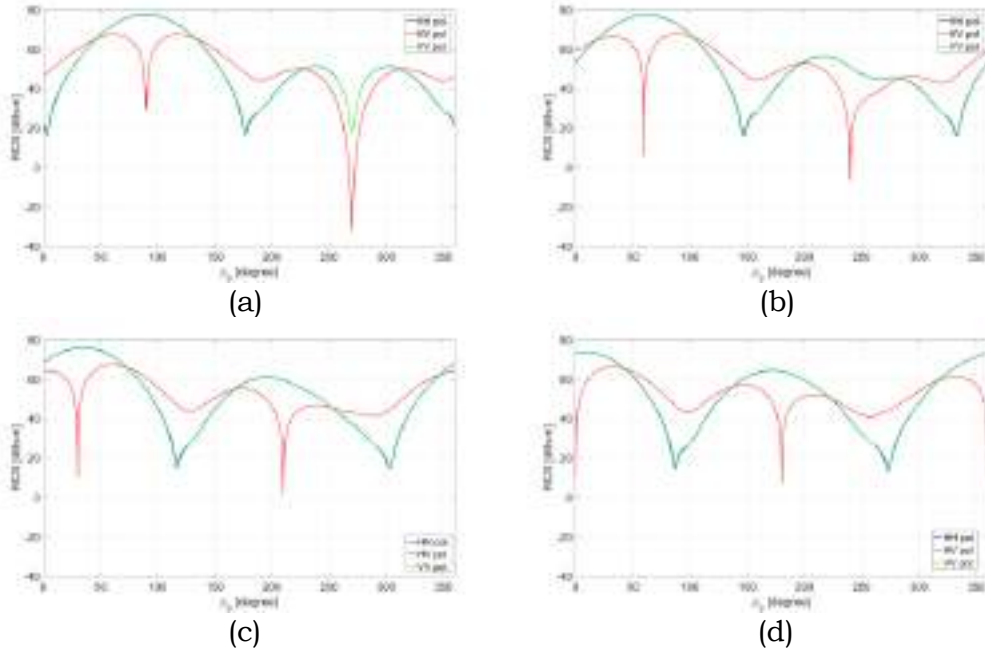


**FIG. 1** – RCS of a ship target at 1.5 GHz as a function of  $\varphi_s$  for (a)  $\varphi = 0^\circ$ , (b)  $\varphi = 15^\circ$ , (c)  $\varphi = 30^\circ$ , (d)  $\varphi = 45^\circ$ .

## REFERENCES

- [1] G. Franceschetti, A. Iodice, and D. Riccio, “A canonical problem in electromagnetic backscattering from buildings,” *IEEE Transactions on Geoscience and Remote Sensing*, vol. 40(8), pp. 1787–1801, 2002
- [2] F. T. Ulaby, R. K. Moore, and A. K. Fung, *Microwave Remote Sensing*. Reading, MA, USA: Artech House, 1982, vol. II.
- [3] D. K. Barton, *Radar Equations for Modern Radar*, 1st Edition. Norwood, MA, USA: Artech House, 2012, cap. 9, pp. 324.
- [4] A. Di Simone, H. Park, D. Riccio, and A. Camps, “Sea target detection using spaceborne GNSS-R delay-doppler maps: Theory and experimental proof of concept using TDS-1 data,” *IEEE Journal of Selected Topics in Applied Earth Observations and Remote Sensing*, vol. 10(9), pp. 4237–4255, 2017.

# THE DELAY AND SUM ALGORITHMS FOR THROUGH THE WALL RADAR IMAGING SYSTEMS

S. Pisa<sup>(1)</sup>, E. Piuzzi<sup>(1)</sup>, E. Pittella<sup>(1)</sup>, G. Sacco<sup>(1)</sup>,  
P. d'Atanasio<sup>(2)</sup>, A. Zambotti<sup>(2)</sup>

<sup>(1)</sup> Dept. of Information Engineering, Electronics and Telecommunications, Sapienza  
University of Rome, Via Eudossiana, 18, 00184 Rome, Italy

<sup>(2)</sup> Italian National Agency for New Technologies, Energy and Sustainable Economic  
Development, Casaccia Research Centre, Rome 00123, Italy

[stefano.pisa@uniroma1.it](mailto:stefano.pisa@uniroma1.it)

## Abstract

*In this paper the delay and sum (DAS) algorithm has been used as imaging technique for a MIMO step frequency (SF) radar system. The DAS has been applied to analytical, simulated, and measured data both in the absence and in the presence of a wall between the antenna and the target. By applying the Fermat principle and antenna calibration this technique was able to accurately reconstruct the position of targets behind a wall.*

**Index Terms** – delay and sum, reconstruction algorithms, through the wall radar imaging systems

## I. INTRODUCTION

Through-the-wall radar imaging (TWRI) systems allow police, fire personnel and defense forces to detect, identify and track subjects inside buildings [1]. At the same time, they can also be used to track older adults inside their home in the ambient assisted living (AAL) context [2]. Generally, these systems utilize a time-division multiplexed (TDM) multiple-input, multiple-output (MIMO) array of antennas and are based on frequency modulated continuous wave (FMCW) [3], ultra-wideband (UWB) [4] or stepped frequency (SF) radars [5]. TWRI systems apply algorithms on the acquired data in order to reconstruct an image of the building interior. In this paper, the delay and sum (DAS) algorithm will be applied to analytical, simulated and measured data and the potentiality and limits of this technique will be evaluated.

## II. RADAR SYSTEM AND SCENARIOS

Fig 1 (a) shows the SF radar structure. The system utilizes a vector network analyzer (VNA) that measures the  $S_{21}$  scattering parameter between a transmitting and a receiving section. A power amplifier (PA) in the transmitting channel and a low-noise amplifier (LNA) in the receiving one are used to achieve the required dynamics. A couple of switches are used to select sequentially a transmitting and a receiving antenna.

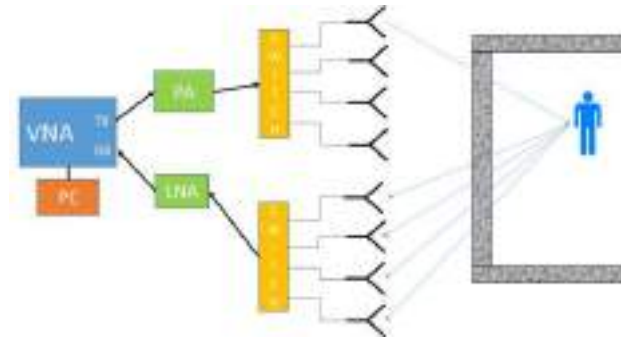


**FIG. 1** – SF radar structure.

To test the DAS algorithms, a typical scenario has been implemented. For the analytical technique 27 point sources and 1 or 2 point scatterers have been considered.

Concerning the numerical solution a typical scenario has been implemented inside the electromagnetic CAD Microwave studio by CST (see Fig. 2a). Two truncated waveguide antennas, operating in the 1-3 GHz band, with their centers at a distance of 36 cm, are moved in the cross range direction by 7.5 cm steps ( $\lambda/2$  at the center frequency of 2 GHz) at 27 positions. A cylindrical metallic target is placed 200 cm far from the array plane and a wall with a thickness  $d = 15$  cm and real relative permittivity equal to 4 has been placed between the two.

An experimental set up has been also realized. It uses as radiating element two truncated waveguides (WR 430) operating between 1.7 and 2.6 GHz. The two waveguides, whose centers are at a distance of 46 cm, are moved at 6 cm steps ( $\lambda/2$  at center frequency) at 31 positions and 801 frequency points are measured with the VNA. The considered scenario is constituted by a water tank, simulating the human body, and a metallic post placed behind a 25 cm thick brick wall located 80 cm far from the antenna (Fig. 2b).

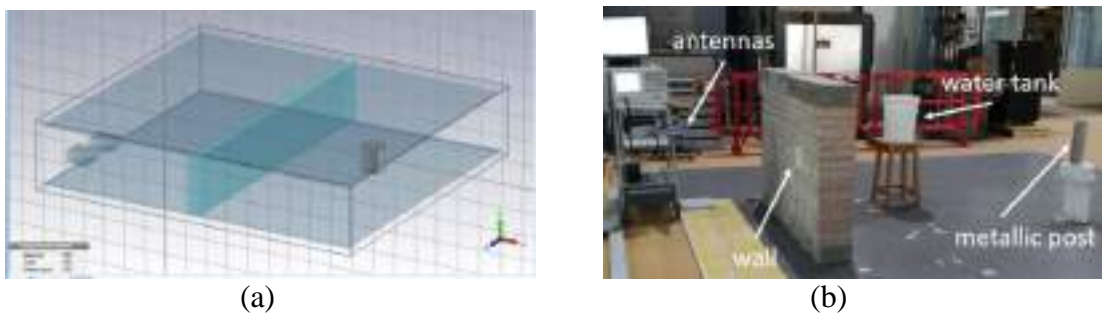


**FIG. 2** – Simulated (a) and measured (b) scenarios.

### III. RECONSTRUCTION TECHNIQUES

The implemented reconstruction technique is the delay and sum algorithm [6]. In this technique, the domain under study is divided in square pixels (i.e. 1 cm  $\times$  1 cm) with (i,j) coordinates and the pixel intensity is evaluated as:

$$I(i, j) = \left| \sum_{k=1}^{N_{pos}} \sum_{l=1}^{N_{freq}} \mathbf{S}_{21}(l) e^{j\frac{2\pi}{\lambda}d(k)} e^{j\frac{2\pi}{\lambda}\tau_D} \right| \quad (1)$$

where  $d(k)$  is the transmitting antenna-pixel-receiving antenna distance,  $N_{pos}$  is the number of antennas and  $N_{freq}$  the number of frequencies. For taking into account the refraction caused by the wall, the Fermat principle of least time [1] has been implemented.

#### IV. RESULTS

For the considered bandwidth ( $B = 2$  GHz) and antenna number ( $N_A=27$ ) placed at distance  $d = \lambda/2$ , the Radar theoretical resolution in range is  $\delta r = c/2B = 7.5$  cm and in angle is  $\delta\phi = 1/(N_A-1) = 0.04$  rad. Fig. 3a shows an image reconstruction achieved by applying the DAS algorithm to analytical data for a point scatterer placed in central position, 1 m far from the antenna array. The 3 dB widths are 8 cm in range (Fig. 3b) and 6 cm in cross-range (Fig. 3c) very close to the 7.5 and 4 cm theoretical values.

Fig. 4a shows the DAS reconstruction for the scenario in Fig. 2a. In these simulations, for taking into account the electrical distance between the waveguide excitation point and the antenna plane, a calibration procedure has been applied. The estimated delay  $\tau_D$  is then inserted in (1). The strong reflection of the wall is well evidenced. By applying the DAS only in the region around the scatterer, its shape is evidenced and located at a distance of 2.22 m. Finally, the further application of the Fermat principle allows a better definition of the target shape and location (2.07m).

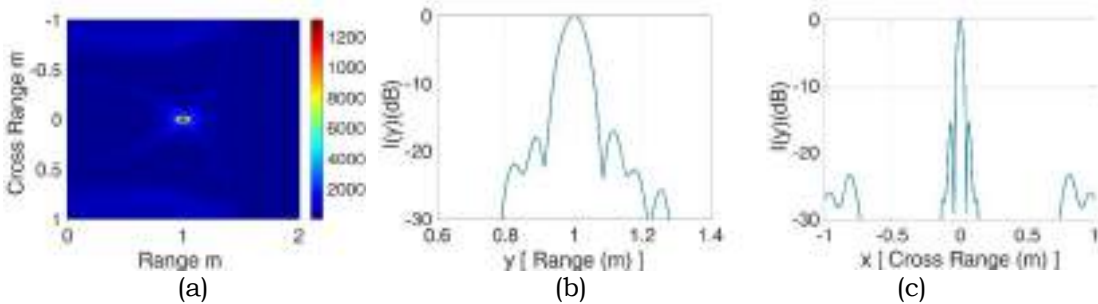


**FIG. 3** – DAS with analytical data for the EM problem.

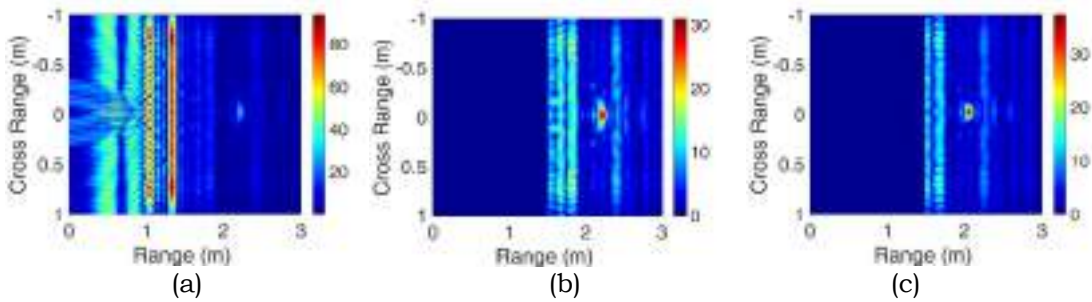


**FIG. 4** – DAS with simulated data for the EM problem.

Measurements have been performed on the scenario depicted in Fig. 2b. In this case, the effect of the wall has been masked by applying a time gating on the measured data. The achieved reconstruction with the DAS algorithm is reported in Fig. 5. The figure shows that the DAS is able to correctly position the two targets.

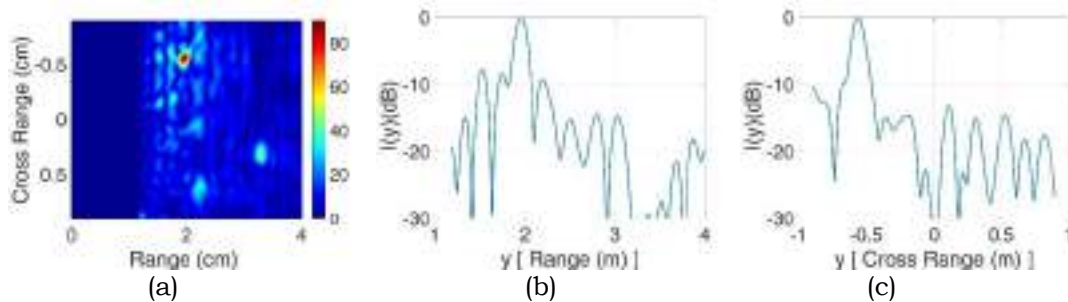


**FIG. 5** – DAS with measured data for the EM problem.

## V. CONCLUSION

The DAS algorithm has been tested on analytical, simulated and measured data. By calibrating the antennas and applying the Fermat principle the target reconstruction and positioning is very accurate.

## ACKNOWLEDGEMENT

This work was supported in part by the Italian Ministry of University and Research under the PRIN 2015: U-VIEW (Ultra-wideband Virtual Imaging Extra Wall for high-penetration high quality imagery of enclosed structures).

## REFERENCES

- [1] M.G. Amin, "Through the wall radar imaging", CRC Press, 2011.
- [2] G. Wang, C. Gu, T. Inoue, C. Li, "A hybrid FMCW-interferometry radar for indoor precise positioning and versatile life activity monitoring," *IEEE Trans. on Microwave Theory and Techniques*, vol. 62 no 11, pp. 2812-2822, 2014.
- [3] J.E. Peabody, G.L. Charvat, J. Goodwin, M. Tobias, "Through-wall imaging radar", *Lincoln Laboratory Journal*, 19 (1), 62-72, 2012
- [4] M. A. Ressler, L. H. Nguyen, F. J. Koenig, G. Smith, "Synchronous impulse reconstruction (SIRE) radar sensor for autonomous navigation", US Army Research Laboratory, 2006.
- [5] X. P. Masbernat, M. G. Amin, F. Ahmad, C. Ioana, "An MIMO-MTI approach for through the-wall radar imaging applications," *Proc. 5th Int. Waveform Diversity and Design Conf.*, Can-ada, 188-192, 2010.
- [6] M. Karaman, P.-C. Li, and M. O'Donnell, "Synthetic aperture imaging for small scale systems," *IEEE Transactions on Ultrasonics, Ferro- electrics, and Frequency Control*, vol. 42, no. 3, pp. 429-442, 1995.

# SOFTWARE-DEFINED RADAR FOR VITAL SIGN MONITORING

A. Raffo<sup>(1)</sup>, V. Cioffi<sup>(1)</sup>, S. Costanzo<sup>(1)</sup>

<sup>(1)</sup> Department of Informatics, Modeling, Electronics and System Engineering, University of Calabria  
Ponte Pietro Bucci, 87036, Arcavacata di Rende, Italy  
[a.raffo@dimes.unical.it](mailto:a.raffo@dimes.unical.it)

## Abstract

*Techniques for contactless detection of small movements claim a wide range of applications in both communication as well as biomedical contexts. A configuration based on the use of a Software-Defined Radar platform is described in this work to offer a flexible, low-cost and compact solution for breathing rate monitoring in health-care and safety usage. A Doppler radar configuration, based on a quadrature receiver and fully implemented via software, is described. Some experimental results are also illustrated to prove the effectiveness of the proposed approach.*

**Index Terms** – Breath detection, Doppler radar, Software-Defined Radar.

## I. INTRODUCTION

The possibility to monitoring breathing and heart rate through the use of microwave Doppler radar has already been indicated since the 70s [1], by showing the effectiveness of such non-invasive measurements, as compared to contact sensors methods, in preserving the physiological integrity of the human subject. In the 2000s, different types of Doppler radars, based on laboratory test equipment or custom hardware on printed/integrated circuits, have been developed to implement physiological sensors. An alternative, flexible and low cost solution can be obtained through the use of an SDR transceiver. This leads to implement a multi-function radar, known as Software Defined Radar (SDRadar) [2], composed by RF hardware modules fully reconfigurable via software. A SDRadar system allows to realize most of the basic operations (e.g. modulation, demodulation, filtering and mixing) by the simple use of programmable software modules, instead of specific hardware components, thus leading to a faster and cheaper development and manufacture, as compared to conventional custom radars [3].

## II. CW DOPPLER RADAR FOR RESPIRATORY SENSING

The CW Doppler radar architecture for respiratory sensing is based on the simplest Doppler radar topology. The architecture based on the quadrature receiver is illustrated in Fig. 1.

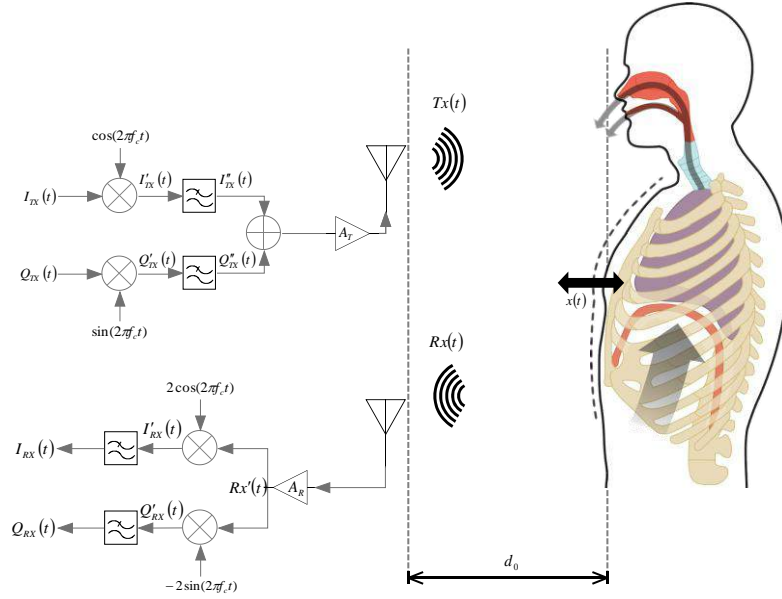


**FIG. 1** – Block diagram of quadrature receiver CW Doppler radar.

These systems typically transmit a CW narrow band signal, which is reflected off a target and then demodulated in the homodyne or heterodyne receiver. In the presence of a single target subject to alternate motions, two parameters can be identified which characterize the motion, namely:

- $x(t)$ , which describes the object oscillatory motion;
- $d_0$ , giving the target range, around which the object oscillates.

A monochrome CW signal is to be transmitted, so the following modulator I/Q components should be fixed:

$$I_{TX}(t) = \cos[2\pi f_{IF}t + \theta_{IF}(t)] \quad (1)$$

$$Q_{TX}(t) = \sin[2\pi f_{IF}t + \theta_{IF}(t)] \quad (2)$$

where  $f_{IF}$  is the intermediate frequency and  $\theta_{IF}(t)$  gives the signal generator phase noise. The I/Q components, applied to different modulator arms, are subject to mixing, filtering, sum and amplification operations, which shift their signal spectrum from the intermediate frequency  $f_{IF}$  to the carrier frequency ( $f_c - f_{IF}$ ) for up-conversion operation. The backscattered I/Q components, received from the radar, keep the same form of the transmitted ones, but they are attenuated of a factor  $L$  and delayed of a ‘round trip time’. After the down-conversion operation of this signal, the transmitted and received I/Q components are multiplied and filtered; then, it is possible to extract the received signal phase from the following equations:

$$I_{B_{LPF}}(t) = \frac{A}{2} \cos \left[ -\frac{4\pi(f_c - f_{IF})d_0}{c} - \frac{4\pi(f_c - f_{IF})x(t)}{c} + \Delta\theta_{TX}(t) \right] \quad (3)$$

$$Q_{BLPF}(t) = \frac{A}{2} \sin \left[ -\frac{4\pi(f_c - f_{IF})d_0}{c} - \frac{4\pi(f_c - f_{IF})x(t)}{c} + \Delta\theta_{TX}(t) \right] \quad (4)$$

Assuming a transmitter residual phase noise  $\Delta\theta_{TX}(t) = 0$ , the motion parameters are easily isolated from phase as follows:

$$\bar{x}(t) = d_0 + x(t) = -\arctan \left[ \frac{Q_{BLPF}(t)}{I_{BLPF}(t)} \right] \frac{c}{4\pi(f_c - f_{IF})} \quad (5)$$

Under the hypothesis that the middle value of signal  $x(t)$  is null in the  $[t_0, t_1]$  acquisition interval, it is possible to finally reconstruct the target motion by the following expression:

$$x(t) = \bar{x}(t) - \frac{1}{t_1 - t_0} \int_{t_0}^{t_1} \bar{x}(t) dt \quad (6)$$

$t \in [t_0, t_1]$

### III. RESPIRATORY ACTIVITY MONITORING THROUGH SDRADAR

In this work, a configuration based on the use of SDRadar is proposed for the monitoring of human respiration. The radar is essentially realized on the transceiver SDR NI USRP 2920, directly interfaced to a PC for data acquisition and processing. Two standard transmitting and receiving antennas, namely a omni-directional dipole in transmission and a strong near field Impinji A0303 in reception, are adopted. The transceiver include an IQ modulator and demodulator, on the TX and RX channels, respectively. The IQ components of the transmitted signal are generated through LabVIEW code. At the receiver, the IQ components, extracted from the demodulator, are acquired on the PC using LabVIEW software. The block diagram shown in Fig. 2 reproduces the modular architecture realized in LabView. The measurement setup has been arranged by including a rigid support for the antennas to be placed in the proximity of the monitored subject, as shown in Fig. 3.

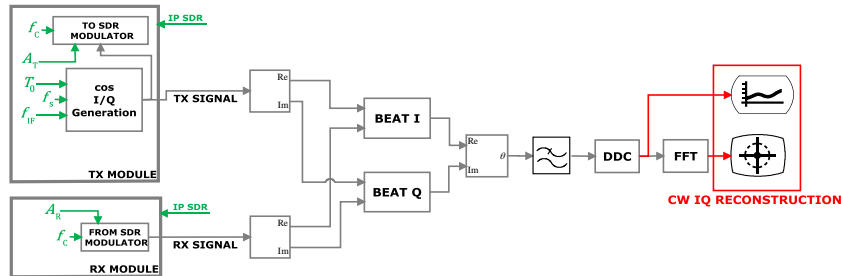


**FIG. 2** – Software-side architecture.

Measured data revealed the system ability to detect the abdominal movements due to the respiratory activity; however, to smooth the data

oscillations, a filtering has been implemented in Matlab environment through a mobile average window (Fig. 3 (c)). The detected movement looks very regular, by highlighting an abdominal shift of about 3 mm (Fig. 3(c)), with a frequency of 30 breaths/min (Fig. 3 (d)), during the normal respiratory activity.

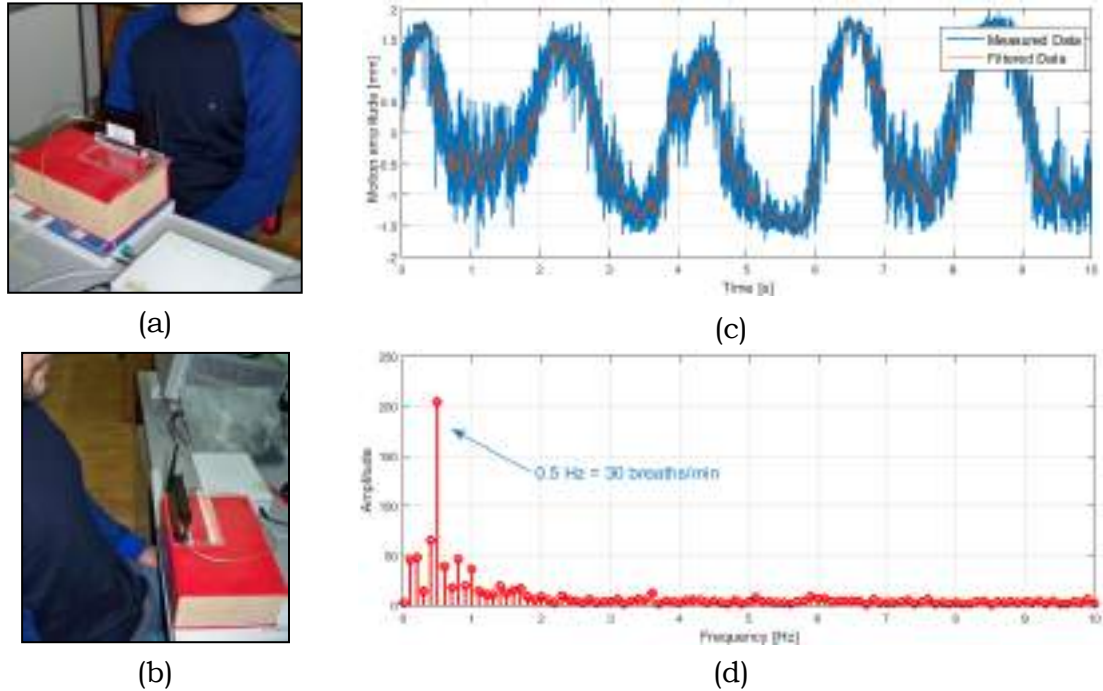


**FIG. 3** – Subject position in relation to the antennas: (a) frontal view; (b) side view. Detected movement during the normal respiratory activity: (c) time-domain; (d) frequency-domain.

#### IV. CONCLUSION

An innovative SDRadar Doppler platform has been proposed and implemented as alternative multipurpose solution to the use of punctual sensors for respiratory activity monitoring. Experimental validations have been performed to prove the accurate detection capability of the proposed system.

#### REFERENCES

- [1] J. C. Lin, "Non-invasive microwave measurement of respiration," *Proc. IEEE*, vol. 63, pp.1530, 1975.
- [2] S. Costanzo, G. Di Massa, A. Costanzo, A. Borgia, A. Raffo, G. Viggiani and P. Versace, "Software-Defined Radar System for Landslide Monitoring," *Advances in Intelligent System and Computing*, pp. 325-331, 2016.
- [3] A. Raffo, S. Costanzo and G. Di Massa, "Software Defined Doppler Radar as a Contactless Multipurpose Microwave Sensor for Vibrations Monitoring", *Sensors*, vol. 17, no. 1, p. 115, 2017.

# DUAL-RECEIVER FMCW RADAR FOR SNOWPACK MONITORING: SYSTEM VALIDATION AND PRELIMINARY RESULTS

Pedro Fidel Espin-Lopez and Marco Pasian

Department of Electrical, Computer and Biomedical Engineering,  
University of Pavia

Via A. Ferrata, 5, 27100 Pavia, Italy

[pedrofidel.espinlopez01@universitadipavia.it](mailto:pedrofidel.espinlopez01@universitadipavia.it)

[marco.pasian@unipv.it](mailto:marco.pasian@unipv.it)

## Abstract

*Microwave radars represent an interesting solution to monitor the internal structure of the snowpack because the measurements are practically instantaneous, non-destructive, and can be remotely controlled to improve the safety of the operators. In particular, an innovative radar architecture based on two receivers can deliver, at the same time, the depth and the dielectric permittivity of the snowpack, this latter directly related to the physical parameters of the snow, such as the density. These parameters are fundamental to provide an accurate forecast for the avalanche formation as well as for estimating the snowmelt for hydrological purposes.*

*This paper presents the validation of the dual-receiver radar architecture for snowpack monitoring. Preliminary experimental results are also presented.*

**Index Terms** – FMCW radar, multi-receiver architecture, snow avalanche, dielectric permittivity, monitoring, and stratigraphy.

## I. INTRODUCTION

Snow avalanches are a persistent risk for several mountain regions, with manifold potential impacts. For example, in the Alpine countries, avalanches threaten the safety of residents (around 20 millions), winter tourists (20 million per year, accounting for a 30 B€ turnover), and transalpine traffic (100 million metric tons of goods per year) [1]. Cost-effective countermeasures inevitably require avalanche forecasting tools. Such forecasting, however, at present still relies largely on manual snowpack analysis. Although very precise, manual analysis also exhibits several disadvantages. Indeed, it is very time consuming (in the order of one hour or more) and its applicability is limited to areas where it can be undertaken within reasonable safety margins for the operators.

For these reasons, solutions based on the use of microwaves, where the internal structure of the snowpack can be analyzed almost instantaneously, non-destructively, and automatically without the presence of the operators, if required, can provide a valuable alternative. Different radar systems have been proposed, but they cannot determine simultaneously the snowpack depth and the dielectric properties of the snowpack itself without auxiliary aids [2]–[4]. In particular, for dry snow the dielectric permittivity is related to the snow density, a fundamental parameter for the models used to forecast avalanches.

## II. DIELECTRIC / PHYSICAL PROPERTIES OF THE SNOW

At microwave frequencies, the dielectric permittivity of dry snow is a function of the snow density [5]. In particular, a widely accepted approximation assumes that the imaginary part of the permittivity is negligible, and that the relative real part  $\epsilon'$  can be described according to a one-to-one relationship between the real part itself and the snow density [5]. Dry snow is a typical condition during the winter season. For example, in Alpine regions, at altitudes where avalanches are mostly triggered (2000 m or higher), snowpacks are normally characterized by dry snow from December to February or March. Standard densities ranges from around 90 kg/m<sup>3</sup> to around 450 kg/m<sup>3</sup>. This means that  $\epsilon'$  can be expected to range around from 1.2 to 1.8, according to [5].

## III. RADAR ARCHITECTURE

The system architecture is shown in Fig. 1 for an upward-looking installation, thus for a system intended to be buried into the ground before the winter season, and remotely controlled.

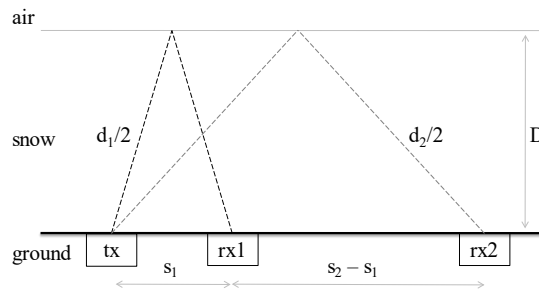


**FIG. 1** – Radar architecture schema showing the transmitter (tx) and the two receivers (rx1 and rx2) installed at ground level under a snowpack with thickness  $D$ . Drawing not to scale.

The radar comprises one transmitter and two receivers. Each transmitter-receiver works as a standard Frequency Modulated Continuous Wave (FMCW) radar, thus delivering the time of flight from the transmitter to the snow-air interface and back to the receiver. In particular, the time of flight is directly related to the wave speed  $\nu$  into the medium. For dry snow, the relative real part of the dielectric permittivity  $\epsilon'$ , as explained in Section II is:

$$\nu \sim c / \sqrt{\epsilon'} \quad (1)$$

where  $c$  is the speed of light. When two receivers are used, as shown in Fig. 1, the following system can be imposed:

$$T_i = d_i / \nu \quad (2)$$

where  $T_i$  for  $i=1,2$  are the times of flight from the transmitter to the receivers, and  $d_i$  for  $i=1,2$  are the propagation distances from the transmitter to the receivers. The propagation distances can be written as:

$$d_i^2 = (2D)^2 + s_i^2 \quad (3)$$

where  $D$  is the snow thickness, and  $s_i$  for  $i=1,2$  are the horizontal distances between the transmitter and the first and second receiver. Manipulating (2)–(3) it is obtained:

$$T_i^2 = ((2D)^2 + s_i^2) / v^2 \quad (4)$$

which represent a system of two equations and two unknowns, the snow thickness  $D$  and wave speed  $v$ , and in turn the density, using (2) and [10].

#### IV. NUMERICAL VALIDATION

The performance of the system is validated using full-wave simulations (using Ansys HFSS). The numerical model consists of one transmitting antenna and two receiving antennas (WR340 open-ended waveguides in the frequency range 2.2 – 3.2 GHz). The antennas radiate into a medium of variable thickness  $D$  and dielectric permittivity  $\epsilon'$ . Particularly,  $D$  varies from 0.5 m to 1 m, while according to Section II  $\epsilon'$  varies from 1.2 to 1.8.

The scattering parameters of the receiving antennas calculated by the full-wave solver are used to calculate the FMCW beat frequency for each receiver. Then, the beat frequencies are processed to obtain  $D$  and  $\epsilon'$  using the equations described in Sec. III. Results for  $s_1 = 30$  cm and  $s_2 = 100$  cm are shown in Table I, obtaining errors better than 15% for all cases.

**TABLE I** - RELATIVE ERRORS  $\delta\epsilon'/\epsilon'$  AND  $\delta D/D$  (IN BRACKETS) OBTAINED IN THE FULL-WAVE SIMULATIONS FOR DIFFERENT SNOWPACKS.

		D(m)					
		0.5	0.6	0.7	0.8	0.9	1
$\epsilon'$	1.2	5% [2%]	5% [3%]	6% [2%]	8% [<1%]	4% [2%]	11% [2%]
	1.5	3% [3%]	5% [2%]	7% [1%]	4% [2%]	5% [<1%]	4% [2%]
	1.8	6% [1%]	7% [1%]	4% [2%]	3% [2%]	7% [<1%]	1% [4%]

#### V. EXPERIMENTAL RESULTS

The proposed radar architecture was validated in a real field test. The experimental site is located in the Italian Alps (Valle d'Aosta, 45°40'30" N 7°19'35" E, a. 2500 m). The inclination of the slope approaches 30 degrees, and it is an historical critical site for the avalanche formation, which threatens part of Pila Ski Resort. The experiment took place in March 2017, and the setup is shown in Fig. 2.

It comprises a vector network analyzer (VNA) from Keysight (FieldFox N9916A) used to generate the FMCW signal and to receive the backscattered echo, three open-ended WR340 open-ended antennas, working from 2.2 GHz to 3.2 GHz, and three coaxial cables to connect the antennas with the VNA. The antennas are mounted on a wooden rail. After the radar measurements, a manual snowpack analysis took place by professional chartered AINEVA (Italian Interregional Association for Snow and Avalanches) experts. To benchmark the achieved results.



**FIG. 2.** EXPERIMENTAL SETUP FOR THE OUTDOOR VALIDATION.

The results of the manual snowpack analysis returned a snow depth  $D = 1.11$  m and density  $\rho = 253$  kg/m<sup>3</sup> ( $\epsilon' = 1.46$ ,  $v = 2.48 \cdot 10^8$  m/s). On the other hand, the FMCW signal processing provided  $T_1 = 4.57$  ns and  $T_2 = 4.68$  ns. This returns  $D = 1$  m and  $\rho = 216$  kg/m<sup>3</sup> ( $\epsilon' = 1.39$ ,  $v = 2.54 \cdot 10^8$  m/s). Consequently, the error with respect to the nominal values is better than 10% and 15% for the snow depth and density, respectively.

## VI. CONCLUSION

This paper presented the working principle and the optimization strategy of a novel FMCW radar architecture for snowpack monitoring. The performance of the system was validated using full-wave simulations. Experimental results performed on real conditions during a field test were shown, returning maximum errors better than 15% with respect to the nominal values obtained after a manual analysis of the snowpack.

## ACKNOWLEDGEMENT

This work was supported by the by the Italian Ministry of Education, University and Scientific Research (MIUR) under the project SIR “SNOWAVE” RBSI148WE5.

## REFERENCES

- [1] K. Lied, SATSIE Avalanche Studies and Model Validation in Europe – Final Report, European Commission 5th Framework Programme, May 31, 2006.
- [2] C. Mitterer, A. Heilig, J. Schweizer, and O. Eisen, “Upward-looking ground-penetrating radar for measuring wet-snow properties,” *Cold Regions Science and Technology*, Vol. 69, pp. 129–138, 2011.
- [3] R. Okorn, et al., “Upward-looking L-band FMCW radar for snow cover monitoring,” *Cold Regions Science and Technology*, Vol. 103, pp. 31–40, 2014.
- [4] L. Schmid, et al., “Continuous snowpack monitoring using upward-looking ground-penetrating radar technology,” *Journal of Glaciology*, Vol. 60, No. 221, pp. 509–525, 2014.
- [5] M. T. Hallikainen, F. T. Ulaby, and M. Abdelrazik, “Dielectric properties of snow in the 3 to 37 GHz range,” *IEEE Transactions on Antennas and Propagation*, Vol. 34, No. 11, pp. 1329–1340, November 1986.

# UPGRADING THE P-BAND RECEIVER OF THE SARDINIA RADIO TELESCOPE FOR SPACE DEBRIS MONITORING

Luca Schirru<sup>(1,2)</sup>, Giacomo Muntoni<sup>(1)</sup>, Giorgio Montisci<sup>(1,2)</sup>

<sup>(1)</sup> Department of Electrical and Electronic Engineering, University of Cagliari

Piazza D'Armi, 09123 Cagliari, Italy

<sup>(2)</sup> National Institute for Astrophysics,  
Cagliari Astronomical Observatory

Via della Scienza n. 5, 09047, Selargius (CA), Italy

[luca.schirru@diee.unica.it](mailto:luca.schirru@diee.unica.it)

## Abstract

*In order to prevent harmful impacts for spacecraft, deriving from the presence of space debris, several surveillance programs of the space environment have been started in recent years. The Sardinia Radio Telescope is a new comer in such a scenario, but it has already shown its potential. However, since the original receiving chain was not optimized for the reception of the echoes scattered from space debris, some modifications have been performed to upgrade the telescope and make it suitable for these types of observations.*

**Index Terms** – Space Debris, Sardinia Radio Telescope, Bi-static Radar

## I. INTRODUCTION

Space debris represent an increasing problem for the ongoing space operations and they are the primary reason of the space environment pollution [1]. The monitoring of the known objects, as well as the detection of new ones, is essential to prevent the risk of collision between debris and spacecraft. Radar measurements are often used to detect debris in the Low Earth Orbit [2]. In the last few years, the Sardinia Radio Telescope (SRT), a fully steerable wheel-and-track 64-m dish located in Sardinia (Italy) has been employed, as a receiver, in a bistatic radar system for space debris monitoring purposes in beam parking mode, using the P band (410 MHz) receiver [1, 3]. Clearly, the SRT P-band receiver has been conceived for radioastronomy observations, and it was not provided with a space debris-dedicated receiving chain, nor a dedicated back-end. To fill this gap, we have made an effort in two directions: first, we have designed and realized a tailored receiving system for space debris detection, then we have developed a specific algorithm to provide the pointing schedule for the SRT both in beam parking and in tracking mode.

The design of the receiving system included: the upgrade of the P band receiver, installed on the primary focus of SRT [4], and the implementation of a performing back-end and, contextually, the development of the down-conversion system.



**FIG. 1** – SRT and detail of P band receiver in primary focus.

## II. UPGRADE OF THE P-BAND RECEIVER

The SRT (see Fig. 1) has recently shown its potential in the detection of relatively small objects orbiting near Earth. With its 64 meter dish, composed by a total of 1008 aluminum panels, the SRT is the second world largest radio telescope equipped with an active surface system [5]. The front-end used for the first experiments on the space debris was the cryogenic P band receiver [1] (Fig. 1), operating between 305 and 410 MHz. In this early configuration (Fig. 2) the two channels at the output of the receiver (one for each polarization), were simply combined and sent to a spectrum analyzer.

Although the experiment described in [1] can be considered a success, the data processing was poor, due mainly to the limitations of the spectrum analyzer, i.e. the slow frequency sweep for low Resolution Bandwidths, thus preventing real time data saving. For these reasons, the choice of a brand new back end was a key point of the upgrade. The P band is a spectral region largely used for radio communication services that can reduce the useful bandwidth and heavily compress the dynamic of the receiver. While radio-astronomical observations use very large bandwidths, radar signals are narrowband.

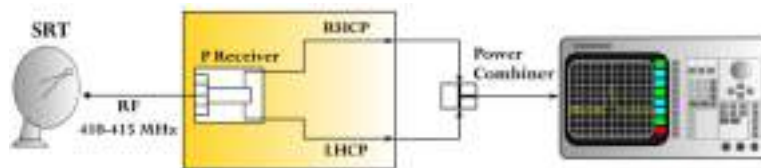


**FIG. 2** – Schematic of the receiving chain in the early space debris detection experiments.

For this reason the receiver block has been modified by inserting in the chain a Band-Pass Filter (BPF) (centered at 410 MHz with a 15 MHz bandwidth) to increase the signal to noise ratio, to mitigate the Radio Frequency Interferences and to remove the image frequency interference, as shown in the schematic in Fig. 3.

The 410 MHz signal, amplified and filtered inside the first block of the chain, is then down-converted to an Intermediate Frequency (IF) at 30 MHz in order to fit the frequency of the dedicated back end. The output signal is further filtered with a BPF centered at 30 MHz with a 5 MHz bandwidth. The mixer chosen for the down conversion works in the

bandwidth 100-2000 MHz, with an isolation between the L-R ports of about 52 dB, and an isolation of about 35 dB between the L-I ports. Since the signals scattered from the debris could be very weak, an amplifier has been placed in the final part of the down conversion block. The main features of the amplifier are: an overall gain of about 40 dB, a noise figure of about 3 dB, and an output power at 1 dB compression point of about 17 dB. In order to avoid the compression point, a wideband (up to 6 GHz) digital step attenuator has been inserted before the amplifier, with a maximum attenuation of 31.75 dB, and a 7 bit parallel control interface that allows to change the signal level in order to take into account the variable size of the debris.

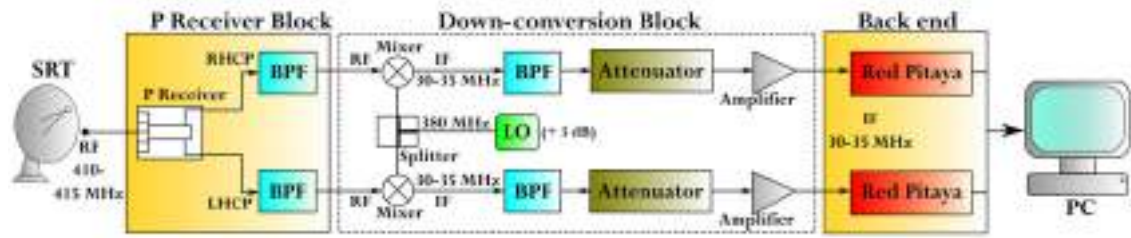


**FIG. 3** – Schematic of the new and upgraded P band receiving chain and photo of the down-conversion block and back end.

The IF signals go through a digital platform based on two Red Pitaya boards [6], one for each polarization. Each orthogonally polarized signal is sampled individually with an ADC, with a resolution of 14 bits and a sampling frequency of 125 MS/s. Once the data are digitized, they are sent to the Xilinx Field Programmable Gate Array (FPGA) installed on the board and then properly processed. After the down-conversion, the signal is filtered with a decimating digital filter in order to remove the unnecessary band and to minimize the output data rate. At this stage, since the signal is mixed with a local oscillator generated by a DDS (Direct Digital Synthesizer) implemented in the FPGA, it is composed of complex samples that are then sent to the PC. This base-band complex signal is stored and subsequently (or simultaneously) a Fast Fourier Transform (FFT) is applied to the data in order to break up the signal in several sub-

bands. The FFT engine could be implemented in the FPGA as well, however the number of spectral points would be limited by the available memory on the FPGA, thus we opted for the implementation of the transform in the CPU/GPU boards.

To detect and possibly track the debris, the SRT must be pointed and driven by a schedule, that contains the azimuth and elevation coordinates of the object. The schedule is generated by an algorithm that takes in input the observation epoch, the Two Line Element (TLEs) of the debris, the geographical coordinates of the radio telescope, the duration and time steps of the tracking.

The proposed system has been experimentally validated for the first time the 29 March 2018: at 7:56:03 UTC with SRT pointing at  $29.93^\circ$  in azimuth and  $24.38^\circ$  in elevation, the Doppler echo of the Tiangong-1 has been received with a Doppler shift of -8.1 KHz (the value predicted by our algorithm was -7.812 KHz) and a SNR of 42 dB (the value predicted by our algorithm was 45 dB). The spectrograms of the observations and the details of the bistatic radar transmitter will be shown during the conference.

### III. CONCLUSION

The research field related to the monitoring of space debris is becoming more and more attractive. The SRT is moving its first steps in this area and has already shown its capabilities. In this work, we have designed and implemented a hardware and software upgrade of the SRT receiving chain, in order to optimize the use of the radio telescope as a receiver for space debris monitoring and tracking.

### ACKNOWLEDGMENTS

Work supported in part by “Sardegna Ricerche” under contract RICERCA\_1C-172 (grant number CUP F21I17000130006) in partnership with Nurjana Technologies S.r.L.

The authors would like to thank the staff of the Astronomical Observatory of Cagliari (INAF) for the support in the system assembling and testing.

### REFERENCES

- [1] G. Muntoni et al., “Space Debris Detection in Low Earth Orbit with the Sardinia Radio Telescope”, *Electronics*, 6(3), 59, August 2017.
- [2] M. Grassi et al., “Enabling Orbit Determination of Space Debris Using Narrowband Radar”, *IEEE Trans. Aerosp. Electron. Syst.*, 51, pp. 1231–1240, April 2015.
- [3] T. Pisanu et al., “SRT as a receiver in a bistatic radar space debris configuration”, *Proc. SPIE*, 9906, August 2016.
- [4] G. Valente, et al., “The Dual Band L-P Feed System for the Sardinia Radio Telescope Prime Focus”, *Proc. SPIE*, 7741, 27 June 2010.
- [5] A. Orfei, et al. “Active surface system for the new Sardinia Radiotelescope”, *Proc. SPIE*, 5495, Astron. Struct. Mech. Technol., 2004.
- [6] [www.redpitaya.com](http://www.redpitaya.com)

# TWO-SCALE MODEL FOR THE EVALUATION OF SEA-SURFACE SCATTERING IN CIRCULAR POLARIZATION

G. Di Martino<sup>(1)</sup>, A. Di Simone<sup>(1)</sup>, A. Iodice<sup>(1)</sup>, D. Riccio<sup>(1)</sup>, G. Ruello<sup>(1)</sup>

<sup>(1)</sup> Department of Electrical Engineering and Information Technology, University of Napoli Federico II  
Via Claudio 21, 80125 Napoli, Italy  
{gerardo.dimartino, alessio.disimone, iodice, dariccio, ruello}@unina.it

## Abstract

*In this paper we propose a polarimetric two-scale model for the evaluation of scattering from the sea surface. The surface is composed of slightly rough facets, for which the small perturbation method can be applied, considering appropriate sea-surface spectra. The facets are randomly tilted, so that the model takes into account both random variations of the local incidence angle and random rotations of the local incidence plane around the line of sight. Using the proposed model, the scattering matrix is analytically evaluated and is used to derive the elements of the polarimetric covariance matrix for circular polarization. The behavior of covariance matrix elements as a function of the wind speed is analyzed.*

**Index Terms** – Electromagnetic scattering, circular polarization.

## I. INTRODUCTION

Analytical models for the evaluation of electromagnetic scattering from the sea surface play a key role in the frame of many remote sensing and radar applications. In particular, polarimetric models can be used to support a wide set of maritime remote sensing applications [1], e.g. estimation of wave spectra and retrieving of wind speed and direction. In the last years, the use of signals of opportunity transmitted by Global Navigation Satellite Systems (GNSS) is fostering the development of new sea surface remote sensing applications [2]. To deal with these signals, which are usually circularly polarized, it is necessary to introduce polarimetric electromagnetic models suitable for the evaluation of the elements of the circular polarization covariance matrix [3].

In this paper we present a polarimetric two-scale model, following the rationale of [4]. The ocean surface is subdivided in slightly rough facets, whose roughness is described by an appropriate sea spectrum. Scattering from the facets is evaluated via the Small Perturbation Method (SPM). The facets are randomly tilted so that the model takes into account both random variations of the local incidence angle and random rotations of the local incidence plane around the line of sight. Once the elements of the covariance matrix for linear polarization are evaluated, an appropriate polarimetric basis change is applied to obtain the expressions of the elements of the covariance matrix for circular polarization. Note that here we focus only on the backscattering case. The obtained expressions show that the backscattering contribution of the

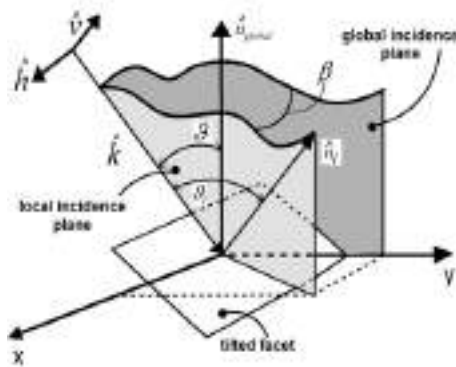


**FIG. 1** – Geometry of the problem.

sea surface is especially weak for the right-hand-transmit/right-hand-receive (RR) configuration, or, equivalently, for the left-hand-transmit/left-hand-receive (LL) one.

## II. POLARIMETRIC TWO-SCALE MODEL

The scattering model is based on a two-scale description of the sea surface, i.e. large-scale variations with superimposed small-scale roughness. The large scale-roughness is approximated using rough facets, large with respect to the wavelength and small with respect to sensor resolution, whose local slopes along  $x$  (azimuth) and  $y$  (range) are equal to  $a$  and  $b$ , respectively. The facets present a small-scale roughness described by the function  $\delta(x, y)$ .

Large-scale and small-scale roughness are modeled as independent stochastic processes. In particular, azimuth and range slopes are independent identically distributed zero-mean  $\sigma^2$ -variance Gaussian random variables, i.e.,  $a, b \sim N(0, \sigma^2)$ . With regard to the small-scale roughness, it is of paramount importance to select a model able to adequately describe the sea surface roughness, in terms of its power spectral density (PSD)  $W(k_x, k_y)$ . The Elfouhaily omnidirectional spectrum provides an accurate description for the case of partially developed sea [1]. At the Bragg resonant wavenumber in L band Elfouhaily spectrum presents a power-law fractal behavior with a *Hurst parameter*  $H_f=0.75$  [4], and its behavior as a function of the local wind is practically the same of the modified Pierson-Moskowitz (PM) omnidirectional spectrum [1]. Due to its simpler expression, in this paper we use the PM spectrum.

The geometry of the problem is illustrated in Fig. 1. The facet random tilt gives rise to a random rotation  $\beta$  of the local incidence plane and to a drift of the local incidence angle  $\theta_i$ , where  $\beta$  and  $\theta_i$  can be expressed as functions of the global incidence angle  $\theta$ , of  $x$ -slope  $a$ , and  $y$ -slope  $b$  [4]. The PTSM takes into account both these effects. The elements of the scattering matrix of the randomly-tilted randomly-rough facet can be evaluated using the first-order SPM and can be expressed as follows:

$$S_{pq} = \frac{k^2 \cos^2 \theta_l}{\pi} \chi_{pq}(\theta_l, \beta) \tilde{\delta}(0, 2k \sin \theta_l) \quad (1)$$

where  $\tilde{\delta}(k_x, k_y)$  is the Fourier transform of  $\delta(x, y)$ ,  $p$  and  $q$  are the polarizations of incident and scattered fields (vertical or horizontal), respectively;  $\chi_{pq}$  are the elements of the matrix

$$\underline{\underline{\chi}}(\theta_l, \beta) = \underline{\underline{R}}_2(\beta) \cdot \begin{pmatrix} F_H(\theta_l, \varepsilon) & 0 \\ 0 & F_V(\theta_l, \varepsilon) \end{pmatrix} \cdot \underline{\underline{R}}_2^{-1}(\beta) \quad (2)$$

wherein  $\underline{\underline{R}}_2(\cdot)$  is the unitary rotation matrix, and  $F_H$  and  $F_V$  are the Bragg coefficients for horizontal and vertical polarization, respectively [4], depending on the sea water relative permittivity  $\varepsilon$ . Therefore, the entries of the covariance matrix of the single facet can be written as follows:

$$\langle S_{pq} S_{rs}^* \rangle_\delta = \frac{Ak^4 \cos^4 \theta_l}{\pi^2} \chi_{pq}(\theta_l, \beta) \chi_{rs}^*(\theta_l, \beta) W(0, 2k \sin \theta_l) \quad (3)$$

wherein  $\langle \cdot \rangle_\delta$  stands for statistical mean with respect to the random variable  $\delta$  and  $A$  is the area of the facet projected on the azimuth-ground range plane. In the hypothesis that the returns from the facets can be considered uncorrelated and for small values of the facets' slope, the covariance matrix of the whole surface can be obtained from the one of the single facet averaging over the surface slopes  $a$  and  $b$ , after a second-order expansion around  $a=0$  and  $b=0$  [4]. In particular, the covariance matrix elements will be function of the  $C_{k,n-k}^{pq}$  Taylor series expansion coefficients, whose expressions are reported in [4].

We want now to evaluate the PTSM expression of the covariance matrix elements for circular polarization. Therefore, we apply an appropriate change of polarimetric basis [3]. We are interested in the following diagonal elements of the covariance matrix for circular polarization:

$$\begin{cases} 4\langle |S_{RR}|^2 \rangle = \langle |S_{hh} - S_{vv} + j2S_{hv}|^2 \rangle = \langle |S_{hh}|^2 \rangle + \langle |S_{vv}|^2 \rangle - 2\text{Re}\{\langle S_{hh} S_{vv}^* \rangle\} + 4\langle |S_{hv}|^2 \rangle \\ 4\langle |S_{RL}|^2 \rangle = \langle |S_{hh} + S_{vv}|^2 \rangle = \langle |S_{hh}|^2 \rangle + \langle |S_{vv}|^2 \rangle + 2\text{Re}\{\langle S_{hh} S_{vv}^* \rangle\} \end{cases} \quad (4)$$

Substituting the elements of the covariance matrix in (4) we obtain

$$\begin{cases} \langle |S_{RR}|^2 \rangle = u_* f_s [ |1 - \beta_r|^2 + f_{RR} \sigma^2 ] \\ \langle |S_{RL}|^2 \rangle = u_* f_s [ |1 + \beta_r|^2 + f_{RL} \sigma^2 ] \end{cases} \quad (5)$$

where  $u_*$  is the wind friction velocity,  $f_s$  depends on  $W(k_x, k_y)$  and on  $F_V(\theta, \varepsilon)$ ,  $\beta_r$  is the ratio between  $F_H(\theta, \varepsilon)$  and  $F_V(\theta, \varepsilon)$ , and  $f_{RR}$  and  $f_{RL}$  depend on  $f_s$  and on the  $C_{k,n-k}^{pq}$  Taylor series expansion coefficients.

According to the expressions in (5),  $\langle |S_{RR}|^2 \rangle$  depends on the difference between the horizontal and vertical Bragg coefficients and, therefore, the

backscattering of the sea surface in this polarization is very low. Conversely,  $\langle |S_{RL}|^2 \rangle$  is related to the sum of the Bragg coefficients, thus maximizing the return from the sea surface, and minimizing potential even-bounce contributions, e.g. due to the presence of ships. Equation (5) highlights the dependence on the large-scale roughness, through the mean square slope  $\sigma^2$ , and the linear dependence on the friction velocity  $u_*$ . Both these quantities can be related to the wind speed at the height of 10 m [1]. In support of the presented discussion, in Fig. 2 we present the graphs of (5) for two different values of wind speed.

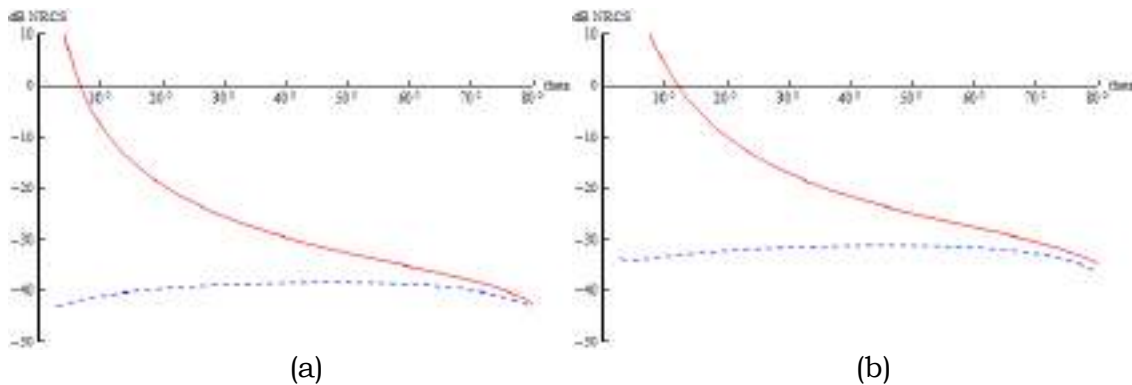


**FIG. 2** – Sea NRCS as a function of the incidence angle for RL (red solid line) and RR (blue dashed line) polarizations. Wind speed: 2 m/s (a), 20 m/s (b).

### III. CONCLUSION

A polarimetric two-scale model for the evaluation of scattering from the sea surface has been presented. Circular polarization covariance matrix elements have been also evaluated in closed form. Extension of the model to the bistatic case, which is of interest in GNSS reflectometry, is ongoing.

### REFERENCES

- [1] F. T. Ulaby, R. K. Moore, and A. K. Fung, *Microwave Remote Sensing*. Reading, MA, USA: Artech House, 1982, vol. II.
- [2] A. Di Simone, H. Park, D. Riccio, and A. Camps, “Sea target detection using spaceborne GNSS-R delay-doppler maps: Theory and experimental proof of concept using TDS-1 data,” *IEEE Journal of Selected Topics in Applied Earth Observations and Remote Sensing*, vol. 10(9), pp. 4237–4255, 2017.
- [3] A. G. Voronovich and V. U. Zavorotny, “Full-Polarization Modeling of Monostatic and Bistatic Radar Scattering From a Rough Sea Surface,” *IEEE Transactions on Antennas and Propagation*, vol. 62(3), pp. 1362–1371, 2014.
- [4] A. Iodice, A. Natale, and D. Riccio, “Retrieval of Soil Surface Parameters via a Polarimetric Two-Scale Model,” *IEEE Transactions on Geoscience and Remote Sensing*, vol. 49(7), pp. 2531–2547, 2011.

# FLOOD MAPPING USING SENTINEL-1 SAR DETECTED IMAGES

Donato Amitrano, Gerardo Di Martino, Antonio Iodice, Daniele Riccio,  
Giuseppe Ruello

Department of Electrical Engineering and Information Technology,  
University of Napoli Federico II

## Abstract

*We introduce a novel method for flood mapping through Sentinel-1 ground range detected images. The work introduces two novelties. As first, the input products, since no applications using these products has been so far presented in literature. Secondly, a new unsupervised methodology, based on the exploitation of opportune layers combined in a fuzzy decision system, is presented. Experimental results showed that our method is able to outperform the most popular classification techniques in terms of standard assessment parameters.*

**Index Terms** – classification; flooding; fuzzy systems; natural disasters; synthetic aperture radar

## I. INTRODUCTION

Floods are among the most frequent natural hazards in the world, causing high damages to people, infrastructure, and economies. The UN estimated that more than the 50% of the total population affected by weather-related disasters is involved in flood issues. Floods are particularly critical in developing countries, where deficient prevention activities and scarce urbanization planning make these phenomena more serious. However, also the “developed world” is frequently interested by catastrophic flood events. As an example, in US more than 225 people were killed and more than 3.5 billion dollars in property were damaged by heavy rainfall and flooding each year between 1993 and 1999. In general, effective response to floods requires the availability of a map of the affected area in a short time.

Synthetic aperture radar (SAR) sensors represent an important tool for rapid flooding mapping due to their all-weather and all-time imaging characteristics, ensuring the imaging of the Earth surface independently from illumination and weather conditions. However, information extraction from SAR acquisitions is typically considered challenging by end-users, also due to the lack of dedicated algorithms implemented in some available software suites. As a result, they often prefer to operate with optical/multispectral sensors. In fact, in this case, beyond the possibility to handle images that can be immediately interpreted for visual inspection, very consolidated techniques for the extraction of the flooded area exist, just think to the exploitation of the normalized difference water index (NDWI) by McFeeters [1]. However, despite their ease of use and popularity among end-users, multispectral

data are often not suitable for emergency due to their sensitivity to weather and illumination conditions.

As aforementioned, the usage of SAR data allows for overcoming this limitation. In this work, we introduce a double innovation. The first is at product level, since we exploit Sentinel-1 ground range detected (GRD) products, i.e. detected images pre-processed by ESA. These products are today still scarcely employed in the SAR literature, despite they are raising a great interest among end-users because they are available for cloud processing within the Google Earth Engine platform.

The second innovation is methodological. We propose two processing chains providing maps with increasing resolution. Chain-one is based on the analysis of a single GRD product. It exploits classic Haralick textural features and the output is a low resolution map obtainable in few minutes. Chain-two is based on change detection between pre- and post-event scene situation. Its output is a map with the full resolution of the input GRD products.

## II. METHODOLOGY

Chain one workflow is depicted in Fig. 1. It takes as input a standard Sentinel-1 GRD (10-meter spatial resolution). Moderate  $3 \times 3$  multilooking is applied for speckle reduction. This brings the image resolution to 30 meters.

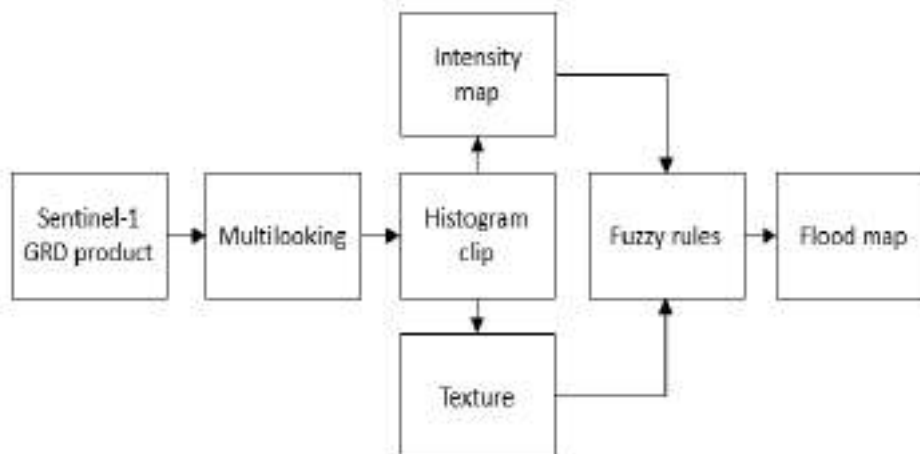


**FIG. 1** – Flood mapping using the single Sentinel-1 GRD product.

After multilooking, histogram clip is performed to compensate the presence of highly reflecting targets [2]. Texture processing consists in the calculation of classic Haralick features [3]. These layers feed the fuzzy decision system assigning automatically the classes “Flood” and “No flood” basing on the calculated membership degree. Permanent hydrography, otherwise indistinguishable from flooded areas, should be externally masked out. The method is fully unsupervised and does not require the application of thresholds.

The change-detection chain is depicted in Figure 3. In this case, the input is a couple of calibrated and coregistered Sentinel-1 GRD

products representing the pre- and the post-event scene situation. Standard despeckling is applied to enhance the contrast between water and land features (here, the refined Lee filter is applied).

Filtered images are subject to cross-calibration using the variable amplitude level equalization introduced in [2] in order to ensure that the same object in different images exhibit the same reflectivity. Then, cross-calibrated images are used to compute a change index map which, together with the post event image, is used as input layer for the fuzzy decision system.

The output map has ten-meter spatial resolution, i.e. the full resolution of the input GRD products, neglecting possible losses due to the applied despeckling. The method is fully unsupervised.

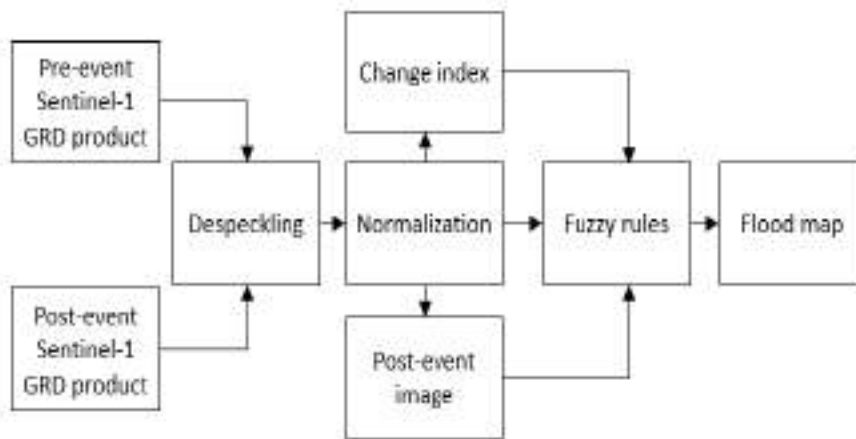


**FIG. 2** – Workflow for flood mapping using change-detection.

### III. EXPERIMENTAL RESULTS

The proposed methodology has been applied to several test cases taken from the Copernicus Emergency Management Service database, in which ground truths as well as masks for the permanent hydrography are available. The obtained results are reported in Table I and Table II for the single image processing and for the change-detection chain, respectively. They are fully satisfying, since allowed for obtaining high accuracy with respect to the available ground truth with negligible impact of false alarms.

**TABLE I – COMPARISON BETWEEN THE PROPOSED SINGLE IMAGE PROCESSING AND POPULAR LITERATURE METHODS FOR SAR IMAGE SEGMENTATION**

Dataset	Proposed		k-mean		SVM		Threshold	
	DR	FA	DR	FA	DR	FA	DR	FA
Ballinasloe	94.5	4.69	78.2	15.8	66.6	3.36	58.7	3.14
Selby	92.1	1.00	86.0	14.2	91.5	2.13	78.7	1.22
Poplar Bluff	96.2	7.33	91.7	15.7	92.2	5.00	63.7	1.30
Jemalong	91.2	13.3	65.4	21.0	64.6	5.00	33.1	4.31

**TABLE II – COMPARISON BETWEEN THE PROPOSED CHANGE-DETECTION PROCESSING AND POPULAR LITERATURE METHODS FOR SAR IMAGE SEGMENTATION**

Dataset	Proposed		k-mean		SVM		Band ratio	
	DR	FA	DR	FA	DR	FA	DR	FA
Ballinasloe	98.6	6.60	59.1	21.9	64.6	3.94	96.6	6.45
Selby	91.8	2.40	90.2	21.2	90.5	3.39	95.7	29.5
Poplar Bluff	84.1	11.1	69.6	11.4	49.0	3.53	49.5	6.28
Jemalong	93.6	12.3	49.5	9.04	66.9	6.11	81.3	12.4

A comparison with several literature methods has been also implemented. We obtained that the proposed methodology outperformed all of them in terms of the adopted classification quality indicators.

#### IV. CONCLUSION

In this work, we presented a new methodology for unsupervised mapping of flooding areas introducing innovation both at product and at processing/methodological level. In fact, we exploit pre-processed Sentinel-1 ground range detected products which are still poorly used in the SAR literature. They constitute the input for two successive processing levels with increasing computational burden, giving as output event maps with increasing resolution. Both the processing levels are fully unsupervised and threshold-free thanks to the adoption of fuzzy classification rules. The obtained results showed that the proposed methodology outperforms the past literature in terms of standard classification quality indicators.

#### REFERENCES

- [1] S. K. McFeeters, “The use of the Normalized Difference Water Index (NDWI) in the delineation of open water features,” *Int. J. Remote Sens.*, vol. 17, no. 7, pp. 1425–1432, May 1996.
- [2] D. Amitrano, G. Di Martino, A. Iodice, D. Riccio, and G. Ruello, “A New Framework for SAR Multitemporal Data RGB Representation: Rationale and Products,” *IEEE Trans. Geosci. Remote Sens.*, vol. 53, no. 1, pp. 117–133, 2015.
- [3] R. M. Haralick, K. Shanmugam, and I. H. Dinstein, “Textural Features for Image Classification,” *IEEE Trans. Syst. Man Cybern.*, vol. SMC-3, no. 6, pp. 610–621, 1973.

# **A NEW METHOD TO ENHANCE SPATIAL RESOLUTION OF MICROWAVE EARTH OBSERVATION MEASUREMENTS**

Matteo Alparone, Ferdinando Nunziata

Dipartimento di Ingegneria, Università degli Studi di Napoli  
Parthenope, 80143 Napoli, Italy  
Centro Direzionale - Isola C4, 80143 Napoli, Italy  
matteo.alparone@uniparthenope.it

## **Abstract**

*In this paper we present a novel technique to enhance the spatial resolution of microwave earth observation measurements collected by meso-scale sensors. The proposed rationale is based on an  $L^p$ -penalization approach with a variable  $p$  exponent, ranging in the interval  $[1.2,2]$ . This allows taking benefits of the advantages of methods operating in both Hilbert and Banach spaces. Experiments are undertaken considering the microwave radiometer and refer to both simulated and actual data. Results demonstrate the benefits of the proposed approach in reconstructing abrupt discontinuities and smooth gradients with respect to approaches in Hilbert and Banach spaces.*

**Index Terms** – Inverse Problems, Microwave Remote Sensing, Resolution Enhancement.

I.

## **INTRODUCTION**

Measurements collected by a microwave probe can be considered as a low-pass filtered version of the geophysical parameters of interest weighted by the system function. Hence, when one attempts at reconstructing the geophysical parameter of interest, an inverse problem is to be addressed. The latter is typically ill-posed since it comes from a direct problem that is, in general, governed by a Fredholm integral equation of the first kind with a smooth kernel. In this study we refer to microwave radiometers, that are instruments designed for a broad number of Earth Observation (EO) applications. Their low spatial resolution limits their use when dealing with regional-scale studies, so that resolution enhancement techniques must be invoked [1]. From a mathematical point of view, this implies that the above mentioned inverse problem that arises when retrieving the geophysical parameters of interest is also undetermined since one attempts to reconstruct the geophysical parameter on a finer resolution grid. In literature such problem is mainly addressed by solving an  $L^p$ -norm minimization problem with  $p=2$  (Hilbert space) and  $p=1.2$  (Banach space) [2]. In this work we present a novel approach, based on the idea of using a variable  $p$  exponent, ranging in the interval  $[1.2,2]$ . The proposed algorithm adapts the  $p$  exponent to the region of the image to be

reconstructed in order to exploit the benefits and avoid the drawbacks of both the constant exponent  $p=2$  and  $p=1.2$  methods.

## II.

### BRIEF THEORETICAL BACKGROUND

To perform the resolution enhancement of radiometer data, the ill-conditioned and underdetermined linear problem  $Ax = b$  must be solved, where  $A$  is the matrix containing the projected antenna patterns related to the radiometer measurements, the unknown vector  $x$  stands for the brightness temperature  $T_B$  and  $b$  is the measurement vector. To solve this problem regularization methods must be invoked and constraints on the signal to be reconstructed must be imposed. The  $L^p$ -norm regularization methods that constrain the reconstructed solution to belong to Hilbert ( $p=2$ ) and Banach ( $p=1.2$ ) spaces have already been covered in previous papers [2] - [4].

$L^p$ -norm minimization method with variable  $p$  exponent is based on the idea that the  $p$  exponent is no longer fixed value; indeed it is a function  $p(t): \Omega \rightarrow [1, \infty]$ . The  $k$ -th iteration of the iterative method of the gradient method using the variable  $p$  exponent is given by :

$$\mathbf{x}_{k+1} = \mathcal{J}_{L^{q(\cdot)}}(\mathcal{J}_{L^{p(\cdot)}}(\mathbf{x}_k) - \lambda_k A^* \mathcal{J}_r(A\mathbf{x}_k - \mathbf{b})) \quad (1)$$

where  $J_{L^{p(\cdot)}}$  and  $J_{L^{q(\cdot)}}$  are the duality maps (that link elements of a normed space with the elements of its dual space) re-adapted to variable  $p$  case  $J_r$  is the duality map of the constant  $p$  case and  $q$  is the Hölder conjugate of  $p$ , i.e.,  $1/p + 1/q = 1$ . Note that a key issue consist of properly re-defining the concept of the  $p$ -norm when  $p$  is variable. Further details can be found in [5].

## III.

### RESULTS

Simulated measurements refer to SSMI-like measurements, whose spatial resolution is 69 km, related to a rect-like reference field. In Fig. 1, the reconstructed fields at enhanced spatial resolution (1 km pixel spacing) are shown for the Hilbert (red line), Banach (yellow line) and variable  $p$  exponent (purple line) methods. Although all the methods succeed in reconstructing the reference field at 1 km spatial grid, the variable  $p$  method allows to wipe out the oscillations due to the Gibbs phenomenon (that typically occurs when  $p=2$  is adopted), and allows to reconstruct fairly the top of the rect-like signal where the  $p=1.2$  method, indeed, exhibit large

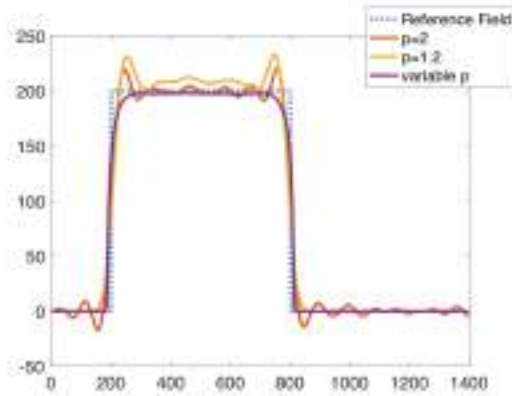


**FIG. 1** – Reference field (blue dotted line) and reconstructed fields obtained using gradient method in Hilbert ( $p = 2$ , red dotted line), Banach ( $p = 1.2$ , yellow line) and variable  $p$  exponent (purple line).

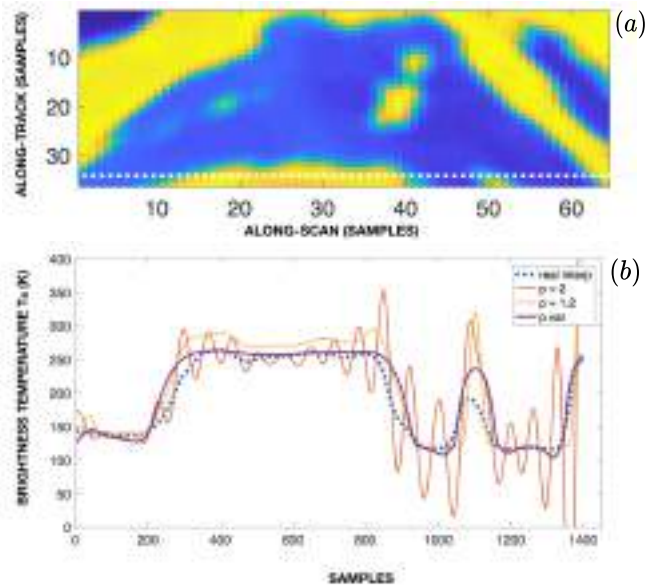


**FIG. 2** – (a) SSM/I 19.3 GHz H-polarized brightness temperature field. The white dotted line shows the along-scan transect selected for our study. (b) Enhanced spatial resolution reconstructions of the selected transect obtained by using gradient method in  $L_p$  spaces. The blue dotted line is the reference field, obtained by a linear interpolation of the measured  $T_B$  on a finer grid.

oscillations. In Fig. 2, experiments undertaken on actual SSM/I measurements refer to the 1998 V-polarized brightness temperature field collected at 19.35 GHz. A transect that includes portions of Northern Africa, Sicily and Italian peninsula is considered (see Fig. 2 (a)). It can be noted that both abrupt (land/sea interface) and spot-like (small islands) discontinuities are present.

The reconstructions at enhanced spatial resolution related to the selected transect are shown in Fig. 2 (b). To evaluate the quality of the

reconstructions, we used as reference field the real measurement (64 samples) linearly interpolated to a finer grid in order to achieve the same dimensions of the solutions (1400 samples). Again, variable  $p$  exponent method performs best in reconstructing the actually brightness profile.

## VI.

## CONCLUSION

A novel approach to enhance the spatial resolution of microwave data has been presented. The reconstruction of the brightness field on a finer resolution grid is achieved using gradient method in  $L^p$  spaces. The innovative theoretical rationale consists of exploiting a variable  $p$  exponent in order to bridge the gap between the Hilbert and Banach space methods. To the best of our knowledge, this is the first time that resolution enhancement techniques in variable exponent Lebesgue spaces are used for the improvement of microwave radiometer data. Results obtained using both simulated and actual radiometer data show the superiority of the variable  $p$  exponent method with respect to Hilbert and Banach methods.

## ACKNOWLEDGEMENT

This work is partially supported by Università degli Studi di Napoli Parthenope under the project ID DING 118.

## REFERENCES

- [1] D. G. Long, "Reconstruction and resolution enhancement techniques for microwave sensors," in *Frontiers of Remote Sensing Information Processing*, C. H. Chen, Ed. Singapore: World Scientific, 2003, ch. 11.
- [2] F. Lenti, F. Nunziata, C. Estatico, and M. Migliaccio, "Conjugate Gradient Method in Hilbert and Banach Spaces to Enhance the Spatial Resolution of Radiometer Data," *IEEE Transactions on Geoscience and Remote Sensing*, vol. 54, no. 1, Jan. 2016.
- [3] F. Lenti, F. Nunziata, C. Estatico, and M. Migliaccio, "On the Spatial Resolution Enhancement of Microwave Radiometer Data in Banach Spaces," *IEEE Transactions on Geoscience and Remote Sensing*, vol. 52, no. 3, pp. 1834–1842, mar 2014.
- [4] F. Lenti, F. Nunziata, C. Estatico, and M. Migliaccio, "Analysis of Reconstructions Obtained Solving  $l_p$ -Penalized Minimization Problems," *IEEE Transactions on Geoscience and Remote Sensing*, vol. 53, no. 9, pp. 4876–4886, sep 2015.
- [5] M. Alparone, F. Nunziata, C. Estatico, M. Migliaccio, and F. Lenti "Spatial Resolution Enhancement of Microwave Radiometer Data in Lebesgue Spaces with Variable Exponent," Submitted to *IEEE TGRS*, 2018.

# A STUDY ON MM-WAVE MULTI-USER BEAMFORMING BASED ON MEASUREMENTS AND RAY TRACING SIMULATIONS

M. Zoli, F. Fuschini

Department of Electrical, Electronic and Information Engineering (DEI),  
University of Bologna  
Viale del Risorgimento 2, Bologna, Italy  
[marco.zoli5@unibo.it](mailto:marco.zoli5@unibo.it)

## Abstract

*This study concerns the evaluation of the impact of the radio channel on beamforming performance in Multi-User indoor environment at mm-Wave band of 70GHz, using both wideband measurements and Ray Tracing simulations.*

**Index Terms** – Millimeter wave, radio propagation, multi-user MIMO/Beamforming, Ray Tracing, SDMA.

## I. INTRODUCTION

Electromagnetic propagation at mm-Wave frequencies is dominated by few multipath components [1]-[3]. In presence of limited multipath richness and low Signal-to-Noise-Ratio, multi-antenna communication schemes can be used to implement beamforming (BF) solutions [3-4] to compensate for the high propagation losses and take advantage of the directional properties of the channel. In order to be compliant to the forthcoming 5G wireless systems, BF must be adaptive [5] and then, in a crowded Multi-User (MU) scenario, the beam-steering procedures should be optimized, aiming at boosting the received signal strength at each user, while reducing the undergone interference. Unfortunately, current beam-scanning techniques are likely to be time consuming and inadequate for a MU scenario. Such problems are studied in this manuscript through 3D directional channel measurements and Ray Tracing (RT) simulations [8] for a small-office environment in the 70GHz band. Results show that the considered RT model is reliable enough to reproduce the general BF performance and also to assist the beam-searching routine, therefore potentially reducing the computational overhead.

## II. CONCEPT OF WORK

Multiuser indoor BF is investigated in this study through the double-track approach sketched in Figure 1, based on both simulated (in blue) and experimental (in red) data. Both radio channel propagation and MU-BF validations have been achieved. Practically, Signal-to-Noise-and-Interference-Ratio (SINR) distributions are addressed in the following not only to compare real measured radio channel versus RT simulations in terms of BF results, but also for a novel assessment of the related system-level performance, in MU indoor environment, where the RT supports the BF decision-making. Part of the results are already included in [9], and are omitted in this paper, for sake of simplicity.

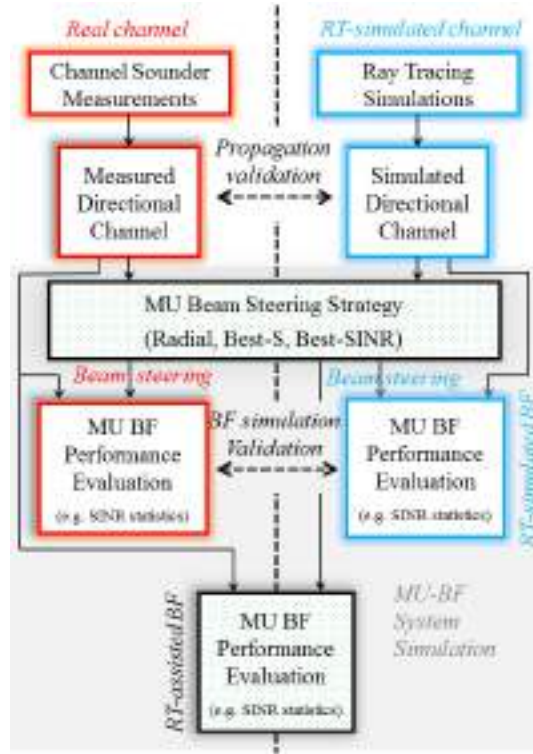


**FIG. 1** – Logical block scheme describing the adopted methodology for the analysis and assessment of MU-BF capabilities.

### III. MEASUREMENTS AND SIMULATIONS

The measurement scenario is a small office where 6 Receiver (Rx) and 2 transmitter positions (Tx1 and Tx2 in the following) are considered. All Tx-Rx links are in Line-of-Sight (LoS), with no people around [8]. The measurements have been performed with a custom mm-Wave M-sequence-based Channel Sounder developed at TU Ilmenau, which exploits an UWB signal up-converted up to 70GHz with more than 4 GHz of bandwidth. The Tx/Rx antennas are cylindrical horn antennas with Half-Power-Beam-Width=15° and a maximum gain of 20dBi, and have been mounted on rotating positioners at both link ends.

### IV. BEAMFORMING SYSTEM SIMULATIONS

System-level simulations take into account all the possible combinations of  $N_{AU}$  active users ( $N_{AU}=2,3$  or 4) in the small-office environment, systematically. Each “Rx drop” includes a different arrangement of the  $N_{AU}$  Rxs over the 6 possible locations [8] and involves a Beam Search performed all over the angular discrete sets, to achieve the best BF solution (e.g. 2 or 3 or 4 beams), according to a Space Division Multiple Access (SDMA) scheme (named ‘Best-SINR BF’), which is an interference-aware, cooperative beam-search solution that maximizes the SINR values for all the active users [9]. In a MU scenario, a high aggregate throughput represents a major goal for an effective BF technique, but at the same time, unbalanced SINR distributions should be also avoided. So a “fairness principle” in the SDMA has been implemented to balance the SINR values among users, also.

## V. RESULTS

The SINR statistics results are shown in Figure 2, where the RT-based SINR CDFs (dotted lines) are shown to match quite well the measurement-based SINR CDFs (solid lines) for 2, 3 and even 4 active users. The root-mean-square-error (RMSE) between the RT-based BF simulations and the measurement-based BF simulations is about 3dB, generally. By increasing  $N_{AU}$  the RMSE raises slightly by 1-2dB, only, and is always kept below 5dB. All of this confirms that RT represents a valid multidimensional radio channel model, and also a reliable tool for the statistical evaluation of beamforming schemes exploiting multidimensional propagation characteristics.

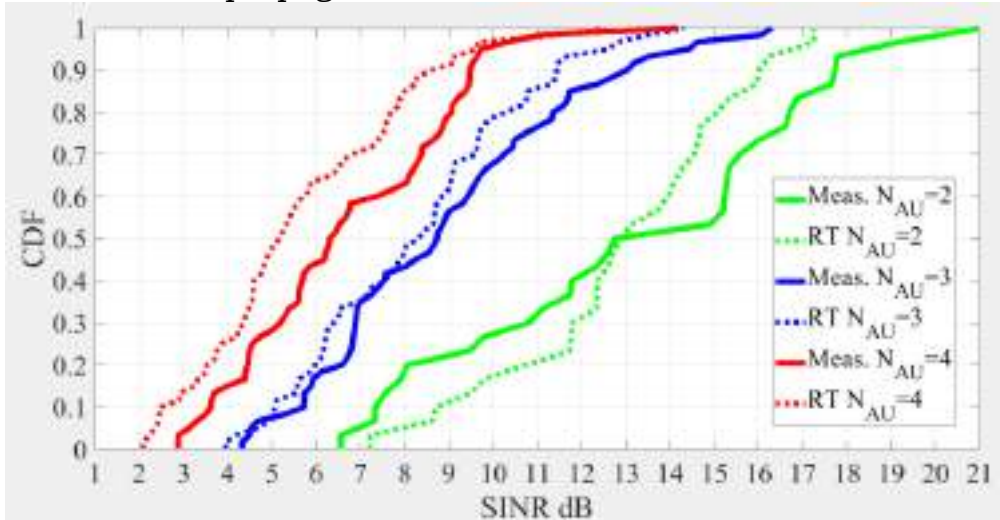


**FIG. 2** – SINR CDF comparison between measurements and RT simulations with  $N_{AU}= 2, 3$  and  $4$  for Tx2, according to Best-SINR BF scheme.

Furthermore, RT has been tested to support the BF Beam Search task, as outlined in the blue track in figure 1. In fact, RT channel information are exploited to pilot the BF decision, totally (RT-driven) or partially (RT-assisted), and then, the related MU-BF system-level results are compared to the measurement-only MU-BF evaluations. Then, results are reported in Table I, where the solution of RT-assisted BF provides a mean error of about 3-4 dB, with respect to the exhaustive BF search based on the measured radio channel. Moreover, the overall search domain for the best BF beams choice for the active users is reduced by a factor of at least  $\times 150$  and  $\times 17700$ , for  $N_{AU}=2$  and  $3$ , respectively, with a proportional dramatic reduction of beam-searching time.

Table I: RT-driven and -assisted BF versus measured-based BF. SINR Errors statics are reported for 50<sup>th</sup> and 90<sup>th</sup> percentiles.

$N_{AU}$	Tx	RT-driven BF		RT-assisted BF	
		50th percentile Error	90th percentile Error	50th percentile Error	90th percentile Error
2	Tx1	6 dB	14 dB	4 dB	6 dB
	Tx2	4 dB	9 dB	3 dB	5 dB
3	Tx1	6 dB	14 dB	3 dB	6 dB
	Tx2	6 dB	14 dB	4 dB	6 dB

## VI. CONCLUSION

In this work, multi-user beamforming is investigated in a small indoor mm-Wave environment. Measurement and simulation analysis shows that the signal-to-interference ratios decreases for bigger number of users, to an extent that the resort to space-division-multiple-access alone for reliable high-speed communications might be doubtful. Anyway, the Best-SINR scheme (i.e. an exhaustive-search algorithm selecting the beam-steering solution maximizing the signal-to-interference ratio) yields overall fair performance. However, the use of such a solution could be impractical due to the long time required by the exhaustive beam-searching phase, especially in joint bidirectional-beamforming case. If accurate localization of the mobile users is available, Ray Tracing can be used as a real-time and/or off-line tool (e.g. database, lookup table) to retrieve the directional characteristics of the radio channel (e.g. Channel State Information) and restrict the search domain in order to speed-up the beam-searching phase. Results show that such a solution gives good results, with an average degradation in terms of SINR of about 3-4 dBs compared to a truly exhaustive search, but with a processing time orders of magnitude lower.

## REFERENCES

- [1] S. Kutty, D. Sen, "Beamforming for Millimeter Wave Communications: An Inclusive Survey", *IEEE Comm. Surveys and Tutorials*, vol. 18, No. 2, 2016;
- [2] S. Sun, T.S. Rappaport, R. W. Heath, A. Nix, S. Rangan, "MIMO for Millimeter-Wave Wireless Communications: Beamforming, Spatial Multiplexing, or Both?", *IEEE Comm. Magazine*, vol. 52, No. 12, December 2014;
- [3] A.F. Molisch, V.V. Ratnam, S. Han, Z. Z. Li, S. Nguyen, L. Li, K. Haneda, "Hybrid Beamforming for Massive MIMO: A Survey", *IEEE Comm. Magazine*, vol. 55, No. 9, September 2017;
- [4] A. Sibille, C. Oestges, A. Zanella, "MIMO From Theory to Implementation", Elsevier Inc., 2011;
- [5] S. Rangan, T. Rappaport, E. Erkip, "Millimeter-Wave Cellular Wireless Networks: potentials and Challenges", *Proc. of the IEEE*, vol. 102, No. 3, March 2014;
- [6] M. Gapeyenko, A. Samuylov, M. Gerasimenko, D. Moltchanov, S. Singh, E. Aryafar, S. Yeh, N. Himayat, S. Andreev, Y. Koucheryavy, "Analysis of human body-blockage in urban millimeter wave cellular communications", *IEEE Int. Conf. on Communications*, Kuala Lumpur (MY), 22-27 May 2016;
- [7] G.R. MacCartney, S. Deng, S. Sun, T. S. Rappaport, "Millimeter-Wave Human Blockage at 73 GHz with a Simple Double Knife-Edge Diffraction Model and Extension for Directional Antennas", *IEEE Veh. Tech. Conf.*, Montreal (CDN), 18-21 September 2016;
- [8] F. Fuschini, S. Häfner, M. Zoli, R. Müller, E. M. Vitucci, D. Dupleich, M. Barbiroli, J. Luo, E. Schulz, V. Degli-Esposti, R.S. Thomä, "Analysis of In-Room mm-Wave Propagation: Directional Channel Measurements and Ray Tracing Simulations," *Vol. 38, No. 6*, pp. 727-744, June 2017;
- [9] Fuschini, F.; Zoli, M.; Vitucci, E. M.; Barbiroli, M.; Degli-Esposti, V., A study on mm-Wave multi-user indoor beamforming, in: *Proceedings of 2017 IEEE-APS Topical Conference on Antennas and Propagation in Wireless Communications (APWC)*, IEEE, 2017, pp. 77 - 80 (atti di: 2017 IEEE-APS Topical Conference on Antennas and Propagation in Wireless Communications (APWC), Verona, Italy, 11-15 Sept. 2017)

## PROGRESS ON THE REALIZATION OF A LoRa® BASED COMMUNICATION SYSTEM FOR ATMOSPHERIC MONITORING PROBES

S. Bertoldo<sup>(1)(2)</sup>, M. Paredes<sup>(1)(3)</sup>, L. Carosso<sup>(1)(2)</sup>, C. Lucianaz<sup>(1)(2)</sup>, M. Allegretti<sup>(1)(2)(3)</sup>, F. Canavero<sup>(1)</sup>, G. Perona<sup>(2)</sup>

(1) Politecnico di Torino, DET, Corso Duca degli Abruzzi 24, 10129, Torino, Italy

(2) Consorzio Interuniversitario Nazionale per la Fisica delle Atmosfere e delle Idrosfere (CINFAI), unità di ricerca presso il DET, Politecnico di Torino, Italy

(3) Envisens Technologies s.r.l., Corso C. Menotti 4, 10138, Torino, Italy

[silvano.bertoldo@polito.it](mailto:silvano.bertoldo@polito.it), [miryam.paredes@polito.it](mailto:miryam.paredes@polito.it)

### Abstract

*The work presents the progress on the realization of the communication system realized for atmospheric monitoring probes. The realization of a link based on the Long Range (LoRa®) technology to connect and exchange data between the probes and the base station located on the ground is the potential adopted solution. After a brief description of the whole project, the realization of the first prototypal transmission system using Adafruit® Feather 32u4 LoRa Radio RFM95 embedded modules is described. First propagation measurements and results are presented.*

**Index Terms** – LoRa, atmospheric probes, propagation measurements, electromagnetic measurements, LoRa measurements, Internet of Things, IoT.

### I. INTRODUCTION

As part of the Horizon 2020 Innovative Training Network Cloud-MicroPhysics-Turbulence-Telemetry project (ITN-COMPLETE), a new kind of ultralight radio probe with an embedded processor, capable of floating in stratocumuli clouds is being developed. The probes must have a fluid-dynamic behavior to allow them to “float” inside warm clouds after been released. They must be equipped with a set of sensors and low power consumption techniques must be implemented in order to allow them to float as longer as possible making ensuring in this way a deeper study of warm clouds [1]. The probes are based on a preliminary feasibility study presented by Bertoldo in 2016 [2]. They acquire information about the surrounding atmosphere characteristics and send them to a receiver located on the ground with a dedicated communication link.

In this work the communication system is briefly presented and some preliminary results about its realization are reported.

### II. LoRa™ BASED COMMUNICATION SYSTEM

LoRa® technology uses a proprietary Chirp Spread Spectrum (CSS) technique to encode information, achieving low power properties and long

communication distances. This modulation scheme allows to improve the receiver sensitivity by the type of modulation itself and accomplishing high tolerance to misalignments in frequency between the transmitter and the receiver. The chirp pulses used in LoRa® modulation allow frequency offsets, equivalent to have timing offsets, between the receiver and the transmitter, increasing in this way the robustness against channel degradation mechanisms such as Doppler Effect, fading and multipath. The reached distances greatly depend on the environment and obstacles, however LoRa® provides better link budget than other similar communication standards. These are the main reasons why the LoRa® technology can be chosen as a communication system for the atmospheric monitoring probes.

The first realization of the communication system is based on the module Adafruit® Feather 32u4 LoRa Radio RFM95. It is an embedded module, which contains a LoRa® transceiver RFM95 and an ATmega32u4 microcontroller. The chip has 32 kB of flash memory and 2 kB of RAM memory. The radio module can be powered using 3.3 volts either by using a micro USB or an external battery. Among its main features, there are the small size (51 mm x 23 mm x 8 mm) and the lightweight (5 g), which are fundamental for the radio probes. Moreover, the operative frequency range is 868-915 MHz, including the band around 868 MHz allowed by the European laws, and the transmitted power ranges between 5 dBm to 20 dBm, thus theoretically allowing to reach distances of a tenth of kilometers. This fact is again a basic point for the choice of this chip.



**FIG. 1** – Adafruit® Feather 32u4 LoRa Radio RFM9 on the left and LoRa Radio RFM9 transceiver module on the right.

Both, the transmitter placed on the final working prototypes of the radio probes, and the receiver located on the ground, will be equipped with the RFM95 transceiver module. The module will be controlled with an Arduino© microcontroller, since the microcontroller of the Adafruit® Feather 32u4 LoRa Radio RFM9 can be programmed with the same libraries of Arduino©, which is the basic chip of the final realization of the system according to the design specifications.

### **III. MEASUREMENTS**

The first preliminary measurements were made using a single transmitter and a receiver located in different positions. Both of them are properly programmed. The transmitter is capable to work with a power supply that can be either a USB cable connected to a PC or a battery. It transmits a set of packets ( $N_{PACKET}=200$ ) with a predefined transmitted power ( $P_{TX}=5$

dBm), at the frequency of 865 MHz with a spreading factor in order to have a channel bandwidth of 125 kHz. The receiver is connected to a PC in order to count the number of correctly received packets, make measurements about RSSI, SNR and log other information. At the same time, next to the receiver, a spectrum analyzer is equipped with the same antenna of the receiver in order to measure also the received power values as far as possible, since the noise floor of the instrument is significantly higher with respect to the sensitivity of the Adafruit® Feather 32u4 LoRa Radio RFM9.

The spectrum analyzer parameters are reported in the Table I. We believe that they can be used as a reference to define a procedure for electromagnetic measurements on LoRa® technologies.

**Table I – Spectrum analyzer parameters for LoRa© measurements**

Center frequency (CF)	865 MHz
Resolution bandwidth (RBW)	10 kHz
Video bandwidth (VBW)	30 kHz
Sweep time	5 ms
Span	500 kHz
Measurement mode	Max hold

Preliminary results of the measurements are reported in the following Table II and Table III, where comparisons between the measured path losses and the free space path losses are reported as well.

For all the measurements, the SNR ranged from +8 at shorter distances to -6 at the longest. The negative values of SNR “indicate the ability to receive signal powers below the receiver noise floor” as reported on the official application note on LoRa™ Technology released by Semtech© [3], and it happens when the range of the communication link is increased.

The RSSI of the packets decreased with distance; however, the majority of the packets were received. For most of the cases, the percentage of packet losses was 0%, while in few cases <1%. Only in the last test, where the separation distance was larger than 800 meters, the percentage of losses reached 4%. At that distance, the Spectrum Analyzer did not measure the received power since the value is below its noise floor. The receiver module correctly received the packets.

**Table II – Preliminary results for indoor measurements**

POSITION #	DISTANCE [m]	SNR (dB)	RSSI [dBm]	LOST PACKETS (%)	Received power (Spectrum) [dBm]	Measured losses [dB]	Free space path loss [dB]	Difference [dB]
1	15	8	-55	1	-35,03	40,03	54,71	14,68
2	29,4	8	-71	0	-54,74	59,74	60,55	0,81
3	41,6	8	-75	0	-54,4	59,4	63,57	4,17
4	57,2	7	-93	1	-75,37	80,37	66,33	-14,04
5	13,3	8	-69	0	-52,63	57,63	53,66	-3,97
6	32,2	8	-85	0	-68,99	73,99	61,34	-12,65
7	27,7	7	-93	0	-77,82	82,82	60,03	-22,79

**Table III – Preliminary results for outdoor measurements**

POSITION #	DISTANCE [m]	SNR (dB)	RSSI [dBm]	LOST PACKETS (%)	Received power (Spectrum) [dBm]	Measured losses [dB]	Free space path loss [dB]	Difference [dB]
1	122	8	-82	0	-69,25	74,25	72,91	-1,34
2	170	7	-87	1	-71,13	76,13	75,79	-0,34
3	376	1	-90	1	-78	83	82,69	-0,31
4	616	-1	-132	1	-85	90	86,98	-3,02
5	839	-6	-140	4	Below noise floor of SA, impossible compute losses with received power measurements		89,66	

#### IV. CONCLUSIONS AND OUTLOOKS

A possible realization of the communication system based on the LoRa® technology is described and some preliminary measurements presented. Particularly detailed measurements will be made in harsh environmental conditions (e. g. rain, fog, drizzle...) in order to simulate a set of possible environmental conditions that can be found inside a warm cloud. A set of prototypes of radio probes will be realized to make further measurements with the final star topology network.

The work presents also a possible configuration for the Spectrum Analyzer to make measurements with LoRa™ technology.

#### ACKNOWLEDGEMENT

The project COMPLETE has received funding from the Marie - Skłodowska Curie Actions (MSCA) under the European Union's Horizon 2020 research and innovation program (grant agreement n°675675).

#### REFERENCES

- [1] T. C. Basso, M. Iovieno, S. Bertoldo, G. Perotto, A. Athanassiou, F. Canavero, G. Perona, D. Tordella, “Disposable radiosondes for tracking Lagrangian fluctuations inside warm clouds”, *IEEE APWC 2017*, 11-15 September 2017, Verona (Italy), pp. 189-192.
- [2] S. Bertoldo, C. Lucianaz, M. Allegretti, G. Perona, “Disposable falling sensors to monitor atmospheric parameters”, *Proceedings SPIE 10001, Remote Sensing of Clouds and the Atmosphere XXI*, 1000104, *SPIE Remote Sensing 2016*, Edinburgh (SCO), 26-29 September 2016.
- [3] AN1200.22 LoRa™ modulation basic. Application Note. May 2015, Revision 2. Semtech Corporation.

# EM WAVE PROPAGATION EXPERIMENT AT E BAND AND D BAND FOR 5G MOBILE NETWORKS

L. Luini<sup>(1)</sup>, G. Roveda<sup>(2)</sup>, M. Zaffaroni<sup>(2)</sup>, M. Costa<sup>(2)</sup>, C. Riva<sup>(1)</sup>

<sup>(1)</sup> DEIB, Politecnico di Milano, Italy  
[lorenzo.luini@polimi.it](mailto:lorenzo.luini@polimi.it)

<sup>(2)</sup> Huawei Microwave Centre, Milan, Italy  
[giuseppe.roveda@huawei.com](mailto:giuseppe.roveda@huawei.com)

## Abstract

*Preliminary results on an electromagnetic wave propagation experiment at E and D band are presented. The research activity is a collaboration between Politecnico di Milano and the Huawei European Microwave Centre in Milan, which has installed short (325 m) terrestrial links operating at 73, 83, 148 and 156 GHz, and connecting two buildings in the university main campus. The experiment aims at investigating and predicting rain attenuation taking advantage of ancillary data collected by a collocated laser-based disdrometer.*

**Index Terms** – 5G mobile networks, electromagnetic wave propagation, measurement, terrestrial links.

## I. INTRODUCTION

The evolution of wireless communication systems is more and more moving towards the use of higher frequency bands due to the need of mobile service providers to support the always increasing data rate and traffic demand [1]. The Fifth Generation (5G) mobile network is expected to employ the millimeter-wave portion of the spectrum, for both backhauling links and radio access (from 26 GHz, up to the optical range), in order to accommodate much higher data rates [1].

Unfortunately, electromagnetic (EM) waves being considered for 5G systems are subject to strong propagation impairments, induced by fog, gases and precipitation. Among them, rain plays the most relevant role: it is of paramount importance to investigate rain attenuation, which is greatly dependent on the operational frequency and on the rain drop dimension, i.e. on the so called Drop Size Distribution (DSD) [2].

This contribution describes a joint research activity on EM wave propagation involving Politecnico di Milano and the Huawei European Microwave Centre in Milan, which has installed full-duplex terrestrial radio links connecting two buildings in the university main campus. The links operate in the E (73 and 83 GHz) and D (148 and 156 GHz) bands and are 325-m long. The D-band link, installed in November 2016, is the first outdoor radio hop deployed worldwide to explore the use of such a band for fixed service in Europe.

## II. SYSTEM ARCHITECTURE

The left side of Fig. 1 shows the transceivers installed on the rooftop of Building 20 of Politecnico di Milano (bottom: E-band, top: D-band), connecting Buildings 14 and 20 in the main university campus (path length  $L = 325$  m). On the right side of Fig. 1 is the table reporting the main system specifics.



Parameter	D-band	E-band
Bandwidth	250 MHz	250 MHz
Transmitter power	+ 5 dBm	+ 10 dBm
Receiver sensitivity	-67 dBm	-71 dBm
Antenna gain	34 dBi	40 dBi
Wave polarization	Linear vertical	Linear vertical
Carrier frequencies	148 and 156 GHz	73 and 83 GHz
Atmospheric fade margin	15 dB	36 dB
Path length	325 m	325 m

**FIG. 1** – Link transceivers (left) and associated system parameters (right).

EM wave propagation data have been routinely collected since February 2017 by sampling the received power,  $P_{RX}$  (dBm), every 3 and 5 seconds, for the E band and the D band, respectively. Both links transmit power  $P_{TX}$  are kept stable by an AGC (Automatic Gain Control) algorithm. Besides the propagation data derived from the link transceivers, a collocated laser-based disdrometer measures the number of rain drops, as well as their falling velocity and size (from which the rain intensity  $R$  can be accurately derived).

## III. RAIN ATTENUATION: MEASUREMENTS AND PREDICTIONS

Gases cause quite a limited attenuation on EM waves in the E and D bands (roughly up to 0.5 dB and 1 dB, respectively). Indeed, we have focused our research activities on quantifying the much higher attenuation caused by rain on the experimental links ( $A_R$ ). To this aim, as a first step, we have identified and isolated rain events by jointly processing the time series of  $P_{RX}$  (from the link) and  $R$  (from the disdrometer). As an example, the blue line in Fig. 2 shows the rain attenuation (in dB) measured on the 29<sup>th</sup> of June 2017 (left side), while the right side of the figure reports the concurrent rain rate measured by the disdrometer.

Besides the rain attenuation derived from  $P_{RX}$ , Fig. 2 also reports  $A_R$  as estimated using recommendation ITU-R P.838-3 [3] (red line in Fig. 3):

$$A_R^{ITU-R} = \gamma_R L = kR^\alpha L \quad (2)$$

In (2),  $R$  is the rain rate obtained from the disdrometer,  $k$  and  $\alpha$  are coefficients that depend on the operational frequency  $f$ , the wave polarization (linear vertical) and link elevation ( $0^\circ$  for the considered terrestrial link). According to (2), the path attenuation is calculated by assuming that the rain intensity is constant along the link, given its short path length.

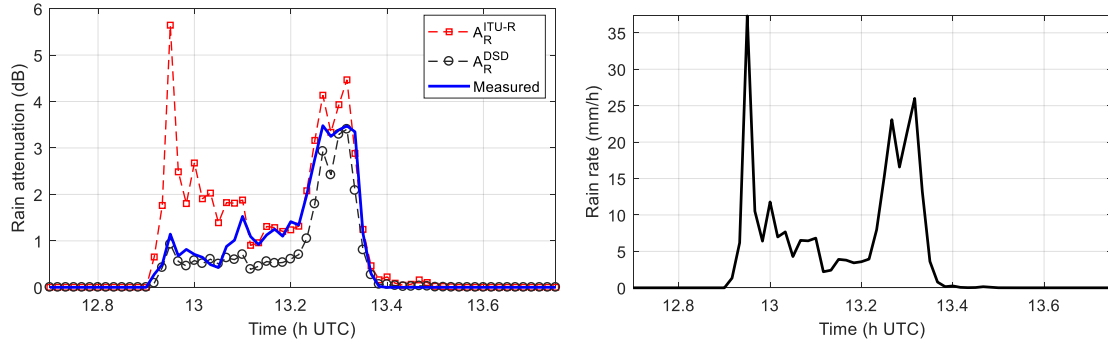


**FIG. 2** – Left side: sample rain attenuation event (blue line for the D band, 148 GHz, 29<sup>th</sup> of June 2017); right side: associated rain rate (disdrometer).

$A_R$  is actually not only function of the precipitation intensity  $R$ , but also of the shape and size of the rain drops [2]. This information is typically provided in terms of the Drop Size Distribution (DSD), which indicates the number of rain drops with given diameter  $D$  contained in  $1 \text{ m}^3$ . More specifically, the DSD is defined as ( $\text{mm}^{-1} \text{ m}^{-3}$ ):

$$N(D_i) = \frac{10^6 n_i}{S v(D_i) T \Delta D_i} \quad (3)$$

In (3),  $n_i$  is the number of raindrops whose diameter falls in the  $i$ -th class (with mean diameter  $0.125 \text{ mm} \leq D_i \leq 8 \text{ mm}$ ),  $\Delta D_i = 0.125 \text{ mm}$  represents the width of each drop-size class,  $S = 4560 \text{ mm}^2$  is the disdrometer sampling area,  $T = 60$  seconds is the instrument integration time,  $v(D_i)$  (m/s) is the terminal velocity of rain drops, measured by the disdrometer as well. Starting from the DSD, the specific attenuation  $\gamma_R$  (dB/km) (as well as  $A_R$ ) at frequency  $f$  is a function of the wavelength  $\lambda$  and of the forward scattering coefficient  $\text{Re}[S_0]$  [4], calculated using the T-matrix approach [5] and the axial ratio defined by Beard and Chuang in [6]:

$$\gamma_R^{DSD} = 4.343 \cdot 10^3 \frac{\lambda^2}{\pi} \sum_{i=1}^N \text{Re}[S_0(D_i, f)] N(D_i) \Delta D_i \quad \rightarrow \quad A_R^{DSD} = \gamma_R^{DSD} L \quad (4)$$

The rain attenuation estimated using this more complex approach is indicated with the black line depicted in Fig. 2.

The two approaches outlined above to predict  $A_R$  provide quite different results: the trend of the three curves is similar, but  $A_R^{DSD}$  is a much better estimate of  $A_R$  than  $A_R^{ITU}$ . More in detail, it is worth pointing out how the peak rain rate exceeding 30 mm/h has actually quite a limited impact on the links: notwithstanding the high rain intensity,  $A_R$  is only slightly higher than 1 dB. This value is well estimated using DSD data, while the ITU-R-based approach strongly overestimate  $A_R$ , as the  $k$  and  $\alpha$  coefficients are independent of the drop dimension. This is actually expected, given the marked dependence of  $\gamma_R$  and the DSD: especially at high frequency, small (e.g.  $D$  around 0.5 mm) and large (e.g.  $D$  around 3 mm) drops definitely have a different impact on EM waves, which the information on the DSD allows to weight properly in calculating  $\gamma_R$  (see (4)).

#### IV. CONCLUSION

This contribution presented a research activity exploring the use of E- and D-band terrestrial links in the near future 5G mobile networks. Data extracted from four links operating at 73, 83, 148 and 156 GHz (path length  $L = 325$  m) were processed to investigate the strong impairments induced by rain.  $A_R$  was derived from the received power level, and afterwards predicted taking advantage of the data collected by a collocated laser-based disdrometer. Preliminary results pointed out the wet antenna effect on the measured attenuation, as well as the usefulness of DSD data to take in due account the different impact of small and large drops on the EM wave. Future work will include extending the collection and processing of the propagation data to at least a full year, investigating and mitigating the wet antenna effect, and further processing to derive rain rate and rain attenuation statistics to be submitted to the Study Group 3 ('Radiowave propagation') of ITU-R.

#### REFERENCES

- [1] T. S. Rappaport et al., "Millimeter Wave Mobile Communications for 5G Cellular: It Will Work!," *IEEE Access*, vol. 1, May 2013, pp. 335–49.
- [2] H.Y. Lam, L. Luini, J. Din, C. Capsoni, A. D. Panagopoulos, "Investigation of Rain Attenuation in Equatorial Kuala Lumpur", *IEEE Antennas and Wireless Propagation Letters*, vol. 11, Page(s): 1002-1005.
- [3] ITU-R P.838-3, Specific attenuation model for rain for use in prediction methods, Geneva, 2005.
- [4] M. Sadiku, Numerical Techniques in Electromagnetics, 2nd Ed., CRC Press, 2001.
- [5] M. Mishchenko, L. Travis, A. Lacis, "Scattering, Absorption, and Emission of Light by Small Particles," *Cambridge University*, 2002.
- [6] K. Beard, C. Chuang, "A New Model for the Equilibrium Shape of Raindrops," *Journal of the Atmospheric Sciences*, Vol. 44 (11), pp. 1509–1524, 1987.

# RAY TRACING PATH LOSS PREDICTION IN URBAN ENVIRONMENT @ 26, 28 AND 38 GHz

Francesco Mani<sup>(1)</sup>, Enrico Maria Vitucci<sup>(1)</sup>, Marina Barbiroli<sup>(1)</sup>,  
Franco Fuschini<sup>(1)</sup>, Vittorio Degli Esposti<sup>(1)</sup>,

<sup>(1)</sup> Dept. of Electrical, Electronic and Information Eng. "G. Marconi",  
University of Bologna, Viale Risorgimento 2, 40136 Bologna, Italy  
[francesco.mani@unibo.it](mailto:francesco.mani@unibo.it), [enricomaria.vitucci@unibo.it](mailto:enricomaria.vitucci@unibo.it), [marina.barbiroli@unibo.it](mailto:marina.barbiroli@unibo.it), [franco.fuschini@unibo.it](mailto:franco.fuschini@unibo.it),  
[v.degliesti@unibo.it](mailto:v.degliesti@unibo.it)

## Abstract

*A ray tracing prediction tool with advanced implementations such as diffuse scattering and vegetation attenuation, is validated vs. mm-Wave frequencies measurements in urban environment at 26GHz and 38GHz. This is one of the first investigations at these frequencies in outdoor scenario. Simulations are compared with measurements in terms of path loss in two different urban scenarios. Results show that the contribution from non-specular components in non-line-of-sight conditions is determinant to achieve a good prediction accuracy at these frequencies and that the excess loss due to vegetation cannot be neglected. To sum up, the prediction accuracy is good and simulations are generally able to track the measurements behavior.*

**Index Terms** – Radio propagation, Channel Modeling, Ray tracing, Diffuse Scattering, Vegetation, mmWave.

## I. INTRODUCTION

Millimeter wave frequencies are being considered for the fifth generation (5G) wireless communications, due to the availability of free bandwidth to accommodate high data rate and the possibility to implement advanced techniques such as beamforming and Massive MIMO [1]. In particular, the band between 26GHz and 38GHz, also known as Ka band, has attracted some attention as a candidate for urban micro-cells and therefore some effort has been spent in characterizing the propagation at these frequencies [2], [3]. Ray Tracing propagation models, able to simulate the multipath characteristics of the propagation channel, can be very useful for channel modeling, e.g. to help the parametrization of pathloss models, and for other applications. In this work a state-of-the-art ray-tracing tool with advanced features [4], [5] is used to predict pathloss (PL) and is validated and tuned vs. a vast outdoor measurement campaigns.

## II. RAY-TRACING ENHANCED FEATURES

Large environments need to be considered for outdoor urban propagation modeling. Ray Tracing (RT) prediction with large input databases including large urban areas and vegetation description may result in impractically large computation times. From the propagation point of view, only the buildings and obstacles in proximity to the Tx-Rx area or in line of sight conditions to the terminals will provide a

significant contribution to propagation [6]. Based on this idea we implemented an automated selection of “active” buildings, based on three geometrical criteria: 1. buildings inside the prediction area, defined as the area encompassing all the receiver positions; 2. buildings in an area between the transmitter and the receivers, defined by a set of ellipses having as foci couples of terminals; 3. prominent buildings not yet selected, defined as those “seen” by either the transmitter or one of the receivers under a view angle larger than a given threshold. Furthermore, an additional feature is added to account for the excess loss for rays intersecting vegetated areas. Two models for vegetation loss have been implemented: the well-known Weissberger model [7] and a simple specific-loss model [dB/m]. Typical values of specific attenuation can be found in the literature [8].

### III. MEASUREMENT SCENARIOS

Measurements were carried out in Shanghai (China) in two different scenarios: The Tengfei office park and the Shanghai Jiao Tong University (SJTU) campus. In both cases the BS were elevated and employing a directional antenna, while the mobile terminal was an omnidirectional antenna at street level (1.5m).



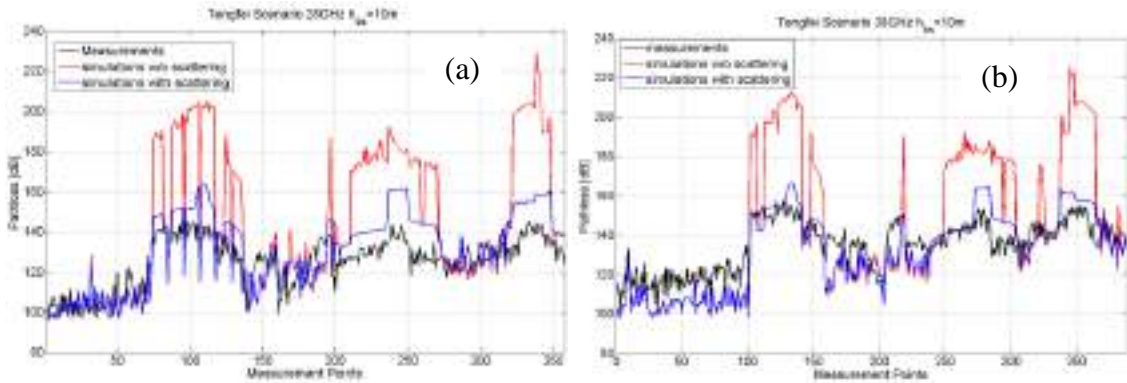
**FIG. 1** – Aerial pictures of the two measurement scenarios: (a) Tengfei scenario; (b) SJTU scenario.

In Tengfei (Fig. 1 (a)) the transmitting antenna is placed on a lift platform at 4 different heights: 5m, 10m, 14m and 17m. The mobile terminal follows multiple routes both in line-of-sight (LOS) and non-LOS (NLOS) conditions, and two measurement frequencies are considered: 28GHz and 38.6GHz. In the SJTU scenario (Fig. 1 (b)) carrier frequency is 26GHz, buildings are surrounded by abundant vegetation, the BS is placed on top of a low building at 10m height while receivers are always located in NLOS conditions with the direct link blocked either by buildings or vegetation.

#### IV. RESULTS

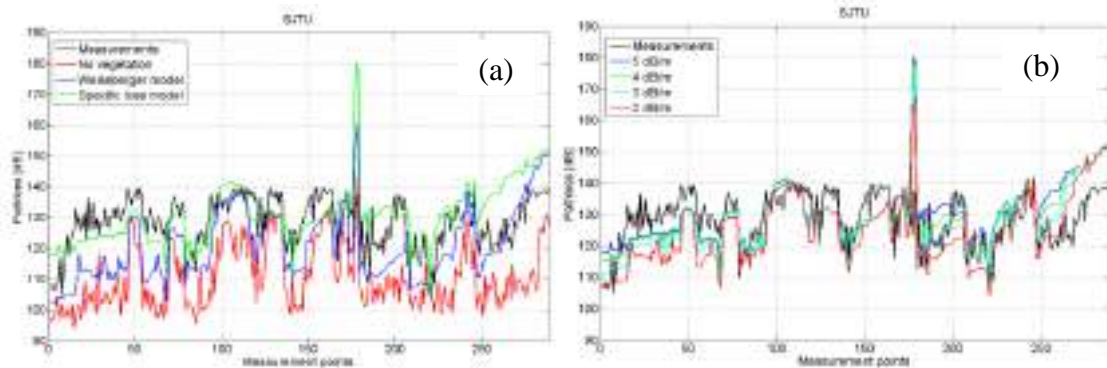
In Tengfei scenario a total of 95 out of 243 buildings are discarded by applying the selection algorithm presented in Section II and therefore simulation time is cut down from 137 to 70 minutes (for a single frequency and BS height value) without any loss in terms of prediction accuracy. In SJTU, 63 out of 231 buildings are discarded, saving 11 hours of simulation time in this much more time consuming scenario, due to the presence of vegetation and to the more complex building shapes. Also in this case there is no prediction accuracy loss.

Fig.2 shows an example of the simulated PL compared with measurements at 28GHz and 38GHz for BS height of 10m. The results clearly show the importance of diffuse scattering to have a realistic prediction in deep NLOS positions where, as it seems, most of the power propagating to the receiver comes from non-specular contributions.



**FIG. 2** – Comparison of measurements with simulations with and without scattering in Tengfei scenario @ 28GHz (a) and 38 GHz (b) for  $h_{BS} = 10m$ .

Fig.3 (a) presents simulation results when vegetation is included or not in the SJTU scenario and a comparison between the two vegetation models. As expected, not including vegetation leads to a significant underestimation of the PL. Also the use of the Weissberger model generates an underestimation and therefore we conclude that the specific loss model is more suitable for such scenario at 26 GHz.



**FIG. 3** – Comparison of measurements and simulations with and without vegetation in SJTU scenario (a) and comparison between measurements and simulations with different excess vegetation loss models in SJTU scenario (b).

As a further investigation we tested different values of the specific attenuation coefficient  $\alpha$ , starting from  $\alpha = 2\text{dB/m}$  up to  $\alpha = 5\text{dB/m}$ . As shown in Fig.3 (b), the best RMSE is achieved between 3 and 4dB/m.

## V. CONCLUSIONS

This paper presents the validation of a RT software against Ka band measurements in two outdoor scenario, a modern office complex and a campus, to assess the prediction capabilities and the improvements achieved thanks to the new implemented features. A speed-up technique aiming at reducing the size of the input environment database has been applied to save computation time which is decreased by almost 50% at no cost in terms of simulation accuracy. Results show that non-specular contributions are decisive to achieve realistic prediction in NLOS conditions and higher values of scattering coefficients are found with respect to previous studies at lower frequencies. Therefore, more specific studies are required to better understand diffuse scattering at mm-Waves in outdoor scenarios. Vegetation penetration loss has also been modeled to deal with the highly vegetated SJTU scenario and a specific loss of approximately 3-4 dB/m is found to give good results in the considered case.

## REFERENCES

- [1] T. S. Rappaport, S. Sun, R. Mayzus, H. Zhao, Y. Azar, K. Wang, G. N. Wong, J. K. Schulz, M. Samimi, and F. Gutierrez, "Millimeter wave mobile communications for 5G cellular: It will work!" *IEEE Access*, vol. 1, pp. 335–349, 2013;
- [2] G. R. MacCartney, J. Zhang, S. Nie, and T. S. Rappaport, "Path loss models for 5G millimeter wave propagation channels in urban microcells," in *2013 IEEE Global Communications Conference (GLOBECOM)*, Dec 2013, pp. 3948–3953.
- [3] J. J. Park, J. Liang, J. Lee, H. K. Kwon, M. D. Kim, and B. Park, "Millimeter-wave channel model parameters for urban microcellular environment based on 28 and 38 GHz measurements," in *2016 IEEE 27th Annual International Symposium on Personal, Indoor, and Mobile Radio Communications (PIMRC)*, Sept 2016, pp. 1–5.
- [4] E. Vitucci, V. Degli-Esposti, F. Fuschini, J. Lu, M. Barbiroli, J. Wu, M. Zoli, J. Zhu, and H. Bertoni, "Ray tracing RF field prediction: an unforgiving validation," *International Journal of Antennas and Propagation*, vol. 2015, 2015.
- [5] F. Fuschini, S. Hafner, M. Zoli, R. Müller, E. Vitucci, D. Dupleich, M. Barbiroli, J. Luo, E. Schulz, V. Degli-Esposti et al., "Analysis of in-room mm-wave propagation: Directional channel measurements and ray tracing simulations," *Journal of Infrared, Millimeter, and Terahertz Waves*, vol. 38, no. 6, pp. 727–744, 2017.
- [6] V. Degli-Esposti, F. Fuschini, E. M. Vitucci, and G. Falciasecca, "Speed-up techniques for ray tracing field prediction models," *IEEE Transactions on Antennas and Propagation*, vol. 57, no. 5, pp. 1469–1480, May 2009.
- [7] M. A. Weissberger, "An initial critical summary of models for predicting the attenuation of radio waves by trees," *ELECTROMAGNETIC COMPATIBILITY ANALYSIS CENTER ANNAPOLIS MD*, Tech. Rep., 1982.
- [8] Y. L. C. de Jong and M. H. A. J. Herben, "A tree-scattering model for improved propagation prediction in urban microcells," *IEEE Transactions on Vehicular Technology*, vol. 53, no. 2, pp. 503–513, March 2004.

# PERFORMANCES ESTIMATION AND MEASUREMENT OF A SOURCE STIRRED REVERBERATION CHAMBER

G. Cerri<sup>(1)</sup>, A. De Leo<sup>(1)</sup>, V. Mariani Primiani<sup>(1)</sup>, P. Russo<sup>(1)</sup>

<sup>(1)</sup> Dipartimento di Ingegneria dell'Informazione, Università Politecnica delle Marche, Via B. Bianche, 60131 Ancona, Italy  
[g.cerri@univpm.it](mailto:g.cerri@univpm.it)

## Abstract

*In this paper, the performances of a reverberation chamber were analyzed both using numerical simulations and through a wide set of measurements. Two stirring techniques were implemented: source stirring, using the multiple monopoles stirring technique, and most traditional stirring technique, the mechanical stirring, obtained by a single rotating paddle. The statistical analysis of the insertion loss parameters and of the electromagnetic fields allowed us to get the most significant indicators of the analyzed reverberation chamber. Apart a similar field uniformity in the working volume, the source stirring method provides a more diffused energy w.r.t. mechanical stirring, quantified by a lower Rician K factor.*

**Index Terms** – reverberation chamber; source stirring; mechanical stirring.

## I. INTRODUCTION

Reverberation Chambers (RCs) are resonating cavities where the electromagnetic field is stirred to achieve the properties of uniformity, depolarization and isotropy (ergodicity). On the principle, there are two possible ways to perform the stirring actions:

- Mechanical stirring actions, based on the variation of the boundary conditions; it can be based on using one or more rotating paddles [1] or moving [2] and vibrating [3] chamber's walls;
- Source stirring actions, based on the variation of the coupling between the source(s) and the chamber's resonating modes. Since 1991 alternative ways to stir the electromagnetic fields inside the working volume of the RC were presented [4] [5], and more recently a source stirring techniques based on an array of fixed antennas placed on RCs' walls was presented [6].

In this paper the analysis of a wide set of full wave numerical simulations is presented to obtain the main RC parameters, simulating and measuring the chamber performances using both mechanical and source stirring techniques. For the first stirring action, a single rotating paddle was considered, whereas for the second one an array of monopoles fed two at a time was considered. The results of full wave numerical simulations were compared to the statistical analysis of a wide set of experimental measurements.

Section II presents the scenario and the corresponding numerical model implemented at the full wave simulation code; at this scope, a commercial tool, CST Microwave Studio, was used. Section III shows the results related to the Insertion Losses (IL); in particular the Quality factor and the Rician K-factor are reported. Section IV contains the electromagnetic field analysis and consequently the calculation of the homogeneity according to the standard [7].

## II. SCENARIO

The RC is a resonating cavity made by galvanic steel having quasi-cubic dimensions ( $1.0 \text{ m} \times 0.9 \text{ m} \times 0.8 \text{ m}$ ). The first eigenmode of the chamber has the cutoff frequency at  $f_0 = 225 \text{ MHz}$ , therefore we focused in the frequency range from 3 times  $f_0$  to 6 times  $f_0$ . Figure 1 (right) depicts the scenario for the source stirred reverberation chamber: the transmitting antennas are two monopoles inserted in two of the 120 holes present in the chamber's walls. As regards the mechanical stirring (Figure 1 left) action, the two transmitting antennas are replaced with a disc-cone antenna, and a Z-folded metallic paddle is used to stir the electromagnetic field inside the cavity. The monopoles' length (75 mm) is chosen to well match them at central frequency of the range  $3f_0 - 6f_0$ .

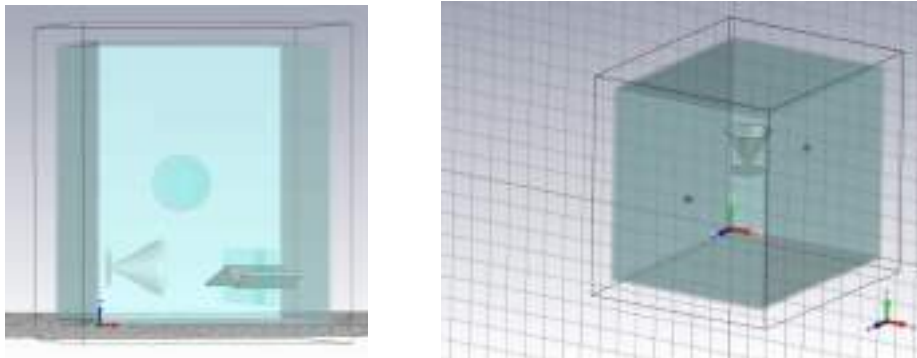


**FIG. 1** – Scenario for the mechanical (left) and source (right) stirring.

For both stirring action 100 different configuration are taken into consideration: 100 different holes position for the first scenario and a stirring angle step of  $3.6^\circ$  for the mechanical stirring.

For the numerical simulations, the chamber was modeled using CST Microwave Studio [12]. The workstation used for these simulations has two CPU Intel Xeon E5640 2.66GHz, 24GB of RAM and a GPU Nvidia Quadro FX1800 - 768MB and using the Time Domain solver, each simulation stood for about one day (26 h).

## III. INSERTION LOSS ANALYSIS

The quality (Q) factor of the RC was computed according to the standard [7]. From the comparison between the two graphics of Figure 2, it can be

seen that the average values of the quality factor, calculated for both stirring actions are similar.

For the measurement, in the lowest frequency range the quality factor behavior is dominated by the effect of the antennas, and  $Q$  increases as the square of the frequency.

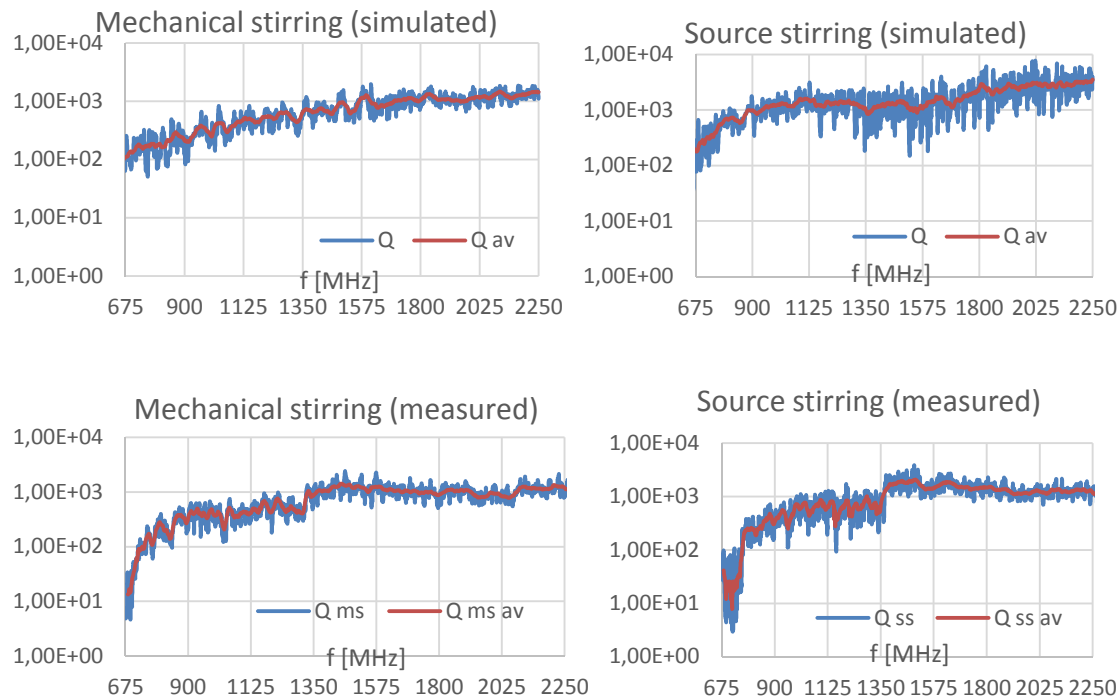


**FIG. 2** – Quality factor simulated (up) and measured (down)

The Rician  $K$ -factor is defined as the ratio of signal power in dominant component over the (local-mean) scattered power [8]. The lower is this value, the better in the stirring action.

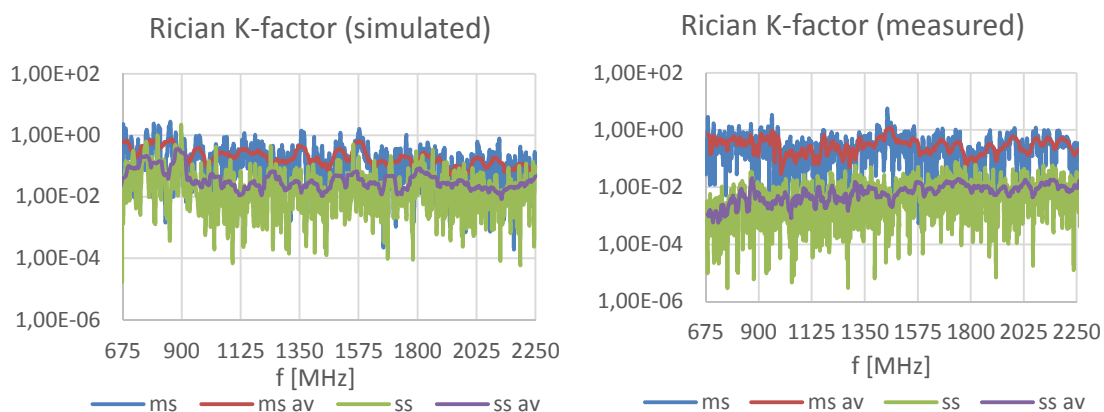


**FIG. 3** – Rician  $K$ -factor simulated (left) and measured (right)

Both in simulations and in measurement the source stirring technique exhibits an enhanced behavior; it can be explained considering that the changing of the position and the polarization of the transmitting

monopoles strongly makes variable the receiving antenna's illumination, so reducing the direct component.

#### IV. ELECTRIC FIELD UNIFORMITY

Table I reports the standard deviation, calculated according to [7] in the 8 vertices of the working volume, defined 10 cm far from the chamber's walls at the frequency of 1.35 GHz. Mechanical stirring technique exhibits lower values, of in all cases the standard deviation is lower than the limit of 3 dB defined by the standard.

**TABLE I - IV. ELECTRIC FIELD UNIFORMITY**

	measured				simulated			
	$\sigma_{24}$ [dB]	$\sigma_{8x}$ [dB]	$\sigma_{8y}$ [dB]	$\sigma_{8y}$ [dB]	$\sigma_{24}$ [dB]	$\sigma_{8x}$ [dB]	$\sigma_{8y}$ [dB]	$\sigma_{8y}$ [dB]
MS	2.3	2.1	2.9	2.9	2.2	2.0	2.8	2.9
SS	2.9	2.5	2.6	2.6	2.7	2.5	2.4	2.5

#### REFERENCES

- [1] J. Clegg, A.C. Marvin, J.F. Dawson, S.J. Porter, "Optimization of stirrer designs in a reverberation chamber," IEEE Trans. on Electromagnetic Compatibility, vol.47, no.4, pp. 824- 832, Nov. 2005
- [2] N.K. Kouveliotis, P. T. Trakadas, C. N. Capsalis, "Theoretical investigation of the field conditions in a vibrating reverberation chamber with an unstirred component," IEEE Trans. Electromagnetic. Compatibility, Vol. 45, No. 1, 77-80, 2003.
- [3] F. Leferink, J. C. Boudenot, W. Van Etten, "Experimental results obtained in the vibrating intrinsic reverberation chamber," IEEE Int. Symp. Electromagnetic Compatibility, 639-644, Washington, 21-25 Aug. 2000.
- [4] T. A. Loughry, "Frequency stirring: an alternative approach to mechanical mode-stirring for the conduct of electromagnetic susceptibility testing", Philips Lab., Tech. Report PL-TR-91-1036, 1991
- [5] Y. Huang and D. J. Edwards, "A novel reverberating chamber: source-stirred chamber," IEE 8th International Conference on Electromagnetic Compatibility, pp.120-124, Edinburgh, UK, September 1992.
- [6] A. De Leo, V. M. Primiani, P. Russo and G. Cerri, "Low-Frequency Theoretical Analysis of a Source-Stirred Reverberation Chamber," IEEE Trans. on Electromagnetic Compatibility, vol. 59, no. 2, pp. 315-324, April 2017.
- [7] Reverberation Chamber Test Methods, International Electrotechnical Commission (IEC), Std. 61 000-4-21, 2011.
- [8] C. L. Holloway, D. A. Hill, J. M. Ladbury, P. F. Wilson, G. Koepke and J. Coder, "On the Use of Reverberation Chambers to Simulate a Rician Radio Environment for the Testing of Wireless Devices," IEEE Trans. on Antennas and Propagation, vol. 54, no. 11, pp. 3167-3177, Nov. 2006.

# AN ITERATIVE TECHNIQUE TO CORRECT PROBE POSITIONING ERROR AFFECTED PLANAR WIDE-MESH SCANNING NF DATA

F. D'Agostino, F. Ferrara, C. Gennarelli, R. Guerriero, M. Migliozi

D.I.In., Università di Salerno, via Giovanni Paolo II, 132 - 84084 Fisciano, Italy  
{fdagostino, flferrara, cgennarelli, rguerriero, mmigliozi}@unisa.it

## Abstract

An efficient technique to correct the positioning errors in the near-field – far-field (NF–FF) transformation with planar wide-mesh scanning (PWMS) is developed and experimentally validated. It is based on a nonredundant sampling representation of the voltage measured by the scanning probe obtained by considering the antenna as enclosed in an oblate ellipsoid. An iterative technique is applied to retrieve the NF data at the points fixed by the sampling representation from the acquired nonuniformly spaced ones. Once the uniform PWMS data have been recovered, those needed by the classical plane-rectangular NF–FF transformation are efficiently evaluated by using an optimal sampling interpolation algorithm.

**Index Terms** – Antenna measurements, NF–FF transformations, nonredundant representations of electromagnetic fields, PWMS, positioning errors compensation.

## I. INTRODUCTION

A nonredundant plane-rectangular (PR) near-field–far-field (NF–FF) transformation using the innovative planar wide-mesh scanning (PWMS) has been recently developed [1] by applying the nonredundant sampling representations [2] to the voltage detected by the scanning probe and considering the antenna under test (AUT) as enclosed in an oblate ellipsoid. It allows a remarkable measurement time saving with respect to that adopting the PR scan [3], since its sampling grid is characterized by meshes becoming larger as their distance from the scanning plane centre increases (Fig. 1). The AUT far field is got by applying again the PR NF–FF transformation, whose input data are accurately reconstructed via fast optimal sampling interpolation (OSI) expansions from the acquired PWMS samples. Unfortunately, due to an inaccurate control of the positioners, it could be impossible to acquire the NF (uniform) samples at the points fixed by the representation, even if the positions of the actual collected (nonuniform) samples can be accurately read by optical devices. Since a direct reconstruction from nonuniform samples is not advisable, a suitable strategy [4] is to recover the uniform samples from the nonuniform ones and then determine the NF data needed for the transformation via an efficient OSI expansion. An iterative technique, converging only if a bi-unique correspondence linking each uniform sampling point to the nearest nonuniform one exists, has been used to recover the uniform samples in a PR grid [4]. Another approach, that doesn't suffer from this drawback, uses the singular value decomposition (SVD) method to retrieve the uniform PWMS samples from the positioning errors affected ones [5], but requires that the uniform samples retrieval can be subdivided in two independent 1-D problems to avoid a huge computational effort.

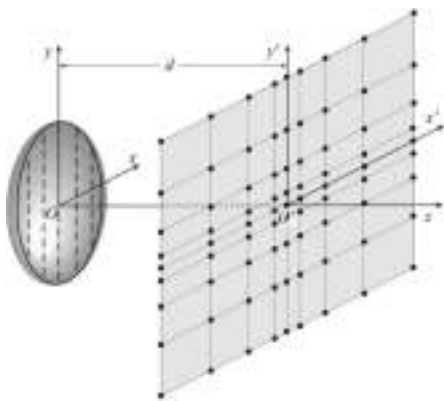


**FIG. 1** – PWMS for a quasi-planar AUT.

Unfortunately, due to an inaccurate control of the positioners, it could be impossible to acquire the NF (uniform) samples at the points fixed by the representation, even if the positions of the actual collected (nonuniform) samples can be accurately read by optical devices. Since a direct reconstruction from nonuniform samples is not advisable, a suitable strategy [4] is to recover the uniform samples from the nonuniform ones and then determine the NF data needed for the transformation via an efficient OSI expansion. An iterative technique, converging only if a bi-unique correspondence linking each uniform sampling point to the nearest nonuniform one exists, has been used to recover the uniform samples in a PR grid [4]. Another approach, that doesn't suffer from this drawback, uses the singular value decomposition (SVD) method to retrieve the uniform PWMS samples from the positioning errors affected ones [5], but requires that the uniform samples retrieval can be subdivided in two independent 1-D problems to avoid a huge computational effort.

Aim of this work is to properly apply the iterative technique to the correction of known positioning errors in the NF–FF transformation with PWMS and to experimentally assess the effectiveness of the so developed procedure.

## II. NONREDUNDANT SAMPLING REPRESENTATION ON A PLANE FROM PWMS SAMPLES

Let us consider a quasi-planar AUT, enclosed in an oblate ellipsoid  $\Sigma$  with major and minor semi-axes equal to  $a$  and  $b$ , and a nondirective probe scanning a plane at distance  $d$  from the AUT centre, assumed as origin of the Cartesian coordinate system  $(x, y, z)$  and of the spherical one  $(r, \vartheta, \varphi)$ . Another reference system  $(x', y', z')$  with the origin  $O'$  at the scanning plane centre (Fig. 1) is also introduced. Since the voltage  $V$  measured by this probe has the same effective spatial bandwidth of the AUT field, the nonredundant representations [2] can be applied to it. Hence, a proper parameter  $\xi$  must be used to describe any curve on the plane, and a suitable phase factor  $e^{-j\psi(\xi)}$  must be extracted from the voltages  $V_y$  and  $V_x$  acquired by the probe and rotated probe. The so introduced “reduced voltage”  $\tilde{V}(\xi) = V(\xi) e^{j\psi(\xi)}$  is spatially quasi-bandlimited to  $W_\xi$  and can be controlled by choosing a bandwidth  $\chi'W_\xi$ , with  $\chi' > 1$  [2]. The bandwidth  $W_\xi$ , the parameter  $\xi$ , and the function  $\psi$  relevant to a radial line, as the  $x'$  (or  $y'$ ) axis, are [1]:

$$W_\xi = \frac{2\beta a}{\pi} E\left(\frac{\pi}{2} \middle| \varepsilon^2\right); \quad \xi = \frac{\pi}{2} \left[ \frac{E(\sin^{-1}u \middle| \varepsilon^2)}{E(\pi/2 \middle| \varepsilon^2)} \right]; \quad \psi = \beta a \left[ v \sqrt{\frac{v^2 - 1}{v^2 - \varepsilon^2}} - E\left(\cos^{-1} \sqrt{\frac{1 - \varepsilon^2}{v^2 - \varepsilon^2}} \middle| \varepsilon^2\right) \right] \quad (1)$$

where  $\beta$  is the wavenumber,  $E(\bullet \middle| \bullet)$  is the elliptic integral of second kind,  $\varepsilon = f/a$  is the eccentricity of the ellipsoid,  $2f$  is its focal distance, and  $u = (r_1 - r_2)/2f$ ,  $v = (r_1 + r_2)/2a$ ,  $r_{1,2}$  being the distances from the foci to the observation point  $P$ .

To factorize the 2-D interpolation algorithm into 1-D OSI expansions along lines, it is necessary to use the same parameter  $\xi$  or  $\eta$  given by (1) for describing all lines parallel to the  $x'$  or  $y'$  axis, respectively. Accordingly, it results [1]:

$$V(\xi(x'), \eta(y')) = e^{-j\psi(x', y')} \sum_{m=m_0-p+1}^{m_0+p} \left\{ G(\eta, \eta_m, \bar{\eta}, M, M'') \sum_{n=n_0-q+1}^{n_0+q} V(\xi_n, \eta_m) e^{j\psi(x'_n, y'_m)} G(\xi, \xi_n, \bar{\xi}, M, M'') \right\} \quad (2)$$

where  $2q \times 2p$  is the number of retained samples,  $m_0 = \text{Int}(\eta/\Delta\eta)$ ,  $n_0 = \text{Int}(\xi/\Delta\xi)$ ,

$$\eta_m = m\Delta\eta = 2\pi m / (2M'' + 1); \quad M'' = \text{Int}(\chi' M') + 1; \quad M' = \text{Int}(\chi' W_\eta) + 1; \quad \bar{\eta} = p\Delta\eta \quad (3)$$

$$M = M'' - M'; \quad W_\eta = W_\xi; \quad \xi_n = n\Delta\xi = n\Delta\eta; \quad \bar{\xi} = q\Delta\xi \quad (4)$$

$\chi > 1$  is an oversampling factor controlling the truncation error [2],  $\text{Int}(x)$  the integer part of  $x$ , and  $G(\alpha, \alpha_k, \bar{\alpha}, L, L'') = \Omega_L[(\alpha - \alpha_k), \bar{\alpha}] D_{L''}(\alpha - \alpha_k)$  the OSI function,  $D_{L''}(\alpha)$  and  $\Omega_L(\alpha, \bar{\alpha})$  being the Dirichlet and Tschebyscheff sampling functions [2].

Relation (2) allows to accurately recover  $V_x$  and  $V_y$  at the points needed by the PR NF–FF transformation [3]. The related formulae in the adopted reference system, when the probe is an open-ended rectangular waveguide, are reported in [6].

## III. UNIFORM SAMPLES RETRIEVAL

Let us assume that the PWMS samples are not evenly spaced and that there is a biunique correspondence linking each of the  $Q$  uniform sampling points to the nearest nonuniform one, so that it is convenient to apply the iterative technique. By applying (2), each of the known  $Q$  nonuniform reduced voltages samples  $\tilde{V}(\tau_k, \sigma_j)$  is expressed in terms of the  $Q$  unknown ones  $\tilde{V}(\xi_n, \eta_m)$ , so getting the lin-

ear system  $\underline{B} \underline{x} = \underline{c}$ , where  $\underline{B}$  is a  $Q \times Q$  sized sparse matrix,  $\underline{x}$  is the vector of the unknown uniform samples, and  $\underline{c}$  is that of the known nonuniform ones. This system can be effectively solved as follows. By splitting  $\underline{B}$  in its diagonal part  $\underline{B}_D$  and nondiagonal part  $\underline{\Delta}$ , multiplying both the members of the system  $\underline{B} \underline{x} = \underline{c}$  by  $\underline{B}_D^{-1}$  and rearranging the terms, the following iterative scheme is obtained:

$$\underline{x}^{(\mu)} = \underline{B}_D^{-1} \underline{c} - \underline{B}_D^{-1} \underline{\Delta} \underline{x}^{(\mu-1)} = \underline{x}^{(0)} - \underline{B}_D^{-1} \underline{\Delta} \underline{x}^{(\mu-1)} \quad (5)$$

where  $\underline{x}^{(\mu)}$  is the uniform samples vector got at the  $\mu$ th iteration. Note that, in the hypotheses done on the distribution of the nonuniform samples, the amplitude of each element on the main diagonal of  $\underline{B}$  is different from zero and larger than the amplitudes of the other elements on the same row or column, so that the necessary conditions [4] for the convergence of the iterative algorithm are satisfied. By rewriting (5) in explicit form, it results:

$$\begin{aligned} \tilde{V}^{(\mu)}(\xi_n, \eta_m) = & \frac{1}{G(\sigma_m, \eta_m, \bar{\eta}, M, M'') G(\tau_n, \xi_n, \bar{\xi}, M, M'')} \left\{ \tilde{V}(\tau_n, \sigma_m) + \right. \\ & \left. - \sum_{\substack{i=i_0-p+1 \\ (i \neq m) \wedge (s \neq n)}}^{i_0+p} \sum_{s=s_0-q+1}^{s_0+q} G(\sigma_m, \eta_i, \bar{\eta}, M, M'') G(\tau_n, \xi_s, \bar{\xi}, M, M'') \tilde{V}^{(\mu-1)}(\xi_s, \eta_i) \right\} \quad (6) \end{aligned}$$

where

$$i_0 = \begin{cases} m & \text{if } \sigma_m \geq \eta_m \\ m-1 & \text{if } \sigma_m < \eta_m \end{cases} ; \quad s_0 = \begin{cases} n & \text{if } \tau_n \geq \xi_n \\ n-1 & \text{if } \tau_n < \xi_n \end{cases} \quad (7)$$

#### IV. EXPERIMENTAL ASSESSMENT

The experimental validation of the developed procedure has been performed via the plane-polar NF measurement facility available at the UNISA Antenna Characterization Lab. In this facility, the probe is mounted on a vertical linear positioner and the AUT on a turntable, whose rotation axis is orthogonal to the linear positioner. The measurement of the NF data, which would be acquired by a PR scanning system or by a PWMS one, is made possible due to the presence of another turntable, placed between the positioner and the probe (an open ended WR90 rectangular waveguide). In fact, this last turntable allows to keep the probe axes always parallel to the AUT ones as required in these scans. The AUT is a vertically polarized dual pyramidal horn situated on the  $xy$ -plane and working at 10 GHz. The horns apertures are  $8.9 \text{ cm} \times 6.8 \text{ cm}$  sized and their centers are 26.5 cm apart. An oblate ellipsoid with  $a = 18.6 \text{ cm}$  and  $b = 6.3 \text{ cm}$  has been adopted to shape the AUT. The nonuniform PWMS samples have been collected in a circle of radius 110 cm on a plane 16.5 cm distant from the AUT, by imposing that the distances in  $\xi$  and  $\eta$  between the positions of the nonuniform samples and those of the corresponding uniform ones are random variables with uniform distributions in  $(-\Delta\xi/3, \Delta\xi/3)$  and  $(-\Delta\eta/3, \Delta\eta/3)$ .

The amplitude and phase of  $V_x$  along the line at  $y' = 3.6 \text{ cm}$ , retrieved from the nonuniform PWMS samples by the iterative procedure, are compared in Figs. 2 and 3 with the directly measured ones. As can be seen, despite the severe values of the positioning errors, the reconstructions are very accurate save for the zones characterized by very low voltage levels. The FF patterns in the E- and H-planes, recovered from 2209 nonuniform PWMS NF data, are compared in Figs. 4 and 5 with those (references) obtained from the  $105 \times 105$  PR NF data directly acquired on a  $140 \text{ cm} \times 140 \text{ cm}$  square. The FF patterns attained without using the iterative

approach are also shown in the same figures. As can be seen, they appear severely worsened, thus further assessing the effectiveness of the developed approach.

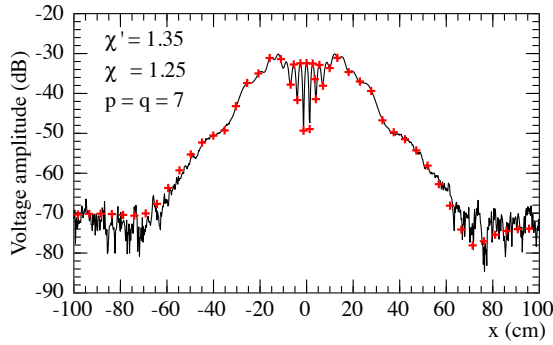


**FIG. 2** – Amplitude of  $V_x$  along the line  $y' = 3.6$  cm. — measured. +++ retrieved from the nonuniform PWMS samples.

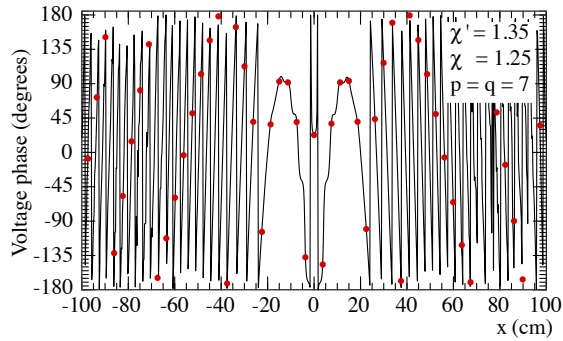


**FIG. 3** – Phase of  $V_x$  along the line  $y' = 3.6$  cm. — measured. .... retrieved from the nonuniform PWMS samples.

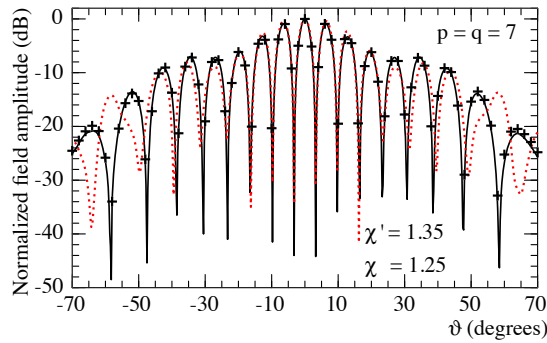


**FIG. 4** – E-plane pattern. — reference. +++ obtained from the nonuniform samples. --- directly obtained from the nonuniform samples without using the iterative technique.

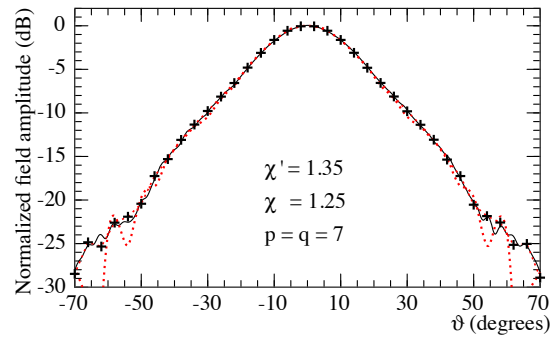


**FIG. 5** – H-plane pattern. — reference. +++ obtained from the nonuniform samples. --- directly obtained from the nonuniform samples without using the iterative technique.

## REFERENCES

- [1] F. D'Agostino, I. De Colibus, F. Ferrara, C. Gennarelli, R. Guerriero, and M. Migliozi, "Far-field pattern reconstruction from near-field data collected via a nonconventional plane-rectangular scanning: experimental testing," *Int. J. Antennas Prop.*, vol. 2014, ID 763687, pp. 1-9, 2014.
- [2] O.M. Bucci, C. Gennarelli, and C. Savarese, "Representation of electromagnetic fields over arbitrary surfaces by a finite and nonredundant number of samples," *IEEE Trans. Antennas Prop.*, vol. 46, pp. 351-359, March 1998.
- [3] E.B. Joy, W.M. Leach, Jr., G.P. Rodrigue, and D.T. Paris, "Application of probe-compensated near-field measurements," *IEEE Trans. Antennas Prop.*, vol. AP-26, pp. 379-389, May 1978.
- [4] O.M. Bucci, C. Gennarelli, and C. Savarese, "Interpolation of electromagnetic radiated fields over a plane from nonuniform samples," *IEEE Trans. Antennas Prop.*, vol. 41, pp. 1501-1508, Nov. 1993.
- [5] F. D'Agostino, F. Ferrara, C. Gennarelli, R. Guerriero, M. Migliozi, G. Riccio, "A singular value decomposition based approach for far-field reconstruction from irregularly spaced planar wide-mesh scanning data," *Microw. Opt. Tech. Lett.*, vol. 49, pp. 1768-1772, 2007.
- [6] F. D'Agostino, F. Ferrara, C. Gennarelli, R. Guerriero, S. McBride, and M. Migliozi, "Fast and accurate antenna pattern evaluation from near-field data acquired via planar spiral scanning," *IEEE Trans. Antennas Prop.*, vol. 64, pp. 3450-3458, Aug. 2016.

# Fast Diagnostics of Large Conformal Array by Matrix Method

Giuseppe Di Massa, Sandra Costanzo  
DIMES - University of Calabria, 87036 Rende (CS), Italy,  
email: giuseppe.dimassa@unical.it

## Abstract

*Near-field data are used as diagnostics tool to reconstruct the aperture field distribution of conformal array antennas and identify any defective element. The Matrix Method is used for the detection of faulty elements in large conformal arrays antennas. The problem of inversion and regularization of the resulting matrix is addressed. A new sampling method is proposed and successfully compared, in terms of computation time, with other existing approaches.*

**Index Terms** – Conical Array, Conformal array, Matrix method

## I. INTRODUCTION

Full array diagnostics is a fundamental tool to identify array antennas failures as an accurate diagnosis allows a fine tuning of active arrays. The use of near field data on planar surfaces for arrays diagnostic is a widely used approach. Usually, the estimation of the array excitations is based on the Backward Transformation Method (BTM) [1], which exploits the high computational efficiency offered by the Fast Fourier Transform (FFT). However, it can be used only in the case of planar arrays, so that other techniques must be applied for other configurations. The method adopted in this work is based on the evaluation of the excitation coefficients through the inversion of the linear system relating them to the measured data on the scanning surface. The above approach, referred in the following as Matrix Method (MM), has been proposed in a number of papers [2]. However, at the best of our knowledge, actual literature studies are applied, with a numeric realistic solution, only to planar arrays. Particular attention is devoted to solve the linear system deriving from the MM. Several techniques are used and compared, in terms of computation time, for a large number of elements. Generally, the number of measurements is greater than the number of array elements, giving an overdetermined system. So, a new matrix sampling technique is experimented to reduce the problem complexity. The results of all methods are compared, in the case of a conical array, by analyzing both computation time and accuracy.

## II. Matrix Method and relative solution

The total electromagnetic field of an array is a linear combination of the fields radiated by the elementary sources, namely:

$$\mathbf{E}(\mathbf{r}_s) = \sum_{e=1}^N \alpha_e \mathbf{E}_e(\mathbf{r}_c) \quad (1)$$

where  $\alpha_e$  is the excitation of the  $e^{\text{th}}$  element,  $N$  is the number of antenna elements,  $\mathbf{r}_c$  gives the position of the elementary source, while  $\mathbf{r}_s$  represents the position of the observation point on the near field surface. The measurements are assumed to be performed within the near field region of the array, but in the far field of each element. The expression (1) can be written in matrix notation as:

$$\mathbf{E} = \mathbf{A}\alpha \quad (2)$$

where  $\mathbf{E}$  is the probe voltage measurement at the point  $r_s$  and  $\mathbf{A}$  is the matrix whose components are determined from the radiated field of each element. The retrieval of the excitation coefficients requires the solution of the following linear system:

$$\alpha = \mathbf{A}^{-1}\mathbf{E} \quad (3)$$

Observe that system (2) is usually overdetermined, and, anyway, due to the presence of noise in the measured data and errors in the model caused by the not exact knowledge of the radiation pattern of each element, a solution generally does not exist and a generalized solution must be looked for. Other problems can also arise, such as a possible ill-conditioning of the matrix caused by the lost of useful data due to the finite dimension of the scanning surface (the so-called truncation error), and the oversampling which introduces rows having some degree of linear dependence in the system. A stable inversion algorithm was obtained by introducing a regularization strategy for the ill-conditioned matrix. Apart from the direct inversion of matrix  $A$ , namely the back slash operator in MATLAB (`mldivide`), several methods can be used to perform the solution of (2). One method is based on the Singular Value Decomposition (SVD). The procedure results from linear algebra which says that any  $M \times N$  matrix  $[A]$  ( $M > N$ ) can be decomposed into the following product :  $[A] = [U][W][V]^T$  where  $[U]$  is an  $M \times N$  orthogonal matrix,  $[W]$  is a diagonal ( $N \times M$ ) matrix whose elements  $w_{ii}$  (the singular values) are positive or zero, and  $[V]$  is an  $N \times N$  orthogonal matrix. This decomposition of matrix  $[A]$  is always possible, whatever its condition number, even when  $[A]$  is singular. The algorithm is slow, but stable, it is robust and does never diverge, and a solution of the kind:

$$[\alpha] = [\mathbf{V}][\mathbf{W}]^{-1}[\mathbf{U}]^T[\mathbf{E}] \quad (4)$$

is always possible.

When the matrix is singular, the Truncated Singular Value Decomposition (TSVD) can be used to regularize the ill-posed problem [3]. TSVD has been widely used for inversion. The method of truncation determines the quality of the solution. Several approaches have been proposed for truncation, taking into account the improvement of the condition number. Recently, some sophisticated algorithms have been applied to the problem in order to reduce the computation time of SVD. We commonly wish to find the best rank- $k$  approximation to the original matrix  $A$  with rigorous error control. The problem to approximate a given  $M \times N$  matrix by another matrix of rank  $k$  which is much smaller than  $N$  and  $M$  can be solved, avoiding the prohibitive times of SVD, by sampling the matrix according to a natural probability distribution. In [4], a randomized algorithm to find the description of rank  $k$  is reported. The algorithm samples a small number of rows (or columns) of the matrix, it scales them approximately to form a small matrix  $S$  and compute the SVD of  $S$ , which is a good approximation to the SVD of the original matrix.

A further robust way to solve problem is based on the use of CVX, a package for specifying and solving convex programs [5]. Another possibility, to overcome the slowness when the dimensions of the problems increase, is to use an iterative regularization methods, such as Landweber method [6]. The procedure is applied in [7], where it is compared with BTM.

In the next paragraph, some of the cited methods are applied to solve the problem of finding fault elements in a conical array and compare the results with a new way to apply the sampling method of matrix.

#### IV. Preliminary results

In the following, some preliminary results for the problem outlined in the previous paragraphs are reported. An array of 72 columns, each one having 8 elements, and arranged on a truncated cone is considered. The cone has an aperture angle equal to  $8^\circ$ . The distance between the elements is equal to 17.5 mm, while the angle between the columns is equal to  $1.67^\circ$ . The angle covered by the array is  $120^\circ$ . The distance between the vertex of the cone and the first element is equal to 1185 mm. Elementary dipoles are assumed as radiating elements. The acquisition surface is a cylinder with a radius  $\rho = a_r = 2 + 6\lambda$ , where  $a_r$  is the minimum diameter enclosing the antenna, and the considered frequency is 9.5GHz. A Taylor amplitude distribution is used along the z-axis, as well as in the azimuthal direction. In (Fig. 1) the z component of the field on the cylindrical scanning surface is reported for several azimuthal angles.

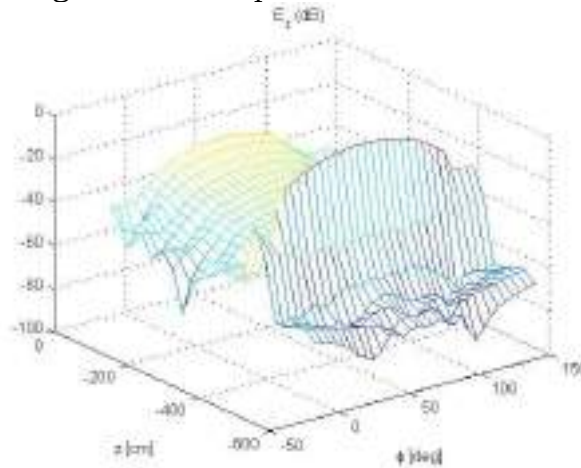
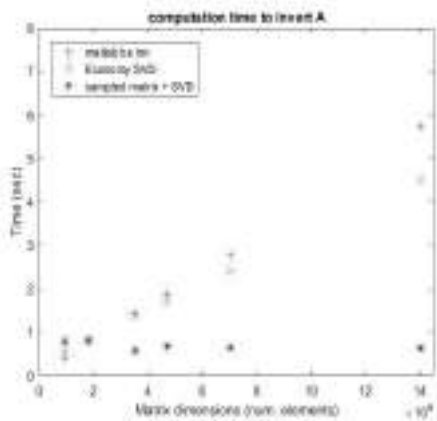


**FIG. 1** – Near Electromagnetic Field as function of z for several azimuthal angles on the acquisition surface.

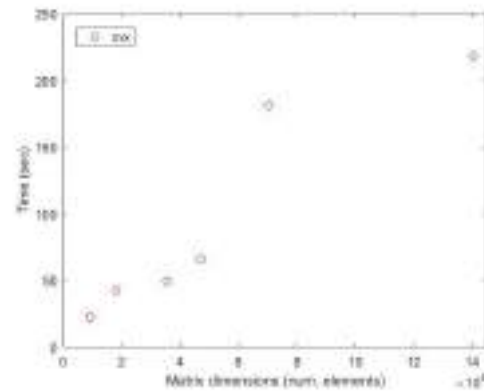
The synthetic near-field data are used to simulate the reconstruction of possible faults in the array elements. As test case, we consider the described conical array with the 32th column switched off. We apply four methods to invert the matrix A with dimensions  $M_r =$  number of observation points for  $N_c =$  number of radiating elements; they are described in the follows:

1. Back slash MATLAB division
2. SVD in economic version
3. Sampled Matrix plus economic SVD
4. CVX

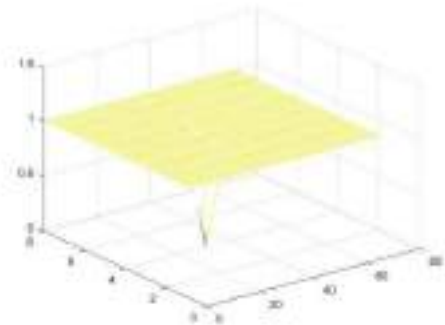
In Fig 2 (a), the computation time of the first three methods is reported as a function of number of element of matrix A. The CVX data are reported under Fig. 2(b) because the range is out of scale. The matrix dimensions vary from 910656 to 14043456. In Fig. 3, the on-off coefficients for one elements fault (a) and one row fault (b) are reported.



(a)



(b)

**FIG. 2** – Computation time.

(a)



(b)

**FIG. 3** – Reconstructed coefficients in the case of one element (a) or 32th column (b) switched off.**REFERENCES**

- [1] J. J. Lee, E. M. Ferren, D. P. Woollen, and K. M. Lee, Near-field probe used as a diagnostic tool to locate defective elements in an array antenna, *IEEE Trans. Antennas Propag.*, vol. 36-6, pp. 884889, Jun. 1988.
- [2] Gattou\_ L., Picard D., Rekiouak A., Bolomey J. Ch., Matrix Method for Near Field Diagnostic Techniques of Phase Array, *Proc. IEEE Int. Symp. Phased Array System and Technology*, 52-57, 1996.
- [3] Per Christian Hansen, The truncated SVD as method for regularization, *BIT Numerical Mathematics*, Volume 27, Issue 4, pp 534553, 1987.
- [4] A. Frieze, R. Kannan, S. Vempala, Fast Monte-Carlo algorithms for finding Low-Rank Approximation, *Journal of the ACM (JACM)*, 51(6), 1025-1041, 2004.
- [5] CVX Research, Inc., CVX: Matlab Software for Disciplined Convex Programming, version 2.0, <http://cvxr.com/cvx>, month = aug, year = 2012.
- [6] Landweber L, An iteration formula for Fredholm integral equations of the first kind, *Am. J. Math.* 73, 615, 1951.
- [7] Bucci O. M., Migliore M. D., Panariello G., Sgambato P., Accurate Diagnosis of Conformal Arrays From Near-Field Data Using the Matrix Method, *IEEE Trans. Antennas Propagat.*, 53, No. 3, March 2005.

# NEAR-FIELD VALIDATION OF THE ELECTROMAGNETIC MODELS FOR LOFAR LBA-OUTER ARRAY

P. Di Ninni<sup>(1)</sup>, P. Bolli<sup>(1)</sup>, F. Paonessa<sup>(2)</sup>, G. Pupillo<sup>(3)</sup>,  
G. Virone<sup>(2)</sup>, S. J. Wijnholds<sup>(4)</sup>

<sup>(1)</sup> INAF - Osservatorio Astrofisico di Arcetri (OAA)  
Largo Enrico Fermi 5, 50125, Firenze, Italy  
[dininni@arcetri.astro.it](mailto:dininni@arcetri.astro.it), [pbolli@arcetri.inaf.it](mailto:pbolli@arcetri.inaf.it)

<sup>(2)</sup> CNR - Istituto di Elettronica ed Ingegneria dell'Informazione e  
delle Telecomunicazioni (IEIIT)  
C.so Duca degli Abruzzi 24, 10129, Torino, Italy  
[fabio.paonessa@ieiit.cnr.it](mailto:fabio.paonessa@ieiit.cnr.it), [giuseppe.virone@ieiit.cnr.it](mailto:giuseppe.virone@ieiit.cnr.it)

<sup>(3)</sup> INAF - Istituto di Radio Astronomia (IRA)  
Via Fiorentina 3513, 40059, Medicina (Bo), Italy  
[g.pupillo@ira.inaf.it](mailto:g.pupillo@ira.inaf.it)

<sup>(4)</sup> Netherlands Institute for Radio Astronomy (ASTRON)  
Oude Hoogeveensedijk 4, 7991 PD, Dwingeloo, The Netherlands  
[wijnholds@astron.nl](mailto:wijnholds@astron.nl)

## Abstract

*The characterization in the Far-Field regime of a radio telescope is an essential step to provide accurate astronomical results. This step represents a challenging task for array with large size and operating in a complex environment. Nowadays, several electromagnetic tools capable to simulate array configurations are commercially available. In this paper, the experimental validation of the electromagnetic model implemented in FEKO is shown for LOFAR LBA-outer array in the Near-Field regime. To this end, measurements acquired by means of an UAV-based system have been employed.*

**Index Terms** – antenna characterization, array radiation pattern, electromagnetic model validation, aperture array radio telescope.

## I. INTRODUCTION

Low Frequency ARray (LOFAR) is an International radio telescope consisting of several array stations distributed over Europe [1], see Fig. 1-a). Each LOFAR station is composed of (i) a High Band Antenna (HBA) array working in 120 – 240 MHz frequency band and (ii) a Low Band Antenna (LBA) array working between 30 and 80 MHz. LBA array is in turn composed of 46 antennas distributed within an approximately circular area featuring a diameter of 30 m (known as LBA-inner array) and of 48 antennas again randomly distributed within a diameter of 85 m (known as LBA-outer array). This paper will concern LBA-outer array.

To provide accurate astronomical results, the characterization in the Far-Field (FF) regime of an antenna array (taking into account the

coupling effects among antennas and the surrounding environment) is a fundamental step. Commercial tools based on full-wave solvers can be potentially employed for this purpose. However, an experimental verification of the numerical model is recommended in order to assess its accuracy and reliability. A procedure to validate the Electro-Magnetic (EM) model by using a system based on an Unmanned Aerial Vehicle (UAV) has been developed by the authors. Such a system has been employed in several measurement campaigns permitting to characterize both a single embedded element and a full array [2]. In all cases, the agreement between simulated and measured data is better than 0.5 dB.

In this paper, the Near-Field (NF) experimental validation method proposed for LBA-inner array [3] has been applied to the LBA-outer array whose distribution of antennas is illustrated in Fig. 1-b).

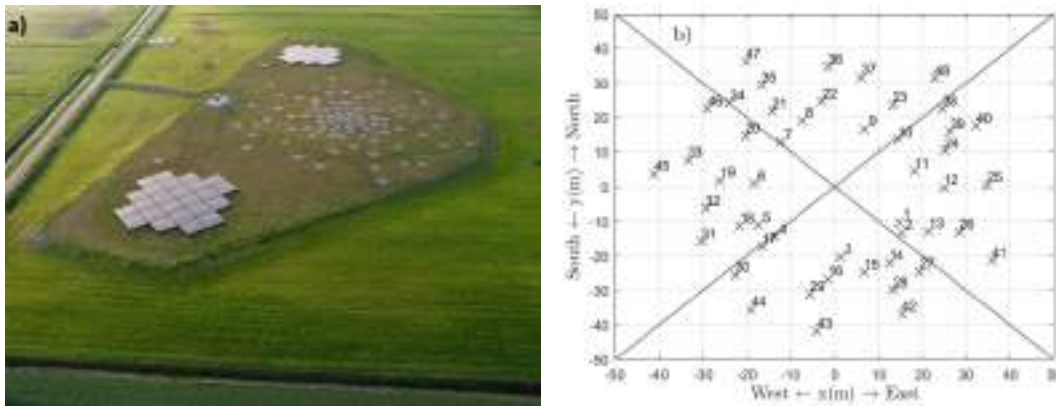


**FIG. 1** – a) Picture of a LOFAR station in The Netherlands; b) Distribution of LBA-outer array antennas (ideal UAV trajectories are also indicated as continuous lines).

## II. MEASUREMENTS CAMPAIGN ON LBA-OUTER ARRAY

The UAV-based system employed during the measurement campaign on the LBA-outer array, considered hereafter, mounted a horizontal dipole as test source emitting linear polarized signals. LBA-outer antennas under test consist of two orthogonal dipoles featuring dual linear polarization: a dipole oriented along the North-East direction, the other one along the South-West direction. Linear UAV trajectories (height about 100m) were carried out in the E-plane and H-plane for one polarization of the LBA-outer array. Positions of the UAV-mounted source were measured using an on-board differential GNSS system. During each flight, a continuous-wave RF signal is transmitted by the test source and it is received by the antennas under test. Complex voltages received by each antenna are then individually measured by the telescope recording system as a function of the curvilinear abscissa providing a NF scan. The same experimental configuration (including both the UAV and LBA-outer) has been simulated using FEKO, a commercial software tool that performs a full-wave analysis by means of the method of moments.

Simulated NF scans have been evaluated for a decimated UAV position series along the considered trajectory [3].

### III. NF EXPERIMENTAL VALIDATION OF THE EM MODEL

In this section, the NF model validation for the LBA-outer array is presented. Measured and simulated NF scan for a linear flight in the array E-plane has been considered for this purpose.

At single embedded antenna level, normalized amplitudes of the NF scans have been evaluated for all antennas composing the LBA-outer array. Figure 2-a) shows the comparison between simulated and measured normalized NF scan for antennas 9, 34, and 43 at 32 MHz frequency. Weighted Differences (WDiff) [4] between simulated and measured normalized amplitudes have been computed for each antenna as a function of the curvilinear abscissa (see bottom panel of Fig. 2-a)). The distribution of the WDiff averaged values has been computed in order to summarize the receiving properties of all the antennas. Such a statistical analysis turns out to be a reliable diagnostic tool to verify the overall antenna pattern measurement performance.

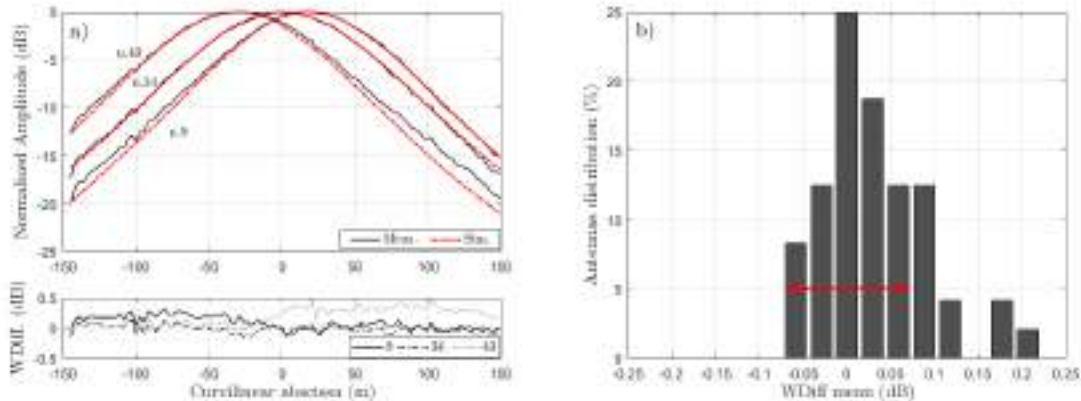


**FIG. 2** – a) Comparison between simulated (red curves) and measured (black curves) normalized amplitudes at 32 MHz; b) distribution of the WDiff averaged values at 32 MHz.

The histogram reported in Fig. 2-b) shows a main distribution centred around zero: about 77% of the LBA-outer antennas have the WDiff averaged values inside 0.12 dB (indicated with a red arrow in Fig. 2-b)), whereas only three antennas have the WDiff averaged values outside two times the half width of the distribution.

At full-array level, Figures 3- a) and -b) show the measured and simulated NF scans focused on the zenith direction (corresponding to the LBA-outer array center) at 32 and 70 MHz frequencies, respectively. Individual simulated and measured NF scans have been summed together [3]. The agreement between simulated and experimental data turns out to be really satisfactory, below 0.5 dB as shown in the WDiff panels of Fig. 3.

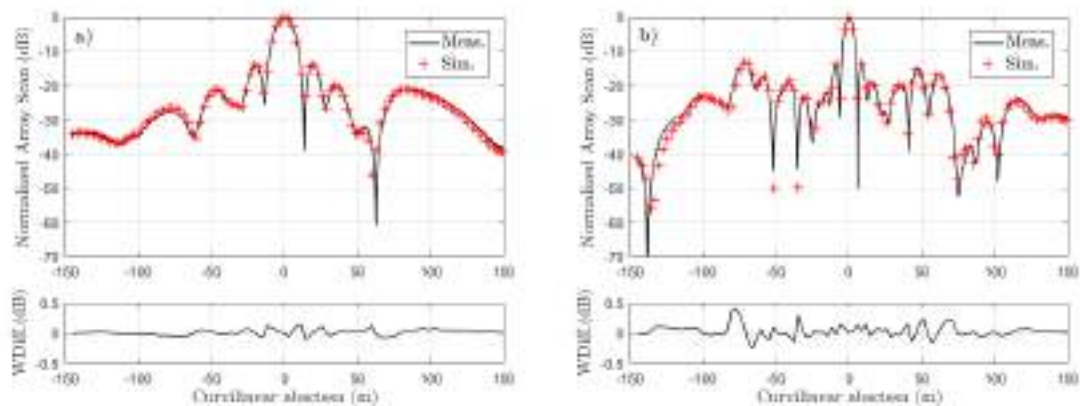


**FIG. 3** – Normalized LBA-outer array NF scans at: a) 32 MHz and b) 70 MHz.

#### IV. CONCLUSION

The UAV-mounted test source makes *in-situ* characterization of radio telescopes based on low-frequency aperture arrays possible. Analysis of the LOFAR LBA-outer array data shows differences between simulated and measured NF scans within  $\pm 0.5$  dB both at single antenna and at full-array level. The experimental results have validated in NF regime the EM model, which in turn can be used to predict the FF array pattern.

#### ACKNOWLEDGEMENT

This work has been supported by the 2014 TECNO INAF project “Advanced calibration techniques for next generation low-frequency radio astronomical arrays”.

#### REFERENCES

- [1] A. W. Gunst and M. J. Bantum, “The LOFAR phased array telescope system,” 2010 *IEEE International Symposium on Phased Array Systems and Technology*, pp. 632-639, Oct. 2010.
- [2] G. Pupillo et al., “Medicina array demonstrator: calibration and radiation pattern characterization using a UAV-mounted radio-frequency source,” *Experimental Astronomy*, vol. 39(2), pp. 405-421, June 2015.
- [3] P. Bolli, G. Pupillo, F. Paonessa, G. Virone, S.J. Wijnholds, and A.M. Lingua, “Near-field Experimental Verification of the EM Models for the LOFAR Radio Telescope,” *IEEE Antennas and Wireless Propagation Letters*, DOI: 10.1109/LAWP.2018.2805999
- [4] S. Pivnenko et al, “Comparison of Antenna Measurement Facilities With the DTU-ESA 12 GHz Validation Standard Antenna Within the EU Antenna Centre of Excellence,” *IEEE Transactions on Antennas and Propagation*, vol. 57(7), pp. 1863-1878, July 2009.

# FIRST TESTS OF A TORALDO PUPIL OPTICAL MODULE FOR THE 32M MEDICINA ANTENNA

L. Olmi<sup>(1)</sup>, P. Bolli<sup>(1)</sup>, L. Carbonaro<sup>(1)</sup>, L. Cresci<sup>(1)</sup>, A. Maccaferri<sup>(2)</sup>, G. Maccaferri<sup>(2)</sup>, P. Marongiu<sup>(3)</sup>, D. Mugnai<sup>(4)</sup>, R. Nesti<sup>(1)</sup>, A. Orfei<sup>(2)</sup>, D. Panella<sup>(1)</sup>, S. Righini<sup>(2)</sup>

<sup>(1)</sup> INAF – OAA, Largo E. Fermi 5, I-50125 Firenze, Italy, [olmi.luca@gmail.com](mailto:olmi.luca@gmail.com)

<sup>(2)</sup> INAF – IRA, Via Fiorentina 3513, I-40059 Villafontana, Italy

<sup>(3)</sup> INAF – OAC, Via della Scienza 5, I-09047 Selargius, Italy

<sup>(4)</sup> CNR – IFAC, Via Madonna del Piano 10, I-50019 Firenze, Italy

## Abstract

*Toraldo Pupils can improve the angular resolving power of an optical instrument beyond the classical diffraction limit (hence the term “super-resolution”) using a filter consisting of finite-width concentric coronae with different amplitude and phase transmittance. Toraldo Pupils represent a viable approach to achieve super-resolution on antennas and radio telescopes. In this work we present a summary of the electromagnetic simulations and laboratory tests of a prototype optical module based on a Toraldo Pupil that has been field-tested on the Medicina 32-m radio telescope.*

**Index Terms** – Astronomical Optics, Diffraction, Super-resolution, Telescopes

## I. INTRODUCTION

One of the fundamental properties of filled-aperture telescopes is their angular resolution, i.e., their ability to separate points of an object that are located at a small angular distance. Apart from other effects which can be either cancelled or mitigated (e.g., aberrations and “seeing”), the diffraction of electromagnetic (EM) waves is generally considered to be a fundamental limit for any imaging device. The concept of *super-resolution* (SR) refers to various methods for improving the angular resolution of an optical imaging system beyond the classical diffraction limit. In optical microscopy several techniques have already been developed with the aim of narrowing the central lobe of the illumination Point Spread Function (PSF). However, microscopy SR techniques cannot be easily applied to astronomical instrumentation, and thus few efforts have been made to overcome the diffraction limit of filled-aperture telescopes.

Variable transmittance pupils represent one viable approach to achieve SR in Radio Astronomy. Toraldo di Francia suggested in 1952 [1] that the classical limit of optical resolution could be improved interposing a filter consisting of finite-width concentric annuli of different amplitude and phase transmittance in the entrance pupil of an optical system, now also known as Toraldo pupils (TPs, hereafter). In this work we present a summary of the most recent results obtained in the context of the “*Pupille Toraldo*” (PUTO<sup>1</sup>) project, which is devoted to a more complete analysis of TPs and how they could be used to implement SR on a radio telescope. During the first part of this project we have performed both EM numerical simulations [2] and laboratory tests [3] at a frequency of 20 GHz that have confirmed and expanded the first measurements carried out in the microwave range [4].

---

<sup>1</sup> <http://www.ifac.cnr.it/PUTO/index.htm>

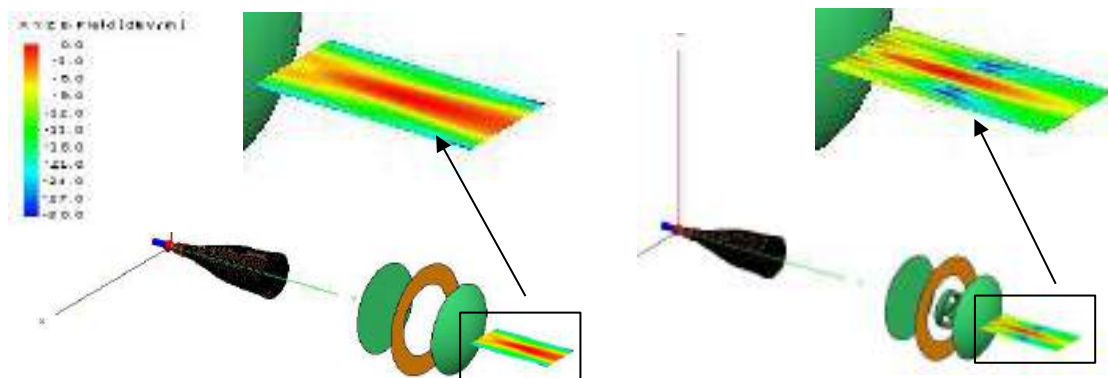


**Fig. 1** FEKO simulations at 20 GHz showing the (normalized) field amplitude at the focus of the collimator without (*left panel*) and with (*right panel*) TP. The collimator is illuminated by the same corrugated feed horn of the K-band receiver at Medicina.

## II. TP OPTICAL MODULE: EM SIMULATIONS AND TESTS

Following these initial experimental tests we have then designed [5] and tested in the laboratory [6] an optical module based on simple TPs that we planned to mount on the Medicina 32-m radio telescope<sup>2</sup>. The current design is based on a two-lens collimator placed after the Cassegrain focus and before the receiver dewar (see Fig.1). The first lens of the collimator generates an image of the primary reflector which is then brought to a subsequent focus by the second lens. The TP is placed at the image of the entrance pupil where it can modify the incident wavefront.

The EM simulations of the optical module were conducted using the commercial software tool FEKO. In the most recent simulations, the 3D model is analyzed in *transmission* rather than in reception. In this model the source was a corrugated feed horn identical to that employed in the K-band receiver operating on the Medicina radio telescope. The results are schematically shown in Fig.1, where the SR effect is visible as the narrower PSF at the focus of the collimator. We then improved the EM model by effectively including the *antenna* optics in the EM simulation. This was performed by using the equivalent parabola to simulate the Medicina Cassegrain telescope (smaller in size but with same focal ratio). Figure 2 shows that while we achieve the correct illumination of the reflector with the basic collimator optics (left panel), we note an anomalous illumination when the TP is applied (right panel). This incorrect illumination is a consequence of the fact that the presence of the TP within the collimator would require a different, optimized feed horn (see Sect. III).

## III. LABORATORY AND FIELD TESTS

The two-lens collimator has been extensively tested in the anechoic chamber of the Osservatorio Astrofisico di Arcetri (Firenze) [6]. During these measurements we illuminated the collimator with the same corrugated feed horn as the one employed on

<sup>2</sup> <http://www.med.ira.inaf.it/>

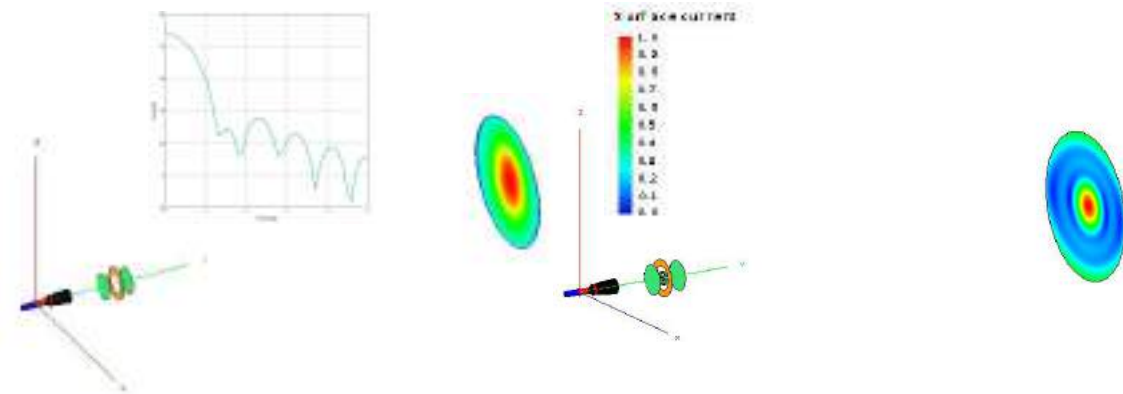


**Fig. 2** FEKO simulations at 20 GHz with the equivalent parabola illuminated by the K-band feed-horn through the two-lens collimator, without (*left panel*) and with (*right panel*) the TP applied. The figure shows the (normalized) surface current distribution on the antenna. The inset in the left panel shows the expected far-field antenna pattern.

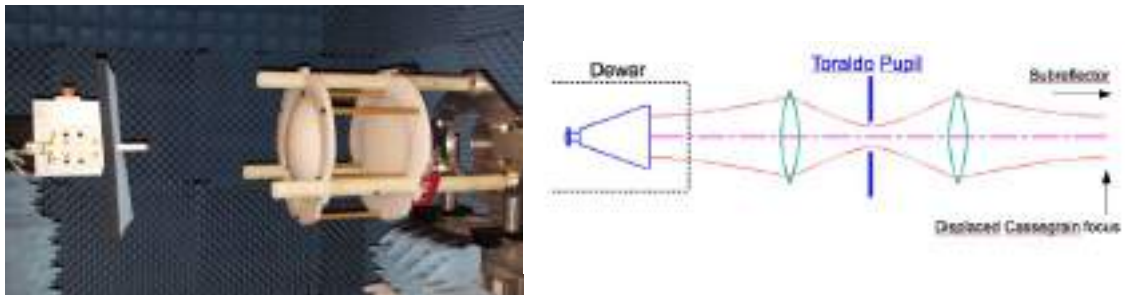


**Fig. 3** *Left panel.* Laboratory setup showing the two-lens collimator, illuminated by a K-band corrugated feed horn. The focus fields are sampled with a an open waveguide. *Right panel.* Gaussian-beam propagation in the collimator.

the K-band receiver at Medicina, while the fields at the focus of the collimator were sampled using a waveguide probe (see left panel of Fig. 3). The results from these tests were quite consistent with the FEKO simulations shown in Fig. 1. However, when the open waveguide at the focus is replaced by the corrugated horn (to simulate the real detection process with the K-band receiver, as shown in the right panel of Fig. 3), the significant mismatch between the PSF at the focus of the collimator and the expected fields on the aperture of the horn completely “washes out” the SR effect when the TP is present. This mismatch is the reason of the anomalous illumination of the reflector in the right panel of Fig. 2.

In March 2018 we finally field-tested the two-lens collimator on the Medicina antenna. The collimator was mounted externally on the dewar of the K-band receiver (see Fig. 4) and then we performed two main series of tests: (i) after mounting the collimator we had to find the new focal position by executing focus scans on point sources, which allowed to optimize the position of the subreflector (see Fig. 3); (ii) then we carried out cross-scans on the point sources, and compared the measured antenna beam with the results obtained without the collimator. During these measurements we used both astronomical point sources and a geostationary satellite (Eutelsat Ka-sat 9a).



**Fig. 4** *Left panel.* Mounting of the collimator at the Cassegrain focus of the Medicina antenna. *Middle panel.* The collimator mounted on the dewar of the K-band receiver. *Right panel.* Example of almost identical antenna beam-patterns obtained during an azimuth scan without (top) and with (bottom) the collimator, but with no TP applied. The raw horizontal scale is not corrected for the different elevations. The vertical scale is raw antenna temperature.

These tests showed that the satellite signal was very difficult to use for focus and pointing scans, especially with a new optical system to be checked. However, the pointing astronomical sources were strong enough to determine the new focus position with the collimator mounted on the receiver and the cross-scans showed that the antenna beam was basically identical with and without the collimator (see the right panel in Fig. 4). When the TP was applied to the collimator it was not possible to make a reliable measurement of the antenna beam, due to the mismatch with the receiver feed-horn, as previously shown during our laboratory tests. An *ad-hoc* receiver and feed horn should be used to fully exploit the SR effect.

#### ACKNOWLEDGEMENT

We gratefully acknowledge the partial support of the Ente Cassa di Risparmio di Firenze (Italy). We also wish to thank all personnel of the Medicina Radio Astronomical Station whose support was fundamental before and during the tests at the antenna.

#### REFERENCES

- [1] G. Toraldo di Francia, "Nuove pupille superrisolventi", *Atti Fond. Giorgio Ronchi*, Vol. 7, 1952.
- [2] L. Olmi, *et al.*, "Super-resolution with Toraldo pupils: analysis with electromagnetic numerical simulations", *Proc. of SPIE*, Vol. 9906, Astron. Telescopes and Instrumentation, 2016.
- [3] L. Olmi, *et al.*, "Laboratory measurements of super-resolving Toraldo pupils for radio astronomical applications", *Experim. Astron.*, Vol. 43, p. 285, 2017.
- [4] D. Mugnai, A. Ranfagni and R. Ruggeri, "Pupils with super-resolution", *Physics Letters A*, Vol. 311, p. 77, 2003.
- [5] L. Olmi, *et al.*, "Design of super-resolving Toraldo Pupils for radio astronomical applications", *URSI GASS*, XXXIInd, 2017.
- [6] L. Olmi, *et al.*, "Design and Test of a Toraldo Pupil Optical Module for the Medicina Radio Telescope", paper accepted for the 2nd URSI AT-RASC, 28 May - 1 June 2018

# A valid angle criterion in near field measurements based on analytical SVD

M. A. Maisto<sup>(1)</sup>

(1) Dipartimento di Ingegneria, Università della Campania L. Vanvitelli,  
Via Roma 29, Aversa (Ce), Italia

[mariaantonia.maisto@unicampania.it](mailto:mariaantonia.maisto@unicampania.it)

## Abstract

In this paper, a new valid angle criterion is proposed within the framework of planar near-field measurement techniques.

**Index Terms** –Near field measurement techniques, Valid angle criterion.

## I. INTRODUCTION

In this paper planar near-field measurement techniques are addressed. While in principle by exploiting the Plane wave formalism, the radiation pattern can be perfectly evaluated from measurements collected over an infinite aperture located in near zone of the antenna, in practice the finiteness of the observation domain introduces errors in the resulting evaluation [1]-[2]. The valid angle concept is a commonly used rule-of-thumb for predicting the region of validity of the calculated far-field pattern in according to observation domain and aperture antenna size and their distance. However, it is based on simple asymptotic arguments which often lead to erroneous estimations. Accordingly, in this contribution, a new valid angle criterion is proposed and compared to the previous one. The new criterion is worked out by studying the eigen-spectrum properties of the relevant radiation operator [3]. It is shown that measurement aperture and the distance (from the antenna under test) can vary according to a hyperbolic law. Finally, previous analysis allows us to obtain an expression of the radiation pattern in terms of the singular functions that can be exploited to avoid the truncated Fourier transform computation. This procedure appears more robust against the noise with respect the one based on Fourier transform and allows to estimate the valid angular region also in presence of the noise.

## II. TRUNCATION ERROR

Consider a linear antenna whose aperture field  $E_a$  is directed along its direction of invariance, the y-axis. The current is supported over the interval  $SD = [-a, a]$  (see Fig. 1) and embedded within a homogeneous host medium with wavenumber  $k$ . In order to estimate the radiation pattern of such an antenna, the only y component of the electric radiated field,  $E(x_o, z_o)$ , is measured over the interval  $OD = [-X_o, X_o]$  parallel to SD and located at a distance  $z_o$  in near-zone. The radiated field measurements can be used to predict the radiation pattern by invoking the plane waves spectrum (PWS) formalism. Indeed, the PSW  $f(k_x)$  of  $E_a$ , is related to  $E(x, z_o)$  by

$$f(k_x) = \int_{-\infty}^{\infty} E(x, z_o) e^{j(k_x x + k_z z)} dx \quad (1)$$

and the far field is related to  $f(k_x)$  by  $E(r) \cong f(k_x) \frac{k_z \sqrt{jk}}{k \sqrt{2\pi r}} e^{-jkr}$ .

In practice, the observation domain OD is bounded. Therefore, (1) must be truncated. This truncation causes errors while evaluating the radiation pattern. The concept of the valid angle is a commonly used rule-of-thumb for predicting the region of validity of the calculated far-field pattern according to the size of the measurement aperture and the radiating system. This is based on asymptotic reasonings and establishes that the radiation pattern can be considered reliable for angles lower than  $\theta_{valid}$  that is  $\theta_{valid} = \tan^{-1} \left( \frac{X_0 - a}{z_0} \right)$ . Despite its simplicity, the VA approach is mainly a qualitative criterion not explicitly linked to the truncation error. Moreover, it appears too restrictive. To address these deficiencies, in the next section we analyse the truncation effect under the light of the radiation operator singular spectrum.

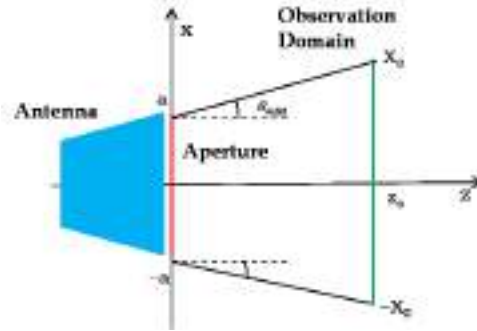


FIG. 1 – Geometry of the problem

### III. NEW VALID ANGLE CRITERION

Consider the operator linking the aperture field  $E_a(x)$  and the near field,  $E(x_0, z_0)$ . It can formally be expressed as

$$\mathcal{A}: E_a \in L^2(\text{SD}) \rightarrow E(x_0, z_0) = \frac{1}{2\pi} \int_{\text{SD}} \int_{-k}^k e^{j(k_x(x-x_0) - k_z z_0)} E_a(x) dx dk_x \in L^2(\text{OD}) \quad (2)$$

with  $L^2$  the set of square integrable. Note that since the field is usually probed at a distance  $z_0$  greater than the wavelength  $\lambda$ , the integration interval in (2) is confined to the visible domain. In order to evaluate  $X_0$  to be used in the radiation pattern estimation, the problem be cast as the determination of the measurement interval size which guarantees a negligible field energy outside OD. In order to get some insights from the previous point of view it is useful to introduce the singular value decomposition of  $\mathcal{A}$ . Note that the singular system is dependent on the observation domain size. Accordingly, let  $\{u_n(x, \infty), \sigma_n^u, v_n(x_0, \infty)\}_{n=0}^{\infty}$  and  $\{u_n(x, X_0), \sigma_n^b, v_n(x_0, X_0)\}_{n=0}^{\infty}$  be the singular systems of  $\mathcal{A}$  when the observation domain is unbounded and bounded respectively. In particular, in [4], it is shown that  $\sigma_n^u$  exhibit a step-like behaviour, in fact they are constant to 1 till their index reaches the critical value  $N^u = \frac{2ka}{\pi}$  beyond they decay exponentially towards zero. As concern  $u_n(x, \infty)$  they are the Prolate Spheroidal Wavefunctions  $\phi_n$ . Moreover, in [4], it is proved

also that  $\sigma_n^b$  exhibit the same step-like behaviour as before, with the only difference that now the knee occurs in correspondence to the index  $N(X_0) = \frac{2(R_{max}-R_{min})}{\lambda}$ , with  $R_{max} = \sqrt{(X_0 + a)^2 + z_0^2}$   $R_{min} = \sqrt{(X_0 - a)^2 + z_0^2}$ . Hence, the main effect due to observing the near field over a finite observation domain is to reduce the number of significant singular values from  $N^u$  to  $N(X_0)$  but not their magnitudes. Accordingly to the above conclusions, the energy of  $E(x_o, z_o)$  outside OD can be estimated as

$$\|E\|_{R-OD}^2 \cong \sum_{n=0}^{N^u} |\langle E_a, u_n(x, \infty) \rangle|^2 - \sum_{n=0}^{N(X_0)} |\langle E_a, u_n(x, X_0) \rangle|^2 \quad (3)$$

with  $\langle \cdot \rangle$  denotes the scalar product. In order to make the energy outside negligible, the first step is to choose  $X_0$  such that  $N^u \cong N(X_0)$ . Of course equality in (3) can never be achieved with finite measurement apertures. Therefore, we must content to determine the minimum  $X_0$  for which  $N^u - N(X_0) = \alpha < 1$ . This means that to observe the field on the entire x-axis should give at most one degree of freedom more with respect to the bounded interval. It easily follows that  $X_0$  solves the following equation

$$\frac{X_0^2}{(1-\eta)^2 a^2} - \frac{z_0^2}{\eta(2-\eta)a^2} = 1 \quad (4)$$

with  $\eta = \alpha \frac{\lambda}{4a}$ . The question arising is how to choose  $\alpha$ . It is evident that as  $\alpha$  increases also  $X_0$  increases. Hence  $\alpha$  should be chosen according to the required valid angle. In order to link such parameter to the valid angle consider  $u_n(x, \infty)$  and  $u_n(x, X_0)$ , It is evident that if  $\lim_{\alpha \rightarrow 0} \sigma_n^b = \sigma_n^u$ , then also  $\lim_{\alpha \rightarrow 0} u_n(x, X_0(\alpha)) = u_n(x, \infty)$ . Accordingly for little value of  $\alpha$ , the following approximation holds  $u_n(x, X_0(\alpha)) \cong \frac{\phi_n(x, c^b)}{\sigma_n^b}$  with  $c^b = ak \left(1 - \frac{\pi\alpha}{2ka}\right) = a\bar{k}$ . By spanning the aperture field in terms of  $u_n(x, X_0(\alpha))$  and performing its Fourier transform we obtain the following expression for the PWS

$$f(k_x) \cong \sum_{n=0}^{N^u} \langle E, v_n(x_o, X_0) \rangle j^n \sqrt{\frac{2\pi\sigma_n^b a}{\bar{k}}} \frac{\phi_n(k_x \frac{a}{\bar{k}}, c^b)}{\sigma_n^b} \quad (5)$$

The (5) allows to introduce the new valid angle criterion. In fact, for  $n \in [0, 1 \dots, N^u]$  the  $\phi_n$ s in are mostly concentrated within the interval  $|k_x| \leq \bar{k}$ . Therefore, it is within this frequency interval that (5) works well in approximating  $f(k_x)$ . Accordingly, the valid angular region is bounded by the following valid angle  $\theta_{valid}^{new} = \sin^{-1} \left(1 - \frac{\pi\alpha}{2ka}\right)$ . Note that the (5) provides a method to compute the radiation pattern without requiring to Fourier transform the measured field. In principle, if series (5) were not truncated at  $N^u$  it would allow to obtain  $f(k_x)$  even beyond  $\theta_{valid}^{new}$ . However, since the step-like behaviour of  $\sigma_n^b$ s, for  $n > N^u$  the coefficients  $\langle E, v_n(x_o, X_0) \rangle$  become vanishingly small and hence more corruptible by noise.

#### IV. NUMERICAL RESULTS

In Fig. 2, the normalised amplitude of  $f(k_x)$  as a function of the observation angle is shown for a triangular aperture. In figure, the two vertical dashed lines identify the corresponding angle valid region. The black line refers to the interval  $[-\theta_{valid}, \theta_{valid}]$  and the violet line to  $[-\theta_{valid}^{new}, \theta_{valid}^{new}]$ . In particular, for this example the  $\theta_{valid}$  returns  $68^\circ$ , while the new valid angle is larger and equal to  $73^\circ$ . As can be seen in the top

panel of the figure, in absence of noise the two curves (blue and yellow lines) are in agreement with the analytical one (red line) within the corresponding valid angles. However, the new valid angle criterion allows to identify a larger region than the valid angle one inside which the estimated PWS can be considered reliable. This becomes more true as the measured field is corrupted by additive Gaussian noise. Indeed, the bottom panel of Fig. 2 shows the same curves as before but now the measured field is corrupted by additive Gaussian noise with  $SNR = 10db$ . As it can be appreciated while the blue line is again in agreement with the analytical one within  $[-73^\circ, 73^\circ]$ , the yellow line is more affected by the noise also within  $[-68^\circ, 68^\circ]$ . This is because the equation (5) retains only the more relevant expansion coefficients, those less corruptible by the noise. Accordingly, this introduces a regularization step that it is not performed within the truncated Fourier transform procedure. This makes the last approach more affected by the noise.

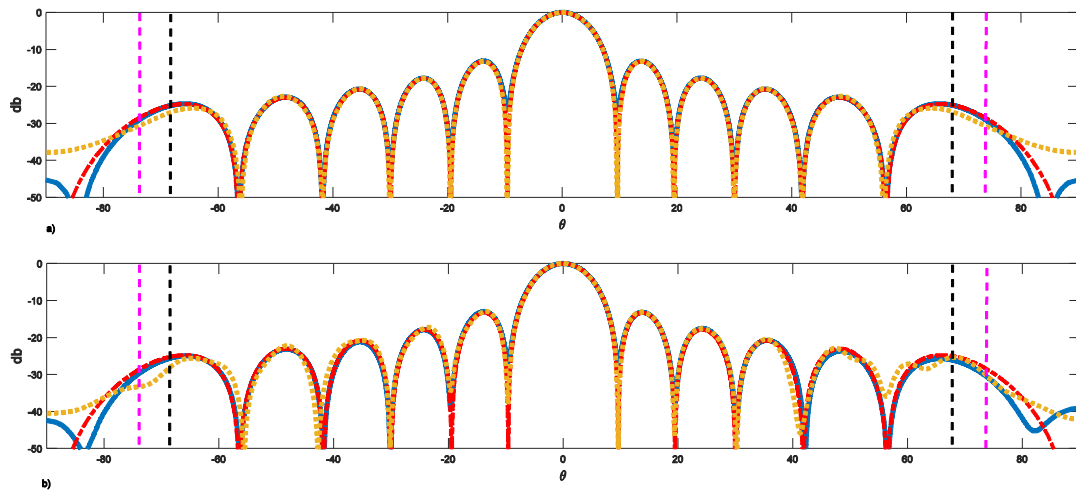


**FIG. 2** – Normalised amplitude of  $f(k_x)$  in db of a rectangular aperture with  $a = 3\lambda$ . The red dotted-dashed line refers to the  $f(k_x)$  evaluated analytically, the blue line to the one evaluated by (5) and the yellow dotted line to the plane wave spectrum evaluated by truncating the Fourier transform. In a) the measures are noise free while in b) are corrupted by additive Gaussian noise with  $SNR = 10db$ . The parameters are  $\alpha = 0.5$ ,  $z_0 = 3\lambda$ .  $k = 2\pi m^{-1}$  and  $X_0 = 10,46\lambda$ .

### Acknowledgement

The author would like to thank Prof. R. Pierri and Prof. R. Solimene for their valuable comments and suggestions.

### REFERENCES

- [1] M. A. Maisto, R. Solimene and R. Pierri "A truncation criterion in planar near field techniques" submitted to IET
- [2] M. A. Maisto, R. Solimene and R. Pierri "A truncation criterion in planar near field techniques" 12<sup>th</sup> European Conference on Antennas and Propagation (EUCAP), London, UK, (2018)
- [3] R. Solimene, M. A. Maisto, and R. Pierri. "Inverse source in the presence of a reflecting plane for the strip case." J. Opt. Soc. Am. A, 31(12), 2814-2820, (2014).
- [4] R. Solimene, M. A. Maisto and R. Pierri "Inverse Source in Near Field: the Case of Strip Current", J. Opt. Soc. Am. A, 35(5), 755-763 (2018)

# MEASUREMENTS-BY-DESIGN: A NOVEL APPROACH FOR FAST AND RELIABLE ANTENNA CERTIFICATION

M. Salucci<sup>(1)</sup>

<sup>(1)</sup> ELEDIA Research Center (ELEDIA@Unitn - University of Trento)  
Via Sommarive 9, I-38123 Trento, Italy  
[marco.salucci@unitn.it](mailto:marco.salucci@unitn.it)

## Abstract

*A novel approach for fast antenna certification is presented. The proposed Measurements-by-Design (MbD) technique allows to accurately estimate both near- and far-field patterns of the antenna under test (AUT) exploiting a suitably generated over-complete basis and a very limited number of measurements. Numerical results are shown to assess the proposed technique.*

**Index Terms** – Antenna measurement, near-field pattern, near-field to far-field transformation (NF-FF), orthogonal matching pursuit (OMP).

## I. INTRODUCTION AND MOTIVATION

With the fast advent of the fifth-generation (5G) communication systems and the unprecedented need for mass production of unconventional radiating systems, fast, reliable, and cost-effective antenna measurement/certification is becoming very attractive [1]-[5].

Many antenna testing techniques rely on near-field and/or compact range measurements [4]. However, standard strategies require a large number of measurement points and, consequently, a long acquisition time [4]. Many efforts have been devoted towards a reduction of the required field samples exploiting *a-priori* knowledge on the antenna under test (AUT). Within this context, several compressive sensing (CS)-based approaches [5], [6] have been proposed to address antenna measurement as a *sparse recovery* problem.

In this paper a novel antenna measurement strategy is presented. The idea behind the proposed Measurements-by-Design (MbD) strategy is to generate a redundant *over-complete* basis able to represent the field radiated by the AUT with a reduced set of near-field samples. Towards this end, *a-priori* information coming from a preliminary *uncertainty analysis* [7] is exploited to provide reliable reconstructions of the radiated pattern also in presence of non-negligible deviations due to manufacturing tolerances or errors.

## II. MATHEMATICAL FORMULATION

With reference to the geometry sketch in Fig. 1, let us consider a planar array of  $N = (N_x \times N_y)$  elements located in  $\mathbf{r}_n = (x_n, y_n)$ ,  $n = 1, \dots, N$ . The near-field distribution of the AUT is measured over the planar surface  $\Omega$  with dimensions  $(W \times L)$  and placed at height  $H$  (Fig. 1).

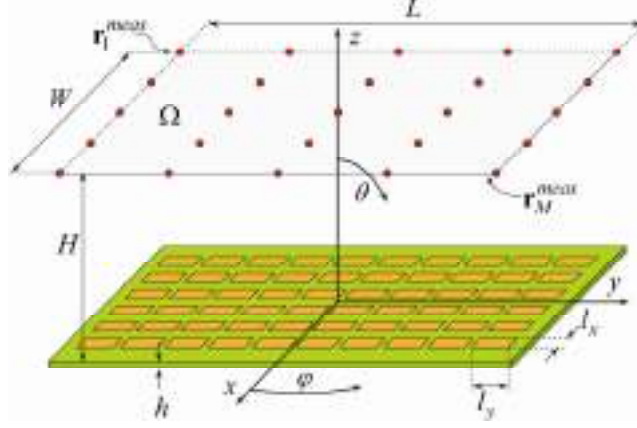


**FIG. 1** – Geometry of the antenna array and of the planar near-field measurement set-up.

A set of  $P$  classes of *uncertainty* that can potentially deviate the radiation features of the *AUT* from the nominal ones is identified exploiting the *a-priori* knowledge on the radiating system and a suitable *uncertainty analysis* [7]. For each identified  $p$ -th class, a set of  $K_p$  full-wave simulations is carried out by considering a variation of the uncertainty parameter within the estimated bounds. Each time the *AUT* near-field distribution is measured over a dense grid of  $T$  equally-spaced positions  $\mathbf{r}_t = (x_t, y_t) \in \Omega$  (Fig. 1), yielding the following set of radiated fields

$$\mathbf{E}_p = \{\mathbf{E}_p^k; k = 1, \dots, K_p\}; p = 1, \dots, P \quad (1)$$

where  $\mathbf{E}_p^k = \{E_p^k(\mathbf{r}_t); t = 1, \dots, T\}$  is the  $k$ -th realization of the *AUT* pattern. The singular value decomposition (SVD) is then applied to each  $p$ -th set, i.e.,

$$\mathbf{E}_p = \sum_{i=1}^{I_p} \sigma_p^i \mathbf{u}_p^i (\mathbf{v}_p^i)^*; p = 1, \dots, P \quad (2)$$

where  $\mathbf{u}_p^i$  and  $\mathbf{v}_p^i$  are respectively the left and right singular vectors,  $*$  being the transpose operator, and  $\sigma_p^i$  are the singular values. In order to regularize the solution, a truncation is applied to Eq. (2) in order to keep the  $Q_p < I_p$  first singular values. The first  $Q_p$  left singular vectors represent a *basis* able to describe the *AUT* near-field under the  $p$ -th cause of uncertainty at the noise level accuracy. An *over-complete* basis can be then straightforwardly obtained as the *union* of the  $P$  SVD-generated bases, i.e.,

$$\mathbf{\Psi} = \cup_{p=1}^P \{\mathbf{u}_p^i; i = 1, \dots, Q_p\}. \quad (3)$$

Once the *over-complete* basis of  $Q = \sum_{p=1}^P Q_p$  vectors is generated, it is possible to retrieve the pattern of the *AUT* starting from a set of (noisy)

measurements taken at  $\mathbf{r}_m^{meas} = (x_m^{meas}, y_m^{meas}) \in \Omega$ ,  $m = 1, \dots, M \ll T$  (Fig. 1) through the following procedural steps:

1. From the  $(T \times Q)$  matrix  $\Psi$  derive the  $(M \times Q)$  sub-matrix  $\Psi'$  by selecting the  $M$  rows corresponding to measurement locations;
2. Apply the orthogonal matching pursuit (OMP) algorithm [8] to solve the following linear system

$$\mathbf{\Gamma} = \Psi' \mathbf{x}. \quad (4)$$

where  $\mathbf{\Gamma} = \{\hat{E}(\mathbf{r}_m); m = 1, \dots, M\}$  contains the noisy samples and  $\mathbf{x} = \{\chi_q; q = 1, \dots, Q\}$  is a *sparse* vector of expansion coefficients.

3. Use  $\mathbf{x}$  to estimate (through the full *dictionary*  $\Psi$ ) the near-field pattern of the *AUT* over the dense grid of  $T$  points belonging to  $\Omega$ .

### III. NUMERICAL VALIDATION

To preliminary assess the proposed *MbD* methodology an exhaustive set of numerical experiments has been carried out. The considered antenna is a planar array of  $l_x = l_y = \lambda/2$ -spaced  $N = 60$  microstrip patches printed on a dielectric substrate of thickness  $h = 0.019\lambda$ , relative permittivity  $\epsilon_r = 4.7$  and loss tangent  $\tan\delta = 0.014$  (Fig. 1). Supposing a row-wise feeding of the radiators, the first class ( $p = 1$ ) of uncertainties affecting the *AUT* is an error in the magnitude of the excitations of each row. Moreover, a second class ( $p = 2$ ) considers a shift of the excitation phases from the broadside ones. An *over-complete* basis of  $Q = 40$  atoms has been generated considering a uniform lattice of  $\lambda/2$ -spaced  $T = 41 \times 41 = 1681$  points  $[(W \times L) = (20 \times 20)\lambda, H = 7\lambda$  - Fig. 1]. The estimation of the near-field has been performed by exploiting a set of  $M = (5 \times 5) = 25$   $5\lambda$ -spaced samples in  $\Omega$  (Fig. 1).

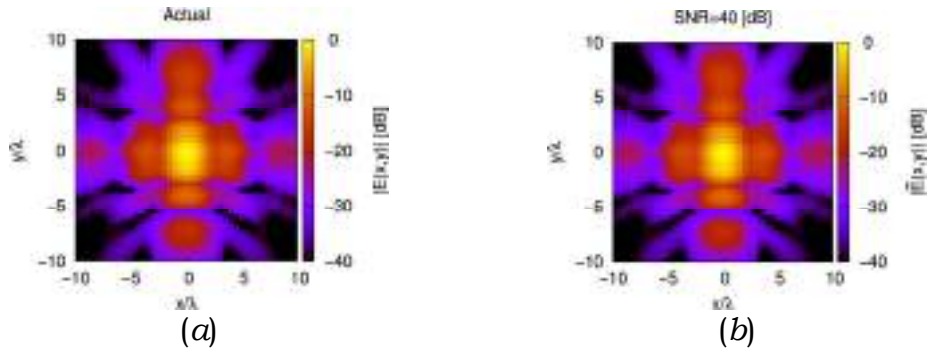


**FIG. 2** – Numerical Assessment ( $N = 60$ ,  $H = 7\lambda$ ,  $T = 1681$ ,  $M = 25$ ,  $SNR = 40$  dB) - (a) Actual and (b) estimated near-field distribution radiated by the *AUT*.

Figure 2 shows the actual [Fig. 2(a)] and retrieved [Fig. 2(b)] near-field when considering a partial failure of the excitations of the third row of the *AUT*. As it can be observed, despite the presence of noise on measurements ( $SNR = 40$  dB) a very accurate estimation of the near-field pattern is yielded. Standard near-field-to-far-field (*NF-FF*) transformation has been applied to the retrieved near-field distribution.

The result is shown in Fig. 3, where the far-field pattern obtained from the retrieved solution [Fig. 3(b)] verifies a very high matching with the actual one [Fig. 3(a)] also in the far side-lobes region.

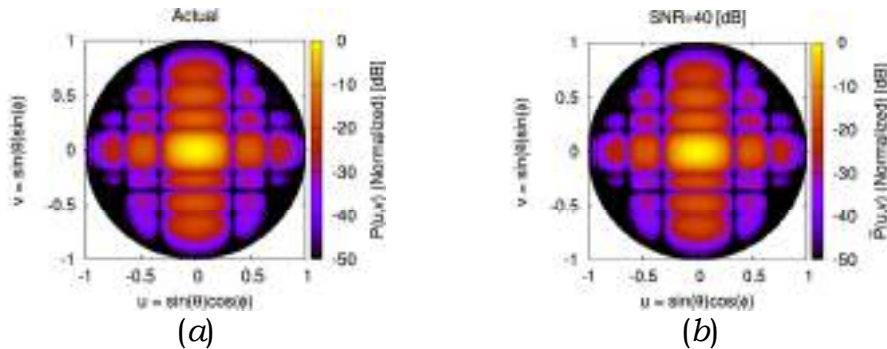


**FIG. 3** – Numerical Assessment ( $N = 60$ ,  $H = 7\lambda$ ,  $T = 1681$ ,  $M = 25$ ,  $SNR = 40$  dB) - Far-field pattern computed through *NF-FF* transformation starting from the (a) actual and (b) retrieved near-field *AUT* distribution.

#### IV. CONCLUSIONS

A novel approach for fast antenna testing has been proposed in this work. The developed *MbD* strategy is based on the generation of an *over-complete* basis able to accurately model the near-field distribution radiated by the *AUT*. Reliable near-field and far-field estimations are yielded exploiting a very limited number of measurements, allowing a fast *AUT* qualification for time- and cost-efficient mass production. Future works will be devoted at experimentally assessing the proposed *MbD* methodology.

#### REFERENCES

- [1] P. Rocca, G. Oliveri, R. J. Mailloux, and A. Massa, “Unconventional phased array architectures and design methodologies - A review,” *Proc. IEEE*, vol. 104(3), pp. 544-560, Mar. 2016.
- [2] G. Oliveri *et al.*, “Co-design of unconventional array architectures and antenna elements for 5G base stations,” *IEEE Trans. Antennas Propag.*, vol. 65(12), pp. 6752-6767, Dec. 2017.
- [3] Y. Qi *et al.*, “5G over-the-air measurement challenges: overview,” *IEEE Transactions Electromagn. Compat.*, vol. 59(6), pp. 1661-1670, Dec. 2017.
- [4] D. Slater, *Near Field Antenna Measurements*. New York: Artech House, 1991.
- [5] M. D. Migliore, “A simple introduction to compressed sensing/sparse recovery with applications in antenna measurements,” *IEEE Antennas Propag. Mag.*, vol. 56(2), pp. 14-26, Apr. 2014..
- [6] A. Massa, P. Rocca, and G. Oliveri, “Compressive sensing in electromagnetics - A review,” *IEEE Antennas Propag. Mag.*, pp. 224-238, vol. 57(1), Feb. 2015.
- [7] N. Anselmi, L. Manica, P. Rocca, and A. Massa, “Tolerance analysis of antenna arrays through interval arithmetic,” *IEEE Trans. Antennas Propag.*, vol. 61(11), pp. 5496-5507, Nov. 2013.
- [8] T. T. Cai and L. Wang, “Orthogonal matching pursuit for sparse signal recovery with noise,” *IEEE Trans. Inf. Theory*, vol. 57(7), pp. 4680-4688, Jul. 2011.

# AN EPIDERMAL CONFIGURABLE ANTENNA SYSTEM FOR THE MONITORING OF BIOPHYSICAL PARAMETERS

C. Miozzi<sup>(1)</sup>, G. Marrocco<sup>(1)</sup>

<sup>(1)</sup> University of Roma “Tor Vergata”, Via del Politecnico 1, 00133, Roma, Italy

## Abstract

*Skin sensors based on Radiofrequency Identification enable non-invasive monitoring of human physiologic parameters. To speed up the experimentations of new sensing modalities and their possible applications, a general-purpose on-skin oriented board is here described. A 3 cm by 3 cm flexible Kapton layer hosts a miniaturized open-loop antenna tuneable in the worldwide UHF RFID band 860-960 MHz, a microchip with internal ADC and pads for interconnecting external sensors and a battery for data-logging mode. When working in Battery Assisted Passive mode it can be read up to 1.5 m and hence the wearer can automatically upload the stored data in mobility. The device is preliminarily experimented in the measurement of the skin temperature and moisture on clothes.*

**Index Terms** – Flexible Electronic, Skin sensor, Radiofrequency Identification.

## I. INTRODUCTION

The measurement of biophysical parameters (temperature, sweat index and pH) directly detected onto the human skin can enable fast and non-invasive health monitoring procedures. The recent progress in epidermal electronics [1] and the consolidating Internet of Things technologies for healthcare [2] are currently stimulating the development of a new class of biocompatible skin-worn devices as an effective and low-cost booster for personal diagnostics and wellness. The wireless connectivity of the epidermal sensor with external nodes can be efficiently provided by the Radio-Frequency Identification (RFID) technology that permits to minimize the complexity of the required electronics.

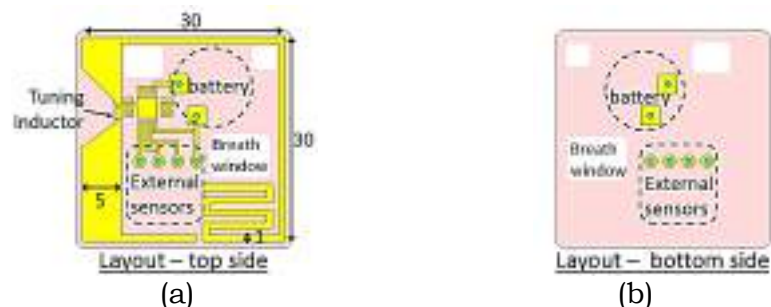


**FIG. 1** – Layout of the RFID skin board: (a) main side with the antenna traces and (b) opposite side with replicated pads. Main sizes in [mm].

As the worldwide interest for skin electronics is continuously increasing, a general-purpose epidermal RFID board could ease the experimentation of new epidermal sensors, like a *lab on skin* [3]. In this perspective, we propose here a small-size flexible RFID antenna on a shaped open-loop layout, working in the UHF band (860-960 MHz). The device is suitable for on-skin placement, includes expansion ports for additional sensors and enables data-logging capability. Some examples of continuous monitoring of skin temperature and clothes moisture are reported.

## II. SKIN ANTENNA LAYOUT

On-skin RFID data-loggers have to be considered as disposable devices and hence the complexity of the involved electronics has to be minimized. Currently the only available all-in-one RFID microchip with sensor-oriented features and capability to store the measured data into an internal memory is the AMS-SL900A IC [4]. This IC provides a native internal temperature sensor and a 10-bit ADC for sampling external sensors. However, this IC cannot be connected to a closed conducting path and, accordingly, conventional impedance matching techniques like the T-match and the Loop- or Slot-match cannot be used. With reference to Fig. 1, the selected antenna comprises a larger vertical trace, where the IC will be interconnected and whose width and gap position have been optimized to match the input resistance of the chip. The meander line portion is used to move the the null of the current so that the two vertical traces will host equal-verse currents. A further degree of freedom is a tuning inductor inserted in series with the chip to change the working frequency of the antenna, e.g. to compensate specific placements over different parts of the body. Finally, the board is provided with some expansion pads for the interconnection of a battery and additional sensors. For improved general use, the terminals are also replicated in the opposite side of the substrate by means of via holes.

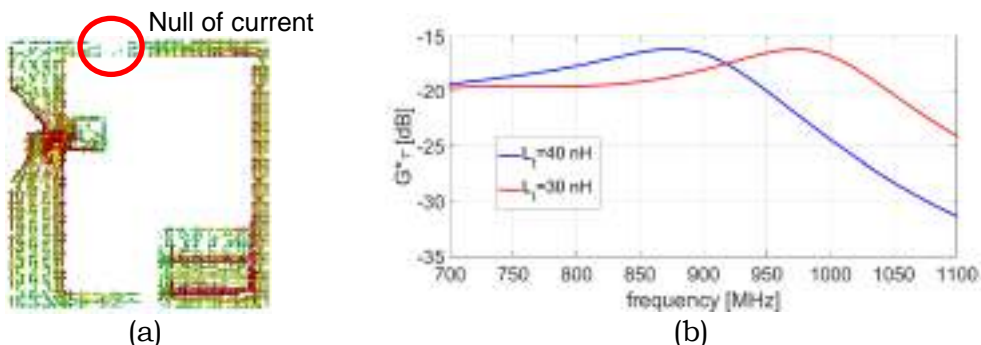


**FIG. 2** – (a) Surface current of the epidermal antenna at 868 MHz and (b) numerically evaluated realized gain for two values of the tuning inductors.

Fig. 2a shows the surface currents onto the antenna when it is placed over an homogeneous box model of human body ( $\epsilon_r = 55.1$ ,  $\sigma = 1.02$  S/m).

The actual combination of the inductor and the meander line length induces the required current pattern so that the antenna can be considered as a miniaturized folded dipole, in spite of the lower open termination. The realized gain for two values of the tuning inductor  $L_t = \{30, 40\} nH$  are shown in Fig. 2b for application in the two extreme boundaries of the UHF RFID band.

The expected read distances in BAP mode are 1.4 m (EU) and 1.5 m (US), by assuming an  $EIRP = 3.2 W$  (EU),  $4 W$  (US). They are suitable for an automatic data download from the device as the user walks across a door that was equipped with an interrogating module.

### III. PROTOTYPES AND PRELIMINARY TEST

A prototype (Fig. 3a) of the skin RFID sensor board was fabricated by etching a copper laminated Kapton substrate ( $50 \mu m$  thickness). A 3 V lithium coin battery was connected in series to the chip throughout a ferrite bead (Murata) to enforce a proper rejection of the RF component versus the chip DC port that will otherwise upset the chip. The resulting device is flexible and can be then embedded into a fabric plaster for healthy and comfortable application onto the skin and easy removal.

The realized gain  $G_R$  was measured by the turn-on method when the antenna was placed over two different parts of the body that are the chest and the rib cage of a female volunteer (Fig 3b). Despite some frequency shift and attenuation, probably due to the different electromagnetic behaviour of the considered body positions, the peak values ( $-17.5 dBi < G_R < -15.5 dBi$ ) are comparable with the simulation ( $-15.5 dBi$ ).

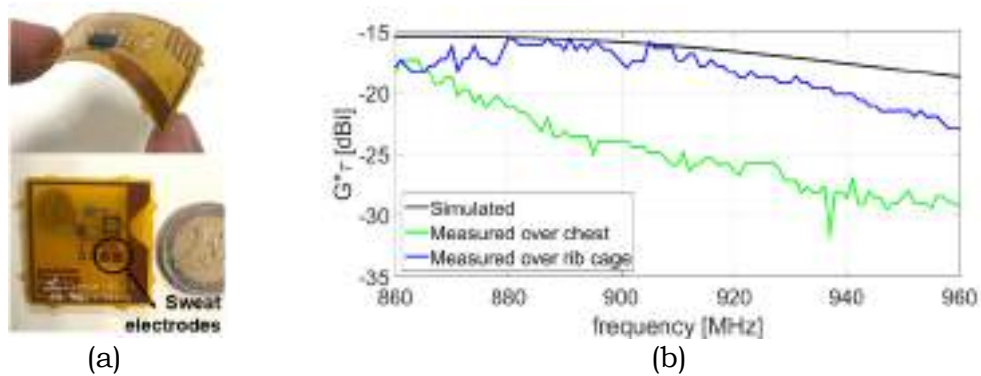


**FIG. 3** – (a) Front and rear sides of the RFID Epidermal Sensor Board prototype with battery mounted onto different faces and (b) measured realized gain when it was placed onto both chest and rib cage of a volunteer.

The RFID skin board was preliminarily demonstrated in the measurement of the skin temperature and the moisture of an underwear cloth. For this purpose, the chip was placed face front the skin and coated with an ultra-thin biocompatible film ( $22 \mu m$  thickness) for sanitary reason, while the battery was soldered in the opposite side. Two

additional copper electrodes were moreover soldered to the expansion ports on the opposite side. The handheld reader to activate the data-logger and download the data was a CAENRFID qIDmini, emitting 150 mW power. An example of measured temperature profile is shown in Fig. 4a and refers to the plaster attached onto the chest of a female volunteer, wearing winter clothes, who moved in the outdoor (13°C for 8 minutes) and then come back inside a university lab (25°C). Finally, Fig. 4b shows the change of surface resistance of a cloth which was artificially humidified with physiologic solution by means of a vaporizer to simulate human sweat production.

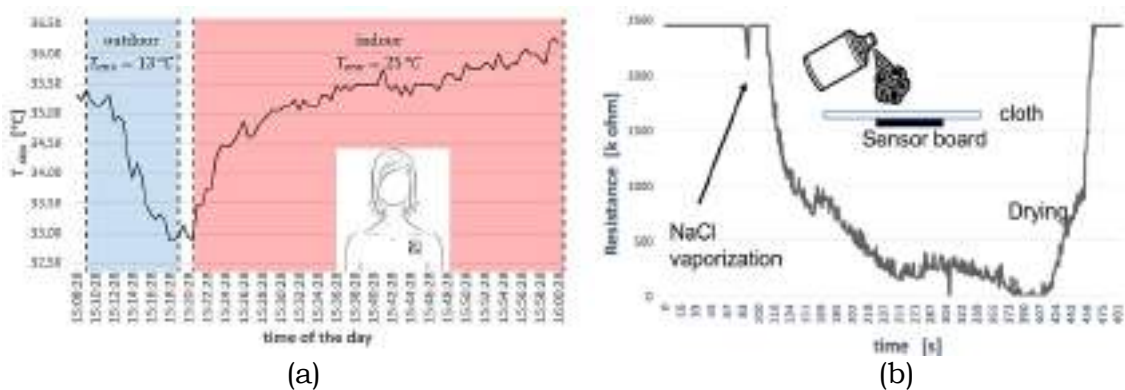


**FIG. 4** – (a) Temperature profile moving from outdoor to indoor environment. (b) Surface resistance of a cloth that was humidified by physiologic solution.

#### IV. CONCLUSION

The proposed epidermal radio-board can be used to test many kinds of sensors suitable to the comfortable monitoring of physiologic parameters in several modalities. The possibility to host a battery could enable a continuous registration of parameters in mobility. The tool is useful for both biomedical applications and diagnostics, as well as to characterize the insulating performance of special clothes, but could be even used in battery-less mode for instantaneous, short-range data download.

#### REFERENCES

- [1] J. A. Rogers et al., *Stretchable Bioelectronics for Medical Devices and Systems*, Springer, 2016.
- [2] S. M. R. Islam et al., "The Internet of Things for Health Care: A Comprehensive Survey", *IEEE Access*, vol. 3, pp. 678-708, 2015.
- [3] Y. Liu et al., "Lab-on-Skin: A Review of Flexible and Stretchable Electronics for Wearable Health Monitoring", *ACS Nano*, Vol. 11(10), pp. 9614-9635, 2017.
- [4] AMS SL900A Tag Chip Datasheet, [Online]. Available: [https://ams.com/ger/content/download/755603/1912935/file/SL900A\\_Datasheet\\_EN\\_v5.pdf](https://ams.com/ger/content/download/755603/1912935/file/SL900A_Datasheet_EN_v5.pdf).

# UHF RFID 3-D LOCALIZATION IN RETAIL SHOP SCENARIOS

A. Motroni, P. Nepa

Department of Information Engineering, University of Pisa  
Via G. Caruso, 56122 Pisa, Italy  
andrea.motroni@ing.unipi.it, p.nepa@iet.unipi.it

## Abstract

***This paper presents the application of the phase-based SARFID technique to locate static tags with respect to a UHF-RFID reader carried by an Unmanned Grounded Vehicle (UGV). The UGV can autonomously move inside a complex indoor environment avoiding obstacles being remote-controlled by humans. The knowledge of the reader antenna trajectory is achieved through a Simultaneous Localization and Mapping (SLAM) procedure. The 3D tag position can be estimated with centimeter error by employing the SARFID technique with two reader antennas. Differently from other localization techniques, neither reference tags (anchor tags), nor large phased array antennas are required.***

*Index Terms* – Passive UHF-RFID system, UHF-RFID localization, Unmanned Ground Vehicles, RFID retail applications

## I. INTRODUCTION

The UHF-RFID technology represents a low-cost and easy-deployable solution to combine localization and tracking of tagged items with real-time inventory, in several scenarios such as warehouses, libraries, hospitals and stores. Several techniques were proposed to develop UHF-RFID localization systems, exploiting both amplitude and phase of the tag backscattering signal measured at the output of the reader coherent receiver. The main goal is to obtain a spatial resolution comparable with the size of the tagged item. Satisfactory performance can be obtained with phase-based methods [1], which are more robust with respect to the multipath propagation phenomena that are typical of a crowded indoor scenario. Multiple reader antennas can be employed to increase the available amount of data to be processed [2]. Alternatively, the relative motion between reader antenna and tags can be exploited to locate moving tagged items with respect to a fixed reader antenna [3]-[4], or fixed tagged items by employing a moving reader antenna, through a Synthetic Aperture Radar (SAR) approach (SARFID method). The antenna motion can be created through a handling system [5], or by mounting the antenna on board of a drone [6].

In this paper, the authors propose the employment of the SARFID localization method to locate static tagged items in retail scenarios, by employing a moving UHF-RFID reader on board of an Unmanned Grounded Vehicle (UGV). The UGV is remote-controlled and can self-localize through a SLAM algorithm. Thus, the 3D UGV/reader antenna

trajectory can be known with centimeter order error in an indoor scenario allowing for the SARFID method application.

## II. THE RFID-BASED UGV-PLATFORM

The UGV platform employed in the experimental setup (Fig. 1a) was the Pioneer 3-AT manufactured by MobileRobots. The robot uses a micro-controller to interface with the motors and to manage the odometry update and the obstacle detection, using the sonar sensors. In order to obtain a satisfactory environment map, the Hokuyo LRF (UTM-30LX) was mounted on the top plate of the original platform. The data from the whole sensor payload (IMU, LRF, and sonar) were integrated into a state-of-the-art SLAM [7] algorithm based on a Rao-Backwellized particle filter [8], thus the UGV was able to avoid obstacles and localize itself with uncertainty of the order of few centimeter.

The Impinj Speedway Revolution R420 UHF-RFID reader was integrated on the UGV with two circularly polarized RFID antennas (WANTENNAX019 by C.A.E.N. RFID). In accordance with the sampling theorem, the UGV/reader has not traveled a distance larger than  $\lambda/4$  [4] when collecting consecutive tag readings. The wireless pilot of the reader was realized through the Wi-Fi module Vonets VAP11G-300.

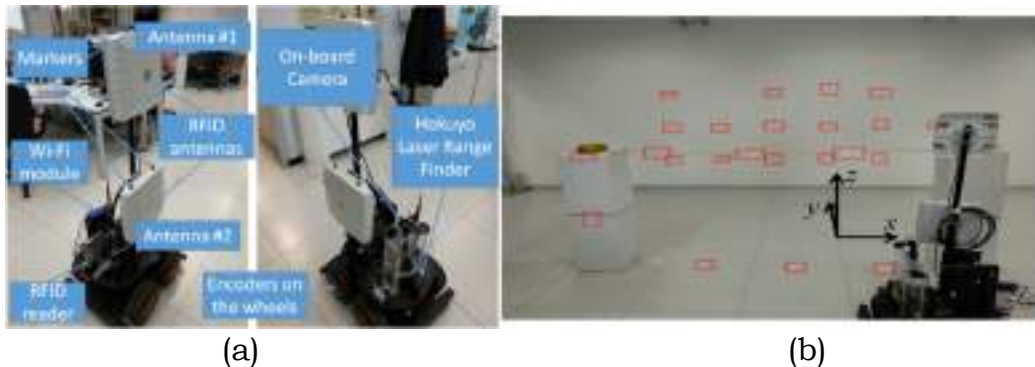


FIG. 1 – (a) Schematic setup of the measurement scenario with the Pioneer 3-AT robot equipped with the RFID reader and the sensor payload for the SLAM algorithm. Infrared markers are used to measure the “ground truth” position of the antennas. (b) Measurement scenario with commercial UHF-RFID inlay tags.

## III. LOCALIZATION METHOD AND EXPERIMENTAL ANALYSIS

When a reader antenna moves in front of tagged items on a shelf according to a rectilinear trajectory (e.g. along the  $\mathbf{x}$ -axis of Fig. 1b) or a planar one (e.g. on the  $\mathbf{xy}$ -plane), it is possible to perform a mono-dimensional or a bi-dimensional localization, respectively, with an error of centimeter order. To obtain an accurate estimation of the third coordinate (3D localization), the reader antenna should also change its height ( $\mathbf{z}$ -coordinate) along the path. Alternatively, two reader antennas at different heights on the UGV can be profitably used. Indeed, each reader antenna measures a different relative phase history being at a

different distance from the tagged items. By multiplying the 3D matching functions obtained from the SARFID method, a new 3D matching function can be extracted from which an accurate estimation of the  $z$ -coordinate is possible. The proposed localization method was tested in an indoor office environment (Fig. 1b). Thirty-eight UHF passive RFID tags were placed in the environment within a volume of  $7\text{ m} \times 5\text{ m} \times 1.5\text{ m}$  and with arbitrary orientation. Different tag typologies with Monza R6 chip (sensitivity of  $-22.1\text{ dBm}$ ) were employed. The antenna #1 was placed at a height of  $z_1=1.25\text{ m}$ , and the antenna #2 at  $z_2=0.75\text{ m}$ . The UGV ran several trajectories on the  $xy$  plane, and the RFID system collected phase samples from all the tags in the scenario ( $f_0=867.5\text{ MHz}$ ,  $P_{TX}=26\text{ dBm}$ , average spatial sampling among consecutive readings of  $5\text{ cm}$ ).

Fig. 2 depicts the 3D matching function projection on the  $xz$ -plane of the estimated  $y$ -coordinate using data from antenna #1 (a), from antenna #2 (Fig. 2b) and by multiplying the matching functions (Fig. 2c). The actual tag position is  $[x_{tag}, y_{tag}, z_{tag}]=[-0.58, -0.58, 1.00]\text{ m}$  and the synthetic aperture lengths are  $D_x=1.51\text{ m}$  and  $D_y=0.78\text{ m}$  along the  $x$ - and  $y$ -directions, respectively. By considering a single antenna with linear trajectory, the main lobe along the  $z$ -axis can be very wide (Fig. 2a), or a secondary lobe can appear (Fig. 2b), depending on the distance of the trajectory heights from the tagged item. Both cases determine an uncertainty in the  $z$ -coordinate that can be solved by multiplying the two matching functions as shown in Fig. 2c. The 3D localization errors are described in Table I.

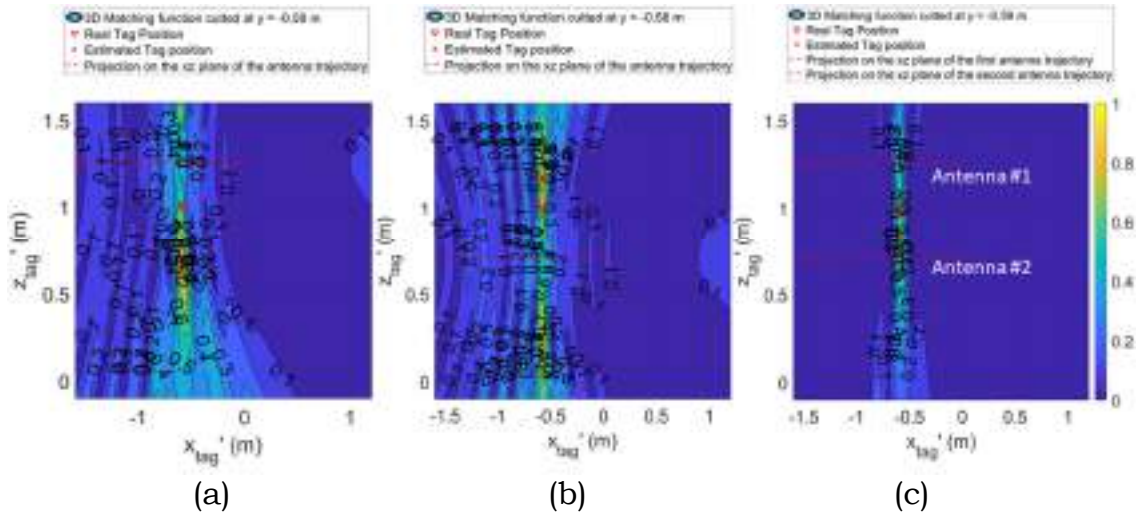


FIG. 2 - 3D matching functions projection on the  $xz$ -plane of the  $y$ -coordinate estimates, obtained by processing data measured (a) at antenna #1, (b) at antenna #2, or (c) by multiplying the matching functions obtained from antenna #1 and antenna #2. The red dashed line denotes the projection of the reader antenna trajectory on the  $xz$ -plane.

TABLE I – LOCALIZATION ERROR

Employed Antenna	$x$ -coordinate error (cm)	$y$ -coordinate error (cm)	$z$ -coordinate error (cm)
#1	1	12	33
#2	1	12	17
#1 and #2	1	5	16

#### IV. CONCLUSION

In this paper, the phase-based SARFID localization technique for UHF-RFID passive tags was applied in a realistic indoor scenario where the tagged items are static, and the reader was moved by a UGV. By performing a planar trajectory of the UGV it is possible to combine the matching function obtained from the data measured at the two reader antennas to determine an accurate 3D tag position.

#### ACKNOWLEDGEMENT

We thank Paolo Tripicchio and Matteo Unetti from Scuola Superiore Sant’Anna of Pisa for their contribution to this work.

#### REFERENCES

- [1] P. V. Nikitin, R. Martinez, S. Ramamurthy, H. Leland, G. Spiess, and K. V. S. Rao, “Phase based spatial identification of UHF RFID tags”, **2010 IEEE Int. Conf. RFID, Orlando**, FL, pp. 102-109, 2010.
- [2] M. Scherhäufel, M. Pichler and A. Stelzer, “UHF RFID Localization Based on Evaluation of Backscattered Tag Signals”, **IEEE Transactions on Instrumentation and Measurement**, vol. 64, no. 11, pp. 2889-2899, Nov. 2011.
- [3] P. Nepa, F. Lombardini, A. Buffi, “Method for determining the location of a moving RFID tag”, EP2533173 (A1), IP: University of Pisa.
- [4] A. Buffi, P. Nepa, F. Lombardini, “A Phase-Based Technique for Localization of UHF-RFID Tags Moving on a Conveyor Belt: Performance Analysis and Test-Case Measurements”, **IEEE Sensors Journal**, vol. 15, no. 1, pp. 387-396, Jan. 2015.
- [5] A. Buffi, M. R. Pino and P. Nepa, “Experimental Validation of a SAR-Based RFID Localization Technique Exploiting an Automated Handling System”, **IEEE Antennas and Wireless Propagation Letters**, vol. 16, pp. 2795-2798, 2017.
- [6] A. Buffi, P. Nepa, R. Cioni, “SARFID on Drone: Drone-based UHF-RFID Tag Localization”, **2017 IEEE Int. Conf. RFID-TA**, Warsaw, 2017.
- [7] G. Pepe, M. Satler e P. Tripicchio, “Autonomous exploration of indoor environments with a micro-aerial vehicle”, **Research, Education and Development of Unmanned Aerial Systems (RED-UAS)**, 2015.
- [8] P. Tripicchio, M. Unetti, N. Giordani, C. A. Avizzano e M. Satler, “A lightweight slam algorithm for indoor autonomous navigation,” **2014 Australasian Conf. Rob. Aut. (ACRA 2014)**, December 2-4, 2014.

# **GOSPER SPACE-FILLING RADIOFREQUENCY-SKIN FOR THE DETECTION AND IDENTIFICATION OF SURFACE CRACKS**

S. Nappi<sup>(1)</sup>, G. Marrocco<sup>(1)</sup>

<sup>(1)</sup> Department of Civil and Informatic Engineering,  
University of Rome Tor Vergata,  
Via del Politecnico 1, 00133 Roma, IT  
[www.pervasive.ing.uniroma2.it](http://www.pervasive.ing.uniroma2.it)

## **Abstract**

*The aging of polymer-based objects (tires, cable harness, paints, gaskets) may appear as the formation of surface defects like cracks and scratches. An early detection of such signs may support the Predictive Maintenance in the Industry 4.0 paradigm of critical polymeric devices before the occurrence of a severe damage. Inkjet printed Space Filling Curves (SFC) are here proposed as an artificial electric skin, suitable to be integrated with an RFID tag, at the purpose to detect and remotely transmit the presence of small aging signs of a surface. Thanks to the particular properties of the Gosper SFC, the size and space resolution of the skin can be easily controlled by few parameters.*

**Index Terms** – Electronic Skin, Material Aging, Printed Electronics, RFID technology.

## **I. INTRODUCTION**

Polymers are increasingly being used in a wide variety of applications where reliability in long-term service in harsh environments is required. These materials are usually greatly involved in aerospace and automotive industries, including civil buildings and infrastructures. The main cause that can lead to a failure during the service is the physical or chemical aging of the materials that could compromise its integrity with catastrophic results. One of the major aging effect [1] [2] is the generation of superficial cracks on the polymer. Accordingly, a regular and hopefully automatic monitoring of the object's health status could extend its lifetime preventing unexpected faults. Currently, there are several cracks detection techniques that usually require cumbersome measure methods and a highly trained operator to collect and interpret data.

This contribution introduces a new idea for the wireless identification of aging signs over plastic surfaces and some preliminary experimental examples. The method is based on an ink-jet printed electronics skin, enveloping the object like a tattoo and connected to an integrated RFID antenna. The alteration of such a skin, due to aging of the surface, will be detected by the RFID microchip transponder and then backscattered to the reader.

## II. GOPSPER SKIN CIRCUITS

Without loss of generality, the defect to be detected are here modeled as a linear crack, of length  $l$ , over the object surface (assumed, for the sake of simplicity, to be planar). A possible family of electrodes to achieve a detection skin is that of Space-filling curves (SFC) [3] [4], that map a multi-dimensional space into the one-dimensional domain. A space-filling curve acts like a thread that passes through portions of the space so that every point is visited only once. The filling density on the surface can be controlled by the selection of the iteration (order) parameter. It can be proved that the minimum length of the detectable crack can be defined as space resolution  $S(N)$  and expressed as:

$$S(N) = \frac{4r\sqrt{3}}{\sqrt{7^{N+1}}} \quad (1)$$

where  $r$  is the radius of the circle enveloping the Gosper island. We consider here the Peano-Gosper curves (Fig. 1) as possible detectors of surface defects since, thanks to their rotational construction, they have the property to uniformly and quickly improve the spatial resolution with respect to the Hilbert curve. The Gosper SFC also possesses the capability of surface tessellation so that several Gosper Islands can be placed one close to another (Fig. 2) in order to widen the area to be monitored. The interrogation of the resulting skin is implemented by connecting the two terminals of each island to the anti-tampering port of an RFID tag. The occurrence of a crack (or more in general of a defect) will not only be identified, by even localized in a macro-region depending on the responding tag with the altered anti-tamper bit.

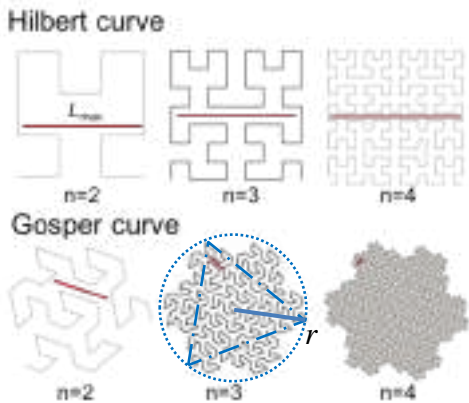


**FIG. 1** Hilbert and Gosper Space-Filling Curves of some orders. The red lines indicate the maximum segment that is not crossed by the curves; such segment can be considered as the lower-bound length of a crack that would not interrupt the line. The blue segment is the radius of the circle enveloping the SFC.

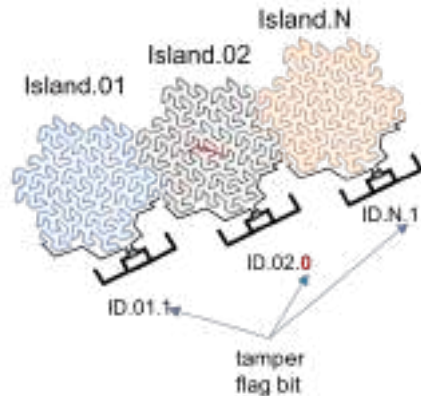


**FIG. 2** Pictorial example of how several Gosper Islands can be mutually displaced in order to fill a large surface. The red '0' indicates the anti-tamper bit in the response of the second tag detecting the occurrence of a damage in the island n.2; in other words, the condition  $l_{crack} > S(N)$  has occurred for that island.

### III. GOSPER SKIN RESISTANCE

A possible fabrication of the space-filling RFID skin involves the conducting inkjet printing process thanks to its capability to produce complex shapes and to deposit ink even onto non planar surfaces. The DC conductivity of the self-sintering ink is  $\sigma^{DC} \approx 1 \cdot 10^7 \text{S/m}$  [5]. In a preliminary test the printing substrate is the PVA coated PET Mitsubishi Paper Mills (Thickness  $135 \mu\text{m}$ ). Fig. 3 shows some single-pass printed Gosper curves of increasing order such to be limited within  $8.5\text{cm} \times 8.5\text{cm}$  square. The critical issue is the non-uniform spread of the deposited ink droplets inside and outside the main trace so that, in high order SFC (closes lines), they may produce a change of the input DC resistance of the curve, measured at the two terminals. Tab. 1 resumes the measured DC input resistance, by a Fluke meter, in case of a continuous line ( $R^{SC}$ ) as well as in case it was interrupted in the middle ( $R^{OC}$ ) by a small cut. Due to the intrinsic ink loss, the short-circuit resistance increases (nearly doubles) along with the order of the curve, i.e. for overall longer traces. With reference to the NXP UCODE G2iM+ chip, the tampering circuit is considered closed (alarm flag = 0) when the port resistance is  $R^{SC} < 2\text{M}\Omega$ , while instead the circuit is considered interrupted (alarm flag = 1) when  $R^{SC} > 20\text{M}\Omega$ . Accordingly, the measured resistances in Tab. 1 show that all the considered Gosper curves can be suitable to interconnection with an RFID tag.



**FIG. 3** Some inkjet-printed Gosper SFCs, with a trace  $250 \mu\text{m}$  of increasing orders, over a PET substrate (left). Magnified photo of the  $n=4$  curve (right).

**TABLE I – MEASURED DC INPUT RESISTANCE AT THE GOSPER SFC IN CASE OF SHORT-CIRCUIT CURVE AND OPEN-CIRCUIT LINE.**

Order (n)	Length [m]	$R^{SC}$ [k $\Omega$ ]	$R^{OC}$ [M $\Omega$ ]
2	0.60	0.7	>2000
3	1.40	1.6	>2000
4	3.86	3.6	>2000

### IV. EXPERIMENTAL VALIDATION

The overall wireless sensing skin (order  $n=3$ ), is finally integrated (Fig. 4) with a meander line dipole, made by a thin wire conductor, embedding the anti-tamper chip NXP UCODE G2iM+. Fig. 4 shows also the realized gain of the skin (in two operative conditions). The SFC acts as a parasitic element that electromagnetically interacts with the MLA antenna depending on its status thus affecting its impedance and radiation pattern. The resonant frequency of the tag shifts from  $921\text{MHz}$ , in absence of the skin, to  $899\text{MHz}$  when the skin is connected to the anti-

tampering part of the chip, and the peak of the gain decreases of 0.5dB. Finally, when the Gosper curve is broken in the middle by a 86 $\mu$ m scratch, the induced current reshapes and the resonance frequency of the tag moves to 903MHz. Overall, being  $P_C=-17.5$ dBm the power sensitivity of the chip, the status of the skin might be read up to 10m in case of an interrogation power EIRP=3.2W at the peak condition.

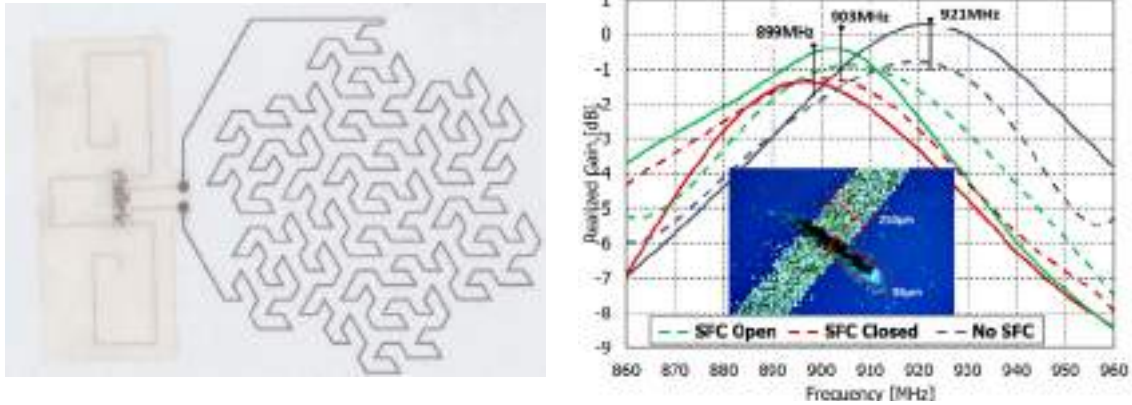


**FIG. 4** Inkjet-printed third-order Gosper skin integrated with an RFID MLA tag (on the left). Measured (dashed) and simulated (solid) realized gain in absence of damage and in case of an interruption of the skin in the middle (on the right).

## V. CONCLUSION

We have presented the idea and a preliminary experimentation of a defect-detecting printed skin to monitor the aging of surface by means of the RFID platform. The Gosper curve looks an interesting option to control the size and the space-sensitivity of the skin by means of few parameters. Despite of the modest quality of the used low-cost inkjet printing, the achieved resistance of the printed trace is low enough to let the anti-tamper chip to discriminate an open circuit skin (a surface defect) from a short circuit case (healthy surface).

## REFERENCES

- [1] F. Awaja, S. Zhang, M. Tripathi, A. Nikiforov, N. Pugno, “Cracks, microcracks and fracture in polymer structures: Formation, detection, autonomic repair Progress”, *Materials Science*, 83, 536 - 573, 2016.
- [2] D. Cangialosi, V. M. Boucher, A. Alegria, J. Colmenero, “Physical aging in polymers and polymer nanocomposites: recent results and open questions”, *Soft Matter*, *The Royal Society of Chemistry*, Vol.9, pp. 8619-8630, 2013.
- [3] H. Sagan, *Space-Filling Curves*, Springer Verlag, New York, 1994.
- [4] H. Fukuda, M. Shimizu, G. Nakamura, “*New Gosper Space Filling Curves*”, *Proceedings of the International Conference on Computer Graphics and Imaging (CGIM2001)*, pp. 34–38 (2001)
- [5] S. Amendola, A. Palombi and G. Marrocco, “Inkjet Printing of Epidermal RFID Antennas by Self- Sintering Conductive Ink”, *IEEE Trans. Microwave Theory Tech.* – Nov. 2017, pp. 1-9.

# TIME-BASED ARRAYS FOR PRECISE TAGS LOCALIZATION

M. Shanawani<sup>(1)</sup>, D. Masotti<sup>(1)</sup>, A. Costanzo<sup>(2)</sup>

<sup>(1)</sup> DEI – University of Bologna, via Risorgimento 2, 40136, Bologna, Italy

<sup>(2)</sup> DEI – University of Bologna, via Venezia 52, 47521, Cesena, Italy

[diego.masotti@unibo.it](mailto:diego.masotti@unibo.it)

## Abstract

*The paper describes a time-modulated compact antenna array suitable for future 5G IoT applications. Each antenna is selectively activated in order to localize tagged objects, randomly distributed in harsh electromagnetic environments, in almost real-time. The system positively exploits a well-known property of the time-modulation technique: the simultaneous radiation at both the carrier frequency and the sideband harmonics created by the superposition of the nonlinear switches driving (or modulation) frequency. Despite their architectural simplicity, these arrays are potential candidate for modern wireless applications because of their ease of reconfiguration. This paper shows some results of a two-element array for localization purposes.*

**Index Terms** – Antenna arrays, nonlinear circuits, localization, time modulation.

## I. INTRODUCTION

The use of time-modulation has been introduced in [1] where the time represents a *fourth* degree of freedom. In a time-modulated array (TMA) system, each antenna port is controlled by a nonlinear switch, whose role is to activate/deactivate the corresponding radiating element through a periodic driving sequence. From Fig. 1 (a), the signal period  $T_M$  and duty cycle  $\tau$  become additional optimization parameters, thus providing an almost infinite multi-dimensional design space in which the proper control sequence has to be chosen. The nonlinear radiating circuit regime is given by the superposition of the carrier radio-frequency ( $f_0$ ) and the modulation frequency ( $f_M$ ) used to periodically drive the switches. Hence, TMAs are able to radiate power at the sideband harmonics ( $f_0 \pm hf_M$ :  $h=1,2,\dots$ ), too. The extreme simplicity of the TMA architecture, which avoids the use of complex phase shifters, makes these arrays very attractive for modern scenarios where sideband radiation can be exploited: these applications range from direction finding [2], to wireless powering [3], and cognitive radio [4] scenarios.

Despite their simplicity, TMAs need an accurate and multi-domain design platform, consisting of the combination of Harmonic Balance-based circuit techniques and full-wave solvers [5]. In this paper, some experimental data of a two-element TMA array to localize RF-ID tags are provided [3].

## II. TMA RADIATION AND LOCALIZATION TECHNIQUES

We assume a linear array of  $N$  antennas operating at the carrier frequency  $f_0$ , with nonlinear switches biased by periodic rectangular pulses  $U_k(t)$ , with period  $T_M=1/f_M$  and duration  $\tau_k$  ( $k = 1, 2, \dots, N$ ). The inclusion of time through the ON/OFF switching in the excitation mechanism leads to a time-dependent array-factor definition:

$$AF(\psi, t) = \sum_{k=0}^{N-1} U_k(t) e^{jk\beta L \cos\psi} = \sum_{h=-\infty}^{\infty} e^{j2\pi(f_0+h f_M)t} \sum_{k=0}^{N-1} u_{hk} e^{jk\beta L \cos\psi} = \sum_{h=-\infty}^{\infty} AF_h(\psi) \quad (1)$$

where a uniform amplitude excitation condition is considered,  $L$  is the element spacing,  $\beta$  is the free-space phase constant, and  $\psi$  is the angle between the alignment direction and the direction of field evaluation. The Fourier expansion of (1) ( $u_{kh}$  are the corresponding complex coefficients) provides harmonic components of the array-factor, which justify the sideband radiation phenomenon, i.e., the radiation at the carrier harmonics  $f_0 \pm h f_M$ , with  $h=0, 1, 2, \dots$ . Therefore, it allows the use of Fourier expansion complex coefficients as design parameters.

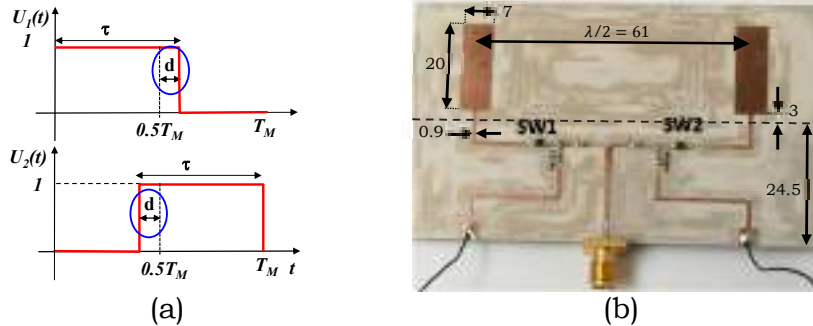


**FIG. 1** – (a) Photo of the two-monopole TMA prototype including the dimensions in millimetres. (b) Excitation pulses waveforms suitable for localization purposes.

A system of two-element array of planar monopoles, as shown in Fig. 1 (b), has been realized on Taconic RF60A ( $\epsilon_r=6.15$ , thickness=0.635 mm) operating at 2.45 GHz and properly operated with the bias sequence shown in Fig. 1(a) [3], where  $d$  represents a tuning parameter for varying the pulse duty-cycle. The two switches are two Schottky diodes. Namely, the Skyworks SMS7630-079. In the present case, they are periodically driven with the sequences of Fig. 1(b), with period  $T_M=40\mu s$  (i.e., a modulation frequency  $f_M = 25$  kHz).

The sideband radiation can be favorably exploited in this case for a  $f_0=2.45$  GHz carrier where the two elements are excited in phase (because of the real nature of the corresponding Fourier coefficient  $u_{0k}$ ), thus providing the standard Sum ( $\Sigma$ ) radiation pattern; simultaneously

for the  $h=\pm 1$  harmonics, where the two dipoles, still in resonant condition, are out-of-phase because of the driving sequence of Fig. 1 (b), a Difference ( $\Delta$ ) radiation pattern takes place. The tuning of the  $\Delta$  using the duty cycle  $d$  independently of  $\Sigma$  gives more freedom for solution-finding ( $u_{0k}$  is real). Fig. 2 (a) shows the result of a first simulation carried out by following the procedure described in [5]. The scanning plane is the dipoles horizontal plane (xz-plane) hence the scanning angle is the elevation ( $\theta$ ).

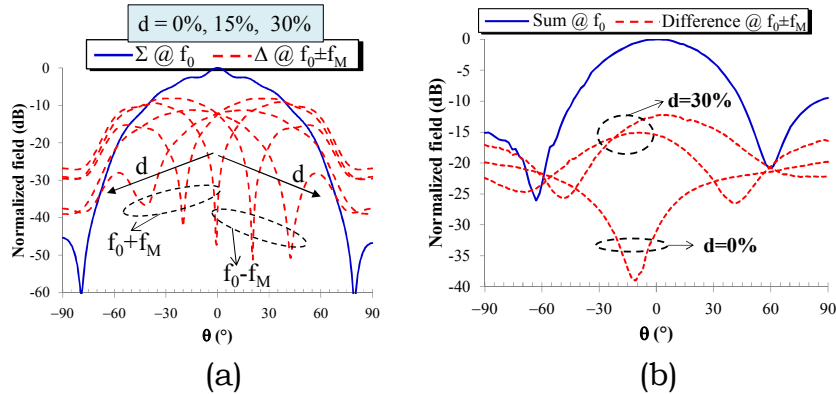


**FIG. 2** – (a) Simulated  $\Sigma$  and  $\Delta$  radiation patterns, showing the tuning capability of the Difference by acting on parameter  $d$ . (b) Measured multiharmonic  $\Sigma$  and  $\Delta$  radiation patterns for  $d=0\%$  and  $d = 30\%$ .

### III. MEASUREMENTS

For the measurements, a microprocessor TI MSP430 is used to drive the diodes with waveforms of the kind of Fig. 1 (a). As a first test, the TMA of Fig. 1 (b) is connected to a signal generator providing the 2.45 GHz signal, and is placed in front of a TDK horn antenna connected to an RF spectrum analyzer. Fig. 3 reports the received spectra when the link direction  $\theta$  is  $0^\circ$ ,  $30^\circ$ , and  $45^\circ$  and the tuning parameter  $d$  assumes the 0% and 30% values.

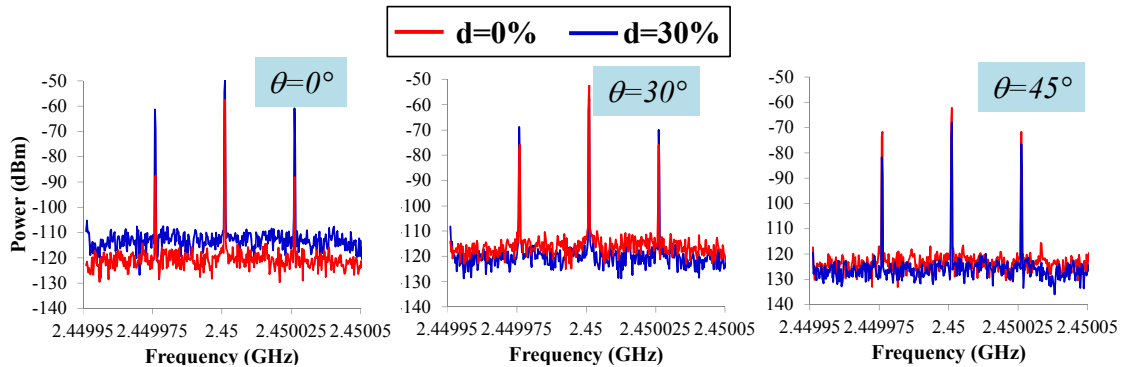


**FIG. 3** – Measured multi-harmonic spectra for different  $\theta$  directions and  $d$  values.

It is clearly visible the sideband radiation phenomenon (limited to the first lateral harmonics  $f_0 \pm f_M$  in the figure), but also its dependency on both the link direction and the pulse duty-cycle: in fact the signal received by the  $\Delta$  pattern at  $f_0 \pm f_M$  increases with increasing values of  $\theta$  if the biasing signals have duty-cycle=50% ( $d=0\%$ ), whereas it decreases if the duty-cycle is increased ( $d=30\%$ ), as confirmed by inspection of Fig. 2 (a), too.

As a second test, the measurement of the  $\Sigma$  and  $\Delta$  radiation patterns for  $d=0\%$ ,  $30\%$  is carried out. The results are shown in Fig. 2 (b) and they reveal a good agreement with the predictions of Fig. 2(a).

#### IV. CONCLUSION

In the localization of crowded RF-ID tags, radiation patterns as those of Fig. 2 can be extremely useful. By considering the backscattered Received Signal Strength Indicator (RSSI) from each illuminated tag, received both by the  $\Sigma$  and the  $\Delta$  patterns of the TMA, the Maximum Power Ratio (MPR) figure of merit can be built as the difference between  $\Sigma_{\text{RSSI}}(\text{dB})$  and  $\Delta_{\text{RSSI}}(\text{dB})$  [6]. The sharp positive peaks of the MPR patterns would guarantee high precision in the detection of tags. And this can be easily obtained with a very simple time-based architecture, rather than traditional phased-arrays [6].

#### REFERENCES

- [1] H. E. Shanks and R. W. Bickmore, "Four dimensional electromagnetic radiators," *Canadian J. of Physics*, 37, 3, 1959, pp. 263-275.
- [2] A. Tennant e B. Chambers, "A Two-Element Time-Modulated Array With Direction-Finding Properties", *IEEE Ant. and Wirel. Prop. Lett.*, 6, 2007, pp. 64-65.
- [3] D. Masotti, A. Costanzo, M. Del Prete and V. Rizzoli, "Time-Modulation of Linear Arrays for Real-Time Reconfigurable Wireless Power Transmission," *IEEE Trans. Microw. Theory Techn.*, 64, 2, Feb. 2016, pp. 331-342.
- [4] P. Rocca, Q. Zhu, E.T. Bekele, S. Yang, A. Massa, "4-D Arrays as Enabling Technology for Cognitive Radio Systems," *IEEE Trans. Antennas Propag.*, 62, 3, March 2014, pp.1102-1116.
- [5] D. Masotti, P. Francia, A. Costanzo, V. Rizzoli, "Rigorous Electromagnetic/Circuit-Level Analysis of Time-Modulated Linear Arrays," *IEEE Trans. Antennas Propag.*, 61, 11, Nov. 2013, pp.5465-5474.
- [6] M. Del Prete, D. Masotti, N. Arbizzani, A. Costanzo, "Remotely Identify and Detect by a Compact Reader With Mono-Pulse Scanning Capabilities," *IEEE Trans. Microw. Theory Techn.*, 61, 1, Jan. 2013, pp.641-650.

# RADIO FREQUENCY SENSORS BASED ON CHIPLESS RFID TECHNOLOGY

F. Costa<sup>(1)</sup>, S. Genovesi<sup>(1)</sup>, S. Terranova<sup>(1)</sup>, G. Manara<sup>(1)</sup>

<sup>(1)</sup> Dipartimento di Ingegneria dell'Informazione, University of Pisa  
Via Caruso 16, 56122 Pisa, Italy  
[filippo.costa@unipi.it](mailto:filippo.costa@unipi.it)

## Abstract

*Chipless sensors are entirely passive devices whose electromagnetic signature is intelligible in time or frequency domain. The variations of the electromagnetic response of these devices can be used to sense environmental parameters at a very limited cost and with a minimum environmental impact. The most relevant configurations for designing environmental sensors are described and the main benefits and drawbacks of this technology are discussed.*

**Index Terms** – Chipless RFID; Humidity sensors; RFID; Sensors.

## I. INTRODUCTION

Low cost wireless sensors are extremely appealing in pervasive sensor networks [1]. The typical configuration of commercial sensors consists of an electronic circuit in which a component induces a certain variation of an observable quantity (frequency shift, phase delay) as a result of the interaction with external environmental parameters such as humidity, temperature, etc. The transducer consists of a material which is frequently referred as a Functional Material [2] or a Chemical Interactive Material (CIM) [3]. The transduction phenomenon is usually monitored at low frequencies or in DC throughout a measurement of currents and voltages. Sensors are usually wired and are interrogated by a direct access to the circuit [4]. The main limitations are the finite lifetime of the battery, which requires periodic maintenance, and the cost that, although modest, is not lower than 20-30 USD.

Nowadays, another class of sensors, cheaper than the abovementioned ones, is emerging on the market: the RFID-based sensors. The advantage of RFID-based sensors relies in the absence of any battery, which can be a huge benefit in terms of maintenance and cost.

The most challenging approach to sense the environment wirelessly is to use an entirely passive device, i.e. without any electronic circuit. In this case, the information is embedded in the electromagnetic footprint of a resonator and the sensing is carried out by detecting the changes in the electromagnetic response of the device. Indeed, as every electromagnetic device, the radio frequency response of these tags depends on the electric or magnetic changes of nearby substrates or particles and on the variation of the surrounding environment. If these variations are suitably controlled and isolated, an indirect measurement of several environmental quantities (or mechanical changes) can be

extracted from the measured backscattering spectrum [5], [6]. This category of sensors is named chipless RFID sensors [7]. This technology is very appealing for designing very low cost, green and embedded sensors. Also, it is worth noting that, due to the absence of any electronic circuit, chipless RFID sensors are potentially suitable for hazardous environments. However, one of the main limitations is that the reliable reading of the sensor can be achieved only under specific conditions. In recent years, the analysis of techniques for the design of chipless RFID sensors has attracted increasing interest. Different environmental parameters can be monitored by exploiting the interaction of CIMs with resonators [8]. Inkjet printing can be also efficiently exploited for the fabrication of chipless sensors [9]. Two main paradigms can be used to sense the change in the electromagnetic response due to external phenomena: time domain [10] or frequency domain [11] sensing. Frequency domain sensor seem to be the most promising option.

## II. FREQUENCY DOMAIN CHIPLESS SENSORS

Two examples regarding a frequency domain humidity sensor, based on a CIM are shown in Fig. 1. There, the CIM is realized by a thin dielectric layer and by silicon nanowires in the examples reported in Fig. 1a and in Fig. 1b, respectively.

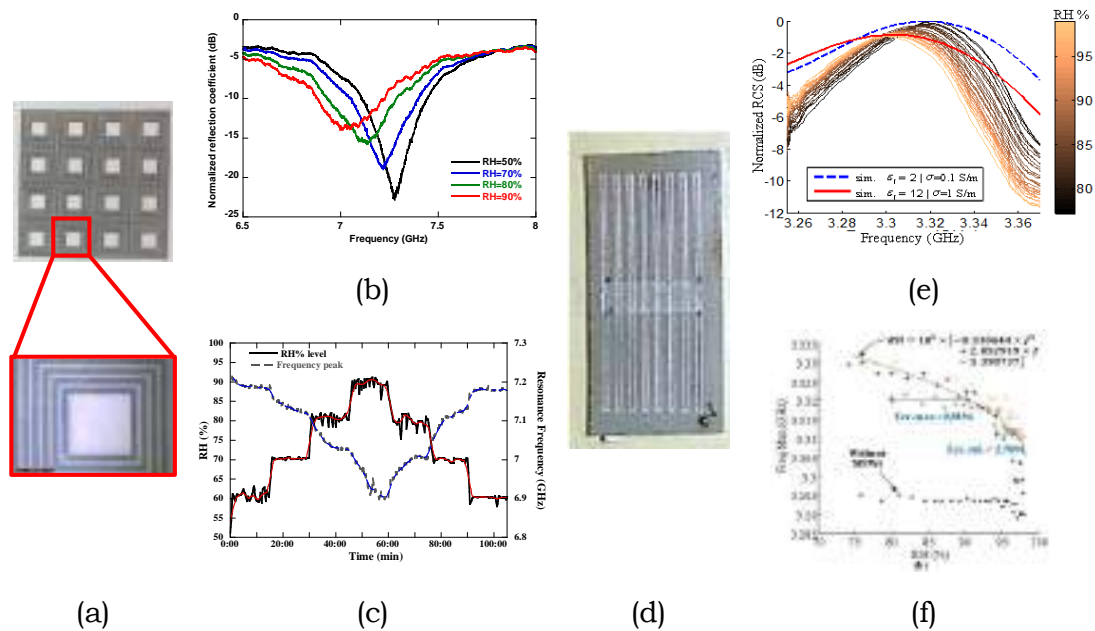


Fig. 1. An inkjet-printed humidity sensor based on the properties of periodic surfaces (a). Measured normalized reflection coefficient at four different humidity levels (b). Resonance frequency of the sensor as a function of the relative humidity level measured in a climatic chamber (c). A humidity sensor based on silicon nanowires (d). Measured normalized reflection coefficient at different humidity levels (e). Resonance frequency of the sensor as a function of the humidity level for three different sensors (f).

The sensor in Fig. 1a consist of a periodic pattern printed on a single-side coated transparency PET film (NB TP 3GU100 Mitsubishi paper)

placed on a grounded cardboard substrate of 3 mm [9]. The pattern is realized with a silver nanoparticle ink through a piezoelectric inkjet printer (Brother DCP-J152W). The paper substrate with the coating layer acts as a CIM, since it is sensitive to humidity variations. The variation of the properties of the thin layer leads to a resonance shift of the frequency response of the resonator. As shown in Fig.1b, a variation of the Relative Humidity (RH) level of the surrounding environment produces an alteration of the electric permittivity of the CIM with a consequent downshift of the deep nulls of the tag response in the frequency spectrum. The sensing mechanism of the tag is based on controlling RH variations through the frequency shift of the backscattered spectrum. This is due to the fact that the paper absorbs the moisture of the external environment, thus increasing its electrical permittivity. The characterization of the sensor was carried out in an ad-hoc designed climatic chamber consisting of a plastic box. The electromagnetic response of the tag was measured at the desired time intervals by a dual polarized horn (Flann DP240), connected to a two ports VNA. The humidity inside the box was controlled with a feedback system driven by a Matlab code. A commercial humidity sensor was used to monitor the RH level inside the box. This system was able to automatically control the RH level inside the box according to a humidity profile and a timetable chosen by the user. During the RH controlled cycle, the electromagnetic response of the chipless tag is collected at the predetermined rate. The RH level within the climatic chamber was increased from 60% to 90% in steps of 10% and then decreased. To test the moisture absorption time of the tag, each humidity level was kept constant for 15 minutes. The measurements of the tags were carried out at intervals of 10 seconds. In order to clearly visualize the shift of the resonance peak as a function of the variation of the RH level, the resonance frequency of the resonator with respect the observation time has been plotted in Fig.1c. In the same Fig.1c, the level of humidity inside the climatic chamber as a function of the observation time, is superimposed. It is apparent that a rapid variation of the resonance frequency is observed with the alteration of the RH level. The response time is in the order of a few seconds and the absorption of the humidity is evidently a reversible process.

To avoid the application of a CIM over the entire resonator, it is possible to place the functional material in the position where the electric field is maximum in the resonator, in order to maximize the frequency variation of the tag response [12]. An example of this second kind of sensors, where a single resonator is loaded with Silicon Nanowires, is depicted in Fig.1d. The variation of the tag response as a function of humidity changes is shown in the same figure. In order to assess the reproducibility of the fabrication process, a set of different resonators loaded with the same material has been characterized. Fig.1e shows the frequency shift of the resonance, measured with respect to the humidity level for three different samples of the sensor. It is shown that the maximum error in the estimation of the humidity level is 10 %.

### III. CONCLUSIONS

A synthetic description of the operating principles brief overview of chipless RFID sensor technology has been presented. Attention has been focused on frequency domain sensors.

### ACKNOWLEDGEMENTS

Work developed within the project funded by the European Union under the H2020 Programme, Call MSCA-RISE-2014 ‘Marie Skłodowska-Curie, Research and Innovation Staff Exchange (RISE)’, GA n. 645771.

### REFERENCES

- [1] “Monitor and Find Everything from the Internet - Wireless Sensor Tags.” [Online]. Available: <http://www.wirelesstag.net/index.html>. [Accessed: 18-Jun-2017].
- [2] J. Weiss, P. Takhistov, and D. J. McClements, “Functional Materials in Food Nanotechnology,” *J. Food Sci.*, vol. 71, no. 9, pp. R107–R116, Nov. 2006.
- [3] C. Di Natale *et al.*, “The exploitation of metalloporphyrins as chemically interactive material in chemical sensors,” *Mater. Sci. Eng. C*, vol. 5, no. 3, pp. 209–215, Feb. 1998.
- [4] F. Lorussi, W. Rocchia, E. P. Scilingo, A. Tognetti, and D. D. Rossi, “Wearable, redundant fabric-based sensor arrays for reconstruction of body segment posture,” *IEEE Sens. J.*, vol. 4, no. 6, pp. 807–818, Dec. 2004.
- [5] E. M. Amin, J. K. Saha, and N. C. Karmakar, “Smart Sensing Materials for Low-Cost Chipless RFID Sensor,” *IEEE Sens. J.*, vol. 14, no. 7, pp. 2198–2207, Jul. 2014.
- [6] B. Ando and S. Baglio, “Inkjet-printed sensors: a useful approach for low cost, rapid prototyping,” *IEEE Instrum Meas Mag*, vol. 14, no. 5, pp. 36–40, Oct. 2011.
- [7] S. Dey, J. K. Saha, and N. C. Karmakar, “Smart Sensing: Chipless RFID Solutions for the Internet of Everything,” *IEEE Microw. Mag.*, vol. 16, no. 10, pp. 26–39, Nov. 2015.
- [8] R. R. Fletcher and N. A. Gershenfeld, “Remotely interrogated temperature sensors based on magnetic materials,” *IEEE Trans. Magn.*, vol. 36, no. 5, pp. 2794–2795, Sep. 2000.
- [9] M. Borgese, F. Dicandia, F. Costa, S. Genovesi, and G. Manara, “An Inkjet Printed Chipless RFID Sensor for Wireless Humidity Monitoring,” *IEEE Sens. J.*, vol. PP, no. 99, pp. 1–1, 2017.
- [10] A. Lazaro, A. Ramos, D. Girbau, and R. Villarino, “Chipless UWB RFID Tag Detection Using Continuous Wavelet Transform,” *IEEE Antennas Wirel. Propag. Lett.*, vol. 10, pp. 520–523, 2011.
- [11] F. Costa, S. Genovesi, and A. Monorchio, “Chipless RFIDs for Metallic Objects by Using Cross Polarization Encoding,” *IEEE Trans. Antennas Propag.*, vol. 62, no. 8, pp. 4402–4407, Aug. 2014.
- [12] A. Vena, E. Perret, D. Kaddour, and T. Baron, “Toward a Reliable Chipless RFID Humidity Sensor Tag Based on Silicon Nanowires,” *IEEE Trans Microw Theory Techn*, vol. 64, no. 9, pp. 2977–2985, Sep. 2016.

# UHF RFID TAG DETECTION IN CYLINDRICAL WAVEGUIDES

A. Michel

- (1) Dipartimento di Ingegneria dell'Informazione, Università di Pisa  
via G. Caruso 16, 56122, Pisa  
[andrea.michel@iet.unipi.it](mailto:andrea.michel@iet.unipi.it)

## Abstract

*The performance of passive RFID tags operating at UHF band, in terms of reading range and read rate, are usually measured or calculated by assuming free-space propagation and local plane wave illumination conditions. In this paper, a practical scenario that does not meet the above assumptions has been analysed. In particular, the RFID signal propagation and tag detection inside a guiding structure has been here considered, where the electromagnetic wave impinging on the tag is a specific propagating mode related to guided structure size.*

**Index Terms** – Cylindrical structures, guided propagation, Radio Frequency Identification

## I. INTRODUCTION

Radio Frequency Identification (RFID) systems have been largely used for logistic, retail and pharmaceutical applications and they are typically subdivided into two main groups, on the basis of the operative frequency band: High Frequency (HF, 13.56MHz) and Ultra High Frequency (UHF, 865-928 MHz) RFID bands. HF RFID systems are employed for short-range applications (e.g. proximity identification and payments) and they are based on inductive coupling between coils. On the other hand, UHF RFID systems are used for both near-field and far-field applications such as localization, sensing and Item Level Tagging (ILT) applications [1], [2]. Generally, different performance parameters are used to estimate the tag detection by means of numerical results, so that the entire RFID system can be properly designed. As an example, the magnetic field distribution is typically considered for HF RFID systems, while the Power Transfer Efficiency and the Modulation Efficiency are among the key-parameters considered for UHF RFID systems [2]-[4]. It is worth mentioning that, in some specific scenarios, the RFID signal propagation model must be accurately defined in order to obtain a reliable tag detection estimation [3]-[6]. For instance, the ray model typically used for long-range UHF RFID systems can not be applied for near-field UHF RFID applications, since the main requirements are not satisfied [1].

In this framework, a particular application in which tag detection requires a specific model consists of tags placed inside closed structures that can be approximated with rectangular or cylindrical waveguides. This is the case of ventilation and sewage pipes shown in Fig. 1 which may be modeled with metallic waveguides [5]. For identification or

sensing purposes, a UHF RFID tag may be placed inside the pipes, attached to the internal surface. However, the tag is not illuminated by a plane wave, as typically considered for free-space applications, but the electric and magnetic fields assume a specific distribution on the basis of the pipe size and operating frequency, i.e. the propagating mode.

In this paper, the analysis concerns the detection of a dipole-like tag placed inside a cylindrical metal pipe. The issue of detecting RFID tags inside guided structures have been already addressed in the past [6], [7]. However, preliminary theoretical considerations supported by both numerical and measured results are here discussed to create a more accurate coupling and propagation model. Numerical results have been obtained by means of CST Microwave Studio®.

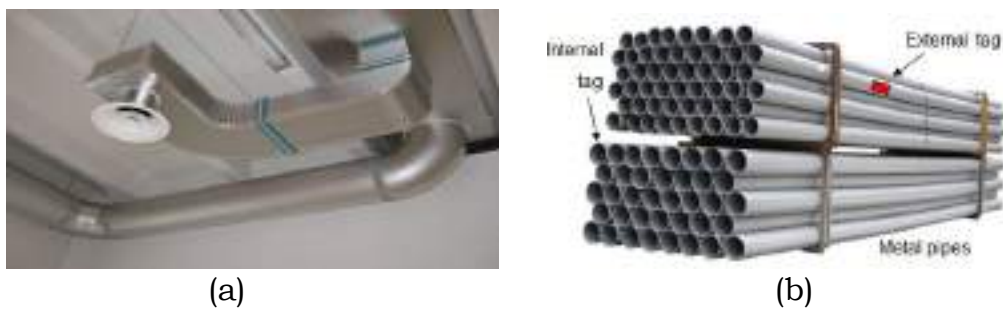


**FIG. 1** – (a) ventilation pipes may be considered as an example of circular and rectangular metal structures. (b) The UHF RFID tag can be attached to the metal pipe for identification or sensing purposes, inside or outside the pipe.

## II. NUMERICAL AND EXPERIMENTAL RESULTS

In Figure 2a, an example of circular waveguide is shown, where an Inlay UH100 (LAB-ID) tag is placed inside. Specifically, the electric field distribution on the transversal section of the guided structure is depicted at the frequency of 866.5MHz, which is the central frequency of the ETSI UHF RFID band (865-868 MHz). It is worth noting that the fundamental mode is excited, i.e. the TE<sub>11</sub>. The propagation of the fundamental mode in a cylindrical waveguide at ETSI UHF RFID band is allowed if the value of the radius  $a$  is between 101mm and 132mm. However, for higher values of  $a$ , at a fixed operating frequency band, higher order modes can propagate in the cylindrical structure, so changing the electric and field distribution on the transversal plane. For this analysis, a cylindrical metal structure with radius  $a=120\text{mm}$  and  $L=1000\text{mm}$  has been considered.

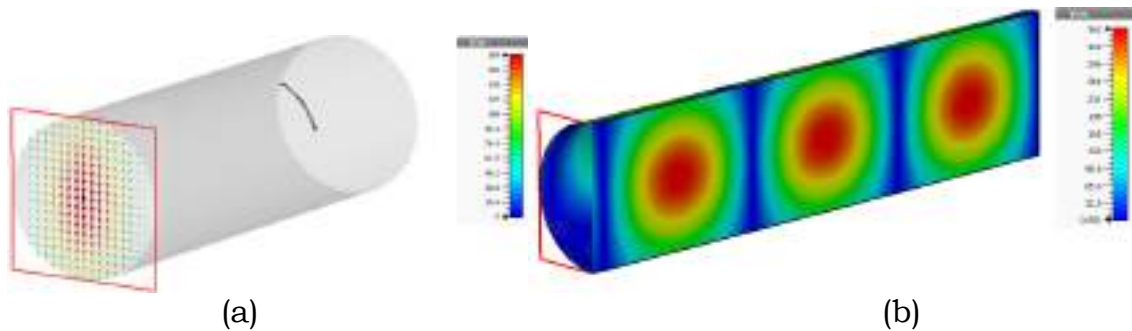


**FIG. 2** – (a) Approximated cylindrical pipe model used for the numerical analysis. (b) Electric field distribution on a longitudinal section when the cylindrical waveguide is terminated on a short circuit.

To model the tag detection inside a guided structure, preliminary tests have been carried out. In particular, to demonstrate that the power collected by a dipole-like UHF RFID tag is proportional to the electric field distribution inside a waveguide, the cylindrical structure has been terminated on a shorting metallic plate, thus obtaining a stationary wave distribution along the longitudinal axis of the waveguide (Fig. 2b). By means of a full-wave analysis, the simulated coupling (S12 parameter) between an UH100 Inlay (LabID) tag model and the fundamental mode (TE11) has been evaluated as a function of the distance of the tag antenna from the short-circuit termination. As expected, a typical stationary distribution is obtained, as represented in Fig. 3.

This result has been experimentally validated by placing a UH100 Inlay (LabID) tag inside a metal cylindrical structure with radius  $a=120\text{mm}$ , at a distance  $D$  from the shorting metal plate (Fig. 3). The Impinj Speedway R420 reader has been used to collect Received Signal Strength Indicator (RSSI) values by increasing the distance  $D$ .

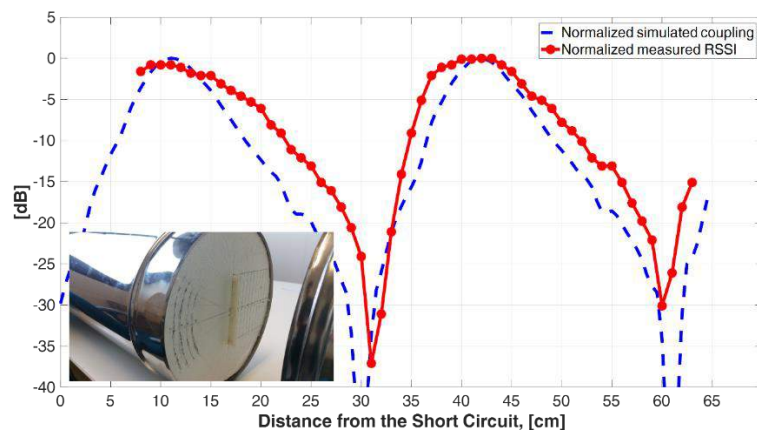


**FIG. 3** – Normalized simulated coupling between the fundamental mode and the dipole-like tag (dashed curve) and normalized measured RSSI (markers) as a function of the distance  $D$ .

The simulated coupling (S12 parameter) and the measured RSSI values are plotted in Fig. 3 as a function of the distance  $D$ . The two curves are

in a good agreement, also with respect to the electric field distribution shown in Fig. 2b. It should be noted that the distance between two consecutive minima of the tag-mode coupling is near to 30cm, which is close to half the guided wavelength of the fundamental mode propagating in the pipe. This confirms that the signal propagation inside metal structures can be used to create an accurate theoretical model of the detection of UHF RFID tags when placed inside those objects approximated by guiding structures.

### III. CONCLUSION

The detection of UHF RFID tags can be estimated by means of signal propagation models, typically based on ray models. However, in specific scenarios, other models must be taken into account. As an example, the detection of a tag placed inside metal structures approximated by waveguides or coaxial cables is strictly related to the propagating mode, which, in turn, depends on the geometrical characteristics of the guided structure. Aims of this work is to create an exhaustive model to predict the tag detection when placed inside a cylindrical waveguide.

### REFERENCES

- [1] A. Michel, P. Nepa, X. Qing and Z.-N. Chen, "Considering High-Performance Near-Field Reader Antennas: Comparisons of Proposed Antenna Layouts for Ultrahigh-Frequency Near-Field Radio-Frequency Identification", *IEEE Antennas and Propagation Magazine*, vol. 60, no. 1, pp. 14-26, Feb. 2018.
- [2] A. Michel, M. Rodriguez-Pino, and P. Nepa, "Reconfigurable modular antenna for near-field UHF RFID smart point readers," *IEEE Transactions on Antennas and Propagation*, vol. 65, no. 2, pp. 1-9, Feb. 2017
- [3] A. Michel and P. Nepa, "UHF-RFID desktop reader antennas: Performance analysis in the near-field region," *IEEE Antennas and Wireless Propagation Letters*, vol. 15, pp. 1430-1433, Dec. 2015
- [4] A. Buffi, A. Michel, P. Nepa, and G. Manara, "Numerical analysis of wireless power transfer in near-field UHF-RFID systems" *Wireless Power Transfer*, 1-12., 2017
- [5] P. V. Nikitin, D. D. Stancil, A. G. Cepni, O. K. Tonguz, A. E. Xhafa and D. Brodtkorb, "Propagation model for the HVAC duct as a communication channel," *IEEE Transactions on Antennas and Propagation*, vol. 51, no. 5, pp. 945-951, May 2003
- [6] A.S. Andrenko. "EM modeling of Metal Pipe Based UHF RFID Tags Activated by R/W Antenna", 2012 International Conference on Electromagnetics in Advanced Applications - ICEEA. Cape Town, South Africa.
- [7] D. D. Arumugam and D. W. Engels, "Characterization of RF Propagation in Helical and Toroidal Metal Pipes for Passive RFID Systems," 2008 IEEE International Conference on RFID, Las Vegas, NV, 2008, pp. 269-276.

# ROTATION-INSENSITIVE RF-TO-DC LINK FOR IPT IMPLANTS

Alex Pacini<sup>(1)</sup>, Francesca Benassi<sup>(2)</sup>

<sup>(1)</sup> Department of Electrical, Electronic and Information Engineering  
“Guglielmo Marconi”, University of Bologna Viale Risorgimento 2,  
Bologna  
[francesca.benassi9@unibo.it](mailto:francesca.benassi9@unibo.it)

## Abstract

*This paper proposes the design and experimental validations of a 6.78 MHz IR-WPT with one conformal transmitter (Tx) and a couple of receiver (Rx) coils, suitable for powering implantable devices. This work is part of a research paper which will be presented at the International Microwave Symposium (IMS) 2018 [1]. The Rx coils are arranged in such a way that quasi-constant dc-output voltage and conversion efficiency are obtained, regardless of the receiver rotation, with respect to the transmitter. A 3-D miniaturized receiver, consisting of two elliptical coils wrapped around a capsule and orthogonal to each other, is faced to a conformal transmitter designed to maximize the magnetic flux in the receiver region. In order to avoid dark areas for energy transfer, due to unknown capsule rotations, each Rx coil is connected to one rectifier and the dc output ports are series-connected.*

**Index Terms** – Implantable device, IR-WPT, Inductive Powering, Class-E rectifier.

## I. INTRODUCTION

In recent years, the problem of wireless powering implants has been addressed with increasing interest [2], but several issues related to system reliability are still under investigation, for both near-field (reactive) and far-field (radiative) implementations. In this study, a near-field inductive powering system at 6.78MHz for an implanted capsule is designed with the goal of being insensitive to the Rx rotation, which is usually unknown. Previous attempts to solve this problem are available in the literature [3], but miniaturization constraints, necessary for implantable devices, are not addressed.

High efficiencies have been demonstrated in [4], in particular for short distances between the coils. However, most proposed links are optimized for static and known positions, rarely taking into account possible movements or misalignments. Indeed, when the coils rotate, the shared flux varies significantly and thus the output power and voltage.

To realize almost constant output dc- voltage and power, for any possible receiver rotation, a 3-D configuration at the Rx side is adopted. It consists of two orthogonal coils wrapped around an ellipsoid plastic capsule; each one is connected to its own rectifier circuit and their dc outputs are

series-connected. In this way a reduced output voltage ripple is obtained for any possible Rx rotation, ensuring continuous powering of the implant. The system design, from the Tx coil to the Rx dc-load, is carried out by means of EM/nonlinear co-simulation. The experimental results, firstly performed for several distances in open air, confirm that the proposed solution allows to remotely provide the minimum required dc-power and voltage to energizing the implantable device, independently of its rotation with respect to the transmitter.

## II. PROJECT IMPLEMENTATION

A large transmitter is optimized to maximize the shared flux, and thus the  $kQ$  [5], in the direction of the miniaturized Rx receiver axis location. The optimized geometrical parameters are:  $h$ ,  $w_1$ ,  $w_2$  and are chosen in such a way to obtain a conformal coil adaptable to be lean on the human body, for example the abdomen, to energize an implantable device in the digestive tract. The Rx side consists of a 3-D structure with orthogonal coils wrapped around an ellipsoid plastic capsule of fixed dimensions (see Fig. 1(b)).

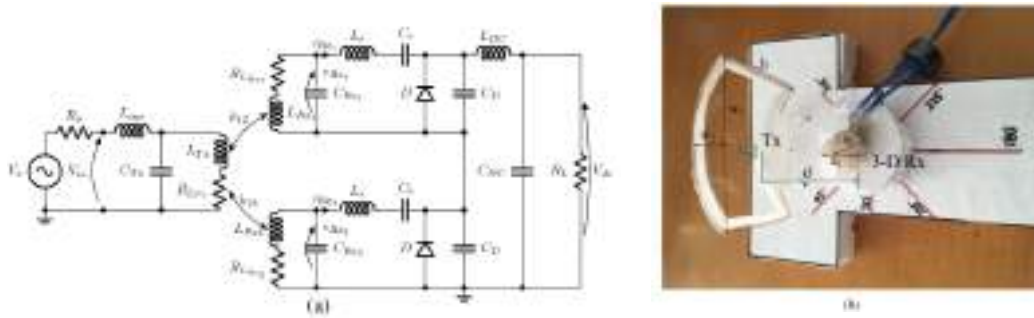


**FIG. 1** – (a), circuit equivalent of the RF-to-dc link; (b), picture of the realized prototype. Two orthogonal coils are wrapped around an ellipsoid plastic capsule with major and minor axes of  $a_1 = 24\text{mm}$  and  $a_2 = 18\text{mm}$ , respectively. The other dimensions are:  $h = 52\text{mm}$ ,  $w_1 = 78.54\text{mm}$ ,  $w_2 = 12\text{mm}$  and  $d = 5\text{ cm to } 7\text{ cm}$  with a  $1\text{ cm}$  step.

From the EM simulations of a set of RF-to-RF links, one for any possible rotation (a  $0^\circ$  rotation corresponds to one coil facing the transmitter and the other one orthogonal to it), the associated equivalent circuits parameters of Fig. 1(a), including the losses, are derived and are listed in Table I. While the self-inductances are unchanged, the coupling coefficients clearly show the different operating conditions of each Rx coil with respect to its position: for a  $0^\circ$ -rotation the  $k_{12}$  is maximum but  $k_{13}$  is negligible, while for a  $90^\circ$ -rotation the coupling coefficients are almost interchanged. A first idea could be to series connect the two Rx coils, but this would simply shift the problem of zero-coupling to other rotations, where  $k_{12}$  and  $k_{13}$  have the same absolute value with opposite signs,

leading to an almost zero-coupling. This is shown in Fig. 2 where the coupling coefficients of the series connected coils [6], are plotted against rotation for several distance  $d$ .

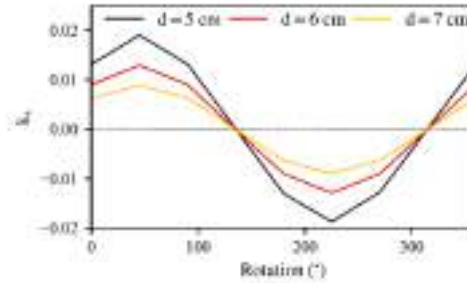


**FIG. 2** – Coupling coefficients values of the RF-to-RF link for various rotations.

A suitable receiver topology can be realized by connecting each Rx coil with its own rectifier and by connecting in series the dc outputs. In this way, large output voltage variations and zero-zones are avoided. A class-E rectifier, shown in Fig. 1(a), is connected to the Rx coil through an LC filter, in order to guarantee a sinusoidal input current. The rectifiers outputs share the same low-pass filter.

A first prototype, resulting from the multi-circuit optimization, that is from the Tx input port to the dc output, is built and a photo is reported in Fig. 1(b). The final component values are listed in Table I: the resistances representing the coils losses are verified using an RLC meter.

**TABLE I – PROTOTYPE COMPONENTS VALUE**

$L_{T_{in}}$	140 nH	$C_{R2}$	10 nF	$D$	HSMS-2822
$R_{L_{T_{in}}}$	1 $\Omega$	$R_{L_{T_{2}}}$	50 m $\Omega$	$C_D$	50 pF
$L_{P2}$	141 nH	$R_{L_{R1}}$	35 m $\Omega$	$L_{DC}$	50 $\mu$ H
$C_{P2}$	3.9 nF	$R_{L_{R2}}$	35 m $\Omega$	$R_{L_{DC}}$	2 $\Omega$
$L_{R1}$	53.2 nH	$L_r$	140 nH	$C_{DC}$	20 $\mu$ F
$L_{R2}$	55.1 nH	$R_{L_r}$	1 $\Omega$	$R_L$	320 $\Omega$
$C_{R1}$	10.3 nF	$C_r$	3.9 nF	$R_s$	50 $\Omega$
		$f$	6.78 MHz		

Finally, the  $\eta_{tot}$ , defined as in [7], is tested over rotations for various distance  $d$  and the results are displayed in Fig.3.

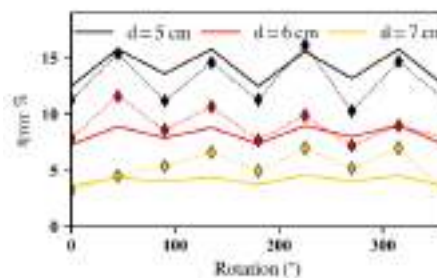


**FIG. 3** –  $\eta_{tot}$  predicted and measured for increasing Tx-Rx distances: diamonds are measurements ( $V_s = 10V$ ).

The design and experimental validation of a 6.78 MHz IRWPT, suitable for implantable applications, has been presented. A couple of miniaturized Rx coils are wrapped around a capsule orthogonal to each other, while a large conformal transmitter (Tx) is used. To solve the problem of dark zones, occurring when the capsule rotation is casual, the received power from each coil is rectified separately and the dc outputs are combined in series. The validation of the prototype, optimized for a reference Tx-to-Rx of 5 cm, is carried out in open air, for different distances and it is shown that a voltage source of 10V is sufficient to remotely provide the dc power to activate an implantable device.

#### ACKNOWLEDGEMENT

The authors would like to thank Professor Alessandra Costanzo and Professor Diego Masotti for their valuable suggestions and supervision throughout the research.

#### REFERENCES

- [1] A. Pacini, F. Benassi, D. Masotti and A. Costanzo, "Design of a RF-to-DC link for in-body IR-WPT with a capsule-shaped Rotation-insensitive receiver", *International Microwave Symposium (IMS)*, June 2018 [Accepted Paper].
- [2] K. Agarwal, R. Jegadeesan, Y.-X. Guo, and N. V. Thakor, "Wireless power transfer strategies for implantable bioelectronics: Methodological review," *IEEE Reviews in Biomedical Engineering*, pp. 1–1, 2017.
- [3] G. Joung and B. Cho, "An energy transmission system for an artificial heart using leakage inductance compensation of transcutaneous transformer," in *PESC Record. 27th Annual IEEE Power Electronics Specialists Conference*. IEEE, 1996.
- [4] R.-F. Xue, K.-W. Cheng, and M. Je, "High-efficiency wireless power transfer for biomedical implants by optimal resonant load transformation," *IEEE Transactions on Circuits and Systems I: Regular Papers*, vol. 60, no. 4, pp. 867–874, apr 2013.
- [5] T. Ohira, "The kQ product as viewed by an analog circuit engineer," *IEEE Circuits and Systems Magazine*, vol. 17, no. 1, pp. 27–32, 2017.
- [6] A. Pacini, F. Mastri, R. Trevisan, D. Masotti, and A. Costanzo, "Geometry optimization of sliding inductive links for position-independent wireless power transfer," in *IEEE MTT-S International Microwave Symposium (IMS)*, May 2016.
- [7] A. Costanzo, M. Dionigi, D. Masotti, M. Mongiardo, G. Monti, L. Tarricone, and R. Sorrentino, "Electromagnetic Energy harvesting and Wireless Power Transmission: A Unified Approach," *Proceedings of the IEEE*, vol. 102, no. 11, pp. 1692–1711, nov 2014.

# FOCUSING THROUGH CYLINDRICAL LEAKY WAVES

Davide Comite and Walter Fuscaldo

Department of Information Engineering, Electronics, and  
Telecommunications, “Sapienza” University of Rome, Via  
Eudossiana, 18, 00184 Rome, Italy  
comite@diet.uniroma1.it, fuscaldo@diet.uniroma1.it

## Abstract

*Bessel-beam launchers with wideband features are required to generate focused pulses in the near field. In this work, we demonstrate the capabilities of backward cylindrical leaky waves, supported by a planar wideband device, of generating nondiffracting beams and pulses at microwave frequencies. The structure consists of a metallic radial waveguide whose upper plate is replaced by an annular metal strip grating. The period of the strips is designed so that the structure supports a fast backward spatial harmonic, as required to focus a Bessel beam in the near field. Experimental results confirm the wideband focusing features of this class of devices, as well as the unprecedented capability of generating X-waves in the microwave range.*

**Index Terms** – Bessel beams, leaky waves, near-field focusing, X-waves.

## I. INTRODUCTION

In radiometry, medical imaging and diagnostics as well as secure communications and military applications, short microwave pulses can be used to improve the inherently low resolution dictated by the operating wavelength. In spite of their relatively large spectral content, such pulses commonly suffer from diffractive spreading as they propagate away from the source. Therefore, the generation of focusing pulses would allow for the design of more efficient devices.

In this context, nondiffracting waves [1] have recently gained much attention, since they represent solutions of Helmholtz equation which do not undergo diffractive spreading in the near-field region. As a matter of fact, the nondiffractive behavior is maintained up to a distance commonly known as the nondiffractive range (NDR) [1]. The most known representatives of nondiffracting waves are Bessel beams and X-waves, being the latter obtained through polychromatic superposition of the former. Along with the peculiar nondiffractive nature, Bessel beams exhibit a transversely localized character (see Fig. 1), while X-waves are longitudinally localized. Even more interestingly, both Bessel beams and X-waves possess the so-called self-focusing property (i.e., the capability to reconstruct themselves if an obstacle obstructs their axis of propagation [1]).

While Bessel beams have been extensively generated both in the very high (i.e., optics) and lower (i.e., mm-waves and microwaves) frequency range, the microwave generation of X-waves is substantially unexplored.

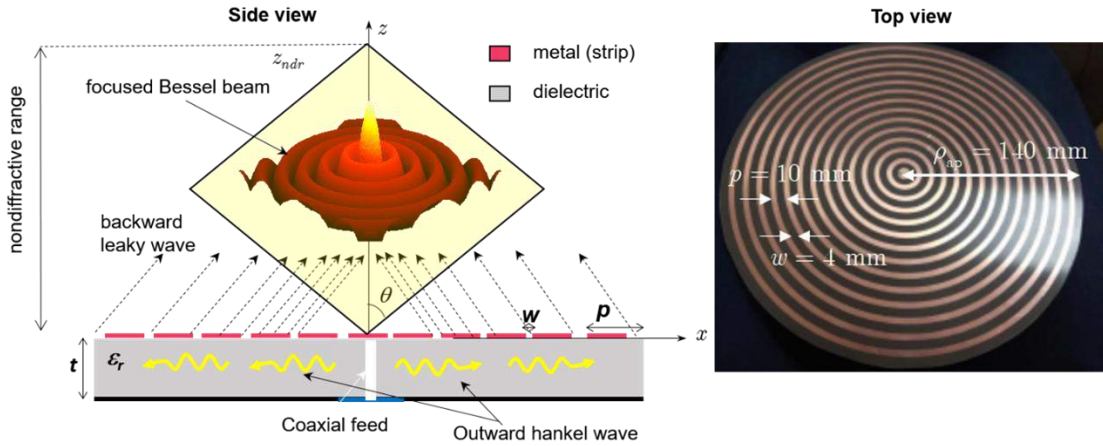


**FIG. 1** – (Left) Ray interpretation of the focusing capabilities of a radially-periodic leaky-wave antenna. (Right) Top view of the fabricated prototype.

This is mainly due to the scarce realizations of wideband Bessel-beam devices in the microwave range (see, e.g., [2, 3] and refs. therein).

In this work, we propose a novel planar radiator, based on low-cost commercial components and fed by a simple 50-Ohm coaxial probe. The structure is designed to support a backward cylindrical leaky wave capable of efficiently generating Bessel beams from 15 GHz to 21 GHz, thus showing an operating bandwidth greater than 30%. A portion of this fractional bandwidth is then used to generate a focusing pulse. A thorough theoretical analysis allows for designing the device with almost arbitrary focusing features. Experimental results obtained by means of a manufactured prototype are presented to corroborate the concept.

## II. FOCUSING FEATURES OF BACKWARD CYLINDRICAL LEAKY WAVES

The radially periodic leaky-wave antenna (RP-LWA) has been shown to be a simple and low-cost solution for the generation of focused beams within a wide frequency band [3]. Indeed, as extensively discussed in [2], backward cylindrical leaky waves (CLWs) allows for generating both Bessel beams and X-waves.

A ray interpretation can be used to explain the focusing capabilities of backward CLWs. As shown in Fig. 1, when a RP-LWA of radius  $\rho_{ap}$  is excited in the center, an outward Hankel wave propagates in the structure. If the grating is designed so that the  $n=-1$  Floquet harmonic is excited, the backward nature of the leaky wave allows for recovering the inward Hankel-wave aperture distribution, which is required to focus energy along the propagating axis [2, 3]. Interestingly, the value of the phase constant ( $\beta_{-1}$ ) of the backward CLW is related to the axicon angle  $\theta_0$  through the relation  $\sin\theta_0 = |\beta_{-1}|/k_0$ , with  $k_0 = 2\pi/\lambda$ ,  $\lambda$  being the operating wavelength. The axicon angle (and, in turn, the phase constant of the CLW) is an extremely important design parameter governing the spot-size  $S_\rho$  and the nondiffractive range of the Bessel beam, which are given by the relations  $S_\rho = 4.81\lambda\text{csc}\theta_0$ , and  $z_{ndr} = \rho_{ap}\cot\theta_0$ , respectively.

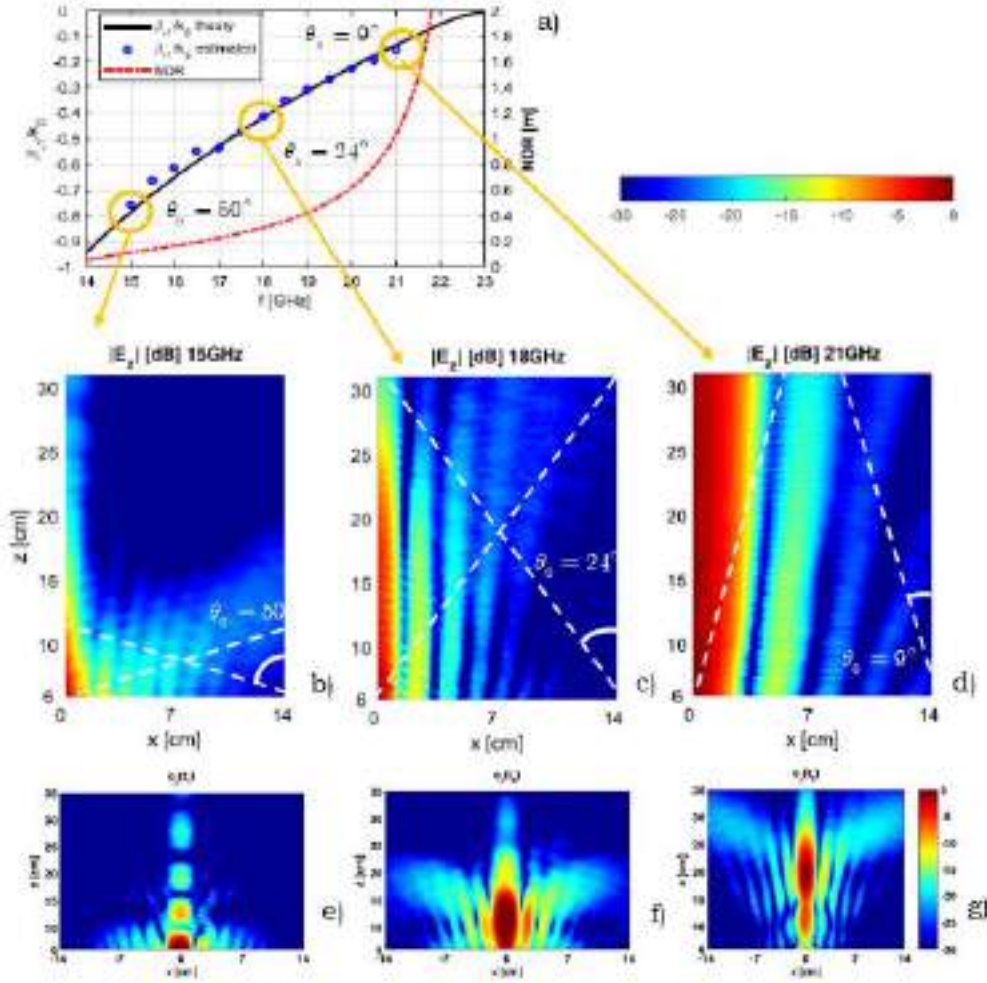


**FIG. 2** – (a) Numerical (black line) and estimated (from experimental data, blue circles) phase constant and NDR (red line) of the CLW. (b)-(d) Measured 2-D near-field maps of  $|E_z|$ . (e)-(g) Intensity of the focused pulse at three different time instants.

### III. DESIGN OF THE WIDEBAND BESSEL-BEAM RADIATOR

As mentioned, a backward CLW can be excited by a RP-LWA. We set here the period  $p$  for the metal strip grating equal to 10 mm and a slot width  $w = 4$  mm. To avoid higher-order modes propagation, the thickness  $t$  of the dielectric slab ( $\epsilon_r=2.2$ ) is set to 3.14 mm. An aperture radius  $\rho_{ap}=14$  cm is chosen to grant an efficiency around 94% [2, 3].

A dispersive analysis, developed by means of an in-house efficient method-of-moments code, is used to characterize the backward CLW supported by the RP-LWA [3], which shows a normalized phase constant  $\beta_1/k_0$  of about -0.4 at 18 GHz (see Fig.2 (a)). In the frequency range 15-21 GHz, the normalized phase constant  $\beta_1/k_0$  changes from -0.15 to -0.75, corresponding to an axicon angle varying from  $\theta_0 = 50^\circ$  to  $9^\circ$  (see Fig. 2(a)). Since the axicon angle is frequency-dispersive (cone dispersion) the  $z_{ndr}$  and the  $S_\rho$  are also expected to change with frequency, as confirmed by the experimental results reported next.

#### IV. EXPERIMENTAL RESULTS

A prototype has been fabricated and characterized (see Fig. 1). Near-field 2-D maps of both the longitudinal and transverse (not shown) components of the radiated electric field over the  $xz$  plane have been measured up to a distance of 31 cm, corresponding to the theoretical  $z_{\text{ndr}}$  at 18 GHz (see Figs. 2(b)-(d)). Experimental results are in good agreement with the numerical dispersion analysis, confirming the expected frequency-dispersive character of the backward leaky wave. All the components of the field (not reported here for space limitations) presents a well-defined nondiffracting behavior, following, within the NDR, the radial profile predicted from the relevant Bessel function [3].

The wideband capability of the device ( $S_{11}$  reported in [3]), can profitably be used to generate an X-wave, i.e., a localized field distribution along both the transverse and the longitudinal axes. The 2-D maps reported in Figs. 2(e)-(g) show the pulse obtained by using a fractional bandwidth of 10% within the available 34% impedance bandwidth. Three different time instants are considered, equal to 0.27, 0.8, and 1.3 ns (see Figs. 2(e), 2(f) and 2(g), respectively). As clearly visible, the pulse maintains its collimated behavior while propagating away from the launcher aperture. As rigorously outlined in [2], larger fractional bandwidths allow for improving the localized nature of the energy over the longitudinal  $z$ -axis. This aspect and further insights on the peculiar nondiffracting features of the leaky-wave-based pulse, supported by an extensive experimental campaign, will be presented at the conference.

#### V. CONCLUSION

A radially-periodic leaky-wave antenna fed by a simple source, supporting a fast backward cylindrical leaky wave, has been proposed for generating nondiffracting beams over a wide bandwidth. Thanks to the traveling-wave nature of the approach, the capabilities of this class of devices of generating localized pulses (i.e., X-waves) have been experimentally demonstrated for the first time in the microwave range. The use of larger fractional bandwidths will enable the generation of extremely short nondiffractive pulses at microwaves, a feature of paramount importance that can open unprecedented possibilities for a wide class of applications.

#### REFERENCES

- [1] H. E. Hernandez-Figueroa, M. Zamboni-Rached, and E. Recami, "Nondiffracting Waves," John Wiley & Sons, 2013.
- [2] W. Fuscaldo, D. Comite, A. Boesso, et al., "Focusing leaky waves: A class of electromagnetic localized waves with complex spectra," *Phys. Rev. App.*, in press, 2018.
- [3] D. Comite, W. Fuscaldo, S. K. Podilchak, et al. "Radially Periodic Leaky-Wave Antenna for Bessel-Beam Generation over a Wide Frequency Range," *IEEE Trans. Antennas Propag.*, in press, 2018.

# SPATIAL CONFINEMENT OF LOCALIZED BEAMS AND PULSES FOR NEAR-FIELD FOCUSING APPLICATIONS AT MILLIMETER WAVES

W. Fuscaldo<sup>(1)</sup> and S. C. Pavone<sup>(2)</sup>

<sup>(1)</sup> Department of Information Engineering, Electronics and Telecommunications (DIET), Sapienza University of Rome, 00184 Rome, Italy, [walter.fuscaldo@uniroma1.it](mailto:walter.fuscaldo@uniroma1.it).

<sup>(2)</sup> Department of Information Engineering and Mathematics (DIISM), University of Siena, 53100 Siena, Italy, [santi.pavone@unisi.it](mailto:santi.pavone@unisi.it).

## Abstract

*Localized beams and pulses, such as Bessel beams and X-waves exhibit remarkable focusing features in the near-field region. We discuss here novel figures of merit for evaluating spatial resolutions of these limited-diffractive, limited-dispersive solutions of wave equation. Specific attention is devoted to the design of planar millimeter-wave launchers, thoroughly addressing the radial wavenumber dispersion that notably affects the propagation of such pulses. The presented results can help in the application-oriented design of X-wave launchers in the microwave and the millimeter-wave range.*

**Index Terms** – Bessel beams, localized pulses, X-waves, millimeter waves, near-field focusing.

## I. INTRODUCTION

In applications such as wireless power transfer, chip-to-chip communications, medical imaging, just to mention a few, it is worth to efficiently focus energy at millimeter waves to benefit of both their non-ionizing character and their short wavelength.

In this context, localized waves, especially Bessel beams and their polychromatic counterpart, i.e., X-waves, are gaining increasing attention in the millimeter-wave community due to their remarkable focusing features [1]. In optics, several designs of Bessel-beam and X-wave launchers have been proposed, and the first experimental realizations date back to the end of the '80s and the end of the '90s, respectively (see [1] and Refs. therein).

However, Bessel beams with different polarizations have been experimentally generated only few years ago (see, e.g., [2-4]), while the first experimental evidence of X-waves in the microwave range has been reported few months ago [5]. Unfortunately, in the millimeter-wave range possible realizations are currently under investigation [6]. One of the main reasons for this temporary lack is due to the non-negligible wavenumber dispersion that notably affects any microwave radiator based on radial waveguides [6]. Indeed, the almost negligible wavenumber dispersion exhibited by the device presented in [5] is paid at the expense of a bulky non-planar design, based on a conical dielectric lens. Conversely, the possibility to develop fully-planar, low-profile near-

field focusing systems would represent a technological breakthrough in millimeter-wave applications. In the following, we will show that, under precise assumptions, such devices can be profitably designed.

## II. THEORETICAL ASPECTS

X-waves can be obtained as a spectral superposition of Bessel beams with the same axicon angle  $\theta$  [1] over a certain frequency bandwidth  $\Delta\omega$  (throughout the paper, we consider only X-waves with a uniform frequency spectrum, without loss of generality).

Specifically, Bessel beams are localized only along the transverse axis and maintain their transverse spot size  $S_\rho$  up to the non-diffractive range  $z_{\text{ndr}} = \rho_{\text{ap}} \cot \theta$  [1], where  $\rho_{\text{ap}} = d_{\text{ap}}/2$  is the aperture radius. In addition, X-waves are also localized along the longitudinal propagating axis (see Fig. 1). However, the longitudinal spot size  $S_z$  is narrow as long as a considerable fractional bandwidth (FBW) is guaranteed [6]. Therefore, to obtain a focused X-wave, an ideal X-wave launcher must show a weakly-dispersive behavior in the frequency band of interest. This requirement is fulfilled either by radial line slot array (RLSA), or by periodic leaky radial waveguides (PLRW) as recently shown in [4] and [7], respectively.

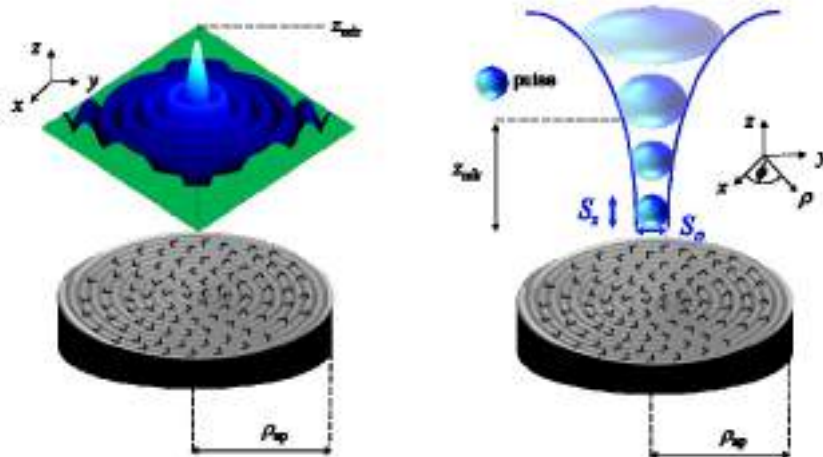


**Fig. 1** – A radial waveguide is able to generate Bessel beams over a wide frequency range. When it is fed by a monochromatic (resp. polychromatic) source, the device generates transversely localized Bessel beams (resp. localized pulses in both longitudinal and transverse directions).

## III. CONFINEMENT CRITERION

As shown in [3], when an X-wave launcher exhibits a weakly-dispersive behavior, the radial and longitudinal spot-sizes of the resulting X-wave are still well-approximated by the ideal, non-dispersive case. Following the theoretical analysis developed in [3], we introduce the longitudinal  $C_z$  and the transverse  $C_\rho$  confinement ratios as the ratios between  $S_\rho$  and  $d_{\text{ap}}$ , and  $S_z$  and  $z_{\text{ndr}}$ , respectively. Then, by using also the assumptions of

limited wavenumber dispersion and uniform frequency spectrum, closed-form expressions for the confinement ratios are obtained, namely

$$C_\rho = \frac{j_{0,1} \csc \theta}{2\pi(\rho_{ap}/\lambda)}, \quad C_z = \frac{2 \sin \theta}{\cos^2 \theta \text{FBW}(\rho_{ap}/\lambda)}, \quad (1)$$

where  $j_{0,1}=2.405$  is the first null of zeroth-order Bessel function of the first kind, and  $\lambda$  is the operating wavelength. Hence, we define the following figure of merit, as a suitable measure of the overall confinement of an X-wave

$$C_{\rho z} = \begin{cases} 1 & \text{if } \max(C_z, C_\rho) > 1 \\ C_\rho \cdot C_z & \text{elsewhere.} \end{cases} \quad (2)$$

The resulting X-wave will be localized along both the transverse and the longitudinal axis if and only if  $C_{\rho z} < 1$ . Furthermore, analytical expressions (not shown here for brevity) to obtain the boundaries for either only transverse or only longitudinal confinement can easily be found by requiring  $C_\rho$  and  $C_z$  less than 1, respectively.

#### IV. NUMERICAL RESULTS

In Fig. 2(a),  $C_{\rho z}$  is represented as a 2D function of  $\theta$  (over the  $y$ -axis) and  $\rho_{ap}/\lambda$  (over the  $x$ -axis), assuming FBW=20%. Such a bandwidth is easily achieved by radial waveguides [6,7]. The dark region represents operating points where the pulse will not result confined, whereas the yellow lines define the boundaries for the only transverse and only longitudinal confinement.

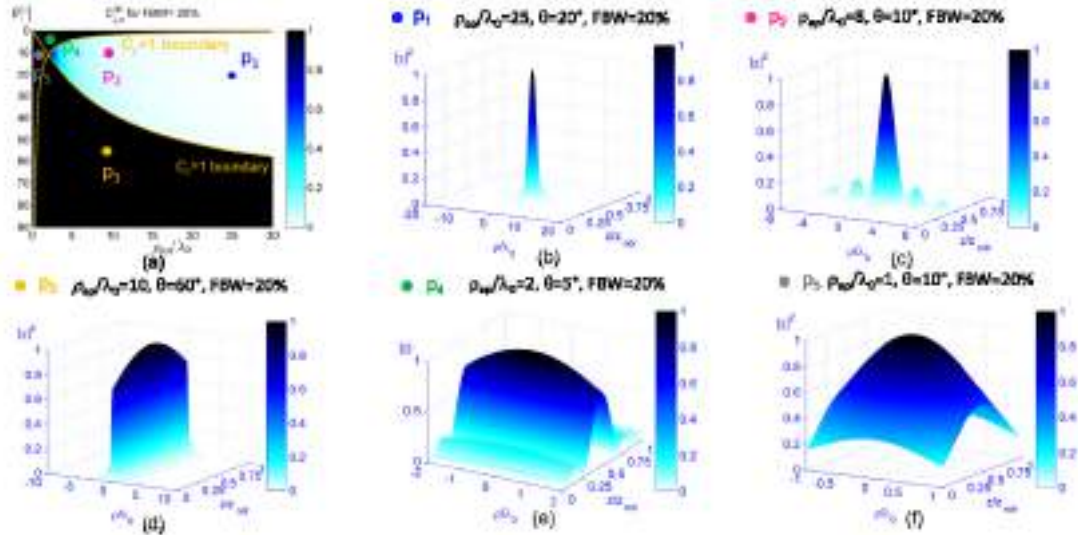


**FIG. 2** – (a)  $C_{\rho z}$  as a 2D function of  $\theta$  and  $\rho_{ap}/\lambda$ , assuming a fractional bandwidth of 20%. (b)-(f) Intensity of the resulting X-wave with parameters as indicated by the respective labels, i.e, p1, p2, p3, p4, p5.

By performing a numerical simulation, colored dots on the contour plot in Fig. 2(a), labelled as  $p_1$ ,  $p_2$ ,  $p_3$ ,  $p_4$ ,  $p_5$  are representatives of X-waves generated with an FBW=20%.

As shown in Fig. 2(b)-(f), at each point of the contour plot of Fig. 2(a) an X-wave satisfying the expected confinement conditions is associated. In particular, pulses in  $p_1$  and  $p_2$  (see Figs. 2(a)-(b)) are confined on both directions, since they are obtained with parameters in the light region of Fig. 2(a), whereas pulses in  $p_3$  and  $p_4$  are confined only along the transverse and longitudinal directions (see Figs. 2(d) and 2(e)), respectively. Finally, a pulse in  $p_5$  (see Fig. 2(f)) is not confined at all, since it lies in the dark region and below both the boundaries of transverse and longitudinal confinements.

## I. CONCLUSION

A useful figure of merit has been derived in analytical form to suitably establish the confinement properties of X-waves. The validity of the proposed theoretical analysis is corroborated by numerical simulations, and allows for defining precise guidelines for the design of fully-planar millimeter-wave radial waveguides fed by polychromatic sources. These devices are expected to represent a technological breakthrough in near-field focusing applications in the millimeter-wave range.

## REFERENCES

- [1] H. E. Hernández-Figueroa, M. Zamboni-Rached, and E. Recami, *Nondiffracting Waves*, John Wiley & Sons, 2013.
- [2] M. Ettorre, S. M. Rudolph, and A. Grbic, "Generation of propagating Bessel beams using leaky-wave modes: experimental validation," *IEEE Trans. Antennas Propag.*, vol. 60, no. 6, pp. 2645-2653, Jun. 2012.
- [3] S. C. Pavone, M. Ettorre, and M. Albani, "Analysis and design of bessel beam launchers: Longitudinal polarization," *IEEE Trans. Antennas Propag.*, vol. 64, no. 6, pp. 2311-2318, Jun. 2016.
- [4] S. C. Pavone, A. Mazzinghi, A. Freni, and M. Albani, "Comparison between broadband Bessel beam launchers based on either Bessel or Hankel aperture distribution for millimeter wave short pulse generation," *Optics Express*, vol. 25, no. 16, pp. 19548-19560, Aug. 2017.
- [5] N. Chiotellis, V. Mendez, S. M. Rudolph, and A. Grbic, "Experimental demonstration of highly localized pulses (X waves) at microwave frequencies," *Phys. Rev. B*, vol. 97, no. 8, 085136, Feb. 2018.
- [6] W. Fuscaldo et al., "Analysis of limited-diffractive and limited-dispersive X-waves generated by finite radial waveguides," *J. App. Phys.*, vol. 119, no. 19, 194903, May 2016.
- [7] W. Fuscaldo et al., "Focusing leaky waves: A class of electromagnetic localized waves with complex spectra," *Phys. Rev. App.*, in press, 2018.

## **ADDITIVE MANUFACTURING OF HIGH PERFORMANCES FILTERS**

G. Addamo<sup>(1)</sup>, O.A. Peverini<sup>(1)</sup>, F. Calignano<sup>(2)</sup>, D. Manfredi<sup>(2)</sup>,  
F. Paonessa<sup>(1)</sup>, G. Virone<sup>(1)</sup>

<sup>(1)</sup> Istituto di Elettronica ed Ingegneria dell'Informazione e delle  
Telecomunicazioni (CNR-IEIIT)  
Corso Duca degli Abruzzi 24, Torino, Italy  
[giuseppe.addamo@ieiit.cnr.it](mailto:giuseppe.addamo@ieiit.cnr.it)

<sup>(2)</sup> DIGEP- Dipartimento di Ingegneria Gestione della Produzione,  
Politecnico di Torino, Corso Duca degli Abruzzi 24, Torino, Italy  
[flaviana.calignano@polito.it](mailto:flaviana.calignano@polito.it)

<sup>(3)</sup> IIT-CSFT  
Corso Trento 21, Torino, Italy  
[Diego.manfredi@iit.it](mailto:Diego.manfredi@iit.it)

### **Abstract**

*In this work the design and Selective Laser Melting (SLM) manufacturing of high performance filters operating in Ku/K bands is reported. An Additive Manufacturing (AM) oriented architecture has been exploited to enhance the manufacture quality. Subsequently a device which integrates bend, twist and filter functionalities is presented. The component has been successfully manufactured exploiting the free-layout capabilities of AM process.*

**Index Terms** – Additive Manufacturing, Selective Laser Melting, Stop-Band Filters, Integrated Component.

### **I. INTRODUCTION**

The design of antenna feed systems for SatCom applications and earth or astrophysical observations requires, nowadays, to take into account more and more demanding requirements in terms of electromagnetic performances and mechanical constraints. Classical electromagnetic architectures are often not feasible for this goal or their realization would require an expansive and complex manufacturing if standard machining processes (e.g. milling, electrical discharge machining, etc.) are exploited. In this framework, Additive Manufacturing (AM) technologies are potential solutions to overcome these limitations thanks to their high integration level characteristics and reduced waste and costs. According to ASTM definition, AM includes different technologies which are based on joining selectively materials (metals, polymers or ceramics) in opposition to subtractive manufacturing methodologies. In the microwave field, the most applied AM process are the Stereolithography (SLA) and Selective Laser Melting (SLM). The latter is particularly suitable for manufacturing antenna feed chains, since it produces parts directly in metal. Unfortunately, the actual SLM

readiness level is not sufficient mature to guarantee a priori the realization of devices with high performances. For this reason, although the exponential growth of publications on this topic in the last decade, further investigations are mandatory. In this contest, the realization of microwave filters, that are key components of any electromagnetic system, is particularly interesting since their intrinsic sensitivity to manufacture tolerances makes their realization particularly cumbersome. As a natural continuation of [1], in this work an AM-oriented architecture of the composite step-stub is discussed and exploited for the SLM realization of high order filters. Subsequently, a set of integrated filters which merges an H-plane bend and 90-deg twist functionalities is presented.

## II. STEP/STUB COMPOSITE FILTER

According to the sensitivity analysis presented in [1], a composite step-step configuration is more stable to manufacturing uncertainties than the usual iris solution. For this reason in [1] some prototypes have been SLM manufactured showing good results in terms of rejection but not excellent return loss performances. This fact is related to the part orientation in the SLM building machine, which is not coincident with the laser axis one to avoid cracks in the realization of the straight stubs. According to the studies reported in [2], the stubs metallic walls become self-supporting if they are tilted by an angle greater than 35 degree. Then the composite step-stub architecture has been modified leading to a slanted version (see Fig. 1). In order to verify the concept, a sixth-order stop-band filter has been designed. The operative frequency bands is the same of that one presented in [1], while more stringent electrical requirements have been considered in terms of isolation (50 dB in the stop-band ([17.5,21.2] GHz), while the requirement on the return loss has been maintained to 30 dB in the pass-band ([12.5,15] GHz). SLM prototypes in both AlSi10Mg and Ti6Al4V alloys have been manufactured each with two different external shapes (see Fig. 2). In one case, it traces the filter internal profile, in the other it has been optimized in order to avoid supporting structure even for the external part. The comparison between the measured and simulated scattering parameters is reported in Table 1. If the silver plating of the internal channel is not applied, the equivalent electrical resistivity  $\rho$  is equal to 300  $\mu\Omega\text{cm}$  and 8  $\mu\Omega\text{cm}$  for the Al- and Ti- based alloys, respectively. On the contrary, after silver plating of the Al-based prototype,  $\rho$  reduces to 20  $\mu\Omega\text{cm}$ . The measured results confirm the conceived AM-oriented architecture confirming that the optimization of the external profile reduces the mechanical stress and, subsequently, permits to enhance the manufacture quality.

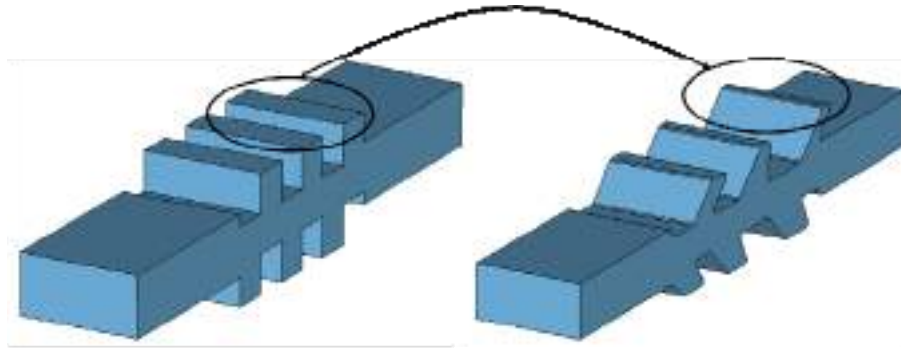


**Figure 1** Classical step-stub composite sixth-order architecture (left) and relevant *AM-oriented* version (right) based on slanting the stubs to achieve self-supporting structures.



**Figure 2** Two sets of prototypes of the sixth-order filter manufactured exploiting the AlSi10Mg and Ti6Al4V alloys. The two sets differ on the external shapes. On the left, it traces the internal profile; on the right, it has been conceived to avoid supporting structures.

### III. INTEGRATED FILTER

Classical feed chain architecture for dual band - dual polarization systems make use of symmetric orthomode junction, which, consequently, requires the use of suitable recombination networks to recombine signals with the same polarization. These networks are formed by different components such as filters, bends and twists [3]. The realization of these components in different single blocks present some drawbacks. From an electromagnetic point of view, the contact regions of different device can generate passive intermodulation products and choke flanges are necessary in the case of high power systems. From a mechanical point of view, the screws and pins used for their connection drive the overall device dimensions. The free-layout feature of Additive Manufacturing technologies can be exploited to overcome these problems. This idea has been verified by designing a Ku/K curved filter which integrates at the same time a 90 degree bend (in the H-plane) and the twist functionality. This subsystem has been designed to exhibit a return loss greater than 30dB in the pass-band

[12.5, 15] GHz and an isolation greater than 60 dB in the stop band [17.5, 21.2] GHz. In order to maximize the power-handling capability of the filter and reduce the sensitivity to manufacturing errors, a ninth-order step-stub configuration has been considered. For comparison, a classical single-blocks implementation would then require an H-plane bend with radius 50 mm and a twist with length 80mm. These values have been chosen according to the return loss specification. In the integrated filter, instead, the bend and twist functionalities have been obtained by rotating the stubs and deforming the common waveguide. First, a curvature radius R of 50 mm has been considered, and then further miniaturization has been obtained reducing R to 40 mm and 30 mm. The latter is the lowest feasible value of R according to the ninth-order filter length. These three prototypes have been SLM manufactured in AlSi10Mg alloy and tested. The overall performances compared to the simulated ones are reported in Table 2. The results are quite good confirming the applicability of SLM for complex and integrated radio-frequency devices.

**Table 1** Comparison between measured and simulated sixth-order filters.

Parameter	Simulation	Prototypes Fig. 2a		Prototypes Fig. 2b	
		AlSi10Mg	Ti6Al14V	AlSi10Mg	Ti6Al14V
Return Loss (dB) [12.5,15] GHz	≥30	≥25	≥27	≥27	≥30
Transmission Coefficient (dB) [17.5,21.2] GHz	≤ -54	≤ -52	≤ -52	≤ -52	≤ -52

**Table 2** Comparison between simulated and measured integrated filter.

Geometry	Curvature Radius R=50 mm		Curvature Radius R=40 mm		Curvature Radius R= 30 mm	
	Simulation	Measurement	Simulation	Measurement	Simulation	Measurement
Return Loss (dB) [12.5,15] GHz	> 30	> 20	>25	>25	>22	>21
Insertion Loss (dB) [12.5,15] GHz	≤ 0.17 ( $\rho=12 \mu\Omega\text{cm}$ )	≤ 0.2	≤ 0.15 ( $\rho=12 \mu\Omega\text{cm}$ )	≤ 0.15	≤ 0.13 ( $\rho=12 \mu\Omega\text{cm}$ )	≤ 0.16
Rejection (dB) [17.5,21.2] GHz	>60	>60	>60	>60	>60	>60

## REFERENCES

- [1] O. A. Peverini, et al. "Additive Manufacturing of Ku/K Band Waveguide Filters for Space Applications", Int. Workshop on Microwave Filters, Toulouse, France, March 2015.
- [2] F. Calignano, D. Manfredi, E.P. Ambrosio, L. Iuliano, and P. Fino, "Influence of process parameters on surface roughness of aluminium parts produced by DMLS," International Journal of Advanced Manufacturing.
- [3] O. A. Peverini, et al., "Integration of an H-Plane Bend, a Twist, and a Filter in Ku/K-Band Through Additive Manufacturing", IEEE Transactions on Microwave Theory and Techniques, Issue 99, 2018.

# PERFORMANCE STUDY OF COMPACT SUBSTRATE INTEGRATED WAVEGUIDE RESONATORS

N. Delmonte<sup>(1)</sup>, C. Tomassoni<sup>(2)</sup>, M. Bozzi<sup>(1)</sup>, L. Perregrini<sup>(1)</sup>

<sup>(1)</sup> Department of Electrical, Computer and Biomedical Engineering,  
University of Pavia, Via Ferrata 1, 27100 Pavia, Italy

<sup>(2)</sup> Department of Engineering, University of Perugia,  
Via G. Duranti 93, 06125 Perugia, Italy

## Abstract

*The substrate integrated waveguide (SIW) technology offers high performance compared to other planar technologies. However, SIW components are larger and bulkier. While there are some techniques that can be used to reduce the size of the components, they tend to increase electromagnetic losses. This paper presents a study on the quality factor of cavity resonators based on different compact SIW technologies. A technique to reduce the losses of compact resonator topologies is also introduced. A two-pole bandpass filter is shown as an example of practical implementation of this technique. The results of the study are validated with the measurement of some physical prototypes.*

**Index Terms** – Cavity resonators, half mode SIW, quality factor, resonator filters, substrate integrated waveguide (SIW).

## I. INTRODUCTION

The new generation of wireless telecommunication systems has increased the performance requirements for microwave devices. In this context, the substrate integrated waveguide (SIW) technology [1] is ideal for the design of high frequency components. Compared to other planar technologies, SIW offers very low power losses and complete electromagnetic shielding, although with a larger component size. In order to reduce the footprint area, multiple solutions have been proposed. In particular, the half-mode SIW (HMSIW) [2] achieves a 50% of size reduction by removing half of the top metallization is removed along the central symmetry plane of the structure. The drawback of this technology is the loss of the electromagnetic shielding and a reduction in performance due to parasitic radiation effects.

An important component that is used as the base building block of other, more complex devices is the microwave resonator. The main figure of merit used to classify the performance of resonant cavities is the unloaded quality factor ( $Q_u$ ), which is inversely proportional to the power loss of the device. This work shows a comparison of the quality factor for different compact resonator topologies based on the SIW technology, and presents a possible solution to improve their performance.

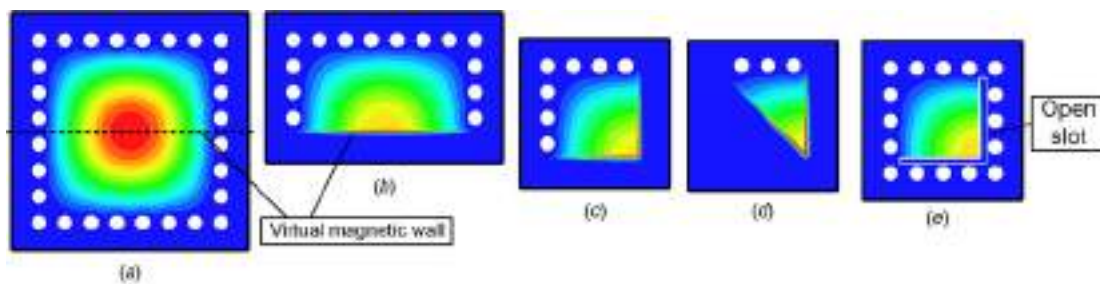


**FIG. 1** – Different compact SIW resonator topologies: electric field distribution for the fundamental resonant mode. (a) Square SIW resonator; (b) Half-mode SIW resonator; (c) Quarter-mode SIW resonator; (d) Eighth-mode SIW resonator; (e) Shielded quarter-mode SIW resonator.

## II. STUDY OF THE RESONATORS

The study has been carried out using the commercial EM simulator software Ansys HFSS. All the components have been designed on a reference Taconic CER-10 substrate ( $\epsilon_r = 10$ ,  $\tan \delta = 0.0035$ , thickness 1.27 mm) and tuned to have a resonant frequency of  $f_0 = 4$  GHz. The first resonator to be analyzed is the standard square SIW cavity (Fig. 1a). There are two main power loss contributions: conductor losses given by the electrical current on the metallic walls of the structure, and dielectric losses in the substrate material. Thick substrates with low dielectric loss tangent are required to maximize the quality factor. The square SIW cavity achieves a quality factor  $Q_u = 223$  with a side length  $l = 17.79$  mm.

The size of the device can be decreased using the half-mode technique [2]. When part of the top metallization is removed, the capacitive effect along the discontinuity can be approximated as a magnetic wall. By placing this virtual boundary condition along the symmetry axis of the fundamental resonant mode, a smaller cavity with the same resonant frequency can be obtained (Fig. 1b). The drawback of the new topology is the presence of a large open side that acts as an additional radiating power loss contribution. For this reason, the half-mode resonator has a quality factor  $Q_u = 79$ . In order to lower radiation losses, the substrate thickness should be reduced. However, as a tradeoff, this leads to an increase of conductor losses.

The resonant mode field distribution of the half-mode structure presents an additional symmetry axis along the middle of the device. Another half of the top metal layer can be removed, obtaining the quarter-mode SIW resonator (Fig. 1c). Aside from the additional size reduction, this topology presents a slight decrease in radiation which translates in an increase of the quality factor, reaching  $Q_u = 106$ .

The quarter-mode structure presents another symmetry axis along its diagonal. By using the same procedure as before, the eighth-mode SIW resonator is obtained (Fig. 1d). The radiating fields of the two open

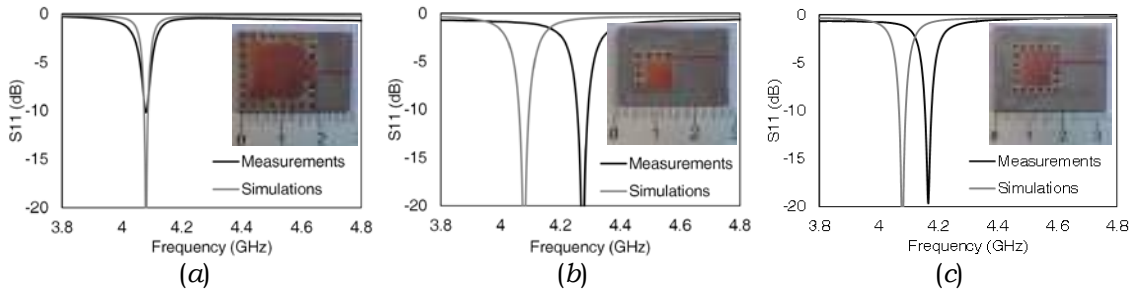


**FIG. 2** – Prototypes and frequency response of the resonators: (a) Standard SIW resonator; (b) Classical quarter-mode SIW resonator; (c) Shielded quarter-mode resonator.

sides partially cancel each other out, further lowering the overall power dissipation. The quality factor of this topology is  $Q_u = 115$ .

While the structures derived from the half-mode technique offer high miniaturization levels, they all suffer from higher losses. Partial electromagnetic shielding can be obtained by placing a row of metallic vias near the open boundaries of the device. The resulting topology is called shielded quarter-mode SIW resonator (Fig. 1e). While this technique leads to a slight increase of the size of the component, it is effective in reducing radiation losses. Using the reference substrate, the component achieves a quality factor  $Q_u = 160$ .

### III. PROTOTYPE RESONATORS AND FILTER MEASUREMENT

The results of the study have been validated by fabricating and measuring physical prototypes of the resonators. The unloaded quality factor of the devices is extracted from the reflection coefficient bandwidth, compensating the external coupling effects [4]. The pictures and frequency responses of the prototypes are shown in Fig. 2. The small shift in frequency of the open structures is due to some slight over-milling of the components. The measured values of the unloaded quality factors are the following:  $Q_u = 167$  for the canonical square SIW resonator;  $Q_u = 72$  for the normal quarter-mode structure;  $Q_u = 124$  for the shielded quarter-mode cavity. In all cases, the measured quality factors are around 25%-30% lower than in the simulations, mainly due to the additional losses provided by the microstrip. The relative performance between the different resonators confirm the effectiveness of the partial shielding to reduce the losses of the open cavities.

Finally, the shielded quarter-mode SIW topology has been used as the base for the design of a two pole bandpass filter, shown in Fig. 3a. The distance between the cavities sets the internal coupling. The filter operates at a central frequency of 4 GHz, with a 9% fractional bandwidth. A physical prototype has been created, and the measurement results presented in Fig. 3b show good agreement with the simulations.

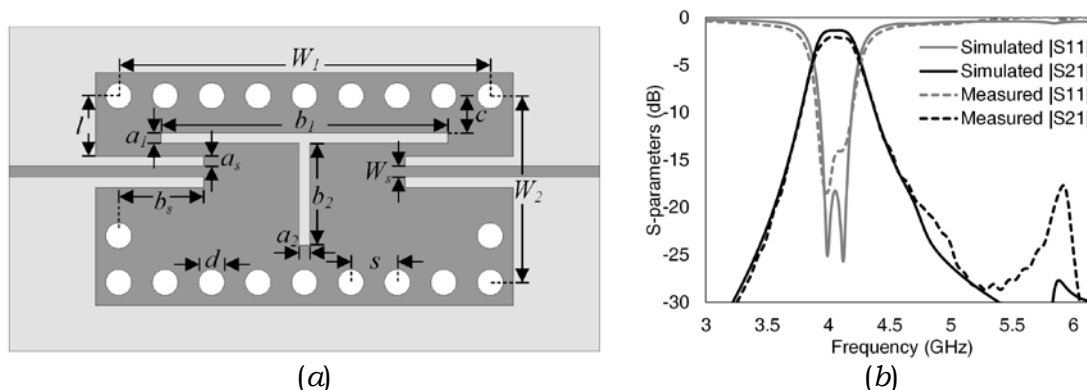


**FIG. 3** – (a) Two-cavity bandpass filter based on shielded quarter-mode SIW resonators (dimensions in mm:  $w_1 = 21.6$ ,  $w_2 = 10.8$ ,  $a_1 = 0.6$ ,  $a_2 = 0.6$ ,  $b_1 = 16.7$ ,  $b_2 = 5.9$ ,  $c = 2.15$ ,  $d = 1.5$ ,  $s = 2.7$ ,  $l = 3.485$ ,  $a_s = 0.6$ ,  $b_s = 4.95$ ,  $w_s = 0.63$ , substrate thickness 0.635 mm); (b) Frequency response of the filter.

#### IV. CONCLUSION

The study shown in this paper demonstrates how partially open SIW resonator topologies offer significant component size reduction, at the cost of lower performance caused by the introduction of radiation losses. This problem can be mitigated by placing a partial electromagnetic shield structure near the open boundaries of the component. A bandpass filter has been shown as a practical application example for the shielded resonator topology. Simulation results have been tested with the creation and measurement of physical prototypes.

#### REFERENCES

- [1] M. Bozzi, A. Georgiadis, and K. Wu, "Review of Substrate Integrated Waveguide (SIW) Circuits and Antennas," *IET Microwaves, Antennas and Propagation*, vol. 5, no. 8, pp. 909–920, June 2011.
- [2] W. Hong et al., "Half mode substrate integrated waveguide: a new guided wave structure for microwave and millimeter wave application," *2006 Joint 31st International Conference on Infrared Millimeter Waves*, Shanghai, 2006, pp. 219-219.
- [3] S. Moscato, C. Tomassoni, M. Bozzi, and L. Perregrini, "Quarter-Mode Cavity Filters in Substrate Integrated Waveguide Technology," *IEEE Transactions on Microwave Theory and Techniques*, Vol. 64, No. 8, pp. 2538-2547, Aug. 2016.
- [4] R. J. Cameron, R. Mansour, and C. M. Kudsia, *Microwave Filters for Communication Systems: Fundamentals, Design and Applications*, John Wiley & Sons, August 2007.

# CORRUGATED RECTANGULAR WAVEGUIDE FOR PULSE COMPRESSION SYSTEMS

G. Di Massa<sup>(1)</sup>, S. Costanzo<sup>(1)</sup>

<sup>(1)</sup> Department of Informatics, Modeling, Electronics and System Engineering, University of Calabria  
Ponte Pietro Bucci, 87036, Arcavacata di Rende, Italy  
[costanzo@dimes.unical.it](mailto:costanzo@dimes.unical.it)

## Abstract

*A two-wall corrugated rectangular waveguide is proposed in this work to realize a simple and compact pulse compression system. The electromagnetic field inside the corrugated waveguide is analyzed to determine the dispersive equation and the relative compression ratio. Numerical simulations are discussed to prove the effectiveness of the proposed configuration.*

**Index Terms** – Microwave pulse compression, corrugated waveguides.

## I. INTRODUCTION

Microwave compressors are typically adopted in those applications requiring ultrahigh power, such as in relativistic electronics, and/or the generation of wide bandwidth pulses, as for high range resolution radar. The simplest way to achieve microwave pulse compression is to adopt a waveguide dispersive line operating close to its cutoff frequency, where a large group velocity difference (strong dispersion) can be observed over a wide frequency range. As a first attempt, conventional regular waveguides have been investigated in literature, due to their relative compactness and ease of realization. However, it was found that, in order to achieve high compression factor, very large waveguide length is required, leading to high losses, and thus to low efficiency. More sophisticated waveguide configurations can be considered to obtain better performances. For example, helically corrugated waveguides have been investigated in literature to generate multigigawatt RF radiation [1] and high compression ratio [2]. In the present work, a simpler configuration is considered, which is basically a rectangular waveguide having corrugations at two opposite sides. The proposed structure is able to produce high pulse compression with relatively short length, thus overcoming disadvantages related to standard rectangular waveguides, but preserving the simplicity and ease of fabrication features. The performance investigation of the proposed rectangular corrugated waveguide is realized by first characterizing the electromagnetic field inside the structure, thus deriving the dispersion equation and the relative slow-wave propagation constant. Numerical

simulations are then performed to demonstrate the pulse compression capabilities of the proposed structure.

## II. THEORY

The corrugated rectangular waveguide proposed in this work is shown in Fig. 1.

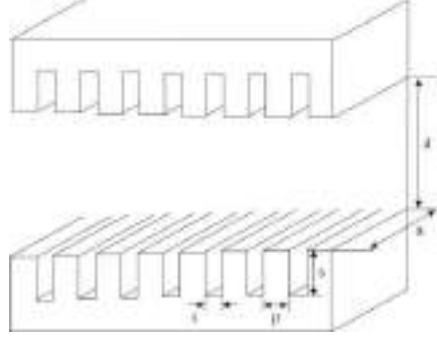


**FIG. 1** – Configuration of corrugated rectangular waveguide.

Assuming the hybrid Longitudinal Section Electric (LSE) mode, the electromagnetic field inside the waveguide can be described in terms of Hertzian potential [], and the following dispersive equation can be written:

$$k_o^2 = \beta^2 + k_x^2. \quad (1)$$

where:

$$k_o^2 = \gamma_n^2 + k_x^2 + \alpha^2. \quad (2)$$

$\gamma_n$  being the propagation constant relative to n-th mode.

In the case of slow waves ( $\alpha = jq$ ), from combination of expression (1) and (2), we obtain:

$$\beta^2 = \gamma_n^2 - q^2. \quad (3)$$

Then, applying the boundary conditions on the air-corrugation interface, the following transcendental equation is obtained:

$$\tanh q \frac{d}{2} = \frac{q}{\beta} \cot \beta s. \quad (4)$$

Finally, the solution of eqs. (3) and (4) gives the propagation constant in the rectangular corrugated waveguide, namely:

$$\gamma_n^2 = \beta^2 + \frac{12}{d^2} - \frac{24}{\beta d^3} \cot \beta s. \quad (5)$$

From eq. (5) the group velocity can be computed as:

$$v_g = \frac{d\omega}{d\gamma_n}. \quad (6)$$

Now, the compression of a frequency-modulated pulse into the corrugated waveguide can be modeled by the propagation of a wave packet through a dispersive medium, with  $\gamma_n = \gamma_n(\omega)$  given by eq. (5). The propagating wave can be so expressed as:

$$u(z, t) = \int_{-\infty}^{+\infty} U(\omega) e^{j\omega t} e^{-j\gamma_n(\omega)z} d\omega. \quad (7)$$

where:

$$U(\omega) = \frac{1}{2\pi} \int_{-\infty}^{+\infty} u_o(t') e^{-j\omega t'} dt'. \quad (8)$$

Let us assume as input signal  $u_o(t) = u(z=0, t)$  a rectangular pulse of duration  $\tau_o$ . The maximum pulse compression occurs at the waveguide termination  $L$ , namely the distance at which all waves meet each other, which is given as:

$$L = v\tau_o. \quad (9)$$

The term  $v$  into eq. (9) is defined as:

$$v = \frac{1}{\frac{1}{v_{g1}} - \frac{1}{v_{g2}}}. \quad (10)$$

where  $v_{g1}$ ,  $v_{g2}$  are the group velocities of the start and end frequencies,  $f_1$  and  $f_2$ , of the microwave pulse.

Taking into account the medium losses, the final expression of the compression ratio  $K$  is given as:

$$K = \Delta f \tau_o e^{-\delta L} = \Delta f L \left( \frac{1}{v_{g1}} - \frac{1}{v_{g2}} \right) e^{-\delta L}.$$

(11)

$\delta$  being the loss factor, and  $\Delta f = f_2 - f_1$ .

### III. NUMERICAL RESULTS

To assess the proposed approach, numerical simulations are performed within X-band on the corrugated structure of Fig. 1, whose dimensions are given as:  $a = 17.5$  mm,  $d = 20.5$  mm,  $p = 3$  mm,  $s = 11$  mm,  $t = 1$  mm,  $L = 30$ cm.

All parameters characterizing the dispersive behavior of the corrugated waveguide, as outlined in Section II, are numerically computed by assuming the above values. In particular, the expected dispersion curve is illustrated in Fig. 2(a), where the comparison with the rectangular waveguide without corrugations is also reported. The same comparison is illustrated in Fig. 2(b) for the compression ratio, by demonstrating the strong enhancement achieved with the proposed corrugated structure.

As a final validation, the compression effect is highlighted by assuming a rectangular pulse of duration  $\tau_0 = 5e-8$  s, as given by eq. (9) with  $f_1 = 9.3$  GHz and  $f_2 = 9.5$  GHz. The output signal computed from eq. (7) shows the expected compressed behavior, as illustrated in Fig. 3.

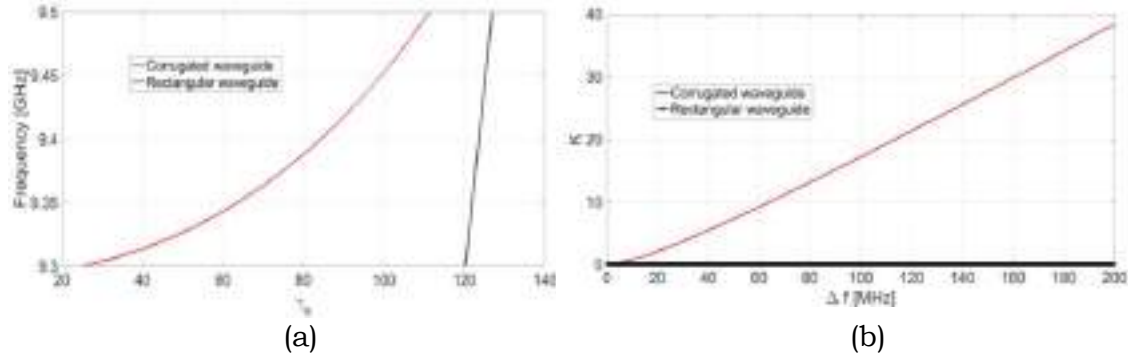


**FIG. 2** – Dispersion curve (a) and compression ratio (b).

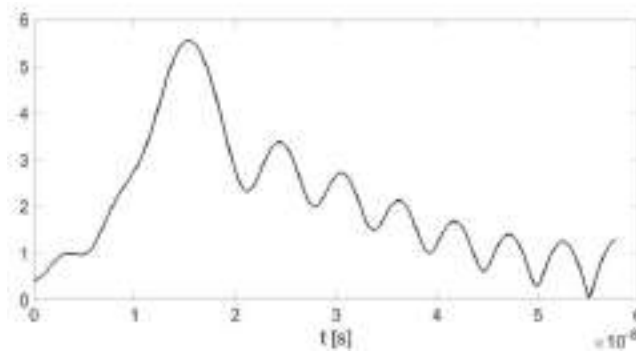


**FIG. 3** – Output (compressed) pulse.

#### IV. CONCLUSION

A corrugated rectangular waveguide has been presented in this work to realize a high-ratio pulse compression system, with a compact and low-cost dispersive structure. Numerical simulations within X-band have been performed to highlight the proper compression feature.

#### REFERENCES

- [1] S. V. Samsonov, A. D. R. Phelps, V. L. Bratman, G. Burt, G. G. Denisov, A. W. Cross, K. Ronald, W. He, and H. Yin, "Compression of frequency-modulated pulses using helically corrugated waveguides and its potential for generating multigawatt rf radiation," *Physical Review Letters*, vol. 92(11), March 2004.
- [2] L. Zhang, S. V. Mishakin, W. He, S. V. Samsonov, M. McStravick, G. G. Denisov, A. W. Cross, V. L. Bratman, C. G. Whyte, C. W. Robertson, A. R. Young, K. Ronald, and A. D. R. Phelps, "Experimental study of microwave pulse compression using a five-fold helically corrugated waveguide," *IEEE Transactions on Microwave Theory and Techniques*, vol. 63(3), pp. 1090-1096, March 2015.
- [3] R. E. Collin, *Field theory of guided waves*, ed. by McGraw Hill, 1960.

# 3D-PRINTED SUBSTRATE INTEGRATED WAVEGUIDE CAVITY FOR FLUIDS CHARACTERIZATION

G. M. Rocco<sup>(1)</sup>, M. Bozzi<sup>(1)</sup>, D. Schreurs<sup>(2)</sup>, S. Marconi<sup>(3)</sup>, G. Alaimo<sup>(3)</sup>,  
F. Auricchio<sup>(3)</sup>

<sup>(1)</sup> Department of Electrical, Computer and Biomedical Engineering,  
University of Pavia, Via Ferrata 5, 27100 Pavia, Italy  
giuliamaria.rocco01@universitadipavia.it, maurizio.bozzi@unipv.it

<sup>(2)</sup> Department of Electrical Engineering,  
KU Leuven, Kasteelpark Arenberg 10, 3000 Leuven, Belgium  
dominique.schreurs@kuleuven.be

<sup>(3)</sup> Department of Civil Engineering and Architecture,  
University of Pavia, Via Ferrata 5, 27100 Pavia, Italy  
stefania.marconi@unipv.it,  
gianluca.alaimo01@universitadipavia.it, auricchio@unipv.it

## Abstract

*In this paper a 3D-printed microwave microfluidic sensor is presented. The sensor, a square substrate integrated waveguide (SIW) cavity with a meandered pipe inside, has been entirely printed by additive manufacturing technology using a photopolymer resin. Through the two open ends of the inner pipe, fluids under test can be injected and their electrical properties determined from the shift in the cavity's resonant frequency and from the changes in the quality factor.*

**Index Terms** – Additive manufacturing, 3D printing, microfluidic sensor, permittivity measurement, substrate integrated waveguide (SIW) technology.

## I. INTRODUCTION

The additive manufacturing technology is increasingly gaining interest in many areas of science and engineering [1]. Among others, the features of 3D-printing technology are suitable to realize new classes of microwave sensors, based on architectures difficult to implement by standard manufacturing techniques.

This paper describes a 3D-printed microfluidic sensor based on a substrate integrated waveguide (SIW) cavity [2]. The innovative aspect in this work consists in 3D-printing a multi-folded micro-pipe which is directly embedded in the dielectric substrate during the printing phase. Moreover, the variation of the infill factor of the cavity is exploited: the structure has been left empty as much as possible in order to decrease the dielectric loss of the cavity, with a consequent increase in the quality factor [3].

This sensor exploits the variation of the resonance frequency of the SIW cavity's fundamental mode and the change in its quality factor to

determine the electrical properties of the liquid injected in the micro-pipe. The proper design of the micro-pipe geometry allows to tailor easily the variation of SIW cavity frequency response through the implementation of fully 3D topologies, thus optimizing the sensitivity of the microfluidic sensor.

The preliminary design of this microfluidic sensor was presented in [4]: in this paper, that idea has been extended by reducing the infill factor and by reporting measurements and corresponding extracted material properties of various sample fluids.

## II. DESIGN OF THE 3D-PRINTED SIW SENSOR

In Fig.1a the microfluidic architecture is shown, which consists of a SIW cavity with a multi-folded pipe embedded in its substrate. The pipe exhibits two open ends through which the liquid is injected, with a consequent change of the substrate's effective permittivity and thus a variation of the resonance frequency of the device.

The dimensions of the SIW cavity, reported in the caption of Fig.1a, have been specifically chosen to operate in the lower portion of the ultra-wide band (UWB) frequency band. Depending on the fluid injected in the pipe, the resonance frequency spans from a maximum value of 3.8 GHz, defined by the fluid with lowest dielectric permittivity (air, in our case), to a minimum value of 3.32 GHz, defined by the fluid with the highest permittivity of interest (distilled water in this proof-of-concept case).

## III. FABRICATION OF THE 3D-PRINTED SIW SENSOR

The substrate, with the pipe and the via holes, has been fabricated by a FORM 2 SLA printer, using a photopolymer resin provided by FormLab, Clear FLGPCL02. After the printing, aluminum tape has been laid on top and bottom faces and steel screws have been put in the vias. In Fig.1b is reported a photograph of the prototype without the metal layers.

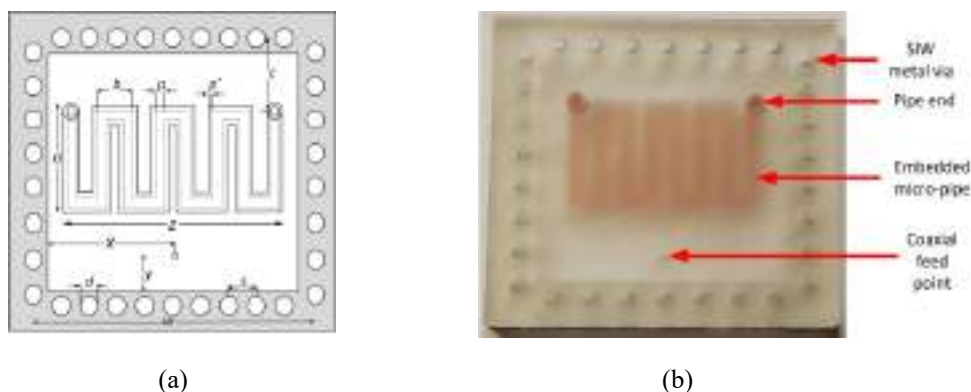


**FIG. 1** – 3D-printed microfluidic sensor: (a) geometry of the proposed structure (dimensions are in mm:  $a = 20$ ,  $b = 5.9$ ,  $c = 12.25$ ,  $d = 3.2$ ,  $p = 2$ ,  $p' = 0.5$ ,  $s = 6$ ,  $w = 48.5$ ,  $x = 20.5$ ,  $y = 8.5$ ,  $z = 32.4$  and substrate thickness  $t = 6$ ); (b) photograph of the cavity.

Since the material used for the substrate is not intended for microwave applications, its electrical properties have to be determined prior to the design of the sensor. Using the waveguide technique, we extracted a dielectric permittivity  $\epsilon_r = 2.73$  and a loss tangent  $\tan\delta = 0.017$  for the resin Clear FLGPCL02.

#### IV. MEASUREMENTS

In order to compute the loss tangent of the fluid injected in the pipe, we need to calculate the unloaded quality factor of the cavity ( $Q_{TOT}$ ), which can be seen as the parallel of the quality factor related to the liquid injected in the pipe ( $Q_L$ ), and the one of the dielectric substrate ( $Q_D$ ):

$$\frac{1}{Q_{TOT}} = \frac{1}{Q_D} + \frac{1}{Q_L} \quad (1)$$

Firstly, using the procedure described in [5], we calculate  $Q_{TOT}$  and  $Q_D$  in the simulation case, and from (1) we find  $Q_L$ . Then, passing to measurement case, we keep  $Q_L$  fixed and we calculate  $Q_D$  as the quality factor of the cavity measured with empty pipe. Finally, substituting these two values in (1), we extract the unloaded quality factor of the measured cavity.

As for the dielectric permittivity calculation, we use the electromagnetic fields theory and we write that:

$$\lambda_{res} = \frac{c}{\left( \sqrt{\frac{\epsilon'}{2}} \cdot \sqrt{1 + (tg\delta)^2} + 1 \right) \cdot f_{res}} \quad (2)$$

where  $\lambda_{res}$  is the cavity's resonant wavelength,  $f_{res}$  is the cavity's resonant frequency,  $\epsilon'$  is the real part of the dielectric permittivity of the material in the cavity and  $tg\delta$  is the loss tangent.

For simplicity we call  $A$  the factor in the brackets at the denominator of (2). If we plot this parameter as function of the shift in the cavity's resonance frequency, we notice that they have a rational dependence (Fig. 2). Thus, from the resonance frequency's shift we calculate  $A$  and then, using the previously calculated loss tangent, we extract the dielectric permittivity of the fluid under test.

Finally, as shown Table I, the results obtained from the electric characterization using our extraction procedures are in very good agreement with the nominal ones obtained with the coaxial probe reference method.

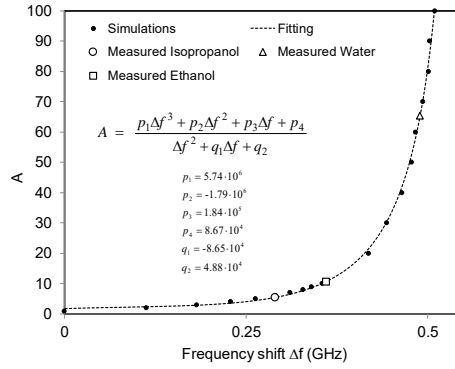


**FIG. 2** – Simulated values and fitting function of  $A$  versus the frequency shift, and experimental validation examples of water, ethanol and isopropanol.

**TABLE I** – COMPARISON BETWEEN LOSS TANGENT AND DIELECTRIC PERMITTIVITY VALUES FOUND USING THE PROPOSED METHOD AND THE ONES EXTRACTED WITH THE COAXIAL PROBE METHOD

Liquid	Nominal $\tan\delta$	Extracted $\tan\delta$	Nominal $\epsilon_r$	Extracted $\epsilon_r$
Ethanol	0.94	0.84	7.5	8.9
Water	0.21	0.21	73.2	64.7
Isopropanol	0.66	0.65	4.4	5

## V. CONCLUSION

A novel microfluidic sensor has been proposed, based on a multi-folded pipe embedded in a SIW cavity and manufactured by the cheap and fast additive manufacturing technology of 3D printing. A prototype has been created and its performance has been successfully verified with the analysis of four fluids (air, isopropanol water and ethanol).

## REFERENCES

- [1] E. MacDonald, *et al.*, "3D Printing for the Rapid Prototyping of Structural Electronics," IEEE Access, Vol. 2, No. 1, pp. 234-242, Dec. 2014
- [2] R. Garg, I. Bahl, and M. Bozzi, Microstrip Lines and Slotlines, Third Edition, Artech House, 2013.
- [3] E. Massoni *et al.*, "Characterization of 3D-Printed Dielectric Substrates with Different Infill for Microwave Applications," IEEE MTT-S International Microwave Workshop Series on Advanced Materials and Processes for RF and THz Applications (IMWS-AMP 2016), Chengdu, China, July 20-22, 2016.
- [4] S. Moscato *et al.*, "Exploiting 3D Printed Substrate for Microfluidic SIW Sensor," European Microwave Conference (EuMC2015), Paris, France, Sept. 7-10, 2015.
- [5] L. F. Chen, C. K. Ong, C. P. Neo, V. V. Varadan, V. K. Varadan, "Microwave Electronics Measurement and Materials Characterization," John Wiley & Sons, 2004.

# LOW-POWER ECO-FRIENDLY SENSORS FOR THE INTERNET OF THINGS

Valentina Palazzi<sup>(1)</sup>, Federico Alimenti<sup>(1)</sup>, Luca Roselli<sup>(1)</sup>, Paolo Mezzanotte<sup>(1)</sup>

<sup>(1)</sup> Department of Engineering, University of Perugia,  
06125, Perugia, Italy  
[paolo.mezzanotte@unipg.it](mailto:paolo.mezzanotte@unipg.it)

## Abstract

*The present research is focused on presenting a new class of battery-less wireless sensors based on the harmonic radar concept, which are intended to produce low environmental footprint, being fabricated by using a paper substrate. Manifold aspects of the new proposed transponders are investigated: manufacturing technology, harmonic generation, antenna and sensor design. Some simple yet robust architectures are identified and some preliminary results are shown. In particular, a one-bit harmonic tag and a harmonic-based crack sensor are reported. All the described circuits are designed to operate in the low-GHz range, but can be tuned to reach higher or lower operating frequencies.*

**Index Terms** – Circuits on paper, crack sensor, flexible electronics, frequency doubler, harmonic radar, slot antenna.

## I. INTRODUCTION

In the near future a large number of everyday objects will be equipped with electronics, so that they could provide useful services and information, make autonomous decisions and assist people during their habitual actions [1]. Short-range wireless sensors are already finding application in several fields, ranging from the monitoring of biological parameters in medicine, to the measurements of mechanical quantities in industrial applications, robot guidance and quality control in supply chain. Consequently, such an approach, involving the use of billions of hardly traceable sensors distributed in the environment, is imposing a deep re-thinking of the next generation electronic apparatuses.

This research is dedicated to the development of a particular class of zero-power wireless sensors relying on the harmonic radar principle. Thanks to the adoption of highly-scalable, simple and robust architectures, the proposed solutions are intended to be suitable for large-scale mass production. All the proposed sensor tags are designed to be fabricated on a paper substrate, to reduce their environmental footprint and ease their integration with the hosting objects.

## II. ONE-BIT HARMONIC TAG ON PAPER

The performance of a one-bit harmonic transponder has been firstly evaluated. The proposed tag is manufactured on paper by using the copper adhesive tape technology [2]. According to this technique, standard photolithography is applied to a foil of copper adhesive tape

and the obtained metal pattern is stuck on the hosting paper substrate via a sacrificial layer. The parameters of the equivalent composite substrate, including both paper and the adhesive layers interposed between each copper layer and paper are as follows:  $\epsilon_r=2.55$ ,  $\tan\delta=0.05$ , and  $h = 0.37\text{mm}$ ; the conductivity of the metal traces corresponds to that of the bulk copper, namely  $\sigma_{\text{cu}} = 5.8 \times 10^7 \text{ S/m}$ .

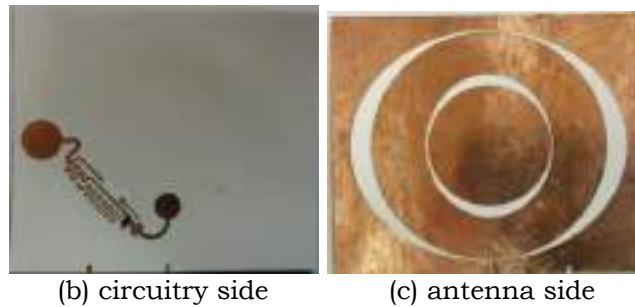
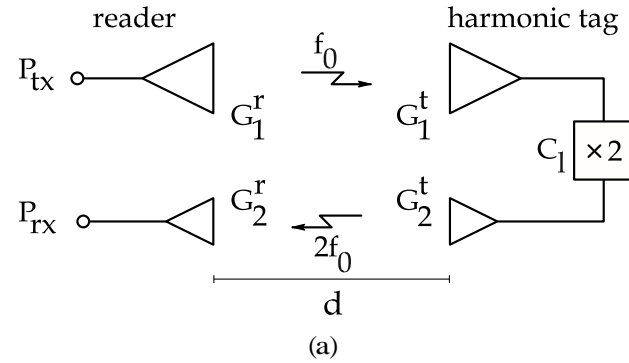


**FIG. 1** – Harmonic radar based system: (a) block diagram (after [3]) and (b)-(c) prototype of the harmonic tag on paper. Overall tag area:  $7.5 \times 6.5 \text{ cm}^2$  [4].

The architecture of the utilized harmonic system is illustrated in Fig. 1(a). The reader transmits a sinusoidal signal with a frequency  $f_0=1.2\text{GHz}$  and has its receiver tuned to  $2f_0=2.4\text{GHz}$  to gather the second harmonic power generated by the transponder. The double-layer transponder, shown in Fig. 1(b)-(c), consists of an input antenna at  $f_0$ , a frequency doubler and an output antenna at  $2f_0$ . All these three elements are designed to be matched to an impedance of  $50\Omega$ , to ease the eventual introduction of additional circuits and sensing blocks.

The harmonic antenna system consists of two nested proximity-fed orthogonally-placed tapered annular slots [4]. This arrangement has been preferred for its compactness and low mutual coupling between radiating elements. Interestingly, the metal surface between the two slots is used as the ground plane for the other components of the tag in microstrip technology. A study about the impact of tapering on the slot performance is reported in [5]. The two antennas, matched to a  $50\Omega$  impedance through circular disc stubs, are well matched, as shown in [4] and feature a mutual coupling below  $-25\text{dB}$  at both frequencies of interest. Moreover, they are linearly polarized and show a maximum gain at their broadside direction of about  $3\text{dBi}$ .

The developed frequency doubler relies on a single lumped component (the low-barrier HSMS-2850 Schottky diode from Broadcom), whereas all the other circuit components are implemented as distributed elements on paper. Besides the afore mentioned non linear component, the circuit includes an input and output matching network and a harmonic filter. An interdigital capacitor with a floating ground plane (number of digits = 5, digit length = 0.8mm, digit width = 0.2mm, digit gap = 0.15mm) is implemented in the output network. The latter structure was also useful to test the pitch and consistency of the adopted technology. The doubler is optimized for power levels in the order of  $-13\text{dBm}$ , where it achieves a conversion loss of  $15.7\text{dB}$ .

The complete prototype was tested in a wireless indoor experiment, demonstrating a coverage of at least 4 meters, insensitive to tag-to-reader rotations (transmitter EIRP  $16\text{dBm}$ ).

### III. HARMONIC-BASED CRACK SENSOR

The proposed architecture for harmonic tags was used to implement a zero-power wireless crack sensor [6],[7]. Fig. 2(a) illustrates the block diagram of the presented transponder. As in the previous case, the reader interrogates the tag. Here, however, the reply depends on the sensor status: if the tag is intact (“intact status”), no second harmonic is generated, as the signal gathered by its input antenna is short-circuited by the stub at the input of the doubler (which is a quarter-wave open-circuited stub). On the other hand, if a crack event occurs (“cracked status”), the input stub is torn off and a second harmonic is generated by the tag and detected by the reader. The detection of a second harmonic is interpreted by the reader as an alarm.

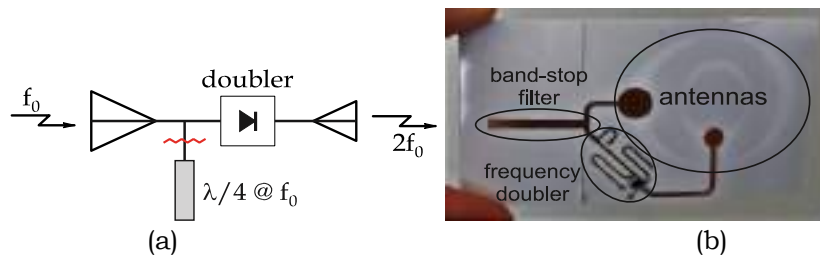


**FIG. 2** – Crack sensor: (a) schematic and (b) prototype on paper [7].

The manufactured prototype shown in Fig. 2(b) is target for  $f_0 = 2.45\text{GHz}$  and weighs only 3 grams. A wireless experiment [6] demonstrates an operating range of the sensor from 1 to 5 m for a transmitted power EIRP of  $25\text{dBm}$ . Since the system is based on an alarm logic (i.e., the second harmonic is generated only in presence of a “crack” event), the system can work in the presence of multiple nodes, without requiring any modification at the reader side [7]: when the tag population is in quiescent condition no second harmonic is received by the interrogating reader, while if one or more of them is cracked, an

alarm is generated, thus configuring a simple yet versatile system for crack sensing. It is worth noticing that sensor is disposable and should be replaced after any crack event.

#### IV. CONCLUSION

Some low-power and long-range wireless transponders, based on the harmonic radar principle, have been presented and discussed. In particular, a one-bit harmonic tag and a disposable crack sensor have been reported. The antenna topology and the frequency doublers have been optimized to guarantee high compactness and low-power operation. The tags have been manufactured by applying the copper adhesive laminate technology to a flexible and recyclable substrate. A minimal amount of lumped components is also adopted. The proposed tags rely only on the power provided by the interrogating signal of the reader for their operation, meaning that no battery is required on-board. This has a very positive impact on their environmental footprint, weight and cost. Consequently, harmonic-based wireless transponders have proved to be an interesting and solution for low-power and low-cost applications in the IoT framework.

#### REFERENCES

- [1] S. A. Nauroze, J. G. Hester, B. K. Tehrani, W. Su, J. Bitto, R. Bahr, J. Kimionis, and M. M. Tentzeris, "Additively Manufactured RF Components and Modules: Toward Empowering the Birth of Cost-Efficient Dense and Ubiquitous IoT Implementations," *Proc. IEEE*, 105(4):702–722, 2017.
- [2] F. Alimenti, C. Mariotti, V. Palazzi, M. Virili, G. Orecchini, P. Mezzanotte, and L. Roselli, "Communication and sensing circuits on cellulose," *Journal of Low Power Electron-ics and Applications*, 5(3):151–164, 2015.
- [3] V. Palazzi, F. Alimenti, P. Mezzanotte, M. Virili, C. Mariotti, G. Orecchini, and L. Roselli, "Low-Power Frequency Doubler in Cellulose-Based Materials for Harmonic RFID Applications," *IEEE Microwave Wireless Compon. Lett.*, 24(12):896–898, December 2014.
- [4] V. Palazzi, F. Alimenti, C. Kalialakis, P. Mezzanotte, A. Georgiadis, and L. Roselli, "Highly integrable paper-based harmonic transponder for low power and long range iot applications," *IEEE Antennas Wirel. Propag. Lett.*, 16:3196–3199, 2017.
- [5] V. Palazzi, M. Del Prete, and M. Fantuzzi, "Scavenging for Energy: A Rectenna Design for Wireless Energy Harvesting in UHF Mobile Telephony Bands," *IEEE Microwave Mag.*, 18(1):91–99, 2017.
- [6] V. Palazzi, F. Alimenti, P. Mezzanotte, G. Orecchini, L. Roselli, "Zero-power, long-range, ultra low-cost harmonic wireless sensors for massively distributed monitoring of cracked walls," *IEEE MTT-S Int. Microwave Symp. (IMS)*, pp. 1–4, 2017.
- [7] V. Palazzi, F. Alimenti, P. Mezzanotte, G. Orecchini, and L. Roselli, "Analysis of a multi-node system for crack monitoring based on zero-power wireless harmonic transponders on paper," *IEEE Topical Conf. Wireless Sensors and Sensor Net-works (WiSNet)*, January 2018.

# A GENERAL PURPOSE APPROACH FOR DIPSTICK ANALYSIS USING SMARTPHONES AND COLORIMETRIC EQUALIZATION CHART

F. Biasion <sup>(1)</sup>, M. Barozzi <sup>(1)</sup>, F. Pasquali <sup>(2)</sup>, A. Tonelli <sup>(2)</sup>, S. Selleri <sup>(1)</sup>

<sup>(1)</sup> Dipartimento di Ingegneria e Architettura - Università di Parma  
Parco Area delle Scienze 181/A, Parma, Italy

<sup>(2)</sup> DNAPhone s.r.l., Viale Mentana n. 150, Parma, Italy  
[stefano.selleri@unipr.it](mailto:stefano.selleri@unipr.it)

## Abstract

*This work presents a smartphone-based approach for colorimetric dipstick analysis. This approach is target-independent and is able to work under different lighting conditions. The system consists of an Android App and a colorimetric reference system printed on a physical support. The App acquires the image containing the dipstick and the colorimetric reference, equalizes colour distortions and returns the chemical value of the analyte. The measurement of the concentration of nitrates in the water has been considered. The proposed system delivered good results also acquiring the test strips under various environmental illumination conditions and represents a new and reliable approach for bio-sensing applications.*

**Index Terms** – Colorimetric measurement, Smartphone, point-of-care, general purpose analysis, diagnostics.

## I. INTRODUCTION

Paper-based colorimetric test strips (Fig. 1) are powerful diagnostic tools that allows to do point-of-care (POC) analyses and low-cost colorimetric diagnostic assays [1].

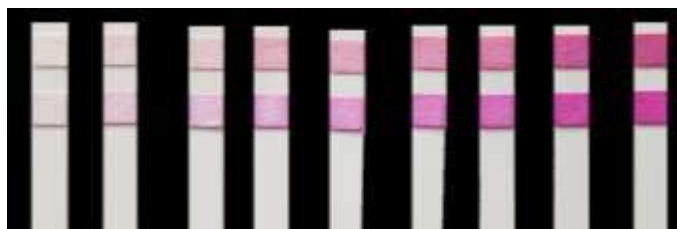


**FIG. 1** – Paper-based colorimetric test strips.

Typically, the analysis is done by naked eye comparing the colour taken by the test strip with a reference scale. Evaluation made by human perception is generally accurate even if some diagnostic errors may occur as the colours might be perceived differently due to the varying lighting conditions. In order to reduce this kind of errors, some digital devices to assist the interpretation of the diagnostic results have been introduced. Digital photography, digital scanners and smartphones

have been utilized to study the effects of light and colours on the chemistry of solutions [1]. In particular, in the last few years, several studies have been carried out on the realization of systems for the automatic reading of the test strips using smartphone technologies [2]. Smartphone-based diagnostic analysis involves few problems related to the variability of the acquisition environment and to the variety of software/hardware components of the available devices. Up to now, to solve these problems two main approaches have been adopted [2]. In first one, the target values are digitally compared with the colours that the test strip can assume [3]. In second one, the target values are acquired in a totally controlled environment [4]. Both of them have limitations. The first one is target-dependent, hence it requires a different reference system for each chemical parameter to be analysed. The second one requires external devices or physical supports to be applied to the smartphone. Here, a new approach is proposed that use the combination of an Android App and a colorimetric reference system to equalize the distortions independently of the target to be analysed.

## II. THE IMPLEMENTED SYSTEM

The system is composed of a mobile App and a target-independent colorimetric reference system, shown in Fig. 2. The App captures the image of the test strip and the reference system. Then, App uses the reference colours to equalize the colour distortions and estimate the chemical value of the analyte.



FIG. 2 – Colorimetric equalization chart.

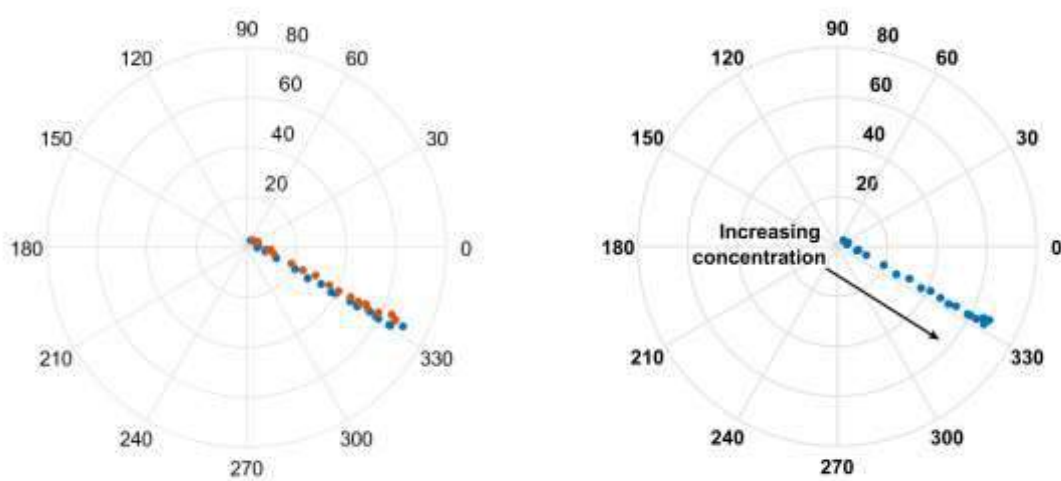
## III. EXPERIMENTAL

In order to test the implemented system in the present work the concentration of nitrates in the water have been measured.

The standard solution of the nitrate was obtained by dissolving 0.41g of potassium nitrate ( $KNO_3$ ) in 50 ml of water ( $H_2O$ ) obtaining a solution with a concentration of 5000 mg/l. Starting from this solution 20 different standards with different concentrations were created using a

dilution process, from a minimum of 5 mg/l up to a maximum of 500 mg/l. For the tests the Quantofix Nitrate-Nitrite test strips were used. The test was performed using the procedure indicated by the test strip reading method: the reactive strip is immersed in the test tube containing the concentration to be analysed, after sixty seconds the strip and the reference system are acquired by the software application in order to process the results.

By using this procedure all dilutions created were analysed twice in order to create two calibration curves and then a mean calibration curve. In Fig. 3a, the polar diagram (C, H) is shown with the values of the equalized colours obtained for each dilution in the two separated calibrations. In Fig. 3b, the polar diagram (C, H) containing the mean calibration values is shown.



(a) Calibrations.

(b) Mean calibration.

**FIG. 3** – Polar diagram (C, H) of the calibration.

The equalized colour of each dilution was compared with each value of the mean calibration curve using the Delta E 94 distance in order to see the precision of the mean calibration curve. In the Tables I and II are shown the results of this test. Using the same method, five unknown samples were also analysed and the Table II show the results obtained with our system.

**Table I - Recalculation of each calibration using the mean calibration as reference system (from 0 to 150 mg/l).**

Concentrations [mg/l]	0	5	10	15	20	25	50	75	100	125	150
<b>Calibration 1</b>	0	5	5	15	20	25	50	75	100	125	125
<b>Calibration 2</b>	0	5	10	15	20	25	50	75	100	150	150

**Table II - Recalculation of each calibration using the mean calibration as reference System (from 175 to 500 mg/l).**

<b>Concentrations [mg/l]</b>	175	200	225	250	275	300	350	400	450	500
<b>Calibration 1</b>	175	150	200	200	275	250	300	350	350	500
<b>Calibration 2</b>	225	275	225	275	300	350	450	450	500	500

**Table III - Results of the analysis of the unknown samples using the calibration as reference system.**

<b>Real [mg/l]</b>	<b>Calculated [mg/l]</b>
150	125
400	350
25	25
100	100
75	75

#### **IV. CONCLUSION**

In this work a general purpose mobile instrumentation for colorimetric dipstick analysis based on smartphone technologies has been presented. The proposed system is very simple being composed of an Android application and a colorimetric reference printed on a physical support. All the tests performed on nitrates in water confirm the effectiveness of the system implemented in removing the distortions of the colour space due to the uncontrolled environmental illumination conditions.

#### **REFERENCES**

- [1] S. F. Cheung, S. K. L. Cheng, and D. T. Kamei, "Paper-based systems for point-of-care biosensing," *Journal of Laboratory Automation*, vol. 20, no. 4, p. 316–333, 2015.
- [2] Z. Geng, X. Zhang, Z. Fan, X. Lv, Y. Su, and H. Chen, "Recent progress in optical biosensors based on smartphone platforms," *Sensors*, vol. 17, no. 11, 2017.
- [3] S. D. Kim, Y. Koo, and Y. Yun, "A smartphone-based automatic measurement method for colorimetric pH detection using a color adaptation algorithm," *Sensors*, vol. 17, p. 1604, Jul 2017.
- [4] Y. Jung, J. Kim, O. Awofeso, H. Kim, F. Regnier, and E. Bae, "Smartphone-based colorimetric analysis for detection of saliva alcohol concentration," *Appl. Opt.* 54, 9183-9189 2015.

# DESIGN OF AN IN-BAND PUMPED DYSPROSIUM-DOPED ZBLAN FIBER AMPLIFIER OPERATING AT 2.9-3.2 MICRON

M. C. Falconi<sup>(1)</sup>, D. Laneve<sup>(1)</sup>, M. Bozzetti<sup>(1)</sup>, T. T. Fernandez<sup>(2)</sup>,  
G. Galzerano<sup>(2)</sup>, F. Prudenzeno<sup>(1)</sup>

<sup>(1)</sup> Department of Electrical and Information Engineering, Politecnico di Bari, Via E. Orabona 4, Bari 70125, Italy

<sup>(2)</sup> Istituto di Fotonica e Nanotecnologie - CNR, Department of Physics, Politecnico di Milano, P. Leonardo da Vinci 32, Milano 20133, Italy

[francesco.prudenzeno@poliba.it](mailto:francesco.prudenzeno@poliba.it)

## Abstract

*A Dy<sup>3+</sup>-doped ZBLAN glass fiber is designed in order to amplify optical signals in the 2.9-3.2  $\mu\text{m}$  wavelength range, via in-band optical pumping. An accurate theoretical model, based on the rate equations for the rare earth populations and the power propagation equations for the optical beams, is employed along with measured spectroscopic and optical parameters. By tailoring the amplifier configuration in terms of fiber length and dopant concentration, an optical gain as high as 14 dB or a noise figure as low as 5 dB are obtained at 2.94  $\mu\text{m}$  wavelength for an input pump power of 1 W at 2.7  $\mu\text{m}$  wavelength.*

**Index Terms** – dysprosium, fiber amplifier, middle infrared, ZBLAN glass.

## I. INTRODUCTION

In the last years, optical amplification in the middle infrared (Mid-IR) wavelength range has attracted much interest due to the increasing need of light sources with high brilliance at wavelengths longer than the conventional ones, i.e. 1.3  $\mu\text{m}$  and 1.55  $\mu\text{m}$ . Free space optical communication, exploiting the 4.5  $\mu\text{m}$ , 9  $\mu\text{m}$  and 12  $\mu\text{m}$  transmission windows of earth atmosphere, is one of the most interesting applications. Its main advantages are the wide bandwidth, the low power, the lightness and the license-free spectrum [1], [2]. Another important application is chemical and biological sensing, due to the efficient interaction of Mid-IR light beams with gas molecules, biological tissues and air/water contaminants. In fact, strong vibrational resonances in the Mid-IR are exhibited by many organic molecules due to the presence of C-H, C-O and C-N chemical bonds. Other applications of Mid-IR light beams include medical surgery, diagnostic investigation, and automotive.

There are several glasses whose spectroscopic characteristics are suitable for the fabrication of rare earth-doped fiber amplifiers operating in the Mid-IR. Chalcogenide glasses are very promising since they exhibit many useful properties such as transparency at very long

wavelengths, beyond 15  $\mu\text{m}$ , high refractive index and capability to host very high rare earth concentrations. However, chalcogenide technology is not yet mature and needs further refinement [3]-[7]. Conversely, tellurite [8], [9] and fluoride glasses [10], [11] are host materials with a higher feasibility level and are widely used in the 2-3  $\mu\text{m}$  wavelength range.

In this work, an accurate theoretical model of an in-band pumped fiber amplifier based on a  $\text{Dy}^{3+}$ -doped ZBLAN glass is developed and numerically solved to investigate its performance in terms of optical gain and noise figure. Realistic values for spectroscopic and optical parameters are employed.

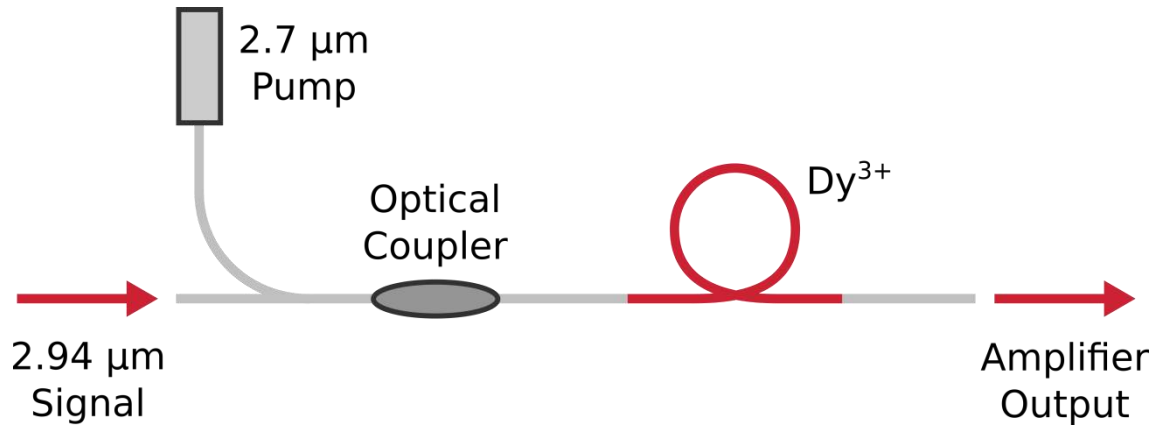
## II. NUMERICAL RESULTS

The model is based on the rate equations for the rare earth populations and the power propagation equations for the optical beams. Population inversion can be achieved by optically pumping the device at 2.6-2.8  $\mu\text{m}$  wavelength. The dysprosium ions are modeled as a two energy levels system. The interaction between light and rare earth is taken into account by means of absorption, stimulated emission, radiative and nonradiative decays. Amplified Spontaneous Emission (ASE) is included too. The parameters employed in the simulation are the following: level 2 radiative lifetime  $\tau_2 = 13.7$  ms, nonradiative decay rate from level 2  $R_{21} = 1539$   $\text{s}^{-1}$ , optical fiber loss  $\alpha = 0.9$  dB/m. Fig. 1 shows the schematic of the device.

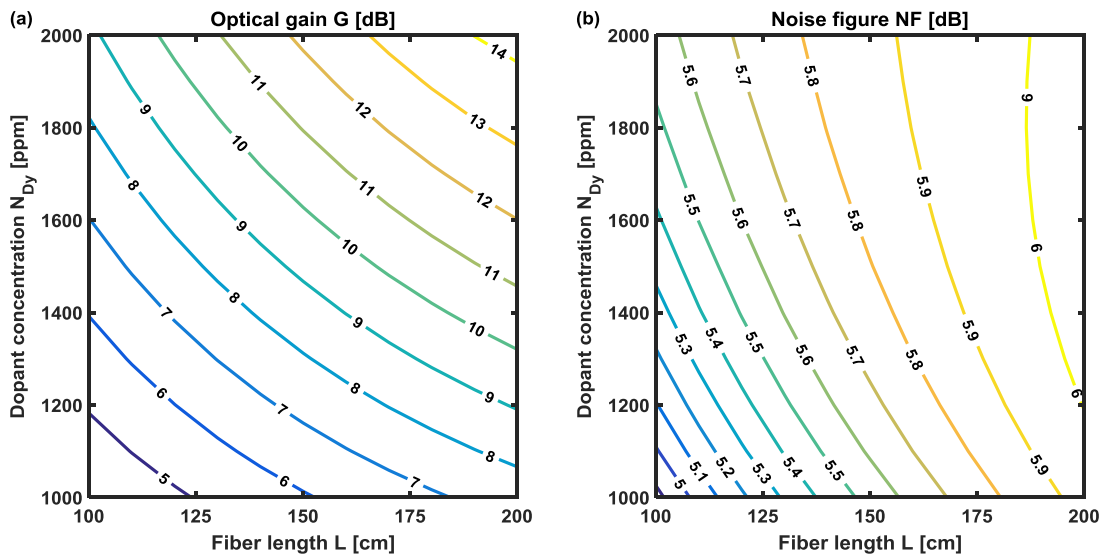
Fig. 2(a) illustrates the optical gain  $G$  of the  $\text{Dy}^{3+}$ -doped ZBLAN fiber amplifier as a function of fiber length  $L$  and dopant concentration  $N_{\text{Dy}}$ . The input pump power is  $P_{p0} = 1$  W, the input signal power is  $P_{s0} = 1$   $\mu\text{W}$ , the pump wavelength is  $\lambda_p = 2.7$   $\mu\text{m}$  and the signal wavelength is  $\lambda_s = 2.94$   $\mu\text{m}$ . The maximum achievable optical gain is about 14 dB. Moreover, long fibers with lower dopant concentrations provide performance similar to that of short fibers with higher dopant concentrations.

Fig. 2(b) illustrates the noise figure  $\text{NF}$  of the  $\text{Dy}^{3+}$ -doped ZBLAN fiber amplifier as a function of fiber length  $L$  and dopant concentration  $N_{\text{Dy}}$ , for the same parameters of Fig. 2(a). The calculated noise figure values are between 5 and 6 dB, with longer fibers exhibiting a worse performance. Therefore, a proper trade-off between optical gain and noise figure is necessary.

In order to improve the performance of the amplifier, i.e. to increase the optical gain or to lower the noise figure, an optimization technique such as the particle swarm algorithm could be used.



**FIG. 1** – Schematic of the Dy<sup>3+</sup>-doped ZBLAN fiber amplifier.



**FIG. 2** – (a) Optical gain  $G$  (in dB) and (b) noise figure  $NF$  (in dB) of the Dy<sup>3+</sup>-doped ZBLAN fiber amplifier as a function of fiber length  $L$  (in cm) and dopant concentration  $N_{Dy}$  (in ppm). Input pump power  $P_{p0} = 1$  W; input signal power  $P_{s0} = 1$  μW; pump wavelength  $\lambda_p = 2.7$  μm; signal wavelength  $\lambda_s = 2.94$  μm.

### III. CONCLUSION

A Dy<sup>3+</sup>-doped ZBLAN fiber amplifier operating by means of in-band pumping was theoretically modeled and its performance in terms of optical gain and noise figure was investigated. Simulation results show that, by choosing a suitable combination of fiber length and dopant concentration, an optical gain as high as 14 dB or a noise figure as low as 5 dB can be obtained at 2.94 μm wavelength, for an input pump power of 1 W at 2.7 μm. In order to further improve the performance of the amplifier, an optimization technique such as the particle swarm algorithm could be exploited. Possible applications of the proposed device include, but are not limited to, free space optical communication, medical surgery and chemical/biological sensing.

## ACKNOWLEDGEMENT

This work was partially supported by EU COST Action under Grant MP1401.

## REFERENCES

- [1] V. W. S. Chan, "Free-space optical communications," *IEEE Journal of Lightwave Technology*, vol. 24(12), pp. 4750-4762, Dec. 2006.
- [2] H. Kaushal, and G. Kaddoum, "Optical Communication in Space: Challenges and Mitigation Techniques," *IEEE Communications Surveys & Tutorials*, vol. 19(1), pp. 57-96, 2017.
- [3] R. S. Quimby, L. B. Shaw, J. S. Sanghera, and I. D. Aggarwal, "Modeling of Cascade Lasing in Dy : Chalcogenide Glass Fiber Laser With Efficient Output at 4.5  $\mu\text{m}$ ," *IEEE Photonics Technology Letters*, vol. 20(2), pp. 123-125, Jan. 2008.
- [4] M. C. Falconi, G. Palma, F. Starecki, V. Nazabal, J. Trolès, S. Taccheo, M. Ferrari, and F. Prudenzano, "Design of an Efficient Pumping Scheme for Mid-IR Dy<sup>3+</sup>:Ga<sub>5</sub>Ge<sub>20</sub>Sb<sub>10</sub>S<sub>65</sub> PCF Fiber Laser," *IEEE Photonics Technology Letters*, vol. 28(18), pp. 1984-1987, Sept. 2016.
- [5] L. Sojka, Z. Tang, D. Furniss, H. Sakr, E. Bereś-Pawlik, A. B. Seddon, T. M. Benson, and S. Sujecki, "Numerical and experimental investigation of mid-infrared laser action in resonantly pumped Pr<sup>3+</sup> doped chalcogenide fibre," *Optical and Quantum Electronics*, vol. 49(21), pp. 1-15, Jan. 2017.
- [6] L. Sojka, Z. Tang, D. Furniss, H. Sakr, Y. Fang, E. Beres-Pawlik, T. M. Benson, A. B. Seddon, and S. Sujecki, "Mid-infrared emission in Tb<sup>3+</sup>-doped selenide glass fiber," *Journal of the Optical Society of America B*, vol. 34(3), pp. A70-A79, Mar. 2017.
- [7] G. Palma, M. C. Falconi, F. Starecki, V. Nazabal, J. Ari, L. Bodiou, J. Charrier, Y. Dumeige, E. Baudet, and F. Prudenzano, "Design of praseodymium-doped chalcogenide micro-disk emitting at 4.7  $\mu\text{m}$ ," *Optics Express*, vol. 25(6), pp. 7014-7030, Mar. 2017.
- [8] L. Gomes, J. Lousteau, D. Milanese, E. Mura, and S. D. Jackson, "Spectroscopy of mid-infrared (2.9  $\mu\text{m}$ ) fluorescence and energy transfer in Dy<sup>3+</sup>-doped tellurite glasses," *Journal of the Optical Society of America B*, vol. 31(3), pp. 429-435, Mar. 2014.
- [9] L. X. Li, W. C. Wang, C. F. Zhang, J. Yuan, B. Zhou, and Q. Y. Zhang, "2.0  $\mu\text{m}$  Nd<sup>3+</sup>/Ho<sup>3+</sup>-doped tungsten tellurite fiber laser," *Optical Materials Express*, vol. 6(9), pp. 2904-2914, Sept. 2016.
- [10] S. D. Jackson, M. Pollnau, and J. Li, "Diode Pumped Erbium Cascade Fiber Lasers," *IEEE Journal of Quantum Electronics*, vol. 47(4), pp. 471-478, Apr. 2011.
- [11] J. Li, L. Wang, H. Luo, J. Xie, and Y. Liu, "High Power Cascaded Erbium Doped Fluoride Fiber Laser at Room Temperature," *IEEE Photonics Technology Letters*, vol. 28(6), pp. 673-676, Mar. 2016.

# ELECTROMAGNETIC PROPAGATION FOR ON-CHIP WIRELESS COMMUNICATIONS

F. Fuschini<sup>(1)</sup>, M. Barbiroli<sup>(1)</sup>, M. Zoli<sup>(1)</sup>, P. Bassi<sup>(1)</sup>,  
G. Bellanca<sup>(2)</sup>, A.E. Kaplan<sup>(2)</sup>, G. Calò<sup>(3)</sup>, V. Petruzzelli<sup>(3)</sup>

<sup>(1)</sup> Dept. of Electrical, Electronic and Information Eng. “G. Marconi”,  
University of Bologna

Viale Risorgimento 2, 40136 Bologna, Italy

[franco.fuschini,marina.barbiroli,marco.zoli5,paolo.bassi}@unibo.it](mailto:{franco.fuschini,marina.barbiroli,marco.zoli5,paolo.bassi}@unibo.it)

<sup>(2)</sup> Dept. of Engineering, University of Ferrara

Via Saragat 1, 44124 Ferrara, Italy

[gaetano.bellanca,kpllmr}@unife.it](mailto:{gaetano.bellanca,kpllmr}@unife.it)

<sup>(3)</sup> Department of Electrical and Information Engineering, Polytechnic of Bari

Via E. Orabona, 4, 70125 Bari, Italy

[giovanna.calo,vincenzo.petruzzelli}@poliba.it](mailto:{giovanna.calo,vincenzo.petruzzelli}@poliba.it)

## Abstract

*Optical Wireless Networks on-Chip are promising solutions to overcome problems of miniaturization and energy consumption in a multicore on-chip environment. In this paper, the optical wireless channel is modeled through a ray tracing approach, and the relationship between the optical antennas gain and the communication range in the on-chip propagation environment is investigated.*

**Index Terms** – Channel Modeling, Ray Tracing, Optical Wireless Networks on Chip

## I. INTRODUCTION

Parallel computation through multi-processors architectures is likely to be a point of no return to cope with the increasing request for greater computation efficiency [1]. Nevertheless, the physical interconnection of many cores currently undergoes several technological impairments, to the extent that wireless network on chip are being investigated as a promising solution [2]. In this work, on-chip wireless connections at optical frequencies are studied by means of a ray-tracing approach, and the impact of path-loss on the communication distance is investigated for different positions and radiation properties of the antennas.

## II. OPTICAL WIRELESS NETWORKS ON CHIP

Although multi-processor chips are widely acknowledged as a promising solution for high-performance computing, prospects towards kilo-cores architectures might be seriously thwarted by interconnects issues, e.g. in terms of complexity, high latency and power consumption [2]. These limitations heavily affect electrical network on chip (NoC), as well as optical NoC (ONoC), although to an overall lesser extent [3]. Wireless networks on-chip (WiNoC) have therefore gained consideration [2] as an effective way to overcome the bottleneck of the physical interconnection between many cores. To overcome the difficulties in antenna integration and energy consumption that obviously rise at UWB/millimeter frequencies, optical WiNoC (OWiNoC) have been recently proposed [3], to

combine the advantages of both ONoC and WiNoC. A crucial aspect of the optical link design is path-loss assessment, which is expected to be a heavy impairment at so large frequency. In spite of the tiny chip size, on-chip wireless communications at optical frequency are likely to occur in far-field conditions, e.g. up to distances by far greater than  $100\lambda$ . Numerical solutions like FDTD are therefore almost impractical, whereas Ray Tracing (RT) can be relied on [4], with noticeable savings in memory and CPU time. The antenna radiation patterns are then calculated by FDTD [3], while the link can be modeled using RT.

### III. RAY TRACING FOR OWiNoC

The on-chip wireless channel is commonly sketched as a layered structure (Fig. 1a), where a plane dielectric slab including the transmitting (TX) and the receiving (RX) antennas is bounded by two different media on the upper and on the lower side. The electromagnetic properties of the materials are considered through their refraction index (values in Fig. 1a refer to wavelength  $\lambda_0=1.55 \mu\text{m}$ ). Planar interfaces are assumed perfectly smooth and infinitely wide at this stage of the work: wave propagation consists then of multiple reflections occurring in the  $xz$  plane (Fig. 1b).

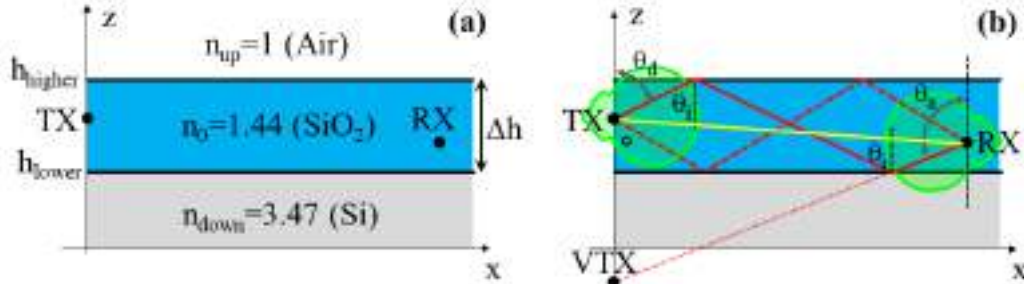


**FIG. 1** – (a) Layered propagation environment; (b) Example: direct and double reflected rays between TX and RX

Therefore, the electromagnetic field radiated to the RX after  $n$  bounces (2 reflections are for instance shown in Fig. 1b) can be expressed as:

$$\vec{E}_n = \vec{E}_{0n} \cdot \frac{e^{-j\beta r_n}}{r_n} \cdot \Pi_n \quad (1)$$

being  $\beta=2\pi n_0/\lambda_0$  the wave number,  $r_n$  the overall length of the ray,  $\Pi_n$  the product of the  $n$  reflection coefficient, and  $E_{0n}$  the TX antenna “emitted field” in the direction of departure of the ray ( $\theta_d$  in Fig. 1b). It is worth mentioning that the path length  $r_n$  can be regarded as the distance between the RX and an “ $n$ th virtual transmitter” (VTX in Fig. 1b) that is the ‘mirror’ image of the TX (if  $n=1$ ) or of the  $(n-1)$ th VTX (otherwise) with respect to the reflecting plane (image principle). In the considered layered scenario, closed-form analytical expressions for the VTXs locations can be easily achieved, meaning that the computation of both  $r_n$  and the incident angles ( $\theta_i$  in Fig. 1b) are straightforward. Then, the (Fresnel) reflection coefficients (and therefore the value of  $\Pi_n$ ) are also immediately available. Finally,  $E_{0n}$  is computed as:

$$E_{0n} = \sqrt{\frac{\eta \cdot P_A \cdot g(\theta_d)}{2\pi n_0}} \cdot p(\theta_d) \cdot e^{-j\beta} \quad (2)$$

where  $\eta=120\pi$ ,  $P_A$  is the overall transmitted power,  $g(\theta_d)$  and  $p(\theta_d)$  are the antenna gain and polarization vector in the direction  $\theta_d$ . As previously mentioned, the power  $P_A$  and the 2D angular description of the antenna gain and polarization, required by the RT engine as input data, are obtained by using the FDTD. Assuming the same antenna at the RX side for the sake of simplicity, the same input information can be exploited to transform the impinging fields into the corresponding received power, once the ray directions of arrival ( $\theta_a$  in Fig. 1b) have been evaluated.

#### IV. RESULTS

The RT model has been tested for the double interface Si-SiO<sub>2</sub>-Air with a layer thickness ranging from 4  $\mu\text{m}$  up to 10  $\mu\text{m}$ , and for different positions of the TX and the RX within the layer. Moreover, different antennas patterns with increasing gain value have been considered at the TX/RX side, assuming an RX sensitivity of -20 dBm and  $P_A = 0$  dBm.

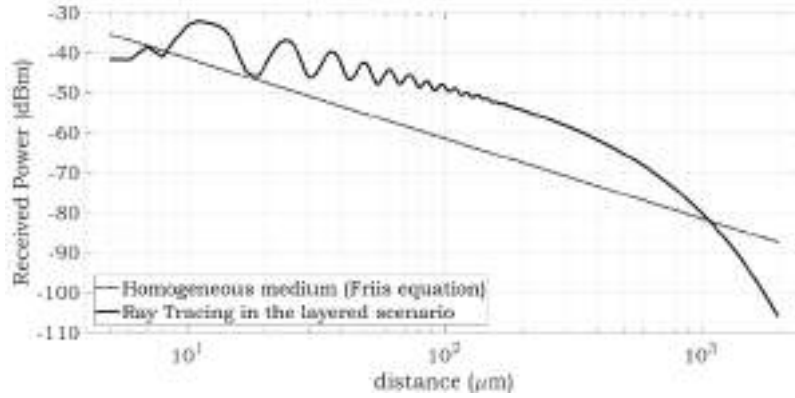


**FIG. 2** – RT modeling of the in-layer propagation (layer thickness=4  $\mu\text{m}$ , TX-RX middle placed, isotropic radiators)

Fig. 2 shows that a guiding effect (i.e. a greater received power compared to a fully homogeneous case) can be highlighted up to a breakpoint (BP) distance, which is strictly related to the layer width (the thinner the layer, the smaller the effect) and to the positions of TX-RX with respect to the lower interface (the closer the position, the weaker the effect). The guiding effect before the BP is mainly due to the overall constructive interference between the received field contributions. Beyond the BP, interference turns to become destructive, resulting in a received power weaker compared to the reference homogeneous case.

Besides the obvious beneficial effect of the layer, which acts as a guide, our analysis shows that the link performance is also affected by its width and by the antenna gain and position. This is shown in Fig. 3, where the maximum link distance, corresponding to a received power equal to the RX sensitivity, is plotted against the antenna gain for different TX-RX positions. If the gain is too low, a large amount of power is lost because

of the large refraction losses of the rays far from grazing incidence, whereas the guiding effect is simply not triggered for gain values corresponding to an excessively narrow radiation lobe.

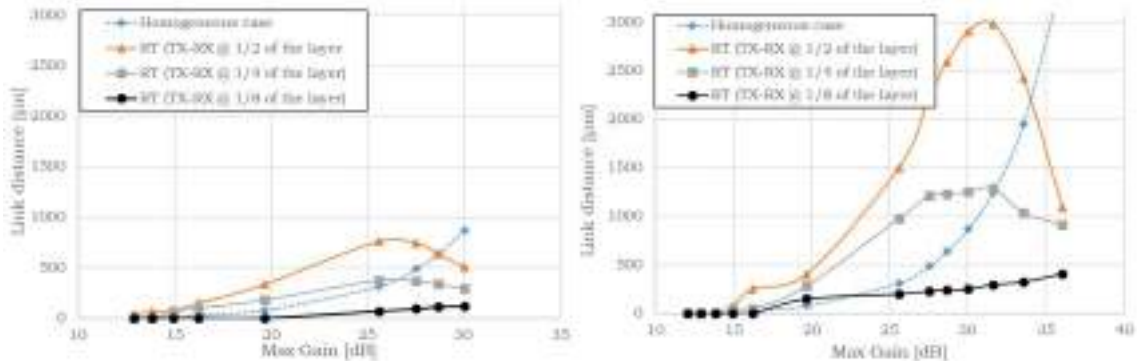


**FIG. 3** – Link distance vs. antenna gain for different layer thickness: (a) 6  $\mu\text{m}$ ; (b) 10  $\mu\text{m}$ .

In both cases, the link distance turns out to be impaired, to an extent which also depends on the layer thickness (Fig. 3a and 3b) and on the TX-RX positions within the layer (different curves in each figure).

## V. CONCLUSIONS

Electromagnetic propagation for optical wireless network on-chip has been investigated using a ray-tracing approach. Assuming a layered layout for the optical wireless channel, which seems reasonable for multi-core chips grown in a multilayered structure, results show that the maximum link length does not increase simply increasing the antenna gain, but also depends on the thickness of the layer and the position of the antennas in the layer. This requires a strong interaction between the e. m. link and the electronic layout designers to find the optimum balance among the whole set of design parameters.

## ACKNOWLEDGEMENT

Research activity supported by MIUR through the PRIN 2015 "Wireless Networks through on-chip Optical Technology - WiNOT" Project.

## REFERENCES

- [1] S. Abdal, M. Iannazzo, M. Nemirovsky, A. Cabellos-Aparicio, H. Lee, E. Alarcon, "On the Area and Energy Scalability of Wireless Network-on-Chip: A Model-Based Benchmarked Design Space Exploration", *IEEE Trans. on Networking*, vol. 23, No. 5, pp. 1501-1513, October 2015;
- [2] S. Deb, A. Ganguly, P. P. Pande, B. Belzer, D. Heo, "Wireless NoC as Interconnection Backbone for Multicore Chips: Promises and Challenges", *IEEE Trans. on Ant. and Propagat.*, vol. 2, No. 2, pp. 228-238, June 2012;
- [3] G. Bellanca, G. Calò, A. E. Kaplan, P. Bassi, V. Petruzzelli, "Integrated Vivaldi plasmonic antenna for wireless on-chip optical communications", *Optics Express*, vol. 25, No. 14, pp. 16214-16227, 2017;
- [4] D. W. Matolak, S. Kaya, "Channel Modeling for Wireless Networks-on-Chips", *IEEE Comm. Magazine*, vol. 51, No. 6, pp. 180-186, June 2013;

# EXPERIMENTAL DEMONSTRATION OF PROTEIN DETECTION USING HOLLOW-CORE TUBE LATTICE FIBERS

F. Giovanardi<sup>1</sup>, A. Cucinotta<sup>2</sup>, A. Rozzi<sup>3</sup>, R. Corradini<sup>3</sup>, F. Benabid<sup>4,5</sup>, L. Vincetti<sup>1</sup>

- (1) Department of Engineering “Enzo Ferrari”, University of Modena and Reggio Emilia, via Vivarelli 10, 41124 Modena, Italy
- (2) Department of Engineering and Architecture, University of Parma, Parco Area delle Scienze, 181/A, 43124 Parma, Italy
- (3) Department of Chemistry, Life Sciences and Environmental Sustainability, University of Parma, Parco Area delle Scienze, 11/a - 43124 Parma, Italy
- (4) GPPMM group, Xlim Research Institute, CNRS UMR 7252, Université de Limoges, 87060 Limoges, France
- (5) GLOphotonics SAS, Ester Technopole, 1 Avenue d'Ester 87069 Limoges Cedex, France  
[luca.vincetti@unimore.it](mailto:luca.vincetti@unimore.it)

## Abstract

*The aim of the present work is to demonstrate that hollow core fibers can be successfully used as sensors for proteins such as streptavidin. After a functionalization of the silica surface, a layer of biotin was deposited on the fiber core inner surface. The fiber was then infiltrated with a solution containing streptavidin and a red shift of the fiber transmission spectrum was experimentally observed.*

**Index Terms** – Fiber optics sensors, Biological sensing and sensors, Microstructured fibers.

## I. INTRODUCTION

Photonic Crystal Fibers (PCF) represent a good platform for the development of sensitive and cheap sensors for the detection of protein and DNA sequence [1]. The holes running along the fiber allows the infiltration of biological substances and for biological layers to attach on the air-dielectric interfaces. In addition, the presence of a hollow core can further increase the infiltration feasibility and the sensor sensitivity.

Recently, the possibility in using hollow core PCFs (HCPCF) based on inhibited coupling waveguiding for label-free DNA detection have been numerically investigated [2]. The sensing is based on the molecular interactions between the surface of the dielectric glass composing the fiber and the target sequence resulting in a generation of a biological layer which modifies the transmission properties of the fiber.

The same mechanism can be exploited for protein detection. In this work, we experimentally investigated the feasibility of a streptavidin sensor [3] based on a silica Hollow Core Tube Lattice Fiber. Experimental results show a spectral red shift in the near infrared region of about 20 nm of the fiber transmission spectrum after infiltration with of a  $0.1 \text{ mg/mL}$  solution of streptavidin.

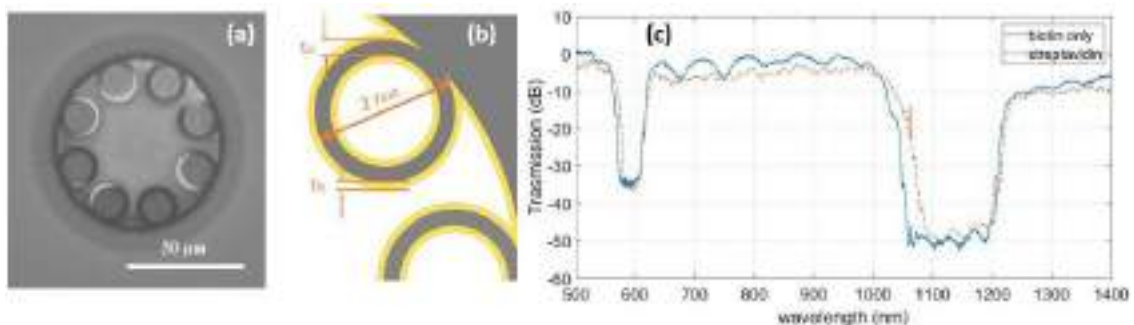
## II. FIBER PROCESSING FOR RECOGNITION ELEMENTS

Fig. 1a) shows the cross section of the fiber used in the experiment. Eight silica tubes placed in a circular shape compose the geometry of this tubular lattice HCPCF. The spectrum of the propagation loss consists in an alternation of high and low loss regions [4], [5]. The spectral location of the high loss regions has a strong dependence on the thickness  $t_{si}$  of the silica tubes according to the following formula [4]:

$$\lambda_m = \frac{2t_{si}}{m} \sqrt{n^2 - 1}$$

where  $n$  is the silica refractive index and  $m$  is an integer number. In the analyzed fiber the thickness of the silica tube is  $t_{si}=610\text{nm}$ , while the tube radius is  $r_{ext}=6.8\mu\text{m}$ .

In order to guarantee the immobilization of the streptavidin to silica surface, a proper treatment of the fiber to immobilize a layer of biotin has been carried out [1]. In this way, the streptavidin can be immobilized on silica surface through bonding with biotin [3]. When a liquid containing a solution of streptavidin is infiltrated inside the hollow core of the fiber, an additional layer is generated on the silica surface as shown in Fig. 1(b). That layer increases the tube thickness and thus determines a red shift in the spectrum of the low transmission spectral regions [4].



**FIG. 1** – (a) cross section of the TLF used in the experiment. (b) details of the silica fiber cross section (gray) with bio-layer (yellow). (c) fiber transmission spectra before (biotin only) and after (streptavidin) the infiltration of a  $0.1 \text{ mg/mL}$  solution of streptavidin.

### III. EXPERIMENTAL RESULTS

The layer on the fiber surfaces has been obtained by infiltrating liquid solutions of reagents induced by a nitrogen overpressure (2 atm). The steps carried out followed similar procedures described earlier for other microstructured fibers [1]. Briefly, first the surface of the channels was cleaned and activated with HCl/Methanol 1:1, then a solution of (3-aminopropyl) triethoxysilane (APTES, 5% in ethanol was infiltrated, followed by rinsing to obtain amino groups at the terminal end. Biotin (5 mM) was then activated using EDC-NHS chemistry (0.25 M both) in a buffered aqueous solution (carbonate buffer, 100 mM, pH 9) and passed through the fiber for 2 hours. The fiber channels were then washed with distilled water.; the resulting functional fiber was then used for the sensing experiments. In these, a solution of streptavidin of 0.1 mg/mL in PBS buffer was used, which was passed through the fiber for 2 hours. The fiber was then washed with distilled water and dried using nitrogen. Measurements were made just before and after streptavidin infiltration. The spectral measurements were obtained by coupling the fiber with a homemade supercontinuum white light source, even though a coherent source is not strictly necessary [2]; an optical spectrum analyzer with a resolution bandwidth of 1 nm was used to measure the output transmission spectrum. Fig. 1c) compare the transmission spectra normalized to the source spectrum of the fiber before (biotin only) and after streptavidin) the infiltration. A red shift of the spectrum around the wavelengths 570 nm and 1045 nm is about 7nm and 20 nm respectively showing that hollow core inhibited coupling fiber can be effectively used as sensor of proteins.

### IV. CONCLUSIONS

In this work, we report on the first experimental results of tubular lattice HCPCF used as protein sensor. A measurable red shift of the transmission spectrum of about 20nm in the near infrared region has been observed after a fiber infiltration with a solution containing 0.1 mg/mL of streptavidin.

### REFERENCES

- [1] M. Barozzi, A. Manicardi, A. Vannucci, A. Candiani, M. Sozzi, M. Konstantaki, S. Pissadakis, R. Corradini, S. Selleri, and A. Cucinotta, "Optical Fiber Sensors for Label-free DNA Detection," *J. Lightwave Technol.* vol. 35, pp. 3461-3472, 2017.

- [2] F. Giovanardi, A. Cucinotta, and L. Vincetti, "Inhibited coupling guiding hollow fibers for label-free DNA detection," *Opt. Expr.* vol. 25, pp. 26215-26220, 2017.
- [3] A. K. Mudraboyina, and J. Sabarinathan, "Protein Binding Detection Using On-Chip Silicon Gratings," *Sensors*, vol. 11, pp. 11295-11304, 2011.
- [4] L. Vincetti, and V. Setti, "Waveguiding mechanism in tube lattice fibers," *Opt. Expr.* vol. 22, pp. 23133-23146, 2010.
- [5] B. Debord, A. Amsanpally, M. Chafer, A. Baz, M. Maurel, J. M. Blondy, E. Hugonnot, F. Scol, L. Vincetti, F. Gérôme, and F. Benabid, "Ultralow transmission loss in inhibited-coupling guiding hollow fibers," vol. 4, pp. 209-217, 2017.

# COUPLED MODE THEORY ASSESSMENT FOR SEMICONDUCTOR CODIRECTIONAL COUPLERS

Ali Emre Kaplan<sup>(1,2)</sup>, Gaetano Bellanca<sup>(1)</sup>, Jos Van Der Tol<sup>(2)</sup>, Paolo Bassi<sup>(3)</sup>

<sup>(1)</sup> DI, University of Ferrara, Italy

<sup>(2)</sup> DEE, Technical University of Eindhoven, The Netherlands

<sup>(3)</sup> DEI, University of Bologna, Italy

[paolo.bassi@unibo.it](mailto:paolo.bassi@unibo.it)

## Abstract

*The Coupled Mode Theory (CMT) is a tool widely used to study the electromagnetic behavior of complex optical devices via the study of the, simpler, composing structures. In this paper, the CMT will be assessed both theoretically and experimentally to show which are the best choices in its formulation to allow its successful use also in the case of closely spaced, high index contrast waveguides.*

**Index Terms** – Coupled Mode Theory, Semiconductor waveguides, Integrated Optics, Numerical Modelling.

## I. INTRODUCTION

The Coupled Mode Theory (CMT) is routinely used to study in a simpler way complicated systems where propagating modes are coupled by structure perturbations. Such coupling can be co-directional (e.g. couplers) or counter-directional (e.g. guides with gratings).

The CMT was first proposed in [1] and then applied also in optics (e.g. [2]). Originally, it was proposed to study only structures with small refractive index changes and coupling, conditions easily fulfilled by the available technologies. The solution considers coupling between the modes of the single waveguides (assumed mutually orthogonal) constituting the complete structure, instead of the interference of its super-modes. This simplifies the approach, since modes of single waveguides can be calculated more easily than the overall structure super-modes. More recently, semiconductor based technologies made the original simplifications no longer realistic. This required revisiting the original approach (e.g. [3]), including mode non-orthogonality.

CMT assessments have been proposed, but always in the 2D case. Recently [4], realistic 3D structures have been studied comparing CMT results for a waveguide coupler to exact ones, calculated with a Finite Element Based software [5], ranging from large to small index contrasts. This study showed also that the extra burden to include mode non-orthogonality was practically useless. It would now be interesting to assess the CMT also with experimental data, as done for example in [6] for a Ti:LiNbO<sub>3</sub> waveguide, which is however a low contrast guide. This work aims to compare the CMT results with experimental ones obtained for couplers realized with the so-called Indium-Phosphide Membranes on Silicon (IMOS) technology [7] which is of interest since its high index contrast allows micron-sized structures comparable to those of Silicon-on-Insulator (SOI). Furthermore, the IMOS technique enables

the integration of electronics (CMOS) and photonics on the same chip. Both active (SOAs, lasers) and passive devices (waveguides, directional couplers) can be fabricated in a single membrane.

After a short introduction to the main equations involved in the study, a brief description of the waveguide characteristics will be given and results will be presented. Finally, conclusions will be drawn.

## II. THE COUPLED-MODE THEORY

Without entering into details of the CMT, (see for example [4]), suffice here to say that possible expressions of the coupling coefficient  $\kappa$  between two modes labeled respectively  $\nu$  and  $\mu$  of the two coupled guides can be found combining the so called transversal coupling coefficient

$$\kappa^t = \kappa_{\nu\mu}^t = \frac{\omega}{4} \int_{S_{\Delta\varepsilon}} \Delta\varepsilon \bar{E}_{t\nu} \cdot \bar{E}_{t\mu}^* dS \quad (1)$$

with the longitudinal one, which, depending on the definition of the single waveguide perturbation  $\Delta\varepsilon$ , given by one of the following expressions

$$\kappa_a^z = \kappa_{\nu\mu}^z = \frac{\omega}{4} \int_{S_{\Delta\varepsilon}} \frac{\varepsilon \Delta\varepsilon}{\varepsilon + \Delta\varepsilon} E_{z\nu} E_{z\mu}^* dS \quad (2)$$

$$\kappa_b^z = \kappa_{\nu\mu}^z = \frac{\omega}{4} \int_{S_{\Delta\varepsilon}} \Delta\varepsilon E_{z\nu} E_{z\mu}^* dS. \quad (3)$$

The following three possibilities will be checked:

$$\kappa = \kappa^t \quad (4)$$

$$\kappa = \kappa^t + \kappa_a^z \quad (5)$$

$$\kappa = \kappa^t + \kappa_b^z. \quad (6)$$

The integrals are calculated only in the region  $S_{\Delta\varepsilon}$  where the perturbation exists. The presence of the longitudinal components contribution and its optimal expression are a critical point. The coupling length  $L$ , i.e. the distance for a complete power transfer between the two waveguides, can be calculated exactly from the super-modes propagation constant mismatch  $\Delta\beta$ , the difference of the even and odd super-mode propagation constants:

$$L = \frac{\pi}{\Delta\beta}. \quad (7)$$

Since it also holds [8]

$$L = \frac{\pi}{2\kappa} \quad (8)$$

one can also find the expression of the coupling coefficient  $\kappa$  which can be considered as the exact one, reference to test expressions (4)-(6):

$$\kappa = \frac{\Delta\beta}{2}. \quad (9)$$

The comparison between this value and the calculated ones will be done in the next section.

## III. THE MEMBRANE TECHNOLOGY BASED COUPLER

The structure which will be studied in the following is illustrated in Fig. 1. The cover is air (refractive index  $n_c = 1$ ), the waveguide is in *InP* ( $n_g = 3.17$ ) and the substrate is in *BCB* ( $n_s = 1.55$ ). The footing layer is 50 nm high, the two

waveguide ribs have a width of 400 nm and a height of 250 nm. The gap ranges from 100 to 500 nm. The operating wavelength is  $\lambda = 1500$  nm.

The main field components of the left waveguide *quasi-TE* and *quasi-TM* modes are shown in Fig. 2 and 3 respectively. The right rib does not exist, but is shown to evidence the strong coupling condition for a 100 nm gap.

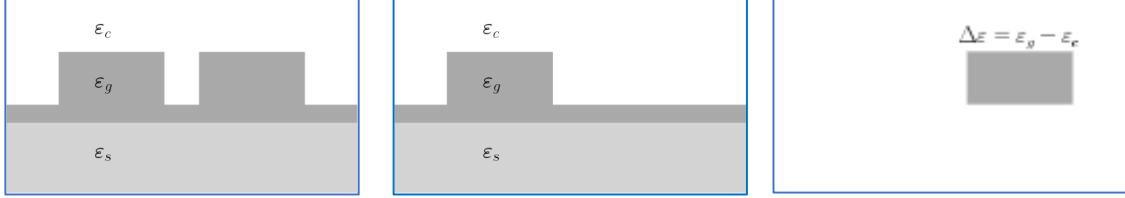


**FIG. 1** – Relative dielectric constants of the coupler (left), of the guide (center) and of the perturbation  $\Delta\epsilon$  (right) used to evaluate (6).

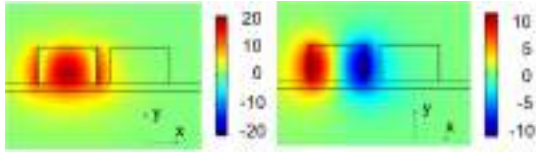


**FIG. 2** – *Quasi-TE* mode distribution:  $\text{Im}(E_x)$  (left),  $\text{Real}(E_z)$  (right).

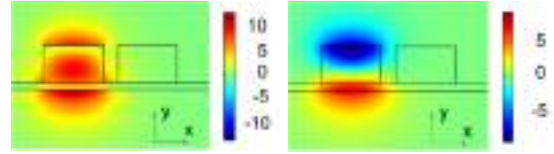


**FIG. 3** – *Quasi-TM* mode distribution:  $\text{Im}(E_y)$  (left),  $\text{Real}(E_z)$  (right).

#### IV. RESULTS

Figures 4 and 5 show the coupling coefficient  $\kappa$  (left) and the coupling length  $L$  (right) calculated for the quasi-TE and the quasi-TM modes respectively. The black long dashed line with open circles comes using (9). The red solid line with crosses shows  $\kappa^t$ . The blue dotted line with triangles shows  $\kappa^t + \kappa_a^z$ . The green dashed-dotted line with squares (almost superimposed to the black long dashed line) shows  $\kappa^t + \kappa_b^z$ .

The best results are obtained using (6). The coupling coefficients of the *quasi-TM* modes are larger than the *quasi-TE* ones, as expected. The effect of the longitudinal coupling coefficient is smaller for the *quasi-TM* modes since  $E_z$  has smaller interactions with the perturbation (see Fig. 2 and 3).

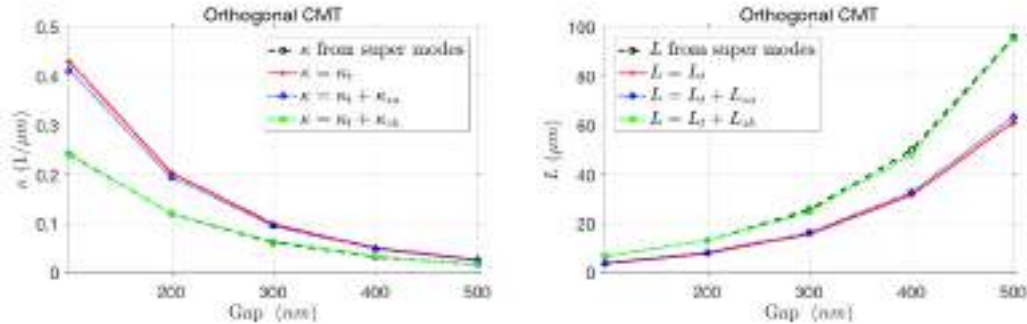


**FIG. 4** – Coupling coefficients (left) and corresponding coupling lengths (right) for the *quasi-TE* mode.

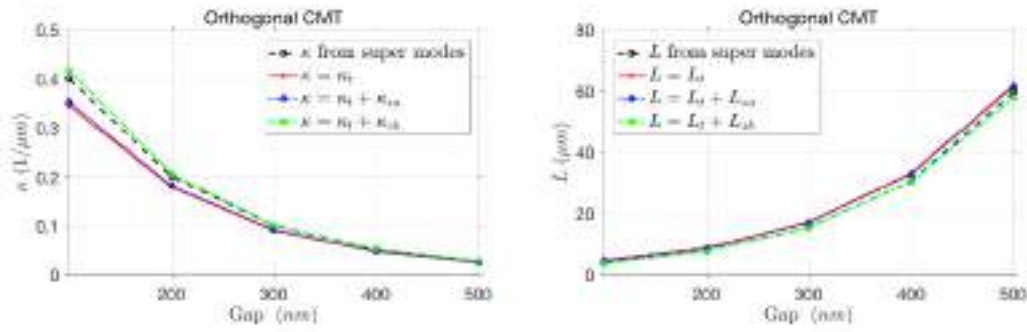


**FIG. 5** – Coupling coefficients (left) and corresponding coupling lengths (right) for the *quasi-TM* mode.

The technological process to fabricate the couplers which will be measured to compare theoretical results with experimental ones is underway. Results will be presented at the conference.

## V. CONCLUSION

The results of some possible implementations of the CMT have been presented in a co-directional coupler and compared with the exact ones obtained using the structure super-modes. Fabrication of the simulated devices is under way to compare theoretical results with the experimental ones.

## ACKNOWLEDGEMENT

The IMOS platform is supported by the “Zwaartekracht”-project, financed by the Dutch government.

## REFERENCES

- [1] S. A. Schelkunoff, “Conversion of Maxwell’s equations into generalized telegraphist’s equations,” *Bell Syst. Tech. J.*, vol. 34, pp. 995–1043, 1955.
- [2] A. Yariv, “Coupled-mode theory for guided wave optics,” *IEEE J. Quantum Electron.*, vol. 9, pp. 919–933, 1973.
- [3] W. Huang, “Coupled-mode theory for optical waveguides: an overview,” *J. Opt. Soc. Am. A*, vol. 11, pp. 963–983, 1994.
- [4] G. Bellanca, P. Orlandi, P. Bassi, “Assessment of the orthogonal and non-orthogonal coupled-mode theory for parallel optical waveguide couplers,” *J. Opt. Soc. Am. A*, vol. 35, pp 577-585, 2018.
- [5] COMSOL Multiphysics Software, <http://www.comsol.com>.
- [6] R. G. Peall, R. R. A. Syms, “Comparison between strong coupling theory and experiment for three-arm directional couplers in Ti:LiNbO<sub>3</sub>,” *J. Lightwave Technol.*, vol. 7, pp. 540–554, 1989.
- [7] J. J. G. M. van der Tol et al., “Indium Phosphide Integrated Photonics in Membranes,” *IEEE J. of Sel. Topics in Quantum Electronics*, vol. 24, pp. 1-9, 2018.
- [8] R. G. Hunsperger, “*Integrated Optics*,” Chap. 8, Springer, 5<sup>th</sup> ed., 2013.

# NON-VOLATILE FERROELECTRIC ACTUATORS INTEGRATED IN SILICON PHOTONIC CIRCUITS

I. Maqueira Albo<sup>(1)</sup>, S. Varotto<sup>(2)</sup>, M. Asa<sup>(2)</sup>, C. Rinaldi<sup>(2)</sup>, M. Cantoni<sup>(2)</sup>, A. Melloni<sup>(1)</sup>, R. Bertacco<sup>(2)</sup>, F. Morichetti<sup>(2)</sup>

<sup>(1)</sup> Dipartimento di Elettronica, Informazione e Bioingegneria  
Politecnico di Milano, 20133 Milano, Italy

<sup>(2)</sup> 2 Dipartimento di Fisica, Politecnico di Milano, 20133 Milano,  
Italy

[francesco.morichetti@polimi.it](mailto:francesco.morichetti@polimi.it)

## Abstract

*In this work, we investigate a novel approach to realize non-volatile phase-actuators integrated in silicon waveguides. We aim to exploit the ferroelectric response of polycrystalline BaTiO<sub>3</sub> (poly-BTO), whose domain can be re-oriented by applying an external electric field so as to induce a large change of the refractive index. Owing to the polarization remanence of ferroelectric materials, such index variation is maintained when the electric field is turned off. Experimental results on poly-BTO demonstrate the possibility to achieve a non-volatile change of the poly-BTO refractive index in the order of 10<sup>-2</sup>, which is consistent with a 90° reorientation of the ferroelectric domains. We also integrated thin poly-BTO films on Si waveguides with a low additional propagation loss (<1 dB/mm), enabling the realization of PICs with the proposed poly-BTO Si-photonics platform.*

**Index Terms** – Integrated optics materials, Ferroelectrics, Optical waveguides, Photonic integrated circuits, Silicon photonics

## I. INTRODUCTION

Low-energy optical actuators are needed in integrated optics to either compensate fabrication tolerances or dynamically control and calibrate the functionality of reconfigurable and programmable circuits. Conventional actuators technologies exploit local heating of the optical waveguides as well as carrier injection/depletion effects in semiconductor waveguides. Albeit being effective and well consolidated, these solutions typically require high power consumption or suffer from large crosstalk that limits PIC scalability. Non-volatile actuators capable to maintain the switching state without an applied control signal are a promising route to tackle this issue. To this aim, several approaches based on phase change materials (GST) [1] and insulator-metal phase transition materials [2] have been proposed, which however mainly provide a control of the imaginary part of the refractive index of the waveguide, thus realizing “intensity actuators” solutions only.

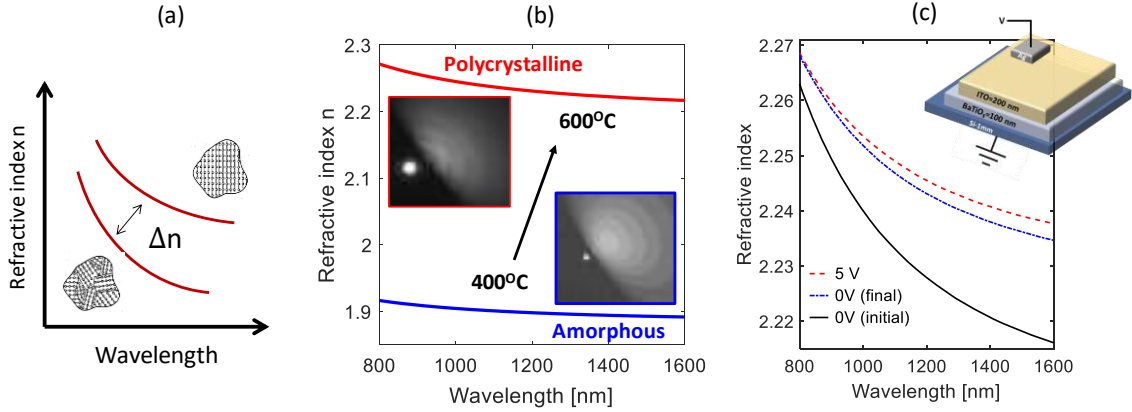


**FIG. 1** – (a) Schematic of the refractive index change associated with domain switching in poly-BTO film. (b) Measured refractive index of amorphous (blue curve) and polycrystalline (red curve) BTO films deposited by PLD at different temperatures. RHEED measurements in the insets confirm the amorphous and polycrystalline nature of the films. (c) Measured refractive index of the poly-BTO film in the pristine state (black solid curve), during the application of a 5V pulse (red dashed curve) and in the final state (blue dash-dotted curve).

In this work, we propose a novel approach to realize self-holding phase actuators integrated in Si waveguides. We aim to exploit the ferroelectric response of polycrystalline BaTiO<sub>3</sub> (poly-BTO) directly deposited on a Si substrate. We observed a large non-volatile change of the poly-BTO refractive index, in the order of  $10^{-2}$ , which is consistent with a  $90^\circ$  reorientation of the ferroelectric domains. We also demonstrated the possibility to integrate thin poly-BTO films as an upper cladding of Si waveguides with a low additional propagation loss ( $<1$  dB/mm), enabling the realization of microring resonators and other integrated devices with the proposed poly-BTO Si-photonics platform.

## II. SELF-HOLDING OPTICAL SWITCHING IN BTO THIN FILMS

Ferroelectric materials are characterized by domains with in-plane ( $a$ -axis) or out-of-plane ( $c$ -axis) orientation, which in polycrystalline films are almost randomly distributed. Domains orientation can be manipulated by applying an external electric exceeding the coercive field of the material and as a consequence of the re-orientation a large change of the refractive index  $n$  can be achieved. Due to the polarization remanence of ferroelectric materials, the refractive index variation is maintained when the electric field is turned off (see Fig 1.a).

BTO films with a thickness of 100 nm were grown by pulsed laser deposition (PLD) on conductive Si(001) substrate, after the removal of native SiO<sub>2</sub> from the substrate surface by standard wet etching in hydrofluoric acid. By controlling the temperature (400 °C - 600 °C) and the oxygen pressure ( $pO_2 = 20$  mTorr - 80 mTorr) during the deposition, BTO films with amorphous and polycrystalline structure were

deposited. A post-annealing at 600°C was performed in 0.5 atm O<sub>2</sub> pressure to fill the oxygen vacancies.

Reflection high-energy electron diffraction (RHEED) measurements (insets of Fig. 1b) indicate that films deposited at 600°C exhibit a polycrystalline structure (poly-BTO), whereas at lower deposition temperatures amorphous films (a-BTO) are obtained. Surface roughness as measured by atomic force microscopy (AFM) is between 0.7-0.9 nm rms. The refractive index  $n$  of  $\alpha$ -BTO films ( $\sim 1.9$  at  $\lambda > 1300$  nm) is lower than poly-BTO films ( $\sim 2.2$  at  $\lambda > 1300$  nm), as measured by spectroscopic ellipsometry (see Fig. 1b), in agreement with data in [3].

To perform switching experiments a 200 nm layer of indium tin oxide (ITO) was sputtered onto the poly-BTO film to realize the top electrode. By applying a 5 V signal (Fig. 1.c), a large change of the refractive index of poly-BTO is induced (red dashed curve) with respect to the initial state (black solid curve), that is as large as  $3 \cdot 10^{-2}$  in the 1550 nm range, with no change in the material loss. Such refractive index variation suggests the occurrence of ferroelectric domains reorientation (from  $a$  to  $c$  axis) in the poly-BTO film [4]. After the electric signal is switched off (blue dashed-dotted curve), the switched state was mostly preserved with only a small relaxation in the refractive index (red dashed curve). We also observed that the pristine state of the film can be restored by heating the sample above the Curie temperature of BTO (120°C).

### III. LOW-LOSS POLY-BTO-COATED SILICON WAVEGUIDES AND CIRCUITS

Polycrystalline BTO was then employed as upper cladding material of Si nanowaveguides. Figure 2(a) shows the cross-sectional SEM photograph of a 220 nm x 400 nm Si waveguide covered with a 200-nm-thin poly-BTO film. For this waveguide geometry, the overlap factor of the guided mode with the BTO material is about 18% for TE polarization and 28% for TM polarization. Given the large  $\Delta n$  measured on poly-BTO films, this would enable a  $\pi$ -phase shift in a waveguide actuator of less than 100  $\mu\text{m}$  length. As shown in Fig. 2(a), at a wavelength of 1550 nm, both modes exhibit a loss change of less than 1dB/mm after the deposition of the BTO layer, thus resulting in less than 0.1 dB actuator loss. The loss decrease observed in the narrowest waveguide (400 nm width) is due to the mitigation of the roughness-induced scattering loss [5].

Figure 2(b) shows the TE transmission measured at the drop port of a silicon microring resonator with a radius of 40  $\mu\text{m}$ . Before the deposition of 200-nm-thick poly-BTO upper cladding (black dashed line), the air-coated silicon microring has a free spectral range of 2.45 nm, a 3 dB bandwidth of about 25 GHz, resulting in a Q factor of about 8000, and an off-band isolation of 18 dB. After the deposition of the BTO cladding (red solid curve), the shape of the transmission spectrum is almost entirely preserved, the Q factor reduction to about 6000 (33 GHz bandwidth) being essentially due to the higher coupling coefficient of the BTO-cladded directional coupler of the microring.

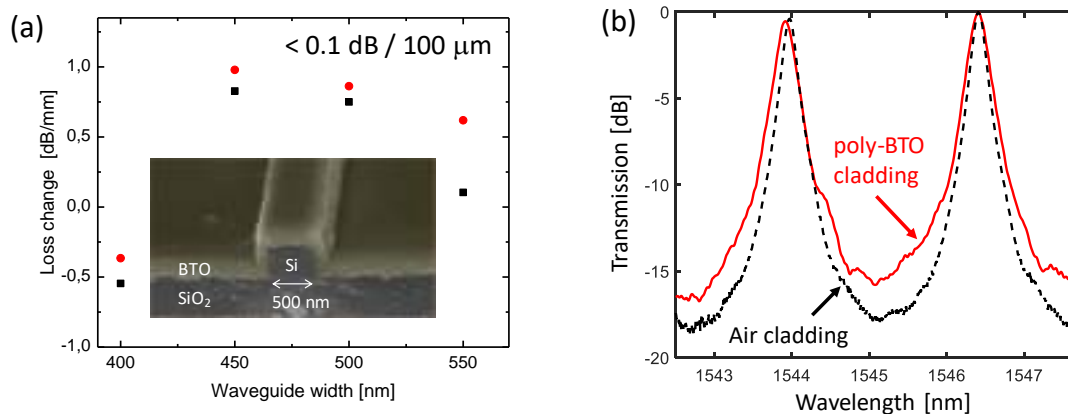


**Fig. 2** - (a) Variation of the propagation loss of a Si nanowaveguide (SEM cross-sectional picture in the inset) after the deposition of a 200 nm thick poly-BTO coating. (b) Normalized transmission at the drop port of a microring resonator before (black dashed curve) and after (red solid curve) the deposition of the poly-BTO upper cladding.

#### IV. CONCLUSION

We demonstrated an electrically-driven non-volatile change of the refractive index of polycrystalline BTO films, which is consistent with a 90° reorientation of the ferroelectric domains. The large refractive index variation ( $3 \cdot 10^{-2}$ ) would enable the realization of compact ( $< 100 \mu\text{m}$ ), low-loss ( $< 0.1 \text{ dB}$ ), self-holding phase actuators integrated in silicon optical waveguides. We also successfully integrated poly-BTO films on Si waveguides and microring resonators, demonstrating the possibility to realize PICs with the proposed poly-BTO Si-photonics platform.

#### V. ACKNOWLEDGEMENT

This work was supported by Fondazione Cariplo Project “Advanced Control Technologies for Integrated Optics (ACTIO)” – Rif. 2016-0881.

#### VI. REFERENCES

- [1] H. Zhang, et al, “Ultracompact Si-GST hybrid waveguides for nonvolatile light wave manipulation,” *IEEE Phot. Journ.*10(1), 2200110 (2018).
- [2] A. Joushaghani, et al., “Sub-volt broadband hybrid plasmonic-vanadium dioxide switches, *Appl. Phys. Lett.* 102, 061101 (2013).
- [3] Thomas, Reji, D. C. Dube, M. N. Kamalasanan, and Subhas Chandra, “Optical and electrical properties of BaTiO<sub>3</sub> thin films prepared by chemical solution deposition”, *Thin solid films* 346 (1-2), 212, (1999).
- [4] M. J. Dicken, L. A. Sweatlock, D. Pacifici, H. J. Lezec, K. Bhattacharya, and H. A. Atwater, “Electrooptic modulation in thin film barium titanate plasmonic interferometers,” *Nanoletters* 8 (11), 4048 (2008).
- [5] D. Melati, A. Melloni, and F. Morichetti, “Real photonic waveguides: guiding light through imperfections,” *Advances in Optics and Photonics*, vol. 6, no. 2, pp. 156-224, May 2014.

# THE REDUCED SCATTERED FIELD AS A TOOL FOR FOCUSING IN AN UNKNOWN SCENARIO

M. T. Bevacqua<sup>(1)</sup>, R. Palmeri<sup>(1)</sup>, L. Crocco<sup>(2)</sup>, T. Isernia<sup>(1,2)</sup>

<sup>(1)</sup> DIIES, Univ. Mediterranea of Reggio Calabria, Italy,  
(martina.bevacqua,roberta.palmeri,tommaso.isernia)@unirc.it

<sup>(2)</sup> CNR-IREA, National Research Council of Italy, Naples, Italy,  
crocco.l@irea.cnr.it

## Abstract

*The orthogonality sampling method has been recently introduced in inverse scattering community as a way to retrieve the morphological properties of unknown targets. Both the simplicity and the flexibility with respect to the performed scattering experiments make this method more appealing than other qualitative methods. Starting from orthogonality sampling method and the inherent concept of ‘reduced scattered field’, in this contribution we propose a new tool to focus the field intensity in an unknown scenario. This novel focusing tool, which can be relevant from both a theoretical and practical point of view, is described and validated with a numerical example.*

**Index Terms** – focusing, inverse scattering problem, orthogonality sampling method, shape reconstruction.

## I. INTRODUCTION

The problem of focusing the field intensity distribution in an unknown medium is relevant from both a theoretical and applicative point of view. Indeed, the problem of determining the array complex excitation in such a way to concentrate the field energy into a given target point of the investigated scenario can be of interest in medical treatments and also near field focusing. However, most of the focusing approaches introduced in literature are based on the exact knowledge of the scenario.

Differently from these latter, the approach in [1] proposes a novel adaptive focusing strategy which, using a number of scattering experiments but avoiding any search for a quantitative imaging of the scenario, allows to determine the excitation coefficients needed to focus the field intensity in a given target point. The method is based on the solution (as well as on the physical interpretation) of the linear sampling method (LSM). LSM is a widely used *qualitative* method which aims at recovering presence, position and shape of unknown targets starting from the knowledge of the fields they scatter.

Many other different qualitative methods have been developed in literature to solve the so called ‘inverse obstacle’, among them it is worth to mention the orthogonality sampling method (OSM) [6], which shows some similarity with respect to LSM. In fact, the rationale behind it is to sample of the scenario under investigation into an arbitrary grid of points,

wherein the *reduced* scattered field and an indicator function are computed in order to provide support information. However, with respect to LSM, OSM exhibits an increased robustness to noise and more flexibility as its application is possible for a wide variety of experiments (single-view, multifrequency, multi-view, to a combination of them) [2]. Last, but not least, it does not require the explicit use of regularization techniques.

Starting from these considerations and the close analogy with LSM, in this contribution we investigate the possibility of using the *reduced* scattered field as a tool for focusing the field intensity in an unknown scenario. In particular, an adaptive two-steps procedure is proposed, wherein a preliminary and qualitative sensing stage of the region of interest is performed via OSM processing. Then, the focusing stage is based on a straightforward exploitation of the *reduced* scattered field to determine the excitation coefficients required to focus the total field in the target point.

Throughout we consider the canonical 2D scalar problem (TM polarization) and we assume and drop the time harmonic factor  $\exp\{j\omega t\}$ .

## II. ORTHOGONALITY SAMPLING METHOD

In the OSM, a key role is played by the so called *reduced scattered field*  $E_s^{red}$ , which is defined as [2]:

$$E_s^{red}(\mathbf{r}, \hat{\mathbf{r}}_t) = \int_{\Gamma} E_s^{\infty}(\hat{\mathbf{r}}_m, \hat{\mathbf{r}}_t) e^{jk_b \mathbf{r} \cdot \hat{\mathbf{r}}_m} d\Gamma = \frac{1}{\gamma} \langle E_s^{\infty}, G_b^{\infty} \rangle_{\Gamma} \quad (1)$$

where  $E_s^{\infty}(\hat{\mathbf{r}}_m, \hat{\mathbf{r}}_t, k_b)$  is the (measured) far field pattern;  $\mathbf{r}$  is the generic position on an arbitrary grid sampling the region under test  $\Omega$  hosting the unknown targets;  $\hat{\mathbf{r}}_t$  is the unit vector which identifies the angular position of the antennas, probing  $\Omega$  and located on a closed curve  $\Gamma$  in the scatterers far-zone;  $\hat{\mathbf{r}}_m$  is the unit vector which identifies the measurements angular position; and  $k_b = \omega \sqrt{\mu_b \varepsilon_b}$  is the wavenumber in the host medium at the frequency  $\omega$ .

The scalar product in (1) assays the *orthogonality* relation between the measured far field pattern  $E_s^{\infty}$  with a test function which corresponds (apart from a constant  $\gamma$ ) to the Green's function  $G_b$  as computed in far-field zone [2]. Once the *reduced* scattered field is computed by means of (1), the OSM indicator function  $I(\mathbf{r})$  is defined as [2]:

$$I(\mathbf{r}, k_b) = \int_{\Gamma} |E_s^{red}(\mathbf{r}, \hat{\mathbf{r}}_t, k_b)|^2 d\hat{\mathbf{r}}_t \quad (2)$$

which is expected to exhibit large values for sampling points  $\mathbf{r}$  belonging to the targets support and limited values outside it.

### III. FIELD INTENSITY FOCUSING VIA OSM

As we are going to argue, the *reduced* scattered field can be exploited to determine the  $N$  array excitations  $I_t$  in such a way concentrate the field intensity in a given target point  $\mathbf{r}_p$  belonging to the target support. To this end, let us consider the minimization of the following cost functional, i.e.:

$$\min_{I_t} \left\| \sum_{t=1}^N I_t(\mathbf{r}_p) E_s^\infty(\hat{\mathbf{r}}_t, \hat{\mathbf{r}}_m) - G_b^\infty(\mathbf{r}_p, \hat{\mathbf{r}}_m) \right\|_\Gamma^2 \quad (3)$$

where one is enforcing on the measurements curve  $\Gamma$  a matching between the scattered fields recombined according to  $I_t$  and the Green function  $G_b^\infty$ , which represents the far field radiated by an elementary current in  $\mathbf{r}_p$ . Therefore, due to the linearity of the scattering phenomena, by minimizing (3) one is looking for a function which modifies the original amplitudes of the primary sources in such a way that their combined effect induces on  $\Gamma$  a scattered field equal to  $G_b$ .

A possible set of array excitations can be provided by the solution of the equation underlying the LSM, as explained in [1]. Another solution can be obtained by furtherly developing the condition in (3). By a simple derivation (whose details are deferred to the Conference) the array excitations  $I_t$  can be in fact related to the *reduced* scattered field (1) as:

$$\sum_{t=1}^N I_t \langle E_s^\infty(\hat{\mathbf{r}}_t, \hat{\mathbf{r}}_m), E_s^\infty(\hat{\mathbf{r}}_{\bar{t}}, \hat{\mathbf{r}}_m) \rangle_\Gamma = \gamma \left( E_s^{red}(\hat{\mathbf{r}}_{\bar{t}}) \right)^* \quad (4)$$

wherein the subscript  $*$  denotes the complex conjugate operation and  $\bar{t}$  identifies a given scattering experiment corresponding to a given angular position  $\hat{\mathbf{r}}_{\bar{t}}$  of the transmitting antenna. Interestingly, by assuming that the scattering experiments are performed in such a way that the scattered fields data are approximatively orthonormal (which can be eventually be achieved by a proper organization of scattering experiments), the array excitations  $I_t$  are finally given by:

$$I_t = \gamma \left( E_s^{red}(\mathbf{r}_t) \right)^* \quad (5)$$

Note the equation (5) means that (the complex conjugate of) the *reduced* scattered field can provide the array excitations required to enforce on  $\Gamma$  a scattered field equal to the field radiated by an elementary current in  $\mathbf{r}_p$ . Hence, by following the same reasoning as in [1], the same excitations can be used to set the amplitudes of the different transmitting antennas in such a way to induce in the investigation domain total fields which are focused in the target point  $\mathbf{r}_p$ . In summary, see (5), the *reduced* scattered field provides a solution to the problem of focusing in unknown scenarios.

#### IV. A NUMERICAL EXAMPLE

In order to verify the capability of (4) to focus the field intensity in a given target point, we performed an extensive numerical analysis. In the following a numerical example dealing with the popular ‘kite’ target, which is known to be a critical situation for [1]. The kite has the leading dimension of about a wavelength and complex permittivity equal to  $2 - 0.36j$ . The target is placed inside a square domain of side  $L = 0.1\text{ m}$  discretized in  $84 \times 84$  cells. Moreover, 16 receivers and transmitters, located on a circumference  $\Gamma$  of radius  $R = 5\text{ m}$ , have been considered. The scattered field data, simulated by means of a full-wave solver based on the method of moments, have been corrupted with a random Gaussian noise with  $\text{SNR} = 30\text{ dB}$ . The working frequency is  $5\text{ GHz}$ .

The performances have been compared with those obtained with LSM [1]. In fig. 1(a) and (d) the maps of the normalized indicators are reported, while in 1(b)-(c) and 1(e)-(f) the normalized square amplitudes of the total field focused in two different target points. As it can be seen, the proposed tool exhibits much better capability with respect to LSM solution, and it also avoids undesired effects in points different from the target one.

More examples and details and an extensive discussion of performances will be given at the conference.

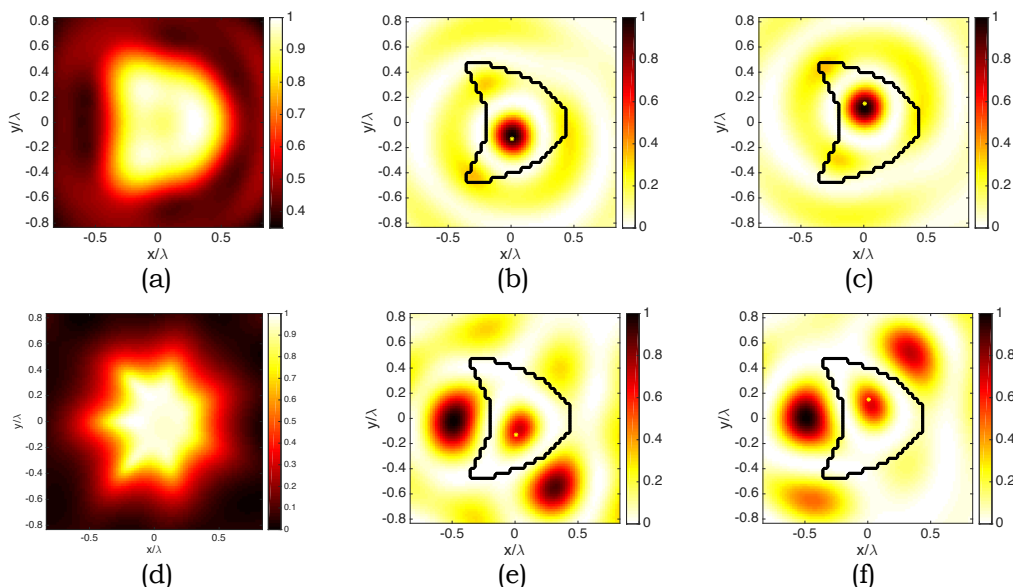


**FIG. 1** – OSM (a) and LSM (d) indicators. Normalized square amplitudes of the total field in two different target points (yellow stars) via (5)(b)-(c), and via LSM [1](e)-(f).

#### REFERENCES

- [1] L. Crocco, L. Di Donato, D. A. M. Iero, T. Isernia, An adaptive method to focusing in unknown scenario, *Progress in Electromagnetic Research*, 130: 563-579, 2012.
- [2] R. Potthast, A study on orthogonality sampling, *Inverse Prob.*, 26(7), 2010.

# THE ROLE OF VIEW DIVERSITY ON LINEAR SCATTERING OPERATOR IN FRESNEL-ZONE

M. A. Maisto<sup>(1)</sup>, F. Munno<sup>(1)</sup>

(1) Dipartimento di Ingegneria, Università della Campania “L. Vanvitelli”  
Via Roma 29, 81031 Aversa, Italia  
[mariaantonia.maisto@unicampania.it](mailto:mariaantonia.maisto@unicampania.it)

## Abstract

*In this paper the role of view diversities in linear inverse scattering problems is analyzed in terms of the singular values behavior of the pertinent scattering operators. In order to obtain analytical results, the analysis is developed within a two-dimensional scalar Fresnel-zone configuration.*

**Index Terms** – Diversities, Inverse scattering, NDF, SVD.

## I. INTRODUCTION

Linear inverse electromagnetic scattering problems deal with the inversion of an integral equation of the first kind in order to recover an object function which is related to the features of the scatterer like the shape, the support, the dielectric contrast, etc. It is known that probing the scattering scene at different spatial positions (multi-view configuration) or at different frequencies (multi-frequency configuration) can improve the achievable performance. However, some degrees of *redundancy* [1] can be expected as not all the data are necessarily independent. The focus here is on establishing the role played by the view diversities on the singular values behavior. Note that this paper is an extension of [1] where the role of redundancy is analyzed in far-zone. The reference scenario is depicted in Fig. 1.

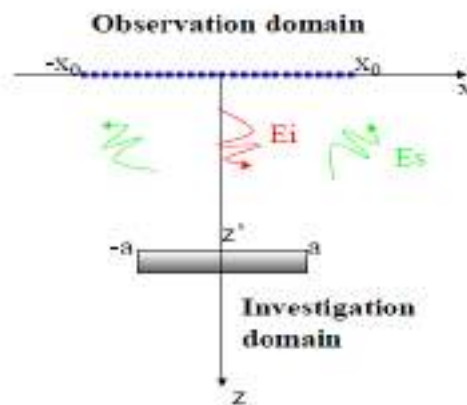


**FIG. 1** – Pictorial view of the scattering configuration considered in this paper.

The scatterer is illuminated by a filamentary current located in  $x_s \in \Sigma = [-x_o, x_o]$ , which also represents the observation domain. The scatterer domain is assumed to be a strip  $I = [-a, a]$  along the  $x$ -axis and the scattered field is collected in the Fresnel-zone. Invariance is assumed along the plane wave polarization direction which in turn is orthogonal

to the strip. Accordingly, the study is developed for a two-dimensional scalar configuration. In this framework, to collect the scattered field by exploiting the view diversity entails to vary  $x_s$ . The paper is organized as follows: in section 2 the multi-view configuration in the Fresnel-zone is presented and the view redundancy is discussed. Finally, conclusions end the paper.

## II. MULTI-VIEW CONFIGURATION

Consider a multi-view configuration. In the Fresnel-zone, exploiting the Born approximation, the scattered operator is

$$\mathcal{A}: \chi(x) \in \mathcal{L}_1^2 \rightarrow E_S(x_s, x_1) = \int_{-a}^a \frac{1}{z'} \chi(x') e^{-j(2k_b z' + \frac{k_b}{2z'}(x_1 - x')^2 + \frac{k_b}{2z'}(x_s - x')^2)} dx' \in \mathcal{L}_2^2(\Sigma \times \Sigma) \quad (1)$$

where  $k_b$  being the wavenumber and  $\chi$  the contrast function. Since the kernel function of equation (1) is a square integrable function, the integral operator is of Hilbert-Schmidt class and hence compact [2]. Therefore its singular system can be introduced. By casting the equations of the shifted eigenvalue problem, the singular system can be found. In particular, with  $\mathcal{A}^\dagger$  being the adjoint operator of  $\mathcal{A}$ , this approach moves from the equation

$$\mathcal{A}^\dagger \mathcal{A} u_n(x') = \sigma_n^2 u_n(x) \quad (2)$$

to the equation

$$\int_{-a}^a \tilde{u}_n(x') \lambda^2 \left\{ \frac{\sin \frac{k_b}{2z'} x_0 [x' - x]}{\pi |x' - x|} \right\}^2 dx' = \sigma_n^2 \tilde{u}_n(x) \quad (3)$$

where  $\tilde{u}_n(x) = u_n(x) e^{-j \frac{k_b}{2z'} x^2}$  and the set  $\{u_n(x)\}_{n=0}^\infty$  forms a complete orthonormal basis for the orthogonal complement of the operator kernel. As depicted in Fig.2, the eigenvalues behavior of the operator  $\mathcal{A}^\dagger \mathcal{A}$  follows the trend of the Fourier transform of the kernel, that is a triangular trend.

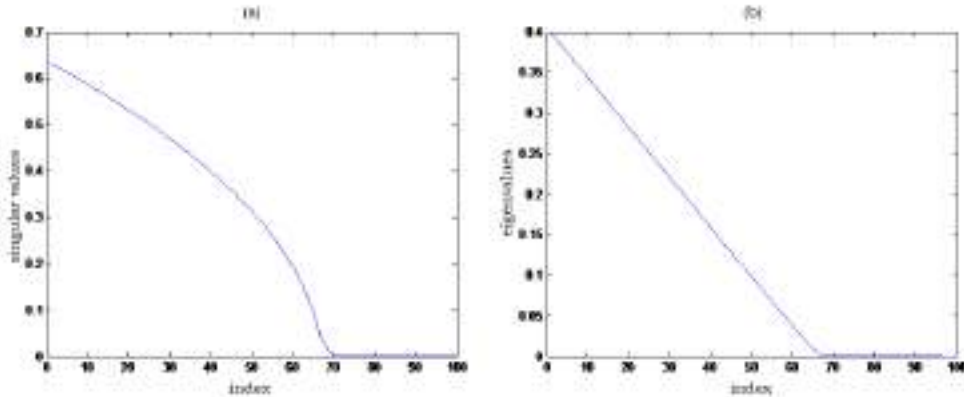


**FIG. 2** – Behavior of the singular values of the operator  $\mathcal{A}$  (a) and of the eigenvalues of the operator  $\mathcal{A}^\dagger \mathcal{A}$  (b).

The trend of the singular values shown in Fig.2(a) can be explained in terms of “redundant” data [1]. In order to obtain an estimation of the maximum number of independent data, let us consider  $M$  uniformly sampled views  $\{x_{s_1}, \dots, x_{s_M}\}$  representing a discrete subset of  $\Sigma$ . The pertinent scattered operator for the Fresnel-zone then writes as:

$$\mathcal{D}: \chi(x) \in \mathcal{L}_I^2 \rightarrow E_s(x_{sn}, x_1) = \int_{-a}^a \frac{1}{z'} \chi(x') e^{-j(2k_b z' + \frac{k_b}{2z'}(x_1 - x')^2 + \frac{k_b}{2z'}(x_{sn} - x')^2)} dx' \in \mathcal{L}_{(\Sigma \times \Sigma)}^2 \quad (4)$$

The singular system of (4) can be found by studying the eigen-spectrum of the associated operator  $\mathcal{D}^\dagger \mathcal{D}$ . This leads to the following equation

$$\int_{-a}^a \sum_{n=1}^M \lambda \frac{\tilde{u}_k(x)}{z'} e^{j\frac{k_b}{z'} x_{sn} [x' - x]} \frac{\sin \frac{k_b}{z'} x_0 [x' - x]}{\pi [x' - x]} dx' = \sigma_k^2 \tilde{u}_k(x) \quad (5)$$

with  $\tilde{u}_k(x) = u_k(x) e^{-j\frac{k_b}{2z'} x^2}$ . Thus, the spectrum of the kernel in (5) is a superposition of  $M$  rectangular windows of amplitude  $\lambda/z'$ , centered in  $\frac{k_b}{z'} x_{sn}$  and with band  $\Omega_n = [\frac{k_b}{z'} x_{sn} - \frac{k_b}{z'} x_0, \frac{k_b}{z'} x_{sn} + \frac{k_b}{z'} x_0]$ . Equation (5) can be expressed in terms of spatial limiting and band limiting projectors  $P_1$  and  $B_{\Omega_n}$  as

$$\mathcal{D}^\dagger \mathcal{D} = \frac{\lambda}{z'} \sum_{m=1}^M P_1 B_{\Omega_m} P_1 \quad (6)$$

For  $M = 2$ , equation (6) produces

$$\mathcal{D}^\dagger \mathcal{D} = \frac{\lambda}{z'} P_1 B_{\Omega_1} P_1 + \frac{\lambda}{z'} P_1 B_{\Omega_2} P_1 \quad (7)$$

For both the operators in (7) the eigenvalues exhibit a step-like behavior with abrupt decay occurring at  $N = [2c/\pi]$  with  $c = ak_b x_0/z'$ . As well known [3]-[4], since  $\Omega_1$  and  $\Omega_2$  are disjoint bands the eigenvalues of the sum of the two operators present a knee at the index  $N = 2[2c/\pi]$ . Of course, the same behavior holds true for the singular values.

Let us now consider  $M = 3$  views,  $\{-x_0, 0, x_0\}$ . In this case, the frequency bands overlap. However,  $\mathcal{D}^\dagger \mathcal{D}$  can be still rearranged so to involve disjoint bands

$$\mathcal{D}^\dagger \mathcal{D} = \frac{\lambda}{z'} P_S B_{\Omega_1} P_S + 2 \frac{\lambda}{z'} P_S B_{\Omega_2} P_S + \frac{\lambda}{z'} P_S B_{\Omega_3} P_S \quad (8)$$

with  $\Omega_1 = [-2\frac{k_b}{z'} x_0, -\frac{k_b}{z'} x_0]$ ,  $\Omega_2 = [-\frac{k_b}{z'} x_0, \frac{k_b}{z'} x_0]$  and  $\Omega_3 = [\frac{k_b}{z'} x_0, 2\frac{k_b}{z'} x_0]$ . The operators in (8) corresponding to the bands  $\Omega_1$  and  $\Omega_3$  present a knee in the eigenvalues trend for  $N = [2c_1/\pi]$  and  $c_1 = a\frac{k_b}{2z'} x_0$ , while the operator corresponding to the band  $\Omega_2$  presents a knee for  $N = [2c_2/\pi]$  and  $c_2 = a\frac{k_b}{z'} x_0$ . Hence, the singular values exhibit a two-step behavior with knees that occur at the indexes  $N_1 = [2c_2/\pi]$  and  $N_2 = N_1 + 2[2c_1/\pi]$ .

This reasoning can be extended to a generic number of views and in this case the singular values exhibit an  $(M - 1)$ -step behavior. The number of singular values on each step is given by  $K_n = \alpha \frac{2c_n}{\pi}$ ,  $\alpha = \begin{cases} 1 & \text{for } n = 1 \\ 2 & \text{for } n \neq 1 \end{cases}$ .

Moreover, on each step the singular values are equal to  $\sigma_{nm} = \sqrt{(M - n)\lambda\lambda_m/z'}$  with  $n = \{1, \dots, M - 1\}$ . This result is very well verified by the example reported in Fig.3(b).

In fact, the singular values exhibit the expected  $M - 1 = 4$  steps. Moreover, also their value estimation is in strict accordance to the numerical result. For example, on the first step, the previous formula returns 0.2828 which well agrees with 0.2836 given by the numerical simulation.

From Fig.2(a) one can appreciate that for only two views the singular values exhibit a single step ( $N = [2c/\pi]$ ). Of course, this single-step behavior allows to identify  $N$  as the number of degrees of freedom. By comparing Fig.3(a) and Fig.3(b) it is evident that the use of more views does not increase the NDF but only the numerical value of the singular values. This is important in the inversion as this entails more stability.

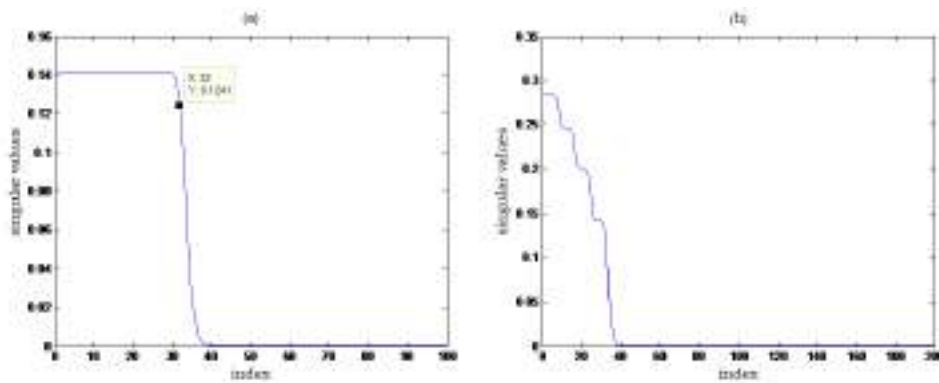


**FIG. 3** – Singular value behavior for only a view (a) and for  $M = 5$  views (b). As can be seen, the foreseen four steps are well evident.

### III. CONCLUSION

The aim of this contribution is to highlight the role played by the parameters of the scattering configuration on the performance achievable in Fresnel-zone. The link between the singular values behavior of the scattering operator and the most used metrics (such as NDF, resolution, information content [4]) which actually are employed to assess the achievable performance in linear inverse scattering problems, justifies the analysis conducted in this paper.

The obtained results show that in order to increase the NDF to the largest extent two *extremal* views are sufficient. By further increasing views does not lead to an increase in the NDF, but entails an increase of the numerical values of the singular values. Moreover, having fixed the noise, higher singular values can lead to a more stable inversion procedure.

### ACKNOWLEDGEMENT

The authors would like to thank Prof. Rocco Pierri and Prof. Raffaele Solimene for their support and suggestions.

### REFERENCES

- [1] Solimene, R., Maisto, M. A., & Pierri, R. (2013). "Role of diversity on the singular values of linear scattering operators: the case of strip objects." *JOSA A*, 30(11), 2266-2272.
- [2] F. Riesz and B. Nagy, "Functional Analysis." (Dover, New York, 1990).
- [3] Solimene R., Maisto M. A., and Pierri R. "Information Content in Inverse Source with Symmetry and Support Priors." *Progress In Electromagnetics Research C* 80 (2018): 39-54.
- [4] Maisto M. A., Solimene R., & Pierri, R. (2016). "Metric entropy in linear inverse scattering." *Advanced Electromagnetics*, 5(2), 46-52.

# FAULTS DIAGNOSTICS OF A CONICAL ARRAY

G. Leone<sup>(1)</sup>, G. Buonanno<sup>(1)</sup>

<sup>(1)</sup> Dipartimento di Ingegneria, Università della Campania

"L. Vanvitelli"

Via Roma 29, 81031 Aversa, Italy

[giovanni.leone@unicampania.it](mailto:giovanni.leone@unicampania.it)

## Abstract

*The inverse problem of the diagnostics of an array of point sources located over a conical surface is addressed by the numerical evaluation of the relevant spectral decomposition. The resulting number of degrees of freedom reveals the maximum number of array elements that can be reliably reconstructed. Spacing between the elements larger than the typical half a wavelength step is required for stable imaging. Some examples of faulty elements diagnostics in presence of noisy data are shown.*

**Index Terms** – Array diagnostics, Conformal antennas, Inverse scattering.

## I. INTRODUCTION

Conformal antennas, i.e. antennas following a nonplanar geometry, have definite advantages in several applications, as for instance, on aircrafts, for a ground surveillance radar achieving a hemispherical coverage, in base stations of wireless network to improve traffic efficiency by dynamic allocation of radiated beams. The source geometry plays a relevant role in defining the number of degrees of freedom (NDF) of the source which is useful to establish the class of patterns that can be radiated [1]. Such a number is also important in array diagnostics to define conditions for reliable determination of array excitation coefficients. This problem is tackled hereafter by resorting to the spectral decomposition of the relevant radiation operator with reference to a conic surface.

## II. FORWARD AND INVERSE MODEL

Consider a conformal array of  $N$  isotropic radiators located on a cone as in Fig. 1. The corresponding array factor can be written as

$$F(\vartheta, \varphi) = \sum_{n=1}^N c_n e^{j\beta r_n [\sin(\pi - \vartheta_0) \sin \vartheta \cos(\varphi - \varphi_n) + \cos(\pi - \vartheta_0) \cos \vartheta]} \quad (1)$$

where  $c_n$  is the excitation coefficient of the  $n$ -th radiator,  $\beta = 2\pi/\lambda$ ,  $\lambda$  is the vacuum wavelength,  $\vartheta_0$  is the half-aperture angle of the conical surface,  $(r_n, \pi - \vartheta_0, \varphi_n)$  are the polar coordinates of the  $n$ -th radiator are the polar coordinates of the far-field observation point.

From the functional analysis point of view, the array factor defines a mapping from a discrete space into a continuous one. Our goal is to evaluate the NDF of this operator, in order to be able to determine the maximum number of elements that can be reliably diagnosed with a certain degree of accuracy. The relevant mathematical tool consists in the the Singular Value Decomposition (SVD) of the operator. Unfortunately,

for the present geometry, the SVD is difficult to be analytically treated, so that we resort to numerical methods. It can be expected that when the half-aperture angle is greater than  $\pi/4$ , the conical surface becomes "close" to a spherical cap, and therefore the NDF is closer to the NDF of a spherical cap enclosing the conical surface [2]. In any case, we assume as NDF the number of singular values, above -20 dB with respect to the maximum one.

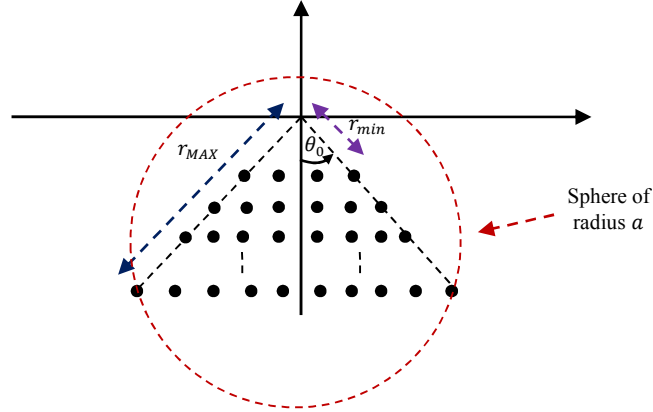


**FIG. 1** – Cut view of an array on a conical surface and of the minimum radius enclosing sphere.

The positions of the conical array elements are defined as follows.

1. The array is composed of  $N_{SUB}$  circular subarrays of different number of elements, located at  $r^{(i)}$  from the origin.
2. The radial spacing between the subarrays is assumed equal to  $\lambda/2$ .
3. The angular step for determining the azimuthal coordinates of the radiators positions in each subarray is chosen equal to  $\Delta\varphi_i^{ARRAY} = 2\pi/(2M_i + 1)$ , where  $M_i = \lceil \beta r^{(i)} \chi \rceil$ ,  $r^{(i)}$  is the radial coordinate related to the  $i$ -th subarray and  $\chi$  is a filling parameter.

As far the discretisation of Eq. (1) is concerned, the following steps are performed.

- A. The height of the cone is determined as  $h = (r_{MAX} - r_{min})\cos\theta_0$ .
- B. The array is rigidly translated along the  $z$ -axis by the  $\Delta z = (h/2) + r_{min}\cos\theta_0$ . In this way,  $z_n = r_n\cos(\pi - \theta_0)$  in Eq. (1) becomes  $\tilde{z}_n = z_n + \Delta z$ , while  $x_n = r_n\sin(\pi - \theta_0)\cos\varphi_n$  and  $y_n = r_n\sin(\pi - \theta_0)\sin\varphi_n$ , remain unchanged.
- C. The smallest sphere that completely enclosing the cone is defined with a resulting radius  $a = \sqrt{(r_{MAX}\sin\theta_0)^2 + (h/2)^2}$ .
- D. The sampling step of the (observation)  $\theta$  angle is  $\Delta\theta = 2\pi/(2N_\theta + 1)$ , where  $N_\theta = \lceil \beta a \chi_\theta \rceil$ ,  $\chi_\theta$  is the oversampling parameter. Therefore the sampling points are  $\theta_i = (i - 1)\Delta\theta$  for  $i = 1, 2, \dots, N_\theta + 1$ .
- E. The sampling step of the (observation)  $\varphi$  angle is  $\Delta\varphi_i = 2\pi/(2M_i + 1)$ , where  $M_i = \lceil \beta a \chi_\theta \sin\theta_i \rceil$  if  $\lceil \beta a \chi_\theta \sin\theta_i \rceil > 7$ , otherwise  $M_i = 7$ , and the  $\varphi$  sampling point are  $\varphi_p^{(i)} = (p - 1)\Delta\varphi_i$  for  $p = 1, 2, \dots, 2M_i + 1$ .

Accordingly, the discretised version of the Eq. (1) can be written in matrix form as  $\underline{F} = \underline{A} \cdot \underline{c}$ .

We denote as  $S$  the number of normalised singular values of the matrix  $\underline{A}$  above  $-20$  dB.  $S$  plays an important role in any diagnostic procedure since it provides the number of independent combinations of array elements that can be reliably reconstructed in presence of uncertainties on data. In fact, if  $S < N$  we expect that some antenna elements excitations exist that cannot be reconstructed by regularized inversion of  $\underline{A}$ . In this circumstance, then, it is impossible to identify an arbitrary located fault element within the array. At the same time,  $S$  represents the maximum number of elements of a conical array allowing for a reliably diagnostic procedure.

### III. NUMERICAL RESULTS

In this section, we show some numerical results that aim at demonstrating difficulties of a reliable diagnosis when  $N$  exceeds the NDF associated with the array factor. We refer to a conical array with  $N_{SUB} = 11$ ,  $\theta_0 = \pi/6$ ,  $r_{min} = \lambda/2$ ,  $r_{MAX} = 5\lambda$  and thus  $h \cong 4.33\lambda$ . So, the radius of the smallest sphere that contains the array is  $a = 3.5\lambda$  and we have chosen  $\chi_\theta = 1.1$ .

In Fig. 2 the behavior of the singular values of the matrix  $\underline{A}$ , for various values of the filling parameter  $\chi$ , and therefore for various  $N$ , are shown. We observe that for  $\chi = 0.7$  the number of antenna elements is larger than  $S$ , while for  $\chi = 0.48$  they nearly agree.

In Figs. 3 and 4 examples of the diagnostic of the two selected cases are shown from far zone data sampled as discussed in Section II. The excitation coefficients of the active elements are assumed  $c_n = 1$ , whereas for the switched off ones  $c_n = 0$ . An array element is assumed off when the reconstructed modulus  $|c_n| < 0.5$ . It can be appreciated that the first array can not be diagnosed even in absence of noise.

### IV. CONCLUSION

The investigation of the number of degrees of freedom of a conical array can provide the way to introduce reliable diagnostic procedure. Some numerical examples show that this results can be achieved when the corresponding elements spacing may be about  $\lambda/2$ .

### REFERENCES

- [1] G. Leone, M.A. Maisto, R. Pierri, "Application of Inverse Source Reconstruction to Conformal Antennas Synthesis", *IEEE Transactions on Antennas and Propagation*, vol 66, n. 3 pp. 1436 – 1445, Mar 2018
- [2] G. Leone, M.A. Maisto, R. Pierri, "First Step Towards a Comparison between 3D Source Geometries for Conformal Antennas", *12th European*

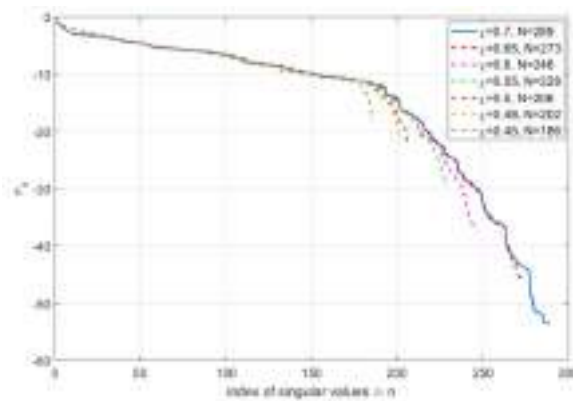


**FIG. 2** – Normalised singular values behaviour for different filling parameter values.

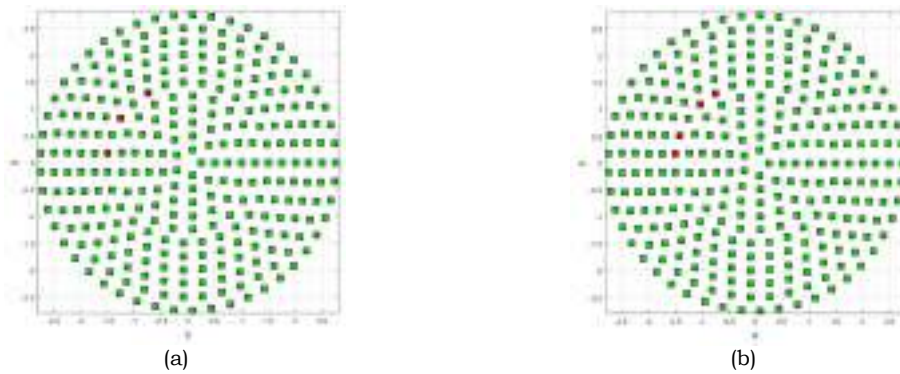


**FIG. 3** – Top views of the first conical array ( $\chi = 0.7$ ) composed by 289 antenna elements, active elements are marked in green, faulty elements are marked in red: a) reference array; b) reconstructed array in absence of uncertainties on data.

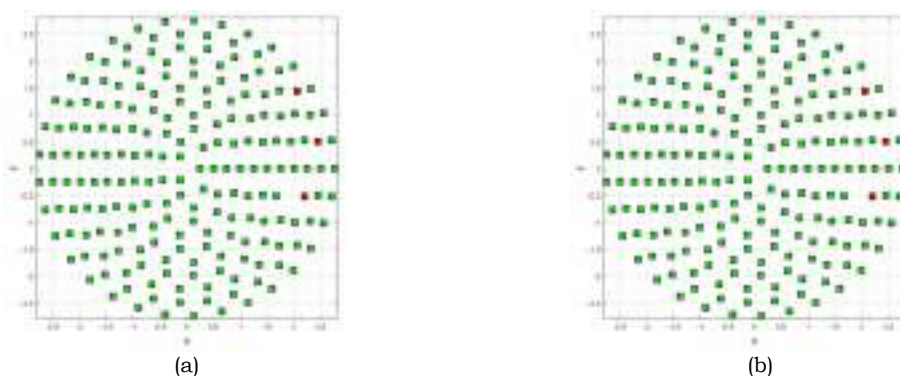


**FIG. 4** – Top views of the first conical array ( $\chi = 0.48$ ) composed by 202 antenna elements, active elements are marked in green, faulty elements are marked in red: a) reference array; b) reconstructed array in presence of uniformly distributed noise on data with a 20 dB Signal-to-Noise ratio.

# On the feasibility of PhaseLift in circular geometry

Maria Antonia Maisto<sup>(1)</sup>, Raffaele Moretta<sup>(1)</sup>, Raffaele Solimene<sup>(1)</sup>, Rocco Pierri<sup>(1)</sup>

(1) Dipartimento di Ingegneria, Università della Campania “Luigi Vanvitelli”  
Via Roma, 81030 Aversa, Italia  
[raffaele.moretta@live.it](mailto:raffaele.moretta@live.it)

## Abstract

*In this paper a methodology based on PhaseLift is applied to reconstruct the radiated field from only magnitude measurements. This methodology requires to collect square amplitude measurements of radiated field and then to solve a problem of low-rank matrix recovery. In addition, a numerical simulation is included. This simulation shows that field reconstruction via PhaseLift is feasible.*

**Index Terms** – amplitude measurements, reconstruction, PhaseLift

## I. INTRODUCTION

At high frequencies it is very difficult to measure the phase of a signal so it has great importance the estimation of radiated field by a source from only intensity measurements of it. This task falls into phase retrieval problem that is a non linear inverse problem. In literature there are different approaches to address this problem. Many of these are based on the minimization of an appropriate functional by an iterative procedure [1]. Unfortunately, such procedures can be trapped into false solutions known as local minima so in order to overcome such difficulty an approach based on lifting is introduced in [2]. This allows to recast the problem as the inversion of a linear operator by re-defining the unknown space. Accordingly, in order to reconstruct the radiated field from only intensity measurements by classical approach, the number of required independent data should be equal to the square of unknown space dimension. Therefore the number of independent data has a crucial role. As illustrated in [3], it is possible to introduce a diversity that increases the number of linearly independent data by collecting the square amplitude of radiated field on multiple observation domains in near zone but, as recently shown in [4], the number of independent data is always less than the required number. For this reason, a procedure based on a problem of low-rank matrix recovery which allows to solve an undetermined problem is exploited. According to such procedure, at first, the phase retrieval problem is linearized lifting up the problem of recovering a vector from quadratic equations into the one of recovering a rank one-matrix from linear equations; then, this new problem is relaxed in a trace minimization problem for a matrix that is solution of the undetermined linear system obtained from lifting. By combining the square amplitude measures of radiated field and the trace minimization problem we obtain a procedure to reconstruct the radiated field.

## II. PHASE RETRIEVAL VIA PHASELIFT

Consider a 2D scalar current source defined within the circle  $\rho < a$ . At a single frequency and for  $\rho > a$ , the field radiated by this source can be expressed as

$$E(\rho, \varphi) \approx \sum_{l=-N}^N c_l \cdot H_l^2(\beta\rho) e^{jl\varphi} \quad (1)$$

where  $\beta a$  is the free space wave number,  $H_l^2$  is the  $l$ -th order Hankel function of second kind and  $N$  is the integer nearest to  $\beta a$ .

Suppose to probe the square amplitude field over  $n$  circles external to the source whose radius are  $\rho_1, \rho_2, \dots, \rho_n$ . Furthermore, each observation circle is sampled with an uniform angular step at  $M_p$  with  $p \in \{1, 2, \dots, n\}$  points. Let be  $M = M_1 + M_2 + \dots + M_n$  the total number of samples.

Our purpose is to estimate the sequence of unknown coefficients  $\{c_l\}$  from square amplitude measurements of radiated field. This task falls into phase retrieval problem which consists in

$$\text{finding } \underline{c} \text{ subject to } |\langle \underline{a}_k, \underline{c} \rangle|^2 = b_k, \quad k = \{1, 2, \dots, M\} \quad (2)$$

where  $\langle \cdot \rangle$  is the scalar product. In our case

- $b_k = |E(\rho_k, \varphi_k)|^2$  where  $\rho_k = \rho_p$  with  $p \in \{1, 2, \dots, n\}$  when  $\sum_{q=1}^{p-1} M_q + 1 \leq k \leq \sum_{q=1}^{p-1} M_q + M_p$ ;
- $\underline{c} \in \mathbb{C}^{2N+1}$  is the column vector which contains the sequence of unknown coefficients  $\{c_l\}_{l=-N}^N$ ;
- $\underline{a}_k \in \mathbb{C}^{2N+1}$  is the column vector which contains the sequence of unknown coefficients  $\{H_l^2(\beta \rho_k) e^{j l \varphi_k}\}_{l=-N}^N$ .

Using the following equations

$$|\langle \underline{a}_k, \underline{c} \rangle|^2 = \text{Tr}(\underline{A}_k \cdot \underline{C}) \quad (3)$$

where  $\underline{A}_k = (\underline{a}_k \cdot \underline{a}_k^H)^t$  and  $\underline{C}$  is the rank one matrix  $\underline{C} = \underline{c} \cdot \underline{c}^H$ , is possible lifting up quadratic measurements and interpreting them as linear measurements.

By introducing the linear operator  $\Lambda : \underline{C} \in \mathbb{C}^{(2N+1) \times (2N+1)} \rightarrow \{\text{Tr}(\underline{A}_k \cdot \underline{C}) \mid k = 1, 2, \dots, M\}$  the phase retrieval can be recast as

$$\text{finding } \underline{C} \text{ from the linear system } \Lambda(\underline{C}) = \underline{b} \quad (4)$$

The linear system  $\Lambda(\underline{C}) = \underline{b}$  is always underdetermined because, as shown in [3], the matrix of coefficient of this system  $\underline{A}_{PL}$  is always rank deficient and for this reason the inversion with classical methods as SVD is not feasible.

In [5] the authors noting that  $\underline{C}$  is a Hermitian positive semi-definite matrix with rank one, rephrase the phase retrieval problem as follows

$$\text{minimize } \text{rank}(\underline{C}) \text{ subject to } \Lambda(\underline{C}) = \underline{b}, \quad \underline{C} \geq 0 \quad (5)$$

where  $\underline{C} \geq 0$  is the constraint which indicates that the unknown matrix  $\underline{C}$  is positive semi-definite. The rank minimization problem is NP hard and for this reason the authors relax this problem in an equivalent convex optimization called PhaseLift which consists in

$$\text{minimize } \text{Tr}(\underline{C}) \text{ subject to } \Lambda(\underline{C}) = \underline{b}, \quad \underline{C} \geq 0 \quad (6)$$

The previous problem is been tackled by minimizing the following functional

$$g(\underline{C}) = \|\Lambda(\underline{C}) - \underline{b}\|^2 + \alpha \cdot \text{Tr}(\underline{C}) \quad (7)$$

where  $\alpha$  is a regularization parameter. The solution of (6) is been reached using a projected gradient method. This iterative method by starting from an initial guest  $\underline{\underline{C}}_0$  defines  $\underline{\underline{C}}_{j+1} = P\left(\underline{\underline{C}}_j - t_j \cdot \nabla g(\underline{\underline{C}}_j)\right)$  where  $t_j$  is such as  $d\underline{\underline{C}}_j/dt_j = 0$ . The operator  $P$  is a projector which dumps the negative eigenvalues and it is defined as follows

$$P\left(\underline{\underline{C}}\right) = \sum_p \max\left(\lambda_p, 0\right) \underline{\underline{u}}_p \cdot \underline{\underline{u}}_p^H \quad (8)$$

where  $\sum_p \lambda_p \underline{\underline{u}}_p \cdot \underline{\underline{u}}_p^H$  is the eigenvalues decomposition of  $\underline{\underline{C}}$ .

Once that rank one matrix  $\underline{\underline{C}}$  has been found, nothing that  $\underline{\underline{C}} = \underline{\underline{c}} \cdot \underline{\underline{c}}^H = \lambda \underline{\underline{u}} \cdot \underline{\underline{u}}^H$  the unknown vector  $\underline{\underline{c}}$  can be reconstructed using the equation

$$\underline{\underline{c}} = \sqrt{\lambda} \cdot \underline{\underline{u}} \quad (9)$$

where  $\lambda$  and  $\underline{\underline{u}}$  are respectively the only eigenvalue and the only eigenvector of matrix  $\underline{\underline{C}}$ .

### III. NUMERICAL RESULTS

To measure the performance of PhaseLift we show a numerical result. The error on the reconstruction is quantified through the relative mean-square error (RMSE). Since the solution to the phase retrieval problem is unique only up to global phase, in order to estimate the relative mean-square error both the ideal solution  $\underline{\underline{c}}$  and real solution  $\hat{\underline{\underline{c}}}$  must be normalized respect to the phase of one of their elements. Accordingly the relative mean-square error (RMSE) is

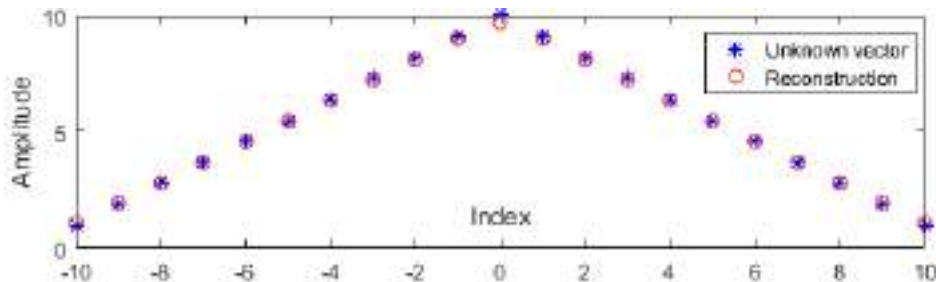
$$RMSE = \frac{\|\underline{\underline{c}}_{norm} - \hat{\underline{\underline{c}}}_{norm}\|}{\|\underline{\underline{c}}_{norm}\|} \quad (11)$$

where  $\underline{\underline{c}}_{norm}$  and  $\hat{\underline{\underline{c}}}_{norm}$  are  $\underline{\underline{c}}$  and  $\hat{\underline{\underline{c}}}$  normalized respect to the phases of their corresponding first element.

As a test case, consider a source whose radiated field is spanned by  $2N + 1$  Fourier - Bessel harmonics so the cylinder of infinite height in which the source is included has a radius  $a = N/\beta = 1,59 \lambda$ . The coefficient of Fourier-Bessel harmonics to be reconstructed are

$$c_l = (-0,9 |l| + 10) \cdot e^{j l \theta}, \quad l \in \{-10, -9, \dots, 9, 10\} \quad (12)$$

The observation domain is supposed to be an ensemble of 2 circle of radius  $\rho_1 = a + 1 \lambda = 2,59 \lambda$  e  $\rho_2 = a + 2 \lambda = 3,59 \lambda$ . For each circle the number of measurements is  $4N + 1 = 41$ , hence the number of total measurements  $M = 82$ . Only numerical noise provides uncertainties on the data. The regularization parameter  $\alpha$  is settled equal to  $10^{-2}$ , the initial guest vector  $\underline{\underline{c}}_0$  is chosen in a random way, the number of iteration in minimization algorithm is settled equal to  $10^5$ . In Fig. 1 the comparison between  $\underline{\underline{c}}_{norm}$  and  $\hat{\underline{\underline{c}}}_{norm}$  is sketched.



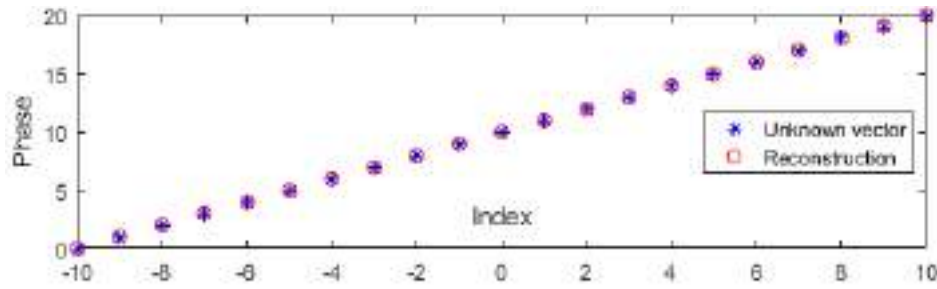


**Fig. 1** - Unknown vector and reconstruction

As can be seen the method works very well, indeed, the value of  $RMSE$  is 0,045. In Fig. 2 the singular values of the matrix  $\underline{\underline{A}}_{PL}$  are sketched. As can be seen, in agreement with [4] the number of significant singular values significant (or in other word the number of independents data) is  $8N = 80$ .

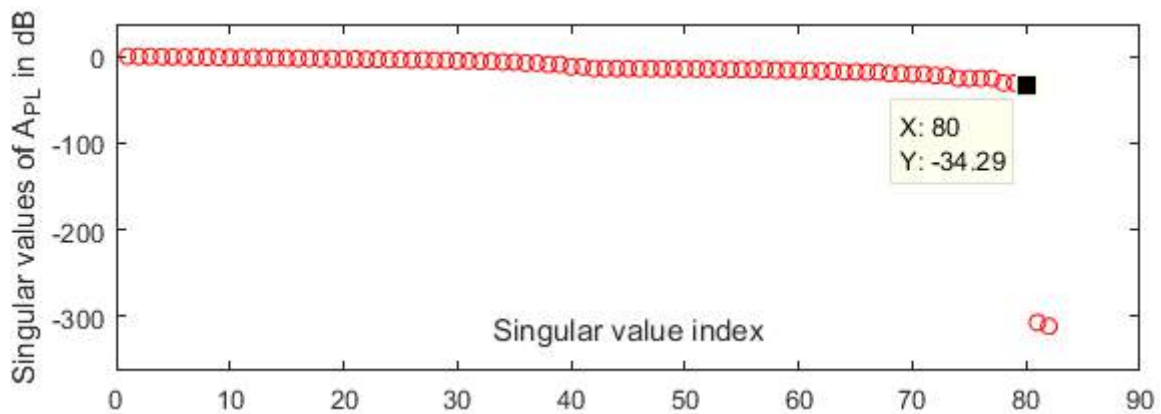


**Fig. 2** - Singular values of matrix  $\underline{\underline{A}}_{PL}$

#### IV. CONCLUSION

In this paper a novel strategy to reconstruct radiated field from only amplitude measurements is addressed. It is shown that combining together a measurement set up consisting in data collection on multiple observation domain and a trace minimization problem provides a powerful approach to solve the problem.

#### REFERENCES

- [1] F. Soldovieri, A. Liseno, G. D'Elia, R. Pierri, "Global convergence of phase retrieval by quadratic approach" (2005). *IEEE transactions on antennas and propagation*, 53(10), 3135-3141.
- [2] T. Isernia, G. Leone and R. Pierri, "A quadratic inverse problem: the phase retrieval". *Inverse methods in action*. Springer, Berlin, Heidelberg, 1990. 285-291.
- [3] R. Solimene, M. A. Maisto and R. Pierri, "On the singular spectrum of the radiation operator for multiple and extended observation domains". *International Journal of Antennas and Propagation*, Volume 2013, 2013.
- [4] M. A. Maisto, R. Moretta, R. Solimene and R. Pierri, "On the number of independent equations in phase retrieval problem". Submitted to *2018 Progress In Electromagnetics Research Symposium*. IEEE Conference.
- [5] E. J. Candes, Y. C. Eldar, T. Strohmer and V. Voroninski, "Phase retrieval via matrix completion". *SIAM J. Imaging Sciences*, Vol. 6, No. 1, 199-225, 2013.

# TWO-DIMENSIONAL PHASE RETRIEVAL AS A ‘CROSSWORDS’ PROBLEM

A. F. Morabito<sup>(1)</sup>, P. G. Nicolaci<sup>(1),(2)</sup>, T. Isernia<sup>(1)</sup>

<sup>(1)</sup> DIIES Department, Università Mediterranea di Reggio Calabria,  
Via Graziella, Loc. Feo di Vito, 89124 Reggio Calabria, Italy

[tommaso.isernia@unirc.it](mailto:tommaso.isernia@unirc.it); [andrea.morabito@unirc.it](mailto:andrea.morabito@unirc.it)

<sup>(2)</sup> Space Engineering S.p.A., Via dei Luxardo, 00156 Roma, Italy

[pasquale.nicolaci@space.it](mailto:pasquale.nicolaci@space.it)

## Abstract

*By taking advantage of existing knowledge and approaches for the retrieval of a 1-D discrete signal from the intensity of its Fourier Transform, we introduce an innovative method for the solution of the corresponding 2-D problem. By exploiting only one measurement surface plus some additional information, and without recurring to global-optimization algorithms, the approach is able to find in a deterministic fashion all the different solutions of the problem.*

**Index Terms** – Antenna measurements, phase retrieval, spectral factorization.

## I. INTRODUCTION

If  $f(x)$  is an unknown signal and  $T$  is an operator such that:

$$F(u) = T[f(x)] = |F(u)|e^{j\phi(u)} \quad (1)$$

then a wide class of Phase Retrieval (PR) problems are formulated as:

*Determine  $f(x)$  from  $|F(u)|$  and some additional information.*

PR is of high interest in those applications wherein the full knowledge of a complex function is needed but phase measurements are not available/convenient, e.g., microscopy, astronomy, and crystallography [1]. The problem has been the object of very many studies also in the Antennas & Propagation Community (because of its interest in antenna characterization and applications involving radio telescopes and inverse-scattering-based imaging), wherein two measurement surfaces are usually required to optimally solve it [2]-[4].

Starting from these observations, we present in the following a new approach to PR which requires only one measurement surface (plus some additional information) and addresses some of the problem’s main difficulties, i.e.,

1. Non-linearity (i.e., even if the available a-priori information theoretically ensures uniqueness of the solution, the cost function can exhibit ‘false solutions’ actually different from the ground truth);
2. Non-availability of some antenna measurements (i.e., the signal domain may be not fully available to the measurement system);
3. Non-uniqueness of the solution (in both 1-D and 2-D cases) due to ‘trivial ambiguities’, i.e., a constant phase, a linear phase, a complex conjugation, or any combination of them;
4. Non-uniqueness of the solution (in the 1-D cases where  $T$  is a Fourier transform operator) as  $|F(u)|^2$  represents a polynomial which can be reduced to a product of first-order factors where ‘zero flipping’ [5] generates multiple phase solutions.

## II. 2-D PHASE RETRIEVAL AS COLLECTION OF 1-D PROBLEMS

Supposing  $T$  is a Fourier transform operator and focusing on 2-D discrete signals, we consider  $f$  as the excitations (say  $I_{nm}$ ) of an array antenna whose elements are uniformly spaced over a square grid. In such a case, denoting with  $u$  and  $v$  the usual spectral variables and with  $N$  and  $M$  the elements' numbers along  $x$  and  $y$  [5], one will achieve:

$$F(u, v) = \sum_{n=0}^{N-1} \sum_{m=0}^{M-1} I_{nm} e^{jnu} e^{jmv} \quad (2)$$

$$|F(u, v)|^2 = P(u, v) = \sum_{p=-N+1}^{N-1} \sum_{q=-M+1}^{M-1} D_{pq} e^{jpu} e^{jqv} \quad (3)$$

wherein (2) is also equal to the array factor, while the coefficients  $D_{pq}$  involved in (3) can be computed starting from the measured data [5].

Under such hypotheses, the proposed PR procedure is as follows:

**STEP 1:** identify along a *vertical* line of the  $u$ - $v$  plane all possible  $F$  behaviors corresponding to the measured power pattern. For instance, along the line  $u = \bar{u}$ , such a 'dictionary of fields' will be determined by applying to the corresponding power-pattern distribution, i.e.,

$$|F(\bar{u}, v)|^2 = P(\bar{u}, v) = \sum_{q=-M+1}^{M-1} \bar{D}_q(\bar{u}) e^{jqv} \quad \text{with} \quad \bar{D}_q(\bar{u}) = \sum_{p=-N+1}^{N-1} D_{pq} e^{jp\bar{u}} \quad (4)$$

the spectral-factorization technique developed in [5] in order to get:

$$F(\bar{u}, v) = \sum_{m=0}^{M-1} \bar{I}_m(\bar{u}) e^{jmv} \quad \text{with} \quad \bar{I}_m(\bar{u}) = \sum_{n=0}^{N-1} I_{nm} e^{jn\bar{u}} \quad (5)$$

Summarizing, by starting from the knowledge of  $P(\bar{u}, v)$  one will solve a 1-D PR problem such to retrieve *all possible*  $F(\bar{u}, v)$  behaviors;

**STEP 2:** determine, in the same manner as step 1, the 'dictionary of fields' along a *horizontal* line of the  $u$ - $v$  plane. For instance, along the coordinate  $v = \hat{v}$ , one will achieve:

$$|F(u, \hat{v})|^2 = P(u, \hat{v}) = \sum_{p=-N+1}^{N-1} \hat{D}_p(\hat{v}) e^{jpu} \quad \text{with} \quad \hat{D}_p(\hat{v}) = \sum_{q=-M+1}^{M-1} D_{pq} e^{jq\hat{v}} \quad (6)$$

$$F(u, \hat{v}) = \sum_{n=0}^{N-1} \hat{I}_n(\hat{v}) e^{jnu} \quad \text{with} \quad \hat{I}_n(\hat{v}) = \sum_{m=0}^{M-1} I_{nm} e^{jm\hat{v}} \quad (7)$$

**STEP 3:** identify, in the same manner as step 1, all possible field behaviors along an *oblique* line of the  $u$ - $v$  plane. For instance, by considering the main diagonal  $u = v$  and denoting by  $w$  the coordinate spanning it, one will achieve:

$$|F(w)|^2 = P(w) = \sum_{h=-2(N+M)}^{2(N+M)} \tilde{D}_h e^{jhw} \quad (8)$$

$$F(w) = \sum_{h=-N-M}^{N+M} \tilde{I}_h e^{jhw} \quad (9)$$

where  $I_h$  and  $D_h$  denote suitable auxiliary sequences. Again, one can deal with an auxiliary 1-D PR problem and, by solving it, he/she will be able to find all the possible  $F$  behaviors along the line  $u = v$ ;

**STEP 4:** apply a ‘crosswords’ approach, as pictorially depicted in Fig. 1, by examining any possible combination of horizontal and vertical fields and, for each couple, looking for the existence of an oblique field correctly intersecting them. In fact, while a proper choice of the corresponding phase constant will allow any oblique candidate field to correctly intersect the candidate vertical field, at the other intersection the phase of the oblique field will generally be different from the one of the horizontal field (see Fig. 1). As a consequence, one will be able to discard a number of possibilities and hopefully identify the correct triple of words (or at least to considerably reduce the number of possibilities).

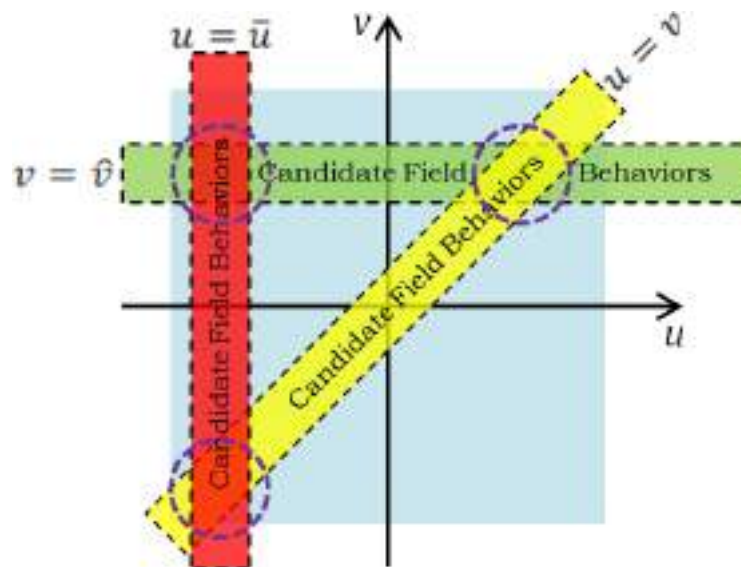


Fig. 1: ‘Crosswords’ (i.e., field dictionaries) intersections in the  $u$ - $v$  plane.

**STEP 5:** Completion of the scheme is rather intuitive for crosswords’ solvers: one will consider additional horizontal, vertical, and oblique lines in order to identify the correct field behavior (i.e., the correct ‘word’) amongst the very many possible ones.

As a distinguishing characteristic, the approach is able to find in a deterministic fashion all the different solutions to the PR problem in case the solution is not unique (including the case of  $u$ - $v$  factorable patterns). Such a capability, deriving from a kind of combinatorial approach to the problem, is paid with a large computational burden. On the other side, one can develop some smart strategy in order to reduce the number of combinations to be explored. For example, starting from a line where many zeroes are present reduces the number of ambiguities on the corresponding 1-D PR problems. Hence, a clever choice of the first three lines in Fig. 1 will be of help. In such a choice, care has to be taken in avoiding that they intersect at a null of  $P$  (wherein phase would make no sense).

### III. A NUMERICAL EXAMPLE IN THE CASE OF ‘SIMPLIFIED’ CROSSWORDS

The proposed procedure results considerably simplified by the knowledge of the reference field’s value in a (low) number of points of the  $u$ - $v$  plane. In fact, if  $F(u_k, v_k)$  is known then all possible field behaviors belonging to the horizontal, vertical, and oblique lines passing through the point  $(u_k, v_k)$  can be ‘normalized’ in such a way that all of them exhibit, in the point  $(u_k, v_k)$ , the correct phase. By so doing, it will be also possible avoiding the trivial ambiguities listed in Section I.

In support of this claim, we show in Fig. 2 the outcomes achieved in the PR of the field radiated by a 100-elements, half-a-wavelength-spaced square array with complex random excitations. As it can be seen, the knowledge, in addition to the square-amplitude far-field distribution, of the excitations’ support and of 3 field’s complex samples along the  $u=v$  diagonal allowed a fully-satisfactory reconstruction.

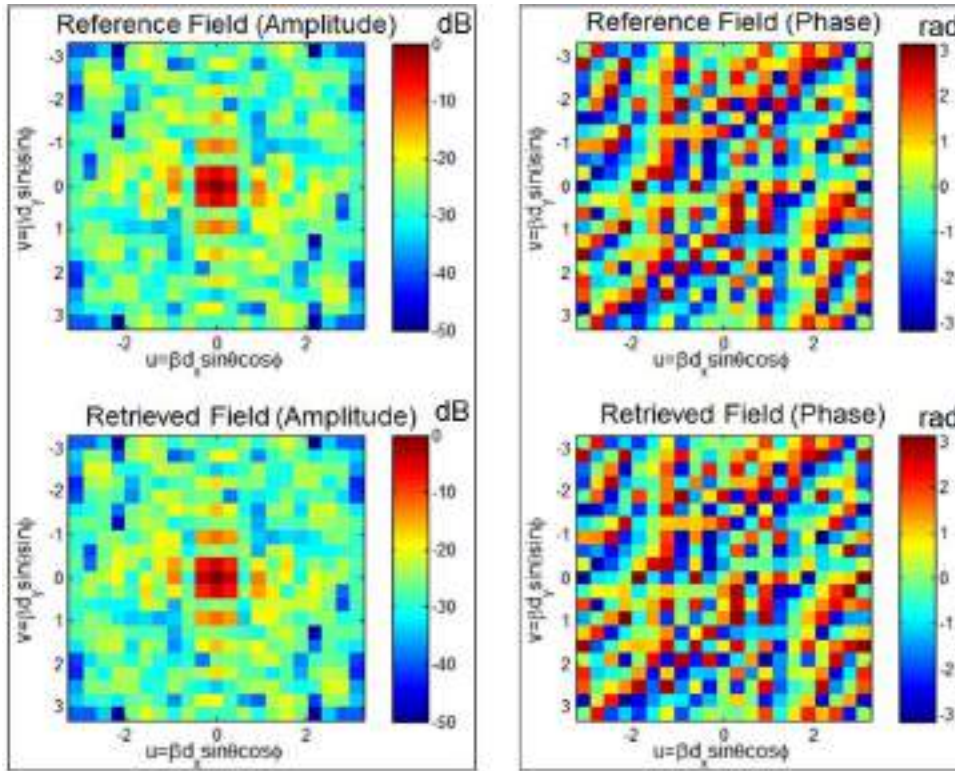


Fig. 2. Reference and retrieved fields for a 100-elements square array.

### REFERENCES

- [1] Rahmat-Samii et al., “Phaseless bi-polar planar near-field measurements and diagnostics of array antennas,” *IEEE Trans. Antennas Propag.*, 1999.
- [2] Isernia et al., “Radiation pattern evaluation from near-field intensities on planes,” *IEEE Trans. Antennas Propag.*, 1996.
- [3] Capozzoli et al., “Phaseless antenna characterization by effective aperture field and data representations,” *IEEE Trans. Antennas Propag.*, 2009.
- [4] G. Junkin, “Planar near-field phase retrieval using GPUs for accurate THz far-field prediction,” *IEEE Trans. Antennas Propag.*, 2013.
- [5] Isernia et al., “Shaped beam antenna synthesis problems: feasibility criteria and new strategies,” *J. of Electromagnetic Waves App.*, 1998.

# THEORETICAL ADVANCES ON NON-DETECTABLE OBJECTS WITH FREQUENCY-SHIFTING AND SPATIAL-SQUEEZING COATINGS

R. Palmeri<sup>(1)</sup>, G. Labate<sup>(2)</sup>

(1) DIIES, Università Mediterranea di Reggio Calabria,  
Via Graziella, 89124 Reggio Calabria, Italy

[roberta.palmeri@unirc.it](mailto:roberta.palmeri@unirc.it)

(2) DET, Politecnico di Torino,

C. so Duca Degli Abruzzi 24, 10129 Torino, Italy

[giuseppe.labate@polito.it](mailto:giuseppe.labate@polito.it)

## Abstract

*In this work, we propose and compare two different methodologies for the design of volumetric and surface coatings for non-detectable objects. The first is based on an inverse scattering problem and it aims to suppress the scattering by acting on the energy of the contrast function in the frequency domain. The second aims to reduce the level of mismatch between object and background by squeezing the scattered energy into the domain of the object itself. Advantages in terms of size and geometry are discussed and numerical results are reported.*

**Index Terms** – Inverse scattering, Fourier Transform, Mie theory.

## I. INTRODUCTION

The idea of designing volumetric and surface coatings to make objects undetectable from external observers is grown in the last years since it has been observed that is possible to be effectively “invisible” to the electromagnetic radiation by means of ad-hoc materials. A lot of techniques have been developed by several research groups around the world to design invisibility cloaks by looking at both volumetric and surface coatings [1]. In this respect, in this work we propose two main methodologies acting on a convenient *relocation* of the energy related to the scattering phenomenon in the frequency and in the spatial domain, respectively. In particular, the first one turns the inverse scattering problem (ISP) as a tool to design a volumetric coat by exploiting the spectral properties of the unknown contrast function with the aim of shifting its scattered energy outside the visible range; the second, based on a matching problem, aims instead to squeeze the scattered energy into the spatial domain where the object is localized.

## II. FREQUENCY-SHIFTING VOLUMETRIC COATINGS

A first approach aiming at “hiding” a given object takes advantage from the ISP, that is a non-trivial diagnostic problem, since to solve it one must face with non-linearity and ill-posedness of the problem itself. Regularization techniques are employed to restore well-posedness, while several approximation methods have been proposed to counteract the

non linearity. For instance, the Born approximation (BA) [2] is valid for weak scatterers since it deals with the approximation of the unknown total field inside the investigation domain by the incident field. Under the BA, it has been demonstrated that the scattered (radiated) field by the object is related to the restriction of the Fourier transform of the unknown contrast function  $\chi(r)$  to the Ewald sphere having radius  $2k_b$  [2],  $k_b$  being the background wavenumber. On the basis of the above, the spectral coverage clearly indicates which kind of profiles can be safely reconstructed: on the other hand, for a hidden object the spectral coverage of  $\chi(r)$  has to be *null* inside the Ewald sphere.

To synthesize a coating  $\Delta\chi(r)$  that makes invisible a given dielectric object  $\chi_0(r)$ , the following optimization problem is solved:

$$\min_{\Delta\chi} \iint_{k_x^2+k_y^2 \leq 4k_b^2} |\tilde{\chi}(k_x, k_y)|^2 dk_x dk_y \quad (1)$$

$\tilde{\chi}$  being the Fourier transform of  $\chi = \chi_0 + \Delta\chi$ , while  $k_x$  and  $k_y$  represent the spectral coordinates. More in details, the problem (1) enforces the energy of  $\tilde{\chi}$  to be minimum inside the Ewald sphere, thus undergoing a *frequency shifting* of such scattered energy.

Obviously, other solution approaches could be pursued, as for instance the “alternate projections” method by iteratively projecting  $\chi \in \mathbb{R}^2$  into the Fourier domain and forcing all the components of  $\tilde{\chi}$  belonging to the circle of radius  $2k_b$  to be zero [3].

Let us note that the approach can be extended to other kinds of linear approximations, but care must be taken with the range of validity of the considered approximations as main starting hypothesis [3].

### III. SPATIAL-SQUEEZING SURFACE COATINGS

The scattered energy generated by the interactions between objects and incoming fields is a function of the level of mismatch between the background and the embedded dielectric particles, related to the configuration of the electric permittivity that generates volumetric sources. The suppression of the scattering is herein obtained by inserting a surface source around the object to be hidden, with the aim of reducing the level of existing mismatch and re-localizing the scattered energy inside the domain of the object itself. This obtained *spatial squeezing* is performed by modeling the object and the background in terms of admittances, defined as magnetic-to-electric field ratio, and inserting a surface admittance to compensate the scattering from the volumetric source of the dielectric object. The 2D electromagnetic fields are expanded in terms of cylindrical harmonic waves, according to Mie theory [4], and the admittance boundary condition is imposed such that:

$$Y_d(ka, n) + Y_s = Y_b(k_b a, n) \quad (2)$$

i.e., there is no mismatch between  $Y_d$  (dielectric admittance) and  $Y_b$  (background admittance) thanks to the insertion of a surface admittance in parallel  $Y_s$ . This happens as a function of  $a$ , the radius of the dielectric particle,  $k_b$  and  $k$ , the wavenumbers in the background and object region, respectively. The invisibility condition is enforced for each harmonic mode  $n$  by computing explicitly the surface admittance as [4]:

$$Y_s = jY_o \left[ \frac{J'_n(k_b a)}{J_n(k_b a)} - \sqrt{\epsilon_r} \frac{J'_n(ka)}{J_n(ka)} \right] \quad (3)$$

where  $Y_o$  is the vacuum admittance and  $\epsilon_r$  is the permittivity of the object. Without any approximation, the dominant contributions to the total scattered energy will increase as a function of the size and permittivity value of the object, requiring a weighted sum to control the enhanced harmonic components with the surface admittance in Eq. (3).

#### IV. RESULTS

In the following examples, we assess and compare the proposed methodologies by first considering a cylinder with dielectric permittivity  $\epsilon_r = 3$  and radius  $a = 0.15\lambda$ , illuminated by an incoming TM plane wave (as assumed for all the examples). The solution of the optimization problem (1) gives rise to a *frequency-shifting* volumetric dielectric coating. Conversely, by means of Eq.(3) a *spatial-squeezing* surface layer is designed. In this example, being in the quasi-static regime, the dominant harmonic mode is the lowest order for the 2D scenario ( $n = 0$ ) and it can be suppressed by both methods, as reported in Fig. 1.

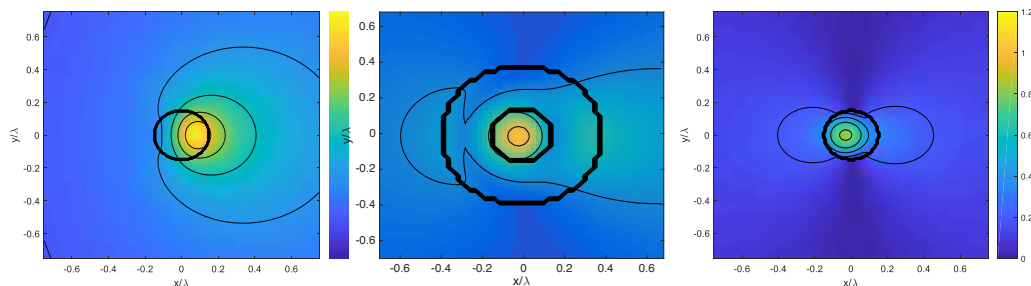


**Figure 1.** Dielectric cylinder: bare case (left), with volumetric coating (center) and with surface coating (right).

In a second example, we consider a different geometry for the two methodologies to show their different ranges of validity. As a matter of fact, a frequency shifting coating can deal with non-canonical objects, but they must be weak scatterers to follow the BA. Conversely, a spatial squeezing surface coat can be applied to canonical geometries, but no limit in dimension and permittivity value is imposed. The achieved performances are shown in Fig.2 and Fig.3 for the two methods, respectively. A non-canonical geometry of three dielectric cylinders with

$\epsilon_r = 1.3$  and  $a = 0.12\lambda$  has been considered for a volumetric coating of radius  $0.6\lambda$ , whereas a dielectric cylinder with  $\epsilon_r = 5$  and radius  $a = 0.3\lambda$  has been adopted for a surface coating. Frequency-shifting and spatial squeezing effects are clearly demonstrated in both cases. Further results and comparisons will be given at the Conference.

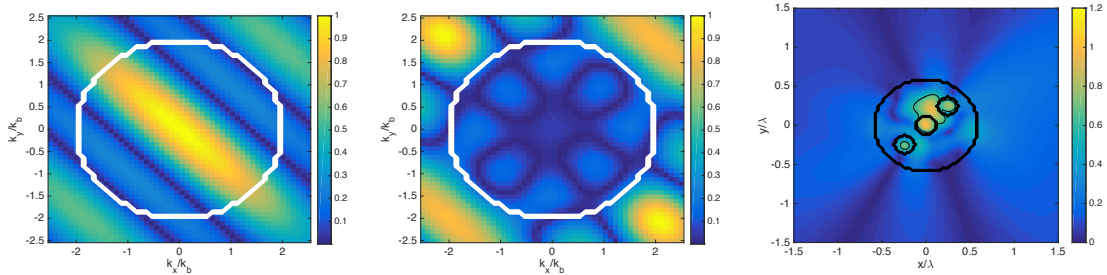


**Figure 2.** Frequency shifting:  $\tilde{\chi}$  energy content for the bare case (left) and for the cloaked case (center) with respect to the Ewald sphere (white line). Achieved scattered field (right).

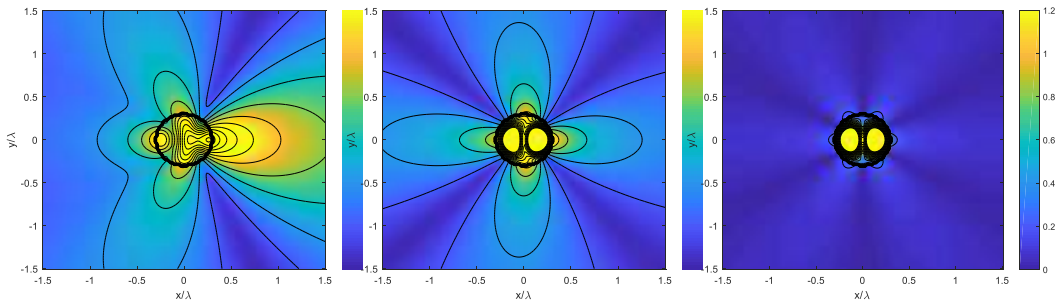


**Figure 3.** Spatial squeezing: suppression of the harmonic wave  $n=0$  (left), of harmonic waves  $n=0,1$  (center) and of harmonic waves  $n=0,1,2$  (right).

## REFERENCES

- [1] R. Fleury, F. Monticone, and A. Alù, "Invisibility and Cloaking: Origins, Present, and Future Perspectives", *Physical Review Applied*, 2015.
- [2] A. J. Devaney, "Mathematical foundations of imaging, tomography and wavefield inversion", Cambridge University Press, 2012.
- [3] R. Palmeri "Synthesis of innovative electromagnetic devices via inverse scattering techniques," PhD Thesis in Information Engineering at Università Mediterranea di Reggio Calabria, 2018.
- [4] G. Labate, A. Alù, L. Matekovits, "Surface-admittance equivalence principle for nonradiating and cloaking problems", *Physical Review A* 95 (063841), 2017.

# NONLINEAR PROPAGATION IN OPTICAL FIBERS FOR SPACE-DIVISION SPACE-DIVISION MULTIPLEX TRANSMISSION

C. Antonelli<sup>(1)</sup>, A. Mecozzi<sup>(1)</sup>, and M. Shtaif<sup>(2)</sup>

<sup>(1)</sup> Department of Physical and Chemical Sciences, University of  
L'Aquila, via Vetoio 1, L'Aquila, Italy

<sup>(2)</sup> Department of Physical Electronics, Tel Aviv University, Ramat  
Aviv, Tel Aviv, Israel  
[cristian.antonelli@univaq.it](mailto:cristian.antonelli@univaq.it)

## Abstract

*The ultimate limit to the capacity of space-division multiplexed transmission on multi-mode and multi-core fibers arises from the fiber linearity, which prevents the indefinite increase of the transmitted power to increase the transmission throughput. In this paper we present the equations that generalize to the multi-mode case the Manakov equation which was originally shown to describe nonlinear propagation in single-mode fibers in the presence of random polarization coupling. We show that in the regime of strong coupling between the propagation modes, the nonlinear evolution is described by a multi-component Manakov equation, whereas the case of multiple groups of strongly coupled modes is modelled by coupled multi-component Manakov equations. The simple form of these equations facilitates considerably the understanding of the nonlinear propagation. In particular, we use them to show that the signal distortion resulting from the nonlinear propagation, reduces with the number of strongly coupled modes.*

**Index Terms** – Fiber optics communications, Mode coupling, Manakov equation, Space-division multiplexing, Nonlinear optics.

## I. INTRODUCTION

Scaling disparities between the demand for data traffic and the capacity of transmission systems based on wavelength-division multiplexing (WDM) technologies indicate that the only viable approach to avoid the incumbent capacity crunch [2] of the global fiber-optic infrastructure is to multiplex transmission into an additional dimension. As is well known, however, space is the only so-far unexploited physical dimension of the optical fiber, thereby making space-division multiplexing (SDM) the solution of choice for scaling the capacity of the future fiber-optic system. However, while the need for SDM is clear, the question of which the most effective implementation of SDM is remains still open, as it entails the challenge of combining capacity scaling and cost reduction. A key-concept in this context is “integrated parallelization,” as it offers the additional degrees of freedom that are necessary to reduce the cost per unit information – the *cost per bit* – while pursuing the increase of the system throughput. The implementation of SDM in multi-mode and multi-core fibers pushes this concept to its ultimate limit by integrating also multiplexed spatial

light-paths in a single fiber. This approach has been intensively investigated in recent years, and several hero experiments have been reported, thereby demonstrating its technical viability.

In this paper we review some of the work that we have recently performed on the modeling of nonlinear propagation in SDM fibers. We discuss the generalization of the Manakov equation that was originally derived to model nonlinear propagation in single-mode fibers with random polarization coupling [3]. The generalized Manakov equations result from a substantial simplification of the underpinning coupled nonlinear Schrodinger equations (NLSE) [4] and constitute the building blocks for the understanding of the nonlinear propagation dynamics in SDM fibers, where the interplay between the random mode coupling and the nonlinear inter-modal interference plays a critical role.

## II. REGIME OF STRONG MODE COUPLING: THE MULTI-COMPONENT MANAKOV EQUATION

We denote by  $\vec{E}(z, t)$  a  $2N$ -dimensional hyper-polarization vector, whose components are the complex envelopes describing the excitations of the  $N$  fiber modes (the factor of 2 accounts for polarization degeneracy). The components of  $\vec{E}(z, t)$  satisfy the following set of coupled NLSE [4,5]

$$\frac{\partial \vec{E}}{\partial z} = i\mathbf{B}^{(0)}\vec{E} - \mathbf{B}^{(1)}\frac{\partial \vec{E}}{\partial t} - i\frac{\mathbf{B}^{(2)}}{2}\frac{\partial^2 \vec{E}}{\partial t^2} + i\gamma \sum_{j,h,k,m} C_{jhkm} E_h^* E_k E_m \hat{e}_j, \quad (1)$$

where  $\mathbf{B}^{(n)}$  ( $n = 0,1,2$ ) are  $2N \times 2N$  Hermitian matrices accounting for linear propagation [5-7],  $\gamma$  is the usual nonlinearity coefficient appearing in the scalar NLSE, and where  $\{\hat{e}_j, j = 1 \dots 2N\}$  is a set of orthogonal unit vectors used to represent the electric field. By the symbols  $C_{jhkm}$  we denote dimensionless constants whose definition involves overlap integrals between the lateral profiles of the fiber modes. In an ideal fiber the matrices  $\mathbf{B}^{(n)}$  are diagonal in the basis of the fiber modes, and no mode coupling exists: the elements of  $\mathbf{B}^{(0)}$  are the propagation constants of the individual modes, those of  $\mathbf{B}^{(1)}$  are the corresponding inverse groups velocity, and those of  $\mathbf{B}^{(2)}$  are the chromatic dispersion coefficients. In real fibers, none of those matrices is diagonal, owing to unavoidable manufacturing imperfections and deployment-related issues, and their perturbations result into random mode coupling. However, in all cases of practical relevance one can safely ignore the perturbations on the group velocity and group velocity dispersion matrices, as the strongest coupling occurs through the perturbations of the optical phase, which are accounted for by  $\mathbf{B}^{(0)}$ .

Modes with similar propagation constants – which we refer to as degenerate or quasi-degenerate modes – are known to couple faster and more strongly than modes characterized by a large wave-vector mismatch [7]. In this section we focus on the case where all modes are degenerate, a situation that can be encountered more easily in multi-

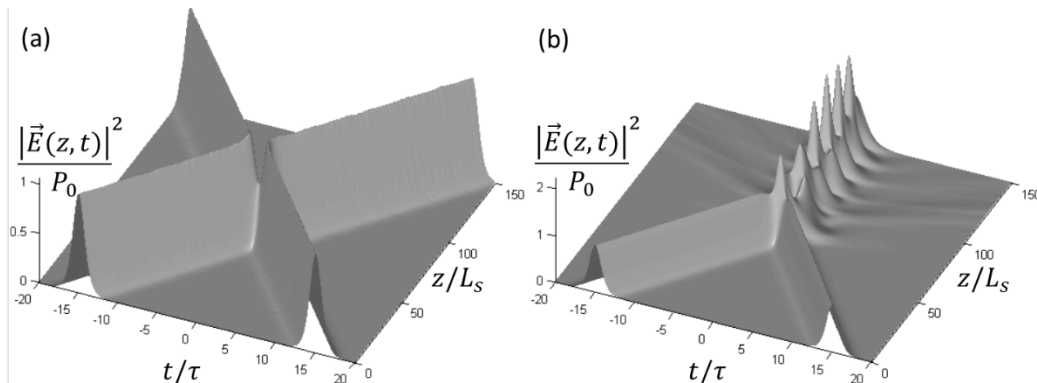


Figure 1. Transmission of two solitons into orthogonal modes, in the presence of strong mode coupling (a) and in the absence of mode coupling (b). The results are obtained in both cases by integrating Eq. (1) with the input soliton parameters given by Eq. (2). The normalization quantities  $P_0$ ,  $\tau$ , and  $L_s$  are the soliton peak power, width, and length. Details in [8].

core fibers [5,8], where the regime of strong coupling between modes is achieved within a length-scale which is by orders of magnitude shorter than the length scale that characterizes the nonlinear propagation. In this situation the orientation of the field vector  $\vec{E}$  becomes uniform in the hyper-polarization space, and the slowly-varying nonlinear term that appears in the coupled NLSEs can be averaged with respect to the random orientation of the field vector. As a result of this procedure, Eq. (1) simplifies to [9]

$$\frac{\partial \vec{E}}{\partial z} = -\beta' \frac{\partial \vec{E}}{\partial t} - i \frac{\beta''}{2} \frac{\partial^2 \vec{E}}{\partial t^2} + i\gamma\kappa |\vec{E}|^2 \vec{E}, \quad \kappa = \sum_{jh} \frac{C_{jhhj} + C_{jhjh}}{2N(2N+1)}, \quad (2)$$

where  $\beta'$  and  $\beta''$  are the group velocity and the dispersion coefficient common to all modes, and where the nonlinearity only enters through the total optical power  $|\vec{E}|^2 = |E_1|^2 + |E_2|^2 \dots + |E_{2N}|^2$ . Note that unlike Eq. (1), Eq. (2) is integrable and admits soliton solutions, a feature that we exploited to assess the correctness of Eq. (2) through numerical simulations. This point is further illustrated in Fig. 1, after [9].

A simple yet very important implication of Eq. (2) is that the nonlinearity coefficient  $\kappa$  must scale as  $\sim 1/2N$ , so that each mode experiences on average the same optical nonlinearity  $\sim |\vec{E}|^2/2N$ . This scaling can be shown to imply that the nonlinear interference noise through which the modes interfere reduces with the number of strongly coupled modes [5], thereby making the nonlinear performance of SDM fibers superior to that of multiple single-mode fibers [8].

### III. MULTIPLE GROUPS OF STRONGLY COUPLED MODES: THE COUPLED MANAKOV EQUATIONS

The most general case is characterized by the presence of multiple groups of degenerate modes, where modes with similar propagation constants (degenerate) undergo strong coupling, whereas modes with different propagation constants couple only very weakly with each other. In this propagation regime the Manakov approach can be applied

within each group of degenerate modes, yielding coupled Manakov equations [10]. In the case of two groups (a and b), they read as

$$\frac{\partial \vec{E}_a}{\partial z} = i\beta_a \vec{E} - \beta'_a \frac{\partial \vec{E}_a}{\partial t} - i \frac{\beta''_a}{2} \frac{\partial^2 \vec{E}_a}{\partial t^2} + i\gamma \left( \kappa_{aa} |\vec{E}_a|^2 + \kappa_{ab} |\vec{E}_b|^2 \right) \vec{E}_a, \quad (3)$$

$$\frac{\partial \vec{E}_b}{\partial z} = i\beta_b \vec{E} - \beta'_b \frac{\partial \vec{E}_b}{\partial t} - i \frac{\beta''_b}{2} \frac{\partial^2 \vec{E}_b}{\partial t^2} + i\gamma \left( \kappa_{ba} |\vec{E}_a|^2 + \kappa_{bb} |\vec{E}_b|^2 \right) \vec{E}_b, \quad (4)$$

where  $\kappa_{aa}$  and  $\kappa_{bb}$  are the generalized self-phase modulation coefficients and  $\kappa_{ab} = \kappa_{ba}$  are the cross-phase modulation coefficients [10].

#### IV. CONCLUSION

We reviewed the modelling of nonlinear propagation in fibers for space-division multiplexing (SDM). We showed that by taking into account the effect of random mode coupling, the coupled nonlinear Schrödinger equations simplify to a set of coupled multi-component Manakov equations, which generalize to the multi-mode case the Manakov equation describing nonlinear propagation in single-mode fibers with polarization coupling. The simple form of the derived equations unlocks the understanding of the multi-mode nonlinear propagation dynamics and of the subsequent nonlinear signal distortions.

#### ACKNOWLEDGEMENT

C. Antonelli and A. Mecozzi acknowledge financial support from the Italian Government under Project INCIPICT (<http://incipict.univaq.it/>).

#### REFERENCES

- [1] P.J. Winzer and D. T. Neilson “*From Scaling Disparities to Integrated Parallelism: A Decathlon for a Decade*,” J. of Lightwave Technol. 35, pp. 1099–1115, March 2017.
- [2] A. R. Chraplyvy, “*The coming capacity crunch*,” European Conference on Optical Communication 2009 (ECOC09), plenary talk (2009).
- [3] D. Marcuse, C. R. Menyuk, and P. K. A. Wai, “*Application of the Manakov-PMD equation to studies of signal propagation in optical fibers with randomly varying birefringence*,” J. Lightwave Technol. 15, pp. 1735–1746, Sept. 1997.
- [4] F. Poletti and P. Horak, “*Description of ultrashort pulse propagation in multi-mode optical fibers*,” J. Opt. Soc. Am. B 25, pp. 1645–1654, Oct. 2008.
- [5] C. Antonelli, A. Mecozzi, and M. Shtaif, “*Modeling of nonlinear propagation in space-division multiplexed fiber-optic transmission*,” J. of Lightwave Technol. 34, pp. 36–54, Jan. 2016.
- [6] C. Antonelli, A. Mecozzi, M. Shtaif, and P. J. Winzer, “*Random coupling between groups of degenerate fiber modes in mode multiplexed transmission*,” Opt. Express 21, pp. 9484–9490, April 2013.
- [7] L. Palmieri and A. Galtarossa, “*Coupling effects among degenerate modes in multimode optical fibers*,” IEEE Photonics Journal 6, pp. 0600408 (1–9), Dec. 2014.
- [8] R. Ryf et al., “*Long-distance transmission over coupled-core multi-core fiber*,” European Conference on Optical Communication 2016 (ECOC16), Post-Deadline Paper session (2016)
- [9] A. Mecozzi, C. Antonelli, and M. Shtaif, “*Nonlinear propagation in multi-mode fibers in the strong coupling regime*,” Opt. Express Vol. 20, No. 11, pp. 11673–11678, May 2012.
- [10] A. Mecozzi, C. Antonelli, and M. Shtaif, “*Coupled Manakov equations in multimode fibers with strongly coupled groups of modes*,” Opt. Express Vol. 20, pp. 23436–23441, Oct. 2012.

# OBSERVING THE BROKEN SYMMETRY OF FERMI-PASTA-ULAM RECURRENCES IN OPTICAL FIBERS

Arnaud Mussot<sup>(1)</sup>, Corentin Naveau<sup>(1)</sup>, Matteo Conforti<sup>(1)</sup>, Alexandre Kudlinski<sup>(1)</sup>, Francois Copie<sup>(1)</sup>, Pascal Szriftgiser<sup>(1)</sup>, and Stefano Trillo<sup>(2)</sup>

<sup>(1)</sup> Univ. Lille, CNRS, UMR 8523 - PhLAM - Physique des Lasers  
Atomes et Molécules, F-59000 Lille, France

<sup>(2)</sup> Department of Engineering, University of Ferrara,  
Via Saragat 1, 44122 Ferrara, Italy

[stefano.trillo@unife.it](mailto:stefano.trillo@unife.it)

## Abstract

*Optical fibres constitute a unique ground to investigate one of the most prolific and controversial discovery of modern physics, namely the Fermi-Pasta-Ulam recurrence, which becomes manifest as the growth and decay cycles of a comb of sideband pairs from a weakly modulated pump, occurring via modulational instability (MI). To date, however, the genuine spontaneous symmetry-breaking nature of the MI recurrence was never observed (in any area of physics) due to intrinsic limitations of the experimental realizations. In this work, we overcome such limitations by implementing a novel experimental technique which allows us to reconstruct the longitudinal evolution in amplitude and phase of frequency modes via heterodyne detection of the backscattered light. As a result, we clearly observe how the control of the input modulation seed results into qualitatively different types of FPU recursive behavior associated with the spontaneously broken symmetry*

**Index Terms** – Modulational instability, Nonlinear Optics, Optical Fibers

## I. INTRODUCTION

Modulational instability (MI) is a universal phenomenon which entails the exponential growth of a triangular comb of symmetric sideband pairs at the expenses of a strong background or pump continuous wave. However, such growth cannot proceed indefinitely. Starting from a weakly modulated pump, when considerable depletion of the pump occurs, the process enters its nonlinear stage where the flow of energy is eventually reversed occurring from the sidebands towards the pump until the weakly modulated input is reconstructed and the process of comb formation starts again. Such a recurrent behavior is a manifestation of the so-called Fermi-Pasta-Ulam (FPU) recurrence principle or paradox, named after Fermi and coworkers, who first discovered it in simulations of model of nonlinear chains of atoms [1]. With their great surprise they observed that modal coupling exhibits recurrent behavior instead of evolving towards the equipartition of energy among all the modes, as expected on

the basis of thermodynamic arguments. Although the recurrent behavior of MI has been observed with reference to the evolution of modal power fractions [2], the analysis and the observation of different, though coexisting, regimes of recurrence remain an open issue that we addressed here both theoretically and experimentally.

## **II. NONLINEAR STAGE OF MODULATION INSTABILITY**

It is well known that the evolution of MI is described by the nonlinear Schroedinger equation (NLSE) for the envelope of the electric field [3], which represents a faultless approximation of Maxwell equations in the regime considered below. Starting from the NLSE, we have developed an accurate model of the nonlinear stage of MI and FPU recurrence based on a Fourier mode truncation to the first three modes (pump and first-order sidebands), which allows to describe the mixing via an equivalent integrable Hamiltonian oscillator [3]. This analysis allows us to establish that different regimes of recurrences exist as a result of a spontaneously broken symmetry which is intrinsically associated with the onset of MI. This in turn entails the coexistence of periodic evolutions around either a single fixed point (representing an invariant eigenmodulation) or two fixed points which are mutually out of phase (in terms of global phase of the mixing, i.e. phase of the sidebands relative to the pump). By analogy, these two qualitatively different types of trajectories correspond to librations versus rotations in a standard pendulum or evolutions in a single versus double well in a quartic potential. In the present case the two evolutions become accessible by injecting a weakly modulated pump and by adjusting the input relative modulation phase to be in-phase or out-of-phase. Globally, the finite-dimensional homoclinic structure of the oscillator accurately reproduces the structure exhibited by the NLSE with infinitely many harmonics (infinite-dimensional phase space) [4].

## **III MEASUREMENT METHOD**

In order to give experimental evidence of such complex behavior, two major challenges need to be faced. The first one concerns the need for measuring the evolution of both the power fractions of Fourier modes and their relative phase along the fiber. A second issue is to compensate the fiber losses, which, though small, can be shown to cause the different initial conditions to evolve accordingly to a single type of recurrent regime. We have developed a setup that implement an original multi-channel vector optical time domain reflectometer (VOTDR) optimized for nonlinear measurements. The phase evolution is extracted from the Rayleigh backscattered light through optical heterodyne. The losses are compensated by exploiting the Raman gain by launching a counterpropagating pump at suitable wavelength detuning.

The main result is shown in Fig. 1. The input pump modulated at 35 GHz (slightly lower than peak MI gain frequency) is shown in Fig. 1(a).

The triangular comb developing from MI at its maximum extension is shown in Fig. 1(b). Then, we show the evolutions along a 7.7 Km long SMF28 fiber of the power fractions, the effective phase, as well as the phase-plane projection for the two regimes of qualitatively different recurrence, as displayed in Fig. 1(c-d-e) and Fig. 1(f-g-h), respectively.

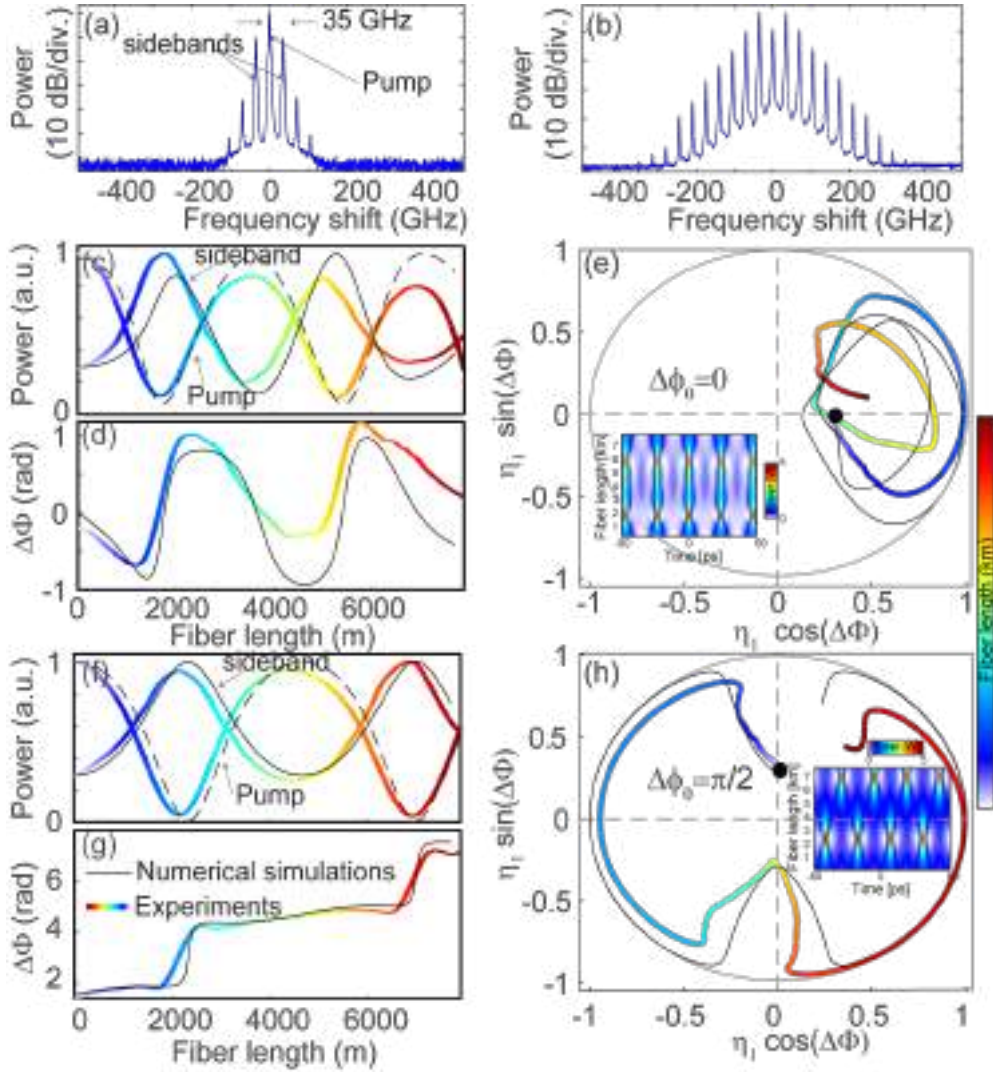


**FIG. 1** – Observed recurrences and their phase plane projections}: (a,b) spectra at (a) the input of the SMF28 (b) the fibre output recorded with an OSA. Evolution along the fibre length of (c,f) the pump power (dashed lines) and the first sideband pair power (dotted lines); (d, g) the relative phase  $\Delta\phi(z)$ . (e,h) Projections of the evolutions in the 3 wave phase plane (the insets show the corresponding temporal evolutions obtained numerically from the NLSE). Numerical simulations are depicted in black lines and experiments in solid rainbow lines. (c,d,e) and (f,g,h) differ only for the initial relative phase of the modulation  $\Delta\phi_0=0$  and  $\Delta\phi_0=\pi/2$ , respectively. Here  $L=7.7$  km, pump power 450 mW, and the input pump-signal power ratio is equal to 8.5 dB. All power plots are normalized to their respective maxima.

In particular, the power evolutions (compare Fig. 1(c) and (f)) show similar recurrent evolutions in terms of power exchange between pump and signal (sidebands). However, the evolution of the phases turn out to be very different, since in the first case (Fig. 1(d)) the phase remain bounded (as for the angle of the librations of a pendulum), while in (Fig. 1(d)) is free running as for a pendulum performing full rotations. We further projected (see Fig. 1(e) and (h)) the trajectories in the phase-plane associated with the reduced nonlinear oscillator arising from mode truncation, characterized by cartesian coordinates  $(\eta_1 \cos \Delta\phi, \eta_1 \sin \Delta\phi)$ ,  $\eta_1$  being the signal fraction and  $\Delta\phi$  the relative (overall) phase. By comparing the measured trajectories in Fig. 1(e) and Fig. 1(h), it is clear that, in the former case, the trajectory is looping around a single center with null phase, while in the latter case the trajectory is a double loop around centers with opposite phases, which further show period doubling (nearly double distance to recover the initial condition).

#### IV CONCLUSIONS

In summary, we presented a new experimental technique that opens new perspectives in the full characterization of parametric mixing processes in guided wave optics, including the regime of phase-sensitive amplification. It allowed the first absolute demonstration of the existence of a spontaneously broken symmetry in the FPU recurrence phenomenon.

#### ACKNOWLEDGEMENT

This work was partly supported by the Agence Nationale de la Recherche through the ANR TOPWAVE, HEAFISY and NoAWE projects.

#### REFERENCES

- [1] E. Fermi, J. Pasta, S. Ulam, in *Collected Papers of Enrico Fermi* (ed. E. Segré) Vol. 2, pp. 977-988 (Univ. Chicago Press, 1965).
- [2] G. Van Simaey, Ph. Emplit, and M. Haelterman, "Experimental demonstration of the Fermi-Pasta-Ulam recurrence in a modulationally unstable optical wave", *Phys. Rev. Lett.* 87, 033902 (2001).
- [3] S. Trillo and S. Wabnitz, "Dynamics of the modulational instability in optical fibers", *Opt. Lett.* 16, 986-988 (1991).
- [4] N. N. Akhmediev, V.M. Eleonskii, and N. E. Kulagin, "Exact first-order solutions of the nonlinear Schroedinger equation", *Theor. Math. Phys.* 72, 809-818 (1987).
- [5] A. Mussot, C. Naveau, M. Conforti, A. Kudlinski, F. Copie, P. Szriftgiser, S. Trillo, "Fibre multiwave-mixing combs reveal the broken symmetry of Fermi-Pasta-Ulam recurrence, *Nature Photonics*, in press.

# MULTI-CORE OPTICAL FIBERS FOR HIGH POWER LASERS

L. Rosa<sup>(1)</sup>, F. Poli<sup>(2)</sup>, S. Selleri<sup>(2)</sup>, L. Vincetti<sup>(1)</sup>, A. Cucinotta<sup>(2)\*</sup>

<sup>(1)</sup> Department of Engineering “Enzo Ferrari”, University of Modena and Reggio Emilia, Italy

<sup>(2)</sup> Department of Engineering and Architecture, University of Parma, Italy

[annamaria.cucinotta@unipr.it](mailto:annamaria.cucinotta@unipr.it)

## Abstract

*We performed Finite Element Method (FEM) simulations of doped Multi-Core Fibers (MCFs) for optical amplification and lasing. The effects of thermal dissipation in the doped core were taken into account by thermal simulation of core heating due to quantum defect and related refractive index variation. We report on the effect of such phenomena on the guided modes of multiple adjacent cores, proving that the thermal index distortion can cause unwanted mode coupling even in optically uncoupled waveguides, and this should be taken into account in the design of MCFs.*

**Index Terms** – Multicore optical fibers, thermal mode coupling, optical amplification, thermal effects, finite-element methods

## I. INTRODUCTION

Diffraction-limited fiber lasers are a fundamental technology for modern industrial applications, providing excellent power scaling capability that is limited by guided mode instability. This is now commonly approached by generating several lower-power beams and combining them coherently to obtain a single higher-power beam, which usually requires a complex setup, making the use of MCFs attractive to guarantee coherence and stability of the resulting beam [1,2]. While optical cross-talk is relatively easy to manage in a multi-core configuration by setting the cores distant enough that the overlap integral between the guided modes becomes negligible, this high-power application entails a strong heat generation, which propagates far across the fiber cross-section. This creates the possibility for thermal cross-talk, where thermally induced refractive index variations in one core are caused by the heat load propagating from another core, producing a form of feedback that can result in unwanted coupling between cores that would normally be optically uncoupled, affecting beam generation and amplification. Simulation results performed for two-core MCFs and considering the LP<sub>01</sub> and LP<sub>11</sub> modes suggest that the feedback can produce resonant phenomena by creating a quasi-periodic refractive index longitudinal variation, with an associated beating between modes [1]. FEM numerical methods are

effective for application to this kind of problem; in fact, the heat-transfer distributions in MCFs with up to 19 cores have been studied in this way [3]. Large-mode area MCFs in amplification applications with closely-packed cores will undergo optical coupling between modes, which will degenerate into a certain number of so-called supermodes [4], whose interaction at high power levels is a risk for mode instability to occur, so the usual approach is to distance the cores so that coupling is negligible, obtaining a better controllable ensemble. While this solves issues related to optical coupling, in high-power amplification and lasing, the fiber is beset by a strong generation of heat, which will propagate unhindered transversally and cause spurious coupling effects.

## II. RESULTS

We study a step fiber cross-section with three in-line cores, called core 1 (left) to core 3 (right). Core/cladding indices are 1.45/1.44992 and core diameter/distance are 50/56  $\mu\text{m}$ . FEM results at 1032 nm are taken by thermal simulation of core-applied heat load, and refractive index is updated with thermal distortion from the temperature profile and an optical simulation gives effective index ( $n_{\text{eff}}$ ) and modal distribution of the heated fiber modes. In Fig. 1, heat is applied to core 1, and  $n_{\text{eff}}$  difference with highest order core 1 LP01 mode shows that the normally uncoupled higher-order LP11 modes in cores 1 and 2 end up crossing the  $n_{\text{eff}}$  of fundamental modes in cores 2 and 3, which can cause spurious coupling harmful for amplification stability and cross-talk. The subscripts ‘v’ and ‘h’ in the figure labels refer to a vertical or horizontal stacking of the two mode lobes, respectively, while the subscripts ‘c1’, ‘c2’, ‘c3’ refers to the three different cores.

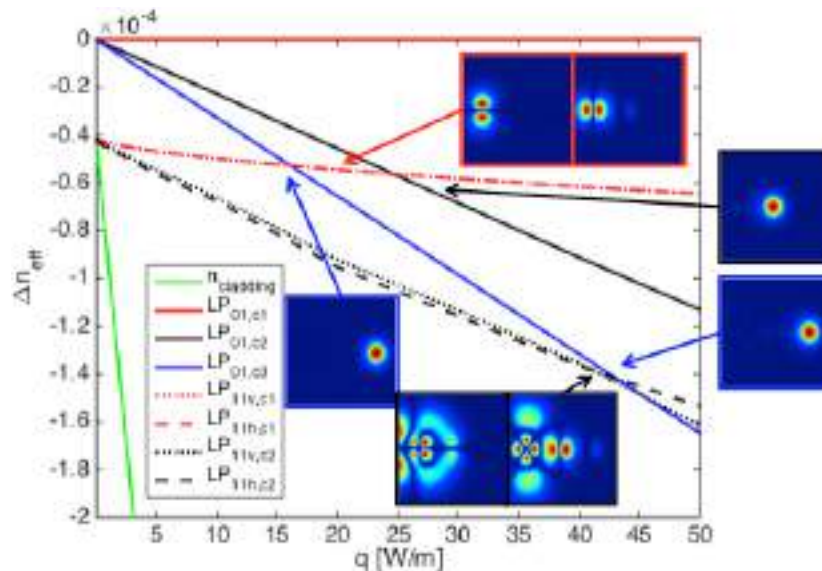


**FIG. 1** – Relative  $n_{\text{eff}}$  difference and evolution of modal field distribution with heat load applied to left-side core 1.

Fig. 2 shows the results when heat is applied to central core 2 instead. In this case the results show that there are also unwanted  $n_{\text{eff}}$  crossings for higher value of  $q$  and, moreover, the symmetry of the refractive index perturbation in this case causes the modes on core 1 and 3 to degenerate, even in absence of optical coupling due to high core distance, forming a quasi-supermode whose nature is currently being investigated.

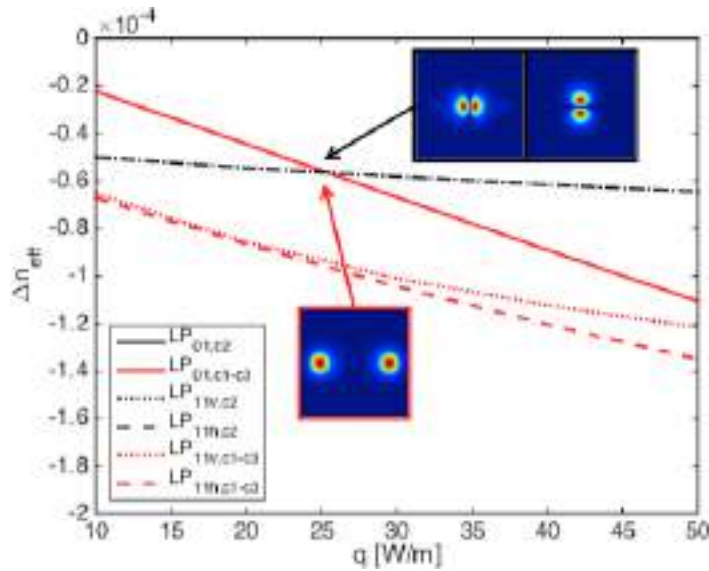


**FIG. 2** – Relative  $n_{\text{eff}}$  difference and evolution of modal field distribution with heat load applied to central core 2.

### III. DUSCUSSION

In order to better illustrate the heat influence on the mode guiding, Figs. 3-5 show the fundamental mode distribution of the three different cores when heat  $q$  is applied to the left core 1 and for increasing values of  $q$ , that is  $q = 0.1 \text{ W/m}$ ,  $q = 1 \text{ W/m}$  and  $q = 10 \text{ W/m}$ . It is clear the asymmetric behaviour of the overall fiber as well as of the central core, given by the asymmetric heat distribution. It is also evident how the heat load in the left core induces a stronger field self-focusing which inhibits coupling with the central core which, in turn, stronger couples to the right one. This behaviour is confirmed by the crossing points in Fig. 1.

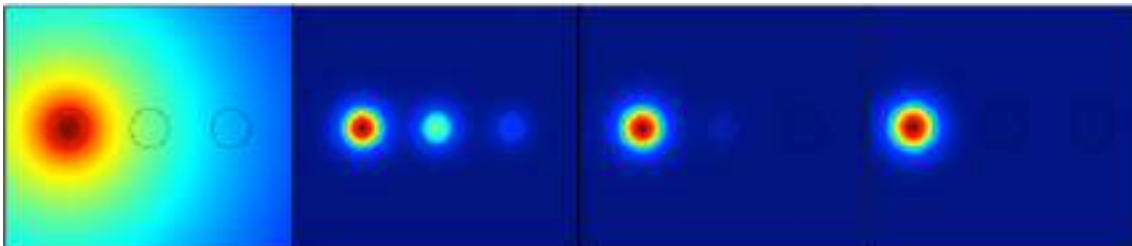


**FIG. 3** – Heat distribution (left) and mode distribution in core 1 for  $q = 0.1 \text{ W/m}$  (center-left),  $q = 1 \text{ W/m}$  (center-right),  $q = 10 \text{ W/m}$  (right).

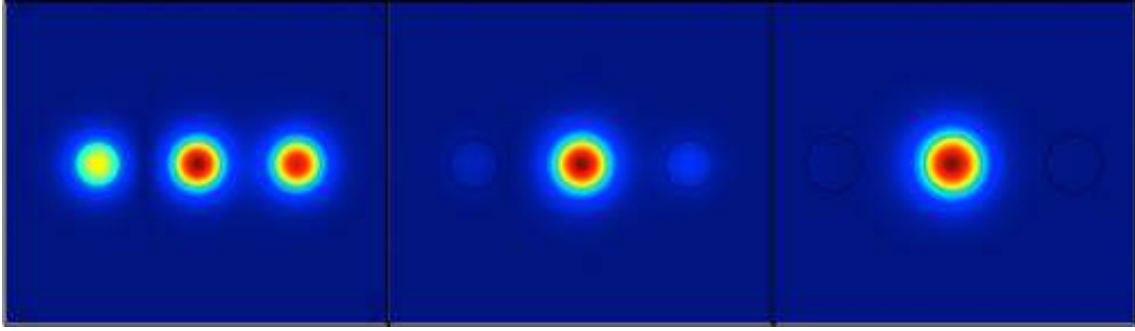


**FIG. 4** – Mode distribution in core 2 for  $q = 0.1\text{W/m}$  (left),  $q=1\text{ W/m}$  (center),  $q=10\text{ W/m}$  (right).

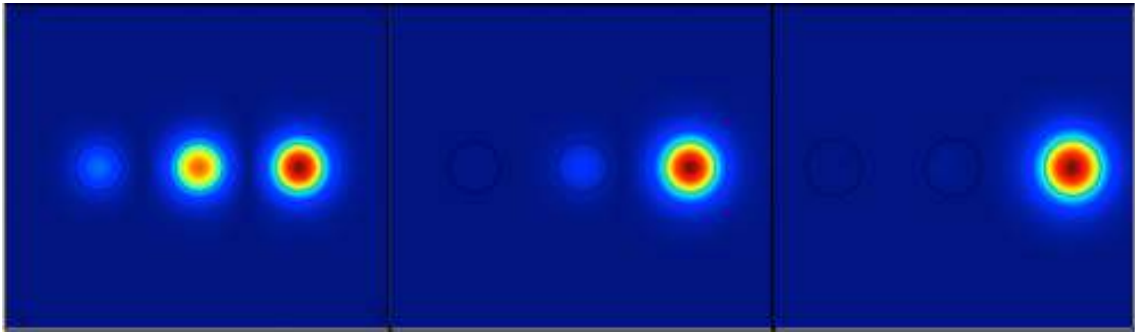


**FIG. 5** – Fig. 5: Mode distribution in core 3 for  $q = 0.1\text{W/m}$  (left),  $q=1\text{ W/m}$  (center),  $q=10\text{ W/m}$  (right).

#### IV. CONCLUSION

In this work, the effects of thermal coupling due to thermal refractive index distortion in a three-core MCF is considered.

In future, more complex MCFs, as the 16-channel multicore fiber [2], will be simulated. In fact, new techniques to manufacture large-area-mode MCF will be developed and the number of cores will further increase. This will allow the demonstration of a new generation of fiber based laser system with Joule level pulse energies.

#### REFERENCES

- [1] H. Otto, A. Klenke, C. Jauregui, F. Stutzki, J. Limpert, and A. Tünnermann, "Scaling the mode instability threshold with multicore fibers," *Opt. Lett.* vol. 39, 2680-2683 (2014).
- [2] A. Klenke, M. Müller, H. Stark, F. Stutzki, C. Hupel, T. Schreiber, A. Tünnermann, and J. Limpert, "Coherently combined 16-channel multicore fiber laser system," *Opt. Lett.* vol.43, 1519-1522 (2018).
- [3] Zheng, Y., Yao, J., Zhang, L. et al, "Thermal distribution analysis of multi-core photonic crystal fiber laser," *Optoelectron. Lett.*, vol. 8, 13-16 (2012).
- [4] C. Jollivet, A. Mafi, D. Flamm, M. Duparré, K. Schuster, S. Grimm, and A. Schülzgen, "Mode-resolved gain analysis and lasing in multi-supermode multi-core fiber laser," *Opt. Express*, Vol. 22, 30377-30386 (2014).

# NESTED PLASMONIC RESONANCES IN OPTICAL ANTENNAS LOADED WITH EPSILON-NEAR-ZERO NANOPARTICLES

D. de Ceglia<sup>(1)</sup>, M. A. Vincenti<sup>(2)</sup>, N. Akozbek<sup>(3)</sup>,  
M. J. Bloemer<sup>(4)</sup>, and M. Scalora<sup>(4)</sup>

<sup>(1)</sup> Department of Information Engineering, University of Padova  
Via Gradenigo 6/a, 35131 Padova, Italy

<sup>(2)</sup> Department of Information Engineering, University of Brescia  
Via Branze, 25128 Brescia, Italy

<sup>(3)</sup> Aegis Techonolgies Inc., Huntsville (AL) - USA

<sup>(4)</sup> US Army AMRDEC, Redstone Arsenal (AL) - USA  
[domenico.deceglia@unipd.it](mailto:domenico.deceglia@unipd.it)

## Abstract

*We propose a nanostructure that supports a nested plasmonic resonance. The system consists of a resonant epsilon-near-zero nanoparticle placed inside the gap of a resonant dipole antenna. Two field enhancement mechanisms are available: one is due to the antenna resonance, the other to the nanoparticle resonance. The cascade of these two effects induces ideal conditions to boost nonlinear optical phenomena at the nanoscale.*

**Index Terms** – Epsilon-near-zero materials, optical antennas, plasmonics, nonlinear optics.

## I. INTRODUCTION

A nanoparticle-loaded optical antenna is proposed, in which the electric-field enhancement is boosted by the cascade of two nested plasmonic resonances (NPRs). Infrared epsilon-near-zero (ENZ) materials are recently attracting growing attention for their remarkable nonlinear optical properties. Large second- and third-harmonic generation enhancements [1] and unity-order refractive-index changes [2] have been demonstrated in planar ENZ films made of indium-tin-oxide (ITO). When ITO or other transparent conducting oxides are degenerately doped, they show metallic, Drude-like dispersion with the real part of the permittivity crossing zero at infrared wavelengths, therefore opening new opportunities for infrared plasmonic devices. The typical signatures of plasmonic resonances are strong field enhancement and the ability to confine light in sub-wavelength dimensions. Both these properties are highly desirable in nanoscale nonlinear optical devices. Another way to boost electric fields at optical frequencies is through metallic optical antennas: Elongated nanoparticles support standing waves formed by counter-propagating surface plasmon-polaritons, and behave as resonant antennas for optical fields [3]. We show that in a nanoparticle-loaded nanoantenna, modes of optical antennas and ENZ nanostructures combine to support a resonance within a resonance, i.e., NPRs. [4]

## II. FIELD ENHANCEMENT

The nanoparticle-loaded nanoantenna is schematized in Fig. 1(a): two gold strips of thickness  $w$  are separated by a gap of height  $d$ . The total nanoantenna length is  $L_{\text{ant}}$ . An ITO cylindrical nanoparticle with diameter  $a$ , is centered in the gap region. The structure is located in vacuo and assumed to be invariant in the  $z$  direction.

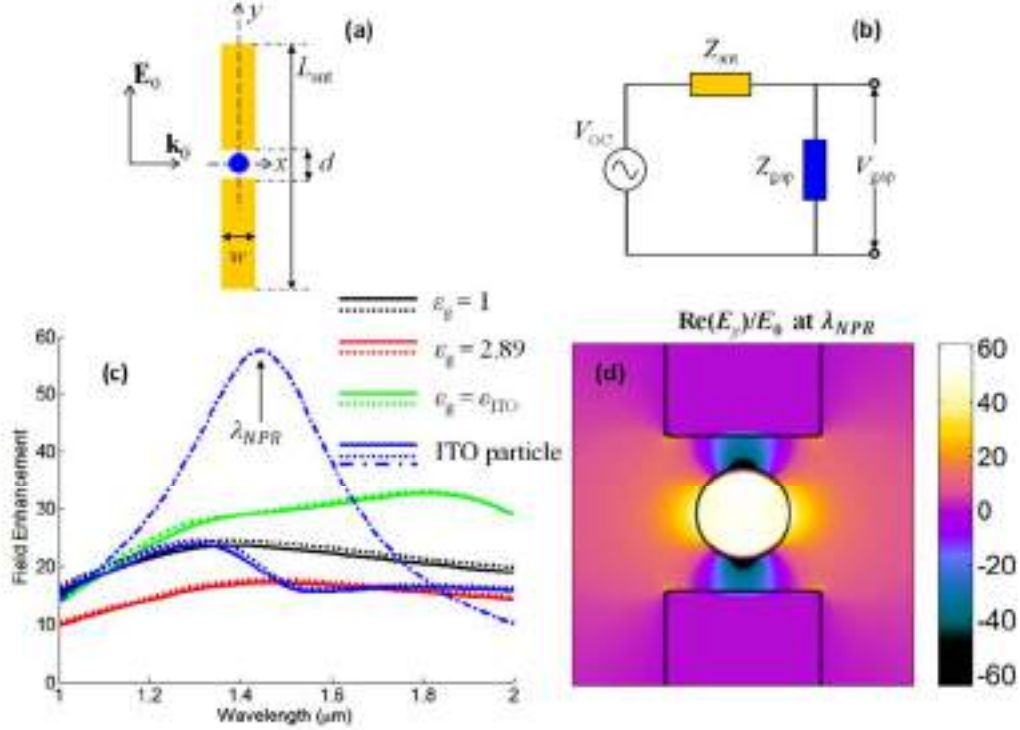


**Fig. 1** (a) Schematic of the Au nanoantenna loaded with an ITO nanoparticle. (b) Circuit model of the loaded antenna. (c) Gap field enhancement vs. wavelength evaluated with the nanocircuit model (solid lines) in the gap of a nanoantenna under plane wave illumination (top-left inset), for the four cases described in the text.

The circuit model of the antenna in receiving mode is illustrated in Fig. 1(b), where  $V_{OC}$  is the open-circuit voltage,  $Z_{ant}$  is the antenna impedance and  $Z_{gap}$  the gap (load) impedance. The permittivity of gold is interpolated with a Drude-Lorentz dispersion model. ITO is modeled as a free-electron gas in a positive ion background, as in Ref. [1]. The incident plane wave is polarized along the antenna long axis ( $y$ -axis). The gold nanoantenna is designed so that the main antenna mode overlaps the zero-crossing wavelength of the ITO-permittivity real-part,  $\lambda_{ENZ} \approx 1.25 \mu\text{m}$ . Hence, we set  $w = d = 10 \text{ nm}$  and  $L_{\text{ant}} = 560 \text{ nm}$ . In Fig. 1(c) we plot the average field enhancement  $|E_y|/E_0$  in the gap region, for the following scenarios: (i) vacuum gap; (ii) gap filled uniformly with a medium having  $\varepsilon_g = 2.89$ ; (iii) gap filled uniformly with ITO,  $\varepsilon_g = \varepsilon_{ITO}$ ; (iv) gap partially loaded with an ITO nanowire with diameter 6 nm. The field enhancement in the gap of these structures is found by retrieving the Thévenin-equivalent

nanocircuit of the antenna in the receiving mode [3] and then compared with full-wave simulations. When the gap is filled with a dispersion-less, loss-less dielectric (i.e.,  $\epsilon_g \geq 1$ ), maximum field enhancement is achieved for  $\epsilon_g = 1$ , i.e., by maximizing the magnitude of the gap impedance  $Z_{\text{gap}} = (-i\omega\epsilon_0\epsilon_g w/d)^{-1}$ . A large and broad field enhancement is found when the gap is filled with a plasmonic medium, as in the case (iii) where  $\epsilon_g = \epsilon_{\text{ITO}}$ . In this scenario a 30-fold enhancement is found over a broad band above  $\lambda_{\text{ENZ}}$ : this effect is due to the complex-conjugate impedance matching between the inductive gap impedance,  $Z_{\text{gap}}$ , and the capacitive antenna impedance,  $Z_{\text{ant}}$ . NPRs are excited in the last scenario (iv), in which the gap is loaded with an ITO nanowire: the field is not uniformly distributed in the gap, especially for wavelengths near and above  $\lambda_{\text{ENZ}}$ , where ITO is metallic. Although the *average* field-enhancement in the nanowire-filled gap (solid and dotted blue curves) is lower than the enhancement experienced by the vacuum- and ITO-filled gaps (black and green curves), the *local* field enhancement inside the ITO is much higher ( $\sim 60$ ). The field distribution [Fig.1(d)] is due to the simultaneous excitation of the main nanoantenna resonant mode and the localized surface plasmon resonance of the ITO nanowire, culminating in the *plasmonic-resonance-within-a-plasmonic-resonance* condition. The vacuum-gap nanoantenna provides a field-enhancement of about 20 in the gap region, whereas a further field-enhancement factor of  $|2/(1 + \epsilon_{\text{ITO}})|$  in ITO is due to the plasmonic resonance in the nanoparticle. The peak of such extra field-enhancement is about 3 and occurs at the NPR wavelength ( $\lambda_{\text{NPR}} \approx 1.4 \mu\text{m}$ ), where  $\epsilon_{\text{ITO}} = -1$ .

### III. HIGHER-ORDER MODES

Our idea is to take advantage of this cascaded field-enhancement effect in order to boost nonlinear optical effects occurring in the nanoparticle, in the nanoantenna and at interfaces. This can be accomplished with two simultaneous mechanisms: (i) by tuning the pump at the NPR, and (ii) by exploiting higher-order antenna modes to increase the far-field radiation rate of harmonic signals generated in the near field region. In Fig. 2, we report all the available antenna modes by plotting the absorption cross section (ACS) spectrum under the illuminations conditions illustrated in Fig. 1. The linear ACS is normalized as follows:  $\int_V \frac{1}{2} \epsilon_0 \omega^2 \epsilon'' |\mathbf{E}|^2 dV / (L_{\text{ant}} I_0)$ , where  $\epsilon''$  is the imaginary part of the relative permittivity,  $\omega$  the angular frequency,  $\epsilon_0$  the permittivity in vacuo,  $I_0$  the input irradiance. The approach to boost nonlinear optical effects in our antenna is to excite mode  $M_1$  with the pump signal (which will be highly enhanced at  $\lambda_{\text{NPR}}$ ), and simultaneously amplify nonlinear signals and out-couple them into the far-field region by exploiting the higher-order modes ( $M_n$ , with  $n \geq 2$ ). In the system under investigation, the free-electron nonlinearity in ITO

and gold is due to convective, Lorentz and gas-pressure forces; its nature is quadrupolar inside ITO and gold, and dipolar on the surfaces due to symmetry breaking. Second-order order ( $\chi^{(2)}$ ) nonlinear effects (second-harmonic generation, spontaneous parametric down-conversion, optical parametric amplification) are mainly driven by free electrons. In contrast, the bound-electron response yields a strong dipole-allowed cubic nonlinearity ( $\chi^{(3)}$ ), both in gold and in ITO. Optical effects that are connected to bound electrons are third-harmonic generation, self-phase modulation, two-photon and saturable absorption.

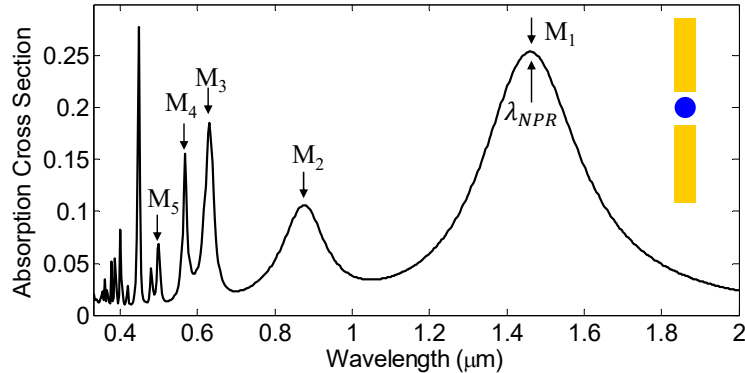


**Fig. 2** Spectrum of the absorption cross section, normalized to the geometrical cross section of the antenna. The absorption peaks are associated with the antenna modes, and they are indicated with the labels  $M_n$ , where  $n$  the mode number.

#### IV. CONCLUSION

An optical antenna loaded with an ENZ nanoparticle realizes a nested-plasmonic resonator. The structure provides unprecedented levels of field enhancement in the volume and on the surface of the plasmonic nanoparticle, therefore it lends itself naturally to boost by several orders of magnitude optical nonlinear effects in nanoscale systems. Nonlinearities may originate from free and bound electrons, as well as from substances placed on the surface or inside the nanoparticle – such as fluorescent, phosphorescent or Raman-active molecules.

#### REFERENCES

- [1] T. S. Luk, D. de Ceglia, S. Liu, G. A. Keeler, R. P. Prasankumar, M. A. Vincenti, M. Scalora, M. B. Sinclair, and S. Campione, “Enhanced third harmonic generation from the epsilon-near-zero modes of ultrathin films,” *Applied Physics Letters* 106, 151103 (2015)
- [2] M. Z. Alam, I. De Leon, R. W. Boyd, “Large optical nonlinearity of indium tin oxide in its epsilon-near-zero region,” *Science* 352, 795-797 (2016)
- [3] M. Agio, and A. Alù, *Optical antennas* (Cambridge University Press, 2013)
- [4] D. de Ceglia, M. A. Vincenti, N. Akozbek, M. J. Bloemer, and M. Scalora, “Nested plasmonic resonances: extraordinary enhancement of linear and nonlinear interactions,” *Optics Express* 25 (4) 3980-3990 (2017)

# TUNABLE OPTICAL ANTENNAS USING VO<sub>2</sub> METAL-INSULATOR PHASE TRANSITIONS

A. Tognazzi<sup>(1)</sup>, F. Baronio<sup>(1,2)</sup>, A. Locatelli<sup>(1,2)</sup>,  
M. A. Vincenti<sup>(1)</sup>, F. Banfi<sup>(3)</sup>, C. Giannetti<sup>(3)</sup> and C. De Angelis<sup>(1,2)</sup>

<sup>(1)</sup> Dipartimento di Ingegneria dell'Informazione, Università degli  
Studi di Brescia

Via Branze 38, 25123 Brescia, Italy

<sup>(2)</sup> Istituto Nazionale di Ottica (INO), Consiglio Nazionale delle  
Ricerche (CNR)

Via Branze 45, 25123 Brescia, Italy

<sup>(3)</sup> Dipartimento di Fisica, Università Cattolica del Sacro Cuore

Via Trieste 17, 25100 Brescia, Italy

[costantino.deangelis@unibs.it](mailto:costantino.deangelis@unibs.it)

## Abstract

*By exploiting VO<sub>2</sub> metal-insulator phase transitions we demonstrate how to effectively control the scattering cross section of optical nanoantennas. We describe the tunability of a gold nanoantenna loaded with VO<sub>2</sub> and then introduce its equivalent circuit to analyze the relevant features of the proposed devices.*

**Index Terms** – Nanophotonics, Optical antennas, VO<sub>2</sub>.

## I. INTRODUCTION

The advances in nanofabrication revolutionized the concept of light manipulation, especially in the visible and infra-red spectral regions. Nanoresonators and metasurfaces are nowadays widely investigated due to their peculiar linear and nonlinear properties and potential applications [1]. Efforts are now focused on achieving dynamically tunable devices that exploit external stimuli to switch their behavior. A variety of approaches has been suggested exploiting thermal, mechanical, electrical as well as optical methods, to obtain dynamically reconfigurable nanostructures [2]. In this framework a promising route is offered by phase transition materials: in contrast with other strongly correlated materials, Vanadium Dioxide (VO<sub>2</sub>) is probably the best candidate for reconfigurable nanostructures because it presents a first order metal-insulator phase transition right above room temperature (~340 K). Since this metal-insulator phase transition can be induced thermally, electrically and even optically, VO<sub>2</sub> attracted much attention for practical applications [3, 4].

In this paper we present an efficient way to exploit VO<sub>2</sub> phase transitions to dynamically control the scattering properties of optical antennas.

## II. RESULTS AND DISCUSSION

In order to describe the role played by the phase transition material, we have used a very simple geometry, i.e. a dipole antenna with parallelepiped arms as described in the insets of Fig. 1. In all our structures, we have performed frequency-domain simulations implemented using the finite-element method in COMSOL. Using gold and VO<sub>2</sub>, we have characterized different dipole nanoantennas in the receiving mode: the antenna is excited with an incident plane wave polarized along the antenna axis as shown in the insets in Fig. 1. We set the width, height and gap at 50 nm, while the arm length is varied between 100 nm and 200 nm. For the complex refractive index values of gold, we use the data reported in [7]. For VO<sub>2</sub> we refer to the data reported in [8], where this material has been thoroughly characterized to demonstrate its tunable and reversible optical properties: for example, at 1 μm, its refractive index and extinction coefficient can be switched from 3.1 to 1.5 and from 0.5 to 1.6, respectively, by increasing the temperature above the transition threshold. In Fig. 1 we compare a gold based nanoantenna with a VO<sub>2</sub> based nanoantenna: we show the normalized dimensionless scattering and extinction cross sections, defined according to [9], as a function of the wavelength: in the panel on the top we report the result for a gold dipole antenna; in the panel on the bottom we report the results for a dipole antenna with VO<sub>2</sub> arms. By comparing continuous lines (low temperature) and dashed lines (high temperature) in Fig. 1 (row at the bottom), we can say that in this configuration the VO<sub>2</sub> nanoantenna is not able to fully exploit the potential of this material for an efficient switching behavior. The poor quality of the switching effect is due to the absence of considerable frequency shifts of the resonances or strong peak intensity dependence upon temperature. Moreover, a comparison between the top row and the bottom row in Fig. 1 shows that gold gives higher values of extinction efficiency and smaller absorption cross sections as compared to the VO<sub>2</sub> nanoantenna.

We thus propose here to fully exploit the potential of phase transition materials by loading the gold nanoantenna gap with VO<sub>2</sub> (see Fig. 2, left); this allows to combine the high performances of the gold dipole antenna with the possibility to control its behavior through tuning of the load. From Fig. 2 it is possible to see that this configuration presents a slightly reduced efficiency and broader resonant peak compared to the gold antenna with air gap; we can clearly see that the resonant peak of the VO<sub>2</sub>-loaded gold nanoantenna at low temperature is red shifted compared to the air gap gold nanoantenna: for this reason the ideal working regime lies in the near infra-red spectral region. Figure 2 also shows that the longer the antenna is, the greater the distance between the high and low temperature peak becomes. This results in a red shift of the high temperature peak for the 100 nm long antenna, and a blue shift for the longer one with respect to the air gap nanoantenna. At the resonant frequency, increasing the temperature changes the normalized scattering efficiency of the longer antenna from ~1.5 to ~15, resulting in a high tunability. The multipolar expansion [10] highlights that the resonant

peak is due to an electric dipole contribution at both temperatures. This is also confirmed by the far field radiation pattern that presents the typical donut shape at both temperatures. The extinction efficiency reported in Fig. 2 outlines the limits where the antenna can be tuned. VO<sub>2</sub> in its metallic phase presents an increasing absorption in the infra-red spectral region that results in an increased extinction efficiency. To obtain the equivalent circuit model of the VO<sub>2</sub> loaded gold nanoantenna we have applied the method proposed in [11] to determine the antenna impedance of a 100 nm long cylindrical gap antenna at the low temperature resonant frequency, whose equivalent circuit is shown in Fig. 2 (left).

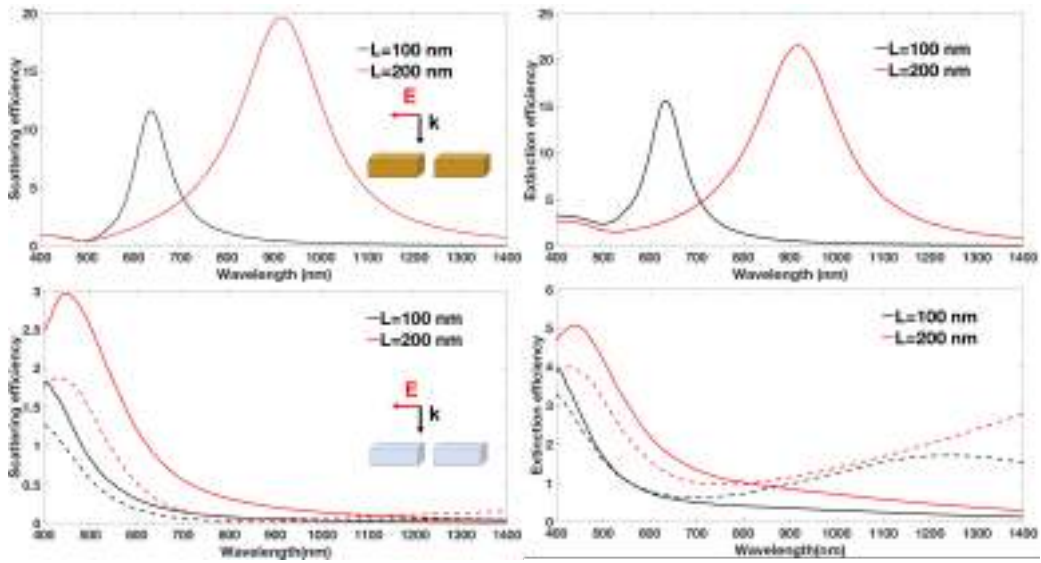


**FIG. 1** – Scattering (left) and extinction (right) cross sections of a gold nanoantenna (row at the top), and a VO<sub>2</sub> nanoantenna (row on the bottom). In the panel at the bottom continuous lines refer to VO<sub>2</sub> in the semiconductor phase, dashed lines refer to VO<sub>2</sub> in the metallic phase.

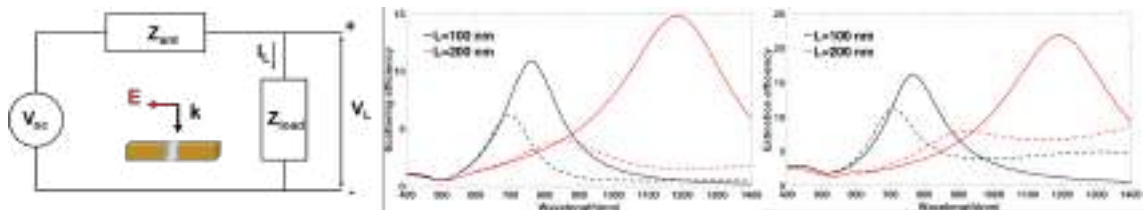


**FIG. 2** – Schematic view and equivalent circuit of the VO<sub>2</sub> loaded gold nanoantenna (left):  $V_{oc}$  is the open circuit voltage,  $Z_{ant}$  is the gold antenna impedance,  $Z_{load}$  is the impedance tunable by means of the VO<sub>2</sub> phase transition. (center-right): Normalized scattering and extinction cross sections of the VO<sub>2</sub> loaded gold nanoantenna: continuous lines with VO<sub>2</sub> in the semiconductor phase; dashed lines with VO<sub>2</sub> in the metallic phase.

At an operating wavelength of 755 nm, we obtain an antenna impedance  $Z_{ant} \sim 100 + 120i \Omega$ ; using the parallel plate approximation the impedance of the lossy capacitor loaded with VO<sub>2</sub> in the gap region is estimated to be

$Z_{\text{load}} = -it/(\omega\epsilon_{\text{VO}_2}S) \sim 37-122i \Omega$ , where  $t$  is the distance between the two antenna arms,  $\omega$  the angular frequency,  $\epsilon_{\text{VO}_2}$  the permittivity of the load and  $S$  the surface of the arm cross section. With these data, we can now use the equivalent circuit in Fig. 2 to predict the behavior of the system without resorting to full wave numerical simulations: using the circuit model and Pocklington's equation we can in fact prove that the exact results of the scattering cross section are well approximated by the results obtained from circuit analysis.

### III. CONCLUSION

We have reported the design of a gold dipole gap nanoantenna loaded with a phase transition material whose optical properties can be tuned by means of thermal, electrical or optical stimulus. Using a simple equivalent circuit, we have provided an effective tool for the modeling of the proposed devices. Our work paves the way toward possible routes for dynamically controlling near as well as far field properties of nanoantennas in the optical domain.

### REFERENCES

- [1] A. Krasnok, M. Tymchenko and A. Alù, "Nonlinear metasurfaces: a paradigm shift in nonlinear optics," *Materials Today* 21, 8 (2017).
- [2] A. M. Haltout, A. V. Kildishev and V. M. Shalaev, "Evolution of Photonic Metasurfaces: From Static to Dynamic," *J. Opt. Soc. Am. B* 33, 501 (2016).
- [3] S. Lysenko, N. Kumar, A. Rúa, J. Figueroa, J. Lu and F. Fernández, "Ultrafast structural dynamics of VO<sub>2</sub>," *Physical Review B* 96, 075128 (2017).
- [4] Z. Zhu, P.G. Evans, R. F. Haglund, Jr., and J.G. Valentine, "Dynamically reconfigurable metadvice employing nanostructured phase-change materials," *Nano Letters* 17, 4881 (2017).
- [5] F. Cilento, C. Giannetti, G. Ferrini, S. Dal Conte, T. Sala, G. Coslovich, M. Rini, A. Cavalleri and F. Parmigiani, "Ultrafast insulator-to-metal phase transition as a switch to measure the spectrogram of a supercontinuum light pulse", *Applied Physics Letters* 96, 021102 (2010).
- [6] A. Alù and N. Engheta, "Tuning the scattering response of optical nanoantennas with nanocircuit loads," *Nature Photonics* 2, 307 (2008).
- [7] R. L. Olmon, B. Slovick, T. W. Johnson, D. Shelton, S. Oh, G. D. Boreman and M. B. Raschke, "Optical dielectric function of gold," *Physical Review B* 86, 235147 (2012).
- [8] J. B. Kana Kana, J. M. Ndjaka, G. Vignaud, A. Gibaud, M. Maaza, "Thermally tunable optical constants of vanadium dioxide thin films measured by spectroscopic ellipsometry," *Optics Communications* 284, 807 (2010).
- [9] C. F. Bohren and D. R. Huffman, "*Absorption and scattering of light by small particles*," 1<sup>st</sup> ed., Wiley Professional Paperback Edition, 1998.
- [10] P. Grahn, A. Shevchenko and M. Kaivola, "Electromagnetic multipole theory for optical nanomaterials," *New Journal of Physics* 14, 093033 (2012).
- [11] C. De Angelis, A. Locatelli, D. Modotto, S. Boscolo, M. Midrio and A. Capobianco, "Frequency addressing of nano-objects by electrical tuning of optical antennas," *Journal of the Optical Society of America B* 25, 997 (2010).

# ANALYSIS OF THE THERMAL EFFECTS ON A FULLY APERIODIC LARGE PITCH FIBER AMPLIFIER

K. Tragni<sup>1</sup>, C. Molardi<sup>1, 3</sup>, F. Poli<sup>1</sup>, R. Dauliat<sup>2</sup>, B. Leconte<sup>2</sup>, D. Darwich<sup>2</sup>,  
R. du Jeu<sup>2</sup>, M.A. Malleville<sup>2</sup>, S. Selleri<sup>1</sup>, P. Roy<sup>2</sup>, A. Cucinotta<sup>1\*</sup>

*1 University of Parma, Dept. of Engineering and Architecture, Parma, Italy*

*2 University of Limoges, CNRS, XLIM, UMR 7252, Limoges, France*

*3 Electrical and Electronic Eng. Dept., Nazarbayev University, Astana, KZ*

*\*[annamaria.cucinotta@unipr.it](mailto:annamaria.cucinotta@unipr.it)*

## Abstract

*A fiber amplifier based on Yb-doped Fully-Aperiodic Large-Pitch Fibers has been numerically investigated. Modal properties and gain competition between FM and first HOM have been calculated in presence of thermal effects, which can compromise the output beam quality. The simulation tool used for this purpose is based on a Finite Element Method modal solver and is coupled with a thermal and an amplifier model, to estimate the variation of guiding properties along the fiber. The main characteristics of the Yb-doped FA-LPF have been derived by the comparison between numerical results and experimental data.*

**Index Terms** – Fiber amplifier, photonic-crystal fibers, thermo-optic effect, large pitch fibers.

## I. INTRODUCTION

In recent years, Photonic Crystal Fiber (PCF) technology has witnessed a huge progress. In particular, Yb-doped double-cladding (DC) PCFs have led to a performance enhancement in high-power fiber lasers and amplifiers, thanks to their interesting characteristics in terms of resilience to thermal effects [1,2]. Namely Fully-Aperiodic Large-Pitch Fibers (FA-LPFs) allow providing high pump power, due to their large mode area, and maintaining the Single Mode (SM) operation and laser beam quality, improving Higher Order Mode (HOM) delocalization out of the gain area [3,4].

In this paper an amplifier based on a Yb-doped FA-LPF is analyzed by means of a full-vector modal solver based on the Finite Element Method (FEM) and an ad-hoc software which considers the power evolution along the amplifier and the related heat distribution through the fiber cross-section [5]. A comparison with experimental data allows validating the numerical model.

## II. FIBER DESIGN AND AMPLIFIER SETUP

The amplifier is made by a DC rod-type fiber with the cross-section shown in Fig. 1. The 19-cell Yb-doped core ( $n = 1.457$ ), denoted in green, has an area of  $2214 \mu\text{m}^2$  and is built over a triangular lattice with pitch of  $34.8 \mu\text{m}$ . The all-solid cladding is made by high-index silica ( $n = 1.457$ ) with fluorine doped inclusions ( $n = 1.444$ ), in pink in Fig. 1, that

break the  $C_{6v}$  symmetry of the triangular lattice and allow the delocalization of HOMs even at high power.

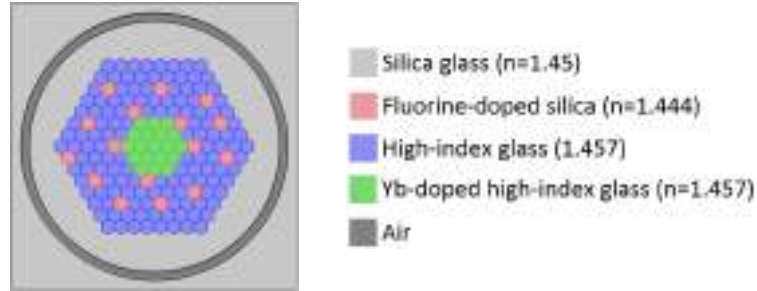


**FIG. 1** – Yb-doped FA-LPF cross-section.

The experimental amplifier setup, in a counter-propagating pump configuration, is represented in Fig. 2.



**FIG. 2** – Schematic illustration of the experimental amplifier setup.

The pump diode delivers up to 400 W of average power at 976 nm, that is coupled into the fiber by lenses L1 and L2. The seed source emits a 20 ps pulse at 1064 nm, with a repetition rate of 40 MHz. The amplified signal is acquired through the dichroic mirror M1.

Experimental results, obtained with this configuration, are compared with numerical values found through an in-house developed tool based on a FEM modal solver. Starting from the calculation of the field distribution of the modes, a spatial amplifier model evaluates the gain competition along the fiber. Moreover, a thermal model calculates the temperature distribution and the thermally-induced change in the refractive index profile over the fiber cross-section, as a consequence of the heat load generated in the Yb doped core due to the quantum defect.

### III. RESULTS

To fit the numerical values with the experimental data, it has been considered a percentage of pump coupled in the fiber equal to 80% and 90%, to take into account the possible losses, and a variable pump absorption. The small signal gain values have been fitted for a pump absorption varying from 17 to 18 dB/m, as shown in Fig. 3. For a pump coupling of 90%, the values of absorbed pump that minimize the mean square error are around 17.5 dB/m. For a lower pump coupling of 80%, the best correspondence is found when the pump absorption is around

17.75 dB/m. Considering these pairs of values, simulations with higher input power have been performed and results have been compared with experimental data obtained with setup shown in Fig. 2.

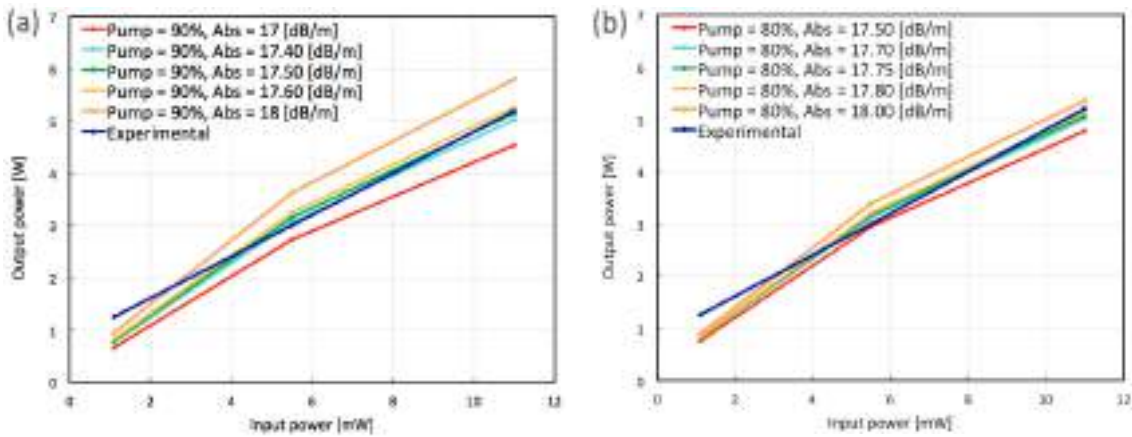


**FIG. 3** – Small signal gain best fitting numerical simulations for a pump coupling = 90% (a) and a pump coupling = 80% (b).

The signal power is equal to 4 W, with a distribution between FM and first HOM of 90% and 10% respectively. The pump power is varied from 0 to 400 W. It can be assumed that it has a Gaussian shape, centered in the core of the fiber, where the FM is more confined and there is an increase of the temperature. To simulate the Gaussian distribution of the pump power, a pre-shaping of it has been performed.

In Fig. 4 the numerical results obtained with the pre-shaped pump, with a coupling of 90% (a) and 80% (b), are compared to the ones given by a pump uniformly distributed through the cross section of the fiber (dashed-line) and the experimental data. The values obtained with the pre-shaped pump fit better with the experimental ones, even if a saturation of the signal for high power occurs.

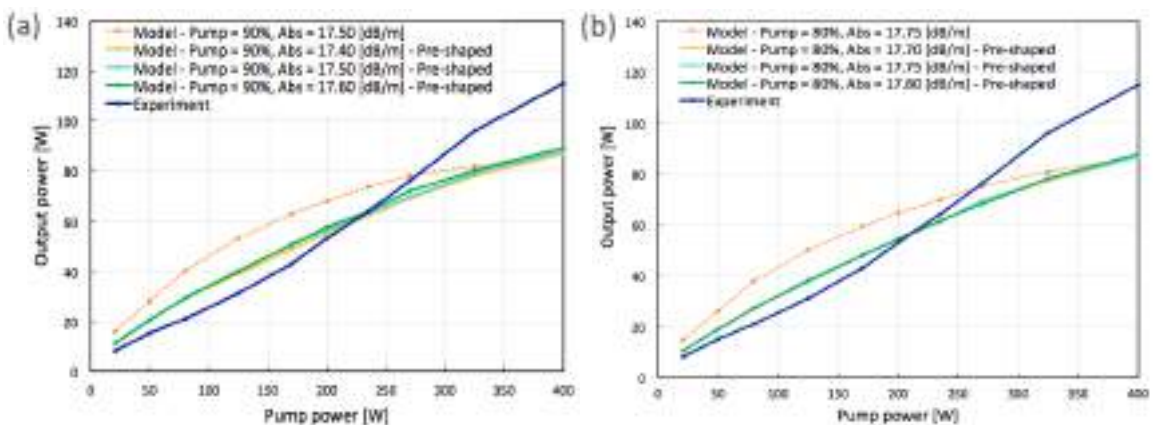


**FIG. 4** – Output power versus pump power characteristic for a pump coupling = 90% (a) and a pump coupling = 80% (b). Input signal of 4 W at 1064 nm.

A second set of simulations has been performed, considering a higher input signal, equal to 9 W. In this case, as the thermal effects have more influence, the FM is better confined in the core and the results

which consider the Gaussian distribution of the pump fit extremely well with the experimental data, as shown in Fig. 5.

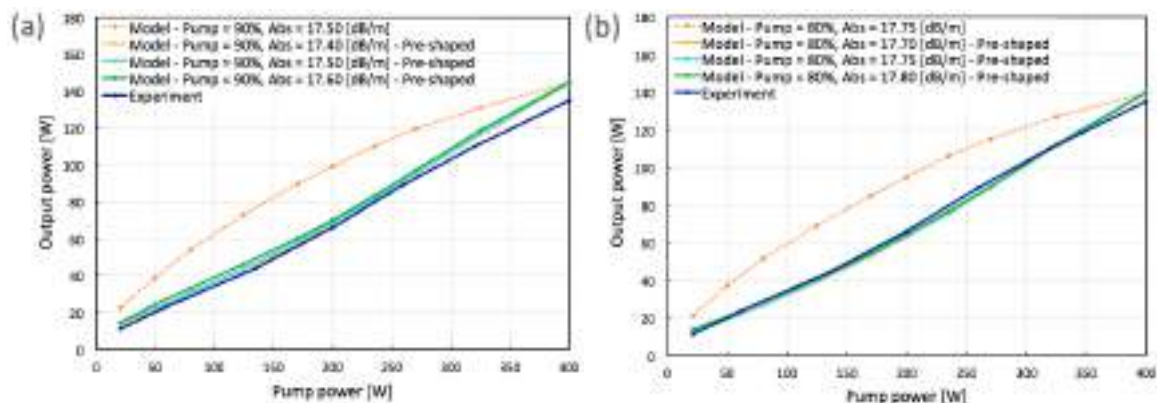


**FIG. 5** – Output power versus pump power characteristic for a pump coupling = 90% (a) and a pump coupling = 80% (b). Input signal of 9 W at 1064 nm.

#### IV. CONCLUSION

In this work a Yb-doped fiber amplifier based on a Fully-Aperiodic PCF has been analyzed with a specific numerical tool, which takes into account the thermal effects due to the high power. Simulations have been performed by considering a counter-propagating pump with an increasing power from 0 to 400 W and an input signal of 4 W and 9 W at 1064 nm. Results, compared to experimental data, have shown that is necessary to consider a Gaussian-shape pump distribution, centered in the core, where the FM confinement is greater with increasing temperature. It is important to take into consideration this behavior for the modeling, making a pre-shaping of the pump power distribution. In this way, for a signal of 9 W with a coupling power of 90% and 80% and an absorbed power around 17.50 dB/m and 17.75 dB/m respectively, we are witnessing an excellent match with the experimental data.

#### REFERENCES

- [1] M.N. Zervas and C.A. Codemard, "High Power Fiber Lasers: A Review," *IEEE JSTQE*, vol. 20, pp. 219–241, 2014.
- [2] A.V. Smith and J.J. Smith, "Mode instability in high power fiber amplifiers," *Opt. Express*, vol. 19, pp. 10180–10192, 2011.
- [3] E. Coscelli, C. Molardi, A. Cucinotta, S. Selleri, "Symmetry-Free Tm-Doped Photonic Crystal Fiber with Enhanced Mode Area," *IEEE JSTQE*, vol. 20, pp. 544–550, 2015.
- [4] R. Dauliat, A. Benoit, D. Darwich, R. Jamier, J. Kobelke, S. Grimm, K. Schuster, P. Roy, "Demonstration of a homogeneous Yb-doped core fully aperiodic large-pitch fiber laser," *Appl. Opt.*, vol. 55, pp. 6229–6235, 2016.
- [5] L. Rosa, E. Coscelli, F. Poli, A. Cucinotta, S. Selleri, "Thermal modeling of gain competition in Yb-doped large-mode-area photonic-crystal fiber amplifier," *Opt. Express*, vol. 23, pp. 18638–18644, 2015.

# REDUCED SIZE PLANAR GRID ARRAY ANTENNA FOR AUTOMOTIVE RADAR SENSOR

E. Arneri, F. Greco, L. Boccia, G. Amendola

Università della Calabria  
[emilio.arneiri@unical.it](mailto:emilio.arneiri@unical.it)

## Abstract

*A new configuration of a planar grid array antenna for automotive radar sensor applications operating in the 76-81 GHz frequency band is introduced. Typically, high resolution direction of arrival (DOA) estimation requires a maximum distance of  $\lambda/2$  between receiving antennas. Proposed antenna consists of reduced size loop elements suitable for this type of applications. In addition, to enhance the gain bandwidth, the antenna adopts variably dimensioned radiation elements.*

**Index Terms** – 77GHz, grid array antenna, automotive radar

## I. INTRODUCTION

For the operation of automotive radar sensors in the millimeter-waves, two frequency bands have emerged. One is the band from 76-77 GHz, which is available worldwide. The second band is the band from 77-81GHz, which has been introduced in Europe to replace radar sensors in the 24GHz band [1]. Several type of antennas have been studied as possible candidate for the automotive radar systems. This work describes the design of a 77-81GHz radar sensor based on the grid array antenna architecture [2]. The grid array antenna possesses many advantages such as high gain, narrow beam, simple feed, and easy construction. The microstrip grid array antenna as shown in Fig. 1 consists of rectangular meshes of microstrip lines on a dielectric substrate backed by a metallic ground plane. If the interval between each receiver antenna is maintained at a fraction of  $\lambda$ , wide angle detection can be achieved by reducing the grating lobe during the angle steering. For this reason the proposed grid array uses reduced size loop elements. Compared to other automotive radar configurations, this antenna design is a completely planar antenna based on a lowcost fabrication technology. The proposed configuration can be used to realize a one-body antenna/transceiver unit for automotive radars sensor applications.

## II. THE GRID ARRAY ANTENNA

Fig. 1 (a) shows a single row grid array antenna composed by a series of 7 rectangular microstrip line loop elements. The radiation properties of the antenna can be explained by analyzing the current flow on a single rectangular element (Fig. 1b). The currents flowing in the x-direction combine constructively, generating a linear polarized radiation. Currents flowing in the y-direction have destructive interference and

does not affect the radiation properties of the antenna. The cell width ( $l1$ ) is set to a half-wavelength and the cell height ( $h$ ) is adjusted for a phase difference of  $180^\circ$  between Q and Q' ( Fig. 1 (b) ). For a broadside radiation, the phase difference between points P and P' has to be  $0^\circ$  (Fig. 1 (c)), which is controlled by the lengths of the connecting lines. Single row design offers narrow beam in elevation and a wide beam in azimuth.

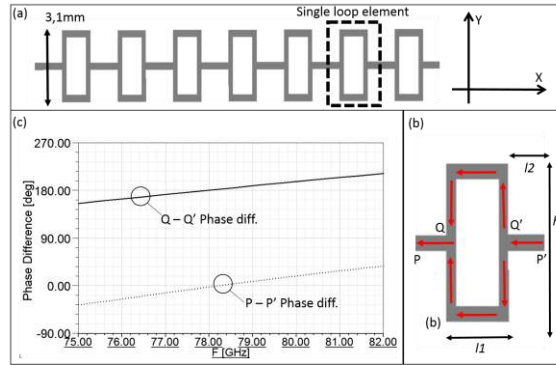


**Fig. 1** (a) Single row grid array antenna. (b) Current flow on fundamental element, c) Simulated phase difference on the fundamental element.

### III. GRID ARRAY ANTENNA MINIATURIZATION

The grid array antenna in its classical configuration is not suitable for applications requiring stringent specification on DOA estimation. The mutual distance of the antenna columns in azimuth is restricted to not much more than half a free-space wavelength. Since the intended element spacing is  $0.5\lambda = 1.9\text{mm}$  (at 79GHz), this value also represents the maximum possible mesh height ( $h$  in Fig. 1b). However, the long side of the mesh presented in the previous section have a height  $h=3,1\text{mm}$ , for this reason classical grid array antenna can't be used in the  $0.5\lambda$  arrangement required for wide angle detection.

#### A. Meandered grid array

The grid array antenna can be miniaturized by meandering the non-radiating side of the mesh (Fig 2a). Fig. 2b shows a miniaturized elementary cell. The new radiation element was designed to have the same radiation properties as the classical configuration presented in previous section. For this reason, the cell length is adjusted for a phase difference of  $180^\circ$  between points Q and Q'; in addition the length  $l2$  has been adjusted to have  $0^\circ$  of phase difference between points P and P' for a broadside radiation (Fig. 2c). The radiation is essentially from the x-oriented sides, with the meandered sides acting mainly as guiding or transmission lines. This is because the current on each short side is basically in-phase, while each long side supports a full wavelength current. With such a current distribution, the maximum radiation would be broadside to the array (as in the classical configuration shown in Fig. 1). With this new configuration the height  $h$  is reduced to 1,7mm (from 3,1mm of the classical configuration).

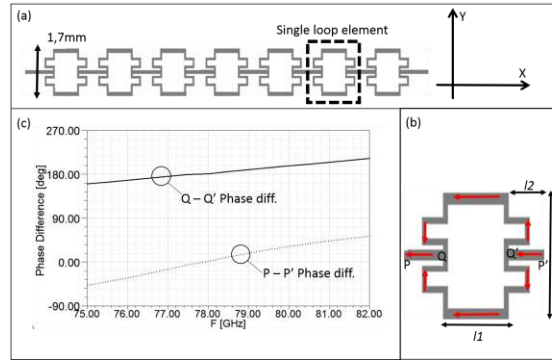


**Fig. 2** (a) Single row meandered grid array antenna. (b) Current flow on fundamental element,  $l_1=1.2\text{mm}$ ,  $l_2=0.6\text{mm}$   $h=1.7\text{mm}$ . (c) Simulated phase difference on the fundamental element.

### B. Meandered –Slanted Grid Array Antenna

Further miniaturization of the elementary cell can be achieved by tilting the meandered lines of about  $45^\circ$ . Fig. 3 shows the new grid array antenna configuration. Similar to the previous configurations the lengths are adjusted to have instantaneous current out of phase on the meandered/sloping side of the cell, and in phase on the the x-directed short sides (Fig. 3 b and c ). With such a current distribution, the maximum radiation would be broadside to the array.

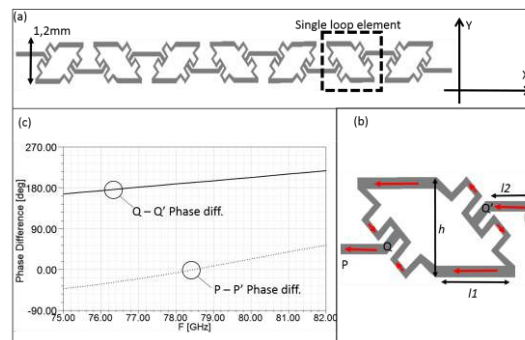


**Fig. 3** (a) Single row meandered-slanted grid array antenna. (b) Current flow on fundamental element,  $l_1=1.2\text{mm}$ ,  $l_2=0.7\text{mm}$   $h=1.2\text{mm}$ . (c) Simulated phase difference on the fundamental element.

### B. Gain and Bandwidth enhancement

The use of a multiresonant radiating structures, like in the log periodic antennas, is a widely used technique for designing wideband antennas. The proposed grid array employs this technique for enhancing the bandwidth: variably dimensioned radiation elements have been adopted, this mean that the antenna will be resonant at different frequencies and that may result in a wideband property. The new configuration offers better performance especially in the lower side of the bandwidth.

#### IV. MEASUREMENT

Fig. 4 shows the manufactured prototype. Fig. 5 shows the measured and simulated matching and Gain. Good agreement has been obtained. Simulated radiation pattern at 78 GHz is shown in fig 5 (c).

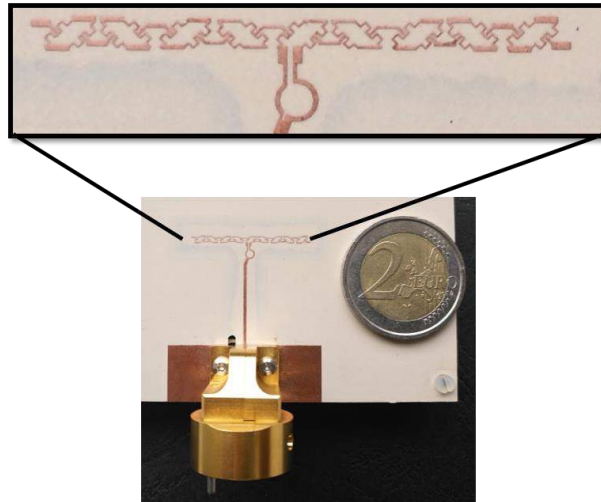


**FIG. 4** – Manufactured Prototype

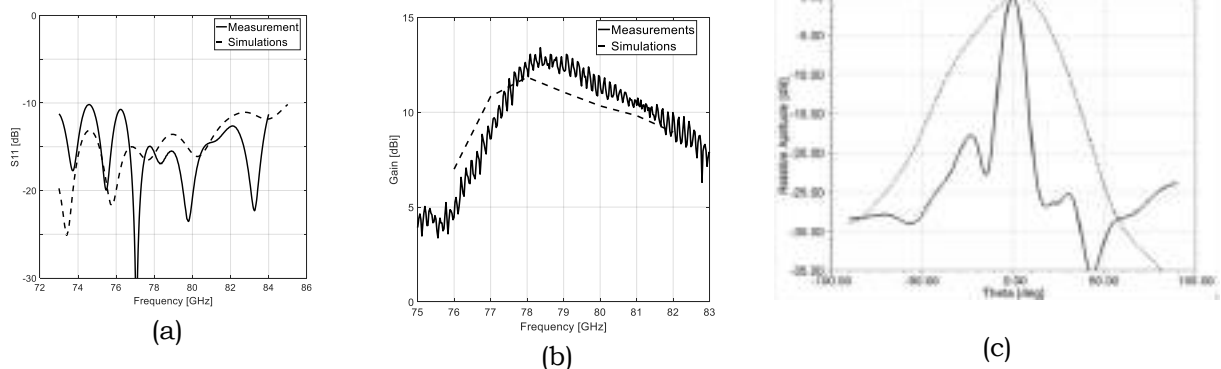


**FIG.5** – Measured results: (a) S11; (b) Gain. (c) Simulated pattern

#### V. CONCLUSION

A planar grid array antenna for automotive radar sensor applications have been presented. Proposed antenna is composed by reduced size loop cells. The antenna shows a wide operating bandwidth in terms of pattern stability, being able to cover the whole frequency range from 77 to 81GHz. Overall 51% size reduction has been achieved as compared to conventional grid array antenna for same frequency band.

#### REFERENCES

- [1] Federal Communications Commission, FCC part 15, sec. 15.253.
- [2] Conti, R., J. Toth, T. Dowling, and J. Weiss, "The wire grid microstrip antenna," IEEE Trans. on Antennas Propagat., Vol. 29, p. 157-166, 1981.

## RECENT ADVANCES ON EBG CAVITY ANTENNAS

P. Baccarelli <sup>(1)</sup>, S. Ceccuzzi<sup>(2)</sup>, V. Jandieri<sup>(3)</sup>, C. Ponti <sup>(1)</sup>, G. Schettini <sup>(1)</sup>

<sup>(1)</sup> Department of Engineering, Roma Tre University  
Via Vito Volterra 62, 00146 Rome, Italy  
[giuseppe.schettini@uniroma3.it](mailto:giuseppe.schettini@uniroma3.it)

<sup>(2)</sup> ENEA, Fusion and Nuclear Safety Department,  
C. R. Frascati, Via E. Fermi 45, 00044 Frascati (Rome), Italy

<sup>(3)</sup> Faculty of Engineering, University of Duisburg-Essen, and  
CENIDE – Center for Nanointegration Duisburg-Essen, D-47048  
Duisburg, Germany

### Abstract

*The activity carried out on EBG cavity antennas is presented explaining in which cases it is possible to obtain good electromagnetic performances. Moreover advancements in terms of understanding of the basic phenomena involved is treated. The possibility of reaching different optimizations is finally investigated showing the obtained results.*

**Index Terms** – Electromagnetic Band Gap (EBG) materials, cavity antennas, leaky waves.

### I. INTRODUCTION

In recent years the study of cavity antennas realized by using dielectric Electromagnetic Band-Gap (EBG) structures for the confinement and steering of the electromagnetic radiation has been addressed in several directions looking at the possibility of reaching very good goals in terms of antenna parameters like directivity, matching, efficiency and bandwidth [1-3]. These studies gave us the possibility of understanding that different optimizations were possible, based on a behavior that, in the first case, is linked to a resonance effect [4-5], while, in the second one, is more strictly referable to the presence of leakage in the structure [6-7].

### II. RESONANT CAVITY ANTENNAS

A resonant cavity antenna (RCA) is a compound radiator, where an EBG superstrate is placed at a suitable distance from a primary elementary source [8-9]. This class can be considered of aperture antennas, since the radiative mechanism is that of an equivalent aperture at the top of the EBG structure. As to the practical realization of the EBG, it is obtained from the period arrangement of a unit cell with 1D, 2D or 3D periodicity. The advantage of RCAs is in the possibility to achieve a high gain with a simple architecture. In their traditional layout, they are resonating structures with a fractional bandwidth of around 4%. A possible way to enlarge the bandwidth is to interrupt the periodicity of the EBG, thus obtaining multiple resonances

that, close in frequency, return a broadband behavior [1]. This can be accomplished from 1D EBGs, i.e., given by a stack of homogenous dielectric layers, alternating layers of different permittivity with high dielectric contrast. An example of implementation is given in Fig. 1(a), where the EBG superstrate is given by an internal layer of PLA ( $\epsilon_r = 2.76$ ), followed by a small internal air cavity, and two touching layers of vetronit ( $\epsilon_r = 7$ ) and polycarbonate ( $\epsilon_r = 3.1$ ), respectively. The primary source is a truncated rectangular waveguide, backed by a ground plane. Therefore, a main cavity is formed, bounded by two mirrors, a perfectly reflecting mirror given by the ground plane, and a partially reflecting one relevant to the EBG superstrate. Thickness of the layers and of the cavity is designed to work in the X band, around a central frequency of 10 GHz. In-plane size of the EBG superstrate, with a side  $L$  of length  $2\lambda$ , is smaller than narrow bandwidth resonator cavity antennas, having side length of at least 4 wavelengths.

The plot of the gain versus frequency is shown in Fig. 2(b). With the non-periodic EBG, a 30% fractional bandwidth is achieved. Maximum gain is 16.9 dB, lower than peak gain achievable in traditional cavity resonator antennas employing periodic EBGs. However, this result is a good compromise between high antenna gain and large bandwidth.

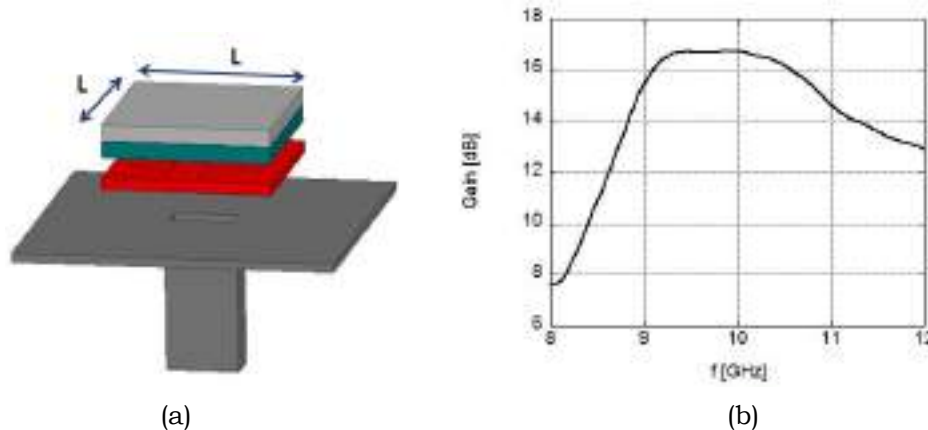


**FIG. 1** – (a) Layout of a wideband EBG resonator antenna. (b) Directivity versus frequency.

### III. THE ROLE OF LEAKAGE IN EBG CAVITY ANTENNAS

Highly directive EBG cavity antennas can be modelled by considering the excitation of slowly attenuating leaky waves that produce a large equivalent field at the antenna aperture. In this framework, the knowledge of the complex propagation wavenumbers of leaky modes supported by 2D EBG waveguides is important for the complete determination of the radiative regions and for the understanding of the fundamental parameters governing the antenna

design [6]. To this aim, a rigorous and efficient full-wave numerical approach devoted to the analysis of leaky modes in 2D EBG waveguides is presented.

The proposed technique allows for the numerical study of bound and leaky modes propagating in artificial periodic structures composed by 2D cylindrical inclusions. The method is based on the Lattice Sums (LSs) related to the periodic arrangement of circular rods and uses the T-matrix and the generalized reflection and transmission matrices to characterize the nature of the cylindrical scatterer and the layered periodic environment [7], respectively. A recently developed fast and accurate calculation procedure for the LSs in case of complex propagation wavenumbers is adopted here, which resorts to original higher-order spectral and spatial Ewald representations and allows for the correct spectral determination of each spatial harmonic constituting the leaky mode [10].

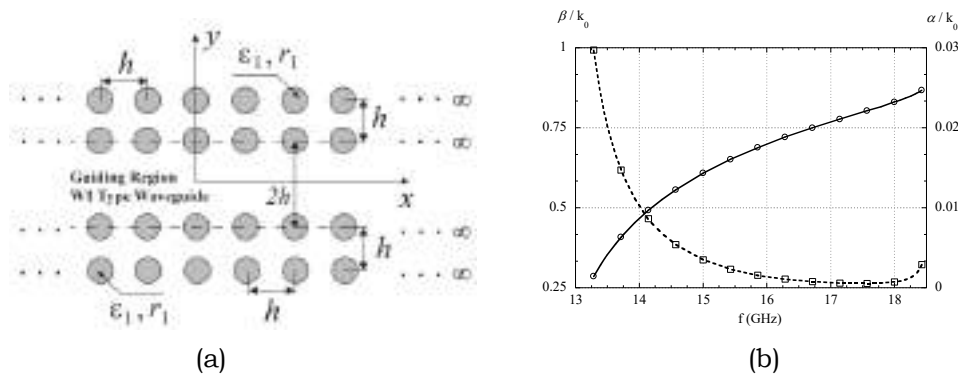


**FIG. 2** – (a) Side view of a 2D planar periodic structure composed by dielectric circular rods periodically distributed in the free space. (b) Dispersion diagrams of the normalized phase and attenuation constants for the radiating harmonic of the lowest order TE leaky mode of the W1 waveguide shown in (a), obtained with the LSs technique (solid and dashed line, respectively) and FSEM with PML (black circles and squares, respectively). The period is  $h = 7\text{mm}$ ; the dielectric permittivity and the radius of the circular rods are  $\epsilon_1 = 11.9 \epsilon_0$  and  $r_1 = 0.2h$ , respectively.

The EBG cavity in Fig. 2(a), formed by removing one row of the dielectric rods from the original square lattice EBG structure, is here considered. The multilayered array of dielectric cylindrical rods with period  $h = 7\text{mm}$  gives rise to an EBG region [7] inside the normalized frequency range  $13.5\text{ GHz} < f < 18.5\text{ GHz}$ . Figure 2(b) shows the normalized phase and attenuation constant,  $\beta/k_0$  and  $\alpha/k_0$ , respectively, for the radiating harmonic of the lowest TE leaky mode of the EBG waveguide. We note that within the EBG frequency range the radiating harmonic is fast, i.e.,  $\beta/k_0 < 1$ , and has an improper determination [6], whereas all other harmonics (not shown here) are slow and proper. Finally, we observe that the modal attenuation constant significantly increases as the wavelength approaches the band edges, due to a decrease of the field confinement by the EBG structure.

The results of the proposed method, based on the LS technique, have been compared with those obtained by means of a well-established Fourier Series Expansion method (FSEM) combined with perfectly matched layers (PMLs) [11]. An excellent agreement has been observed in all cases, while the computation time of the proposed approach, based on the LSs, was in average about 1000 time faster than that of the PML-FSEM.

#### REFERENCES

- [1] A.A. Baba, R.M. Hashmi K.P. Esselle, Q. Xue, "Achieving a Large Gain-Bandwidth Product from a Compact Antenna," *IEEE Transactions on Antennas and Propagation* vol. 65(7) pp. 3437-3446, July 2017.
- [2] S. Ceccuzzi, L. Pajewski, C. Ponti, G. Schettini, "Directive EBG Antennas: a Comparison Between Two Different Radiating Mechanisms," *IEEE Transactions on Antennas and Propagation*, vol. 62(10), pp. 5420-5424, October 2014.
- [3] S. Ceccuzzi, V. Jandieri, P. Baccarelli, C. Ponti, G. Schettini, "On beam shaping of the field radiated by a line source coupled to finite or infinite photonic crystals," *Journal of the Optical Society of America A*, vol. 33(4), pp. 764-770, April 2016.
- [4] S. Ceccuzzi, C. Ponti, G. Schettini, "Low-permittivity EBG materials for antenna superstrates," Proc. of the IEEE Ant. and Prop. Society (AP-S 2015) International Symposium, 19-24 July 2015, Vancouver, Canada, pp.1106-1107.
- [5] C. Ponti, P. Baccarelli, S. Ceccuzzi, G. Schettini, "Tapered EBG Superstrates for high-gain EBG resonator antennas," Proc. XXI Riunione Nazionale di Elettromagnetismo (RiNEM 2016), Parma, 12-14 September 2016, pp. 103-106.
- [6] D. R. Jackson and A. A. Oliner, "Leaky-wave antennas", in Balanis, C.A. (ed.), *Modern Antenna Handbook*, Wiley, New York, NY, 2008, Ch. 7.
- [7] K. Yasumoto, *Electromagnetic Theory and Applications for Photonic Crystals*, Boca Raton, FL: CRC Press, 2005, Ch. 3.
- [8] A.R. Weily, L. Horvath, K.P. Esselle, B.C. Sanders, and W.S. Park, A planar resonator antenna based on a woodpile EBG material, *IEEE Trans Antennas Propag* 53 (2005), 216-223.
- [9] Y.J. Lee, J. Jeo, R. Mittra, and T.S. Bird, Application of electromagnetic bandgap (EBG) superstrates with controllable defects for a class of patch antennas as spatial angular filters, *IEEE Trans Antennas Propag.* 53 (2005), pp. 224-235.
- [10] P. Baccarelli, V. Jandieri, G. Valerio, and G. Schettini, "Efficient computation of the lattice sums for leaky waves using the Ewald method," *11-th European Conference on Antennas and Propagation*, Paris, France, 19-24 March, 2017, pp. 3222-3223.
- [11] D. Zhang and H. Jia, "Numerical analysis of leaky modes in two-dimensional photonic crystal waveguides using Fourier series expansion method with perfectly matched layer," *IEICE Trans. Electron.*, E90-C, pp. 613-622, 2007.

# PROPOSAL OF A MILLIMETER-WAVE ANTENNA ARRAY FOR CUBESATS

G. Buttazzoni<sup>(1)</sup>, F. Pelusi<sup>(1)</sup>, R. Vescovo<sup>(1)</sup>

<sup>(1)</sup> Department of Engineering and Architecture, University of Trieste  
Via A. Valerio 10, 34127 Trieste, Italy  
[gbuttazzoni@units.it](mailto:gbuttazzoni@units.it)

## Abstract

*This paper describes the preliminary phase of design of a microstrip antenna array composed by subarrays, intended to be mounted on a CubeSat operating in the millimeter-wave frequency range. A three-step procedure is described, consisting in the development of the single-element, of the subarray and of the complete array. Different configurations of the subarray and of the complete array are investigated and mutually compared.*

**Index Terms** – Antenna arrays, CubeSats, Millimeter-wave communications, Circular polarization.

## I. INTRODUCTION

CubeSats belong to a particular class of small satellites. Introduced in the late Nineties with educational and scientific purposes, their field of application has rapidly been extended to the industrial, commercial and military contexts. So, in order to guarantee the new variety of services, CubeSat structures have become more complex. For example, a telecommunication satellite is required to support high data-rates, which cannot be achieved at the amateur radio frequencies commonly used by the early CubeSat antennas. Thus, in recent years, in order to increase the transmission capacity of such category of satellites, a shift to higher frequencies has been introduced. The antenna proposed in this paper operates at 37 GHz, in the Ka-frequency band. As is well-known, at higher frequencies the free space path loss is higher and the propagation in the ionosphere is much more critical. Thus, the use of high gain circularly polarized (CP) antennas is mandatory. The literature offers some proposals of CubeSat antennas operating in the Ka-frequency band [1], [2]. In this context, however, attention has never been focused on direct radiating antenna arrays of microstrip patches. An advantage of such structures is their planar nature, which fits on a CubeSat face and does not require any deployment system, which would further complicate the structure of the satellite. Moreover, they are cheap and can be easily manufactured and easily integrated with other electronic equipments.

The paper is organized as follows. In the next section the adopted design procedure is described in detail. Then, Section III presents two candidate subarray configurations and in Section IV three different

geometries are proposed for the array, and are mutually compared. The conclusions are summarized in Section V.

## II. THREE-STEP DESIGN PROCEDURE

In this paper, the design of a CP antenna array of microstrip patches is accomplished through a three-step procedure, which has been well validated in the previous literature [3]. Precisely, first the single element is designed, as a square patch with truncated corner. The dimensions of the square edge and of the truncation are evaluated according to [4] and then optimized with the electromagnetic software CST [5]. As a second step, in order to improve the final performance in terms of axial ratio and operational bandwidth, the sequential rotation technique is then adopted to suitably arrange four radiators in a subarray configuration [6]. The third step consists in the development of the final array. This technique can lead to different geometrical configurations for the subarray, and consequently to different final arrays. In the next section two candidate subarrays are presented.

## III. SUBARRAY DEVELOPMENT

The sequential rotation technique has been applied by grouping four radiators in a subarray. Each radiator is obtained by rotating the previous one of  $90^\circ$ , and a  $90^\circ$  phase change has been sequentially applied to the four radiators. Two candidate configurations are shown in Fig. 1. In the subarray of Fig. 1(a) the four radiators are placed in correspondence of the vertices of a square of edge 7.2 mm (however, other dimensions have also been simulated). In the subarray of Fig. 1(b) the radiators are arranged in correspondence of the middle points of the 8.8 mm edges of a square (however, other dimensions have also been simulated). The two structures give similar performances (gain of 11.33 dB and 11.53 dB, respectively, with axial ratio lower than 5 dB in the main beam region, and an RHCP/LHCP isolation greater than 15 dB), but can be arranged in different ways in the final array.

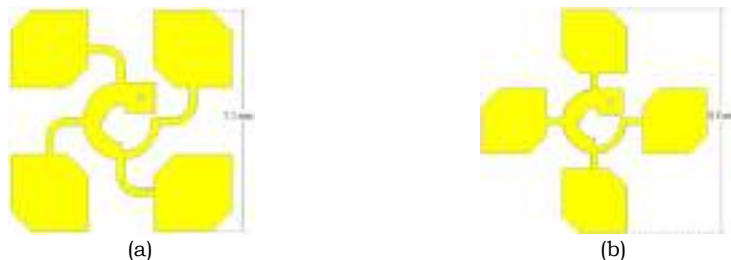


**FIG. 1** – Two different candidate configurations for the subarray.

#### IV. ARRAY GEOMETRY DEVELOPMENT

The proposed antenna array is required to occupy one face of a CubeSat, thus the net available surface is a square of side 85 mm. Nevertheless, a number of geometries may be obtained with the two above described subarrays. In this paper, attention has been focused on the three configurations shown in Fig. 2. It is to be noted that, in this preliminary design, the mutual coupling effects between the subarrays have not been considered, and the array far-field pattern is obtained by multiplying the element factor (i.e., the pattern of the subarray) by the array factor. For reasons of space, only the main results are summarized in Table I. The pattern cuts on the principal planes ( $\phi = 0^\circ - 180^\circ, 45^\circ - 225^\circ, 90^\circ - 270^\circ, 135^\circ - 315^\circ$ ) are shown in Fig. 3.

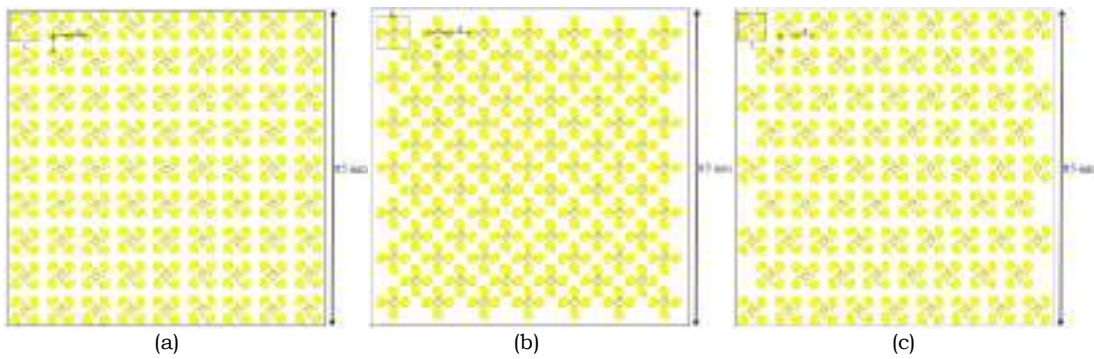


**FIG. 2** – The three analyzed array geometries.

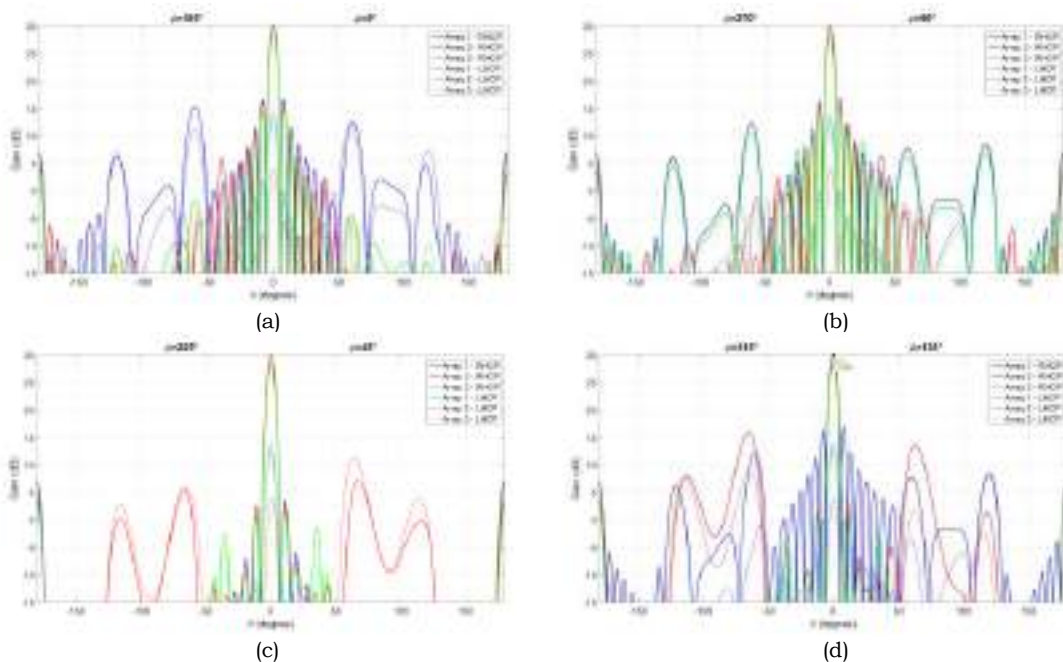


**FIG. 3** – Radiation pattern cuts on the principal planes for the three array geometries of Fig. 2 (Array 1 corresponds to that of Fig. 2(a), Array 2 corresponds to that of Fig. 2(b), Array 3 corresponds to that of Fig. 2(c)). (a)  $\phi = 0^\circ - 180^\circ$ , (b)  $\phi = 90^\circ - 270^\circ$ , (c)  $\phi = 45^\circ - 225^\circ$ , (d)  $\phi = 135^\circ - 315^\circ$ .

**TABLE I – COMPARISON OF THE THREE ARRAY GEOMETRIES**

	Array of Fig. 2(a)	Array of Fig. 2(b)	Array of Fig. 2(c)
Number of subarrays	81	85	77
Gain [dB]	30.0	29.9	28.5
Maximum SLL [dB]	-13.2	-13.4	-13.7
RHCP/LHCP isolation [dB]	17	24	17

## V. CONCLUSION

In this paper a proposal of a high-gain CP microstrip antenna array of subarrays has been presented, with each subarray constructed by adopting the sequential rotation technique. The array is suited for a face of a CubeSat and operates in the Ka-frequency band. The design procedure has been described and two different subarray configurations have been selected and analyzed. Finally, the performance of three different array geometries have been compared in terms of gain, maximum sidelobe level and polarization purity. In the next step of the design, the mutual coupling effects will be analyzed and the feeding network will be designed, possibly including phase variations for the subarray element excitations and/or pattern reconfiguration capability.

## REFERENCES

- [1] J.F. Sauder, N. Chahat, R. Hodges, E. Peral, Y. Rahmat-Samii, M. Thomson, "Designing, building, and testing a mesh Ka-band parabolic deployable antenna (KaPDA) for CubeSat", *54th AIAA Aerospace Sciences Meeting*, Jan. 4-8 2016, San Diego, CAL, USA.
- [2] R.E. Hodges, D.J. Hoppe, M.J. Radway, N.E. Chahat, "Novel deployable reflectarray antennas for CubeSat communications", *IEEE MTT-S International Microwave Symposium*, May 17-22 2015, Phoenix, AZ, USA, pp. 1-4.
- [3] J. Huang, "A Ka-band circularly polarized high-gain microstrip array antenna," *IEEE Transactions on Antennas and Propagation*, vol. 43(1), pp. 113-116, Jan 1995.
- [4] G. Buttazzoni, M. Comisso, A. Cuttin, M. Fragiaco, R. Vescovo, R. Vincenti Gatti, "Reconfigurable phased antenna array for extending cubesat operations to Ka-band: Design and feasibility," *Acta Astronautica*, vol. 137, pp. 114-121, Jan 2017.
- [5] CST, <https://www.cst.com/>
- [6] P. S. Hall, J. Huang, E. Rammos and A. Roederer, "Gain of circularly polarised arrays composed of linearly polarised elements," *Electronics Letters*, vol. 25(2), pp. 124-125, Jan 1989.

# A COMPACT SERIES ARRAY FOR SHORT RANGE COMMUNICATION

S. Maddio, G. Pelosi, M. Righini, S. Selleri

Department of Information Engineering, University of Florence  
Via di S. Marta, 50139 Florence, Italy  
(stefano.maddio, giuseppe.pelosi, monica.righini, stefano.selleri)@unifi.it

## Abstract

*We present a linearly polarized series-array antenna, suitable for dedicated short range communications, optimized for operation in C-band. The array is printed on a commercial substrate, and it is optimized for compactness. Experimental validations confirm a maximum gain of 8 dB at 5.8 GHz and 5 dB at 5.9 GHz, enabling both Electronic Toll Collection and low-latency WiFi operation for vehicular communications, i.e. the novel 802.11p standard.*

**Index Terms** – series-array antenna, linear polarization, dedicated short range communications.

## I. INTRODUCTION

Many world standard organizations have assigned part of the C-band to vehicular Dedicated Short Range Communications (DSRC), both for safety services and for commercial service, such as Electronic Toll Collection (ETC).

In this contribute we propose an antenna array suitable for operation at 5.8 GHz and 5.9 GHz, optimized for efficient DSRC according to the ETSI-EN 300674 European standard [1]. In this context, both compactness and price considerations are of paramount importance.

Series array configuration is the best choice, since it offers the advantage to minimize the feed line lengths, thus reducing both losses and spurious radiation, hence increasing array efficiency, avoiding the need of a complex feeding network. Furthermore, this configuration permits a single-layer via-less implementation, with obvious repercussions on the easiness of fabrication.

The only drawback for this class of antenna arrays is the difficulty to synthesize a perfect broadside condition. Indeed this is not a problem for the application in exam, since the beam pointing accuracy in the base stations for ETC applications, typically arranged within a Road-Side-Unit, is not a critical issue.

In view of these consideration, this paper proposes the design of a linearly polarized three element series-fed array, working at 5.8 GHz and 5.9 GHz, with reduced dimension.

This paper is organized as follows: Section II shows the architecture of the designed structure while in Section III the comparison between simulated and measurements result are presented.

## II. ARRAY ARCHITECTURE

The designed antenna is a series array based on three rectangular patches printed on a single layer of FR408 dielectric substrate.

Patches were initially considered identical and designed according to the classical patch design rules. The transmission lines connecting each patch with the next one are implemented as tapered lines, to achieve the maximum level of versatility.

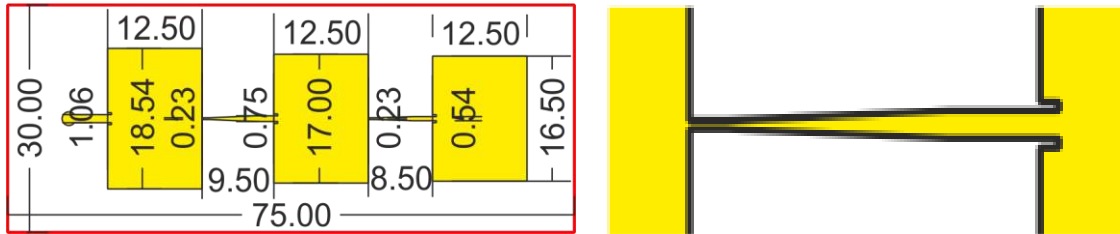


**Fig. 1** – Top view of the proposed series array and a detail of the tapered line

To synthesize the best broadside condition, each element must be in phase, with an adequate amplitude tapering among the patches. The problem of the exact feeding is quite complex for a series-fed array. Here, by exploiting the degree of freedom given by the tapered lines, the inset feeding, the patches dimensions and mutual distances as optimization parameters and frequency band, broadside gain and compactness as optimization goal within an automatic multi-objective optimization procedure [2], the layout given in Fig. 1 is obtained, corresponding to the realized prototype in Fig. 2. The prototype is fabricated by a standard low-cost photo-etching procedure on a commercial FR408 substrate (thickness = 1.6mm,  $\epsilon_r=3.75$ ,  $\tan \delta=0.01$ ).

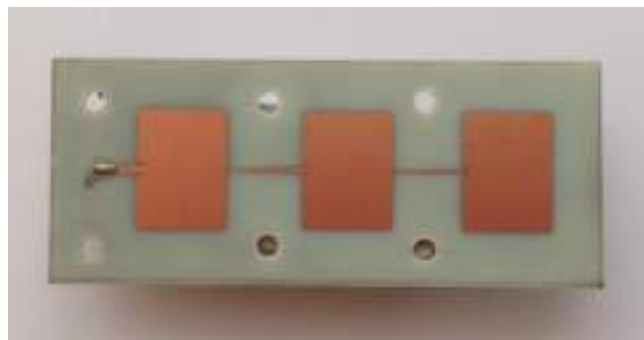


**Fig. 2** –Photograph of the prototype of the designed antenna.

### III. EXPERIMENTAL VALIDATION

The measurements are taken with a Keysight 5242A Keysight Vector Network Analyzer, inside an anechoic chamber. The measured reflection coefficient of the antenna is depicted in Fig. 4. A Return loss exceeding 15 dB is observed at the frequency of 5.8 GHz.

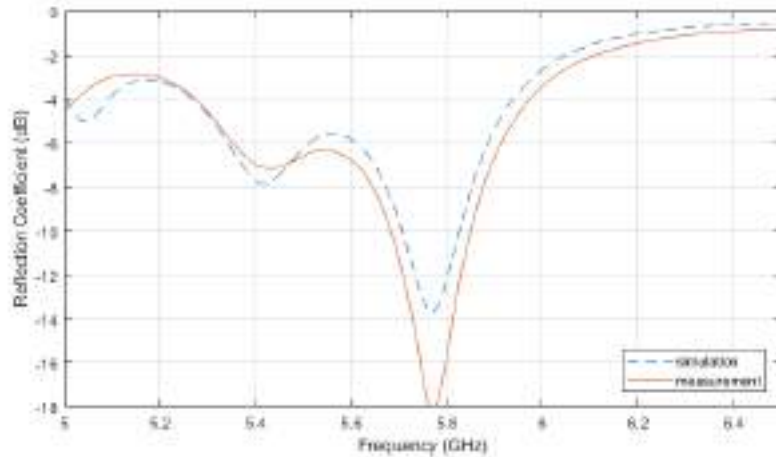


**Fig. 3** – Comparison between the simulated (blue lines) and measured (red lines) reflection coefficient of the proposed antenna.

Fig. 5 shows the Gain pattern of the proposed antenna both at 5.8 GHz and at 5.9 GHz. The measurements match very well with the simulations. A maximum gain of 8.5 dB is observed with a squint of 3 degrees respect to the nominal boresight direction, which is not a problem for the application of this antenna. The HPBW are about 90° on the H plane and 40° on the E plane, suitable to cover the area of single car lane, as prescribed by the standard.

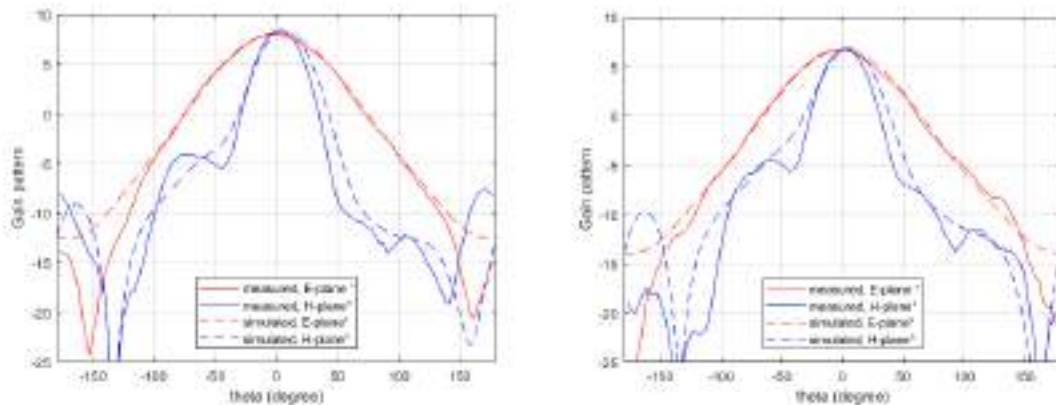


**Fig. 5** – Comparison between the simulated and measured gain pattern of the proposed antenna. Left: comparison at 5.8 GHz, Right: comparison at 5.9 GHz

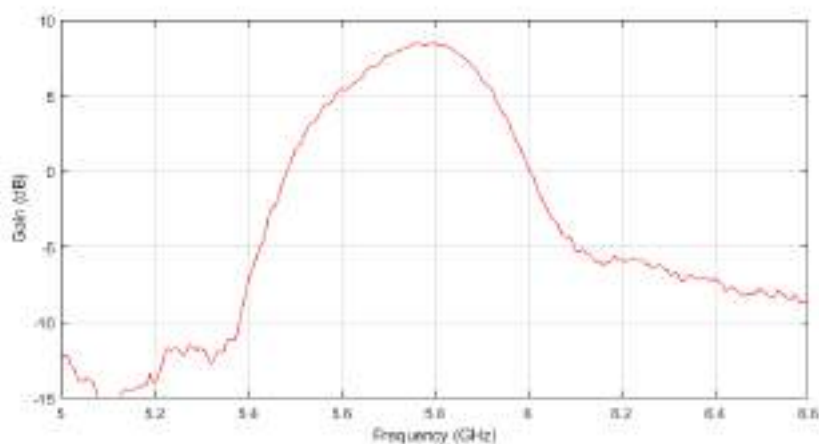


**Fig. 6** – Maximum Gain versus frequency for the proposed antenna

Finally, Fig. 6 shows the maximum gain of the proposed antenna as a function of the frequency within the C-band. The smooth behavior around the center frequency confirms that the device is suitable also for operation at 5.9 GHz, which is allocated for the 802.11p vehicular-to-vehicular (v2v) WiFi standard.

#### **IV. CONCLUSION**

A compact linearly polarized series-fed array antenna array is proposed. The array is realized as a single-layer via-less board, composed of three rectangular patch antennas fed with sections of tapered transmission lines. The device has been optimized for operation at 5.8 GHz. Thanks to the degrees of freedom, the optimal condition of 8.5 dB of gain within the dimensions of 30 mm x 75 mm have been achieved. In addition, the proposed device is suitable for operation at 5.9 GHz, for v2v, and even for normal WiFi operation at 5.6 GHz

#### **REFERENCES**

- [1] European Standard for Electromagnetic Compatibility and Radio Spectrum Matters: 'EN300674-1 V1.2.1, Electromagnetic compatibility and Radio spectrum Matters (ERM); Road Transport and Traffic Telematics (RTTT); Dedicated Short Range Communication (DSRC) transmission equipment (500 kbits/250 kbits) operating in the 5.8 GHz Industrial, Scientific and Medical (ISM) band', 2012.
- [2] G. Pelosi, S. Selleri, R. Taddei, "A Novel Multiobjective Taguchi's Optimization Technique for Multibeam Array Synthesis," *Microwave and Optical Technology Letters*, Vol. 55, N. 8, 2013, pp. 1836-1840;

# ESTIMATION OF THE ANTENNA PHASE CENTER POSITION IN ANECHOIC CHAMBER

C. Esposito<sup>(1)</sup>, A. Gifuni<sup>(2)</sup> and S. Perna<sup>(2),(1)</sup>

<sup>(1)</sup> Institute for Electromagnetic Sensing of the Environment (IREA) of Consiglio Nazionale delle Ricerche (CNR), Napoli, Italy;

e-mail: esposito.c@irea.cnr.it

<sup>(2)</sup> Dipartimento di Ingegneria (DI), Università degli Studi di Napoli “Parthenope”, Napoli, Italy;

e-mail: {gifuni, perna}@uniparthenope.it

## Abstract

*An algorithm for the calculation of the position of the antenna phase center is presented. It exploits field measurements carried out in anechoic chamber, and overcomes the main limitation of the two-point approach available in the literature. In particular, the proposed procedure is capable of accounting for the possible presence of an undesired and unknown misalignment between the geometric axis of symmetry of the Antenna Under Test (AUT) and the rotation axis of the turntable where the AUT is placed within the chamber.*

*The algorithm has been tested in the anechoic chamber of the Dipartimento di Ingegneria of the Università degli Studi di Napoli “Parthenope” on a radar antenna operating at X-band.*

**Index Terms** – Antenna Phase Center, Anechoic Chamber.

## I. INTRODUCTION

The antenna Phase Center (PhC) position [1]-[2] is a key information in many fields, such as air and naval traffic control, biomedical sensing and remote sensing of the environment. In literature, several methods have been proposed to calculate the antenna PhC position. They can be essentially divided into two classes: the first class includes the methods based on analytical models capable of describing the antenna radiating properties [2]-[9], whereas the second one includes the procedures that exploit measurement data [2], [10], [11]. In this work, we propose a procedure belonging to the latter class. In particular, the presented algorithm exploits amplitude and phase measurements of the electromagnetic field received by the Antenna Under Test (AUT) within an Anechoic Chamber (AC), and extends a method available in the literature, known as Two-Point Approach (TPA), [2].

More specifically, similarly to the TPA, also in our case the AUT is placed over a turntable mounted in the AC and receives the field radiated by a transmitting antenna located in a fixed position of the chamber. However, differently from the TPA, our method is effective even in the presence, quite usual in realistic measurement scenarios [15], of an undesired (and unknown) misalignment between the axis of symmetry of the AUT and the turntable’s rotation axis.

The effectiveness of the developed algorithm has been tested on an X-band radar antenna.

## II. RATIONALE OF THE DEVELOPED APPROACH

The measurement setup for the calculation of the antenna PhC position in AC is sketched in Fig. 1. In the figure, a polar reference system with origin  $O$  located on the turntable's rotation axis is considered. The AUT, which operates in receiving mode, is placed over the turntable, whereas the transmitting antenna (TXA) is fixed. In the figure, the PhCs of the TXA and AUT are highlighted in blue and red, respectively. Note that while the TXA transmits, the turntable rotates around its vertical axis. Accordingly, during the rotation of the turntable, the generic angular coordinate, say  $\vartheta_k$ , of the AUT PhC changes, and in turn the distance  $R(\vartheta_k)$ , briefly  $R_k$ , between the PhCs of the AUT and the TXA changes as well, see again Fig.1. The terms  $a$  and  $b$  in the figure represent the unknown longitudinal and transverse misalignments, respectively, between the origin  $O$  and the AUT PhC when the AUT observes the TXA at the boresight. As a matter of fact, in the literature it is assumed  $b$  known and equal to zero, and only the quantity  $a$  needs to be estimated in order to calculate the antenna PhC position [2]. However, in realistic measurement scenarios, a misalignment between the rotation axis of the turntable and the geometric axis of symmetry of the AUT can be accidentally introduced when manually placing the AUT over the turntable. This means that the quantity  $b$  is typically different from zero and, more important, it is unknown. For this reason, in our approach, the problem of finding the antenna PhC position is formulated as the estimation of two unknowns, namely  $a$  and  $b$ , and not just one as in [2]. To this aim, as shown in [15], we have derived a linear model that relates the unknowns  $a$  and  $b$  to the following phase difference:

$$\varphi(\vartheta_k) - \varphi(\vartheta_0) = \frac{2\pi}{\lambda} [R(\vartheta_k) - R(\vartheta_0)] \quad (1)$$

where  $\varphi$  is the phase of the electromagnetic field received by the AUT within its main beam,  $\vartheta_k$  and  $R(\cdot)$  have been defined above, and  $\vartheta_0$  is the angle where the amplitude pattern received by the AUT is maximum. Starting from the phase difference in (1) it is thus possible to find the desired unknowns through a linear inversion. In particular, the proposed algorithm provides the best estimate in the least-square error sense of the term  $a$  in the presence of the unknown transverse misalignment  $b$ . Further details on the proposed procedure can be found in [15].

## III. EXPERIMENTAL RESULTS

In this Section we assess the effectiveness of the developed algorithm. In particular, we report the results obtained on the antenna (serial number MAA-935985-V) of a radar system operating at X-Band [16]. The experiments have been carried out in the AC of the

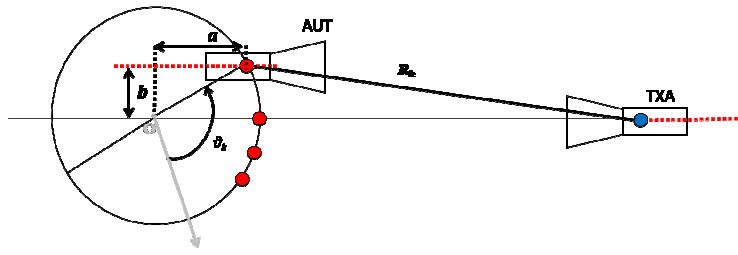


**Figure 1.** Measurements setup for calculating the phase center in anechoic chamber.

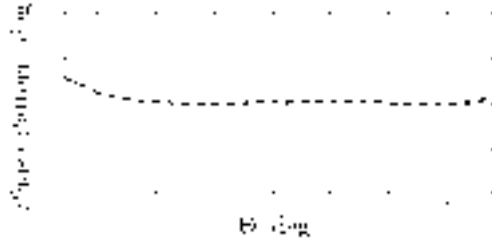


**Figure 2.** Phase pattern of the AUT within the main beam around the estimated PhC.

Dipartimento di Ingegneria of the Università degli Studi di Napoli “Parthenope”. The TXA is a standard rectangular aperture pyramidal horn antenna [13]. The measurement setup includes also a Vector Network Analyzer (VNA), model Agilent E8362B [14], a turntable and concerning controller, models Newport RV240PP and Newport MM40006, respectively, a radiofrequency (RF) rotary joint, model Sage 344AF, RF cables, X- band waveguides, adapters, and connectors to properly realize the necessary RF connections. Measurements were acquired in free run. The turntable was continuously run while the concerning controller generated trigger pulses each 0.2 degrees, which were sent to the VNA to trigger measurements.

The measurements were performed in the H-plane at 9.55 GHz. By applying the proposed method, we have obtained  $\hat{a}=7.8$  cm and  $\hat{b}=0.1$  cm, where the symbol  $\hat{\phantom{x}}$  stands for estimate. Then, in order to appreciate the accuracy of the achieved results, we have measured the phase pattern by rotating the AUT around the estimated PhC position. By doing so, we have achieved in the main beam the phase pattern shown in Fig. 2. As can be seen, it is almost constant (its standard deviation is about 0.06 deg), in agreement with the definition of antenna phase center [1]. Finally, to compare the performances of our procedure and that available in the literature, we have verified (the results can be found in [15]) that under the conditions considered in the experiment above (that is, the misalignment  $b$  on the order of 1 mm) the TPA in [2] becomes ineffective.

#### IV. CONCLUSION

An algorithm for calculating the position of the antenna PhC in an anechoic chamber has been proposed. Differently from the methods

available in the literature, the approach is effective even in the presence, quite common in realistic measurement scenarios, of an unknown transverse misalignment between the rotation axis of the turntable of the chamber and the geometric axis of symmetry of the AUT. The algorithm has been tested on a X-band radar antenna. The obtained results show the effectiveness of the proposed procedure. In particular, by rotating the AUT around the estimated phase center position, we have obtained an almost flat phase pattern, in agreement with the definition of antenna phase center.

## REFERENCES

- [1] IEEE Standard Definitions of Terms for Antennas," in IEEE Std 145-1983, 1-31, June 22 1983.
- [2] M.Teichman, "Determination of Horn Antenna Phase Centers by Edge Diffraction Theory," IEEE Trans. Aerosp. Electron. Syst., 9, 6, 875-882, 1973.
- [3] K.Baur, "The phase center of aperture radiators," Arch. Elekt. Ubertragung, 9, 541-546, 1955.
- [4] D.Carter, "Phase centers of microwave antennas," IRE Trans. Antennas Propag., AP-4, 597-600, 1956.
- [5] S.Sander and D.Cheng, "Phase center of helical beam antennas," 1958 IRE International Convention Record, New York, NY, USA, 1958, pp. 152-157.
- [6] E.R.Nagelberg, "Fresnel Region Phase Centers of Circular Aperture Antennas," IEEE Trans. Antennas Propag., 13, 3, 479-480, 1965.
- [7] H.Ujiie, T.Yoneyama, S.Nishida, "A Consideration of the Phase Center of Aperture Antennas," IEEE Trans. Antennas Propag., 15, 3, 478-480, 1967.
- [8] E.I.Muehldorf, "The phase center of horn antennas," IEEE Trans. Antennas Propag., AP-18, 753-760, 1970
- [9] D.Waidelich, "The phase centers of aperture antennas", IEEE Trans. Antennas Propag., 28 , 2, 263-264, 1980.
- [10] P.N.Betjes, "An Algorithm For Automated Phase Center Determination And Its Implementation", 29th Annual Symposium of the Antenna Measurement Techniques Association, 2007.
- [11] S.Perna, C.Esposito, A.Pauciullo and A.Gifuni, "An algorithm for the antenna phase center calculation," 2017 International Conference on Electromagnetics in Advanced Applications (ICEAA), 1433-1435, 2017.
- [12] S.M.Kay, Fundamentals of Statistical Signal Processing – Estimation Theory, Prentice Hall International Editions, 1993.
- [13]<http://datasheets.globalspec.com/ds/2851/NardaMicrowaveEast/BB1A0388-DEBB-4269-B6BA-4EA72AD4F5B9>.
- [14] Agilent Technologies, "PNA microwave network analyzer datasheet," 5988-7988EN, Printed in USA, August 3, 2006.
- [15] C. Esposito, A. Gifuni, S. Perna, "Measurement of the Antenna Phase Center Position in Anechoic Chamber", submitted to the IEEE Antennas and Wireless Propagation Letters.
- [16] C.Esposito, A.Natale, P.Berardino, G.Palmese, R. Lanari, S.Perna, "AXIS: An Airborne X-Band Interferometric FMCW SAR System", accepted for inclusion in the IGARSS 2018 program.

# SPATIAL DISPERSION OF METASURFACES FOR LEAKY-WAVE ANTENNAS IN THE TERAHERTZ RANGE

S. Tofani<sup>(1)</sup>, W. Fuscaldo<sup>(1)</sup>, D. C. Zografopoulos<sup>(2)</sup>, P. Baccarelli<sup>(3)</sup>,  
P. Burghignoli<sup>(1)</sup>, R. Beccherelli<sup>(2)</sup>, and A. Galli<sup>(1)</sup>

<sup>(1)</sup> Department of Information Engineering, Electronics and  
Telecommunications (DIET), “Sapienza” University of Rome,  
Via Eudossiana 18, 00184, Rome, Italy

[silvia.tofani@uniroma1.it](mailto:silvia.tofani@uniroma1.it)

<sup>(2)</sup> Institute for Microelectronics and Microsystems (CNR-IMM),  
National Research Council, 00133, Rome, Italy

<sup>(3)</sup> Department of Engineering, “Roma Tre” University,  
00146 Rome, Italy

## Abstract

*In this work, three metasurfaces with a patch-like, a strip-like, and a fishnet-like unit cell are compared in terms of their surface impedance for different angles of incidence in the terahertz range. The fishnet-like metasurface shows a TE-TM polarization independent behavior and a spatially nondispersive response, thus offering very interesting possibilities for the design of efficient Fabry-Perot cavity leaky-wave antennas at terahertz frequencies.*

**Index Terms** – Leaky-wave antennas, leaky waves, Fabry-Perot cavity antennas, terahertz, metasurfaces, frequency selective surfaces.

## I. INTRODUCTION

Different kinds of antennas have recently been proposed for working in the terahertz (THz) spectrum, but the improvement of their radiating performance usually requires either structure complexity or high fabrication costs [1].

Fabry-Perot cavity leaky-wave antennas (FPC-LWAs) [2] have been employed from the microwave to the visible range, but, in the THz band, valid configurations are still lacking. FPC-LWAs allow for achieving high radiating properties at a low cost and with reduced complexity of fabrication. A possible simple arrangement of a FPC-LWA is constituted by a grounded dielectric slab covered by a metallic patterned metasurface, which acts as a partially reflecting sheet (PRS) able to improve the directional features of the beam [3].

The aim of this work is to show how the combination of two conventional metasurface topologies, namely the patch array and the strip grid, into the fishnet metasurface (see Fig. 1), may lead to properties inaccessible by simply employing one of the first two configurations.

## II. MODEL DESCRIPTION

The PRSs are characterized by a periodic arrangement of subresonant elements, with a period  $p \ll \lambda_0$ , where  $\lambda_0$  is the wavelength in the vacuum. Under this condition, a PRS can be described with a single homogenized impedance. In the typical homogenization limit (i.e., when  $p < \lambda_0/4$ ), the dependence of the surface impedance both on the frequency (temporal dispersion) and on the angle of incidence (spatial dispersion) has to be taken into account for an accurate modeling of the PRS.

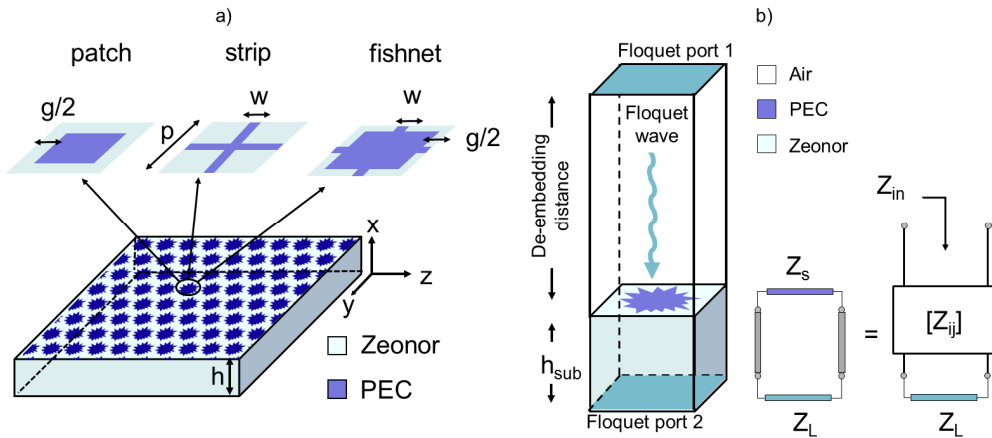


**FIG. 1** – a) Three different geometries for the unit cell of a homogenized metasurface are reported with their relevant geometrical parameters; b) the transmission-line model employed for extracting the surface impedance of a fishnet-like PRS element.

The unit-cell geometry is presented in Fig. 1a. The width of the strips (which corresponds to the width of the arms in the fishnet topology) is fixed in the examples as  $w = p/10$ , and the spacing between the patches  $g$  (which corresponds to the length of the arms in the fishnet topology) has been chosen equal to  $w$  as well. For the substrate, a cyclo-olefin ( $\epsilon_r = 2.3$  and  $\tan \delta = 0.001$  at 1 THz [4]) is selected as a suitable dielectric material due to its low THz losses. The metal is treated, at a first approximation, as a perfect electric conductor (the use of more realistic models will be discussed at the conference). For this reason, no ohmic losses are expected and the PRSs can be described by purely imaginary impedances  $Z_s = jX_s$ .

As is known [5], the grid impedance of *i*) patches for a transverse-electric (TE) polarization and *ii*) strips for a transverse-magnetic (TM) polarization exhibits a spatially dispersive character because the surface impedance depends on the angle of incidence  $\theta$ . For the estimation of the surface impedance of the fishnet PRS, a fishnet-like unit cell has been simulated with a CAD tool (HFSS). The model for extracting the surface impedance of a periodic fishnet element is

described in Fig. 1b, where  $Z_L$  represents the characteristic impedance of the Floquet port.

A Floquet wave impinges at different angles of incidence on the PRS and the impedance matrix is obtained at the PRS level by setting a proper de-embedding distance. An equivalent transmission-line circuit model has been exploited to retrieve the value of the scalar surface impedance value (no TE-TM cross-coupling is expected for the considered geometries [3]) from the impedance matrix parameters. The same analysis has also been performed for both the patch array and the strip grid. However, HFSS simulations are in very good agreement with the homogenization formulas [5], thus only the latter results will be shown. All the surface impedances are estimated in the frequency range between 0.5 and 1.5 THz for angles of incidence varying from  $\theta = 0^\circ$  and  $\theta = 80^\circ$  with an angular step of  $10^\circ$ .

### III. SPATIAL DISPERSION ANALYSIS

The surface reactances for the three different metasurface patterns are presented in Fig. 2.

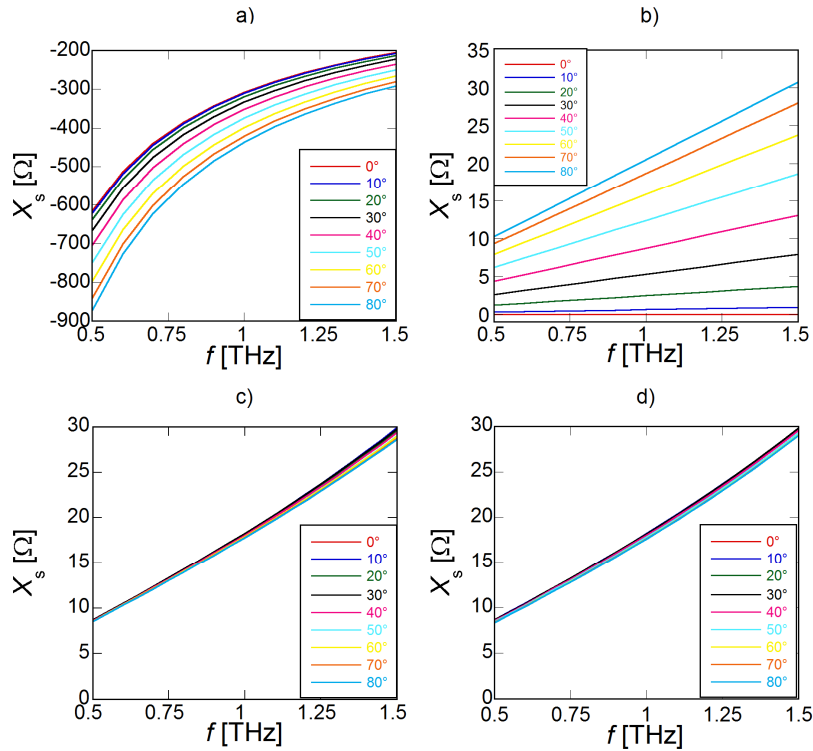


**FIG. 2** – Surface reactance  $X_s$  vs. frequency in the range  $0.5 < f < 1.5$  [THz]: a) patch PRS for TE polarization; b) strip PRS for TM polarization; c) fishnet-like unit-cell for TE polarization; d) fishnet-like unit-cell for TM polarization.

As predicted by the relevant homogenization formulas [5], the surface reactances of the patch array (Fig. 2a) and of the strip grid (Fig. 2b) show a non-negligible spatial dispersion.

Conversely, HFSS simulations confirm that the surface reactance of the fishnet-like metasurface is essentially spatially nondispersive for both TE (Fig. 2c) and TM (Fig. 2d) polarizations. Interestingly, this property is satisfied by all the fishnet-like unit cells within the homogenization limit, regardless of the values of their geometrical parameters (further validations performed by means of HFSS simulations are not shown here for brevity). In addition to this, it is noted that the TE and TM impedances of the fishnet attain almost the same values, thus resulting independent of the polarization of the field. This is an extremely attractive property that allows for having FPC-LWAs with equalized patterns over the principal planes.

The spatially nondispersive behavior of such printed metasurfaces represents a very interesting feature for the development of advanced THz FPC-LWAs, as recently shown in [3]. There, the promising features of a fishnet-like unit-cell have been profitably employed for designing different layouts of FPC-LWAs with either a remarkable directivity at broadside (i.e.,  $\theta = 0^\circ$ ) and narrow fractional bandwidth or vice-versa.

#### IV. CONCLUSION

The surface impedance of three different metasurface geometries has been investigated for different angles of incidence at terahertz frequencies. The comparison between the unit-cell geometries showed that the patch array and the strip grid have a high spatially dispersive behavior. On the other side, the fishnet metasurface, i.e. the superposition of a patch and a strip geometry, is essentially spatially nondispersive for both TE and TM polarizations, thus paving the way for the realization of promising Fabry-Perot cavity leaky-wave antennas in the THz range.

#### REFERENCES

- [1] G. Chattopadhyay, "Technology, capabilities, and performance of low power terahertz sources," *IEEE Trans. Terahertz Sci. Technol.*, vol. 1(1), pp. 33–53, 2011.
- [2] D. R. Jackson and A. A. Oliner, "Leaky-wave antennas," in *Modern Antenna Handbook*, C. A. Balanis, Ed. John Wiley & Sons, Inc., 2008, pp. 325–367.
- [3] W. Fuscaldo, S. Tofani, D. C. Zografopoulos, P. Baccarelli, P. Burghignoli, R. Beccherelli, and A. Galli, "Systematic design of thz leaky-wave antennas based on homogenized metasurfaces," *IEEE Trans. Antennas Propag.*, vol. 66(3), pp. 1169–1178, Mar. 2018.
- [4] D. C. Zografopoulos and R. Beccherelli, "Tunable terahertz fishnet metamaterials based on thin nematic liquid crystal layers for fast switching," *Sci. Rep.*, vol. 5, Aug. 2015.
- [5] O. Luukkonen et al., "Simple and accurate analytical model of planar grids and high-impedance surfaces comprising metal strips or patches," *IEEE Trans. Antennas Propag.*, vol. 56(6), pp. 1624–1632, Jun. 2008.

# THE QV-LIFT PROJECT: A GROUND SEGMENT FOR THE FUTURE Q/V BAND SATELLITE SYSTEMS.

G. Amendola<sup>(1)</sup>, L. Boccia<sup>(1)</sup>, F. Greco<sup>(1)</sup>, E. Arnieri<sup>(1)</sup>, C. Riva<sup>(2)</sup>, L. Luini<sup>(2)</sup>, R. Nebuloni<sup>(3)</sup>, G. Codispoti<sup>(4)</sup>, G. Parca<sup>(4)</sup>, G. Valente<sup>(4)</sup>, G. Goussetis<sup>(5)</sup>, S. Kosmopoulos<sup>(5)</sup>, M. Siegler<sup>(6)</sup>, R. Martin<sup>(7)</sup>, J. Moron<sup>(7)</sup>, R. Eleuteri<sup>(8)</sup>, M. Bergmann<sup>(8)</sup>, F. Massaro<sup>(9)</sup>, R. Campo<sup>(9)</sup>, F. Vitobello<sup>(10)</sup>

(1) CNIT-Università della Calabria (I), (2) CNIT- Politecnico di Milano(I),  
(3) IEIIT/CNR (I), (4) ASI – Agenzia Spaziale Italiana (I), (5) Heriot Watt  
University (UK), (4) ERZIA (S), (6) Ommic (F), (7) Skytech (I), (8) Eutelsat  
(F), (9) European Commission  
[g.amendola@dimes.unical.it](mailto:g.amendola@dimes.unical.it)

## Abstract

*This paper presents a summary of the design of the Q/V band Ground Segment currently under development in the framework of the project: “Q/V band earth segment Link for Future high Throughput space systems” (QV-LIFT - [www.qvlift.eu](http://www.qvlift.eu)), that has recently been funded in the framework of the EU program Horizon 2020. The project is focusing on the development of up to date hardware and software technologies for the Ground Segment of the future Q/V band terabit Satcom infrastructure. In the following, a description of the system and an account of the developments related to the RF systems are presented.*

**Index Terms** – Q/V band terabit Satcom infrastructure

## I. INTRODUCTION

The European Commission defined in its Digital Agenda that all European households shall have access to internet connections of more than 30 Mbps from 2020 onwards, so the volume of digital data communications are expected to double by 2020 [1]. This calls for a dramatic improvement in the satellite communication technologies as they are a fundamental part of the global communication infrastructure. In order to provide the necessary “Terabit connectivity”, an evolution to “beyond Ka-band frequencies” is necessary. In fact, the future High Throughput Satellite (HTS) systems will move up to Q and V bands (around 40 GHz for downlink and 50 GHz for uplink) since they offer larger bandwidth availability for the feeder links and the opportunity to dedicate the Ka-band to user links where revenues are generated. Moreover, Q/V-band offers attractive bandwidth for specific segments requiring high data rates such as aeronautical in-flight services. The QV-LIFT project started on November 16th 2016 and it will last for about three years developing hardware and software building blocks and integrating them in a Q/V band SatCom system. To do this, the project will integrate the Aldo Paraboni Q/V band payload host by Alphasat which will be used to set up both feeder and user links. In this paper a description of the QV-LIFT Ground Segment and an account of the developments related to the RF building blocks are presented.

## II. THE QV-LIFT GROUND SEGMENT

In Fig.1 is shown the overall QV-LIFT system. It is built around the Aldo Paraboni QV band payload on board of Alphasat, developed by the Italian Space Agency (ASI) and currently in operation. The QV-LIFT ground segment includes two already operational Earth Stations, owned and operated by ASI, Earth station 1, located in Tito Scalco (Italy), and Earth Station 3, located in Spino d'Adda (Italy). A further Q/V band ground station (Earth Station 2) and a Q/V band Aeronautical Terminal are also included in the system and are both currently in development. The Earth Station and the terminal will make use of a Block Up Converters based on a power combined GaN MMICs, and high efficiency antennas developed in the project. Also shown in Fig. 1, is the Gateway Management System (GMS) which takes in charge the network control functions needed to support smart handover of communications between multiple gateway nodes (smart gateway).

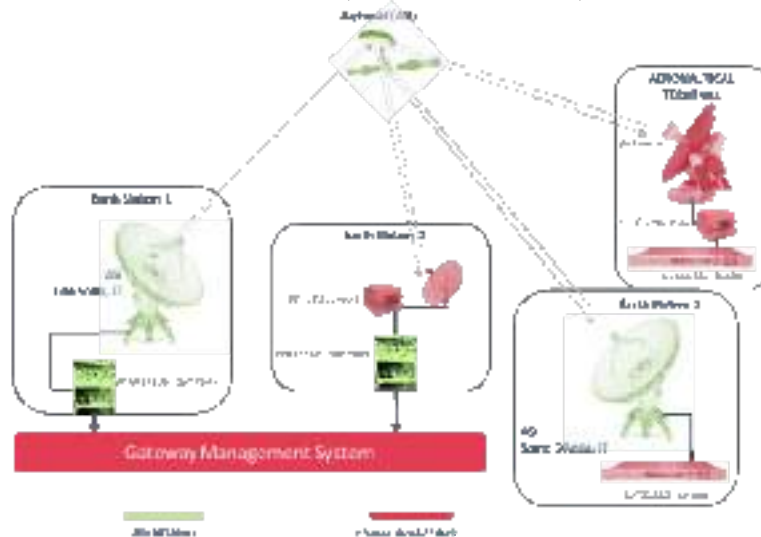


FIG. 1 – The QV-LIFT System

## III. QV-LIFT RF DEVELOPMENTS

The QV-LIFT Ground System includes existing and operational earth stations available with the Italian Space Agency (ASI) and newly built systems. For the new systems, the consortium is currently developing the following major building blocks: V band MMIC amplifier, V band power combining SSPA (Solid State Power Amplifier), V band BUC (Block Up Converter), Q band LNB (Low Noise Block down converter), Q/V band (RX/TX) antennas for mobile terminals, Q/V band (RX/TX) antenna for fixed station, Tracking and pointing systems for the mobile and fixed antennas. As it will be detailed in the following sections, due to the high performance required and to the high frequency of operation, up to date technologies are needed to realize the previous components. As an example, MMIC are based on the recently delivered OMMIC GaN technology and they are power combined in a metallic

waveguide divider/combiner to provide a high power SSPA. The LNB is based on a low noise GaAs LNA produced by OMMIC. The antenna for the mobile terminal is an Axially Displaced Gregorian reflector with a corrugated feed. This arrangement aims at an aperture efficiency larger than 70% which ensures good performance in both uplink and downlink. The fixed earth station is based on an Axially Displaced reflector with a 1.5m diameter. In the following the involved components will be described giving details of specifications and showing the intermediate results available.

#### a. **SSPA, BUC AND LNB**

The SSPA is based on a MMIC GaN amplifier currently in development. The MMIC is developed in GaN technology by OMMIC. The MMIC specs are: Bandwidth 47.2-50.2GHz; Output Power P2dB 37 dBm (5W); Output Power PSat 39dBm (8W); Gain>16dB; Gain Flatness +/- 1.5dB; PAE 20%.

The MMIC is realized with the Ommic D01GH – 100nm. Simulated results for Gain, Output Power, Power Added Efficiency are shown in fig. 2 for three compression levels (1dB, 2dB, 3dB).

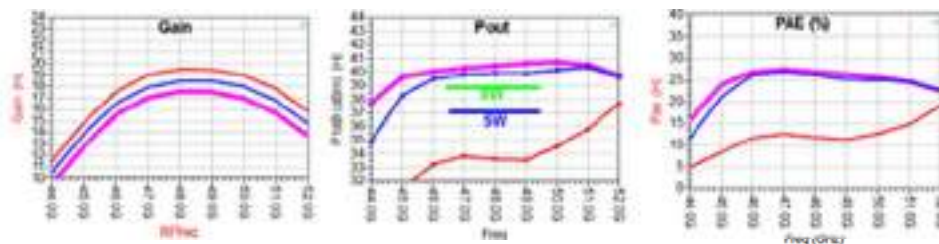


**FIG. 2** – Simulated Output Parameter of the V band GaN MMIC amplifier under development

4 MMICs will be power combined in waveguide to reach the power level needed by the BUC. The power dividing and combined structure is based on 4X1 (1X4) metallic waveguide T magic with low insertion loss. The power combining/dividing structure is designed to cover the bandwidth from 46.5GHz to 49.5GHz.

The BUC specifications are : Input frequency 1.5 GHz; Bandwidth 500 MHz; Output frequency 46.5 – 49.5 GHz; Output power 15 W (41.7 dBm); Gain 40 - 60 dB; S11, S22<-10 dB. The LNB specifications are : Input frequency 37.5 – 42.5 GHz; Bandwidth 500 MHz; Output frequency 1.25 – 1.75 GHz; Input power -130 dBm; Noise Figure <3.5 dB; Gain>50 dB; S11, S22<-10 dB.

The LNB is based on the CGY2122XUH/C2 LNA developed by OMMIC with NF=1.5dB. The LNB has a bandwidth from 37.5GHz to 42.5GHz and output Gain > 50 dB. The simulated Noise Figure is 3dB.

#### b. **ANTENNAS**

Link budget analysis [4] indicates the adoption of high efficiency antennas. In particular, considering a link margin larger than 2.5 dB,

one needs antennas with  $G/T > 14\text{dB/K}$  and  $\text{EIRP} > 56 \text{ dBW}$ . Considering antennas with diameters 45cm and 60 cm and the BUC and the LNB presented in the previous section, one finds that antenna needs to have 70% aperture efficiency. These performances may be reached with axially displaced reflectors which can maintain very good performance on a large frequency band.

In Fig. 3 are shown the radiation diagram of the 45 cm antenna at 37.5GHz (RX) and 48.5 GHz (TX). Also indicated is the maximum gain achieved which is 43.82 dB in RX and 45.5 dB in TX which correspond to an aperture efficiency close to 80%. The antenna is able to cover from 37GHz to 50 GHz with a good match. Similar results are achieved for the 60 cm antenna which shows 45.9 dB in RX and 47.7 dB in TX. The 1.5 m antenna is currently under development but preliminary results show an aperture efficiency of 60% which is already enough to close the link budget thanks to the large antenna size.

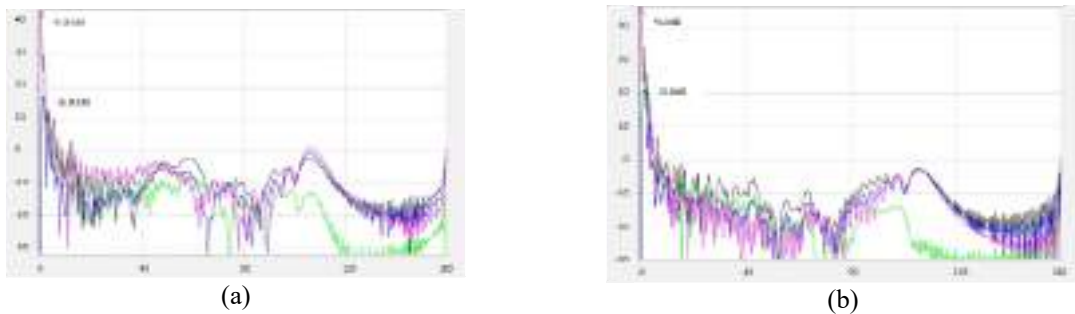


**Fig. 3.** Radiation diagram of the 45cm mobile terminal antenna at 37.5GHz (a) and 48GHz (b)

#### IV. CONCLUSION

The QV-LIFT project, funded by EU in the framework of the H2020 program, aims at realizing the software and hardware building blocks for the Ground Segment of the future Q/V band satellite links. In this paper we have presented a short description of the system under development and the characteristics of some of the RF blocks. A more detailed account of the system and the most recent results will be given in the course of the presentation.

#### REFERENCES

- [1] [www.qvlift.eu](http://www.qvlift.eu)
- [2] Communication from the Commission to the European Parliament, the Council, the European Economic and Social Committee and the Committee of the Regions, “Connectivity for a Competitive Digital Single Market – Towards a European Gigabit Society”, COM(2016) 587 final, Brussels, 14/09/2016.
- [3] F.Massarò et al. “QV-LIFT Project: Using the Q/V Band Aldo Paraboni Demonstration Payload for Validating Future Satellite Systems”, 23rd Ka and Broadband Communications Conference, Trieste, Italy, October 16 th-19th, 2017.
- [4] QV-LIFT project, D2.3 System Analysis and Requirements, Confidential, qv-lift\_d2.3\_v1.0.

## **INVERSE SCATTERING METHODOLOGIES AND APPLICATIONS @ ELEDIA RESEARCH CENTER**

N. Anselmi<sup>(1)</sup>, A. Gelmini<sup>(1)</sup>, G. Gottardi<sup>(1)</sup>, G. Oliveri<sup>(1)</sup>, L. Poli<sup>(1)</sup>, P. Rocca<sup>(1)</sup>, M. Salucci<sup>(1)</sup>, and A. Massa<sup>(1)(2)</sup>

<sup>(1)</sup> ELEDIA Research Center (ELEDIA@UniTN, University of Trento)  
via Sommarive 9, I-38123 Trento, Italy

<sup>(2)</sup> ELEDIA Research Center (ELEDIA@UC3M – Universidad Carlos III de Madrid) Avenida de la Univesidad 30, 28911 Madrid, Spain  
[andrea.massa@eledia.org](mailto:andrea.massa@eledia.org)

### **Abstract**

*A review of inverse scattering methodologies recently developed at the ELEDIA Research Center is presented. The paper describes advances and novelties introduced by such methods with respect to approaches at the state-of-the-art, mainly focusing on Compressive Sensing (CS), Learning-by-Examples (LBE) and multi-resolution (MR) strategies.*

**Index Terms**—Compressive Sensing, Ground Penetrating Radar Imaging, Evolutionary Optimization, Inverse Scattering, Microwave Imaging, Multi-Resolution Methods, Non-Destructive Testing/Non-Destructive Evaluation, Learning-by-Example Methods.

### **I. INTRODUCTION**

Inverse scattering methods are aimed at retrieving the physical features of an inaccessible region by inverting the scattered field measured through a set of probes after illuminating the area with low-power incident microwaves. Such methods are of interest for a wide range of applications, among which biomedical imaging, non-destructive testing and evaluation (NDE/NDT) and subsurface sensing, however the solution of the arising inverse problem generally requires coping with several issues, namely non-linearity, ill-posedness, ill-conditioning and high computational costs. In this framework, the ELEDIA Research Center has proposed in the past years several methodologies to efficiently cope with such challenges, with particular attention to a suitable exploitation of the *a-priori* information of the imaged scenario [1], [2]. Focusing on the last years, several advances have been proposed concerning CS [1]-[5] and LBE-based [6]-[10] techniques as well as deterministic [11]-[13] or stochastic [14] optimizations based on multi-scaling approaches [4], [11]-[14], for ground-penetrating radar (GPR) imaging [5], [11]-[14], NDE/NDT [7], [8] and biomedical applications [9], [10].

## II. INVERSE SCATTERING @ ELEDIA – METHODOLOGIES AND APPLICATIONS

Compressive Sensing-based techniques for inverse scattering have widely proven their effectiveness for retrieving the dielectric features of targets of different nature, ranging from weak scatterers to perfect electric conductors and considering different kinds of illuminations (i.e., transverse magnetic and transverse electric waves, multi-frequency approaches, etc.) [2]. However, the sparsity constraint which has to be satisfied on the problem unknowns with respect to a known expansion basis (e.g., pixel or Haar wavelet basis) implies the need of some *a-priori* information on the shape of the targets to be reconstructed [2]. The work presented in [3] relaxes such a requirement by proposing a hierarchical multi-level approach where at the first step multiple *sparsity-regularized* reconstructions are carried out considering a *dictionary* of basis functions and then a sparsity criterion is applied to determine the most reliable solution among the set of retrieved unknown vectors. Iterative schemes have been also proposed in order to increase the amount of information, besides the target sparsity, to be exploited during the reconstruction process [4], [5]. More in detail, innovative multi-resolution (MR) [4] and frequency hopping (FH) [5] approaches have been developed with the aim of progressively acquiring additional information throughout iterative procedures. A customized Relevance Vector Machine (RVM) has been used to find the solution at each iteration, constrained to encode the information on the zoomed region of interest detected at the previous iteration, in order to limit the search space.

Advanced multi-resolution/multi-scaling methods, that combine the iterative procedure with a multi-frequency approach for a suitable exploitation of the frequency diversity of the wide-band GPR measurements, have been also proposed in [11] and [14], based on deterministic (the conjugate gradient method) and stochastic (the particle swarm optimizer) techniques, respectively.

Innovative LBE approaches have been also investigated [6]-[10]. LBE methods have proven to be interesting approaches for enabling real-time accurate and robust inversion of data for several applications [6]. Such strategies involve an *off-line* training phase for generating a suitable database of known input-output pairs, based on which the predictions are made during the *on-line* phase when processing new measurements. Innovative LBE methodologies have been developed at the ELEDIA Research Center, using support vector regression (SVR) [7]-[8], [10] or support vector machine (SVM) [9] algorithms for making prediction in different applicative frameworks, such as the crack characterization in conductive structures [7], the retrieval of the characteristics of a defect in a nondestructive testing and evaluation framework [8] by exploiting eddy current testing (ECT) signal, the real-time detection of brain strokes [9] and human chest monitoring [10].

### III. NUMERICAL EXAMPLE

A selected numerical example is presented in this Section in order to assess the effectiveness of the iterative MR-CS method [4]. A lossless ‘E-shaped’ cylinder [shown in Fig. 1(a)] having contrast  $\tau = 0.1$  is placed within a square investigation domain of side  $L_D = 6.0\lambda$ ,  $\lambda$  being the wavelength corresponding to the frequency of the  $V = 60$  transverse magnetic plane-waves with incident angles  $\theta_\nu = 2\pi \times (\nu - 1)/V$ ,  $\nu = 1, \dots, V$ , illuminating the region. The synthetic scattered field data have been computed in  $M = 60$  points equally spaced on a circular investigation domain of radius  $\rho = 4.5\lambda$ . Figure 1(b) shows the reconstructed profile obtained at the step  $S = 4$  of the iterative multi-focusing strategy considering a signal-to-noise ratio on the scattered field of  $SNR = 10$  [dB]. The result shows that the position of the scatterer has been correctly identified and its dielectric permittivity has been accurately retrieved despite the non-negligible amount of noise affecting the scattered field data.

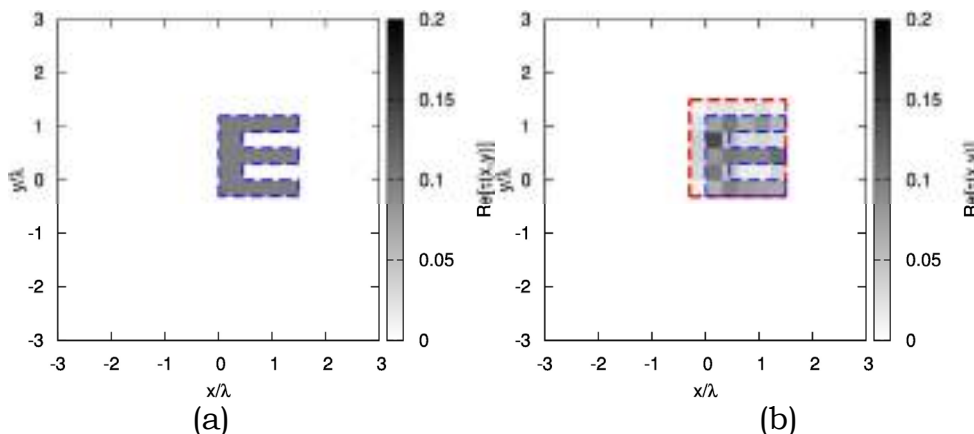


**FIG. 1** – [*E-shaped Scatterer*,  $\tau = 0.1$ ,  $SNR = 10$  [dB],  $L_D = 6\lambda$ ] – (a) Actual target profile and (b) MR-CS retrieved profile.

### IV. CONCLUSION

In this paper a review of inverse scattering methodologies recently developed at the ELEDIA Research Center has been presented. The main aspects of the developed methods have been briefly discussed along with the novelties introduced with respect to the SoA approaches and their exploitation in different applicative scenarios.

### ACKNOWLEDGEMENT

This work has been partially supported by the Italian Ministry of Foreign Affairs and International Cooperation, Directorate General for Cultural and Economic Promotion and Innovation within the SNATCH Project (2017-2019) and it benefited from the networking activities carried out within the Cátedra de Excelencia UC3M-Santander funded by the Universidad Carlos III de Madrid (Spain) (Prof. A. Massa).

## REFERENCES

- [1] A. Massa, P. Rocca, and G. Oliveri, "Compressive Sensing in Electromagnetics - A review," *IEEE Antennas Propag. Mag.*, pp. 224-238, vol. 57, no. 1, Feb. 2015.
- [2] G. Oliveri, M. Salucci, N. Anselmi, and A. Massa, "Compressive sensing as applied to inverse problems for imaging: theory, applications, current trends, and open challenges," *IEEE Antennas Propag. Mag.*, vol. 59, no. 5, pp. 34-46, Oct. 2017.
- [3] N. Anselmi, G. Oliveri, M. A. Hannan, M. Salucci, and A. Massa, "Color compressive sensing imaging of arbitrary-shaped scatterers," *IEEE Trans. Microw. Theory Techn.*, vol. 65, no. 6, pp. 1986-1999, Jun. 2017.
- [4] L. Poli, G. Oliveri, and A. Massa, "Multi-resolution compressive sensing inversion of scattering data," *11th European Conference on Antennas and Propagation (EUCAP 2017)*, Paris, France, pp. 1599-1602, March 19-24, 2017.
- [5] M. Salucci, A. Gelmini, L. Poli, G. Oliveri, and A. Massa, "Progressive compressive sensing for exploiting frequency-diversity in GPR imaging," *Journal of Electromagnetic Waves and Applications*, in press.
- [6] A. Massa, G. Oliveri, M. Salucci, N. Anselmi, and P. Rocca, "Learning-by-examples techniques as applied to electromagnetics," *Journal of Electromagnetic Waves and Applications*, pp. 1-16, 2017.
- [7] M. Salucci, N. Anselmi, G. Oliveri, P. Calmon, R. Miorelli, C. Reboud, and A. Massa, "Real-time NDT-NDE through an innovative adaptive partial least squares SVR inversion approach," *IEEE Trans. Geosci. and Remote Sens.*, vol. 54, no. 11, pp. 6818-6832, Nov. 2016.
- [8] S. Ahmed, M. Salucci, R. Miorelli, N. Anselmi, G. Oliveri, P. Calmon, C. Reboud and A. Massa, "Real time groove characterization combining partial least squares and SVR strategies: application to eddy current testing," *Journal of Physics: Conference Series*, vol. 904, pp. 1-8, 2017.
- [9] M. Salucci, J. Vrba, I. Merunka, and A. Massa, "Real-time brain stroke detection through a learning-by-examples technique - an experimental assessment," *Microwave and Optical Technology Letters*, vol. 59, no. 11, pp. 2796-2799, Aug. 2017.
- [10] M. Salucci and A. Massa, "An innovative learning-by-examples method for real-time electrical impedance tomography of the human chest," *2018 IEEE AP-S International Symposium and USNC-URSI Radio Science Meeting*, Boston, Massachusetts, USA, July 8-13, 2018.
- [11] M. Salucci, G. Oliveri and A. Massa, "GPR prospecting through an inverse-scattering frequency-hopping multifocusing approach," *IEEE Trans. Geosci. Remote Sens.*, vol. 53, no. 12, pp. 6573-6592, Dec. 2015.
- [12] M. Salucci, L. Tenuti, L. Poli, G. Oliveri, and A. Massa, "A computational method for the inversion of wide-band GPR measurements," *Journal of Physics: Conference Series*, vol. 756, pp. 1-6, 2016.
- [13] M. Salucci, L. Poli, and A. Massa, "Advanced multi-frequency GPR data processing for non-linear deterministic imaging," *Signal Processing*, vol. 132, pp. 306-318, Mar. 2017.
- [14] M. Salucci, L. Poli, N. Anselmi, and A. Massa, "Multi-frequency particle swarm optimization for enhanced multi-resolution GPR microwave imaging," *IEEE Trans. Geosci. and Remote Sens.*, vol. 55, no. 3, pp. 1305-1317, Mar. 2017.

## **EM EDUCATION TOOLS & PROGRAMS @ ELEDIA RESEARCH CENTER**

N. Anselmi <sup>(1)</sup>, G. Oliveri <sup>(1)</sup>, L. Poli <sup>(1)</sup>, A. Polo <sup>(1)</sup>, F. Robol <sup>(1)</sup>, P. Rocca <sup>(1)</sup>,  
M. Salucci <sup>(1)</sup>, and A. Massa <sup>(1)(2)</sup>

<sup>(1)</sup> ELEDIA Research Center (ELEDIA@UniTN, University of Trento)  
via Sommarive 9, I-38123 Trento, Italy

<sup>(2)</sup> ELEDIA Research Center (ELEDIA@UC3M – Universidad Carlos III de  
Madrid) Avenida de la Univesitat 30, 28911 Madrid, Spain  
[andrea.massa@eledia.org](mailto:andrea.massa@eledia.org)

### **Abstract**

*This paper presents an overview of novel educational activities and tools for motivating, training, and supporting students as well as teaching staff in the field of Electromagnetism and Engineering science. Proposed approaches have been designed and experimentally validated within Bachelor and Master degree courses of the ELEDIA Research Center.*

**Index Terms** – educational tools, motivating students, online examination, scientific exams, tutoring, training.

### **I. INTRODUCTION**

During the last years, institutions from high school to Ph.D. programs have started to introduce new teaching approaches and tools for improving the world of education and prepare students for their professional career. The role of teaching staff is not limited to standard activities such as frontal lessons and examination, but it includes the tasks of motivating students, sharing methodologies and tools for self-evaluation, providing hints, options, and paths for their own grow both in industrial and research fields. In this framework, this work presents two relevant activities carried out by the ELEDIA Research Center for both educational and examination purposes.

### **II. ELEDIA TALENT RESEARCH PROGRAM (ETRP)**

The ELEDIA Talent Research Program (*ETRP*) has been recently introduced by the ELEDIA Research Center as a novel approach to teaching and students education. *ETRP* is mainly focused on cultivating the students' self-motivation as well as their critical analysis, for future interdisciplinary talents [1]. In such a framework, one of the key aspects is represented by the definition of a course or program and a set of exercises and exam problems, capable of providing a successful experience to the participants, encouraging them in improving their skills and capabilities, while reducing the high natural dropout of traditional courses, where practical works are somehow limited or neglected [2].

In particular, such a new teaching approach has been applied in the last years as the advance to the Electromagnetic Fields course of the

Bachelor Degree in Telecommunication Engineering at the University of Trento, since the academic year 2011-2012. During the *ETRP* program, several software laboratory exercises are carried out, allowing students to develop a more practical comprehension of the investigated topics that may appear difficult to understand if presented only from a theoretical point of view. To this end, additional hands-on activities are presented to students, which are free to participate to the program as volunteers without any obligation nor relation with the university career exams. For most of the students, the Bachelor Electromagnetic Field course is their first approach to such topics, therefore it is quite essential to motivate them and to improve the actual comprehension of the addressed topics. Therefore, students are involved in software and practical exercises mainly focused, at the beginning, on the analysis and learning of commonly used electromagnetic simulators both at research and industrial level. Prototyping is also carried out after an improved knowledge of the software suites, in order to improve the practical flavour of students as well as enhancing their expertise in antenna design and synthesis procedures. Students are also pushed to improve their capabilities in writing technical documentation, describing the developed activities and analysing and discussing the obtained results in a critical way. *ETRP* students develop their activities under the supervision of a tutor, who is in charge of supporting and driving their training, while introducing them to the research teams actually working on the same or similar topics. Of course, one of the main goals of the tutor is enhancing the spirit of team collaboration, giving credit to the students results as part of the research team. In addition, depending on the students skills and wills, specific topics may be addressed in view of their future career. It is worth remarking the importance that laboratories and hands-on projects have on curricula, as giving credit to the capabilities and to the knowledge the students acquire during courses.

### **III. SELF-EVALUATION AND FINAL EXAMINATION TOOLS**

In recent years, online examination systems have gained more and more popularity not only in distant education and massive open online courses, but also within high schools and academic institutions [2]. The traditional written examination is a very laborious and long process for teaching staff. In particular, the exam paper preparation and the correction require very careful attention as might lead to batch errors. Online examination systems are tools aimed to help both students and teachers within all phases of the process. In particular, the proposed system "*ELEDIA E-XAM*" supports and simplifies the examination process *(i)* by providing self-assessment evaluation that students can conduct anytime and anywhere in order to understand the preparation on each course topic, *(ii)* by granting security and fairness during the final examination as results are computed semi-automatically against formal rules implemented in the software, *(iii)* by minimizing the time

required for each exam session by the teaching staff to prepare and correct submitted exams, to publish marks, and finally (iv) by supporting the students consultation of corrected exam and the teacher during oral session, when required. The *E-XAM* system is based on state-of-the-art web technologies, any device equipped with an Internet browser can be used for taking the exam (e.g., a standard computer room as shown in Fig. 1) and for administration tasks such as the management of new exam calls and their correction. The examination service can be restricted to the Intranet of any local Institution or can be deployed remotely through the Internet accordingly to the modern cloud-oriented paradigm.

The evaluation questionnaire is typically defined as a set of Multiple Choice Questions as shown in Fig. 2. The *E-XAM* platform provides also guidelines and tools for reformulating theoretic checks, theorems and exercises in the form of Boolean answers (i.e., student answers if the proposed statement is correct or wrong). For example, a theorem can be tested by having student to confirm the correctness of each step of the demonstration in which some conceptual, logical, or mathematical mistakes have been introduced. Nevertheless, the system supports more question types such as numerical input which is validated against given accuracy. A key feature of the proposed *E-XAM* system is the questions management. Once the master database of the course is initialized (populated with enough questions accordingly to examination complexity and length), new exam sessions can be created in few clicks as the system supports the pseudo-random selection of questions fitting objectives defined by the teacher, such as having a given number of questions for each topic. The initial creation and the maintenance of the master database is supported by semi-automated procedures for importing rich text, images and math (e.g., formatted in LaTeX), as well as by the inline question editor. The generated exam papers can be different for each student (i.e., questions and their statements are shuffled). Each answer provided by the student is associated to a positive or negative arbitrary score, in the case answer is correct or wrong, respectively. The exam correction and mark assignment is semi-automated and instantaneous, nevertheless the teacher can modify and tune the approach used to convert the student score to the final mark in the given grade scale.

#### IV. CONCLUSION

In this work, paradigms and tools for motivating students and supporting teaching staff have been presented. Since the first launch of the *ETRP* program in 2011, more than 100 students have experienced the proposed track with success and willingness, considerably improving their academic and cultural growth. Moreover, the proposed online examination system *E-XAM* has been adopted in 22 international courses and schools in the field of Electromagnetism since 2016.



**FIG. 1** – A picture of Bachelor students taking the *E-XAM* of the course of “Electromagnetic Fields” in a standard computer room.

**Domanda No. 9**

Una linea di trasmissione lunga  $7\lambda/12$  viene collegata ad un generatore sinusoidale avente una tensione a circuito aperto pari a 10 V ed una frequenza di 300 MHz. Alla linea vengono connessi un carico  $Z_L=20 \Omega$  e una seconda linea di trasmissione, di lunghezza  $\lambda/2$  e terminata su un circuito aperto, di impedenza caratteristica pari a  $Z_0=50 \Omega$ . Si vuole determinare, se possibile, l'impedenza caratteristica della linea affinché la stessa sia adattata.

Il diagramma mostra un generatore  $C$  con tensione  $V_0=10V$  e frequenza  $f=300MHz$  collegato a una linea di trasmissione di lunghezza  $L_1=7\lambda/12$  e impedenza caratteristica  $Z_0=50\Omega$ . Questa linea è collegata a un carico  $Z_L=20\Omega$  e a una seconda linea di trasmissione di lunghezza  $L_2=\lambda/2$  e impedenza caratteristica  $Z_0=50\Omega$ , terminata in un circuito aperto.

Si indichi se ciascuna delle seguenti affermazioni è VERA o FALSA.

L'impedenza di ingresso del tutto di linea con lunghezza $L_1$ terminato su circuito aperto è pari a $Z_0=0$	<input type="button" value="Ignora"/>	<input type="button" value="VERO"/>	<input type="button" value="FALSO"/>
L'impedenza di ingresso del tutto di linea con lunghezza $L_1$ terminato su circuito aperto è pari a $Z_0=10$	<input type="button" value="Ignora"/>	<input type="button" value="VERO"/>	<input type="button" value="FALSO"/>
L'impedenza di ingresso del tutto di linea con lunghezza $L_1$ terminato su circuito aperto è pari a $Z_0=10$	<input type="button" value="Ignora"/>	<input type="button" value="VERO"/>	<input type="button" value="FALSO"/>

**FIG. 2** – A screenshot of the online exam of “Electromagnetic Fields” showing an exercise on transmission lines formulated as Multiple-Choice question

### ACKNOWLEDGEMENT

This work benefited from the networking activities carried out within the Càtedra de Excelencia UC3M-Santander funded by the Universidad Carlos III de Madrid (Spain) (Prof. A. Massa).

### REFERENCES

- [1] X. Su, T. Wang, J. Qiu and L. Zhao, "Motivating students with new mechanisms of online assignments and examination to meet the MOOC challenges for programming," *2015 IEEE Frontiers in Education Conference (FIE)*, El Paso, TX, pp. 1-6, 2015.
- [2] P. Fonseca, P. Pedreiras, P. Cabral, J. N. Matos, B. Cunha and F. Silva, "Motivating first year students for an engineering degree," *2016 2nd International Conference of the Portuguese Society for Engineering Education (CISPEE)*, Vila Real, pp. 1-7, 2016.

## ANTENNA SYNTHESIS AND OPTIMIZATION @ ELEDIA RESEARCH CENTER

N. Anselmi<sup>(1)</sup>, R. Azaro<sup>(1)</sup>, P. Bui<sup>(1)</sup>, A. Gelmini<sup>(1)</sup>, G. Gottardi<sup>(1)</sup>, M. A. Hannan<sup>(1)</sup>, G. Oliveri<sup>(1)</sup>, L. Poli<sup>(1)</sup>, A. Polo<sup>(1)</sup>, F. Robol<sup>(1)</sup>, P. Rocca<sup>(1)</sup>, M. Salucci<sup>(1)</sup>, and A. Massa<sup>(1)(2)</sup>

<sup>(1)</sup> ELEDIA Research Center (ELEDIA@UniTN, University of Trento)  
via Sommarive 9, I-38123 Trento, Italy

<sup>(2)</sup> ELEDIA Research Center (ELEDIA@UC3M – Universidad Carlos III de Madrid) Avenida de la Univesitad 30, 28911 Madrid, Spain  
[andrea.massa@eledia.org](mailto:andrea.massa@eledia.org)

### Abstract

*In this work a review of synthesis and optimization methods for the design of next generation antennas for telecommunication and radar applications developed at the ELEDIA Research Center is presented. The main challenges and future trends are discussed, focusing on the design of clustered array architectures and complex electromagnetic devices.*

**Index Terms** – Antenna optimization, array clustering, contiguous partition method, System-by-Design, tiling.

### I. INTRODUCTION

The radar and telecommunication industry is nowadays interested on advanced antenna systems able to afford high radiation performances and meet tight requirements in terms of physical size, modularity and implementative costs [1]. As instance, phased array antennas, usually characterized by high architectural complexity and costs, have recently become a key technology for new generation mobile communications systems [2]. Consequently, the development of synthesis and optimization methods, able to provide optimal trade-offs between costs/sizes and radiation performances, is still an active research area. According to the design constraints, different optimization paradigms/approaches, such as deterministic and evolutionary algorithms (EAs) [2]-[9], compressive sensing (CS) [10], [11], system-by-design (SbD) [12]-[16], as well as useful mathematical theorems [3]-[7], have been exploited in order to provide optimal trade-off solutions to the antenna synthesis problem. Accordingly, this work presents an overview of the last innovative optimization-based methods developed at the ELEDIA Research center, as applied to the design of clustered array architectures, and high-complexity electromagnetic (EM) systems and devices.

## II. INNOVATIVE DESIGN METHODS OF CLUSTERED ARRAY ARCHITECTURES

The design of clustered array architectures has been widely studied starting from the seminal works addressing the problem of high quantization lobes arising when high clustering ratios and periodic sub-array configurations are considered [1], [2]. The contiguous partition method (*CPM*) has been successfully applied for the optimization of linear and planar arrays, affording sum and/or difference beams, partitioned into a fixed number of clusters [3]. The sub-array amplitude coefficients have been optimized using efficient excitation matching techniques or optimal convex optimizations. Recently a novel *CPM*-based method has been proposed for the optimization of linear non-uniformly clustered arrays, generating two different beams using the phases at sub-array level [4]. The clustering configuration is obtained by means of a global optimizer, while optimal compromise phase coefficients are computed using an excitation matching strategy. When the sub-arrays are required to have pre-fixed sizes and shapes, modular-constraint methods have to be used. As instance, the synthesis of clustered arrays [10]-[11], starting from a dictionary of sub-arrays having fixed sizes, has been proposed for linear geometries, using a CS-based technique. When dealing with planar array layouts, tiled array methods have been recently presented [5]-[7]. By exploiting mathematical tiling theorems, the optimal (i.e., complete) covering of the antenna aperture is assured, in order to maximize the directivity and the aperture efficiency of the array. The possibility to build the entire antenna as a tessellation of few tiles shapes, further decreases the production costs and allows an easier maintenance of the array. In this framework, domino [5], [6] and diamond [7] tiles shapes have been proposed as simple elementary building blocks of rectangular and hexagonal shaped arrays, respectively. Efficient tiling algorithms have been exploited for the optimization of irregular sub-array configurations by means of exhaustive methods and genetic algorithm (*GA*)-based optimizers, in order to deal with small and large aperture arrays [5]. Moreover, multi-objective optimizations approaches have been also recently investigated [6]. Future extensions of the proposed methods regard the optimization of very-large array, exploiting suitable graph-based representation of the solution space, enabling the use of efficient local search techniques and exploiting the symmetries among different tiling solutions.

## III. SYNTHESIS OF COMPLEX ELECTROMAGNETIC SYSTEMS AND DEVICES THROUGH THE SYSTEM-BY-DESIGN PARADIGM

Complex *EM* design problems are still a challenging task in terms of required computational resources and simulation time. Even if powerful computational machines are nowadays available, the synthesis of complex *EM* systems and devices is still difficult to solve in a reasonable

amount of time. By exploiting the recently introduced *SbD* paradigm [12]-[16] *AEs*-based approaches have been enabled for addressing complex synthesis problems, such as the design of metamaterials based devices [13] and wide-angle impedance matching (*WAIM*) layers [14]. More recently, the *SbD* has been proposed as an effective strategy for the synthesis of antennas for satellite communications [15], affording satisfactory designs in reasonable amount of time. Moreover, the synthesis of electrically-large radomes for airborne applications has been addressed in [16] exploiting a Learning-by Examples (*LBE*) technique for efficiently evaluating each trial solution without the need of accurate but time-consuming *EM* full-wave simulations.

#### IV. CONCLUSION

A review of the optimization and synthesis techniques for the design of antennas for telecommunication and radar applications, recently developed at the ELEDIA Research Center, has been presented. The last methodological advancements and future trends, focusing on the optimization of clustered/tiled array architectures and the synthesis of complex *EM* systems within the *SbD* framework, have been discussed.

#### ACKNOWLEDGEMENT

This work benefited from the networking activities carried out within the Càtedra de Excelencia UC3M-Santander funded by the Universidad Carlos III de Madrid (Spain) (Prof. A. Massa) and within the FET Open CSA PROJECT NANOARCHITECTRONICS (Grant Agreement n. 737135) funded by the European Union in the framework of the Horizon 2020 – the Framework Programme for Research and Innovation (2014-2020). This work benefited also from the networking activities carried out within the Project "Antenne al Plasma - Tecnologia abilitante per SATCOM (ASI.EPT.COM)" funded by the Italian Space Agency (ASI) under Grant 2018-3-HH.0 (CUP: F91I17000020005).

#### REFERENCES

- [1] P. Rocca, G. Oliveri, R. J. Mailloux, and A. Massa, "Unconventional phased array architectures and design Methodologies - A review," *Proc. IEEE*, vol. 104(3), pp. 544-560, Mar. 2016.
- [2] G. Oliveri, G. Gottardi, F. Robol, A. Polo, L. Poli, M. Salucci, M. Chuan, C. Massagrande, P. Vinetti, M. Mattivi, R. Lombardi, and A. Massa, "Co-design of unconventional array architectures and antenna elements for 5G base station," *IEEE Trans. Antennas Propag.*, vol. 65(12), pp. 6752-6767, Dec. 2017.
- [3] P. Rocca, L. Manica, and A. Massa, "An improved excitation matching method based on an ant colony optimization for suboptimal-free clustering in sum-difference compromise synthesis," *IEEE Trans. Antennas Propag.*, vol. 57, no. 8, pp. 2297-2306, Aug. 2009.
- [4] P. Rocca, N. Anselmi, M. Salucci, G. Gottardi, L. Poli, and A. Massa "A novel analytic beam steering approach for clustered phased array

architectures," *2017 IEEE AP-S International Symposium and USNC-URSI Radio Science Meeting*, San Diego, California, USA, pp. 2013-2014, July 9-15, 2017.

[5] N. Anselmi, P. Rocca, M. Salucci, and A. Massa, "Irregular phased array tiling by means of analytic schemata-driven optimization," *IEEE Trans. Antennas Propag.*, vol. 65(9), pp. 4495-4510, Sept. 2017.

[6] N. Anselmi, P. Rocca, G. Gottardi, M. Salucci, and A. Massa, "Tiling optimization of orthogonal-polygon shaped aperture for phased array antennas," *2017 IEEE AP - S International Symposium and USNC - URSI Radio Science*, San Diego, California, USA, pp. 2025 - 2026, July 9-15, 2017.

[7] N. Anselmi, L. Poli, P. Rocca, and A. Massa, "Diamond tiling optimization for hexagonal shaped phased arrays," 12th European Conference on Antennas and Propagation (EUCAP 2018), London, United Kingdom, April 9-13, 2018.

[8] L. Poli, G. Oliveri, P. Rocca, M. Salucci, and A. Massa, "Long-Distance WPT Unconventional Arrays Synthesis" *Journal of Electromagnetic Waves and Applications*, vol. 31(14), pp. 1399-1420, Jul. 2017.

[9] M. Salucci, G. Gottardi, N. Anselmi, and G. Oliveri, "Planar thinned array design by hybrid analytical-stochastic optimization," *IET Microwaves, Antennas & Propagation*, vol. 11(13), pp. 1841-1845, Oct. 2017.

[10] G. Oliveri, M. Salucci, and A. Massa, "Synthesis of modular contiguously clustered linear arrays through a sparseness-regularized solver," *IEEE Trans. Antennas Propag.*, vol. 64(10), pp. 4277-4287, Oct. 2016.

[11] N. Anselmi, G. Oliveri, and A. Massa, "Synthesis of clustered arrays based on a total variation compressive sensing approach," *11th European Conference on Antennas and Propagation (EUCAP 2017)*, Paris, France, pp. 862-864, March 19-24, 2017.

[12] G. Oliveri, P. Rocca, M. Salucci, and A. Massa, "Efficient synthesis of complex antenna devices through system-by-design," *2014 IEEE Symposium Series on Computational Intelligence (IEEE SSCI 2014)*, Orlando, Florida, USA, pp. 1-6, December 9-12, 2014.

[13] M. Salucci, G. Oliveri, N. Anselmi, G. Gottardi, and A. Massa, "Performance enhancement of linear active electronically-scanned arrays by means of MbD-synthesized metalenses," *Journal of Electromagnetic Waves and Applications*, vol. 32(8), pp. 927-955, 2018.

[14] G. Oliveri, M. Salucci, N. Anselmi and A. Massa, "Multiscale System-by-Design synthesis of printed WAIMs for waveguide array enhancement," *IEEE J. Multiscale Multiphysics Computat. Techn.*, vol. 2, pp. 84-96, 2017.

[15] A. Massa and M. Salucci, "Dealing with complexity in electromagnetics through the system-by-design paradigm - New strategies and applications to the design of airborne radomes," *2018 IEEE AP-S International Symposium and USNC-URSI Radio Science Meeting*, Boston, Massachusetts, USA, July 8-13, 2018.

[16] M. Salucci, D. Marcantonio, F. Greco, G. Amendola, and A. Massa, "Looking for the optimal trade-off between computational costs and reliability in synthesizing high-complexity electromagnetic systems - The case of satellite communications antenna design," *2018 IEEE AP-S International Symposium and USNC-URSI Radio Science Meeting*, Boston, Massachusetts, USA, July 8-13, 2018.

## **DISTRIBUTED WIRELESS SENSING, MONITORING, AND DECISION SUPPORT: CURRENT ACTIVITIES @ ELEDIA RESEARCH CENTER**

M. Bertolli<sup>(1)</sup>, G. Oliveri<sup>(1)</sup>, A. Polo<sup>(1)</sup>, F. Robol<sup>(1)</sup>, P. Rocca<sup>(1)</sup>, F. Viani<sup>(1)</sup>,  
and A. Massa<sup>(1)(2)</sup>

<sup>(1)</sup> ELEDIA Research Center (ELEDIA@UniTN, University of Trento)  
via Sommarive 9, I-38123 Trento, Italy

<sup>(2)</sup> ELEDIA Research Center (ELEDIA@UC3M – Universidad Carlos III de  
Madrid) Avenida de la Univesidad 30, 28911 Madrid, Spain

[andrea.massa@eledia.org](mailto:andrea.massa@eledia.org)

### **Abstract**

*Wireless sensing technologies are widely exploited nowadays as enabling several applications and diversified services. Indeed, monitoring systems are often the base for advanced processing and analysis mechanisms, that allow to enhance the amount of information collected by the sensing devices and, in turn, to support daily life operations. Therefore, the capability to sense heterogeneous data with delocalized small devices spread around even large environments, as well as performing real-time acquisition and processing, has allowed the extensive use of wireless sensing technologies. In such a framework, the paper discusses the recent advances the ELEDIA Research Center is carrying out regarding pervasive computing and monitoring systems, also referring to applicative examples, experimentally validated, mainly concerned with the preservation of cultural heritage, the increase of road safety, and the precision farming paradigm, through specific sensing platforms and decision support systems designed and implemented for the scope.*

**Index Terms** – Decision support systems, distributed wireless monitoring, pervasive computing, wireless sensor network

### **I. INTRODUCTION**

Recent advances in communication and wireless technologies have lead to an increasing interest for distributed wireless monitoring and pervasive computing applications. In particular, Wireless Sensors Networks (WSNs) represent a widely used technology, thanks to the provided features such as low-cost and easy installation, which allowed a rapid increase in the use of wireless-based systems as an alternative to wired-based networks [1].

Among all, particular focus is given to those applications aimed at improving situation and security awareness as well as supporting daily life decisions, which may be related to several applicative fields, such as preserving cultural heritage works, improving road security, or enhancing the efficiency and the quality of farming productions.

To this end, the use of low-cost and low-power wireless technologies is highly exploited, thus allowing the design of innovative solutions toward the definition of smarter environments, improving the overall exploitation of finite resources available nowadays.

In this framework, the ELEDIA Research Center is working on the study and design of innovative solutions through the implementation of wireless sensing platforms to be spread around the scenario under analysis and whose data are accurately processed and managed by ad-hoc decision support systems developed in order to improve and simplify end-users' actions, as the actual response to the sensed environment. Therefore, the paper is focused on the discussion about the recent advances and results obtained in the field of distributed wireless monitoring and decision support systems.

## **II. WIRELESS SOLUTIONS FOR CULTURAL HERITAGE**

Cultural heritage represents an inestimable asset as inherited by ancient ages, composed by artworks of any kind, such as statues, frescos or even entire buildings. Therefore, particular focus is given to the health monitoring of such structures. In detail, several methodologies have been defined at the state of the art, mainly classified as destructive and non-destructive testing. In the former case, the test implies the analysis of the structure material, thus allowing the possibility to determine material features not identifiable via non-destructive testing. Nevertheless, this implies the structure impairment in order to collect structure samples to be analyzed. Considering non-destructive testing, instead, continuous inspection of the structure must be performed, such as visual inspection, but thanks to the advances in sensing technologies and computer science, several approaches based on the analysis of propagating waves (i.e., acoustic, mechanical, electromagnetic waves) can be efficiently exploited [2]. Therefore, in such a framework, a wireless monitoring system for damage detection is under design and development, taking advantage of the heterogeneous data acquired by diversified sensors (i.e., temperature, humidity, accelerometer, vibration sensors), subsequently processed by a machine learning approach in order to investigate if potential damages may arise in the monitored structure [3]. Preliminary results demonstrate the potentialities of the proposed system, allowing an appreciable detection accuracy (i.e., about 67%).

## **III. WIRELESS SOLUTIONS FOR ROAD SECURITY**

Security on roads is transversely investigated nowadays, in order to improve drivers' awareness of risks they may be involved in, as well as trying to properly prevent them by assisting road-users while driving. In

such a framework, particular attention is also given to the wildlife monitoring at the road sides in order to prevent potential collisions with the incoming vehicles.

To this end, a distributed wireless monitoring system has been developed for the real-time detection of wildlife road-approaching and road-crossing events. In particular, the implemented system is based on the Doppler radar technology, which allows the definition of the so-called “security area” at the road sides, where wildlife is promptly detected. In addition, the system has been validated on a real test-site in the Alp regions for more than one year, demonstrating good detection capability of road-crossing events, about the 78% of all the occurred real events, as well as good system robustness and stability [4], [5].

Additional activities are currently under development in order to improve the system potentialities, making it conformable to different wildlife species, such as boars, which actually represent a relevant problem for the road security in the north-mid Italy as well as in many other countries.

#### **IV. WIRELESS SOLUTIONS FOR PRECISION FARMING**

Wireless technologies have been widely adopted for precision agriculture applications, such as smart irrigation management [6], continuous monitoring of the crop status, and phytosanitary treatment [7].

In such a framework, a decision support system has been developed in order to sustain the farmer decision and activity in agro-chemical treatment processes. In particular, starting from a set of wireless sensing devices, spread around the orchard, the heterogeneous acquired data are properly processed by the implemented spatialization algorithm and accurately integrated with additional external information, such as models and weather forecast. This mechanism allows to reduce the need for high density WSNs and to manage different set of data, which can be correlated a-posteriori, improving the actual set of knowledge about the monitored crop.

The proposed system thus actually allows the support to the farmer in decisions making on the usage of phytosanitary products and, for each treatment, the farmer is also supported on the quantification of the proper dosage in order to optimize the amount of agro-chemical product to be used. This mechanism also allows different spatial treatment concentration sprinkling, depending on the actual needs of the local crop as well as on the effective evolution of investigated parasites, as determined by the implemented methodology.

An experimental testing on a real vineyard in the north Italy has validated the actual working of the system, demonstrating good capability in the detection of localized arising infections, as well as in the identification of the agro-chemical product and related dosage to be applied.

## V. CONCLUSION

The paper has been focused on a general review of the main recent activities carried out by the ELEDIA Research Center regarding distributed wireless monitoring systems and decision support systems. The discussed solutions take advantage of both such paradigms, namely starting from the sensed data, additional improved processing is applied in order to support end-users' actions.

## ACKNOWLEDGEMENT

This work has been partially supported by the Italian Ministry of Foreign Affairs and International Cooperation, Directorate General for Cultural and Economic Promotion and Innovation within the SNATCH Project (2017-2019) and it benefited from the Project "WATERTECH - Smart Community per lo Sviluppo e l'Applicazione di Tecnologie di Monitoraggio Innovative per le Reti di Distribuzione Idrica negli usi idropotabili ed agricoli" (Grant no. SCN\_00489) funded by the Italian Ministry of Education, University, and Research within the Program "Smart cities and communities and Social Innovation" (CUP: E44G14000060008).

## REFERENCES

- [1] F. Viani, F. Robol, A. Polo, P. Rocca, G. Oliveri, and A. Massa, "Wireless Architectures for Heterogeneous Sensing in Smart Home Applications: Concepts and Real Implementation," in *Proceedings of the IEEE*, vol. 101, no. 11, pp. 2381-2396, Nov. 2013.
- [2] M. Donelli and F. Viani, "Remote Inspection of the Structural Integrity of Engineering Structures and Materials With Passive MST Probes," in *IEEE Transactions on Geoscience and Remote Sensing*, vol. 55, no. 12, pp. 6756-6766, Dec. 2017.
- [3] M. Salucci, J. Vrba, I. Merunka, and A. Massa, "Real-time brain stroke detection through a learning-by-examples technique - an experimental assessment," *Microw. Opt. Technol. Lett.*, vol. 59, pp. 2796-2799, Aug. 2017.
- [4] F. Viani, F. Robol, A. Polo, and E. Giarola, "Wildlife road-crossing monitoring system: Advances and test site validation," *10th European Conference on Antennas and Propagation (EUCAP 2016)*, Davos, Switzerland, April 11-15, 2016.
- [5] F. Viani, A. Polo, E. Giarola, M. Salucci and A. Massa, "Principal component analysis of CSI for the robust wireless detection of passive targets," *2017 International Applied Computational Electromagnetics Society Symposium - Italy (ACES)*, Florence, pp. 1-2, 2017.
- [6] L. G. Paucar, A. R. Diaz, F. Viani, F. Robol, A. Polo and A. Massa, "Decision support for smart irrigation by means of wireless distributed sensors," *2015 IEEE 15th Mediterranean Microwave Symposium (MMS)*, Lecce, 2015, pp. 1-4.
- [7] F. Viani et al., "A wireless monitoring system for phytosanitary treatment in smart farming applications," *2016 IEEE International Symposium on Antennas and Propagation (APSURSI)*, Fajardo, pp. 2001-2002, 2016.

# THE CASE OF MICROWAVE DISINFECTION OF RAISED BEDS CULTIVATIONS – NUMERICAL ASSESSMENT

S.Casu<sup>(1)</sup>, A. Fanti<sup>(1)</sup>, M.B. Lodi<sup>(1)</sup>, M. Spanu<sup>(1)</sup>, M. Renzi, G. Mazzarella<sup>(1)</sup>

<sup>(1)</sup> Department of Electrical and Electronic Engineering, University of  
Cagliari

Piazza D'Armi, 09123 Cagliari, Italy

[alessandro.fanti@diee.unica.it](mailto:alessandro.fanti@diee.unica.it)

## Abstract

*Microwave-induced heating can be regarded as an interesting, cost-effective and eco-friendly possibility to solve issue related to agriculture. This paper deals with the computational modelling of nonlinear microwave heating of soils in metal raised bed cultivations inside greenhouses. Non-linear Multiphysics simulations are carried out modeling dielectric properties of soil, in terms of composition and actual temperature, and accounting for the exact thermal and electromagnetic conditions in raised beds inside the greenhouse. The disinfection is directed to noxious agents, such as fungi, insects or weeds, such as Sclerotium rolfsii, Mediterranean Fruit Fly and ryegrass or fleabane. Simulations results for microwave disinfection procedure are critically discussed and compared to the traditional solarization technique.*

**Index Terms** – computational modeling, disinfection, mediterranean fruit fly, rf in agriculture, microwave.

## I. INTRODUCTION

Farmlands and cultivations preservation from agricultural pests is a relevant issue in agricultural production [1]. Scientific community is searching an innovative technique with the potential of eliminating insects, soilborne pathogens and/or weeds avoiding the use of chemicals, minimizing the impact on the product quality and which can be employed on bare soil, in greenhouses and raised beds [1], [2].

Raised beds are employed to face the increasing demand for production, reducing water consumption and CO<sub>2</sub> emissions for several crops of shallow, medium and deep rooting, namely tomatoes, corn, cucumber, watermelon, rice [2]. Heat treatments are the most popular non-chemical way to reduce and control the populations of soilborne pathogens [1]. Thermal quarantine methods have the aim of rising system temperature over a lethal threshold value to inactivate noxious targets. Thermal death, long-term lethal effect and chronic mortality are caused by denaturation or coagulation of cellular proteins, irreversible damage to the cell wall and accumulation of toxic products [1]. The most traditionally employed thermal methods is solarisation, i.e. the use of solar energy to heat the

soil and then disinfect it [1]. This method is very low-cost but its duration is several months long. On the other hand, use of microwaves (MWs) for soil sterilization, instead, is a faster, though more expansive, way to eliminate soilborne pathogens [1], [3], and can be used beside farmland geographical location. However, because of its cost, MW heating requires a careful trade-off between time and cost to devise the most effective treatment [4]. This trade-off can be only performed if accurate evaluation of the interaction between soil and MW and the thermal fluxes in the soil itself is available [3], [4]. As a matter of fact, this evaluation requires the knowledge of soil physical properties and the non-linear interaction between thermal and microwave field.

## II. SOIL ELECTROMAGNETIC PROPERTIES, THERMAL MODEL AND GEOMETRY

Soil is a heterogeneous medium, i.e. a mixture of clay, silt, sand and grave, but also water and air, and its texture is one of the most determinant of the amount of water (humidity) retained in its pores [3]. The complex dielectric constant depends on all these components [4], and therefore it is possible to write it as:

$$\begin{aligned}\varepsilon'_{mixture}(T) &= \vartheta_w \cdot \varepsilon'_w(T) + \vartheta_s \cdot \varepsilon'_s + \vartheta_a \cdot \varepsilon'_a \\ \varepsilon''_{mixture}(T) &= \vartheta_w \cdot \varepsilon''_w(T) + \vartheta_s \cdot \varepsilon''_s\end{aligned}\quad (1)$$

where  $\theta_w$  is the volume fraction of water in wet soil,  $T$  is the temperature, whereas  $\varepsilon_w$  is the dielectric constant of water [5] and  $\theta_s$  is the solid volume fraction, whilst  $\varepsilon_s$  is the dielectric constant of the solid components [4] and  $\theta_a$  is the dielectric constant of air in the soil, determined as the difference between porosity and  $\theta_w$ . In this work is considered a soil with 29% of sand, 50.1% of silt, 20.9% of clay.

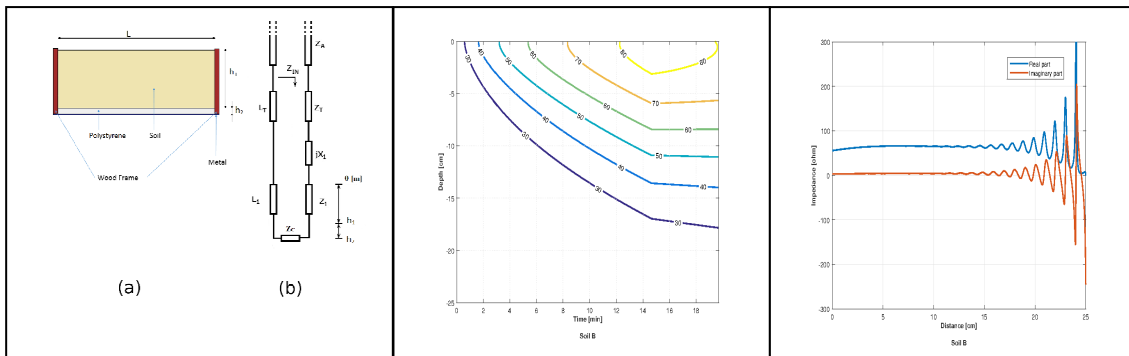


**Fig. 1.** a) Raised bed cultivation system in greenhouses. The system consists of a box in metal or wood with a length  $L = 60$  cm, a width of 30 cm (here not shown) and a height  $h = h_1+h_2 = 1$  m. Soil is deposited on a thermal insulant polymeric film, e.g. Styrofoam. b) The equivalent transmission line model for soil, Styrofoam and the bottom, assuming an impinging plane wave of  $11 \text{ kW m}^{-2}$  at 2.45 GHz. c) Spatio-temporal distribution of soil temperature. Microwave power is turned off at 15 min. d) Local impedance as a function of soil depth inside the raised bed, for different time during MW exposure.

For the raised bed system shown in Fig. 1a, assuming an incident plane wave at the working frequency of 2.45 GHz, with a power of  $11 \text{ kW m}^{-2}$  it is possible to calculate the dielectric constant and the field inside the raised bed using a transmission line model (Fig. 1b) [4], whose parameters depend from the field. This leads to a non-linear coupling between thermal and electromagnetic (EM) field, which is solved using a Finite Difference Time Domain (FDTD) scheme as described in Ref. [4]. at the end of the system the impedance is the input impedance of the dielectric insulating layer, backed by the PEC, and is therefore equal to  $Z_c = j\zeta_p t_p \tan(\beta_p)$ , where  $\zeta_p$  and  $\beta_p$  are the characteristic impedance and the propagation coefficient of the styrofoam, and  $t_p$  its thickness. To describe and quantify the space- and time-variant nature of the soil heating, the following heat equation must be solved:

$$\rho C \frac{\partial T}{\partial t} = \kappa \nabla^2 T + P_T = \kappa \frac{\partial^2 T(z,t)}{\partial z^2} + P_T \quad (2)$$

where  $k$  is soil thermal conductivity ( $2.47 \text{ W m}^{-1} \text{ K}^{-1}$ ), whilst  $\rho$  its density ( $1400 \text{ kg m}^{-3}$ ), and  $C$  is the specific heat at constant pressure ( $893 \text{ J kg}^{-1} \text{ K}^{-1}$ ). The term  $P_t$  is the thermal power generated by MW heating, in  $\text{Wm}^{-3}$ .

The biological target is Mediterranean fruit fly in this work [6]. The death kinetics of these insects is reported to respect the following relation [6]:

$$\frac{d\left(\frac{N}{N_0}\right)}{dt} = -k_t \left(\frac{N}{N_0}\right)^n \quad (3)$$

where  $k_t$  is thermal death rate constant in  $\text{min}^{-1}$  and has an Arrhenius-like dependence from temperature [6],  $n$  is reported to be equal to 0.5

[6] and  $N$  and  $N_0$  are the surviving and initial numbers of insects respectively. Data are available for 46, 48, 50, and 52°C. The simulation was run to obtain a total disinfection, i.e.  $N/N_0 \sim 1e-9$ .

### III. RESULTS

The temperature distribution against time and raised bed depth is presented in Fig. 1c for the soil under investigation.

This simulation indicated that any egg or third instar of a Mediterranean fruit fly in the soil can be killed after 15 min at 83 °C [6]. Comparing the temperature pattern obtained in the raised bed case with non-linear one [4], which consider a semi-infinite space, it is possible to notice that wave reflection determines a different dielectric heating. This result in higher temperature values and heating rate, which can be defined as the average temperature increase in 1 min. This heating rate is around 3.33°C/min for the semi-infinite soil and increases to 4.6°C/min in our case. Hence raised beds may allow an effective MW disinfection treatment with respect to open cultivation case.

The propagation into the bed soil depends in a significant way on the metallic termination, and this influences heating. Therefore, the modulus of the local impedance as a function of depth at the initial time is depicted in Fig. 1d.

The impedance exhibits an almost constant trend for the first few centimeters, i.e. circa 12 cm, and then starts to oscillate. When the feeding MW power starts heating the soil bed, the local impedance slightly varies from the initial situation, as reported in Fig. 1d. The performed analysis allows to devise a suitable matching of the radiant device and hence to optimize the disinfection performance for any given field.

### REFERENCES

- [1] J. Hansen, D. Winter, "History and use of heat in pest control: a review", *International journal of pest management*, 2011, 57, pp. 267-289.
- [2] G. Abate, "Local food economies: driving forces, challenges, and future prospects", *Journal of Hunger & Environmental Nutrition*, 2008, 3, pp. 384-399.
- [3] M. Spanu, A. Fanti, M. B. Lodi, S. Casu, F. Desogus, B. Bisceglia, G. Mazzarella, "Microwaves disinfection of farmland", *Journal of Electromagnetic Waves and Applications*, 2016, 30, pp. 2165-2173.
- [4] A. Fanti, M. Spanu, M. B. Lodi, F. Desogus, G. Mazzarella, "Nonlinear Analysis of Soil Microwave Heating: Application to Agricultural Soils Disinfection", *IEEE J. Multiscale and Multiphysics Computational Techn.*, 2017, 2, pp. 105-114.
- [5] P. S. Ray, "Broadband complex refractive indices of ice and water", *Applied Optics*, 1972, 11, pp. 1836-1844.
- [6] Y. Gazit, Y. Rossler, S. Wang, J. Tang, S. Lurie, "Thermal death kinetics of egg and third instar Mediterranean fruit fly (Diptera: Tephritidae)". *Journal of Economic Entomology*, 2004, vol. 97, no. 5, pp. 1540-1546.

# DESIGN OF AMC STRUCTURES FOR UHF APPLICATIONS

G. A. Casula<sup>(1)</sup>, G. Montisci<sup>(1)</sup>, P. Maxia<sup>(1)</sup>

<sup>(1)</sup> Department of Electrical and Electronic Engineering, University of Cagliari  
Cagliari  
Piazza D'Armi, 09123 Cagliari, Italy  
[a.casula@diee.unica.it](mailto:a.casula@diee.unica.it)

## Abstract

*In this work a uniplanar electromagnetic bandgap structure is presented, for antennas and microwave circuits working in the UHF frequency band. The proposed configuration is fully planar, easy to fabricate, and based solely on metallic surfaces on layer interfaces, without the use of vias or other kinds of vertical connections.*

**Index Terms** – AMC cells, UHF applications, UC-PBG Structures.

## I. INTRODUCTION

Electromagnetic bandgap (EBG) structures are becoming very important in modern design of antennas and microwave components, since these periodic structures resonate at certain frequencies, presenting filtering characteristics which can be used in the microwave region of the electromagnetic spectrum, in the design of filters or for reducing the coupling between circuit components [1]. The central frequency and extent of the stopband can be controlled by the geometry of the metallic cell constituting the EBG structure. These bandgap properties can be exploited for the design of microwave components, providing features like compactness, broadband behavior or high gain. An EBG structure can be designed in order to act like an artificial magnetic conductor (AMC) at certain frequencies. In AMCs, the surface current effects are negligible with respect to a PEC, and the image current (referred to the ground plane of the structure) is in phase with the current source. Therefore, AMCs are very promising in the design of microwave components, where they are typically used to replace the metallic ground planes. The central frequency and extent of the stop-band of an EBG cell can be controlled by the geometry of the cell itself. Some well-known EBG structures are the uniplanar compact photonic band gap (UC-PBG) proposed by Itoh [2] and the Sievenpiper “mushroom” high-impedance surface [3]. The mushroom-like structure [3] has been extensively used and implemented, but the presence of several via holes and vertical metallic connections places a severe constraint on the fabrication process and limits potential applicability of this kind of EBG structure. Planar EBGs allow to avoid the complexity of via connections

[4]–[7], and can use interdigital structure with increased fringe capacitances in order to tune the resonant frequency [6], or a more expensive (and more difficult to realize) multilayer implementation [7]. We are interested here in planar periodic structures designed to act as an artificial magnetic conductor (AMC) or high-impedance electromagnetic ground plane over a desired frequency range, corresponding to the forbidden frequency band. Hence, the key feature of these structures is the reflection of an incident plane wave with no phase reversal, unlike normal metal surfaces [3]. In the present literature, the AMC structures working in the UHF band are designed over expensive substrates with a very high dielectric permittivity [6, 7], and this strongly limits the widespread of these structures. In order to fill this gap, we propose here a compact, easy to fabricate, AMC structure, working within the UHF frequency band at 868 MHz, based on totally planar layouts without vias, with an uniplanar implementation, having the structure on top of a single dielectric layer. The proposed structure can be used for several applications, such as wireless communications, and it is especially suitable for RFIDs, where the production cost and the component size are critical points.

## II. EBG DESIGN

The design of the fundamental cell of an AMC structure is generally performed using different approaches, such as fractal geometries, or genetic programming techniques [8]. On the other hand, in this work we decided to start with a classical bi-dimensional cell, namely the “Jerusalem cross” proposed by Itoh [7], which we designed through a “cut and try” procedure, since in this way we are able to easily control the cell optimization. We selected a Rogers RT 6010LM substrate, with a dielectric constant equal to  $\epsilon_r = 10.2$ , with  $\delta = 0.0025$ , and a thickness of 3.94 mm, and the proposed cell has a very compact size (25 mm), with an operating frequency of 868 MHz. The proposed structure can be considered equivalent to a parallel LC circuit, with a resonant frequency given by:

$$f_0 = \frac{1}{2\pi\sqrt{LC}} \quad (1)$$

Considering the periodic structure of an EBG, the capacitance  $C$  of (1) is strictly related to the gap between two adjacent elementary cell composing the EBG structure, and can be computed following [9] as:

$$C = \frac{W\epsilon_0(1 + \epsilon_r)}{\pi} \cdot \cosh^{-1}\left(\frac{W + g}{g}\right) \quad (2)$$

where  $g$  is the gap between two adjacent cells,  $\epsilon_0$  and  $\epsilon_r$  are respectively the dielectric constant of free space and of the dielectric substrate, and

W is the width of the metallic patch. The inductance L of eq. (1) is due to the thin microstrip lines connecting the elementary cells, and can be estimated as [10]:

$$L = \frac{Z_0 \cdot l \cdot \sqrt{\epsilon_1}}{c} \quad (3)$$

where  $Z_0$  is the characteristic impedance of the microstrip line, and  $l$  is the length of the microstrip line connecting the central patches of the structure. The resonant frequency of the EBG cell can be modulated by modifying the values of the capacitance and/or of the inductance given by (2) and (3). Starting from the cell proposed by [7], we modified the gap between the cells equal to 0.2 mm, in order to have a higher capacitance C, and modified the width of the microstrip lines (3.8 mm for the central cross, and 2.27 mm for the lateral arms), so as to obtain a higher inductance L. With these choice, the resonant frequency is still too high (far beyond 900 MHz), therefore we inserted a thin slot cut in each of the four lateral arms (0.5x7 mm), and four squares with size 0.77x0.77mm close to each of the four cell borders so as to decrease the resonant frequency of the cell. With these choices, we obtained a resonant frequency around 868 MHz. and the resulting layout is shown in Fig.1.

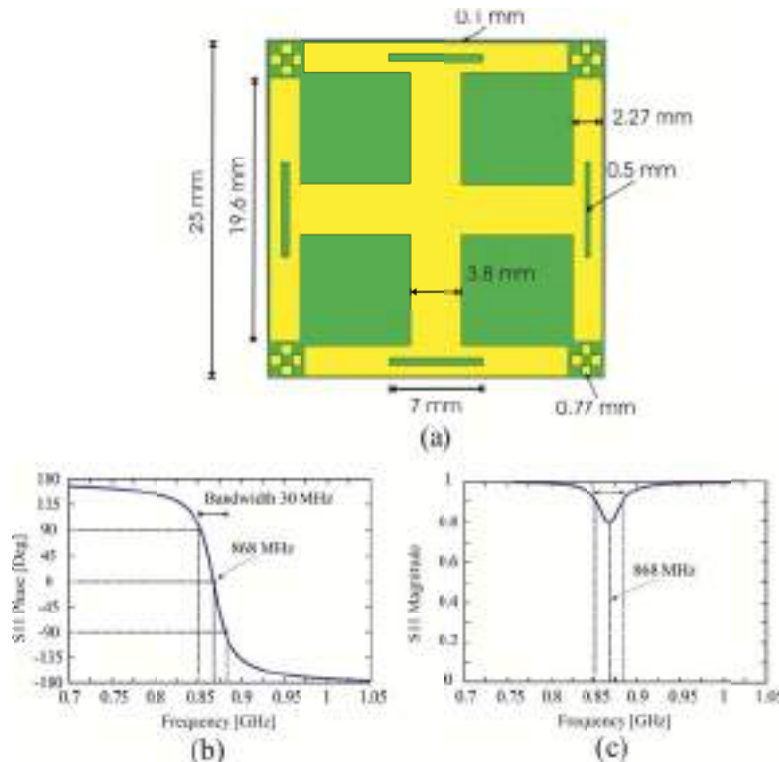


**FIG. 1** – (a) Layout of the elementary cell of the designed AMC;(b) Reflection coefficient phase, and (c) magnitude of the designed AMC.

In Fig. 1.b, and 1.c the simulated reflection coefficient phase and magnitude of the designed structure are shown, respectively, confirming

that the EBG structure has a resonant frequency of 868 MHz, with a working bandwidth (reflection coefficient phase within  $-90^\circ$  and  $90^\circ$ ) of about 30 MHz.

### III. CONCLUSION

An EBG structure working in the UHF frequency band is presented. The proposed EBG is very compact, has an easy fabrication, and is fully planar, without the use of vias or other kinds of vertical connections. The proposed structure can be used for wireless communications in the UHF band, and is particularly suited for RFIDs, where the production cost and the component size are critical points.

### REFERENCES

- [1] F. Yang and Y. Rahmat-Samii, *Electromagnetic Band Gap Structures in Antenna Engineering*. Cambridge, U.K.: Cambridge Univ. Press, 2009.
- [2] F. R. Yang, K. P. Ma, and Y. Qian, "A novel TEM waveguide using uniplanar compact photonic-bandgap (UC-PBG) structure," *IEEE Transactions on Microwave Theory and Techniques*, vol. 47, no. 11, pp. 2092–2098, 1999.
- [3] D. Sievenpiper, L. Zhang, R. Broas, N. Alexopoulos, and E. Yablonovitch, "High-impedance electromagnetic surfaces with a forbidden frequency band," *IEEE Trans. Microw. Theory Tech.*, vol. 47, no. 11, pp. 2059–2074, 1999.
- [4] B. Lin, X. Wen, "A novel uniplanar compact EBG incorporated with interdigital structure," *Micr. Opt. Technol. Lett.*, vol. 50, no. 3, 2008.
- [5] E. Rajo-Iglesias, Ó. Quevedo-Teruel, and L. Inclán-Sánchez, "Mutual coupling reduction in patch antenna arrays by using a planar EBG structure and a multilayer dielectric substrate," *IEEE Trans. Antennas Propag.*, vol. 56, no. 6, pp. 1648–1655, 2008.
- [6] D.J.Kern, D.H.Werner, A.Monorchio, L.Lanuzza, M.J.Wilhelm, "The design Synthesis of Multiband Artificial Magnetic Conductors Using High Impedance Frequency Selective Surfaces", *IEEE Transactions on Antennas and Propagation*, Vol.53, No.1, January 2005.
- [7] J.R.Sohn, T.Heung-Sik, J.G.Lee, J.H.Lee, "Comparative analysis of four types of high-impedance surfaces for low profile antenna applications, *Antennas and Propagation Society International Symposium*, 2005 IEEE (Volume:1A ), 3-8 July 2005.
- [8] L. Deias, G. Mazzarella, G. Montisci, and G. A. Casula, "Synthesis of Artificial Magnetic Conductors Using Structure-Based Evolutionary Design," *International Journal of Antennas and Propagation*, vol. 2013, pp. 1–7, 2013.
- [9] D.F. Sievenpiper, *High-Impedance Electromagnetic Surfaces*, Ph.D. dissertation, University of California, Los Angeles, CA.
- [10] R.B.Watherhouse, D.Novak, "A small electromagnetic bandgap structure", proceedings of Microwave Symposium Digest, 2006, *IEEE MTT-S International*, pp 602-605, June 2006, San Francisco, CA.
- [11] Md. Shaidul Alam, N. Misran, B. Yatim and M. T. Islam, "Development of electromagnetic Band Gap Structures in the perspective of microstrip antenna design", *International Journal of Antennas and Propagation*, Volume 2013.

# ENHANCED COLE-COLE DIELECTRIC MODEL FOR ACCURATE BLOOD GLUCOSE SENSING

V. Cioffi

DIMES, University of Calabria  
Via Pietro Bucci, 87036 Rende, CS, Italy  
[v.cioffi@dimes.unical.it](mailto:v.cioffi@dimes.unical.it)

## Abstract

*An improved dielectric model for the prediction of complex permittivity of blood as a function of frequency and glucose concentration is proposed in this work to strongly enhance the accuracy in the design of microwave sensors for blood glucose sensing. Preliminary numerical simulations are also discussed to support the proposed approach.*

**Index Terms**—Blood glucose, Microwaves, Microstrip sensor, Non-invasive sensor.

## I. INTRODUCTION

One of the most appealing topic in current research is the study of the interactions between electromagnetic fields and biological systems, such as human body. Studies are particularly addressed to the development of innovative technologies being able to exploit electromagnetic diagnostics methods for the non-invasive monitoring of biological parameters, to be helpful in the framework of healthcare systems. Diabetes is one of the most widespread chronic diseases in the world, which is more and more spreading, due to increasing aging population and wrong lifestyles. Nowadays, the main drawback is due to the fact that usual monitoring tools, such as glucometers, are mostly invasive in nature, and they inhibit a continuous monitoring of blood. To face this problem, the adoption of microstrip technology has been recently proposed for the realization of low-cost microwave sensors able to exploit the correlation between the blood permittivity and the blood glucose levels. However, most of existing microwave sensor designs assume approximated dielectric models, thus limiting the accuracy in the reconstruction of blood glucose concentration (BGC). In this present work, a new enhanced version of the Cole-Cole model is proposed, which properly considers the variation of both real and imaginary parts of the blood permittivity when changing the glucose concentration and the operating frequency. Preliminary numerical results are also reported to show the effectiveness of the proposed approach.

## II. ENHANCED COLE-COLE DIELECTRIC MODEL

The Cole-Cole model gives an efficient and accurate representation of biological tissue behavior, being at present the most reliable dielectric representation versus frequency. The expression in the form of multiple dispersion is given as [1]:

$$\varepsilon_r(\omega) = \varepsilon_\infty + \sum_n \frac{\varepsilon_{sn} - \varepsilon_\infty}{1 + (j\omega\tau_n)^{1-\alpha}} + \frac{\sigma}{j\omega\varepsilon_0}. \quad (1)$$

In the above form, the Cole-Cole model has a strong limit, as no correlation exists between the complex permittivity and the blood glucose concentration. For this reason, the Cole-Cole model in the form of multiple dispersion (1), with two poles (n=2), was modified in [2] to include the glucose level  $g$ , but uniquely in the real part. This modified form of the Cole-Cole model is expressed as:

$$\begin{aligned} \varepsilon_r(\omega) = & \text{Re} \left[ \varepsilon_\infty + \sum_{n=1}^2 \frac{\varepsilon_{sn} - \varepsilon_\infty}{1 + (j\omega\tau_n)^{1-\alpha}} + \frac{\sigma}{j\omega\varepsilon_0} \right] \cdot (-0.001445 \ g + 1.145882) + \\ & + \text{Im} \left[ \varepsilon_\infty + \sum_{n=1}^2 \frac{\varepsilon_{sn} - \varepsilon_\infty}{1 + (j\omega\tau_n)^{1-\alpha}} + \frac{\sigma}{j\omega\varepsilon_0} \right]. \end{aligned} \quad (2)$$

In the present work, an enhanced version of the Cole-Cole model is proposed, basically adopting the two poles Cole-Cole equation (1), but extending the modified equation (2) by including also a correlation between the imaginary part of the blood permittivity with the glucose concentration and the operating frequency. In order to obtain the result, a curve fitting was carried out using experimental data from different water-glucose solutions, which exhibit the same dielectric behavior when changing the glucose concentration and the frequency. The proposed dielectric model for blood plasma is given as:

$$\begin{aligned} \varepsilon_r(\omega) = & \text{Re} \left[ \varepsilon_\infty + \sum_{n=1}^2 \frac{\varepsilon_{sn} - \varepsilon_\infty}{1 + (j\omega\tau_n)^{1-\alpha}} + \frac{\sigma}{j\omega\varepsilon_0} \right] \cdot (-0.001445 \ g + 1.145882) + \\ & + \text{Im} \left[ \varepsilon_\infty + \sum_{n=1}^2 \frac{\varepsilon_{sn} - \varepsilon_\infty}{1 + (j\omega\tau_n)^{1-\alpha}} + \frac{\sigma}{j\omega\varepsilon_0} \right] \cdot \left\{ [0.1256 + (0.000011 \ g)] \cdot \frac{\omega}{2\pi} + [0.2817 + (0.000074 \ g)] \right\}. \end{aligned} \quad (3)$$

It can be easily observed a dependency of the imaginary part from the glucose concentration as well as from the operating frequency.

## III. PRELIMINARY NUMERICAL VALIDATIONS

In this section, the accuracy improvement introduced by the proposed model (3) is numerically validated on the microwave sensor configuration first reported in [3]-[4]. It is a standard inset-fed patch

antenna working in the ISM-band around a frequency  $f_0=2.4$  GHz. In the present work, a stratified medium well simulating the human finger [6] is considered, as reported in Fig. 1.

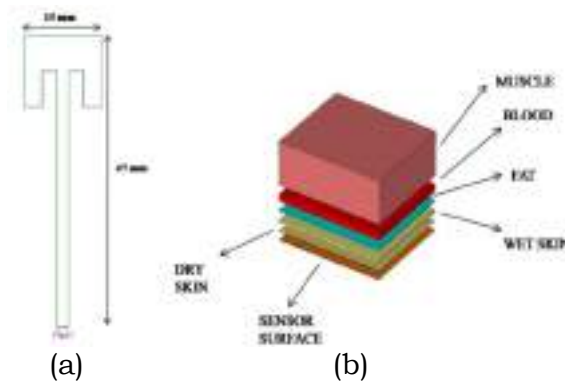


**FIG. 1**–Microwave sensor (a) and stratified configuration(b) for numerical validations.

As a first step, the dielectric model(2) is considered, which assumes the variation of the real part of the permittivity with respect to BGC, and the relative curves obtained from the sensor simulations on Ansys software are reported in Fig. 2.

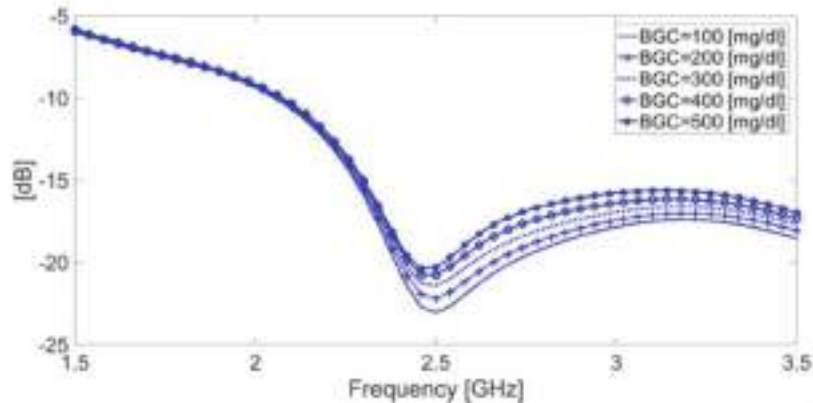


**FIG. 2**–Simulated return loss for different BGC (model as given by eq.(2)).

As a second step, the enhanced model (3) proposed in the present work is applied in order to obtain the simulations results reported in Fig.3.

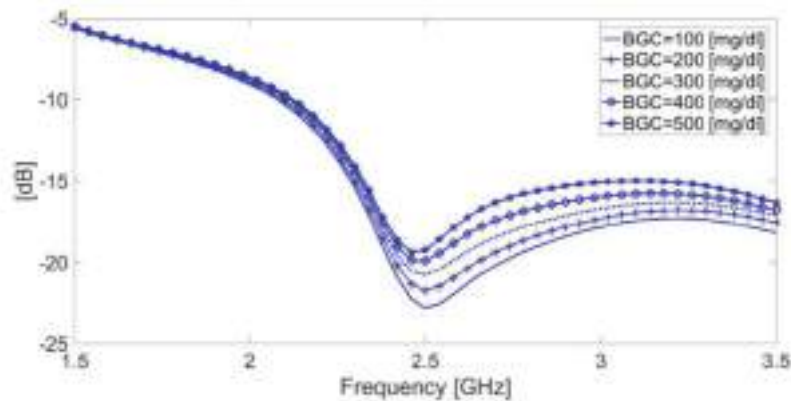


**FIG. 3**–Simulated return loss for different BGC (model as given by Eq.(3)).

Finally, in Fig.4, the comparison between the return loss amplitude obtained from the two models at various BGC is reported.

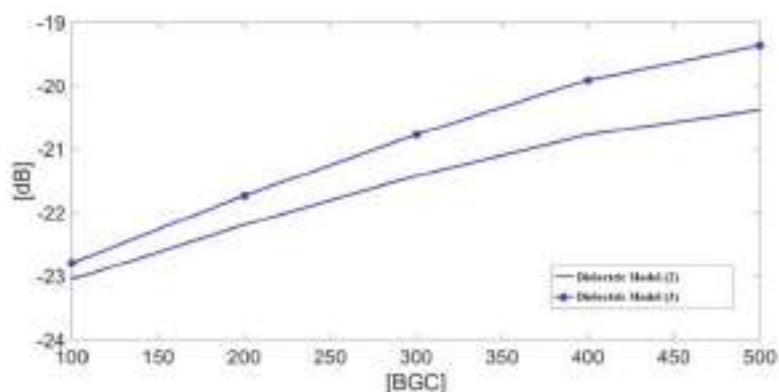


**FIG. 4**–Comparison of return loss amplitude vs BGC obtained from models (2) and (3).

It is evident that the dielectric model proposed in this work gives higher amplitude variations when changing the BGC, thus revealing a better characterization of the loss tangent effect.

#### IV. CONCLUSION

An enhanced Cole-Cole dielectric model, accurately predicting both the real part as well as the imaginary part of the blood permittivity as a function of both frequency and glucose concentration, has been proposed in this work. Numerical simulations have been performed as a preliminary validations, and the improved accuracy with respect to existing approaches in literature has been successfully demonstrated.

#### REFERENCES

- [1] S. Gabriel, R. W. Lau, C. Gabriel, “The dielectric properties of biological tissues: III. Parametric models for the dielectric spectrum of tissues,” *Physics in Medicine and Biology* 41, 2271-2293 (1996).
- [2] J. Venkataraman, B. Freer, “Feasibility of non-invasive blood glucose monitoring,” *In: 2011 IEEE AP-S/URSI Int. Symp.*, 603-606 (2011)..
- [3] S. Costanzo, “Non-invasive microwave sensors for biomedical applications: new design perspectives,” *Radioengineering* 26, 406-410 (2017).
- [4] S. Costanzo, “Loss tangent effect on the accurate design of microwave sensors for blood glucose monitoring,” *In: 11th EuCAP, Paris (France)*(2017).
- [5] S. Kumar, J. Singh, “Measuring blood glucose levels with microwave sensor,” *Int. Journal Computer Applicat* 72, 4-9 (2013).

# ANALYSIS OF PROPAGATION IN URBAN AREAS AT 3.7 AND 28 GHz FOR 5G WIRELESS NETWORKS

Gerardo Di Martino, Antonio Iodice, Daniele Riccio, Giuseppe Ruello

(1) Department of Electrical Engineering and Information Technology,  
University of Napoli Federico II  
Via Claudio 21, 80125 Napoli, Italy  
{[gerardo.dimartino](mailto:gerardo.dimartino@unina.it), [iodice](mailto:iodice@unina.it), [daniele.riccio](mailto:daniele.riccio@unina.it), [ruello](mailto:ruello@unina.it)}@unina.it

## Abstract

*Electromagnetic propagation in urban areas at 3.7 and 28 GHz, two frequencies currently employed for the first preliminary experiments of 5G networks in Italy and in USA, is here considered. The analysis is performed both by theoretical considerations and by using a raytracing solver, previously developed by the authors to deal with traditional mobile networks and now adapted to the new range of frequencies to be used in the near future.*

**Index Terms** – 5G, Electromagnetic propagation, millimeter waves, urban areas.

## I. INTRODUCTION

The demand for faster and faster data transfer, and the development of the Internet of things (IoT) and of machine-to-machine (M2M) communications, are urging toward a new generation of wireless networks, namely, the fifth generation (5G). The most obvious way to obtain the necessary bandwidth is to move towards higher frequencies, so that use of millimeter (mm) waves is being considered [1]. Accordingly, a strong effort is being made by researchers to characterize propagation of mm waves in complex environments, such as urban areas [2]. This year, some mobile phone companies in Italy are starting an experimentation of 5G networks to test the achievable quality of service (QoS) [3]. This experimentation is performed at 3.7 GHz (the frequency band released by the Italian Government for this purpose), but a possible aim is to try to “scale” obtained results also to the higher, 28 GHz, band, for which some results are available in recent literature [4].

In order to support such ongoing studies and experimentations, here we present an analysis of propagation at 3.7 and 28 GHz, both by theoretical considerations and by using a properly adapted version of a raytracing solver that we developed some years ago [5-6].

## II. ELECTROMAGNETIC SOLVER

The electromagnetic solver input is a digital description of the scene and of the transmitting antenna. The scene description is provided by a vectorial file in Planet or kml (Keyhole Markup Language) formats describing the buildings, and a raster file describing the terrain topography (Digital Terrain Model, DTM). Buildings' walls and terrain relative permittivity and conductivity can be also stored to account for the electromagnetic properties, that are frequency dependent.

A vertical-plane-lunching (VPL) raytracing algorithm is employed that considers direct, reflected and diffracted rays. Reflections are treated by using Geometrical Optics (GO), whereas diffraction is evaluated by using the Uniform Theory of Diffraction (UTD).

The electromagnetic field is computed on one or more regular 2-D grids ("layers") placed on surfaces at different fixed heights above the ground (or above the rooftop, if the grid point is in correspondence of a building).

## III. RESULTS

Differences between the propagation results at the two considered frequencies may be due, of course, to the different values of electromagnetic parameters of building walls and soil. Another significant difference is the increase of scattered and absorbed power by small obstacles (cars, people, etc.) and by vegetation at the higher frequency. However, the main dependence in the line-of-sight (LoS) case is expected to be the free-space power loss increase with the square of frequency (for fixed-gain receiving antennas). In the non-line-of-sight (NLoS) case, where the main propagation mechanism is diffraction, a further power loss increase proportional to frequency is added, so that an overall loss increase with the cube of frequency is expected. This theoretical expectation is mostly confirmed by solver simulations. For instance, in Fig. 1 simulated field levels in an area in the Naples city center at 3.7 (a) and 28 (b) GHz are shown. In the area A, characterized by a LoS link, an average difference of about 18 dB (corresponding to the square of the frequency ratio) between results at the two frequencies is obtained; and in the NLoS area B, in which the dominant mechanism is diffraction, an average difference of about 27 dB (corresponding to the cube of the frequency ratio) is present. Finally, in the NLoS area C, characterized by the so-called "canyoning" effect, in which both reflections and diffractions play a role, an intermediate average difference of about 22 dB is obtained.

It must be finally noted that, while atmospheric gases do not appreciably affect propagation at any of the two considered frequencies, attenuation by rain may significantly affect propagation at 28 GHz, see Fig. 2, where attenuation as a function of rain rate at 3.7 and 28 GHz is

plotted by using the empirical formulas of Olsen, Rodgers and Hodge, as reported in [7], page 404. The optional possibility to account for this further attenuation has been added to the solver of [5]-[6].

#### IV. CONCLUSIONS

Electromagnetic propagation in urban areas at two frequency bands of interest for 5G wireless networks has been considered. Main sources of differences between propagation behaviors in urban areas at the two considered frequencies have been briefly analyzed.

Performed analysis has only considered the received signal strength. However, the employed raytracing solver is also able to compute delay spread and angular spread: the former also affect the final QoS, and the latter can be exploited to devise the use of reconfigurable directive receiving antennas. Future work on these issues is planned.

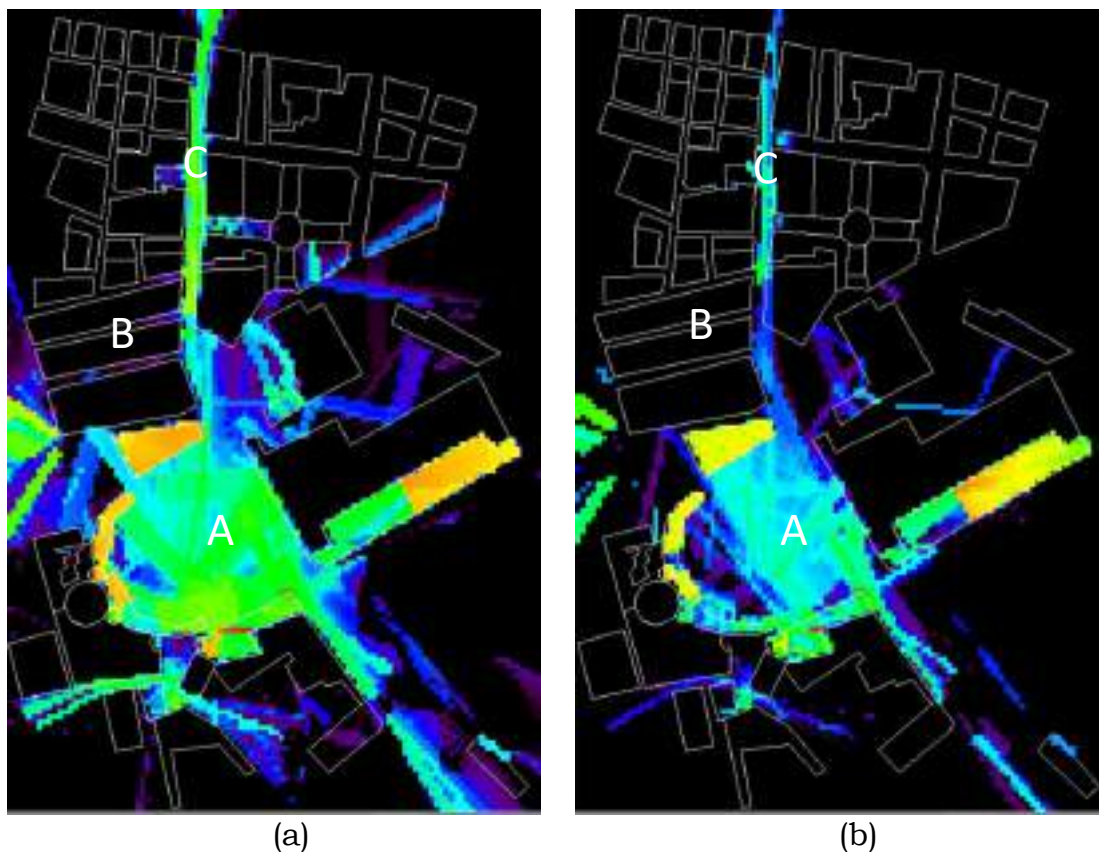


**FIG. 1** – Received signal strength  $L$ , in dBm, in the area of Piazza Plebiscito, Naples, Italy. The (omnidirectional) transmitting antenna is represented by a red diamond. Transmitted power is 5 W. (a) 3.7 GHz (black:  $L < -100$  dBm, red:  $L > -40$  dBm). (b) 28 GHz (black:  $L < -100$  dBm, red:  $L > -60$  dBm).

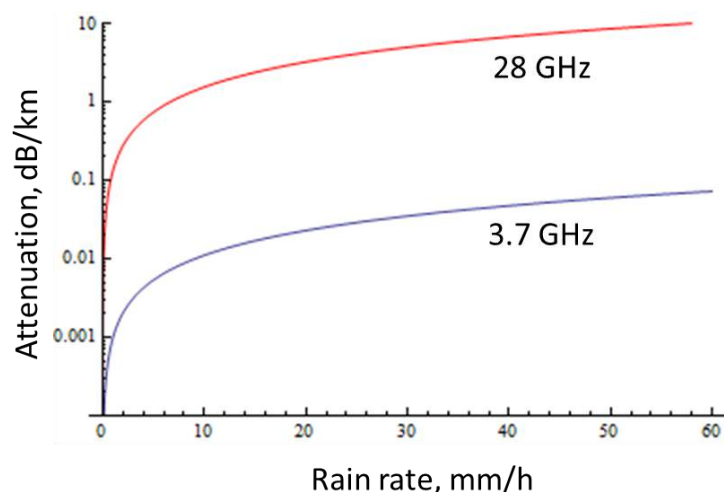


**FIG. 2** – Attenuation by rain (in dB/km) as a function of rain rate (in mm/h) at 3.7 and 28 GHz.

## REFERENCES

- [1] M. Agiwal, A. Roy, N. Saxena, “Next Generation 5G Wireless Networks: A Comprehensive Survey,” *IEEE Communications Survey & Tutorials*, vol.18(3), pp. 1617-1655, 2016.
- [2] T. S. Rappaport, Y. Xing, G. R. MacCartney, A. F. Molisch, E. Mellios, J. Zhang, “Overview of Millimeter Wave Communications for Fifth-Generation (5G) Wireless Networks—With a Focus on Propagation Models,” *IEEE Transactions on Antennas and Propagation*, vol. 65(12), pp. 6213-6230, Dec. 2017.
- [3] <http://www.sviluppoeconomico.gov.it/index.php/it/198-notizie-stampa/2037116-5g-in-5-citta-al-via-la-sperimentazione-della-tecnologia-mobile-di-v-generazione> , accessed on April 3, 2018.
- [4] T. S. Rappaport, G. R. MacCartney, M. K. Samimi, S. Sun, “Wideband Millimeter-Wave Propagation Measurements and Channel Models for Future Wireless Communication System Design,” *IEEE Transactions on Communications*, vol. 63(9), pp. 3029-3056, Sep. 2015.
- [5] G. Franceschetti, A. Iodice, D. Riccio, G. Ruello, “A Tool for Planning Electromagnetic Field Levels in Urban Areas”, *Proceedings of the Antennas and Propagation Society International Symposium*, Monterey (USA), 2004, pp. 2211-2214.
- [6] G. Franceschetti, A. Iodice, D. Riccio, G. Ruello, “Determinazione della Radiocopertura per Reti di Telecomunicazioni”, *Atti della XV Riunione Nazionale di Elettromagnetismo*, Cagliari, 2004, pp.477-480.
- [7] R. E. Collin, *Antennas and Radiowave Propagation*, McGraw-Hill, New York, 1985.

# ON THE REPEATABILITY OF THE EXPERIMENTAL CHARACTERIZATION UP TO 50 GHz OF *EX-VIVO* BREAST TISSUES

S. Di Meo<sup>1</sup>, P. F. Espin-Lopez<sup>1</sup>, A. Martellosio<sup>1</sup>

<sup>1</sup>Dept. of Electrical, Computer and Biomedical Engineering University of Pavia, Pavia, Italy  
simona.dimeo01@universitadipavia.it

## Abstract

*Breast cancer is one of the leading causes of death among women. In recent years, there has been an increase in the incidence rate, but the rate of death has decreased. This is also due to the improvement of diagnostic techniques, which are making possible to have diagnoses ever more precocious. However, all the techniques currently in use show limitations (such as the use of ionizing radiation) and therefore new imaging techniques are being studied. Microwave and millimeter waves imaging systems, based on the different behavior of healthy and tumorous tissues in the interest band, can be a viable alternative, so it is crucial to characterize the different human breast tissue up to 50 GHz. In 2014, in collaboration with the European Institute of Oncology in Milan, Italy, and in a project funded by the Italian Association for Cancer Research, a first experimental campaign on ex-vivo samples was conducted. In this paper, the results of a second experimental campaign, conducted in 2016 by the same team, are shown.*

**Index Terms** – Breast cancer detection; dielectric characterization; ex-vivo samples; dielectric properties; microwave and mm-wave imaging; sensitivity; specificity.

## I. INTRODUCTION

Breast cancer is the most diffused disease among women in the world. Nowadays, it is one of the first cause of death between women. However, during the last years, the improvement in diagnostic techniques and in knowledge about cancer are allowing to decrease the death rate, despite the increase in the incidence rate [1], [2].

Nevertheless, the well recognized limitations of the actual screening methods for breast cancer detection are requiring new imaging techniques. In particular, the three most commonly used techniques are the X-ray mammography, the ultra-sound echography, and the magnetic resonance imaging. However, all of them show important limitations, such as the woman exposition to ionizing radiation (X-ray mammography), the operator dependence as well as the suitability of making diagnosis only for dense breasts (ultrasound echography), and the requirement of very expensive machines (breast magnetic resonance), so for all these reasons new imaging techniques are welcome.

Microwave imaging has been proposed as a promising alternative to the current methods. A number of prototypes have been proposed up to

now around the world at microwave frequencies [3]–[8]. However, the low central working frequency and the narrow band involved, do not give the possibility of making an early diagnosis fundamental point to increase the possibility of having successful pharmacological treatments [3], [9].

For this reason, higher central working frequencies and larger bandwidths are envisaged [10], [11]. This requires the dielectric characterization of breast tissues up to 50 GHz. In collaboration with the European Institute of Oncology in Milan, Italy, and in the framework of a project funded by the Italian Association for Cancer Research, a first experimental campaign on ex-vivo breast tissues have been performed in 2014, showing the high dielectric contrast between healthy and tumorous tissues up to 50 GHz [12], [13].

This paper presents the results a second experimental campaign, performed in 2016, aimed at validating the results achieved in 2014. This second experimental campaign was carried out at the Pathological Anatomy Department of the European Institute of Oncology in Milan, Italy, involving the same experimental setup used in 2014 [12], [13]. It included 124 breast samples, 81 healthy and 43 tumorous, taken from 45 different patients.

## II. EXPERIMENTAL CAMPAIGN

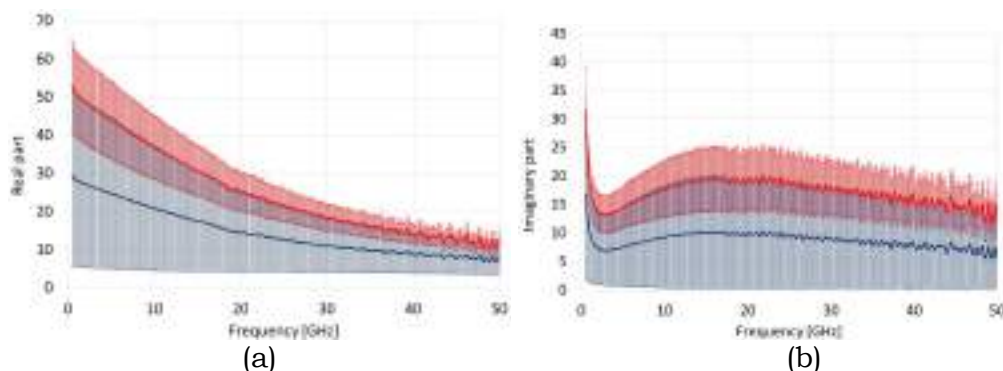
The measurement setup is composed by an high precision open-ended coaxial probe (Keysight 85070E Dielectric Probe Kit), able of making measurements in a broad range of frequency [0.5-50] GHz, connected through an high-performance flexible coaxial cable to the Vector Network Analyzer, which is used to retrieve and store the dielectric permittivity of the sample under test. Fig. 1 shows the measurement system, same as for [12], [13].

Fig. 2 shows the comparison in terms of mean values and a variable region defined by  $\pm 1$  standard deviation.

It can be appreciated that the results are very similar to those reported in [12] in terms of mean values, thus confirming the database, with variable regions that tend to be larger because of the reduced number of samples with compared to [12].



**Fig. 1** – Measurement setup.



**Fig. 2** – Comparison between the relative dielectric permittivity of normal and tumorous tissues: (a) real part; (b) imaginary part.

In addition, since each diagnostic technique is evaluated basing on its quality of identifying as sick one person which is really sick and on the contrary as healthy one person which is healthy (two percentage parameters take named *Sensitivity* and *Specificity*), these two values have been computed using the procedure explained in [14]. Fig. 3 shows the achieved results.

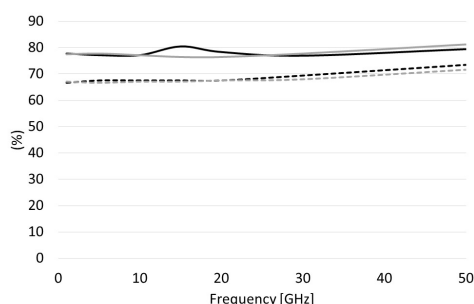


**Fig. 3** – Plot of *Sensitivity* (solid lines) and *Specificity* (dotted lines) versus frequency calculated for real (black lines) and imaginary (grey lines) part of the relative dielectric permittivity.

### III. CONCLUSIONS

In this paper, the second experimental campaign on ex-vivo samples performed at the European Institute of Oncology in Milan, Italy, on 124 breast samples, 81 healthy and 43 tumorous, taken from 45 different patients, was shown. Results are in agreement with [12].

### ACKNOWLEDGEMENT

The authors would like to thank all the medical staff of the European Institute of Oncology in Milan for their help during the work, the Italian Association for Cancer Research, and Alessia Iuele and Laura Suma for their work during the analysis of the experimental results.

### REFERENCES

- [1] “International Agency for Research on Cancer,” <http://globocan.iarc.fr/>.
- [2] “Cancer Treatment and Survivorship Facts & Figures 2014-2015,” *Atlanta: American Cancer Society; 2014*.
- [3] N. K. Nikolova, “Microwave imaging for breast cancer,” *IEEE Microwave Magazine*, Vol. 12, No. 7, pp. 78–94, December 2011.
- [4] M. Klemm, *et al.*, “Radar-based breast cancer detection using a hemispherical antenna array - experimental results,” *IEEE Transactions on Antennas and Propagation* Vol. 57, No. 6, pp. 1692–1704, June 2009.
- [5] T. M. Grzegorzczuk *et al.*, “Fast 3-D tomographic microwave imaging for breast cancer detection,” *IEEE Trans. Med. Imag.*, Vol. 31, No. 8, pp. 1584–1592, August 2012.
- [6] E. C. Fear, *et al.*, “Microwave breast imaging with a monostatic radar-based system: a study of application to patients,” *IEEE Transactions on Circuits and Systems*, Vol. 61, No. 5, pp. 2119–2128, May 2013.
- [7] M. J. Burfeindt, *et al.*, “Beamforming-Enhanced Inverse Scattering for Microwave Breast Imaging,” *IEEE Trans. Ant. and Prop.*, Vol. 62, No. 10, pp. 5126–5132, June 2009.
- [8] H. Bahramiabarghouei, *et al.*, “Flexible 16 antenna array for microwave breast cancer detection,” *IEEE Transactions on Biomedical Engineering*, Vol. 62, No. 10, pp. 2516–2525, October 2015.
- [9] M. Klemm, I. J. Craddock, and A. W. Preece, “Contrast-enhanced breast cancer detection using dynamic microwave imaging,” *2012 IEEE Ant. Propag. Society International Symposium*, Chicago, U.S.A., July 8–14, 2012.
- [10] S. Di Meo, *et al.*, “On the Feasibility of Breast Cancer Imaging Systems at Millimeter-Waves Frequencies,” *IEEE Trans. Microw. Theory Techn.*, Vol. 65, No. 5, pp. 1795-1806, May 2017.
- [11] S. Moscato, *et al.*, “A mm-Wave 2D ultra-wideband imaging radar for breast cancer detection,” *Int. J. Antennas Propag.*, Vol. 2013, Article ID 475375, 8 pages, 2013, doi:10.1155/2013/475375.
- [12] A. Martellosio, *et al.*, “Dielectric properties characterization from 0.5 to 50 GHz of breast cancer tissues,” *IEEE Trans. Microw. Theory Techn.*, Vol. 65, No. 3, pp. 998-1011, March 2017.
- [13] A. Martellosio, *et al.*, “0.5-50 GHz Dielectric Characterization of Breast Cancer Tissues,” *IET Electron. Lett.*, Vol. 51, No. 13, pp. 974-975, June 2015.
- [14] S. Di Meo, *et al.*, “Experimental Validation of the Dielectric Permittivity of Breast Cancer Tissues up to 50 GHz”, *IEEE MTT-S Intern. Microw. Workshop Series*, Pavia, Italy, September 20-22, 2017.

# **SVM CLASSIFICATION OF ALZHEIMER'S DISEASE USING MRI AND fMRI**

C. Dachena<sup>(1)</sup>, A. Allocca<sup>(1)</sup>, I. Meloni<sup>(1)</sup>, A. Fanti<sup>(1)</sup>, G. Mazzarella<sup>(1)</sup>

<sup>(1)</sup> Department of Electrical and Electronic Engineering, University of Cagliari  
Cagliari  
Piazza D'Armi, 09123 Cagliari, Italy  
[alessandro.fanti@diee.unica.it](mailto:alessandro.fanti@diee.unica.it)

## **Abstract**

*Magnetic resonance imaging has the clinical potential of helping diagnosis in providing to doctors structural and functional information of several neurological disorders. Linking the structural results to functional findings through the Spearman's correlation coefficient, 69 subjects from ADNI open-database, 33 Alzheimer's patients and 36 healthy controls, were analyzed. In HC group 9 ROIs presented correlation between structural and functional features, whereas in AD only 4 ROIs were correlated. To discriminate Alzheimer's disease, a support vector machine classification (SVM) was applied, to combine information from MRI, fMRI and clinical data from MMSE.*

**Index Terms** – Alzheimer's Disease, Biomedical image processing, graph theory, magnetic resonance imaging, medical diagnostic imaging.

## **I. INTRODUCTION**

Magnetic Resonance Imaging (MRI) and functional Magnetic Resonance Imaging (fMRI) of brain have become popular methods of inquiry in neuroscience [1]. MRI can be used to probe the structural environment and fMRI can be employed to detect changes in Blood Oxygenation Level Dependent (BOLD) signals. One of the most spread neurodegenerative disorder is Alzheimer's disease (AD), characterized by a severe derangement of cognitive functions and structural changes. In functional imaging, the BOLD signal reflects the activity degree of brain areas. New approaches founded on the graph theory [2], have been proposed to investigate in vivo alterations in cerebral functional and structural networks.

In this paper, MRI data were processed to extract structural features, while fMRI features were exploited to evaluate connectivity measures. Moreover, we evaluate the possibility of correlating the grey matter volume (GMV) with the clustering coefficient (CC). Finally, the measurements from three features, i.e. GMV, CC and MMSE, are combined to discriminate between AD and HC, through a Support Vector Machine (SVM).

## **II. METHODS AND PROCEDURE**

### *A. MRI and magnetic mechanism of BOLD signal*

The desire to extract biological information from intact biological systems using MRI and fMRI introduced new technologies that allowed the study of human brain activity with greater detail and resolution [3]. MRI offers more contrast possibility than radiological methodology. Contrast helps in recognizing different biological tissues and structure. However, it depends on both the longitudinal relax time (T1) and transversal relax time (T2\*). To perform studies on AD using MRI images, data acquired with high T1 and low T2 are necessary. In this way, structural features can be adequately evaluated [3].

BOLD signal represents the hemodynamic response of cerebral activation. Deoxyhemoglobin and oxyhemoglobin present paramagnetic and diamagnetic compartments respectively, leading to a shift of the local magnetic susceptibility [1]. In MRI, material's magnetization is directly proportional to magnetic field [3]. For this reason, different magnetization provokes different signals in fMRI.

#### *B. Data acquisition and preprocessing*

All subjects used in this study were selected from the Alzheimer's disease Neuroimaging Initiative (ADNI) database. A total of 69 subjects, 33 AD and 36 HC, were considered. Subjects demographic data are summarized in Table. I. Resting state data and structural MRI scans were acquired with 3.0 T Philips Medical System scanner. MRI data include high-resolution T1-weighted scans and an 8-channel receive-only head coil. Parameters include: sagittal plane, Slices = 170, TR = 6.77 ms, TE = 3.13 ms, TI = 0 ms, FA = 9°, Matrix = 256x256, Voxel size = 1.0 x 1.0 x 1.2 mm<sup>3</sup>. All the resting state scans consist of 140 functional volumes. Parameters include: TR = 3000 ms, TE = 30 ms, flip angle = 80°, slice thickness = 3.313 mm, 48 slices. Images were processed using the CONN functional connectivity toolbox v15.a (nitrc.org).

#### *C. Structural and functional measurements*

Employing the Wake Forest PickAtlas software (fmri.wfubmc.edu), masks were limited to a priori regions of interest (ROIs) through the Automated Anatomical Labelling atlas. This atlas included 90 ROIs. These masks were employed to quantify ROI volume and connectivity as in [4]. In this study, we make use of connectivity matrices 90x90. Each value in matrices represents functional connectivity that is defined as statistical dependencies among remote neurophysiological events [5]. Connectivity matrices are used to perform the network measure, i.e. a clustering coefficient [6]. This measure was calculated with the Brain Connectivity Toolbox (BCT) (n-connectivity-toolbox.net).

#### *D. Support Vector Machine (SVM)*

Support Vector Machine is an efficient supervised learning method which can organize large dimensional data classification. In this study the SVM classifier was implemented in Matlab. This method is useful

when there is only two class of data; classification is done such that the marginal between the two class is as more as possible. To train the SVM classifier 35 subjects were employed as training set, whereas 34 for test set.

### **III. RESULTS**

The correlation analysis between grey matter volume and clustering coefficient in the ROIs was assessed. In this work, across groups, GMV and clustering coefficient were correlated in 7 ROIs; higher GMV was associated with high CC in the right supplementary motor area ( $\rho = 0.3107$ ). Within HC group, 9 ROIs presented correlation between grey matter volume and CC. Higher GMV was associated with higher correlation coefficient in the left calcarine ( $\rho = 0.4597$ ). Within AD group, only 4 ROIs presented correlation between GMV and CC. Higher GMV was associated with higher CC in the left hippocampus ( $\rho = 0.4014$ ). Positive correlation coefficient demonstrates that for GMV decreasing had lower clustering coefficient, implying that pathology caused reduction in structural features and functional variables.

Finally, the SVM classification was performed. Firstly, it was tested the performance of unimodal classification method in identification of AD from healthy control, based on MRI and fMRI. Specifically, when using only MRI data, it is possible to achieve a classification accuracy of 68.57%, a sensitivity of 50%, and a specificity of 88%. On the other hand, for classifying AD subjects from HC ones relying on fMRI data only, the method shows a classification accuracy of 64.10%, a sensitivity of 50%, and a specificity of 78.94%. In the end, the combined measurements of MRI, fMRI and MMSE was investigated. As it can be noticed from Fig. 1, the combination of the three measurements achieves a more accurate classification and discrimination between AD and HC. In this case the method can achieve a classification accuracy of 88.57%, a sensitivity of 77%, and a specificity of 100%.

### **IV. CONCLUSIONS**

In this paper, morphological MRI and functional MRI images processing was analyzed to verify the possibility of correlating anatomical and functional data and to confirm the difference between the AD and HC groups through the SVM. First, the potential association between GMV and CC in the ROIs was analyzed to try to correlate anatomical and functional results. AD group showed positive correlation in 4 ROIs, while in HC group there are 9 ROIs correlated. This result makes it possible to put in relationship morphological and functional data. Finally, the SVM classification was performed. In our study we have put in prominence the capability to discriminate better between AD group and HC combining the structural, functional, and clinical feature. Additional studies could provide further analysis and could confirm

these findings. The correlation between grey matter volume and clustering coefficient can be used to stress other features or to better investigate this aspect without non-invasive imaging techniques. Instead, through the use of a classifier, it is possible to discriminate AD patients from healthy control, and this could be a potential use in clinical applications.

TABLE I  
DEMOGRAPHIC AND NEUROPSYCHOLOGICAL CHARACTERISTICS OF SUBJECTS

	HC subjects	AD patients	P-value
Number of Subject	36 (21F/15M)	33 (18F/15M)	>0.99 <sup>b</sup>
Age, years	72.51 (±5.40)	72.72 (±7.52)	p > 0.05 <sup>a</sup>
MMSE	26.6667 (±1.36)	22.6667 (±2.45)	p = 2.828e-12 <sup>a</sup>

<sup>a</sup> The  $P$  value was obtained by a two-sample two-tailed  $t$  test

<sup>b</sup> The  $P$  value was obtained by Pearson  $\chi^2$  two tailed test

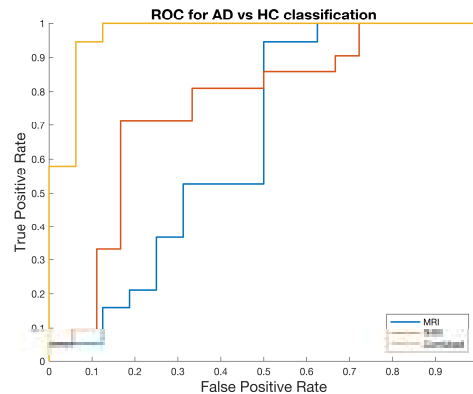


Fig. 1. ROC curves of different methods, for AD classification

## REFERENCES

- [1] F. Winter, C. Bludszweit-Philipp, O. Wolkenhauer, "Mathematical analysis of the influence of brain metabolism on the BOLD signal in Alzheimer's disease," *Journal of Cerebral Blood Flow & Metabolism*, vol. 0, pp. 1–13, Jan. 2017.
- [2] M. Rubinov, O. Sporns, "Complex network measures of brain connectivity: uses and interpretations," *Neuroimage*, vol. 52, pp. 1059–1069, Sept. 2010.
- [3] M. Coriasco, O. Rampado, G. B. Bradac, "Elements of Magnetic Resonance," in *Imaging&Formation*, 1<sup>st</sup> ed, Italy: Springer-Verlag 2014, ch. 6.
- [4] P. Fransson, G. Marrelec, "The precuneus/posterior cingulate cortex plays a pivotal role in the default mode network: Evidence from a partial correlation network analysis," *Neuroimage*, vol.42, pp. 1178-1184, Sept. 2008.
- [5] K. J. Friston, "Functional and effective connectivity in neuroimaging: a synthesis," *Human brain mapping*, vol. 2, pp. 56–78, Sept. 1994.
- [6] C. J. Stam, C. R. Jaap, "Graph theoretical analysis of complex networks in the brain," *Nonlinear biomedical physics*, vol. 1, 2007.

# EFFECTIVE ANTENNA DESIGN METHODOLOGIES FOR NEW GENERATION 5G MIMO SYSTEMS

G. Gottardi<sup>(1)</sup>

<sup>(1)</sup> ELEDIA Research Center (ELEDIA@Unitn - University of Trento)  
Via Sommarive 9, I-38123 Trento, Italy  
[giorgio.gottardi@unitn.it](mailto:giorgio.gottardi@unitn.it)

## Abstract

*The massive data-rate required from future generation mobile systems demands a new prospective in the development of design methodologies of antenna arrays for mobile communications. This work is aimed at showing that data-rate performance of a mobile communication system can be maximized only if the design methodology takes into consideration the behavior of the propagation scenario rather than “conventional” pattern parameters. A numerical example, in a real test-case scenario, is shown to provide a preliminary proof of the proposed concept.*

**Index Terms**—5G, array design, innovative design methodologies, MIMO, mobile communications

## I. INTRODUCTION

Multiple-input multiple-output (MIMO) architectures for new generation mobile communication systems are required to deliver high data rates to multiple users with low connection latencies [1], [2]. In order to fulfill these challenging requirements, new antenna topologies such as Massive MIMO antenna arrays, have been addressed [2]. However, the complexity introduced from these new architectures further increases the need of methodologies able to deal with the design problem in an effective manner. Nowadays design methodologies for MIMO antenna array architectures are mainly focused on the design of solutions with optimal trade-offs in terms of pattern parameters [3], [4] and architecture complexity [5], [6]. The goal of this work is to provide a preliminary proof that the fulfillment of stringent constraints on the radiated pattern does not imply the optimization of the data-rate performance. On the contrary, architectures with an optimal data-rate performance can be achieved only by taking into consideration the characteristics of the propagation scenario within the design process.

## II. MATHEMATICAL FORMULATION

Let us consider a point-to-point downlink MIMO scenario where one Base Station (BS) device, with  $N$  elements, is serving one User Equipment (UE) device with  $M$  elements. At the BS device, the input data stream is fed to the  $N$  radiating elements through the Beam-forming Network (BFN)  $\mathbf{b}_{TX}$ .

At the receiver side, the  $m$ -th element of the UE device collects the signal

$$g_m(t) = \sum_{n=1}^N \int_{-\infty}^{+\infty} h_{mn}(t-\tau) s_n(\tau) d\tau + z_m(t); \quad m = 1, \dots, M \quad (1)$$

where  $s_n(t)$  is the signal transmitted from the  $n$ -th radiating element of the BS device,  $z_m(t)$  is the noise signal and  $h_{mn}(t)$  is the Green's function of the propagation channel. Finally, signals from the  $M$  elements of the UE device are decoded into the output data-stream by means of the BFN  $\mathbf{b}_{RX}$ .

When considering an *AWGN* noise with variance  $\gamma$  and a transmitted power  $P_{in}$ , the capacity value can be computed as [1],[7],[8]

$$C = \log_2 \left[ \det \left( 1 + \frac{1}{\gamma} \mathbf{b}_{RX} \mathbf{H} \mathbf{b}_{TX} P_{in} \mathbf{b}_{TX}^H \mathbf{H}^H \mathbf{b}_{RX}^H \right) \right] \left[ \frac{bps}{Hz} \right] \quad (2)$$

where  $^H$  is the complex-conjugate transpose operator and  $\mathbf{H}$  collects the Green's functions of each BS and UE elements pair.

The Green's functions in Eq. (2) have a fundamental impact on the data-rate performance that the system can achieve. In fact, it has been shown in [1], [7], [8] that the system can achieve the maximum capacity only if both BS and UE devices have a perfect knowledge of the propagation channel. Indeed, it has been shown in [1], [8] that the optimal sets of BFN weights  $\mathbf{b}_{TX}^{opt}$  and  $\mathbf{b}_{RX}^{opt}$  can be computed from the single value decomposition (SVD) of the channel matrix  $\mathbf{H} = \mathbf{U} \mathbf{\Sigma} \mathbf{V}^H$  by choosing

$$\mathbf{b}_{RX}^{opt} = \mathbf{u}_1^* \quad (3)$$

and

$$\mathbf{b}_{TX}^{opt} = \mathbf{v}_1 \quad (4)$$

where  $\mathbf{u}_1^*$  is the first column of  $\mathbf{U}^H$  and  $\mathbf{v}_1$  is the first column of  $\mathbf{V}$ .

### III. NUMERICAL RESULTS

Let us consider a mobile MIMO communication system operating in the realistic urban scenario, modeled as a "Madrid-grid" urban micro-cell environment [2], shown in Fig. 1.

The BS device, placed in  $\mathbf{r}_{TX} = [129.0, 205.0, 7.0][m]$ , has been modeled as a  $4 \times 8 = 32$  planar array with dipole elements placed with an inter-element distance equal to  $d_{TX} = 0.5[\lambda]$ . The UE device, placed in  $\mathbf{r}_{RX} = [287.24, 264.12, 1.5][m]$ , has been modeled as  $M = 2$  dipole elements placed along the  $z$ -axis at  $d_{RX} = 0.5[\lambda]$  distance. Due to its position in the scenario and according to the "Madrid-grid" environment model the UE device will experiment a Non-Line-of-Sight (NLOS) condition [2]. The system operates at a frequency of 2 [GHz], the power

transmitted from the BS is equal to  $P_{in} = 0[dB]$  and the AWGN noise variance at the receiver is equal to  $\gamma = -94[dB]$ .

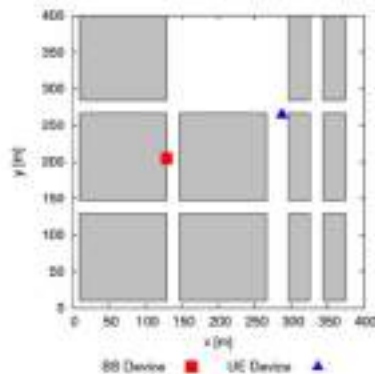


**FIG. 1** – 2D sketch of the considered scenario.

In order to prove the proposed concept, the set of Green’s functions that characterizes the MIMO system in Fig. 1 have been simulated by means of the QuaDRiGa channel generator [9]. The data-rate performance as well as “classical” pattern parameters have been evaluated when considering: (i) optimal BFN weights of Eq. (4) at the transmitter and (ii) the set of BFN weights with uniform amplitude values maximizing the radiation pattern directivity in the UE direction. In both test-cases  $\mathbf{b}_{TX}$  has been normalized in order to have  $\|\mathbf{b}_{TX}\| = 1$  and  $\mathbf{b}_{RX} = \mathbf{b}_{RX}^{opt}$  as in Eq. (3).

Fig. 2 shows the normalized power pattern as a function of the direction cosines, for the optimal BFN weights [Fig. 2(a)] and for the uniform amplitude weights [Fig. 2(b)]. Moreover,  $SLL$  and  $D_{max}$  pattern performance, as well as the capacity values, are reported and compared for the two test-cases in Table I.

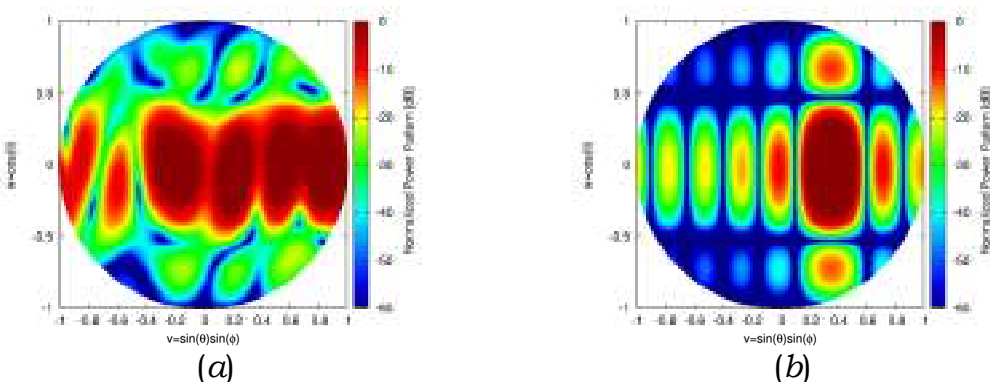


**FIG. 2** – Normalized power pattern in the (v,w) plane of (a) optimal BFN weights and (b) uniform amplitude weights

By analyzing Table I and Fig. 2 it can be noticed that the pattern performance achieved in the second test-case is considerably better than the performance achieved in the first test-case.

**TABLE I – PATTERN PARAMETERS AND CAPACITY VALUES COMPARISON**

		Optimal BFN weights	Maximum directivity BFN weights
$SLL$	[dB]	-0.52	-12.80
$D_{\max}$	[dB]	10.21	16.64
$C$	[bps/Hz]	0.265	0.019

However, Table I shows that the capacity value in the second test-case is notably lower if compared with the capacity value achieved in the first test-case.

#### IV. CONCLUSION

In this work it has been shown that design methodologies for new generation mobile communication systems must take into consideration the characteristics of the propagation channel to achieve solutions with the optimal data-rate performance. Moreover, it has been shown that optimal performance in terms of pattern parameters, such as the sidelobe level or the directivity, does not imply optimal performance in terms of achieved data-rate.

#### REFERENCES

- [1] A. J. Paulraj, D. A. Gore, R. U. Nabar, and H. Bloskei, "An overview of MIMO communications - a key to gigabit wireless," *Proc. IEEE*, vol. 92, pp. 198-218, Feb. 2004.
- [2] P. Kyosti, J. Lehtomaki, J. Medbo, and M. Latva-aho, "Map-Based Channel Model for Evaluation of 5G Wireless Communication Systems," *IEEE Trans. Antennas Propag.*, vol. 65, no. 12, pp. 6491-6504, Dec. 2017.
- [3] L. Manica, P. Rocca, and A. Massa, "Design of subarrayed linear and planar array antennas with SLL control based on an excitation matching approach," *IEEE Trans. Antennas Propag.*, vol. 57, pp. 1684-1691, Jun. 2009.
- [4] G. Oliveri, M. Salucci, and A. Massa, "Synthesis of modular contiguously clustered linear arrays through a sparseness-regularized solver," *IEEE Trans. Antennas Propag.*, vol. 64, no. 10, pp. 4277-4287, Oct. 2016.
- [5] P. Rocca, G. Oliveri, R. J. Mailloux, and A. Massa, "Unconventional phased array architectures and design methodologies - A review," *Proc. IEEE*, vol. 104(3), pp. 544-560, Mar. 2016.
- [6] G. Oliveri, G. Gottardi, F. Robol, A. Polo, L. Poli, M. Salucci, M. Chuan, C. Massagrande, P. Vinetti, M. Mattivi, R. Lombardi, and A. Massa, "Co-design of unconventional array architectures and antenna elements for 5G base station," *IEEE Trans. Antennas Propag.*, vol. 65(12), pp. 6752-6767, Dec. 2017.
- [7] A. Goldsmith, *Wireless Communications*, 3rd Ed. New York, NY: Cambridge University Press, 2005.
- [8] M. A. Jensen and J. W. Wallace, "A Review of Antennas and Propagation for MIMO Wireless Communications," *IEEE Trans. Antennas Propag.*, vol. 52, no. 11, pp. 2810-2824, Nov. 2004.
- [9] S. Jaeckel, L. Raschkowski, K. Borner, and L. Thiele, "QuaDRiGa: A 3-D multi-cell channel model with time evolution for enabling virtual field trials," *IEEE Trans. Antennas Propag.*, vol. 62, no. 6, pp. 3242-3256, Jun. 2014.

# FEASIBILITY STUDY ON THE USE OF MICROWAVE IMAGING FOR IN-LINE MONITORING OF FOOD CONTAMINATION

L. Farina<sup>(1)</sup>, J. A. Tobon Vasquez<sup>(1)</sup> and R. Scapaticci<sup>(2)</sup>

<sup>(1)</sup> DET, Politecnico di Torino, Torino, Italy

<sup>(2)</sup> IREA, National Council of Research of Italy, Naples, Italy

[scapaticci.r@irea.cnr.it](mailto:scapaticci.r@irea.cnr.it)

## Abstract

*This communication describes the outcomes of a feasibility study on the use of microwave imaging for detecting food contamination in products moving along the production chain. To cope with this challenging scenario, in which the measurement time is reduced and only a limited amount of data is available, an imaging strategy taking advantage of the target's movement and of the small size of the sought contamination is developed. The rationale of the approach is described and assessed in a simple, yet meaningful case.*

**Index Terms** – microwave imaging, non-invasive diagnostics, food inspection, food security, food safety.

## I. INTRODUCTION

Foreign body contamination is among the main causes of costumers' complaint against food manufacturers, resulting in loss of brand loyalty and large recall expenses [1]. Food industry is particularly exposed to these type of problems, especially nowadays that aware consumers place much more attention to the quality and integrity of purchased food.

To cope with these issues, technologies such as metal detectors (MD), X-ray (XRI) and near infrared (NIR) imaging are currently adopted. However, the occurrence of incidents remains significant. As a matter of fact, these technologies suffer several limitations. For instance, MD can only detect metallic objects, whereas XRI cannot easily recognize low-density foreign objects such as most plastics, thin glass and wood (the most common type of contaminants) and can be harmful for operators. Finally, NIR techniques are rapid and safe but limited by the short penetrating length and the strong absorption in water. For these reasons, novel technologies must be developed to address all the requirements of food-industry.

Among the possible candidates, microwave technologies represent an attractive, cost-effective option [2]. In fact, food characteristics (e.g., water content) affect the food EM properties at microwaves, which are in turn detected by EM devices.

In this communication, the use of microwave imaging for food inspection is investigated with respect to a challenging case study relevant to a broad range of users. In particular, the validation concerns the assessment of a plastic or glass jar containing semi-solid food (e.g., jam, chocolate-based spreads, honey or baby food), moving along the production chain.

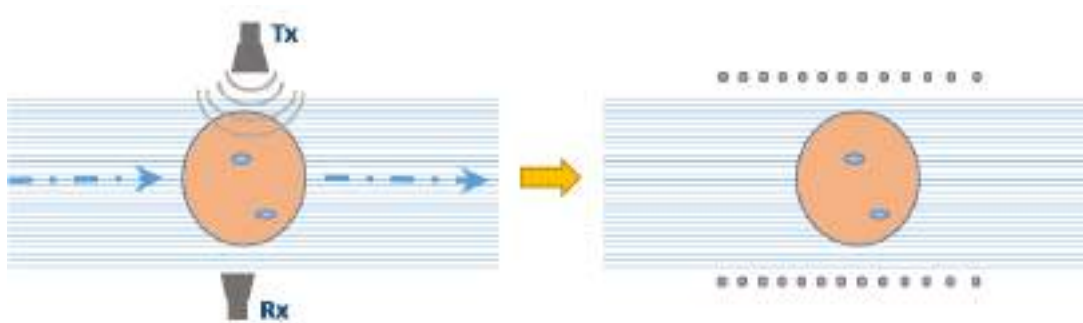


**FIG. 1** – Conceptual scheme of the microwave device for food monitoring. (a) The target moving along the production chain probed by the two-antennas system; (b) the scenario modeled in the imaging problem.

The goal is to detect the presence of foreign bodies (e.g., plastic or glass fragments), whose size is as small as a few millimetres.

## I. RATIONALE OF THE DEVELOPED MONITORING SYSTEM

In the considered scenario, the movement of the object under test poses definite constraints on the speed of acquisition (and therefore amount of available data) and elaboration. As such, developing an MWI device capable to assess products without interrupting or delaying the production process requires suitable strategies to cope with these aspects.

To this end, we have explored the feasibility of a “synthetic aperture” approach, by considering just a pair of antennas placed at the sides of the chain, see Fig.1(a). The relative movement of the object under test with respect to the measurement device is exploited to introduce the “diversity” in observation needed to implement a tomographic imaging algorithm, see Fig1(b). It is important to highlight that, in this arrangement, no “cross-position” information is however available.

In addition, to enable real-time monitoring, a “model-based” differential imaging approach based on the distorted Born approximation [3] has been developed. In particular, the tomographic images are obtained by processing the data obtained from the difference of the signals measured for the object under test and those measured for a “standard” – i.e., uncontaminated - object. Such an approach is reasonable in this kind of applications, wherein objects are indeed expected to be identical. Moreover, given the small size of the sought contaminations, it is further reasonable to assume a linearized model of the electromagnetic scattering, as the one underlying the adopted approximation.

## II. IMPLEMENTATION AND NUMERICAL ASSESSEMENT

By relying on the distorted Born approximation, the differential data from the current jar with respect to the reference one is given by

$$\Delta S(\mathbf{r}_p, \mathbf{r}_q) = \frac{-j\omega\epsilon_b}{4} \int_D \mathbf{E}_b(\mathbf{r}_p, \mathbf{r}) \cdot \mathbf{E}_b(\mathbf{r}, \mathbf{r}_q) \Delta\chi(\mathbf{r}) d\mathbf{r} = L(\Delta\chi), \quad (1)$$

where  $D$  is the domain of interest,  $p$  and  $q$  are the transmitter and the receiver probes' indexes and  $\Delta\chi$  is the variation of the contrast with respect to the reference scenario due to the food contamination.  $\mathbf{E}_b$  is the total field radiated by the  $p$  antenna in absence of  $\Delta\chi$  (and in presence of the uncontaminated jar).  $L$  is the linear scattering operator, which relates the data  $\Delta S$  to the unknown  $\Delta\chi$  of the problem.

The tomographic image is formed by using the Truncated Singular Value Decomposition (TSVD) scheme [4]:

$$\Delta\chi = \sum_{n=1}^T \frac{1}{\sigma_n} \langle \Delta S, u_n \rangle v_n \quad (2)$$

where  $[u_n, \sigma_n, v_n]$  is the singular value decomposition of  $L$  in eq. (1), while  $T$  is the truncation index representing the regularization parameter of the linear and ill-posed inverse problem in (1) and it is chosen as a trade-off between accuracy and stability of the reconstruction.

The considered testbed is the monitoring of a 3 mm thick glass jar filled with hazelnut-cocoa cream. The validation has been carried out with respect to a canonical 2D geometry, modelling the jar as an infinite cylinder and the antennas as line currents aligned with the cylinder axis. The first part of our feasibility study has dealt with the setting of the frequency range. A broad numerical analysis has shown that a frequency of about 10 GHz represents the best trade-off between penetration depth and achievable spatial resolution. Hence, nine evenly spaced frequencies with a step of 250 MHz in the range [9 – 11] GHz have been selected and used in the numerical validation.

As a second aspect, the number of data points has been determined. To this end, assuming that the spacing between the jars moving along the chain is the same as their size (8.5 cm in diameter), a measurement line 12 cm long, centred with respect to the jar, has been considered. By so doing, the antenna does not “sense” the presence of the previous or the following jar. The measurement line is positioned at 3 cm from the side of the jar (given the typical size of the belt) and 13 sampling positions (spaced of 1cm) have been considered.

In the adopted frequency range, the electric properties of glass and cocoa cream are  $\epsilon_{\text{glass}}=4.7$ ,  $\sigma_{\text{glass}}=0$  S/m and  $\epsilon_{\text{cream}}= 3$ ,  $\sigma_{\text{cream}}=0.25$  S/m, respectively. The contaminant has been modelled as two plastic inclusions of 2mm in size, whose electric properties in the frequency range of interest are  $\epsilon_{\text{plastic}}=2.3$ ,  $\sigma_{\text{plastic}}=0$  S/m . The testbed scenario is depicted in Fig. 2a. Synthetic data have been corrupted with a Gaussian noise with SNR = 60 dB on the total field.

In Fig.2b, the reconstruction obtained via TSVD is shown. As can be seen, some replicas in the direction orthogonal to the measurement line are present. This occurrence is due to the lack of measurements on the left and right sides of the jar and is consistent with the spatial spectral

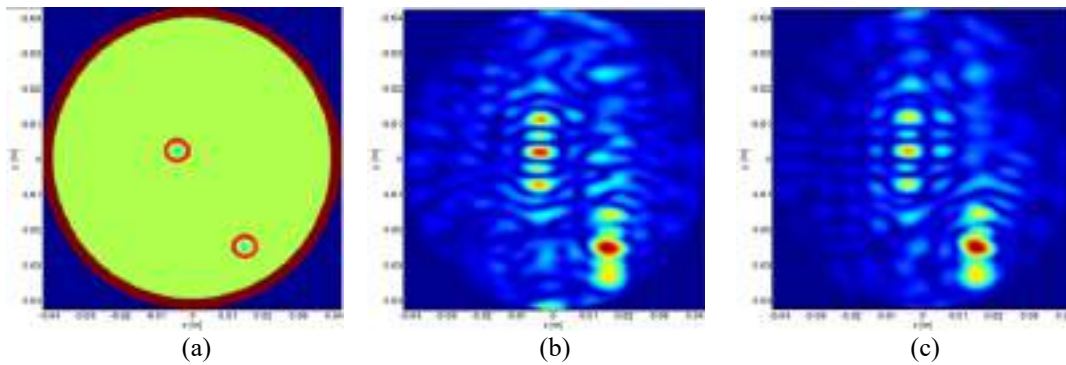


**FIG. 2** – Numerical example. (a) Reference profile. Red circles highlight the two plastic inclusions; (b) Normalized TSVD reconstruction; (c) Projection of the actual contrast onto the first  $T$  singular functions of  $L$ .

content of the operator  $L$  (not reported for the sake of brevity). To illustrate such an aspect and assess the obtained result, Fig2c reports the projection of the ground truth onto the first  $T$  singular functions  $v_n$ . As can be seen the two tomographic images are almost identical, confirming that the obtained result is the optimal one in the considered conditions.

### III. CONCLUSIONS

We have presented a feasibility study on the use of microwave technology for food contamination monitoring, possibly exploitable on the production chain. The results from the presented analysis are promising, motivating further investigation concerned with an experimental proof-of-concept.

### ACKNOWLEDGMENT

This work was supported by Compagnia di San Paolo, under the research project “Microwave Imaging Technology for Food Contamination Monitoring” (MIT-food).

### REFERENCES

- [1] <https://www.foodprocessing.com/articles/2011/conveyor-innovation/>
- [2] K. Wang, D.-W. Sun, H. Pu, Emerging non-destructive terahertz spectroscopy imaging technique: Principle and applications in the agri-food industry, Trends in Food Science & Technology, vol.67, pp.93-105, 2017.
- [3] M. Pastorino, “Microwave Imaging”, Wiley, 2010.
- [4] M. Bertero and P.Boccacci, Introduction to Inverse Problems in Imaging, Bristol, U.K.: Inst. Phys., 1998.

# SOLUTION-PROCESSABLE ORGANIC SEMICONDUCTORS FOR INTEGRATED PHOTONICS APPLICATIONS

I. Maqueira Albo<sup>(1)</sup>, M. Caironi <sup>(2)</sup>, F. Morichetti<sup>(1)</sup>

<sup>(1)</sup> Dipartimento di Elettronica, Informazione e Bioingegneria  
Politecnico di Milano, 20133 Milano, Italy

<sup>(2)</sup> Center for Nano Science and Technology, Istituto Italiano di  
Tecnologia, Via Pascoli 70/3, 20133 Milano, Italy  
[francesco.morichetti@polimi.it](mailto:francesco.morichetti@polimi.it)

## Abstract

*In this work, we investigate the optical properties of solution-processable organic semiconductors that are widely employed in the field of large-area, flexible and portable electronics. The refractive index and extinction coefficient of an n-type organic semiconductor (P(NDI2OD-T2)) were measured in the visible and near infrared range by means of spectroscopic ellipsometry. We also demonstrated integration of P(NDI2OD-T2) as a coating film of low-loss silicon oxynitride waveguides (SiON). Results suggest the possibility to integrate solution-processable electronic devices on photonic integrated circuits and to realize organic transistors on photonic platforms.*

**Index Terms** – Organic semiconductors, Integrated optics materials, Optical waveguides, Photonic integrated circuits

## I. INTRODUCTION

As photonics integrated circuits evolve toward complex on-chip architectures, integration of photonic devices with electronics is becoming mandatory to implement more sophisticated control and read-out operations. Organic molecular materials, offering flexibility and low-cost fabrication, can enrich conventional photonics platforms with new functionalities in order to develop next-generation photonic devices [1].

Solution-processable organic semiconductors have been widely studied in the field of large-area, flexible and portable electronics [2]. These compounds together with soluble conductors and dielectrics enables the fabrication of complex organic devices solely through solution-based methods. Among these materials, poly{[N, N'-bis(2-octyldodecyl)-naphthalene-1,4,5,8-bis(dicarboximide)-2,6-diyl]-alt-5,5'-(2,2'-bithiophene)} (P(NDI2OD-T2)) is a notable example of n-channel type polymeric semiconductor with high electron mobility in the order of  $0.1 - 0.96 \text{ cm}^2\text{v}^{-1}\text{s}^{-1}$ . [3]. However, few works report on the optical performance of solution-processable organic semiconductors, and the integration itself of organic electronic devices, such as organic transistors, on a photonic chip has still to be demonstrated.

In this work we characterized the optical properties of P(NDI2OD-T2) in the visible and near infrared range and we integrated this material as a coating layer of silicon oxynitride (SiON) waveguides. Results suggest

the possibility to use P(NDI2OD-T2) as a an organic semiconductor material for the realization of electronic circuits integrated on an optical platform.

## II. FILM DEPOSITION AND OPTICAL CHARACTERIZATION

P(NDI2OD-T2) thin films were deposited by spin-coating from a 5mg/ml toluene solution on a glass substrate for ellipsometry analysis. The film was then annealed in air at 80 °C for 15 min in order to evaporate the solvent and the final thickness determined by Atomic Force Microscopy (AFM) was of 60 nm. Consequent studies by AFM reveals the random orientation of the polymer fibril structures with the presence of elongated rod-like features and a surface roughness of 0.6 nm rms (Fig.1b), which is well in line with the requirements of optical applications.

Spectroscopic ellipsometry was performed on P(NDI2OD-T2) thin films (Fig. 1c) in the range between 400 nm to 1650 nm taking into account the anisotropic nature of the material. The absorption P(NDI2OD-T2) spectra in the UV-Vis range is characterized by two spectral features, one high energy peak around 390 attributed to the  $\pi$ - $\pi^*$  transition and a broader and lower energy band between 600 to 800 nm, depending on the solvent employed in the solution, attributed to the charge-transfer

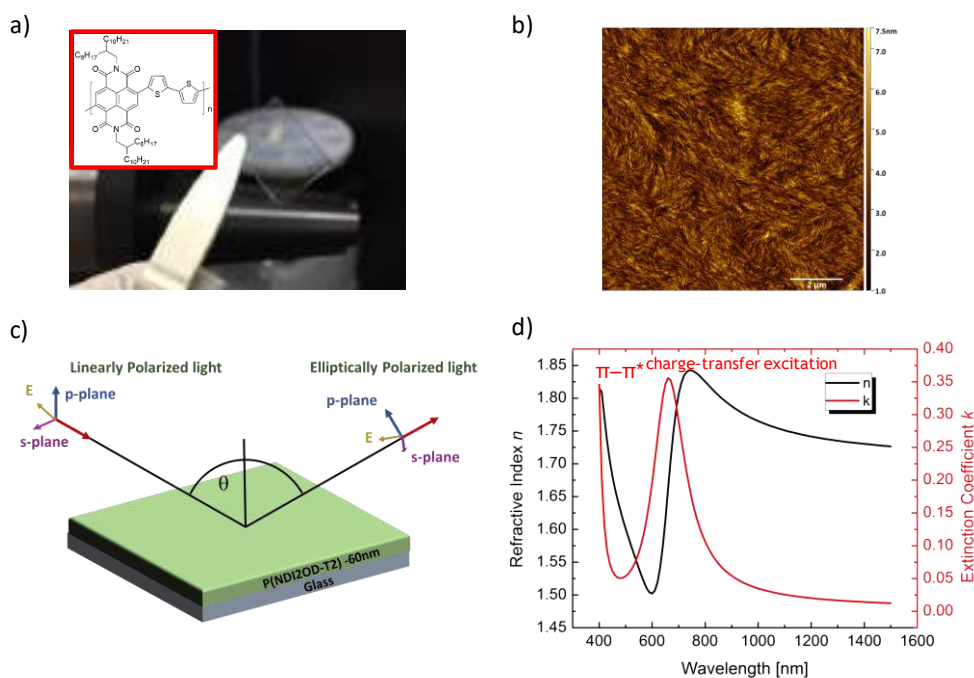


**FIG. 1** – (a) P(NDI2OD-T2) molecular structure (inset) and thin film photograph after spin-coating on a glass substrate. (b) AFM topography of the polymer film, exhibiting random orientation of the fibril structures. (c) Schematic representation of the film stack used for the ellipsometric measurements. (d) Refractive index *n* and extinction coefficient *k* in the wavelength range between 400 and 1600 nm of the P(NDI2OD-T2) determined by spectroscopy ellipsometry.

(CT) transition. For the ellipsometric data modelling were used two Lorentz oscillators at 390 nm and 660 nm. In the visible range, the refractive index of P(NDI2OD-T2) presents a minimum value of 1.5 at 600 nm and maximum value of 1.84 at 800 nm, which is in agreement with results reported in the literature [4]. At  $\lambda > 1300$  nm, the refractive index is around 1.7 and the extinction coefficient  $k$  was found to be lower than the accuracy provided by the experimental setup ( $<10^{-2}$ ) (Fig.1d).

### III. P(NDI2OD-T2)-COATED SILICON OXYNITRIDE WAVEGUIDES

In order to accurately evaluate the transparency of P(NDI2OD-T2) in the near NIR range, a thin film of this material was used as coating material of optical waveguides. To this aim, we employed SiON rib waveguides with a cross-sectional geometry as shown in Fig. 2a. A 2.2- $\mu\text{m}$ -thick SiON core layer with a refractive index of 1.497 was deposited by plasma enhanced chemical vapour deposition (PECVD) on a  $\text{SiO}_2$  surface and was then etched by 500 nm by reactive-ion etching. The resulting waveguide index contrast is about 3.6 %. A solution of P(NDI2OD-T2) was then spin-coated on top the waveguides. Figure 2b shows the cross-sectional SEM image of a fabricated waveguide, where the 60-nm-thick P(NDI2OD-T2) films well follows the waveguide profile, demonstrating the effectiveness of the solution process deposition method for optical waveguide applications.

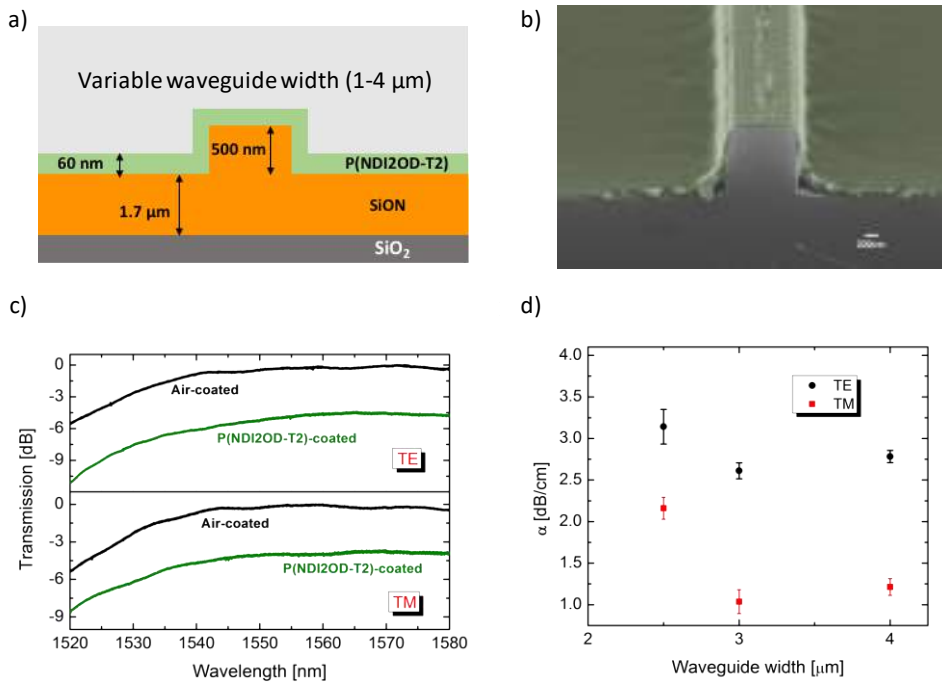


**Fig. 2** - (a) Schematic of the SiON waveguide covered by a thin film of P(NDI2OD-T2). (b) SEM cross-sectional image of a SiON rib waveguide after the deposition of a 60-nm-thick P(NDI2OD-T2) coating. (c) Normalized transmission of 1 cm long SiON waveguide before (black curve) and after (green curve) the deposition of the polymer upper cladding. (d) Attenuation of the P(NDI2OD-T2) film integrated in the SiON waveguide versus the waveguide width for TE (black circles) and TM (red squares) polarization.

The waveguide fabrication process was performed at Polifab, the micro- and nanofabrication facility of Politecnico di Milano.

Figure 2c shows the transmission of a 1-cm-long waveguide with a width of 2.5- $\mu\text{m}$  for TE and TM input polarization, before (black line) and after (green line) the deposition of the P(NDI2OD-T2) coating. A wavelength-independent loss increase by about 2 dB and 3 dB was observed for TE and TM polarizations, respectively. Taking into account the confinement factor of the TE and TM guided modes in the P(NDI2OD-T2), amounting to about 0.4% and 0.6%, respectively, the extinction coefficient  $k$  of the material was found to be around  $1.5 \cdot 10^{-3}$ . This low  $k$  value was confirmed by transmission measurements performed in the 1550 nm wavelength range on SiON waveguides with a different width (Fig. 2d). Results suggests that across the typical length of organic transistors (in the order of 100- $\mu\text{m}$ ), optical loss would be almost negligible ( $<0.03$  dB), thus demonstrating the possibility to integrate organic electronic devices directly on top of optical waveguides.

#### IV. CONCLUSION

The optical properties of P(NDI2OD-T2) organic-semiconductor were measured by spectroscopic ellipsometry in the 400 nm - 1600 nm wavelength range. The refractive index  $n$  presents a minimum value of 1.5 at 600 nm and maximum value of 1.84 at 800 nm. In the NIR  $n = 1.7$  and the extinction coefficient  $k$  is less than  $10^{-2}$ . SiON waveguides covered with a P(NDI2OD-T2) thin film show losses in the order of 3 dB/cm, corresponding to an extinction coefficient  $k = 1.5 \cdot 10^{-3}$ . Results suggest the possibility to employ solution-processable P(NDI2OD-T2) as an organic semiconductor to realize electronic devices, such as organic transistors, on a photonic chip.

#### V. ACKNOWLEDGEMENT

This work was supported by Fondazione Cariplo Project "Advanced Control Technologies for Integrated Optics (ACTIO)" – Rif. 2016-0881. This work was performed at Polifab, the micro- and nanofabrication facility of Politecnico di Milano.

#### VI. REFERENCES

- [1] Zhang, C.; Zou, C.-L.; Zhao, Y.; Dong, C.-H.; Wei, C.; Wang, H.; Liu, Y.; Guo, G.-C.; Yao, J.; Zhao, Y. S., Organic printed photonics: From microring lasers to integrated circuits. *Science Advances* 1 (2015).
- [2] Large Area and Flexible Electronics. Wiley-VCH, Verlag GmbH &Co. KGaA: Boschstr. 12, 69469 Weinheim, Germany, 2015.
- [3] Luzio A.; Criante L.; D'Innocenzo V.; Caironi M., Control of charge transport in a semiconducting copolymer by solvent-induced long-range order. *Scientific Reports* 3, 3425 (2013).
- [4] R. A. DeCrescent, et al., "Model-blind characterization of thin-film optical constants with momentum-resolved reflectometry," *Opt. Express* 24, 28842 (2016).

# ADDITIVE MANUFACTURING OF A SUBSTRATE INTEGRATED SLAB WAVEGUIDE FOR SINGLE-MODE BANDWIDTH ENHANCEMENT

E. Massoni<sup>(1)</sup>, L. Silvestri<sup>(1)</sup>, G. Alaimo<sup>(2)</sup>, S. Marconi<sup>(2)</sup>,  
M. Bozzi<sup>(1)</sup>, L. Perregrini<sup>(1)</sup>, and F. Auricchio<sup>(2)</sup>

<sup>(1)</sup> Department of Electrical, Computer and Biomedical Engineering,  
University of Pavia  
Via Adolfo Ferrata, 5, 27100 Pavia, Italy  
[enrico.massoni02@universitadipavia.it](mailto:enrico.massoni02@universitadipavia.it)

<sup>(2)</sup> Department of Civil Engineering and Architecture,  
University of Pavia  
Via Adolfo Ferrata, 3, 27100 Pavia, Italy

## Abstract

*A broadband substrate integrated waveguide (SIW) by an additive manufacturing technique is presented in this communication. A Ninjaflex<sup>®</sup> filament has been adopted as 3D-printable material to implement the prototype via the fused deposition modeling (FDM) technique. This solution allows for the regulation of the infill percentage, thus affording the possibility to fabricate and characterize materials with different dielectric properties. In that way, two regions of different material's density, produced using the same filament but with different infill percentage, have been used for the implementation of a substrate integrated slab waveguide (SISW), which allows increasing the single-mode bandwidth compared to a typical SIW. From the experimental results, it has been observed a 50 % bandwidth enhancement when comparing the fundamental and second modes of SIW and SISW.*

**Index Terms** – 3D printing, additive manufacturing, broadband interconnects, slab waveguide, substrate integrated waveguide.

## I. INTRODUCTION

Nowadays, the implementation of the next generation of wireless sensors networks and the Internet of Things (IoT) require a thorough study on the novel possibilities enabled by the manufacturing of microwave components and systems by additive techniques and 3D printing [1]. In fact, beyond rapid prototyping and low fabrication cost, the 3D printing offers unprecedented flexibility and a completely new design scenario.

Furthermore, one of the most common additive manufacturing techniques is represented by the fused deposition modeling (FDM), that permits to control the local printing density, leading to a modification of the dielectric characteristics of the 3D-printed elements with different infill percentage, in only one-pass fabrication process. [2]

A substrate integrated slab waveguide (SISW) [3], which is a modified version of the standard substrate integrated waveguide (SIW) [4], [5] with increased single-mode bandwidth, is presented in this communication.

## II. ADDITIVE MANUFACTURING AND MATERIAL CHARACTERIZATION

The adopted material is the thermoplastic polyurethane called Ninjaflex® (filament diameter 1.75 mm), printed by using the commercial FDM Leapfrog Creatr 3D printer. To fully exploit the potentialities of the FDM technology, the variation of the infill percentage has been examined, leading to the possibility to vary the density of the 3D-printed material theoretically from 100 % (completely filled structure) to 0 % (hollow structure) [2]. This work benefits from this opportunity and it allows to design, manufacture and test both SIW and SISW structures. Both narrow-band (waveguide set-up) and wide-band (two lines method) measurements have been performed to retrieve values of the complex dielectric permittivity versus the infill percentage for the Ninjaflex®. [5],[6]

## III. DESIGN OF THE SUBSTRATE INTEGRATED SLAB WAVEGUIDE

This Section is dedicated to the comparison of the bandwidth performance between a classical SIW and a broadband SISW, 3D-printed with the Ninjaflex® material. In particular, the SIW has been designed with 100 % nominal infill material ( $\epsilon_r = 3.05$  and  $\tan \delta = 0.05$ ), to operate with cutoff frequency of the fundamental mode  $f_1 = 3$  GHz. The modal analysis of the unit cell leads to the geometrical dimensions  $w = 32$  mm,  $d = 3$  mm,  $s = 6$  mm (Fig. 1a), resulting in a single-mode band spanning from  $f_1 = 3.00$  GHz to  $f_2 = 6.00$  GHz. Subsequently, the SISW was designed by using the commercial software Ansys HFSS with a cutoff frequency of the fundamental mode around  $f_1 = 3$  GHz. The SISW consists of a central portion with high-permittivity material (in this case, 100 % nominal infill, i.e.,  $\epsilon_r = 3.05$  and  $\tan \delta = 0.05$ ) and two side portions with low-permittivity material (obtained by decreasing the infill) [3], [5].

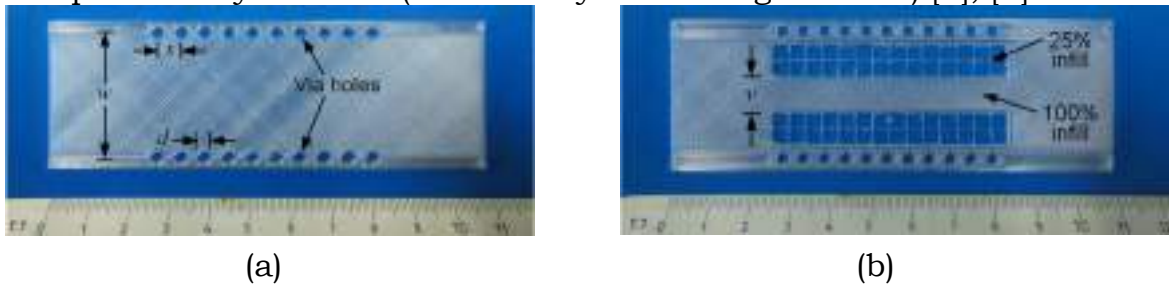


**FIG. 1** – 3D-printed prototypes photos without aluminum foils attached:  
 (a) 100% infill percentage SIW;  
 (b) 100% infill (central portion) and 25% infill (side portions) SISW.



**FIG. 2** – 3D-printed prototypes photos with aluminum foils attached:  
 (a) Prototype for the excitation of the fundamental  $TE_{10}$  mode;  
 (b) Prototype for the excitation of the second  $TE_{20}$  mode.

The single-mode bandwidth increases by decreasing the infill of the lateral portions, and that an optimal width  $\nu$  exists (infill below 25% is not considered as it does not guarantee sufficient mechanical stability). The maximum bandwidth was achieved with 25 % nominal infill (i.e.,  $\epsilon_r = 1.70$  and  $\tan \delta = 0.01$  and width  $\nu = 8.4$  mm, without changing the other dimensions (Fig. 1b) [single-mode band spanning from  $f_1 = 3.06$  GHz to  $f_2 = 7.48$  GHz]. Consequently, the use of the SISW topology leads to a 50 % enhancement of the single-mode bandwidth performance.

#### IV. EXPERIMENTAL RESULTS

Fabricated prototypes of the SIW and SISW (substrate thickness 1 mm) are shown in Fig 2a and Fig 2b, respectively. Metal layers have been implemented by pasting adhesive aluminum foils and copper rivets have been adopted for the implementation of the metal vias [5]. Tapered microstrip transitions have been implemented for launching the fundamental mode of the two structures (Fig. 2a). Moreover, to assess the bandwidth performance, launchers for the second mode of the two structures have been implemented, by using a balanced power divider with  $180^\circ$  output phase shift (Fig. 2b), with the sole aim to identify the cutoff frequency of the second mode. Attenuation and propagation constants of the SIW and SISW have been determined experimentally by adopting the technique described in [7], which permits to de-embed the effect of the transitions.

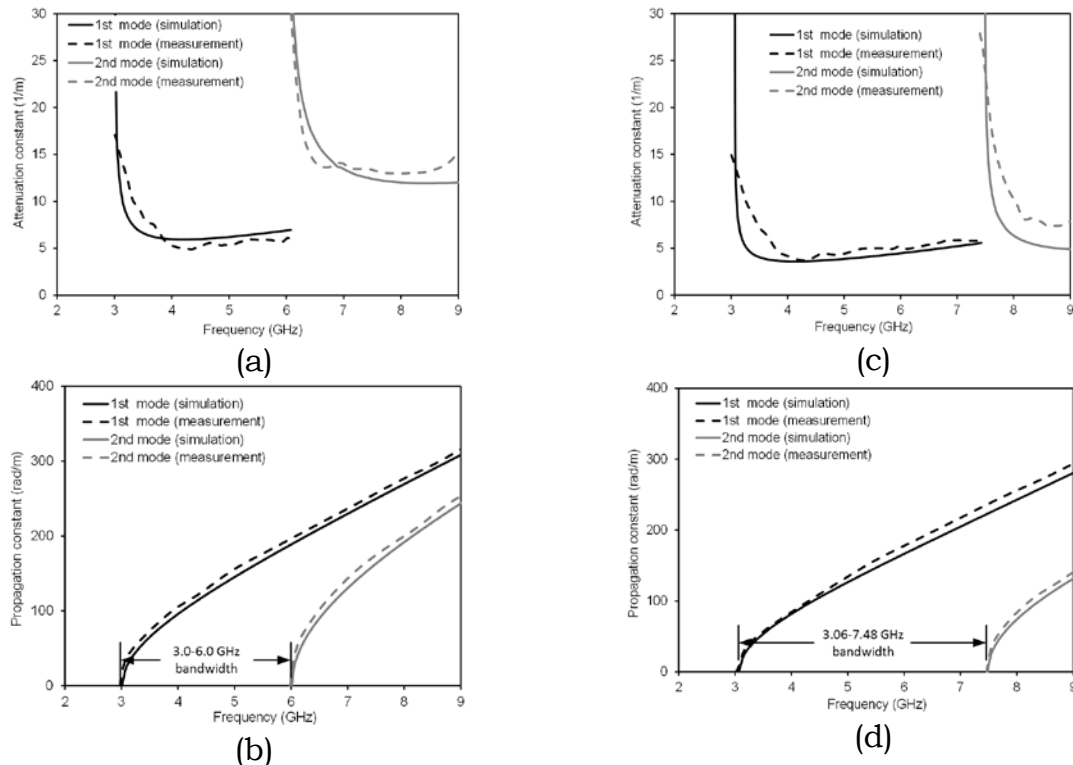


**FIG. 3** – Simulated and measured dispersion characteristics versus frequency of the first and second modes: (a) Attenuation constant for the SIW structure; (b) Propagation constant for the SIW structure; (c) Attenuation constant for the SISW structure; (d) Propagation constant for the SISW structure.

Simulated and measured dispersion curves of the first and second modes of the SIW structure, as in [5], are shown in Fig. 3a and Fig. 3b, highlighting a single-mode bandwidth of 3 GHz. Similarly, Fig. 3c and Fig. 3d show the simulated and measured dispersion curves of the first and second modes of the SISW structure: in this case, the single-mode bandwidth is almost 4.5 GHz, confirming the 50 % bandwidth enhancement with respect to the classical SIW structure. In addition, the attenuation constant of the second mode in the SISW (Fig. 3c) is smaller than in the second mode of the SIW (Fig. 3a): this is due to the lateral air-filled portions of the substrate in the SISW, where the electric field of the second mode is more intense. This feature could be of interest for those structures that exploit the second mode, e.g., leaky-wave antennas.

## V. CONCLUSION

Implementation and testing of a broadband SIW by an additive manufacturing technique has been highlighted in this communication. By exploiting the features of the FDM procedure, materials with different dielectric permittivity have been fabricated, tested and used for the implementation of a SISW, which covers a single-mode band 50 % larger than a standard SIW. Besides the broader operation bandwidth, the interesting characteristic of the proposed waveguide is the possibility to realize the structure in one-pass fabrication and using one single thermoplastic filament. While nowadays losses of 3D-printed structures are still large, many materials are currently under development for 3D printing, which are expected to exhibit significantly lower losses in the near future.

## REFERENCES

- [1] E. MacDonald et al., "3D Printing for the Rapid Prototyping of Structural Electronics," *IEEE Access*, Vol. 2, pp. 234-242, Dec. 2014.
- [2] C. Tomassoni, R. Bahr, M. Bozzi, L. Perregrini, and M. Tentzeris, "3D Printed Substrate Integrated Waveguide Filters with Locally Controlled Dielectric Permittivity," *46th European Microwave Conference (EuMC2016)*, London, UK, Oct. 3-7, 2016.
- [3] M. Bozzi et al., "Efficient Analysis and Experimental Verification of Substrate Integrated Slab Waveguides for Wideband Microwave Applications," *International Journal of RF and Microwave Computer-Aided Engineering*, Vol. 15, No. 3, pp. 296-306, May 2005.
- [4] M. Bozzi, A. Georgiadis, and K. Wu, "Review of Substrate Integrated Waveguide (SIW) Circuits and Antennas," *IET Microwaves, Antennas and Propagation*, Vol. 5, No. 8, pp. 909-920, June 2011.
- [5] E. Massoni et al., "3D-Printed Substrate Integrated Slab Waveguide for Single-Mode Bandwidth Enhancement," *IEEE Microwave and Wireless Components Letters*, Vol. 27, No. 6, pp. 536-538, June 2017.
- [6] H.-M. Chang and C. Liao, "A Parallel Derivation to the Maxwell-Garnett Formula for the Magnetic Permeability of Mixed Materials," *World Journal of Condensed Matter Physics*, Vol. 1, pp. 55-58, 2011.
- [7] M.D. Janezic and J.A. Jargon, "Complex permittivity determination from propagation constant measurements," *IEEE Microwave and Guided Wave Letters*, Vol. 9, No. 2, pp. 76-78, Feb. 1999.

# DESIGN OF ROBUST WEARABLE UHF RFID TAGS THROUGH THE OPTIMUM POSITIONING OF A PIFA RADIATING ELEMENT ON A COMPACT GROUND PLANE

A. Michel<sup>(2)</sup>, R. Colella<sup>(1)</sup>, G. A. Casula<sup>(3)</sup>, P. Nepa<sup>(2)</sup> L. Catarinucci<sup>(1)</sup>, G. Montisci<sup>(3)</sup>, G. Mazzarella<sup>(3)</sup>, G. Manara<sup>(2)</sup>,

<sup>(1)</sup> Dept. of Innovation Engineering, Univ. of Salento, 73100 Lecce.  
[riccardo.colella@unisalento.it](mailto:riccardo.colella@unisalento.it); [luca.catarinucci@unisalento.it](mailto:luca.catarinucci@unisalento.it)

<sup>(2)</sup> Dept. of Information Engineering, Univ. of Pisa, 56126 Pisa.  
[andrea.michel@iet.unipi.it](mailto:andrea.michel@iet.unipi.it); [p.nepa@iet.unipi.it](mailto:p.nepa@iet.unipi.it); [g.manara@iet.unipi.it](mailto:g.manara@iet.unipi.it)

<sup>(3)</sup> Dept. of Electrical and Electronic Engineering, Univ. of Cagliari, Piazza D'Armi, 09123 Cagliari.  
[a.casula@diee.unica.it](mailto:a.casula@diee.unica.it); [giorgio.montisci@unica.it](mailto:giorgio.montisci@unica.it);  
[mazzarella@diee.unica.it](mailto:mazzarella@diee.unica.it)

## Abstract

*The electric and magnetic energy density distributions are key-parameters to improve the robustness of a wearable UHF RFID tag to the human body proximity, since they allow for a ground plane shaped while maintaining a limited antenna size. In this paper, such theoretical considerations have been discussed and assessed through both numerical analysis and experimental measurements, by optimizing the position of the radiating element of a wearable grounded UHF RFID tag operating at the ETSI band (865-868 MHz), with respect to its ground plane. In particular, the tag sensitivity has been measured as a function of the antenna-body distance by using an ad-hoc flexible tag characterization and performance evaluation platform.*

**Index Terms** – Body-antenna coupling, human-body proximity, RFID tag, wearable antenna

## I. INTRODUCTION

The human body proximity represents a critical issue for wearable antennas performance [1], since, being a non-homogeneous lossy material, it considerably affects the antenna input impedance and radiation efficiency by causing a detuning of the antenna. This aspect is particularly critical in wearable Radio Frequency Identification (RFID) applications where a fully-passive tag is used to perform both RF energy harvesting and communication with the reader by using a really limited amount of energy. In this case, for instance, losses introduced by the human body can definitively break down the performance of the whole tag [2].

In general, even though single-layer antennas may be used for wearable applications, it is well-formed opinion that a relatively large ground plane is beneficial to limit the effect of the human body proximity on the antenna performance [1]. However, at low frequency bands (e.g.  $f < 1\text{GHz}$ ), there is no room to implement a large ground plane able to decouple the antenna from the body, nor does the wearer's body act as

an effective reflector to reduce back radiation and increase antenna gain [1]. Hence, in [3] an energy-based design criterion has been proposed to improve the robustness of a wearable antenna by properly shaping its ground plane.

In this paper, the position of a wearable radiating element with respect to its ground plane has been optimized by considering the design criterion proposed in [3]. Without loss of generality, a UHF RFID PIFA antenna has been considered, operating in the ETSI band (865-868 MHz). A built-in-lab tag characterization system is used to measure the antenna performance as a function of both antenna-body distance and ground-plane placement, so experimentally validating the effectiveness of the described design considerations.

## II. ANTENNA DESIGN AND NUMERICAL ANALYSIS

Starting from [5], an ad-hoc RFID tag PIFA antenna has been designed and fabricated on two 1.57-mm-thick RT/duroid 5870 substrates ( $\epsilon_r=2.3$ ,  $\tan\delta=0.002$ ) in a stacked configuration, obtaining an antenna thickness  $H=3.2$  mm. The antenna prototype is shown in Fig. 1a, while Fig. 1b shows the layout of the simulated model, and its geometrical dimensions are listed in Table 1. The overall antenna size is  $53\text{mm}\times 53\text{mm}$ , which corresponds to  $0.154\lambda\times 0.154\lambda$ , being  $\lambda$  the free-space wavelength at 866.5MHz. The antenna design has been optimized to achieve a power transmission coefficient ( $\tau$ ) higher than 0.8 with a Monza 3 chip ( $Z_{\text{CHIP}}=13-j151\ \Omega$ ).

In order to improve the antenna robustness with respect to the human body coupling, the ground plane size must be suitably increased to optimize the antenna performance, without enlarging too much the overall antenna size. The approach discussed in [3] suggests a ground plane extension toward the region where the electric energy density exhibits a peak. On such basis three antenna versions have been considered (Fig. 1) for the proposed study: **Config. A** represents the original antenna, whose dimensions are listed in TABLE 1; **Config. B** is obtained from **Config. A** by increasing the ground plane size and placing the PIFA open side close to the ground plane edge; **Config. C** is obtained from **Config. A** by increasing the ground plane size and placing the PIFA open side far from the edge.

In order to numerically analyze the interaction between the antenna and the human body, an equivalent model at 866.5 MHz, consisting in a 5-cm-thick material with  $\epsilon_r = 2/3*\epsilon_{r,\text{muscle}} = 36$ , and  $\sigma = 2/3*\sigma_{\text{muscle}} = 0.62$  S/m, has been considered during the simulation phase.

The wearable antenna performance robustness has been studied by means of two metrics,  $\tau$  and  $\tau\times\eta$ , which are computed as a function of both  $d$  and frequency, in the ETSI UHF RFID operative band by varying the distance  $\Delta L$  between the PIFA open side and the ground plane border from  $\Delta L=0\text{mm}$  (**Config. B**) to  $\Delta L=25\text{mm}$  (**Config. C**).

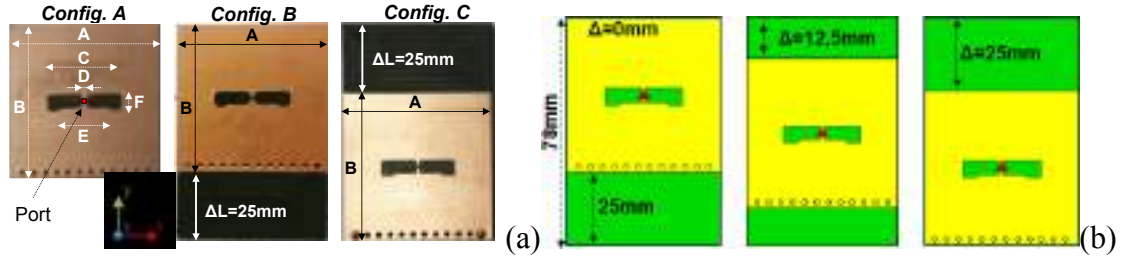


**FIG. 1** - (a) Prototype of the designed wearable UHF-RFID PIFA and two modified versions with enlarged ground plane. (b) simulated antenna model

**TABLE 1 - ANTENNA GEOMETRICAL PARAMETERS**

Parameter	Value	Parameter	Value
<b>A</b>	53 mm	<b>E</b>	17 mm
<b>B</b>	53 mm	<b>F</b>	6 mm
<b>C</b>	27 mm	<b>D</b>	1 mm

In Fig. 2, the  $\tau$  (Fig. 2a) and  $\tau \times \eta$  (Fig. 2b) curves have been plotted as a function of the antenna-body distance, for the three layouts of Fig. 1, and for two frequencies of the ETSI band: 865 MHz, and 868 MHz.

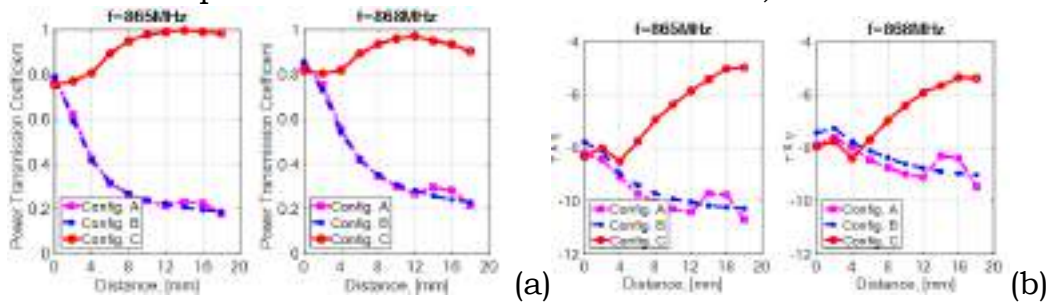


**FIG. 2** - Simulated results for (a)  $\tau$  and (b)  $\tau \times \eta$  vs. the antenna-body distance, for the three configurations shown in Fig. 1 in ETSI UHF RFID band.

It should be noted that the **Config. C** performance is generally better and more stable than the **Config. A** and **Config. B**, both in terms of  $\tau$  and  $\tau \times \eta$ . In particular, when the antenna-body distance varies from 0 to 18mm, the parameter  $\tau$  of **Config. C** assumes values higher than 0.8, while its  $\tau \times \eta$  is always higher than -8 dB. On the other hand, **Config. A** and **Config. B** have similar performance when varying the antenna-body distance, but their behavior is significantly worse than **Config. C**. Therefore, increasing the ground plane size towards the direction of the PIFA short-circuit side, not only makes the antenna more obtrusive but is also useless from the performance improvement point of view.

### III. EXPERIMENTAL RESULTS

An antenna performance validation has been carried out to assess the numerical analysis presented in Section II. In particular, the behavior of  $\tau \times G_{\text{tag}}$  (where  $G_{\text{tag}}$  is the maximum gain of the tag antenna) as a function of the antenna-body distance, has been evaluated through the tag characterization platform proposed and validated in [4]. As for the setup, an artificial model of the human tissue has been synthesized in the laboratory by means of a specific saline solution, to mimic the body

average dielectric properties. The saline solution has been inserted in a PVC tank, arranged in front of the reader board antenna, and placed in anechoic environment, as shown in Fig. 3a.

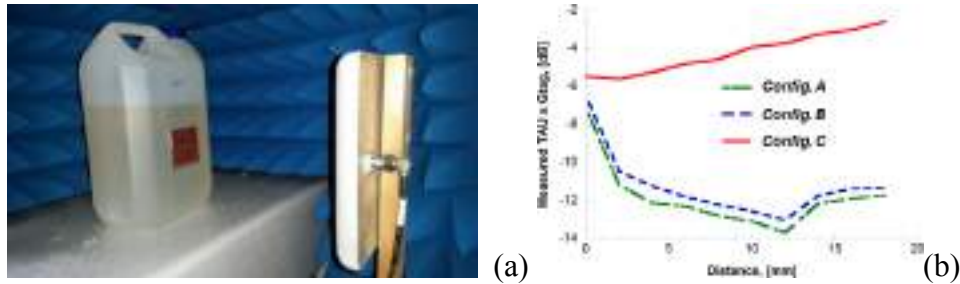


**FIG. 3** – (a) The tag under test applied on the saline solution tank emulating the human tissue. (b) Results in terms of  $\tau \times G_{\text{tag}}$

By assuming a chip sensitivity equal to  $-20\text{dBm}$ , the  $\tau \times G_{\text{tag}}$  product has been estimated and plotted in Fig. 3b, as a function of the tag-reader antenna distance,  $d$ , in the range between 0 (tag attached to the human body) and 18 mm. The good agreement in terms of curves behavior with simulated results of Fig. 2 confirms that **Config. C** is the one assuring the better performance, thanks to the ground plane extended toward the direction of a peak of electric density.

#### IV. CONCLUSION

In this work the analysis of the proper positioning of the radiating element of a wearable UHF RFID PIFA with respect to its ground plane borders has been carried out both numerically and experimentally. Results confirm that antenna robustness is improved when the electric energy peaks appearing in the antenna reactive near-field region are far from the borders of the ground plane and provides guidelines for the development of compacts and efficient wearable RFID tags.

#### REFERENCES

- [1] P. Nepa and H. Rogier, "Wearable antennas for off-body radio links at VHF and UHF bands (below 1 GHz): challenges, state-of-the-art and future trends," *IEEE Ant. Propag. Magaz.*, vol. 57, no. 5, pp. 30-52, Oct 2015.
- [2] T. Kellomaki, "On-Body Performance of a Wearable Single-Layer RFID Tag," *IEEE Antennas and Wireless Propagation Letters*, vol. 11, pp. 73-76, 2012
- [3] G.A. Casula, A. Michel, P. Nepa and G. Montisci, "Robustness of Wearable UHF-Band PIFAs to Human-Body Proximity", *IEEE Trans. Antennas Propag.*, vol. 64, no. 5, pp. 2050-2055, May 2016.
- [4] R. Colella, L. Catarinucci, P. Coppola, and L. Tarricone, "Measurement Platform for Electromagnetic Characterization and Performance Evaluation of UHF RFID Tags," *IEEE Trans. on Instrumentation and Measurement*, vol. 65, no. 4, pp. 905-914, Apr 2016.
- [5] C. Occhiuzzi, S. Cippitelli, and G. Marrocco, "Modeling, design and experimentation of wearable RFID sensor tag", *IEEE Transactions on Antennas and Propagation*, 58(8), pp. 2490-2498, 2010.

# MODELING AND EXPERIMENTATION OF A UHF-RFID TRANSCUTANEOUS WIRELESS COMMUNICATION SYSTEM FOR THE MYOELECTRIC CONTROL OF PROSTHETIC HAND

C. Miozzi<sup>(1)</sup>, S. Guido<sup>(1)</sup>, G. Saggio<sup>(1)</sup>, E. Gruppioni<sup>(2)</sup>, G. Marrocco<sup>(1)</sup>

<sup>(1)</sup> University of Roma "Tor Vergata", Via del Politecnico 1, 00133,  
Roma, Italy

<sup>(2)</sup> INAIL Centro Protesi, Research and Training Area, Budrio (BO),  
Italy

## Abstract

*Modern active hand prostheses include myoelectric controlled electronics and actuators to restore the lost biomechanical functionalities. The feasibility of a wireless transcutaneous telemetry link based on the UHF Radiofrequency Identification is here investigated. The link should interconnect one or more implanted battery-less antennas with an external miniaturized and conformal reader's antenna integrated with the prosthesis socket. Numerical models and preliminary laboratory experimentations demonstrated the possibility to successfully establish an RFID data link with a multiplicity of implanted tags even by using a low-power embedded reader (0.25 W) with a displacement-tolerance among interrogating and sensor antennas of 1-2 cm.*

**Index Terms** – Radiofrequency Identification, Robotic limb, Transcutaneous wireless communication, Implantable device.

## I. INTRODUCTION

The hand is one of the most complex systems of the human body and its loss has a serious physical and psychological impact. Among the most advanced prosthetic hands available today, there are that can be controlled by the electromyographic signals generated during the contraction of the residual muscles of the arm's stump.

The mostly used electrodes for the acquisition of the myoelectric signal are surface-mounted ones, which have several disadvantages related to the skin-electrode interface: skin impedance variation, sweating, risk of detachment and misplacement, distance from the source of signal. To overcome some of above limitations, myoelectric sensors could be implanted in the arms and a transcutaneous wireless link throughout the body needs to be established for the data retrieving.

As most of the transcutaneous upper-limb prosthesis system have been studied in High Frequency band [1]-[2], this paper is aimed at exploring the feasibility of a different kind of link involving the Radiofrequency Identification (RFID) technology in the UHF band (860-960 MHz), with the purpose to evaluate: *i*) the link budget in terms of power, *ii*) the read region inside the arm that can be achieved with the

typical power of embedded readers, *iii*) the tolerance to the mutual displacement of the implants with respect to the query unit.

## II. MODEL OF TRANSCUTANEOUS COMMUNICATION LINK

The considered transcutaneous communication system involves an external interrogating antenna and one or more implanted transponders inserted between the fat layer and the muscles. As the electromagnetic interactions occur in the very near field, the transcutaneous link is properly modelled by a two-port network (Fig. 1).

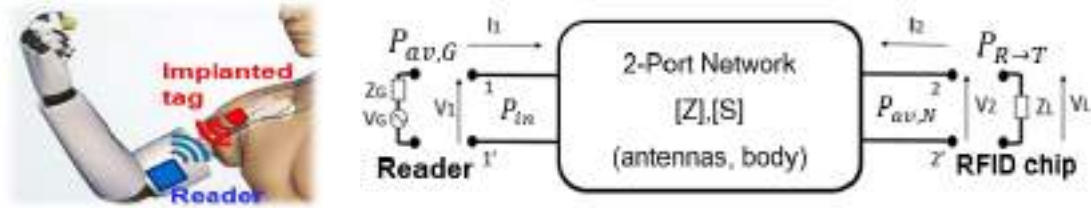


**FIG. 1** – Two-port network model of the transcutaneous link.

In order to establish an RFID link, the power delivered by the reader to the tag's chip  $P_{R \rightarrow T}$ , must exceed the chip sensitivity  $p_C$ . The communication performance is thus quantified in terms of *Transduction Power Gain* ( $G_T$ ), i.e. the ratio between  $P_{R \rightarrow T}$  and the power available from the reader generator  $P_{av,R}$  [3]:

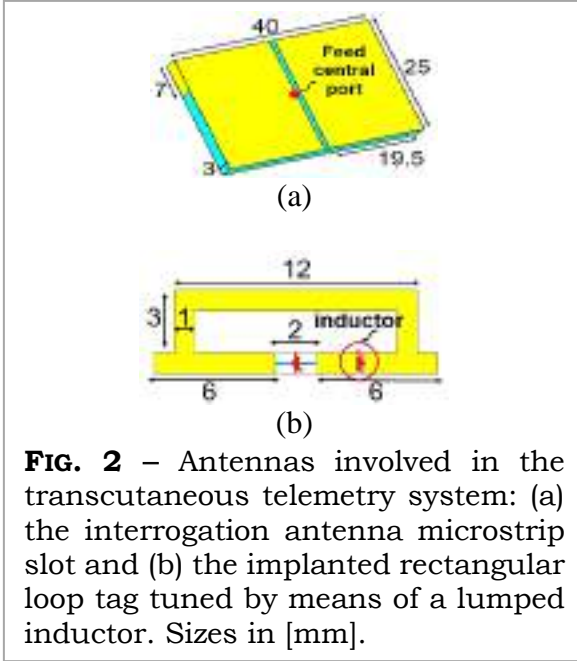
$$G_T = \frac{P_{R \rightarrow T}}{P_{av,R}} = \frac{4R_C R_G |Z_{21}|^2}{|(Z_{22} + Z_C)(Z_{11} + Z_G) - Z_{12}Z_{21}|} \quad (1)$$

where  $[Z_{ij}]$  are the entries of the impedance matrix of the two port-network, related to the port of the reader's antenna and of the implanted sensor antenna. Finally, the minimum power the reader has to produce in order to activate the tag ( $P_{R \rightarrow T} = p_C$ ) is:

$$P_{min} = \frac{p_C}{G_T} . \quad (2)$$

This parameter is an effective link budget indicator to be compared with the typical power emitted by battery-sourced small-size RFID readers spanning in the range 0.25 - 1 W.

The selected interrogation antenna is a microstrip slot (Fig. 2a), made of two patches facing each other and shorted to the ground plane at opposite edges by means of two vertical stripes, suitable for tuning the antenna at 870 MHz.



The implantable tag antenna layout is a rectangular loop made of a copper trace ( $35 \mu\text{m}$ ) deposited onto a PET substrate ( $135 \mu\text{m}$ ) and covered with a thin film of common polyethylene ( $10 \mu\text{m}$ ) (Fig. 2b).

The above models of antennas were hence applied to evaluate the minimum power required (2) to source the transmitting antenna in order to activate the implanted tag in several positions P1-P8 in a realistic multi-layered forearm model, partly levelled on top to easily allocate the patch antenna (Fig. 3a).

The histogram in Fig. 3b resums the results of the numerical analysis concerning the minimum input power. All the positions, except for P6, are compatible with an input power of just 0.25 W (24 dBm). By also accounting for the symmetry, the read region at the fat-muscle interface can be approximated by a rectangle of 2 cm by 1 cm size that hence quantifies the tolerable reader-tag displacement when just 0.25 W power is available.

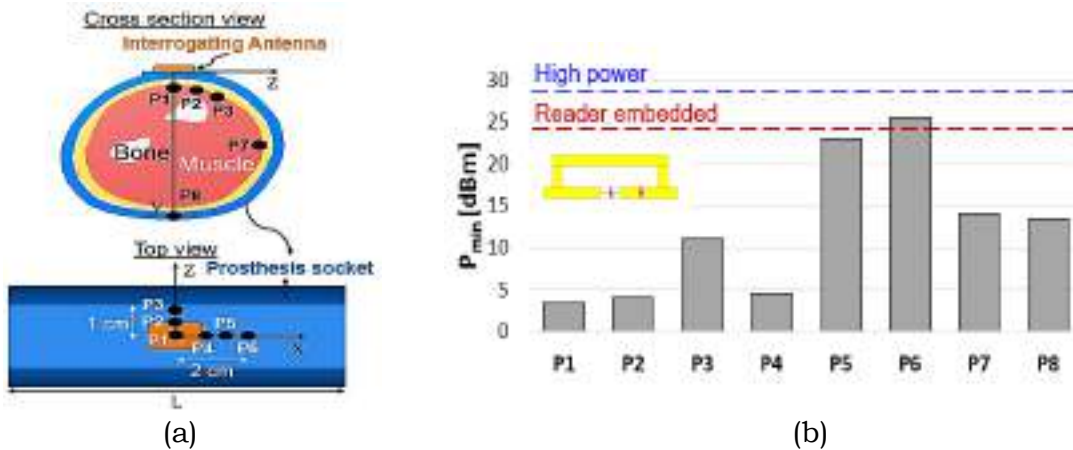


**FIG. 3** – (a) Multi-layered forearm model ( $L = 25 \text{ cm}$ ) and (b) minimum activation power for the tag implanted in the selected positions P1-P8.

### III. PROTOTYPES AND EXPERIMENTAL EVALUATION

The prototypes of both interrogating and implanted antennas are shown in Fig. 4a. The implanted tag under test has been equipped with the G2iL NXP microchip,  $Z_c = (16.6 - j51)\Omega$   $p_c = -18 \text{ dBm}$ .

A pork limb emulated the stump of the forearm so that all the relevant tissues were realistically accounted for. The tag was implanted

subcutaneously (Fig. 4a). The stump was hence inserted into a real prosthetic socket and the slotted patch was placed onto its external surface (Fig. 4a) and connected to a Thing Magic M5e reader.

The minimum power to activate the tag was measured by the turn-on method over the 840-960 MHz band. Fig. 4b shows the minimum activation powers for reader-tag arrangement as in P1, P7 and P8. The first two configurations are associated with a robust reading within the entire frequency band by using less than 24 dBmW input power. Instead, to interrogate the tag placed in the most distant position P8 a slight higher amount of power is requested.

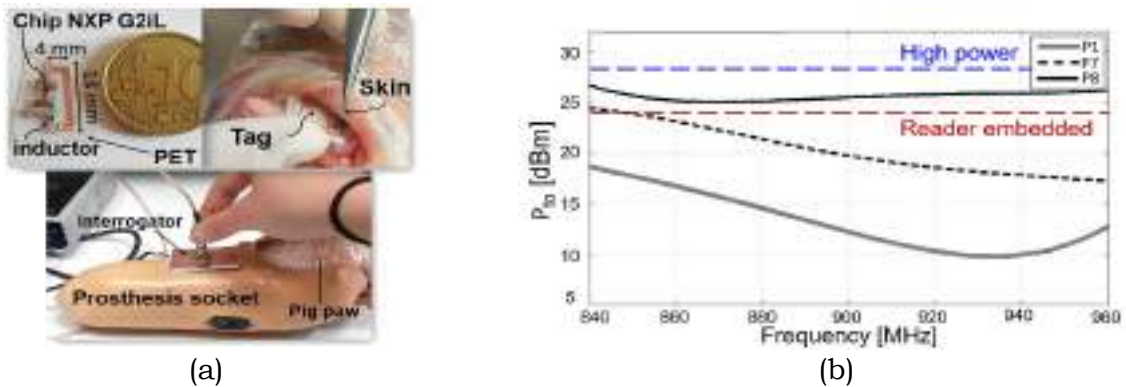


**FIG. 3** – Experimental measurements: (a) prototypes, set-up and (b) turn-on power for the transcutaneous links P1, P7 and P8.

#### IV. CONCLUSION

Numerical and experimental analysis demonstrated the preliminary feasibility of a UHF transcutaneous link based on backscattering communication. Most of the considered positions of the implanted tag permitted to establish an UHF-RFID link with a power less than 0.25 W, compatible with embedded readers. The tolerance against a possible misalignment of the reader’s antenna w.r.t. the implanted sensor is more than 1 cm. On comparing simulated and measured results, it is apparent that there are still relevant margin of improvement in the impedance matching of the tag, thus farther reducing the request of power.

#### REFERENCES

- [1] B. D. Farnsworth et al., "Wireless in vivo EMG sensor for intelligent prosthetic control ", *Solid-State Sensors, Actuators and Microsystems Conference*, June 21-25 2009, Denver, CO, USA, 4pp.
- [2] P. F. Pasquina et al., "First-in-man demonstration of a fully implanted myoelectric sensors system to control an advanced electromechanical prosthetic hand", *Journal of Neuroscience Methods*, vol. 244, pp. 85-93, Apr. 2015.
- [3] V. Di Cecco et al., "Finger-Augmented RFID System to Restore Peripheral Thermal Feeling", *11<sup>th</sup> Annual IEEE International Conference on RFID*, May 9-11 2017, Phoenix, AZ, USA, 7pp.

# DESIGN OF ACTIVE WAVEGUIDE OMT FOR RADIO ASTRONOMY RECEIVER ARRAY IN THE 3 MM BAND

A. Navarrini<sup>(1)</sup>, G. Valente<sup>(1)</sup>, P. Serres<sup>(2)</sup>, F. Schaefer<sup>(3)</sup>, F. Thome<sup>(4)</sup>,  
O. Garnier<sup>(2)</sup>

<sup>(1)</sup> INAF-Osservatorio Astronomico di Cagliari, via della Scienza 5,  
Selargius, Italy, [alessandro.navarrini@inaf.it](mailto:alessandro.navarrini@inaf.it)

<sup>(2)</sup> IRAM-Istitut de RadioAstronomie Millimétrique, Grenoble, France

<sup>(3)</sup> MPIfR-Max Planck Institute for Radio Astronomy, Bonn, Germany

<sup>(4)</sup> IAF-Fraunhofer Inst. Appl. Solid State Physics, Friburg, Germany

## Abstract

*We describe the design of an integrated cryogenic receiver module based on an “active” waveguide Orthomode Transducer (OMT) for dual-polarization radio astronomy observations across 75-116 GHz (3-mm band). The receiver module consists of passive and active sections that can be incorporated in a very compact mechanical assembly suitable for integration in a focal plane array.*

*The passive section of the receiver module employs a broadband backward-coupler waveguide OMT while the active section consists of ultra-low noise MMIC (Monolithic Microwave Integrated Circuit) amplifiers.*

**Index Terms** – Orthomode Transducer (OMT), MMIC, Low Noise Amplifier (LNA), integrated receiver, millimeter-wave radio astronomy.

## I. INTRODUCTION

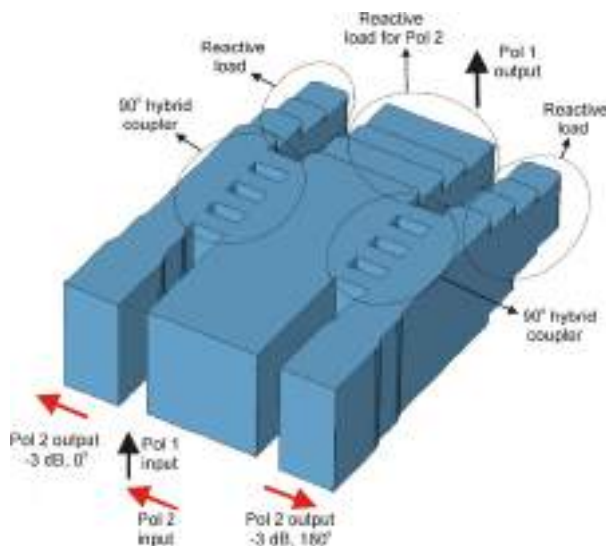
Orthomode Transducers (OMTs) are key components of dual-polarization receivers for radio astronomy [1]. An OMT has three physical ports but exhibits electrical properties of a four-port device. The input common port, usually a waveguide with a square or a circular cross-section, has two electrical ports carrying two orthogonal independent linearly polarized RF signals. Symmetric OMT structures allow achieving large relative bandwidth with  $\Delta\nu/\nu_c > 30\%$ . Wideband waveguide OMT designs that have proved to work well at millimeter wavelengths are based on Boifot junction [2], turnstile junction [3] and dual-ridge designs [4]. An OMT based on reverse-coupling waveguide junction was proposed in [5]. Here, we describe the design of a dual-polarization receiver module based on a waveguide OMT employing the broadband symmetrical reverse-coupling OMT structure presented in [6]. The OMT integrates MMIC LNAs (Low Noise Amplifiers,) designed and fabricated at IAF [7], and waveguide-to-microstrip transitions to be fabricated at IRAM.

This active waveguide OMT is developed in the framework of Work Package 1 of the AETHRA (Advanced European Technologies for Heterodyne Receiver for Astronomy) programme, aiming at investigating the new 35 nm gate length mHEMT (Metamorphic High Electron Mobility Transistor) technology for improving MMIC LNA performance. Our goal is

to develop a prototype of dual-polarization receiver array and to install it on the focal plane of the IRAM 30-m radio telescope on Pico Veleta, Spain.

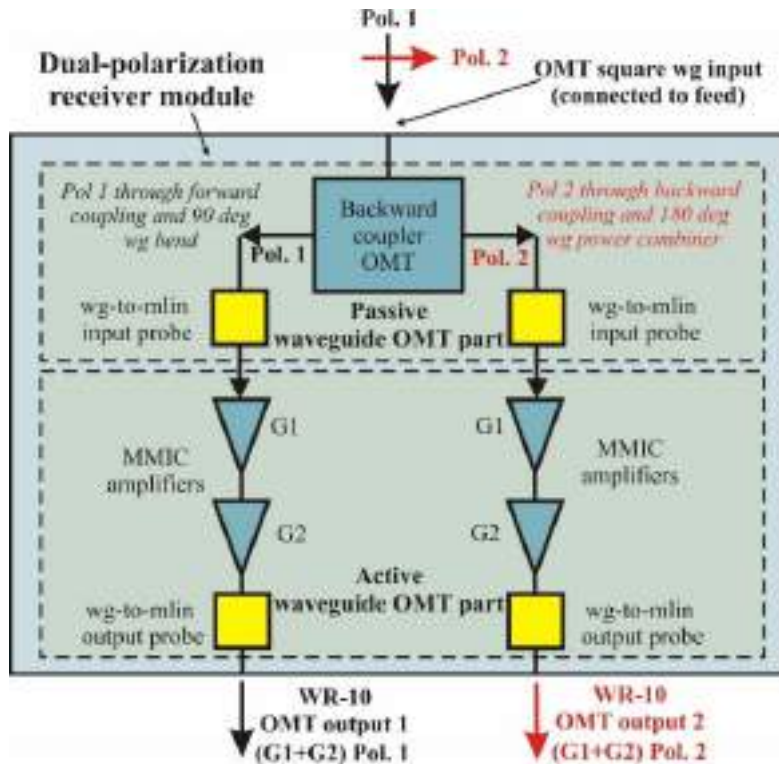
## II. DESIGN OF THE DUAL-POLARIZATION RECEIVER MODULE

Fig. 1 shows the inner section of the symmetric reverse-coupling waveguide OMT described in [6]. The OMT consists essentially of: 1) a square waveguide input (size  $2.54 \times 2.54 \text{ mm}^2$ ) carrying Pol 1 and Pol 2; 2) a dual-step transition to rectangular waveguide output for Pol 1 (forward coupling); 3) two  $90^\circ$  hybrid couplers based on 3 dB E-plane branch-line waveguide coupling structures with four branches for Pol 2. The outputs of both  $90^\circ$  hybrid couplers are terminated with reactive loads so that Pol 2 input signal is backward coupled to two rectangular waveguide outputs parallel to the square waveguide input. The signals in the two Pol 2 rectangular waveguide outputs are out-of-phase and carry half of the power (-3 dB) of the Pol 2 signal in the square waveguide. The Pol 2 outputs are combined with a  $180^\circ$  deg power combiner (not shown).



**FIG. 1** – 3D view of the inner part of the symmetric reverse-coupling waveguide OMT. The incoming Pol 1 signal at the square waveguide input is forward-coupled to a single rectangular waveguide output through a dual-step transition. The incoming Pol 2 signal at the square waveguide input is backward-coupled to two rectangular waveguide outputs at 3 dB with  $180^\circ$  phase difference.

Fig. 2 and Fig. 3 show the block diagram and the design of the dual-polarization active waveguide OMT receiver module, respectively. The device consists of the “passive” OMT based on the backward coupler waveguide structure shown in Fig. 1 and of an “active” waveguide circuitry with MMIC LNAs packaged in a single mechanical module. The passive waveguide OMT utilizes a square input for connection to a dual-polarization feed-horn. The OMT separates the two orthogonal linearly polarized input signals in two independent waveguides with oval shape located inside the module (visible in Fig. 3).



**FIG. 2** – Block diagram of dual-polarization receiver module based on a passive OMT part and on an active part integrating MMIC LNAs.

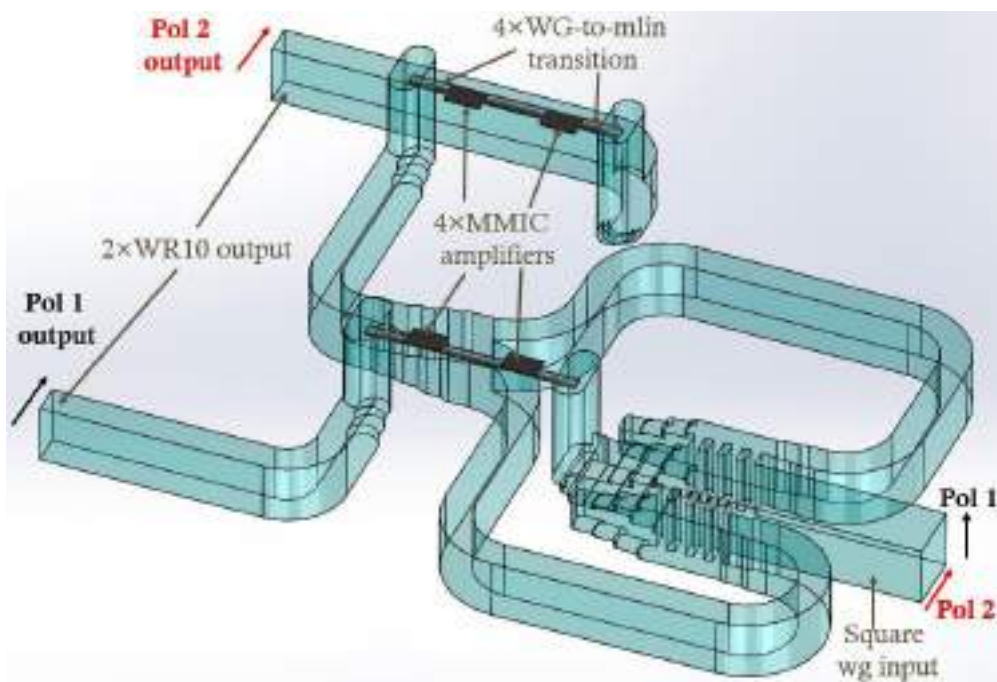


**FIG. 3** – 3D view of the inner part of the dual-polarization receiver module showing the passive and active waveguide OMT parts, including the waveguide circuitries and the MMIC amplifiers. The square waveguide input at OMT input (on the figure right) has size  $2.54 \times 2.54 \text{ mm}^2$ ; it will be connected to a dual-polarization feed-horn. The two WR10 waveguides ( $2.54 \times 1.27 \text{ mm}^2$ ) at OMT output with amplified Pol 1 and Pol 2 signals are parallel and in-line with the input.

Each polarization signals is coupled to the “active” circuitry consisting of a cascade of two MMIC amplifiers through waveguide-to-microstrip transitions based on quartz substrate with Gold beam-lead interconnection. The two MMICs of each cascade are interconnected through a microstrip line fabricated on quartz and located inside a channel. The signals at the output of the second MMIC amplifier of the cascade is coupled back to waveguide through a microstrip-to-waveguide transition. Sections of standard WR10 waveguides are used to route the signals amplified by the MMICs to suitable positions at the output of the module. The waveguide outputs are parallel and in-line with the waveguide input. Two amplified signals, one per polarization channel, are available at the WR10 waveguide outputs of the receiver module. The dual-polarization receiver module shown in Fig. 3 can be fabricated in three mechanical blocks and assembled in a compact unit with external dimension  $43 \times 25 \times 35 \text{ mm}^3$ , thus allowing to mount two standard UG387 waveguide flanges at the device outputs. The waveguide circuitry of the OMT passive part would be incorporated in two of the mechanical blocks, while the active part in a single block of the three-block unit.

### III. ACKNOWLEDGEMENTS

This project has received funding from the European Union’s Horizon 2020 research and innovation programme under grant agreement No 730562.

### REFERENCES

- [1] J. D. Kraus, “Radio Astronomy”, McGraw-Hill Book Company, 1966.
- [2] A. M. Boifot, E. Lier, T. Schaug-Pettersen, “Simple and broadband orthomode transducer” IEEE Proceedings, Vol. 137, Pt. H, No. 6, December 1990, pp. 396-400.
- [3] A. Navarrini and R.L. Plambeck, “A Turnstile Junction Waveguide Orthomode Transducer,” IEEE Trans. Microwave Theory Tech., 54, n. 1, 272-277, 2006.
- [4] A. Dunning, “Double Ridged Orthogonal Mode Transducer for the 16-26 GHz Microwave Band”, Proc. of the Workshop on the Applications of Radio Science, February 20-22, 2002.
- [5] O. Peverini, R. Tascone, G. Virone, A. Olivieri, R. Orta, “Orthomode Transducer for Millimeter-Wave Correlation Receivers,” IEEE Trans. Microwave Theory Tech., vol. 54, n.5, May 2006.
- [6] A. Navarrini, R. Nesti, “Symmetric reverse-coupled waveguide orthomode transducer for the 3mm band,” IEEE Trans. Microw. Theory Tech., vol. 57, no. 1, pp. 80-88, Jan. 2009.
- [7] F. Thome, A. Leuther, J. D. Gallego, F. Schäfer, M. Schlechtweg, and O. Ambacher, “70--116-GHz LNAs in 35-nm and 50-nm Gate-Length Metamorphic HEMT Technologies for Cryogenic and Room-Temperature Operation,” IEEE MTT-S Int. Microw. Symp. Dig., Jun. 2018, pp. 1495-1498.

# INVESTIGATING EM WAVE DEPOLARIZATION DUE TO RAIN USING A PHYSICALLY-BASED MODEL

E. Regonesi<sup>(1)</sup>, L. Luini<sup>(1)</sup>

<sup>(1)</sup> Dipartimento di Elettronica, Informazione e Bioingegneria (DEIB),  
Politecnico di Milano,  
Via Ponzio 34/5, 20133 Milano, Italy  
[eric.regonesi@polimi.it](mailto:eric.regonesi@polimi.it)

## Abstract

*Electromagnetic wave depolarization is a key effect to be taken into account in dual polarization systems. Clouds and hydrometeors in the troposphere affect Earth-satellite links working in the Extremely High Frequency (EHF) band, causing the additional detrimental effect of depolarization. This contribution presents the current activities carried out at Politecnico di Milano on the investigation of the Cross-Polar Discrimination (XPD) measured in past electromagnetic wave propagation campaigns (Italsat, Alphasat). A physical based model is under development to support the analysis of the XPD.*

**Index Terms** – Depolarization, ice, rain, satellite links.

## I. INTRODUCTION

The use of dual polarization Earth-satellite communication systems is widespread nowadays to increase the channel capacity made available. Satellite links working in the EHF band experience additional impairments caused by precipitation phenomena present in the troposphere [1]. Rain and ice crystals have been widely investigated in literature. The model included in recommendation ITU-R P.618-13 provides an average prediction of the depolarization effects with separate terms for rain and ice [2], but it cannot catch the large variability of XPD induced by the troposphere. This contribution presents the physically-based model under development at Politecnico di Milano, which aims at thoroughly investigating the impact of all the atmosphere constituents (e.g. rain, ice, melting particles and clouds) on the overall wave depolarization. The main aim of the model is to provide a reliable tool for satellite systems design, but it could also be useful, for example, to support and enhance precipitation retrievals using polarimetric weather radars.

## II. THE ITALSAT EXPERIMENT MEASUREMENTS

The Italsat electromagnetic wave propagation experiment included the transmission of two orthogonal linear polarization signals at V band (49.5

GHz) with very high switching rate (933 Hz) [1]. The data collected at the ground station of Spino d'Adda (Italy), with elevation angle of  $37.7^\circ$ , were used to develop a simple yet effective model. The scatterplot between the Co-Polar Attenuation (CPA) and the Cross-Polar Discrimination (XPD) is reported in Fig. 1. The figure also includes the ITU-R P.618-13 model (solid line with circles) as reference, as well as the mean and the 10%-90% percentiles values of data (solid and dashed lines, respectively).

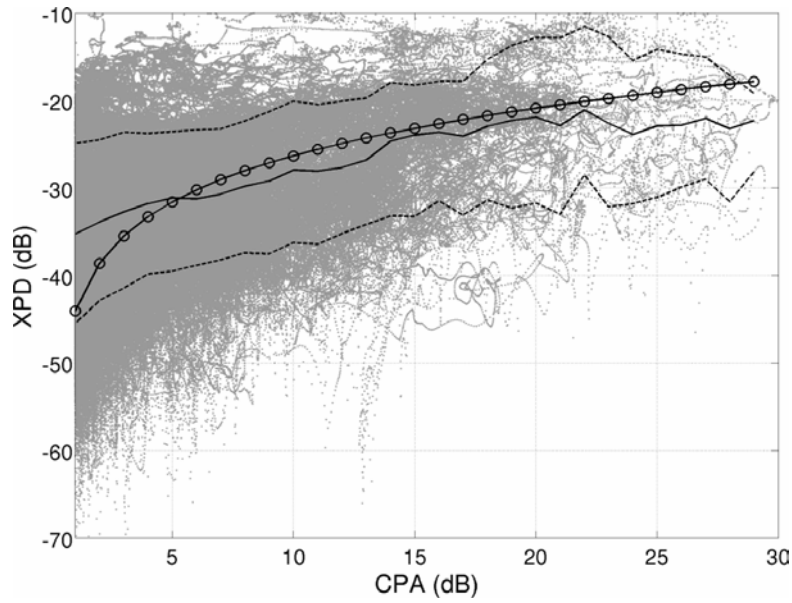


**FIG. 1** – CPA and XPD scatterplot for two orthogonal polarizations measured at Spino d'Adda at 49.5 GHz

As is clear from Fig. 1, the ITU-R model is very simple and cannot catch the high variability observed in XPD measurements, especially at mid-low values of the CPA. On the contrary, this is one of the goals of the model, whose development is briefly described in the next section.

### III. THE PHYSICALLY-BASED MODEL

The physical modeling of the precipitation starts from the single particles. It has been found that raindrops have irregular shapes, which can be well approximated by oblate spheroids [3]. The approximation is typically also extended to ice particles. The problem of expressing the particles axial ratio as a function of their equivalent diameter has been addressed in many works [4], [5], considering different forces acting on the water and the mean shape resulting from the raindrop vibration. As a further step, the Particle Size Distribution (PSD) has been linked to the rain rates [6], which are easily retrievable worldwide. The rain height in the model corresponds to the mean yearly  $0^\circ\text{C}$  isotherm height of the local area [7]. Frequency and elevation angles are freely tunable, according to the analysis to be performed. We set the values of the Italsat experiment to

validate the model by comparing its outputs against the experimental data. Further details on the model can be found in [8].

#### IV. INPUT RAIN MAPS

As an example of the potentialities of the XPD model under development, we have used as input rain maps (80 km×80 km with spatial resolution of 0.5 km×0.5 km) derived from the Spino d’Adda research weather radar. Specifically, we have taken into account a stratiform rain event recorded on the 24<sup>th</sup> January of 1992, consisting of 118 rain maps. As for the PSD, we have used in the model the one proposed by Marshall and Palmer [6]. Fig. 2 shows the results for different axial ratio models along with the ITU-R P.618-13 model curve. Note that here ITU-R curve does not include the ice term.

By comparing Fig. 1 and Fig. 2 we can observe that the polarization introduced by rain drops cannot fully catch the variability in the Italsat measurements: indeed, the high XPD associated to low CPA shown in Fig. 1 are likely associated to ice particles. Furthermore, lowest XPD values at mid-CPAs might require an additional refinement in the model, e.g. considering the effects of drop vibration or linking the particle size parameters to the rain intensity.

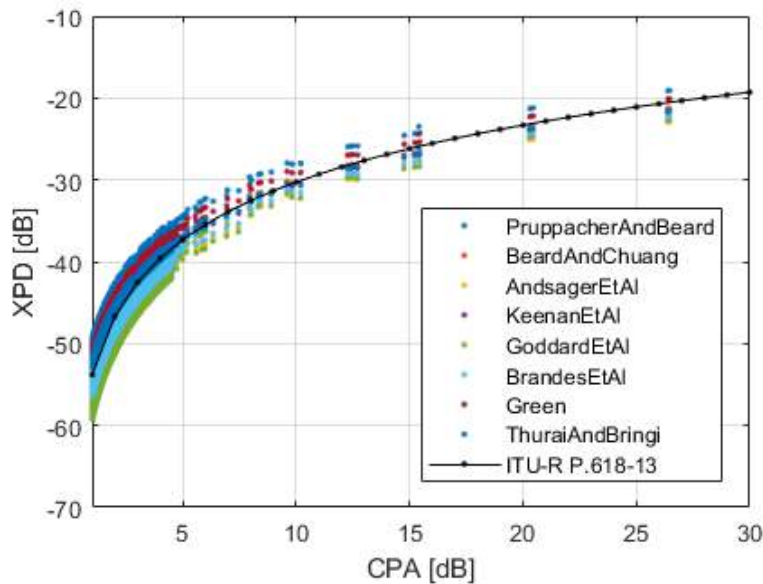


**FIG. 2** – CPA/XPD scatterplot for the selected stratiform event (circular polarization)

#### V. CONCLUSION

A model is being developed at Politecnico di Milano to support the investigation of the depolarization affecting EHF band satellite links. The results obtained by using as input to the model rain maps derived from

the research weather radar installed at Spino d'Adda fall in the range of the XPD data measured during the Italsat experiment, but also point out that additional atmospheric elements (e.g. ice particles) need to be taken into due account to catch the large XPD/CPA spread shown in the experimental data. We are encouraged to further extend the investigation by enlarging the model so as to include also the contribution of ice crystals in clouds and the particles in the melting layer [9], [10]. Indeed, even in presence of a negligible attenuation, as in clear sky conditions, cirrus ice clouds may affect significantly the measured signal [1]. Though the main aim of the model is to provide a reliable tool for satellite systems design, it could also be useful, for example, to support and enhance precipitation retrievals using polarimetric weather radars.

### REFERENCES

- [1] A. Paraboni, A. Martellucci, C. Capsoni and C. Riva, "The Physical Basis of Atmospheric Depolarization in Slant Paths in the V Band: Theory, Italsat Experiment and Models" *IEEE Transactions on Antennas and Propagation*, vol. 59(11), pp. 4301-4314, August 2011.
- [2] "Propagation data and prediction methods required for the design of earth-space telecommunication systems", ITU-R P.618-13, 2017.
- [3] H. R. Pruppacher and R. L. Pitter, "A semi-empirical determination of the shape of cloud and rain drops", *Journal of the atmospheric sciences*, vol. 28(1), pp. 86-94, January 1971.
- [4] A. W. Green, "An approximation for the shapes of large raindrops", *Journal of Applied Meteorology*, vol. 14(8), pp. 1578-1583, December 1975.
- [5] E. Gorgucci, L. Baldini and V. Chandrasekar, "What is the shape of a raindrop? An answer from radar measurements", *Journal of the atmospheric sciences*, vol. 63(11), pp. 3033-3044, November 2006.
- [6] C. W. Ulbrich, "Natural variations in the analytical form of the raindrop size distribution." *Journal of Climate and Applied Meteorology*, vol. 22(10), pp. 1764-1775, 1983.
- [7] S. M. Uppala et al., "The ERA-40 re-analysis" *Quarterly Journal of the Royal Meteorological Society*, vol. 131, pp. 2961-3012, October 2005.
- [8] E. Regonesi, C. Capsoni and C. Riva, "Radio wave depolarization simulator based on the SC EXCELL model" *Antennas and Propagation (EuCAP), 10<sup>th</sup> European Conference on*, pp. 1-3, April 2016.
- [9] L. Luini, "A Comprehensive Methodology to Assess Tropospheric Fade Affecting Earth-Space Communication Systems", *IEEE Transactions on Antennas and Propagation*, vol. 65(7), pp. 3654-3663, July 2017.
- [10] L. Luini and A. Quadri, "Investigation and Modeling of Ice Clouds Affecting Earth-space Communication Systems", *IEEE Transactions on Antennas and Propagation*, vol. 66(1), pp. 360-367, January 2018.

# A FMCW RADAR AS ELECTRONIC TRAVEL AID FOR VISUALLY IMPAIRED SUBJECTS

G. Sacco, E. Piuzzi, E. Pittella, S. Pisa  
Dept. of Information Engineering, Electronics and Telecommunications,  
Sapienza University of Rome  
Via Eudossiana, 18, 00184 Rome, Italy  
[giulia.sacco@uniroma1.it](mailto:giulia.sacco@uniroma1.it)

## Abstract

*In this paper design and test of a frequency modulated continuous wave (FMCW) radar to be used as electronic travel aid for visually impaired subjects are presented. The sensor is based on the Infineon BGT24MTR11 integrated circuit. Transmitting and receiving serial arrays of patch antennas have been suitably designed and tested. An amplifying circuit, with a shaped gain, has been used to enhance and filter the received signal. The radar range accuracy has been experimentally investigated with different modulation signals and targets, finding a worst-case uncertainty lower than 6 cm for all the distances of interest.*

**Index Terms** – Digital Signal Processing (DSP), ETA device, FMCW radar, patch antennas.

## I. INTRODUCTION

The mobility in unknown environments is one of the major problems for visually impaired people [1]. Currently, there are some electronic travel aids (ETAs) for visually impaired people mobility [2]. They are based on ultrasonic or optical systems. However, such systems have a limited range and have difficulty to operate in the presence of very reflective surfaces and with a low incidence angle. Recently, the possibility of using electromagnetic radiation for the detection of obstacles has been explored [3], [4]. Ultra-wideband radars can be used for realizing ETA devices. These radars have high resolution but require bulky antennas [5]. On the contrary, frequency modulated continuous wave (FMCW) radars use compact planar antennas and have the further remarkable advantage of being realized in integrated technology resulting in a very compact device. Finally, thanks to its small dimension the FMCW radar can be easily integrated in the white cane that is largely used by visually impaired subjects. In this paper, the design of a portable device for the mobility of visually impaired people, using an FMCW Radar, is addressed and some characterization tests are performed.

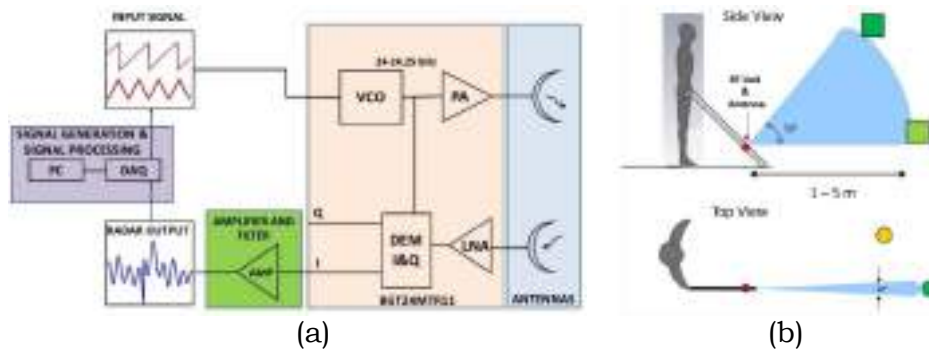


**FIG. 1** – Block scheme of the FMCW radar system (a), scheme of the considered scenario (b).

## II. RADAR SYSTEM OVERVIEW

A radar system based on the BGT24MTR11 integrated circuit (IC) by Infineon has been designed. For preliminary tests a NI PXI 6251 DAQ card controlled by a graphical user interface developed in the LabVIEW environment for ramp generation and signal acquisition has been used (see Fig. 1a). The BGT24MTR11 IC is based on a voltage controlled oscillator (VCO in Fig. 1a). The VCO is driven by a ramp or a triangular wave signal with a repetition rate (RR) of 100 Hz and 50 Hz respectively and generates a chirp from 24 to 24.25 GHz ( $B=250$  MHz). The power delivered by the power amplifier (PA) to the radiating antenna is about 11 dBm. The receiving channel is constituted by a low noise amplifier (LNA) and an I&Q demodulator. The collected signal is then amplified and filtered (AMP) in order to remove the DC component and reduce the noise. The output of the amplifier is acquired by the DAC and processed on a PC by a Matlab algorithm to extract the frequency component associated with the distance.

## III. ANTENNA DESIGN

A serial patch array has been chosen both for the transmitting and receiving antennas to obtain a system compact enough to be put on a cane for visually impaired subjects. Fig. 1b shows a scheme of the radar on the white cane together with the position of possible obstacles.

To design the array the Microwave Studio software by CST has been used. In order to guarantee a field of view between one and five meters, with an azimuthal resolution of about  $10^\circ$ , a serial array of 8 patches was necessary. In particular, since the radar output is differential, a balanced antenna has been realized for the TX section (see Fig. 2a bottom). The receiving antenna (RX) uses the same array attached to a Wilkinson power combiner whose two outputs have a phase difference of  $180^\circ$  with each other (see Fig. 2a top). Figs. 2b and 2c show the measured reflection coefficient for the RX and TX antennas, respectively. The figure shows the good matching of the antenna in the 24 GHz ISM band.

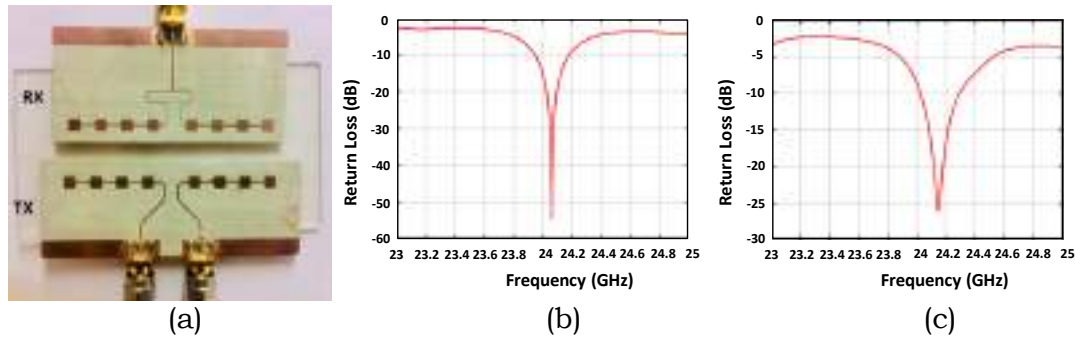


**FIG. 2** – Layout of the designed RX and TX patch antennas (a) and return loss of the RX (b) and TX (c) antennas as a function of frequency.

#### IV. SIGNAL PROCESSING

Both the generation of the ramp and the acquisition of the IF signal have been performed at a sample rate of 10 kHz. For each ramp 100 samples are acquired, the first and the last 10 samples are deleted since they are close to modulation signal discontinuities and the remaining are zero padded up to 256 samples. Because of the non-perfect isolation between the transmitting and the receiving channel, the received signal is affected by crosstalk and a triangular offset is superimposed to the IF signal. To reduce this effect the signal is filtered with a moving average filter using a window of 3 samples. Finally, FFT is applied to the signal and the spectrum peak frequency is extracted and converted into distance.

#### V. RESULTS

In order to test the performance of the system, a metallic reflecting panel ( $90 \times 90$  cm) and a water-filled plastic tank ( $30 \times 20 \times 10$  cm) have been positioned in front of the radar at different distances from the antenna. The system has been calibrated to eliminate the residual time delay due to cables connecting the antenna to the radar. Fig. 3a shows the FFT of the received signal without any processing (red curve), with the application of the zero padding (green curve) and with the further application of the moving average (blue curve). Only in this last case the 480 Hz peak due to the panel located at a distance of 2.9 m far from the antenna is well evidenced. The complete set of measured results is reported in Fig. 3b. It is possible to notice a good agreement between the measured distances and the real ones with both targets. This conclusion is better evidenced by the error defined as the absolute value of the difference between the measured distance and the real one. The error reaches in the worst cases 5.21 cm and 5.99 cm using the panel and the water tank, respectively.

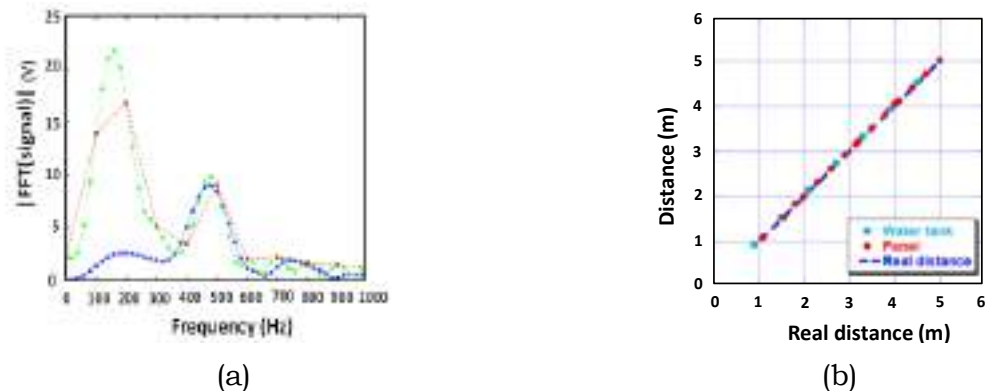


**FIG. 3** – Magnitude of the FFT of the received signal (a), measured distance as a function of the real one for a panel and a tank (b).

## VI. CONCLUSIONS

In this paper, a FMCW radar system has been investigated. Transmitting and receiving antennas have been designed and realized. An analog filtering circuit has been developed to amplify the signal and select the frequency components of interest. A Graphical User Interface and a signal processing software have been realized. The entire system has been tested using a metallic reflecting object and a water tank. Measured distances are in good agreement with the real ones, confirming the possibility of using the proposed radar as travel aid for visually impaired subjects. As future developments, the radar will be implemented on a single board controlled by a Digital Signal Processor (DSP) and installed on a white cane.

## VII. REFERENCES

- [1] C. Corcoran, G. Douglas, S. Pavey, A. Fielding, M. McLinden and S. McCall, "Network 1000: the changing needs and circumstances of visually-impaired people: project overview", *The British Journal of Visual Impairment*, vol. 22, No. 3, 2004, ISSN 0264-6196.
- [2] D. Dakopoulos, N.G. Bourbakis, "Wearable obstacle avoidance electronic travel aids for blind: a survey", *IEEE Transactions on Systems, Man, and Cybernetics, Part C*, vol.40, no.1, pp. 25-35, Jan. 2010.
- [3] L. Scalise, V. Mariani Primiani, P. Russo, D. Shahu, V. Di Mattia, A. De Leo, and G. Cerri, "Experimental investigation of electromagnetic obstacle detection for visually impaired users: a comparison with ultrasonic sensing", *IEEE Transactions Inst. Meas.*, vol. 61, no. 11, November 2012.
- [4] S. Pisa, E. Pittella, E. PiuZZi, "Serial patch array antenna for an FMCW radar housed in a white cane", *International Journal of Antennas and Propagation*, vol. 2016, Article ID 9458609, 10 pages, 2016. doi:10.1155/2016/9458609
- [5] E. Pittella, P. Bernardi, M. Cavagnaro, S. Pisa, and E. PiuZZi, "Design of UWB antennas to monitor cardiac activity", *J. Appl. Comput. Eletromagn. (ACES)*, vol. 26, no. 4, pp. 267-274, April 2011.

# FIRST EXPERIMENTAL ASSESSMENT OF A MICROWAVE IMAGING PROTOTYPE FOR CEREBROVASCULAR DISEASES MONITORING

J. A. Tobon Vasquez<sup>(1)</sup>, R. Scapaticci<sup>(2)</sup>, G. Turvani<sup>(1)</sup>, G. Dassano<sup>(1)</sup>, N. Joachimowicz<sup>(3)</sup>, B. Duchêne<sup>(4)</sup>, M. R. Casu<sup>(1)</sup>, L. Crocco<sup>(2)</sup>, and F. Vipiana<sup>(1)</sup>

<sup>(1)</sup> DET, Politecnico di Torino, Torino, Italy, [francesca.vipiana@polito.it](mailto:francesca.vipiana@polito.it)

<sup>(2)</sup> IREA, National Council of Research of Italy, Naples, Italy

[{scapaticci.r, crocco.l}@irea.cnr.it](mailto:{scapaticci.r, crocco.l}@irea.cnr.it)

<sup>(3)</sup> GeePs, CNRS – CentraleSupélec - Université Paris Saclay, Gif-sur-Yvette, France [joachimowicz@paris7.jussieu.fr](mailto:joachimowicz@paris7.jussieu.fr)

<sup>(4)</sup> L2S, CNRS – Centrale Supélec – Univ Paris Sud, Gif-sur-Yvette, France [Bernard.Duchene@l2s.centralesupelec.fr](mailto:Bernard.Duchene@l2s.centralesupelec.fr)

## Abstract

*This communication deals with a novel device aimed at continuously monitoring brain stroke, in order to timely detect its uncontrolled growth and inform clinicians on the effectiveness of the therapies. In particular, the present paper describes some advancements towards the realization of the first prototype specifically designed for this goal, as well as the first preliminary experimental testing of the realized hardware.*

**Index Terms** – microwave imaging, stroke monitoring, antennas, switching matrix.

## I. INTRODUCTION

Brain stroke is one of the main cause of death or serious disablement in the world. The main imaging technology used for the diagnosis of a stroke are magnetic resonance imaging (MRI) and computerized tomography (CT). However, both these technologies are time consuming, not cost effective and not portable and, in the CT case, harmful due to the use ionizing radiations. Hence, they are not convenient for continuous monitoring purposes, where repeated examinations are generally required. For this reason, microwave imaging (MWI) has been recently proposed as a complementary technique to monitor a patient after the stroke onset and follow up the effectiveness of the therapies. MWI exploits the difference in dielectric properties of tissues and it has been shown that an electric contrast exists, at microwave frequencies, between healthy brain tissues and ischemic or haemorrhagic stroke areas [1].

The present paper describe our ongoing work with respect to the realization of a prototype MWI system, specifically designed for monitoring purposes [2,3]. In its final realization, it will be made of an array of antennas conformal to human head, where each single antenna

will act as both transmitting and receiving element, so to provide multiview-multistatic microwave data.

The system design and a feasibility study of the whole system has been reported in [2,3]. In the following, description of the already realized hardware will be described and a first experimental testing of the prototype shown in Fig. 1, preliminarily used in a 2D configuration, will be reported.



**FIG. 1** – Prototype microwave system overview.

## **II. REALIZED HARDWARE**

The developed prototype, in its current version, is represented by an array of 24 antennas, as a result of the study in [3], connected to a control unit so to enable each antenna to work in both transmitting and receiving mode. The designed and built antennas are printed monopoles (see insert of Fig. 2) whose size has been properly optimized to allow positioning them in the head conformal array configuration described in [3]. According to the system feasibility study in [4], the working frequency band of the system is 0.8-1.2 GHz and the RX/TX antennas are immersed in a coupling medium with dielectric constant of around 20. The coupling medium is realized with a mixture of triton x-100 and water [5]. The measured reflection coefficient of each built antenna immersed in the coupling liquid is shown in Fig. 2, confirming a good matching has been obtained in the working frequency band.

The control electronics is represented by a switching matrix, shown in Fig. 3. It consists of two SP4T, eight SP6T and twenty-four SPDP electromechanical coaxial switches, which are connected with semi-rigid coaxial cables in order to realize a 2 by 24 switching matrix – see Fig. 3. All the different paths of the switching matrix have been measured in the frequency range 0.8-1.2 GHz: the maximum insertion loss is -0.8dB (average -0.5dB).

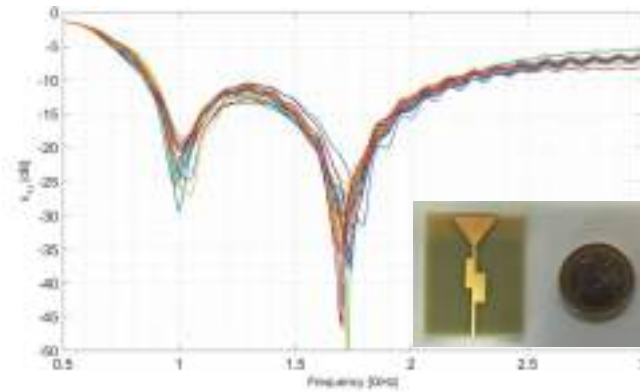


**FIG. 2** – Measured amplitude of the reflection coefficient ( $S_{11}$ ) of the realized 24 antennas immersed in the coupling liquid (each line corresponds to an antenna).



**FIG. 3** – Built 2X24 switching matrix (each black cable is conneted to an antenna).

### III. PRELIMINARY 2-D EXPERIMENTAL RESULTS

The currently developed system has been preliminarily tested with respect to a 2-D scanning. To this end, the realized 24 antennas have been mounted on a circle (see the numbered dots in Fig. 4) inside a tank filled with the coupling liquid having a dielectric constant of 23.1 and a conductivity of 0.3 S/m at 1 GHz. The target is a plastic cylinder filled with water with diameter of 15 mm. The gathered 24x24 scattering matrix is processed by means of a well assessed algorithm based on the Truncated Singular Value Decomposition of the scattering operator [6]. The reconstructed image is shown in Fig. 4, where the exact position and size of the water cylinder is indicated with a red circle, showing a good agreement with the reconstructed ones (yellow spot).

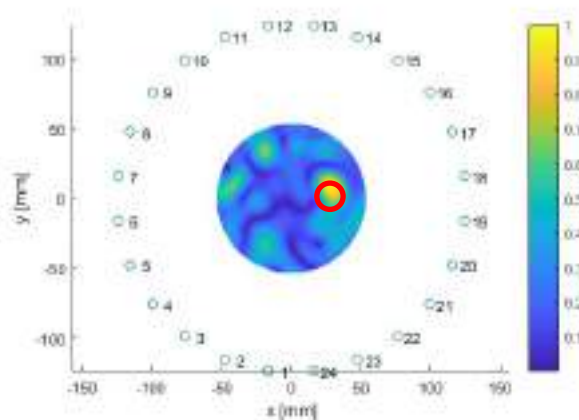


**FIG. 4** – Example of a reconstructed image together with the 24 antenna positions; the red circle denotes actual lesion position and size.

#### IV. CONCLUSIONS AND FUTURE WORK

We have presented the current stage of the realization of a novel microwave imaging device for the monitoring a patient after the stroke onset. The next step of the research activity is the realization of the antenna array conformal to the human head to perform 3-D imaging experiments with realistic anthropomorphic head phantoms.

#### ACKNOWLEDGEMENT

This work was supported by the Italian Ministry of University and Research (MIUR) under the PRIN project “MiBraScan - Microwave Brain Scanner for Cerebrovascular Diseases Monitoring.

#### REFERENCES

- [1] S. Semenov, T. Huynh, T. Williams, B. Nicholson, A. Vasilenko, “Dielectric Properties of Brain Tissue at 1 GHz in Acute Ischemic Stroke: Experimental Study on Swine”, *Bioelectromagnetics*, 38, pp. 158-163, 2017.
- [2] J. A. Tobon et al., “A feasibility study for cerebrovascular diseases monitoring via microwave imaging”, *Proc. of the Int. Conf. on Electromagnetics in Advanced Applications (ICEAA)*, Verona (Italy), Sept. 2017.
- [3] R. Scapatucci, et al., “Optimized design of the antenna array in a microwave imaging system for brain stroke monitoring”, accepted to the 12th European Conf. on Antennas and Propagation (EuCAP), London (UK). 2018.
- [4] R. Scapatucci, L. Di Donato, I. Catapano, L. Crocco, "A feasibility study on microwave imaging for brain stroke monitoring", *Progress in Electromagnetics Research B*, Vol. 40, 305-324, 2012 (doi:10.2528/PIERB12022006).
- [5] S. Romeo, L. Di Donato, O. M. Bucci, I. Catapano, L. Crocco, M. R. Scarfi, R. Massa, “Dielectric characterization study of liquid-based materials for mimicking breast tissues”, *Microw. Opt. Technol. Lett.*, 53: 1276–1280, 2011 (doi:10.1002/mop.26001).

# NOVEL CLASS OF DUAL-MODE AIR FILLED SIW FILTERS

C. Tomassoni<sup>(1)</sup>, L. Silvestri, M. Bozzi, L. Perregrini<sup>(2)</sup>, A. Ghiotto<sup>(3)</sup>

<sup>(1)</sup> University of Perugia, Department of Engineering, Perugia, Italy

<sup>(2)</sup> University of Pavia, Department of Electrical, Computer and Biomedical Engineering, Pavia, Italy

<sup>(3)</sup> University of Bordeaux, IMS Laboratory, CNRS UMR 5218, IPB, 33405 Talence, France

[lorenzo.silvestri01@universitadipavia.it](mailto:lorenzo.silvestri01@universitadipavia.it)

## Abstract

*This paper presents the design and implementation of a novel class of substrate integrated waveguide (SIW) filters, based on partially air-filled dual mode cavities. Dual-mode cavities, called doublets, can be obtained by removing the dielectric in a portion of the SIW cavity. A modal analysis of the air-filled resonant cavity based on transmission lines representation and a detailed study of the doublet permit to demonstrate a full control of the operation frequency, pass bandwidth, spurious-free region, and position of the transmission zeros of the filter. The design, fabrication and measurement of two-pole filter are presented.*

**Index Terms** – Dual-mode filters, Filters, Substrate Integrated Waveguide.

## I. INTRODUCTION

The advent of the Internet of Things (IoT) is leading the microwave community towards the investigation of novel technologies, in particular in the field of the Substrate Integrated Waveguide (SIW) [1]. SIW implements the classical rectangular waveguide in planar form, based on a dielectric substrate with top and bottom metal layers and two lateral rows of conductive vias. SIW components are ease to integrate, present low cost manufacturing techniques and a shielded structure. Instead, one of the main minuses, in comparison with rectangular waveguide, is related to the dielectric losses. A possible solution is based on the use of air-filled SIW structure [2]. Instead, when the size reduction, in the case of filters, is one necessary request the use of dual-mode resonators can be a very useful topology [3], [4]. In this paper, a novel class of SIW filters is studied, combining the best features of dual-mode cavities and air-filled SIW. By partially removing the dielectric material from the SIW cavity, the resonance frequency of the first cavity modes (pass band of the filter) and the possibility to maximize spurious-free bandwidth can be controlled. An exhaustive study of the cavity demonstrates the full control of the operation frequency, pass bandwidth, spurious-free region and position of the transmission zeros of the filter. A prototype of doublet has been designed, realized and measured.

## II. THEORY OF DUAL-MODE AIR-FILLED CAVITY

An efficient transmission line theoretical model (instead of eigen-mode simulations) is proposed to obtain a characteristic equation of the air-filled cavity. The partially air-filled cavity is divided in three homogeneous

portions (a central air-filled part and two external dielectric filled parts), and each portion is described as a transmission line. A transverse resonance technique is used to obtain the resonance modes of the overall (piecewise homogeneous) cavity, relating the  $TM_{mn0}$  mode resonant frequencies with the cavity dimensions. The cavity comprises a dielectric of relative permittivity  $\epsilon_{r1}$  at its two ends, and a central air-filled region of relative permittivity  $\epsilon_{r0}=1$  and length  $a$ . Defining the equivalent impedance  $Z_{e0mn0}$  at the cavity symmetry plane (looking toward one side) the odd modes (odd values of  $m$ ), at the cavity resonance  $f_{TM_{mn0}}$ , can be found when  $\text{Im}(Z_{e0mn0})=\infty$ , whereas for even modes (even values of  $m$ ), at the cavity resonance  $f_{TM_{mn0}}$ ,  $\text{Im}(Z_{e0mn0})=0$ .

In Fig. 1 (b) the first four mode resonance frequencies are plotted for an air-filled cavity of width  $B = 19$  mm,  $A=50$  mm and  $\epsilon_{r1}=10.5$ , versus the air-filled area length  $a$ .

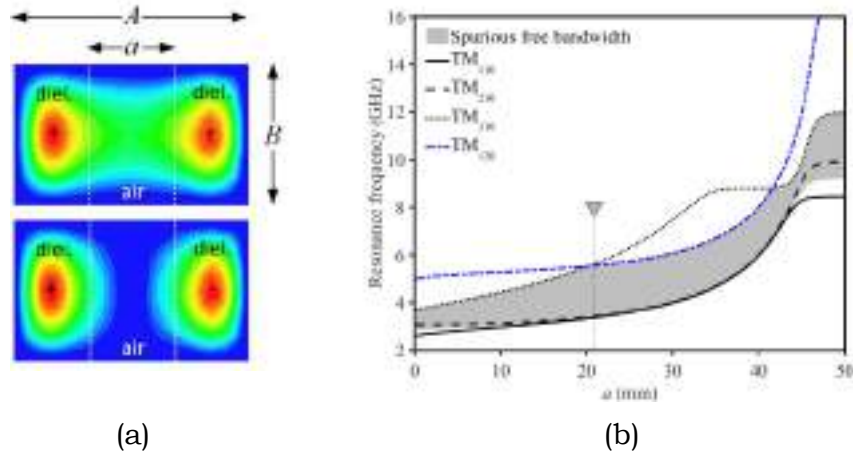


**FIG. 1** – (a) Electric modal field of the first two resonant modes in the air-filled cavity; (b) Theoretical first four resonance frequencies and spurious free bandwidth versus dimension  $a$ .

The first two modes ( $TM_{110}$  and  $TM_{210}$ ) have very close resonant frequencies for  $a$  in the range from 10 mm to 35 mm because of the mode distribution, as shown in Fig. 1 (a). By selecting the appropriate dimension  $a$  for a certain value of  $B$ , the relative frequency separation  $\Delta f$  between the  $TM_{110}$  and  $TM_{210}$  modes can be modified. Fig. 2 is a two-dimensional plot of the central frequency  $f_c$  versus dimensions  $a$  and  $B$  with the isocurves of the relative resonance frequency separation (black straight lines) and relative spurious free bandwidth (white straight lines). With fixed  $f_c$  and resonance frequency separation, two sets of values  $a$  and  $B$  can be chosen. However, one of the two set provides a larger spurious-free bandwidth.

### III. INVESTIGATION OF THE DOUBLET

This section describes the design strategy of a doublet based on the air-filled dual-mode SIW cavity. These are capable of two poles and two transmission zeros and can be used as building blocks to obtain higher-order filters.

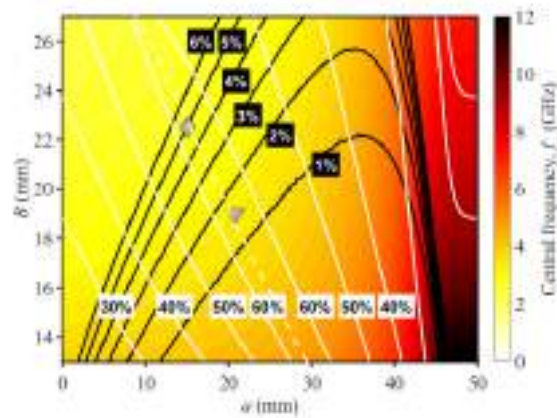


**FIG. 2** – Theoretical central frequency  $f_c$ : black straight lines represent the isocurves of the relative resonance frequency separation and white straight ones the relative spurious free bandwidth. Instead the optimal relative spurious free bandwidth is plotted with white dotted line versus dimensions  $a$  and  $B$  ( $A = 50$  mm,  $\epsilon_{r1} = 10.5$ ).

The air-filled dual-mode SIW cavity is studied to implement the topology shown in Fig. 3 (c). The filter passband mainly depends on the resonance frequencies  $f_1$  and  $f_2$  of the first two cavity modes and, as shown in the previous section, they are fully controllable through the dimensions of the cavity. The coupling of the first two resonant modes can be controlled by the inductive iris of width  $w$ . The larger the width  $w$ , the higher the couplings values  $M_{S1}$  and  $M_{S2}$ .

$A=50.54$	$B=23.04$	$a=15.64$	$b=20.04$
$c=5.85$	$d=7.85$	$e=9$	$f=3$
$g=1$	$h=7.5$	$s=9.05$	$w=9$

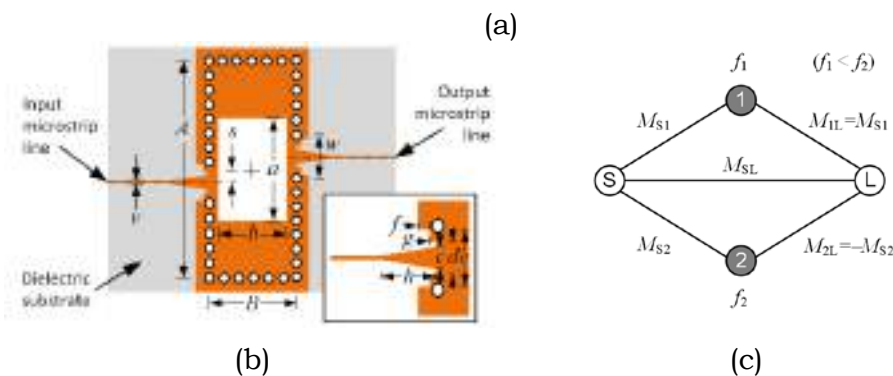


**FIG. 3** – Geometry of the doublet: (a) Dimensions of the filter (mm); (b) microstrip feeding; (c) Transversal topology of the doublet

In case of the microstrip feeding shown in Fig. 3 (b), the coupling is controlled by the microstrip taper ( $c$  and  $h$ ) and the aperture of width  $e$ . Three coupling values with the same sign and the fourth with an opposite sign are required (Fig. 3 (c)) and for this the SIW and microstrip feeding lines are positioned anti-symmetrically.

In the considered topology, the capability to implement and control the first transmission zero is related to the ratio  $Ms_1/Ms_2$  and can be changed with the offset  $s$  shown in Fig. 3 (b). A second transmission zero is obtained with the direct SL coupling, through higher order modes.

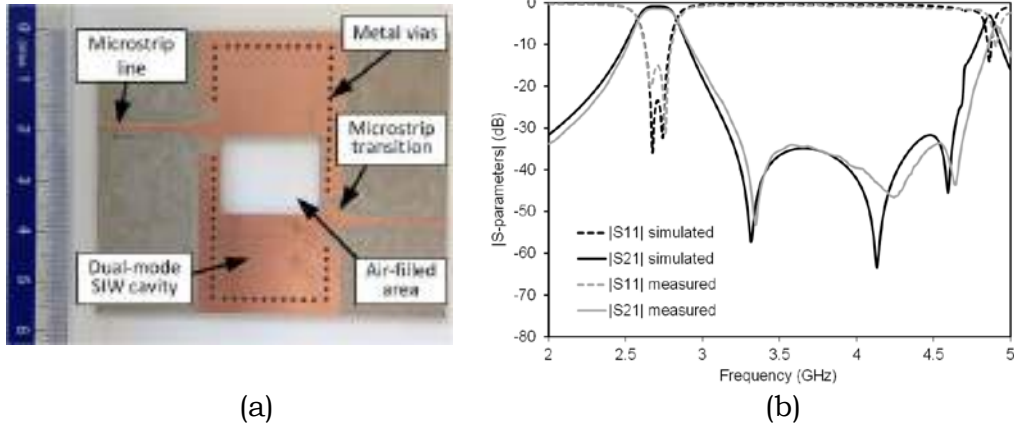


**FIG. 4** – (a) Photograph of the prototype; (b) Simulation and measurement

The filter has been fabricated by milling technique on a dielectric laminate Taconic CER-10 (with  $\epsilon_r=10.5$ ,  $\tan\delta=0.0035$ , and thickness 1.27 mm) and dimensions shown in Fig. 3 (a). The photograph of the prototype is shown in Fig. 4 (a), before the closing of the top/bottom air-filled area by copper sheets. Measurements have been performed by using an Anritsu Universal Test Fixtures (UTF) 3680 and an Anritsu 37347C VNA. A comparison between simulations and measurements is shown in Fig. 4 (b) confirming the theoretical studies.

#### IV. CONCLUSIONS

This paper presents a novel class of SIW filters combining the advantages of the dual-mode resonant cavities with the recently proposed air-filled SIW. The doublet structure, able to provide two poles and two zeros, has been detailed investigated, showing a full control on it. A prototype has been reported to show the validity of the proposed study.

#### REFERENCES

- [1] M. Bozzi, A. Georgiadis, and K. Wu, "Review of Substrate Integrated Waveguide (SIW) Circuits and Antennas," *IET Microwaves, Antennas and Propagation*, vol. 5, no. 8, pp. 909–920, June 2011.
- [2] F. Parment, A. Ghiotto, T. P. Vuong, J. M. Duchamp, and K. Wu, "Air-Filled Substrate Integrated Waveguide for Low-Loss and High Power-Handling Millimeter-Wave Substrate Integrated Circuits," *IEEE Trans. Microw. Theory Techn.*, vol. 63, no. 4, pp. 1228-1238, April 2015
- [3] S. Bastioli, C. Tomassoni, and R. Sorrentino, "TM Dual-Mode Pseudoelliptic Filters using Nonresonating Modes," *IEEE MTT-S 2010 International Microwave Symposium*, Anaheim, CA, 23-28 May 2010.
- [4] C. Tomassoni, L. Silvestri, M. Bozzi, L. Perregrini, and A. Ghiotto, "A dual-mode quasi-elliptic filter in air-filled substrate integrated waveguide technology," *47th European Microwave Conference (EuMC)*, Nuremberg, Germany, 10-12 Oct. 2017

# GRAPHENE MICROSTRIP ATTENUATOR WITH HIGH TUNABILITY AND MINIMUM REFLECTION

M. Yasir<sup>(1)</sup>, M. Bozzi<sup>(1)</sup>, L. Perregrini<sup>(1)</sup>

<sup>(1)</sup> Department of Electrical, Computer and Biomedical Engineering,  
University of Pavia  
Pavia, Italy  
[muhammad.yasir01@universitadipavia.it](mailto:muhammad.yasir01@universitadipavia.it)

## Abstract

*In this work, an innovative tunable microstrip attenuator based on few layer graphene flakes is presented. This novel attenuator is composed of two pairs of grounded vias connected to graphene flakes. The graphene flakes are in turn connected to a 50  $\Omega$  microstrip line. An applied voltage bias can be used to tune the resistance of the graphene flakes thus tuning the insertion loss of the attenuator. The design is such that it minimizes the reflection from the attenuator while increasing the insertion loss. A prototype of the proposed design is fabricated and measurements are compared with simulations. The attenuator provides a tunable range of 25dB operating in the frequency band of DC to 10 GHz.*

**Index Terms** – Electronically controlled attenuators, Few-Layer Graphene Flakes, Graphene, Tunable microwave components.

## I. INTRODUCTION

The tunable properties of graphene at the microwave frequencies have brought it significant attention in the recent years [1]-[2]. Specifically, the tunable conductivity of graphene has been exploited in implementing novel devices, systems and components at the microwave and millimeter wave frequencies [3], [4]. Even more interesting is the fact that graphene keeps its tunable conductive properties when implemented in multiple layers [5]. This largely increases the simplicity of the fabrication procedure and reduces the cost since at microwave frequencies large quantities are required [4], [5].

The tunable conductivity of graphene has been exploited in implementing electronically controlled microwave attenuator. A simple approach has been used in [4] based on a microstrip line with a gap where the flakes were deposited. The flakes were biased by a DC bias voltage which would increase their conductivity reducing the insertion loss. This version was improved in [5] and a structure based on a pair of grounded vias was proposed as shown in Fig. 1(a). The vias were separated from a microstrip lines by the graphene flakes. In this case, an increase in the bias voltage would reduce the graphene resistance increasing the current passing through the flakes into the ground, which would increase the

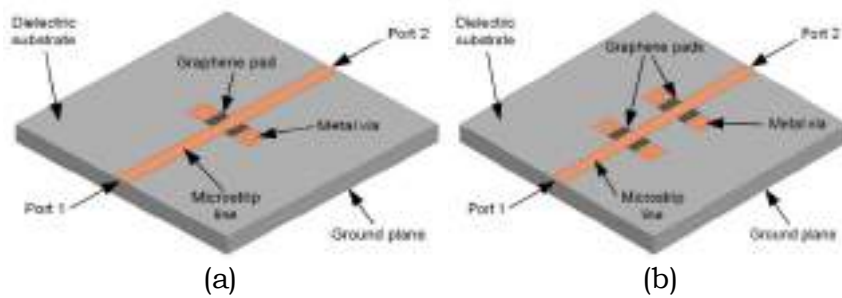


**FIG. 1** – Geometry of the graphene based tunable attenuator: (a) two post design;(b) four post design.

insertion loss. Conversely, with a reduced bias voltage, the graphene flakes bore high resistance which meant low current passing and thus higher signal on the line and a lower insertion loss. The insertion loss in this case is a result of a reflective and dissipative part.

In this work the number of vias were increased from two to four. This is referred to as the four-post design as shown in Fig. 1(b). The frequency band of operation has been maximized by regulating the midline section between the pair. This proposed design works in a similar manner as the previous design but has significantly higher insertion loss with reduced reflection.

## II. DESIGN OF THE TUNABLE GRAPHENE ATTENUATOR

The proposed attenuator as shown in the Fig. 1. (b) is a modified version of the attenuator of the Fig. 1 (a) as in [5]. Transmission through the microstrip line is tuned by the help of a control voltage applied to the graphene pads. Application of a voltage bias reduces graphene resistance thus increasing the current passing through the pads into the ground resulting in a highly attenuated signal.

The proposed attenuator is designed on the Taconic RF-60 dielectric substrate of thickness  $h=0.64$  mm. It has an  $\epsilon_r=6.15$  and  $\tan \delta=0.0028$ . The  $50 \Omega$  line has a width of  $0.94$  mm. The graphene pads have lengths  $1.40$ mm and widths  $0.66$ mm. The metallic via has a  $0.8$  mm diameter. Simulations were performed with the four-post design by using commercial FEM solver, HFSS. Graphene flakes were modelled as infinitely thin resistive sheets. The insertion loss from the simulated results suggest that the dynamic range of the insertion loss for the four-posts case shown in Fig. 2 (b) is almost twice as much as that of the two-post case of Fig. 2(a). Another important aspect that can be seen is that the frequency band of operation has been doubled. The maximum insertion loss for  $40 \Omega$  graphene resistance for the two cases is  $14$  dB and  $24$  dB for two and four-posts respectively.

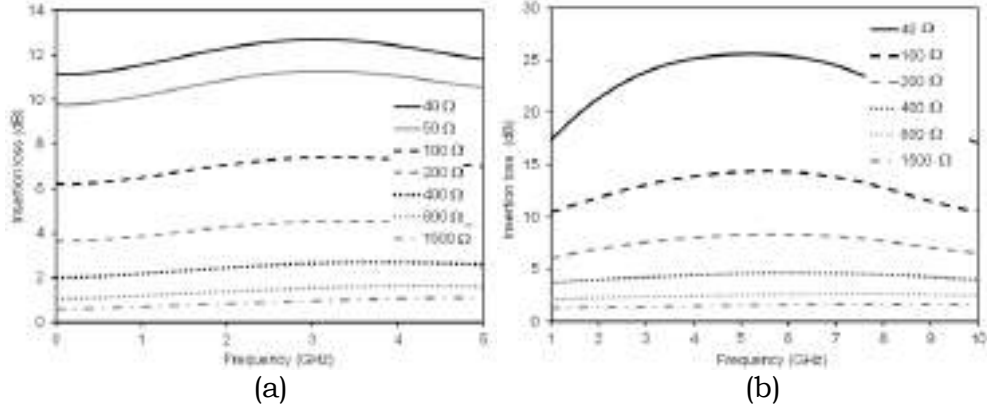


**FIG. 2** – Simulated insertion loss of the graphene attenuator with assigned graphene sheet resistances: (a) two-post design; (b) four-post design.

### III. MEASURED RESULTS

A prototype of the proposed attenuator has been fabricated and graphene flakes deposited by the same procedure as [5]. The attenuator prototype was measured by the help of an anritsu test set as shown in the Fig. 3 (a). The prototype for the two-post can be seen in the Fig. 3(b) and the four-post proposed in this work can be seen in the Fig. 3(c).

During the application of the bias voltage, current is measured from which the resistance values are derived ( $R=V/I$ ) as shown in the Fig. 3(d), which is similar for both design. Simultaneously, measurements of the scattering parameters are carried out and insertion loss is derived as shown in the Fig. 5(a). When compared to the insertion loss of the two-post of [5], a drastic increase of the insertion loss of almost 10 dB has been acquired. Due to such a high increase in the insertion loss in the case of the four-post attenuator, it was suspected that the reflective contribution towards the total insertion loss had also been increased. In order to acquire a complete picture of the insertion losses: dissipative as well as reflective, simulation and measurements were compared as shown in the Fig. 5(b). It can be seen that major portion of the insertion loss is dissipative.

### IV. CONCLUSION

A new version of graphene based electronically-controlled tunable attenuator has been presented. The attenuator is composed of four grounded vias, two on each side of a microstrip line separated from the microstrip line by the graphene flakes. Functionality of the attenuator has been improved in terms of increased insertion loss, reduced reflection and twice as much bandwidth. The reported insertion loss is 24dB as compared to 14 dB of the previous design with 10 GHz of operating band unlike 5GHz of the one proposed earlier.

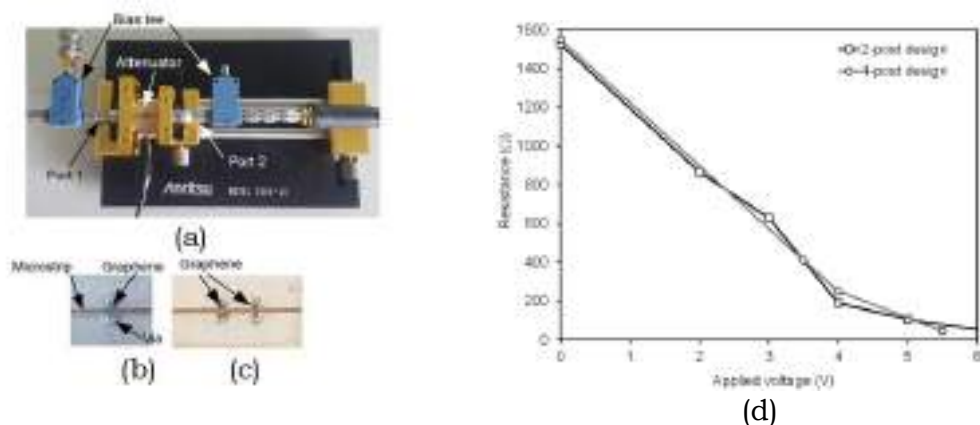


**FIG. 4** – Prototype and measurements: (a) measurement setup; (b) two-post design;(c) four-post design;(d) Tunable resistance for the two attenuators.

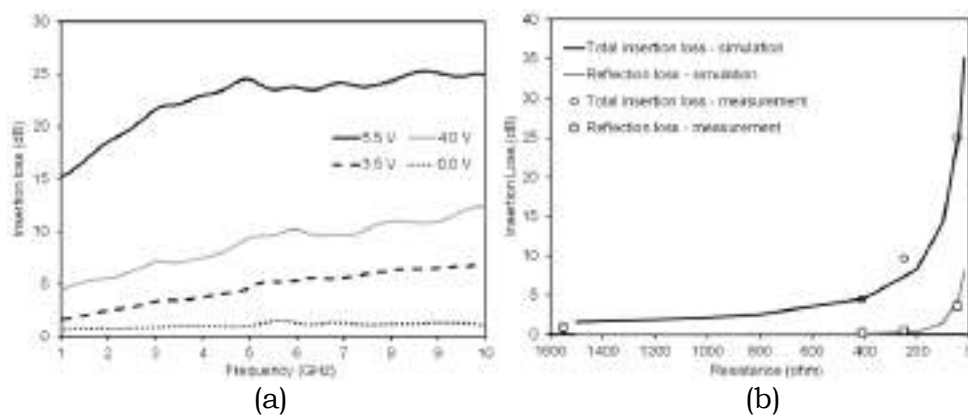


**FIG. 5** – Measured Insertion loss: (a) change in IL for each applied voltage; (b) Simulated and measured insertion loss and reflection loss vs. resistance at the frequency of 5 GHz;

## REFERENCES

- [1] S K.S. Novoselov *et al.*, “Electric field effect in atomically thin carbon films,” *Science*, Vol. 306, No. 5696, pp. 666–669, 2004.
- [2] M. Bozzi, L. Pierantoni, and S. Bellucci, "Applications of Graphene at Microwave Frequencies," *Radioengineering*, Vol. 24, No. 3, pp. 661-669, Sept. 2015
- [3] R. Quhe *et al.*, “Tunable band gap in few-layer graphene by surface adsorption,” *Scientific Reports*, Vol. 3, No. 1794, May 2013.
- [4] L. Pierantoni *et al.*, “Broadband Microwave Attenuator Based on Few Layer Graphene Flakes,” *IEEE Transactions on Microwave Theory and Techniques*, Vol. 63, No. 8, pp. 2491-2497, Aug. 2015.
- [5] M. Yasir, S. Bistarelli, A. Cataldo, M. Bozzi, L. Perregrini, and S. Bellucci, “Enhanced Tunable Microstrip Attenuator Based on Few Layer Graphene Flakes,” *IEEE Microwave and Wireless Components Letters*, Vol. 27, 2017.